Understanding Liquid Metal Electrode Interfaces for Intermetallic, Metallic, and Semiconductor Growth

by

Joshua P. Hazelnis

A dissertation submitted in partial fulfillment
of the requirements for the degree of
Doctor of Philosophy
(Chemistry)
in the University of Michigan
2025

Doctoral Committee:

Professor Stephen Maldonado, Chair
Professor Bart M. Bartlett
Professor Ageeth Bol
Professor Roy Clarke

Joshua P. Hazelnis

jphazeln@umich.edu

ORCID iD: 0000-0003-0726-3754

© Joshua P. Hazelnis 2025

Dedication

"To my ever-loving and supportive wife, Maria Catharina."

Table of Contents

Dedication ii

List of Tables viii

List of Figures ix

List of Appendices xxii

Abstract xxiv

Chapter 1 Thesis Introduction 1

1.1 Motivation 1

1.2 Electrochemical Liquid-Liquid-Solid Growth 2

1.3 Addressing the Knowledge Gap in ec-LLS 2

1.3.1 Supersaturation by an Electrochemical Driving Force 4

1.3.2 Controlling the Location of Nucleation and Crystal Growth 5

1.3.3 Influence of the Local Atomic Structure and Composition of Liquid Metal Electrodes 11

1.4 Using Liquid Metal Electrodes a Reactant for Material Synthesis 20

1.5 Overview of Thesis 21

1.6 References 25

Chapter 2 Detection of Ge-Containing Adlayers at the Liquid Hg/Water Interface by In Situ X-Ray Reflectivity in Aqueous Borate Electrolytes Containing Dissolved GeO_2 30

2.1 Preface 30

2.2 Introduction 30

2.3 Experimental 32

2.3.1 Materials and Chemicals 32

2.3.2 Potential of Zero Charge Measurement 32
2.3.3 X-Ray Reflectivity Measurements 32
2.3.4 Modelling of XRR Data. 33
2.4 Results 36
2.5 Discussion 51
2.6 Conclusion 58
2.7 References 59
Chapter 3 X-Ray Reflectivity and Scattering of Hg-In Alloy Electrodes 64
3.1 Preface 64
3.2 Introduction 64
3.3 Experimental 67
3.3.1 Materials 67
3.3.2 X-Ray Reflectivity Measurements and Analysis 67
3.4 Results 69
3.5 Discussion 90
3.5.1 Observance of Yoneda Signatures at Liquid Metal Interfaces 94
3.5.2 Chemistry of Hg-rich Surface Layer in Hg-In Liquids 96
3.6 Conclusion 98
3.7 References 99
Chapter 4 Electrosynthesis of Quasi-Epitaxial Crystals on Liquid Metals 104
4.1 Preface 104
4.2 Introduction 104
4.3 Experimental 106
4.3.1 Electrochemical Cell 106
4.3.2 Pb Electrodeposition 107

4.3.3 Bi Electrodeposition 107

4.3.4 Pd Electrodeposition 109

4.3.5 Mn Electrodeposition 109

4.3.6 Materials Characterization 109

4.4 Results 111

4.4.1 Electrochemical Behavior of Ga in 1.25 M NaOH Electrolyte 111

4.5 Discussion 128

4.5.1 Probable Source of Preferred Orientation 128

4.5.2 Origin of Preferred Orientation 131

4.5.3 Factors that Prevent 'Quasi-Epitaxial' Crystal Growth in Electrodepositions with Liquid Metal Electrodes 132

4.6 Conclusions 140

4.7 References 141

Chapter 5 Discovery of Metal-Ga Intermetallics via 'Quasi'-Epitaxy at Liquid Ga/Water Interfaces 145

5.1 Preface 145

5.2 Introduction 145

5.3 Experimental 146

5.3.1 Chemical and Materials 146

5.3.2 Electrolyte Characterization 146

5.3.3 Electron Microscopy Sample Preparation 147

5.3.4 Electron Microscopy 147

5.3.5 MicroED Data Workup 150

5.4 Results 151

5.4.1 Synthesis of Transition Metal-Ga Hexagonal Particles 151

5.5 Discussion 170

5.5.1 Lattice Structure 170
5.5.2 Quasi-Epitaxy 172
5.6 Conclusion 183
5.7 References 184
Chapter 6 Open Electrochemical Liquid Phase Epitaxial Growth of Crystalline Ge Films 188
6.1 Preface 188
6.2 Introduction 188
6.3 Experimental 191
6.3.1 Materials and Chemicals 191
6.3.2 Liquid Metal Alloy Preparation 191
6.3.3 Electrochemical cell 191
6.3.4 Linear Sweep Voltammetry 193
6.3.5 Electrodeposition of Ge Films 194
6.3.6 Contact Angle Measurements 194
6.3.7 Materials Characterization 194
6.4 Results 197
6.4.1 Wetting Characteristics 197
6.4.2 Linear Sweep Voltammetry 197
6.4.3 'Open' ec-LPE 200
6.5 Discussion 213
6.5.1 Epitaxial Germanium Films 213
6.5.2 Liquid Metal Characteristics 216
6.5.3 Suggestions for refined 'open' ec-LPE Strategies 219
6.6 Conclusions 221
6.7 References 222

Chapter 7 Unresolved Work 226
7.1 Preface 226
7.2 Overview 226
7.3 Context of Future Directions 228
7.4 Electrochemistry of Gallium 229
7.4.1 Proposed Operative Reactions 236
7.5 Flat Liquid Metal Electrodes 238
7.6 Isolating and Characterizing Products of Liquid Metal Electrodeposition 241
7.7 References 252
Appendices 255

List of Tables

Table 2.1 Parameters of the best fits of the XRR data by *Equation* 2.5 [a,b,c] 42

Table 2.2 Parameters of the best fits of the XRR data collected in 0.1 M $Na_2B_4O_7$ + 0.05 M GeO_2 at -0.2 V[a] 50

Table 3.1 Specular and Diffuse Scattering Features 73

Table 3.2 Values of Best Fit for $X_{Hg,First}$ = Gibbs Adsorption Theorem for Ideal Solution Behavior[a] 86

Table 3.3 Values of Best Fit for $X_{Hg,First}$ = 1.00 (Full Hg Coverage)[a] 87

Table 3.4 Fit Parameters for XRR Data in Figure 4[a] 88

Table 4.1 Standard redox potentials (E^0) of the metal cations of interest in this work Mn^{2+}, Bi^{3+}, Pb^{2+}, and Pd^{2+} 113

Table 4.2 Packing density calculation for the $PdGa_5$ planes highlighted in Figure 4.14 along the perpendicular [001] direction to the liquid Ga interface 134

Table 4.3 Packing density calculation for the possible in-plane ordering arrangement of liquid Ga layers nearest the liquid Ga/electrolyte interface shown in Figure 4.15. 136

Table 4.4 Packing density calculation for the $MnGa_4$ planes highlighted in Figure 4.16 along the perpendicular [111] direction to the liquid Ga interface. 138

Table 5.1 Calculated total packing densities in the estimated $Fe_{0.14\pm0.01}Ga_{0.86\pm0.01}$ and $Fe_{0.08\pm0.01}Co_{0.06\pm0.01}Ga_{0.86\pm0.01}$ structures 175

Table 5.2 Calculated total packing densities of $FeGa_3$ 178

Table 5.3 Calculated packing densities of Ga atoms in $FeGa_3$ 179

Table 5.4 Calculated Ga atom packing densities in the estimated $Fe_{0.14\pm0.01}Ga_{0.86\pm0.01}$ and $Fe_{0.08\pm0.01}Co_{0.06\pm0.01}Ga_{0.86\pm0.01}$ structures 180

List of Figures

Figure 1.1 a) Schematic representation of ec-LLS crystal growth steps including metal precursor X^{n+} reduction to zero-valent X^0, dissolution into the liquid metal electrode M, nucleation and subsequent crystal growth of X^0. b) Schematic depiction of a complete ec-LLS reaction cell with a liquid metal electrode. Colored boxed insets highlight three distinct: (purple) location of the nucleation and crystal growth events, (red) ordering of alloy species at the liquid metal interface, and (blue) isothermal driving force on crystal growth and product species. 3

Figure 1.2 (a) Schematic depiction of (1) an e^- beam causing the reduction of dissolved GeO_2 in solution to Ge^0, followed by (2) dissolution into the liquid metal nanodroplet, then (3) crystal nucleation, and finally (4) Ge nanowire growth. (b) Frame grabs from an *in situ* transmission electron video of a Ge ec-LLS event with a Ga nanodroplet immersed in an aqueous solution containing 0.05 M GeO_2 and 0.01 M $Na_2B_4O_7$. (c) A plot of Ge nanowire length *vs* time for four separate Ge nanowire growth events. The steady-state growth rates were estimated from the linear-least-squares fitting of the data (red lines). (d) The phase diagram for the Ga-Ge system is shown with the inclusion of data from four different Ge nanowire growth events. The colored data points correspond to the inferred Ge concentration in the Ga nanodroplets at the time just before nucleation. (e) A plot showing the volume change of the Ga nanodroplet as a function of time before Ge nucleation occurred. 6

Figure 1.3 (a) Schematic depiction of ec-LLS inside a microwell which is sufficiently deep enough that no solute reaches the bottom interface and instead preferentially nucleates and grows crystals homogeneously within the liquid metal. (b) Same as in (a) except the microwell is shallow that solute can reach the bottom interface and preferentially nucleate and grow a crystal heterogeneously. Scanning electron micrographs of Ge ec-LLS experiments performed in aqueous solution containing 50 mM GeO_2 and 10 mM $Na_2B_4O_7$ at $E = -1.6$ V for 30 min at $T =$ 40°C using (c) 27 μm and (d) 8 μm thick e-GaIn microelectrode. (e) Summary view of an electrochemical liquid phase epitaxy (ec-LPE) film growth concept with a thin liquid metal electrode with thickness h. (f) Schematic depiction of the relevant steps in ec-LPE, where an oxidized species X^{n+} dissolved in the electrolyte is reduced to X^0 by heterogeneous electron transfer, partitions into the liquid metal film, and then diffuses some distance away from the liquid electrolyte/liquid metal interface before precipitating out. When h is too thick homogenous nucleation will occur preferentially. However, if h is sufficiently thin, preferential heterogeneous nucleation and crystal growth is possible at the bottom interface between the liquid metal and a seed substrate. (g) Exploded view of the ec-LPE cell. The cell has a compression stack design to facilitate the formation of a stable liquid metal film over a large two-dimensional area. Upon assembly, liquid metal is flowed into a thin cavity with the side walls and bottom defined by photoresist patterned on a seed substrate, respectively, and the top comprised of a porous membrane that is permeable to electrolyte flow but resists infusion by the liquid metal. 8

Figure 1.4 (a) Representative chronoamperometric trace of an ec-LPE deposition of a Ge film using the following conditions: $E = -1.6$ V vs E(Ag/AgCl), $T = 90$ °C, and an aqueous electrolyte containing 70 mM $Na_2B_4O_7$ and dissolved GeO_2 at a formal concentration of 225 mM. (b) Optical photograph of a Ge film prepared by ec-LPE with the same conditions as in (a) on top of a n^+-Si(100) seed substrate. (c) Scanning electron micrograph of a cross-section of a Ge film prepared by ec-LPE with the same conditions as in (a). The underlying seed substrate is n^+-Si(100). (d) Representative high resolution annular dark-field scanning transmission electron micrograph of the interface between the Ge film and Si substrate. Electron diffraction patterns for the Ge film and the Ge/Si interface are shown in (e) and (f), respectively. (g) Chronoamperometric data for Si ec-LPE performed on an n^+-Si(100) seed substrate using eutectic GaIn liquid metal thin-film electrodes within an ec-LPE cell filled with propylene carbonate containing 0.1 M $(C_4H_9)_4NCl$ with 0.5 M $SiCl_4$ at T = 125°C. (Inset) Excitation waveform (h) Cross-section scanning electron micrograph of Si film grown by ec-LPE (i) Plan view optical photograph of electrodeposited Si film prepared by ec-LPE at the conditions in Figure g. (j) Bright field transmission electron micrograph of a cross section of an epitaxial Si film prepared by ec-LPE on a n^+-Si(100). The dashed circles correspond to the position of the selected area aperture in 1-3. Insets: Partially indexed selected area electron diffraction patterns from just the epifilm, the epifilm-substrate interface, and the substrate respectively. (k) High magnification brightfield scanning transmission electron micrograph of Si epifilm grown by ec-LPE. (l) Representative high angle annular dark field high-resolution scanning transmission electron micrograph of the interface between the Si film and Si substrate. 10

Figure 1.5 Schematic illustration of the electrochemical cell and the X-ray beam path used for in situ X-ray reflectivity measurements. 13

Figure 1.6 R_F-normalized X-ray reflectivity of (a) liquid Hg and (b) liquid $Hg_{0.3}In_{0.7}$ in 0.1 M $Na_2B_4O_7$ at a potential of $E = -1.4$ V. The solid lines in (a, b) indicate the best fit. Insets: Schematic representations of the interface structure for each liquid metal. Schematic depiction of Ge crystal nuclei growth in (c) pure Hg (d) and Hg_xIn_{1-x} where indium has a higher affinity for Ge facilitating better transport within the liquid metal and therefore causing larger Ge crystallites to be observed as In content increases. 16

Figure 1.7 Scanning electron micrographs of as-prepared crystalline Ge electrodeposited with Hg, $Hg_{1-x}In_x$, and In electrodes from solutions containing 0.05 M GeO_2 and 0.01 M $Na_2B_4O_7$. Corresponding schematic depiction of the influence of In on the surface diffusion of Ge on the resultant morphology of the Ge crystallites as a function of In concentration. Scale bars: (a) 0.5 μm; (b, c, d) 1 μm. 18

Figure 1.8 Photographs of Pd electrodeposited onto $Hg_{1-x}In_x$ alloy electrode at (a) $t = 0$ s and (b) $t = 7900$ s. (c) Powder X-ray diffractograms of Pd electrodeposited on $Hg_{1-x}In_x$ and solid In electrodes under the same reaction conditions. Reference peaks are shown for polycrystalline Pd, In, HgPd, In_7Pd_3, and InPd. (d) Shift in the peak position for the [100], [200], [211], and [220] InPd peaks as a function of the fraction of In in the Hg-In alloy used for material synthesis. (e) Schematic depiction of the formation of In-M intermetallics by ec-LLS. (1) M^{n+} is reduced at the Hg-In/electrolyte interface. (2) The resultant M^0 is dissolved into the Hg-In electrode and is solvated. (3) Nucleation occurs to form a Hg-M solid phase. (4) Lattice site exchange of In for Hg to for In-M. (5) Crystal growth and buoyancy of In-M. 19

Figure 2.1 Voltammetric responses for a mercury electrode immersed in 0.1 M $Na_2B_4O_7$ (aq) (dashed line) and 0.1 M $Na_2B_4O_7$ + 0.05 M GeO_2 (aq) (solid line). Scan rate: 0.02 V s^{-1} 38

Figure 2.2 a) Schematic depiction of the model function for the electron density profile along the surface normal that was employed in the fitting of the XRR data. Contributions from the electrolyte, the Hg 'adlayer', and bulk Hg as well as the central fit parameters are indicated. b) Plot of the X-ray reflectivity normalized to the Fresnel reflectivity, R/R_F, vs. surface-normal momentum transfer, q_z, for a Hg electrode immersed in deaerated 0.1 M $Na_2B_4O_7$ (*aq*) (orange) or 0.01 M NaF(*aq*) (black) at -0.2 V. Solid lines denote best fits of the data with the model given by *Equation* 2.5. The resulting values of the model parameters are listed in Table 2.1. The corresponding electron density profiles are shown in c). 40

Figure 2.3 a) Plots of the absolute X-ray reflectivity vs. momentum transfer perpendicular to the surface for a Hg electrode immersed in deaerated electrolyte containing either 0.1 M $Na_2B_4O_7$(*aq*) or 0.01 M NaF(*aq*). These data were normalized in Figure 2.2 of the main text. b) Plots of the absolute X-ray reflectivity vs. momentum transfer perpendicular to the surface in 0.1 M $Na_2B_4O_7$(*aq*) at four different potentials: E = -0.2 V (red circles), -0.5 V (blue circles), -0.7 V (green circles), and -0.9 V (purple circles). These data were normalized in Figure 2.4 of the main text. c) Plots of the absolute X-ray reflectivity vs. momentum transfer perpendicular to the surface in 0.1 M $Na_2B_4O_7$ (*aq*) and 0.05 M GeO_2. For the data at E < -0.2 V, the solid black lines denote the corresponding best fit of the data using *Equation* 2.2, For the data at E = -0.2 V, the solid black lines indicate the best fit following the model of *Equation* 2.5. These data were normalized in Figure 2.5 of the main text. In all panels, curves are offset for visual clarity. 41

Figure 2.4 a) Plots of the normalized X-ray reflectivity curves for a Hg electrode immersed in 0.1 M $Na_2B_4O_7$ (*aq*) at -0.2 V (red), -0.5 V (blue), -0.7 V (green), -0.9 V (purple). Solid black lines denote the corresponding best fits of the data. Data were normalized to the Fresnel reflectivity. b) Electron density profiles corresponding to the best fits of the data in (a). Insets show an enlarged view of the electron density profile in the adlayer region (-5 $Å^{-1} \leq z \leq$ -2 $Å^{-1}$). 44

Figure 2.5 a) Plots of the normalized X-ray reflectivity curves for a Hg electrode immersed in deaerated electrolyte containing 0.1 M $Na_2B_4O_7$ + 0.05 M GeO_2 (*aq*) at -0.2 V (red), -0.5 V (blue), -0.7 V (green), and -0.9 V (purple). The XRR data at -0.2 V were recorded after keeping the potential for 15 min. at this value. The solid black lines denote the corresponding best fit of the data. b) Electron density profiles corresponding to the fitted data shown in (a). Insets show an enlarged view of the electron density profile in the adlayer region (-5 $Å^{-1} \leq z \leq$ -2 $Å^{-1}$). 45

Figure 2.6 a) Comparison of the normalized X-ray reflectivity curves and corresponding fits for Hg electrodes immersed in either 0.1 M $Na_2B_4O_7$ (*aq*) (solid circles and black solid lines) or 0.1 M $Na_2B_4O_7$ + 0.05 M GeO_2 (*aq*) (hollow squares and red solid lines) at -0.50 V, -0.70 V, and -0.90 V. b) (top) Potential-dependent adlayer density determined from fits of the data in (a). (middle) Normalized surface tension, γ, measurements for Hg pendant drop electrodes (inset) in 0.1 M $Na_2B_4O_7$ (*aq*). (bottom) Normalized surface tension measurements for Hg pendant drop electrodes in 0.1 M $Na_2B_4O_7$ + 0.05 M GeO_2 (*aq*). 46

Figure 2.7 Plots depicting the reflected X-ray intensity at (top) $q_z = 0.30$ Å^{-1} and (middle) 0.85 Å^{-1}, recorded concurrently with (bottom) the electrochemical current during a voltammetric scan at 0.05 V s^{-1} for a Hg electrode immersed in 0.1 M $Na_2B_4O_7$ + 0.05 M GeO_2 (*aq*). The arrows denote the voltammetric sweep direction. 49

Figure 2.8 a) Plot of the absolute X-ray reflectivity vs. momentum transfer perpendicular to the surface for a Hg electrode immersed in deaerated electrolyte containing 0.1 M $Na_2B_4O_7$ (*aq*) and a formal concentration of 0.05 M GeO_2 at E = -0.2 V (closed red circles). The fit of the data using *Equation* 2.6 assuming $\Theta_{GeO2} = 1$ and all other parameters listed in Table 2.2 is shown (black line). The Fresnel reflectivity of an interface with a monotonic electron density profile with no surface roughness is also presented (grey dashed line). b) The same XRR data as in (a) but normalized to the Fresnel reflectivity. c) Electron density profiles corresponding to the fitted data shown in (b). 52

Figure 2.9 Interface structure of Hg electrodes in 0.1 M $Na_2B_4O_7$ + 0.05 M GeO_2 (*aq*) at -0.2 V. a) Schematic depiction of the three-component model (*Equation* 2.7) used to fit the XRR data at this potential, consisting of a surface fraction with a bilayer of solid GeO_2 (top) and a Hg surface with adsorbed $HGeO_3^-$ (bottom). The best fits were obtained with a rutile-like bilayer structure, oriented with the [110] direction along the surface normal, and a layer of adsorbed $HGeO_3^-$ on top. b) XRR curve shown in Figure 2.5a together with best fit by this model (dashed black line), corresponding to a bilayer coverage of $\theta_{GeO2} = 0.27 \pm 0.01$. c) Electron density profile corresponding to the fit shown in (b). 53

Figure 3.1 Schematic illustration of an X-ray reflectivity measurement where an X-ray beam of vertical height $2W_V$ at an incident angle, α_i interacts with the surface of a liquid metal. 66

Figure 3.2 a) Example of the reflected beam signal from a liquid $Hg_{0.50}In_{0.50}$ immersed in 0.1 M $Na_2B_4O_7$(*aq*) for a fixed incident angle $q_z = 0.10$ Å^{-1}. b) Line scans of the measured specular and diffuse scattering intensity integrated along q_z across the orange box in (a) for $Hg_{0.35}In_{0.65}$ (black), $Hg_{0.50}In_{0.50}$ (red), and $Hg_{0.95}In_{0.05}$ (blue). Intensities for $q_z < 0.7$ Å^{-1} scaled by 1, 5, 20 times, respectively. c) Example integrated profiles of the specular beam for the same liquid metals measured at $q_z = 0.30$ Å^{-1}. d) $FWHM_{Specular}$ as a function of Hg-In bulk composition. e) $FWHM_{Yoneda}$ as a function of Hg-In bulk composition. f) Normalized Yoneda intensity (I_Y/I_0) as a function of Hg-In bulk composition. g) Normalized Yoneda intensity as a function of radius of curvature (*r)* of the liquid metal for measurements with $q_z = 0.08$ Å^{-1} 70

Figure 3.3 Example integration of the reflected beam intensity profile for $Hg_{35}In_{65}$ (black), $Hg_{50}In_{50}$ (red), and $Hg_{95}In_{05}$ (Blue) for incident angle $q_z = 0.08$ Å^{-1}. Intensity at angles smaller than $q_z \approx 0.7$ Å^{-1} scaled by 1, 2, 10 times, respectively. 71

Figure 3.4 Yoneda intensity (I_Y / I_0) as a function of radius of curvature (*r)* of the liquid metal determined from *Equation* 3.3 and the fitted specular width from *Equation* 3.2 for the $q_z = 0.10$ Å^{-1} showing an increasing trend in intensity as the surface becomes more curved. 74

Figure 3.5 Potential dependence of I_Y/I_0 for a) $Hg_{0.35}In_{0.65}$, b) $Hg_{0.50}In_{0.50}$, and c) $Hg_{0.95}In_{0.05}$ electrodes when the measurement was performed at a constant applied potential and the incident beam was aligned at this potential. Analogous measurements were performed for d) $Hg_{0.35}In_{0.65}$,

e) $Hg_{0.50}In_{0.50}$, and f) $Hg_{0.95}In_{0.05}$ electrodes where the potential was continuously scanned at 10 mV s^{-1} between -1.00 V to -1.40 V while scattering data was recorded. The dashed vertical lines denote the initial potential where the incident beam was aligned. All measurements were performed using an incident angle of q_z = 0.10 $Å^{-1}$ 76

Figure 3.6 Plots of a) $q_{z,peak,specular}$ b) $FWHM_{specular}$ c) $sk_{specular}$ d) $q_{z,peak,Yoneda}$ e) $FWHM_{Yoneda}$ and f) sk_{Yoneda} versus applied potential (E) for fitting the diffuse scans of $Hg_{35}In_{65}$ (blue circle), $Hg_{50}In_{50}$ (orange circle), $Hg_{95}In_{05}$ (green circle) at a fixed incident angle of q_z = 0.08 $Å^{-1}$ using *Equation* 3.2. 77

Figure 3.7 Plots of a) $q_{z,peak,specular}$ b) $FWHM_{specular}$ c) $sk_{specular}$ d) $q_{z,peak,Yoneda}$ e) $FWHM_{Yoneda}$ and f) sk_{Yoneda} versus applied potential (E) for fitting the diffuse scans of $Hg_{35}In_{65}$ (blue circle), $Hg_{50}In_{50}$ (orange circle), $Hg_{95}In_{05}$ (green circle) at a fixed incident angle of q_z = 0.10 $Å^{-1}$ using *Equation* 3.2. 78

Figure 3.8 Plot of the a) $Hg_{35}In_{65}$ b) $Hg_{50}In_{50}$ c) $Hg_{95}In_{05}$ sample alignment (S_z) versus applied potential (E). d) Slope of the linear trendlines (ΔS_z / ΔE) used to fit the data in a-c versus liquid metal composition. 79

Figure 3.9 Plot of the normalized $q_{z,peak,Yoneda}$ position as function of Hg-In for fixed q_z = 0.08 $Å^{-1}$ (blue circles) and q_z = 0.10 $Å^{-1}$ (orange circles). The red line is the calculated value of the critical angle for the Hg-In/water interface assuming the refractive index of the bulk Hg-In composition. 80

Figure 3.10 Plots of the normalized X-ray reflectivity curves (R/R_F) for a) $Hg_{0.35}In_{0.65}$, b) $Hg_{0.50}In_{0.50}$, and c) $Hg_{0.95}In_{0.05}$, electrodes immersed in 0.1 M $Na_2B_4O_7$ (aq) at applied potentials of −1.00 V (red), −1.10 V (blue), −1.20 V (green), −1.30 V (purple), −1.40 V (yellow) vs E(Ag/AgCl). Solid black lines denote the corresponding best fits of the data using the third approach outlined in the text. Data were normalized to the Fresnel reflectivity, R_F (denoted by grey dashed line). 84

Figure 3.11 Plots of the absolute X-ray reflectivity vs. momentum transfer perpendicular to the surface for a a) $Hg_{35}In_{65}$ b) $Hg_{50}In_{50}$ or $Hg_{95}In_{05}$ deaerated electrolyte containing 0.1 M $Na_2B_4O_7$(aq) at potentials of: E = -1.00 V (red circles), -1.10 V (blue circles), -1.20 V (green circles), -1.30 V (purple circles), and -1.40 V (yellow circles).These data were normalized in Figure 3.10 of the main text. In all panels, curves are offset for visual clarity 85

Figure 3.12 Electron density profiles corresponding to the best fits of the data shown in Figure 3.10 of the main text at potentials of: E = -1.00 V (red), -1.10 V (blue), -1.20 V (green), -1.30 V (purple), and -1.40 V (yellow). Profiles are offset for visual clarity. 89

Figure 3.13 Plot of σ_i vs. applied potential for $Hg_{0.35}In_{0.65}$ (black squares), $Hg_{0.50}In_{0.50}$ (red circles), and $Hg_{0.95}In_{0.05}$ (blue triangles) electrodes immersed in 0.1 M $Na_2B_4O_7$ (aq). 91

Figure 3.14 Trends in a) $X_{Hg,first}$ b) $\rho_{e,first}$ / $\rho_{e,bulk}$ c) d_{bulk} and d) σ_{first} versus the applied potential (E) as determined by the fit of the data in Figure 3.10 using *Equation* 3.4. Results for $Hg_{35}In_{65}$, $Hg_{50}In_{50}$, and $Hg_{95}In_{05}$ are the black squares, red circles, and blue triangles, respectively. 92

Figure 3.15 a) Plot of the fitted $X_{Hg,first}$ values for the data in Figure 4 compared to the bulk composition (dashed black line), the predicted first layer composition from the Gibbs adsorption theorem (dashed green line), and the assumption of a pure Hg surface (dashed blue line). b) Plot of d_{first} values from the fitting approach where $X_{Hg,first}$ was allowed to vary. Values of d_{first} for pure Hg (2.87 ± 0.09 Å) and pure In (3.14 ± 0.01 Å) are taken from the literature. 93

Figure 4.1 Schematic depiction of the short-range in-plane atomic layering in the near surface region of a liquid metal/electrolyte interface which decreases monotonically into the bulk liquid metal. Atomic layers (dashed grey lines) are defined by the diameter of a Ga atom (Δd_{Ga}) to highlight deviations of the atomic layering as the short-range order behavior trends toward that of a liquid traversing deeper into the bulk away from the electrolyte. 105

Figure 4.2 a) Schematic depicting the electrochemical cell with a liquid Ga working electrode for electrodeposition and cyclic voltammetry measurements. b) Cyclic Voltammetry of a blank 1.25 M NaOH electrolyte in contact with a liquid Ga working electrode at 1.0 V s^{-1}. c) Current-time transient responses from potential step experiments to (blue) -1.30 V and (red) -1.47 V (red) vs. Hg/HgO (1.25M NaOH) in blank 1.25 M NaOH solution for an initial 15 minutes prior to electrodeposition. d-g) Current-time transients for electrodeposition potentials of -1.30 V (blue) and -1.47 V (red) where t = 0 minutes is defined as the time when an aliquot of d) 15 mM $PbClO_4$, **e)** 1. 0 ± 0.01 mM Bi_2O_3, f) 1.20 ± 0.01 mM $PdCl_2$, or g) 0.120 mM $Mn(NO_3)_2$ is spiked in. ... 108

Figure 4.3 a) Current-time transients with data points collected every t = 0.01 second for electrodeposition potentials of -1.30 V (blue) and -1.47 V (red) where t = 0 seconds is defined as the time when an aliquot of a) 15 mM $PbClO_4$ b) 15 mM $PbClO_4$ c) 1.20 ± 0.01 mM $PdCl_2$, d) 1. 0 ± 0.01 mM Bi_2O_3 or e) 0.120 mM $Mn(NO_3)_2$ is spiked in..... 114

Figure 4.4 a) SEM analysis of a liquid Ga electrode following electrodeposition of 2.5 mM $PbClO_4$ ● H_2O at -1.30 V vs. Hg/HgO (1.25 M NaOH) b) EDS mapping of Ga, Pb and O at the liquid Ga electrode interface which maps the dendrites as Pb highlights an appreciable O signal otherwise not observed at -1.47 V. 115

Figure 4.5 SEM and corresponding elemental mapping of the particles produced after metal electrodeposition at -1.47 V including a) Pb triangular particles (inset scale bar = 10 μm) b) Bi nanoribbons and triangular particles (inset scale bar = 25 μm) c) $PdGa_5$ square particles (inset scale bar = 25 μm) d) $MnGa_4$ nanoribbons and triangular particles (inset scale bar = 5 μm). Corresponding cross-sectional HR-TEM bright field image of the e) [112] direction of a Pb triangular particle, f) [1120] direction of a Bi triangular particle, g) [110] direction of a $PdGa_5$ square particle, h) [110] direction $MnGa_4$ hexagonal particle with the face of the particle probed highlighted in red (inset) and a guiding overlay of the atomic arrangement corresponding to the unit cell viewed in that crystallographic direction for Ga (green) and Pd or Mn (purple). (i-l) Corresponding FFT of (e-h) respectively and experimental selected area electron direction for m) Pb, n) Bi, o) $PdGa_5$, and p) $MnGa_4$ in the orientation shown in (e-h) respectively. 117

Figure 4.6 a) SEM/EDS analysis of a liquid Ga electrode following electrodeposition (t > 15 hours) of 0.20 mM Bi_2O_3 at -1.47 V vs. Hg/HgO (1.25 M NaOH) showing evidence of more coalesced and thicker triangles and nanoribbon Bi particles compared to electrodeposition at t = 3 hrs and b) corresponding current-time transient c) SEM/EDS analysis of a liquid Ga electrode

following electrodeposition (t > 15 hours) of 2.5 mM $PbClO_4$ ● H_2O at -1.47 V vs. Hg/HgO (1.25 M NaOH) showing evidence of more coalesced and larger side length Pb triangles 118

Figure 4.7 SEM of the final TEM sample prepared for analysis by plasma focused ion beam milling with corresponding liftout site (inset) for a) a Pb triangular particle, b) a Bi triangular particle, c) a $PdGa_5$ square particle, and d) a $MnGa_4$ hexagonal particle. 120

Figure 4.8 STEM-EDX analysis of the 0.2 mM Pd^{2+} electrodeposition at -1.47 V onto a liquid Ga electrode. a) HAADF image of the Pd particle area with the spectra area for EDX acquisition indicated. b) EDX mapping for Pd and c) Ga d) EDX Spectra for the spectra area indicated in (a) with the calculated sample composition for Pd and Ga noted in atomic % without considering contributions of the TEM grid or sample spacers. 122

Figure 4.9 STEM-EDX analysis of the 20 μM Mn^{2+} electrodeposition at -1.47 V onto a liquid Ga electrode. a) HAADF image of the Mn particle area with the spectra area for EDX acquisition indicated. b) EDX mapping for Mn and c) Ga. d) EDX Spectra for the spectra area indicated in (a) with the calculated sample composition for Mn and Ga noted in atomic % without considering contributions of the TEM grid or sample spacers. 123

Figure 4.10 Grazing incidence x-ray diffraction data of the Ga electrode interface following electrodeposition in 1.25 M NaOH electrolyte containing either a) 2.5 mM $PbClO_4$ ● H_2O at -1.30 V (blue) and -1.47 V (red) with peaks corresponding to the {111} preferred orientation of the deposition product Pb highlighted in yellow, b) 2.0 mM $PdClO_4$ (blue) and 0.2 mM $PdClO_4$ (red) with peaks corresponding to the {001} preferred orientation of the deposition product $PdGa_5$ highlighted in yellow c) 0.2 mM Bi_2O_3 at -1.47 V (red) and corresponding reference XRD spectra for a polycrystalline Bi sample with peaks corresponding to the preferred {0001}orientation of the electrodeposition product Bi highlighted in yellow. 124

Figure 4.11 (left) Forward-scattered Electron Detector Image of thin, elongated electrodeposited Bi crystals on a frozen Ga interface. (right) The corresponding electron backscatter diffraction map indicating orientation mapping. 125

Figure 4.12 a) SEM of a $MnGa_4$ hexagon which was isolated onto carbon tape from the interface of liquid Ga for further attempted EBSD analysis with corresponding EDS mapping b) Different $MnGa_4$ hexagon also isolated onto carbon tape and imaged at a 52° tilt angle. 127

Figure 4.13 Graphical summary of the key electrodeposition steps in nucleus formation by quasi-epitaxy starting with the (1) electrochemical reduction of a dissolved metal precursor (M_1^{n+}) to achieve one of three observed products: a) polycrystalline metal (M_1^0) dendrites by heterogeneous nucleation on the solid surface oxide, b) single crystalline M_1^0 by nucleation of M_1^0 via self-segregation at the interface in a close-packed form, or c) single crystalline intermetallic via nucleation governed by the in-plane packing of M_2^0. In both (b) and (c), a fraction of electrodeposited metal atoms do not participate in nucleation at the interface and will instead dissolve into the liquid metal bulk (M_2^0). 130

Figure 4.14 a) Tetragonal $PdGa_5$ projected along the [110] crystallographic cross-section with the perpendicular [001] direction pointed upwards. Two planes belonging to the {001} are

highlighted in b) red and c) blue which are considered for the packing arrangement prior to Pd atom insertion within the liquid Ga layers at the interface. 133

Figure 4.15 Potential a) cubic b) pentagonal or c) hexagonal in-plane packing arrangements the liquid Ga surface layers with the defined planar area highlighted in red. 135

Figure 4.16 a) Cubic $MnGa_4$ projected along the [110] crystallographic cross-section with the perpendicular [111] direction pointed upwards. Two planes belonging to the {111} are highlighted in b) red and c) blue which are considered for the packing arrangement prior to Mn atom insertion within the liquid Ga layers at the interface. 137

Figure 5.1 ICP-MS concentration profile showing the measured change in Fe concentration (ΔC_{Fe}) with time (t) over ≈100 hours for a 1.25 M NaOH (aq) solution in contact with liquid Ga. 148

Figure 5.2 Example FIB samples prepared for (S)TEM characterization. The inset graphic denotes the viewing angle for each corresponding crystal image..... 149

Figure 5.3 a) Picture of the glass vial where liquid Ga is reacted in alkaline aqueous solution of 1.25 M NaOH with Fe(II) and Co(II) of varying observations. b) SEM of the principle observation of the reaction which is the formation of hexagonal particles at the liquid metal interface. The reaction shown is the liquid metal surface after reacting with 10 mg L^{-1} Fe(II) salt dissolved in solution for t = 48 hours. 152

Figure 5.4 SEM of the Ga interface following a reaction with a 0.5 mM Fe(II) $(ClO_4)_2 \bullet xH_2O$ solution showing cubic particles that formed 154

Figure 5.5 Representative SEM and EDS of the Ga interface following the reaction with 10,000 µg L^{-1} Co(II) and a) 1,078 µg L^{-1} Fe(II) or b) 10,078 µg L^{-1} Fe(II) dissolved in 1.25 M NaOH (aq) solution 155

Figure 5.6 SEM analysis of synthesized $Fe_{0.85}Ga_{0.15}$ and $Fe_{0.08\pm0.01}Co_{0.06\pm0.01}Ga_{0.86\pm0.01}$ Particles using varied amounts of Fe(II) and Co(II) concentration in 1.25 M NaOH solution. 156

Figure 5.7 Representative SEM and EDS of the $Fe_{0.14\pm0.01}Ga_{0.86\pm0.01}$ hexagons lifted off the liquid Ga interface 157

Figure 5.8 Collected EDX data for the a) $Fe_{15}Ga_{85}$ and b) $Fe_{0.08\pm0.01}Co_{0.06\pm0.01}Ga_{0.86\pm0.01}$ hexagonal particles..... 158

Figure 5.9 HAADF images of the plan-view [left], cross-section along the hexagon corner [middle] and side [right] for the a) $Fe_{0.85}Ga_{0.15}$ and b) $Fe_{0.08\pm0.01}Co_{0.06\pm0.01}Ga_{0.86\pm0.01}$ particles. Orange and green hexagons are used to denote the repeating honeycomb features observed imaging the plan-view direction, particularly for the $Fe_{0.08\pm0.01}Co_{0.06\pm0.01}Ga_{0.86\pm0.01}$ structure. A repeating 7-layer stack was observed for both $Fe_{0.08\pm0.01}Co_{0.06\pm0.01}Ga_{0.86\pm0.01}$ and $Fe_{0.14\pm0.01}Ga_{0.86\pm0.01}$ both cross-sectional directions with a measured height of 11.8 Å..... 160

Figure 5.10 a) High angular dark-field (HAADF) and corresponding b) integrated differential phase contrast (iDPC) image of the $Fe_{0.08\pm0.01}Co_{0.06\pm0.01}Ga_{0.86\pm0.01}$ plan-view 161

Figure 5.11 Comparison of the cross-sectional HAADF imaging looking down an axis intersecting the corner of the hexagonal a) $Fe_{0.14\pm0.01}Ga_{0.86\pm0.01}$ and $Fe_{0.08\pm0.01}Co_{0.06\pm0.01}Ga_{0.86\pm0.01}$ particles. Green arrows represent the repeating 7-layer stack, and blue arrows represent the non-periodic stacking faults observed in the $Fe_{0.14\pm0.01}Ga_{0.86\pm0.01}$ structure. 162

Figure 5.12 Selected area electron diffraction (SAED) of the a) $Fe_{0.85}Ga_{0.15}$ and b) $Fe_{0.08\pm0.01}Co_{0.06\pm0.01}Ga_{0.86\pm0.01}$ particle plan-view with the less intense (red) and more intense (yellow) spots circled for clarity, c) $Fe_{0.85}Ga_{0.15}$ and d) $Fe_{0.08\pm0.01}Co_{0.06\pm0.01}Ga_{0.86\pm0.01}$ cross-section along the hexagon corner, and e) $Fe_{0.85}Ga_{0.15}$ and f) $Fe_{0.08}Co_{0.06}Ga_{0.86}$ cross-section along the hexagon side 164

Figure 5.13 a) Schematic depiction of the microED experimental analysis of the hexagonal particles. Example microED frame data from -70° to 70° tilt angles for the b) $Fe_{0.14\pm0.01}Ga_{0.86\pm0.01}$ and c) $Fe_{0.08\pm0.01}Co_{0.06\pm0.01}Ga_{0.86\pm0.01}$ particles with frame nearest 0° having rotation orientation indicated with a green hexagon. Contrast and brightness have been adjusted to improve clarity. d) Plotted radial integrations of the -70° to 70° tilt angles for the $Fe_{0.14\pm0.01}Ga_{0.86\pm0.01}$ and $Fe_{0.08\pm0.01}Co_{0.06\pm0.01}Ga_{0.86\pm0.01}$ particles. 166

Figure 5.14 Radially integrated $Fe_{0.14\pm0.01}Ga_{0.86\pm0.01}$ experimental microED data plotted as a function of with 2θ using $Cu_{K\alpha}$ (1.54 Å) and the custom Python code presented in Section S4 compared to the powder X-ray diffraction profiles of common pure Ga and Fe-Ga phases. 168

Figure 5.15 Spatially correlated, atomic resolution HAADF STEM images and EDS maps of a hexagonal $Fe_{0.08\pm0.01}Co_{0.06\pm0.01}Ga_{0.86\pm0.01}$ platelet 169

Figure 5.16 Atomic resolution (S)TEM-EDX of $Fe_{0.14\pm0.01}Ga_{0.86\pm0.01}$ along the hexagonal particle a) corner and b) side 171

Figure 5.17 a) Estimated hexagonal unit cell structure with $a = b = 8.22$ Å and $c = 11.8$ Å of $Fe_{0.14\pm0.01}Ga_{0.86\pm0.01}$ and $Fe_{0.08\pm0.01}Co_{0.06\pm0.01}Ga_{0.86\pm0}$. Green spheres denote Ga atoms and brown spheres denote Fe or Co atomic sites. b) Simulated HAADF images for the structure shown in part a with the respective unit cell outlined in red. 173

Figure 5.18 The estimated structure of hexagonal $Fe_{0.14\pm0.01}Ga_{0.86\pm0.01}$ and $Fe_{0.08\pm0.01}Co_{0.06\pm0.01}Ga_{0.86\pm0.01}$ projected along the [010] crystallographic cross section with sliced projections within the {001} family of planes shown. These slices are colored red (layer 1), blue (layer 2), yellow (layer 3), and pink (layer 4) are considered when calculating the total (Table 5.1) and Ga packing densities (Table 5.4). Green atoms are Ga and brown are Fe or Fe/Co in $Fe_{0.08\pm0.01}Co_{0.06\pm0.01}Ga_{0.86\pm0.01}$. 174

Figure 5.19 The thermodynamic expected phase, tetragonal $FeGa_3$ projected along the a) [001] b) [010] c) [110] and d) [110] crystallographic cross sections with sliced projections within the {100}, {001}, {111}, and {110} family of planes shown alongside each of these projections, respectively. These slices are colored red (layer 1), blue (layer 2), yellow (layer 3), and pink

(layer 4) where applicable are considered when calculating the total (Table 5.2) and Ga packing densities (Table 5.3). Green atoms are Ga and brown are Fe. 177

Figure 5.20 SEM and EDS of a) a gold coated $Fe_{0.14\pm0.01}Ga_{0.86\pm0.01}$ particle on scotch tape following exfoliation and b) section of the $Fe_{0.14\pm0.01}Ga_{0.86\pm0.01}$ exfoliated particle which appears transparent when imaged with a 12 kV electron beam. 182

Figure 6.1 a) Schematic depiction of electrochemical liquid phase epitaxy (ec-LPE) with compression where electroreduced solute dissolves through a porous membrane in the liquid metal with a thickness *h* and diffuses to a boundary with a solid to nucleate at that interface. Preferential heterogeneous nucleation at the liquid metal/seed substrate interface is probable when *h* is sufficiently small with the compressive membrane ensuring the electrocapillarity does not change *h*. b) Schematic depiction of open ec-LPE where a seed substrate is immersed into a liquid metal electrode pool. The white line denotes the macroscopic view of how far the seed substrate is immersed in the liquid metal. The blue box denotes where the three-phase boundaries occur between the liquid metal, liquid electrolyte, and solid seed substrate. 190

Figure 6.2 Sketch and specification of the PMMA tweezer holder [red] and cell cap [blue] for the custom O-ring cell used for electrodeposition with corresponding top-down and side view schematics of the electrochemical cell. 192

Figure 6.3 SEM of the final TEM sample prepared by plasma focused ion beam milling with corresponding liftout site for Ge electrodeposited film using a) $Hg_{0.35}In_{0.65}$ and b) *e*-GaIn..... 196

Figure 6.4 Wetting contact angle, α measurements between a Ge(100) wafer substrate and either liquid a) Ga, b) *e*-GaIn, c) Hg, or d) $Hg_{0.35}In_{0.65}$. 198

Figure 6.5 Linear sweep voltammetric responses for liquid a) Hg, b) $Hg_{0.35}In_{0.65}$, c) Ga, and d) *e*-GaIn in N_2 purged aqueous 0.1 M $Na_2B_4O_7$, both (black line) without and (red line) with 0.05 M GeO_2. 199

Figure 6.6 Linear sweep voltammetry of a) Hg b) $Hg_{0.35}In_{0.65}$ c) Ga and d) *e*-GaIn in 0.01 M $Na_2B_4O_7$ electrolyte with [red] and without [black] the addition of 0.05 M GeO_2. 201

Figure 6.7 a) Representative current-time responses for the chronoamperometric electrodeposition of 0.05 M GeO_2 in aqueous 0.1 M $Na_2B_4O_7$ using either liquid Hg, $Hg_{0.35}In_{0.65}$, Ga, or *e*-GaIn. In all traces, the applied bias was -1.5 V vs. *E*(Ag/AgCl). Zoomed-in view of the first 0.25 h (inset). b) Optical photographs of a Ge(100) wafer section immersed into liquid *e*-GaIn at (top) t = 0 h and (bottom) t = 3 h of the experiment. 202

Figure 6.8 Plot of the thickness electrodeposited Ge film using a) Ga and b) $Hg_{0.35}In_{0.65}$ as a function of distance (x) from the interface between liquid metal, substrate, and electrolyte 204

Figure 6.9 Representative images of various Ge(100) wafer sections following 3 h attempts at 'open' ec-LPE of Ge epi-films using either liquid a,b) Hg, c-f) $Hg_{0.35}In_{0.65}$, g-j) Ga, or k-n) *e*-GaIn. Panels a), c), g) and k) show the macroscopic view of the resultant films. The immersion level of each wafer section is indicated with a white dashed line. The top of the epi-film is denoted with a blue dotted line. The bottom edge of the epi-film is marked with an orange dot-

dashed line. Panels b, d), h) and l) illustrate representative scanning electron micrographs of the top edge of the electrodeposited material. Inset in l shows the nuclei observed towards the bottom edge of the *e*-GaIn film. Panels e-f), i-j), and m-n) indicate the representative Kikuchi patterns and corresponding pole figures measured by electron back scatter diffraction for each film prepared with liquid $Hg_{0.35}In_{0.65}$, Ga, and *e*-GaIn, respectively. 205

Figure 6.10 Optical micrographs of the a) front and b) back of the Ge electrodeposited film using *e*-GaIn at -1.5 V vs. Ag/AgCl in 0.1 M $Na_2B_4O_7$ and 0.05 M GeO_2 for 3 hours 206

Figure 6.11 a-c) Cross-sectional scanning electron micrographs at two different positions along the vector perpendicular to the white lines in Figure 6.9 for Ge epi-films electrodeposited with liquid *e*-GaIn pool electrodes biased at -1.5 V vs. *E*(Ag/AgCl) for *t* = a) 1 h, b) 3h, and c) 18 h. d) Thickness vs distance along the vector perpendicular to the white lines in Figure 6.9 for Ge epi-films prepared with liquid *e*-GaIn biased at -1.5 V vs. *E*(Ag/AgCl) for *t* = 1, 3, and 18 h. The lines are the best fits according to *Equation* 6.1. 208

Figure 6.12 Scanning electron micrograph of the Ge electrodeposited film in plain a) and close-up b) views using Ga for 18 hours and the corresponding current-transient curve c) 209

Figure 6.13 Scanning electron micrographs of a) bottom left and b) top right of an electrodeposited Ge film using *e*-GaIn before and after submerged in *e*-GaIn droplet under -1.5 V vs. Ag/AgCl in 0.1 M $Na_2B_4O_7$ for 18 hours 210

Figure 6.14 Cross-sectional electron micrographs of the interface between a Ge(100) seed substrate and electrodeposited Ge-epifilm using either liquid a,b) $Hg_{0.35}In_{0.65}$ or c,d) *e*-GaIn liquid metal electrodes. Panels a) and c) illustrate high-angle annular dark-field (HAADF) scanning transmission electron micrographs of the respective interfaces. Panels b) and d) show high resolution bright-field images of the respective interfaces, with selected area electron diffraction images obtained from the respective seed substrate and Ge epi-films. 212

Figure 6.15 a) High-angle annular dark field scanning transmission electron micrograph (HAADF – STEM) of the interface between the Ge film grown using $Hg_{0.35}In_{0.65}$ and Ge substrate with corresponding energy dispersive spectroscopy signal for Ge, In and Hg with the corresponding b) EDS spectra showing the peak signals of each element. c) Zoomed EDS spectra in the region around the less intense Hg and In peak signal. 214

Figure 6.16 a) High-angle annular dark field scanning transmission electron micrograph (HAADF – STEM) of the interface between the Ge film grown using *e*-GaIn and Ge substrate with corresponding energy dispersive spectroscopy signal for Ge, Ga, and In. b) HAADF – STEM image of Ga droplet occluded in the Ge electrodeposited film with corresponding energy dispersive spectroscopy signal for Ge and Ga. 215

Figure 6.17 Schematic depiction of the a) initial and b) latter stages of the 'open' ec-LPE process at the three-phase boundary. The dashed arrow labeled 'i.' denotes transport of electroreduced Ge adatoms along the liquid metal surface. The dashed arrow labeled 'ii.' indicates the dissolution of electroreduced Ge adatoms into the bulk liquid metal. The solid arrow labeled 'iii.' illustrates diffusion of electroreduced Ge adatoms along the solid surface of a Ge crystal. The solid arrow labeled 'iv.' shows the diffusion of Ge dissolved in the bulk liquid metal. The

assumption in this work is that the solid arrows are rate-limiting with respect to epi-film growth while the dashed arrows are not. 218

Figure 6.18 Schematic depiction of three different time points a) t_1 < b) t_2 < c) t_3 in a hypothetical 'open' ec-LPE process where the seed substrate is vertically translocated through the liquid metal pool electrode. 220

Figure 7.1 Picture of the electrochemical cell used for the electrochemical characterization of liquid Ga in aqueous 1.25 M NaOH electrolyte. The liquid Ga pool was housed in a custom Teflon bowl and contacted using a Pt wire. The counter electrode was a pure Pt wire, the reference a Hg/HgO (1.25 M NaOH) and the cell was maintained under inert N_2 atmosphere. 230

Figure 7.2 Cyclic Voltammetry of liquid Ga in 1.25 M NaOH (*aq*) solution at a scan rate of 10 mV s^{-1}. A total of 35 cycles were performed from a) -1.32 V to -1.47 V or b) -1.20 V to -1.55 V with the last cycle highlighted in red to clearly represent the change in the voltametric profile over time. 232

Figure 7.3 Cyclic Voltammetry of liquid Ga in 1.25 M NaOH (*aq*) solution at scan rates of 100 to 1,000 mV s^{-1} in 100 mV intervals. 234

Figure 7.4 Cyclic Voltammetry of solid Ga on a FTO glass substrate in 1.25 M NaOH (*aq*) solution at a scan rate of 10 mV s^{-1}. A total of 35 cycles were performed from a) -1.32 V to -1.47 V or b) -1.20 V to -1.55 V with the last cycle highlighted in red to clearly represent the change in the voltametric profile over time. 235

Figure 7.5 a) As prepared Cu/$CuGa_2$/Ga foil electrode by mechanically spreading Ga across the Cu foil in the presence of concentrated HCl. b) Top and c) side view of the Cu/$CuGa_2$/Ga foil electrode in a 'platform' configuration to better probe the characteristics of the liquid metal/electrolyte interface. 240

Figure 7.6 a) Custom electrochemical cell fitted with a flat quartz-glass window to view and video with an optical camera the behavior of the Cu/$CuGa_2$/Ga 'platform' electrodes shown in Figure 7.5 when an electrochemical bias is applied. b) Cyclic voltammetry from -1.0 to -1.7 V vs. Ag/AgCl in an aqueous 0.1 M $Na_2B_4O_7$ electrolyte solution in contact with the Cu/$CuGa_2$/Ga 'platform' electrode. c) Zoom-in on the cyclic voltammetry shown in b to highlight the peak features present at more positive potentials. d) Interface of the liquid Ga/electrolyte in a blank 0.1 M $Na_2B_4O_7$ electrolyte solution. e) Interface after holding at negative -1.7 V vs. Ag/AgCl for t > 18 hours in 0.1 M $Na_2B_4O_7$ and 0.05 M GeO_2. Accumulation of Ge crystallites and hydrogen bubbles are observed but the interfacial curvature is unchanged. 242

Figure 7.7 a) Picture of a piece of Kapton tape after touching the interface of liquid Ga which had been decorated with particles. Subsequent contact with 1.25M NaOH was performed to remove any bulk liquid metal that may have transferred. b) Image taken with a 50x microscope objective of the piece of tape shown in part a showing hexagonal particles which were transferred. 244

Figure 7.8 a) Picture of a typical Ga ingot which has been frozen with liquid N_2 following electrodeposition of particles on the surface. b) Image of a Si wafer after an ingot like what is

shown in part a is gently 'streaked' onto the wafer to transfer particles of interest which may be contained on the surface..... 246

Figure 7.9 SEM images of a single particle FIB transfer onto an Au patterned electrode array. a) Attachment of the omniprobe needle to the particle. b) Initial lift-off from the substrate surface which fragments a piece of the particle. c) Movement of the particle the Au patterned electrode area. d) Particle cut free from the omniprobe needle. e) Platinum is patterned between the Ga-based hexagonal particle and the Au electrodes to make electrical contact. Corresponding EDS is shown. 249

Figure 7.10 a) Optical image of the 2-probe measurement performed by making contact to the Au electrode strips. b) i-v curve response when the potential bias is swept from ± 0.10 V across the as prepared $Fe_{0.08\pm0.01}Co_{0.06\pm0.01}Ga_{0.86\pm0.01}$ particle shown in Figure 7.9..... 250

Figure 7.11 Using the FIB procedure in Figure 7.9 but for a Ge nanowire. a) Ge NW is affixed to the omniprobe needle. b) The Ge NW is brought near the Au patterned electrode array prior to being cut free from the needle. c) Platinum is patterned between the Ge NW and the Au electrodes to make electrical contact. 251

Appendix Figure.A.1 Pictorial representation of an 'adlayer'of $HGeO_3^-$ ions. The gray dashed lines indicate the layers of atoms that are described by a Gaussian term with the atomic form factors of either Ge or O, respectively. 257

Appendix Figure A.2 Pictorial representation of a rutile bilayer of GeO_2 along the <110> direction used in fitting the data collected at E = -0.2 V. The gray dashed lines indicate the layers of atoms within each of the respective structures which are described by Gaussian terms with the atomic form factors of Ge or O, respectively. Each layer is defined by a coverage (Θ), position (z), and roughness (σ). The relative positions of atoms within this structure are determined by the lattice bond distances and orientation. 260

Appendix Figure D.1 Linear sweep voltammetry responses at 10 mV s^{-1} for three distinct liquid Ga electrodes in 0.1 M $Na_2B_4O_7$ and 0.05 M GeO_2 electrolyte solution where a) repetitive cycling with allowing the electrode to go to OCP in-between scans, b) repetitive 10 mV s^{-1} sweeps but with multiple sweeps not at 10 mV s^{-1} taken in-between and c) repetitive cycling without going to OCP was performed. 310

Appendix Figure D.2 Background corrected linear sweep voltammetry responses at 1, 5, 10, 50, and 100 mV s^{-1} for a liquid Ga electrode in 0.1 M $Na_2B_4O_7$ and 0.05 M GeO_2 electrolyte solution. 310

List of Appendices

Appendix A: Supporting Information for Chapter 2 255

A.1 Contents 255

A.2 Refinement to *Equation* 2.2 to Describe Enrichment Hg Interface with General Gaussian Terms 256

A.3 Refinement to *Equation* 2.2 to Describe Enrichment of H_2GeO_3/$HGeO_3^-$ at Hg Interface 257

A.4 Description of the Distance-Dependent Electron Density Profile for a Hg interface 258

Appendix B: Supporting Information for Chapter 3 262

B.1 Contents 262

B.2 Full XRR Scan Fitting Python Code 263

B.2.1 Fitting File 264

B.2.2 DCMLayer and DCMPers File 270

B.2.3 XRR.Layer File 276

B.2.4 XRR Model Approach File 281

B.2.5 XRR.lmfit File 282

B.3 Code Used to Describe the Yoneda Feature 284

B.4 References 300

Appendix C: Supporting Information for Chapter 5 301

C.1 Contents 301

C.2 Example Python Code Used to Radially Integrate MicroED Frame Data 302

C.3 Example Python Code Used to Convert MicroED (.mrc) Frame Data to .tif 307

Appendix D: Supporting Information for Chapter 6 308

D.1 Contents 308

D.2 Additional Voltammetric Measurements on Multiple Liquid Ga pools 309

Abstract

This thesis presents an atomic-level understanding of liquid metals obtained via in-situ X-ray reflectivity and leverages this insight to develop novel approaches for growing single-crystalline inorganic materials. First, the efficacy of using X-ray reflectivity to probe unary or binary liquid metal/electrolyte interfaces *in situ* has been described. Second, it introduces the first known method of electrochemical single-crystalline material synthesis at a liquid metal/liquid interface, a process termed 'quasi'-epitaxial growth. Third, this work outlines how interfacial liquid metal surface ordering directly influences the single-crystalline growth of both known and previously unknown inorganic materials.

The first chapter describes the important aspects of liquid metals used in ec-LLS and ec-LPE. First, ec-LLS experiments have similarities in supersaturation behaviors observed with traditional melt growth and vapor-liquid-solid methods but done so electrochemically. Second, the location of nucleation and crystal growth can be controlled. Third, the local atomic structure and liquid metal composition influences the product of ec-LLS.

Chapter 2 and Chapter 3 of this thesis details the theory and approach in probing liquid Hg and Hg_xIn_{1-x} electrode interfaces *in-situ* using XRR. First, pure Hg in contact with aqueous $Na_2B_4O_7$ solutions does not exhibit any adsorption at the liquid metal interface. Second, a pure Hg electrode in the presence of dissolved H_2GeO_3 and/or $HGeO^{3-}$, at sufficiently positive potentials forms monolayer coverages of polygermanates via a condensation reaction. Additional insights made using Hg_xIn_{1-x} alloys show that there is Hg surface enrichment beyond what was previously predicted by the Gibbs Adsorption Isotherm for ideal mixtures. Additionally, an intense Yoneda signal was confirmed for Hg_xIn_{1-x} that shows a noticeable dependence on the radius of curvature and bulk composition.

Chapters 4 and 5 introduce a new concept in ec-LLS, referred to as 'quasi'-epitaxy. Directed crystal growth of metallic material is observed during low flux electrodeposition onto a 'clean' liquid metal interface devoid of oxides. Liquid Ga at constant, ambient conditions was used to electrodeposit pure single crystalline forms of Pb[111], Bi[0003], PdGa5[001], and MnGa4[111]. A similar approach was also used for synthesizing previously unreported intermetallic phases, $Fe_{0.14\pm0.01}Ga_{0.86\pm0.01}$ and $Fe_{0.08\pm0.01}Co_{0.06\pm0.01}Ga_{0.86\pm0.01}$.

Chapter 6 describes an alternative approach coined 'open' ec-LPE, for observing single-crystal semiconductor growth at room temperature and ambient pressures. Ge(100) epi-films were synthesized electrochemically on a Ge seeding substrate mechanically inserted into a liquid metal electrode. Differences between Hg, $Hg_{35}In_{65}$, Ga, and *e*-GaIn are described based on differences in wetting interactions with the seed wafer and solubility toward Ge.

The last chapter of this work outlines unresolved work to assist future researchers working with liquid metal electrodes. Attempts at understanding the complex electrochemistry of liquid Ga in alkaline aqueous electrodes are discussed. Additionally, efforts in making a flat liquid Ga electrode by using $CuGa_2$ as a more wettable conductive substrate is presented. Lastly, methods for isolating and electronically characterizing the products of ec-LLS and ec-LPE are discussed.

This work paves the way for future studies on interfacial ordering in liquid metal electrodes and its impact on crystal growth while expanding the prospects of liquid metals in synthetic electrochemical applications.

Chapter 1 Thesis Introduction[1]

1.1 Motivation

Liquid metals were essential to the discovery and the synthesis of many historically important crystalline inorganic materials. Dating back to the onset of semiconductor materials science, liquid metals were crucial in both the fundamental understanding of material crystallization[1] and the practical realization of high quality materials for optoelectronic devices.[2] Interest in liquid metals as platforms for materials science continues to this day.[3-7]

A particularly vibrant and comparatively new direction focuses on metals and metal alloys that are specifically molten at or near room temperature.[8] Room temperature liquid metals have enabled the syntheses of several previously unimagined material phases and compositions.[9-13] For example, the preparation of ultra-thin (i.e. two dimensional) oxides is now possible at a liquid metal alloy because the surface composition can be selectively enriched, affording control over the surface oxide composition.[10] Similarly, the synthesis of two-dimensional metal films (e.g. gallanene)[14, 15] has been demonstrated. A major appeal of liquid metals for these types of syntheses is mechanical separation of the bulk product material is straightforward.[10, 16]

Given the surge in popularity in room-temperature liquid metals for inorganic crystal growth,[8] there is value in both understanding and subsequently developing synthetic processes which utilize room-temperature liquid metals. Thus, the scope of this thesis is two-fold: (1) Increase the atomic understanding of liquid metals during inorganic crystal growth conditions and (2) Describe the use of liquid metals as an electrochemical and metallurgical reaction medium for single crystalline inorganic materials synthesis. To contextualize the new findings described in the later chapters of this thesis, a summary is first provided here of the prior work of the Maldonado group.

[1] Reprinted (adapted) with permission from Wu, H.; Hazelnis, J. P.; Maldonado, S., Understanding and Expanding the Prospects for Electrosynthesis with Liquid Metal Electrodes. *Accounts of Chemical Research* 2023, *56* (7), 846-855. Copyright 2023 American Chemical Society.

1.2 Electrochemical Liquid-Liquid-Solid Growth

About a decade ago,[17] our group described a new hybrid strategy for synthesis of inorganic semiconductors centered on the virtues of liquid metals. The electrochemical liquid-liquid-solid (ec-LLS) concept merges and leverages simultaneously liquid metals as chemical solvents and as electronic current collectors. Specifically, the use of a liquid metal as an electrode during material electrodeposition affords the possibility of obtaining a crystalline form of that electrodeposit (Figure 1.1a). An appeal of this approach is that the common three electrode cell design in electrodeposition becomes a highly versatile melt crystal growth reaction vessel (Figure 1.1b).

The ec-LLS method has several tangible advantages. Ec-LLS is natively simple to execute. Changes in temperature are not required to drive crystallization. Accordingly, ec-LLS can be performed isothermally, even at room temperature! Ec-LLS is not specific to just the common liquid metals in electrochemistry (i.e. Hg). Ec-LLS has been performed with other pure liquid metals and liquid metal alloys.[18-21] Ec-LLS is agnostic towards electrolyte type, i.e. it can be performed with molecular and ionic electrolyte solvents.[22, 23] Ec-LLS can be performed with large or minute volumes of liquid metals, dictating the 'yield' and 'form' of the crystalline material.[24, 25]

Still, ec-LLS is deceptively complex to optimize. Beyond engineering challenges, leveraging the ec-LLS concept to its fullest extent requires a more complete understanding of what is and is not possible and/or relevant. Simply, there are several critical and fundamental knowledge gaps in how to think about liquid metal solvent electrodes. In general, the atomic structure and depth-dependent composition are significantly more nuanced for liquid metal solvents than for molecular liquids.[26, 27] More specifically, a detailed understanding of liquid metals in contact with liquid electrolytes with and without an applied bias is almost entirely lacking at the atomic scale. Separately, crystal growth by an electrochemical potential gradient rather than a thermal gradient is fundamentally different than any traditional melt crystal growth process. Even for well understood materials, the consequences of this difference are difficult to predict.

1.3 Addressing the Knowledge Gap in ec-LLS

In the more recent years, further work by the Maldonado group on ec-LLS has focused on defining how crystalline solids form in a liquid metal electrode, leveraging the ec-LLS concept towards realizing more advanced materials targets, or both. The cumulative observations, inferences, and conclusions of the research was guided by three main questions (Figure 1.1): (*1*) What are the

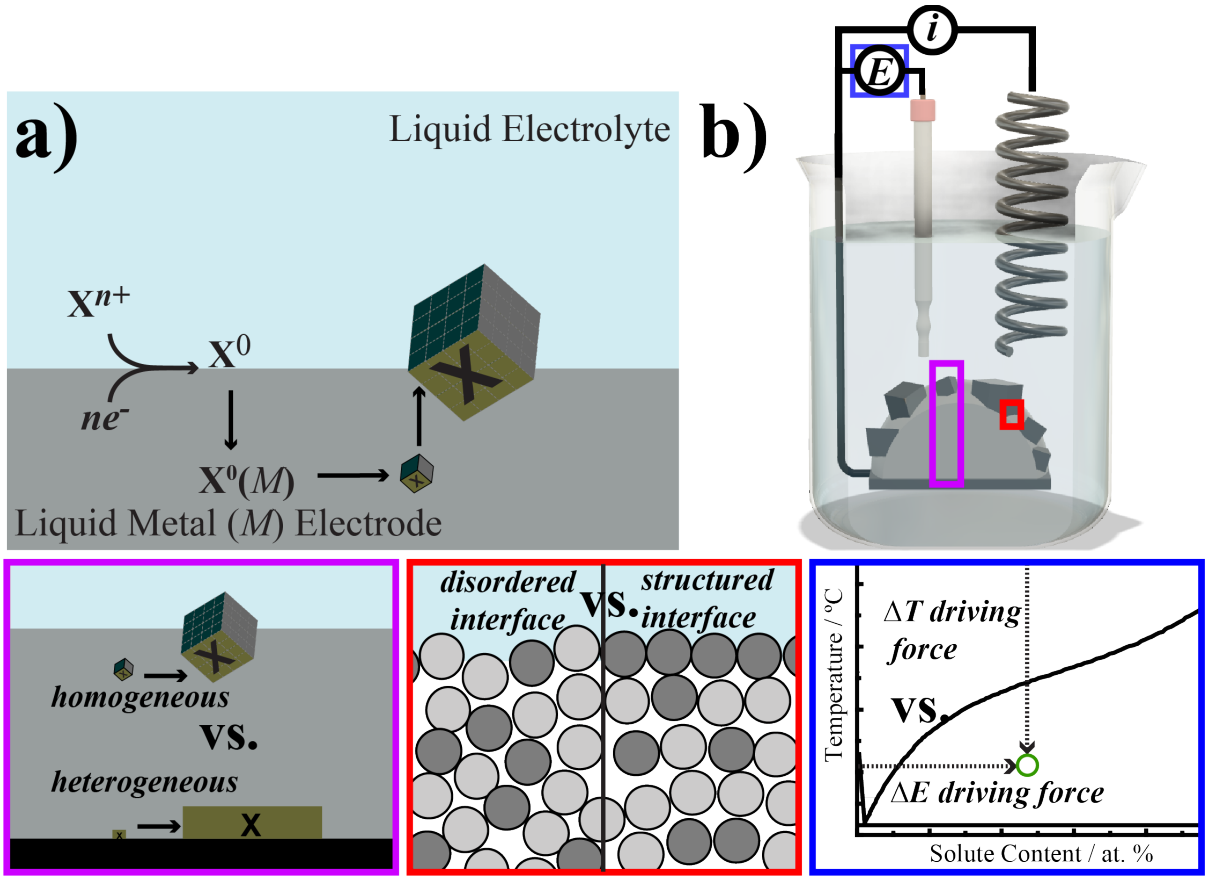

Figure 1.1 a) Schematic representation of ec-LLS crystal growth steps including metal precursor X^{n+} reduction to zero-valent X^0, dissolution into the liquid metal electrode *M*, nucleation and subsequent crystal growth of X^0. b) Schematic depiction of a complete ec-LLS reaction cell with a liquid metal electrode. Colored boxed insets highlight three distinct: (purple) location of the nucleation and crystal growth events, (red) ordering of alloy species at the liquid metal interface, and (blue) isothermal driving force on crystal growth and product species.

consequences of reaching supersaturation by an electrochemical rather than a thermal driving force for crystal growth in ec-LLS? (*2*) Can the location of nucleation and subsequent crystal growth be controlled? (*3*) Does the atomic structure of the liquid metal affect product formation in ec-LLS?

1.3.1 Supersaturation by an Electrochemical Driving Force

A consistent observation in the Maldonado lab was that the appearance of crystalline materials in ec-LLS was not necessarily instantaneous. The lack of crystalline products did not correspond to an initial deposition of amorphous/disordered solute as we never observed this outcome in any ec-LLS configuration.[22, 28-30] Instead, we suspected that an appreciable amount of electrodeposited solute was accumulating within the liquid metal electrodes prior to crystal growth.

An initial set of in-situ measurements were performed with eutectic gallium indium (*e*-GaIn) microdroplets of precisely defined volumes using X-ray diffraction. The premise was that diffraction from (111) planes would serve as a marker for the formation of Ge crystals in ec-LLS by the electroreduction of dissolved GeO_2.[31] Linear correlations of the X-ray diffraction signal intensity vs time (*t*) were consistently observed at several different temperatures, but none of the collected data sets had intercepts at t=0. Instead, extrapolation of these linear data sets indicated a delay in the first appearance of Ge crystals between 15 and 45 s. Complementary 1D models of diffusion and nucleation/crystal growth in the liquid metal microdroplets indicated that these delay times might be better understood as induction times. That is, these data implied that driving forces, $\Delta\mu$, for nucleation and crystal growth of 14 kJ mol^{-1} were attained. Similarly, these driving forces corresponded supersaturation levels of Ge $>10^2$ in *e*-GaIn during ec-LLS. These driving force and supersaturation levels were surprising, as they implied two important points. First, the activation barrier for nucleation in at least some low temperature ec-LLS processes is much higher than the thermal energy. Second, the liquid metal electrodes in ec-LLS are, with respect to solubility, solvents far from equilibrium. The first point was consistent with reports suggesting that liquid metals that are poorer solvents for Ge require high supersaturations to grow Ge crystals.[32] The equilibrium solubility for Ge in *e*-GaIn near room temperature is much lower in comparison to the solubility of Ge in Au (~0.2 mol L^{-1}), [33, 34] Still, our data also suggested the activation barrier for nucleation strongly depended on the size of the microdroplet (*vide infra*). The fact that the liquid metal droplets were in contact with multiple surfaces introduced some uncertainty as to the interpretation of the apparent activation barriers for nucleation. The second point provided some

context as to why crystallographic defects are consistently observed in crystals prepared by ec-LLS. Still, the sensitivity of X-ray diffraction further introduced uncertainty with regards to the precise induction times and the actual supersaturation levels.

To provide further clarity, we pursued an alternative method for in-situ analysis, liquid cell transmission electron microscopy (TEM).[35] This technique[36] allows direct visualization of the initial moments of nucleation and crystal growth in liquid solvents. An added benefit is the possibility of the electron beam for imaging also being used to drive electrochemical processes.[37] In the context of ec-LLS, this latter aspect afforded biasing isolated liquid metal droplets 'floating' in aqueous electrolyte (Figure 1.2a). When the appropriate ec-LLS precursor is dissolved in the electrolyte, the incident electron beam can stimulate electroreduction. Figure 1.2b shows representative frames from different times of one such experiment for a Ge ec-LLS event at room temperature that produced a Ge nanowire from a Ga nanodroplet. The temporal resolution was limited by the quality of the digital detector, with state-of-the-art detectors capable of significantly faster frame rates. Nevertheless, individual nanowire growth rates were easily accessible through these experiments (Figure 1.2c). More interestingly, quantitative analysis of the projected volume of the liquid metal prior to, during, and after the emergence of the Ge crystal could be performed. These volumes indicated the loading of Ge into the liquid Ga nanodroplet (Figure 1.2e). Extremely high atomic concentrations of >50% were consistently observed for both liquid Ga and In droplets, i.e. the droplets were momentarily composed of more Ge than liquid metal. To put this into context, the binary phase diagram for Ge and Ga is shown in Figure 1.2d. At room temperature, the equilibrium solubility of Ge in Ga is vanishingly small. But under the conditions of ec-LLS, i.e. under the action of an applied electrochemical stimulus, Ga-Ge liquid mixtures reach supersaturations that are equivalent to a supercooling of ~Δ775°! The ability of an electrochemical bias to realize such supercooled liquids was subsequently and independently observed.[38] Thus, these experiments indicated that while ec-LLS experiments have many similarities with traditional melt crystal growth approaches like vapor-liquid-solid methods, ec-LLS also affords both unique and potentially controllable conditions for materials synthesis.

1.3.2 Controlling the Location of Nucleation and Crystal Growth

The aforementioned works in our labs also hinted how to dictate where nucleation and crystal growth occurred with liquid metal electrodes. Figure 1.3a and Figure 1.3b highlight a

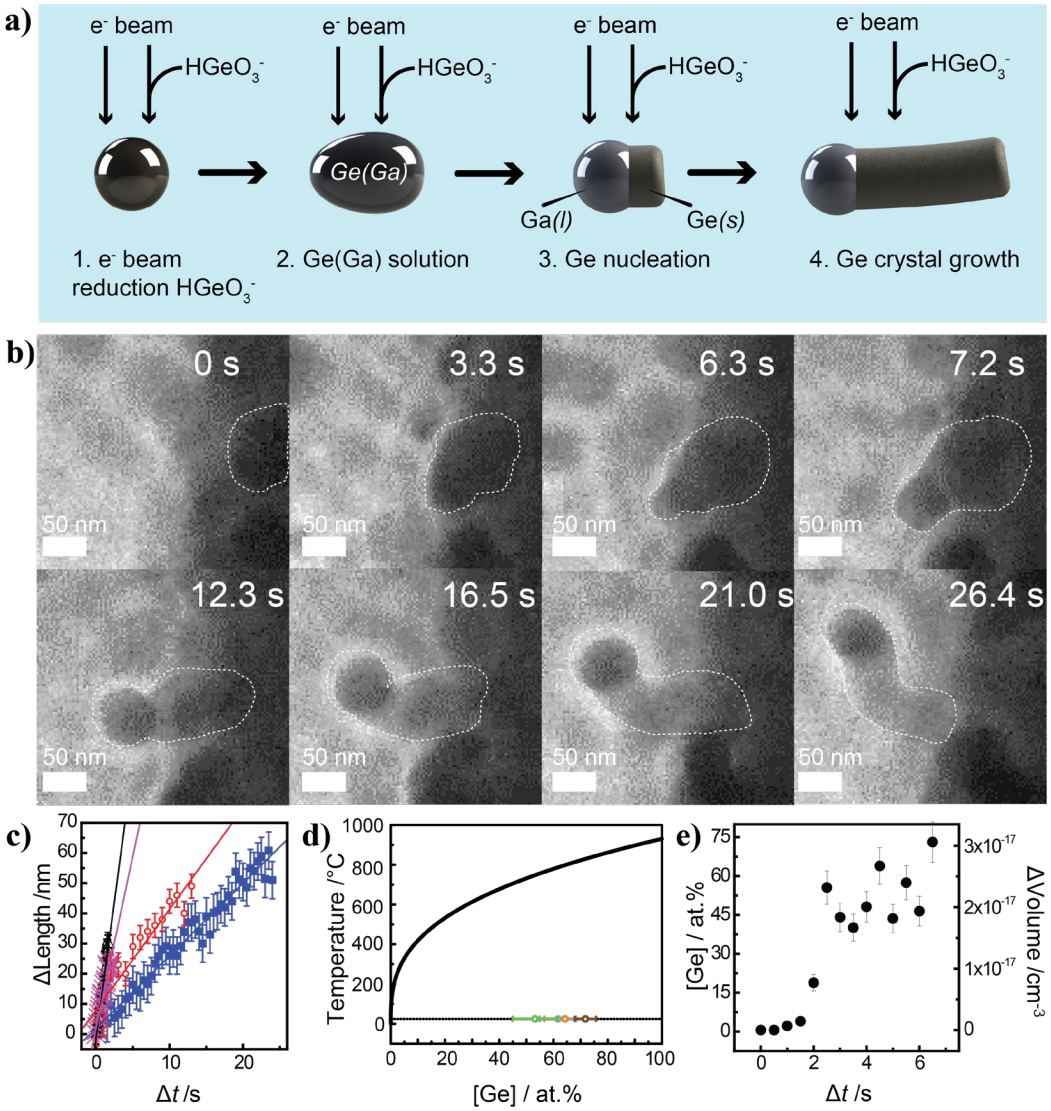

Figure 1.2 (a) Schematic depiction of (1) an e^- beam causing the reduction of dissolved GeO_2 in solution to Ge^0, followed by (2) dissolution into the liquid metal nanodroplet, then (3) crystal nucleation, and finally (4) Ge nanowire growth. (b) Frame grabs from an *in situ* transmission electron video of a Ge ec-LLS event with a Ga nanodroplet immersed in an aqueous solution containing 0.05 M GeO_2 and 0.01 M $Na_2B_4O_7$. (c) A plot of Ge nanowire length *vs* time for four separate Ge nanowire growth events. The steady-state growth rates were estimated from the linear-least-squares fitting of the data (red lines). (d) The phase diagram for the Ga-Ge system is shown with the inclusion of data from four different Ge nanowire growth events. The colored data points correspond to the inferred Ge concentration in the Ga nanodroplets at the time just before nucleation. (e) A plot showing the volume change of the Ga nanodroplet as a function of time before Ge nucleation occurred.

hypothesis that we tested initially with liquid metal microdoplets.[31] Specifically, using narrow, lithographically patterned microwells, we assessed where Ge crystals grew with liquid metal microdroplet electrodes possessing different thicknesses. We posited that at a given temperature and electrochemical potential, liquid metals with an appreciably thickness would consistently and solely support homogeneous nucleation and crystal growth. Given the buoyancy of Ge crystals in *e*-GaIn, these crystals would float and accumulate at the top liquid metal/liquid electrolyte interface. Conversely, liquid metals that were sufficiently thin would favor nucleation and crystal growth at the bottom liquid metal/solid substrate interface. Representative results from these experiments are shown in Figure 1.3c and Figure 1.3d. At a temperature just above the melting point of *e*-GaIn, liquid metal droplets thicker than 20 μm showed numerous Ge crystallites at the top interface. Conversely, liquid metal droplets thinner than 10 μm supported the electrodeposition of a crystalline Ge microwire. Nucleation occurred exclusively at the bottom interface and crystal growth continued specifically at the liquid metal/solid Ge interface. No solid material nucleated or accumulated on the side walls of the photoresist. This general feature was observed at other temperatures, except the apparent thickness threshold for observing 'clean' microwire growth increased at higher temperatures.

It was inferred that the thickness threshold for ensuring that ec-LLS resulted in heterogeneous nucleation at the bottom interface was not unique to the microwell platform. That is, if a sufficiently thin but *wide* liquid metal electrode were used for ec-LLS, the electrodeposited material would grow exclusively as a *film* at the bottom interface with the substrate (Figure 1.3e and Figure 1.3f). Although fabricating arbitrarily wide wells in photoresist is trivial, we empirically found that features with aspect ratios greater than ~2 (i.e. the width divide by the thickness) could not be reliably wet by and filled with liquid metals. Accordingly, alternate strategies were necessary to test this hypothesis.

Liquid metals can be spread uniformly over a large area if the solid substrate exhibits some wettability for the liquid metal. For metals like *e*-GaIn, this requirement is seemingly satisfied by the majority of solid surfaces. However, this wettability is facilitated specifically by the native oxide of the liquid metal. Ec-LLS requires cathodic potentials that partially or completely remove surface oxides from all investigated liquid metals. This point, in conjunction with the electrocapillarity of liquid metals (i.e. their propensity to deform when their surface charge is changed by an applied bias)[39] results in the loss of continuity across a thin liquid metal film

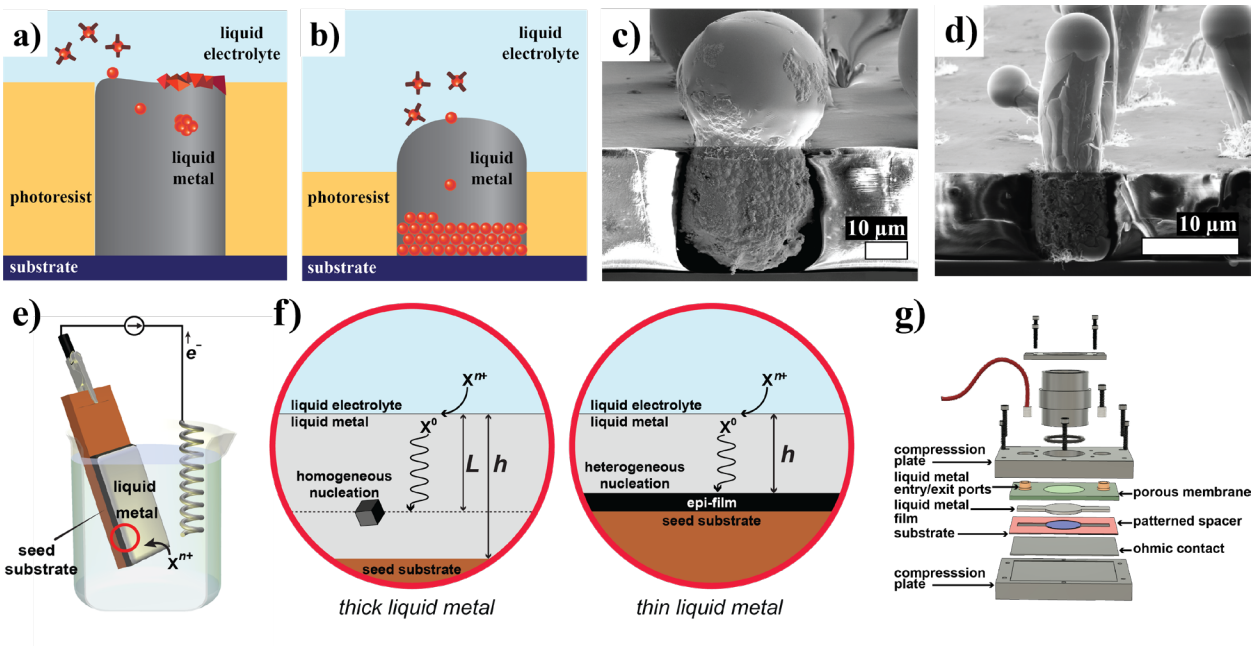

Figure 1.3 (a) Schematic depiction of ec-LLS inside a microwell which is sufficiently deep enough that no solute reaches the bottom interface and instead preferentially nucleates and grows crystals homogeneously within the liquid metal. (b) Same as in (a) except the microwell is shallow that solute can reach the bottom interface and preferentially nucleate and grow a crystal heterogeneously. Scanning electron micrographs of Ge ec-LLS experiments performed in aqueous solution containing 50 mM GeO_2 and 10 mM $Na_2B_4O_7$ at $E = -1.6$ V for 30 min at $T = 40$°C using (c) 27 µm and (d) 8 µm thick e-GaIn microelectrode. (e) Summary view of an electrochemical liquid phase epitaxy (ec-LPE) film growth concept with a thin liquid metal electrode with thickness h. (f) Schematic depiction of the relevant steps in ec-LPE, where an oxidized species X^{n+} dissolved in the electrolyte is reduced to X^0 by heterogeneous electron transfer, partitions into the liquid metal film, and then diffuses some distance away from the liquid electrolyte/liquid metal interface before precipitating out. When h is too thick homogenous nucleation will occur preferentially. However, if h is sufficiently thin, preferential heterogeneous nucleation and crystal growth is possible at the bottom interface between the liquid metal and a seed substrate. (g) Exploded view of the ec-LPE cell. The cell has a compression stack design to facilitate the formation of a stable liquid metal film over a large two-dimensional area. Upon assembly, liquid metal is flowed into a thin cavity with the side walls and bottom defined by photoresist patterned on a seed substrate, respectively, and the top comprised of a porous membrane that is permeable to electrolyte flow but resists infusion by the liquid metal.

electrode in ec-LLS. That is, liquid metal films break up into discrete liquid metal macro-, micro-, and nanodroplets. This observation was particularly true for liquid metal films spread over single-crystalline semiconductor substrates.

For this purpose, Demuth et al invented a new type of electrodeposition cell. Figure 1.3g summarizes the key elements. In this compression cell, a semiconductor wafer substrate is patterned with an insulating material that defines a liquid metal reservoir with a large area but shallow depth. The depth is defined by the insulator thickness but intentionally kept ≤ 10 μm. This cavity is filled with liquid metal and the substrate is then sandwiched between a support platform and a porous membrane. The porous membrane constrains the liquid metal to prevent dewetting and deformation but allows transport of the electrolyte. In this way, the membrane holds the liquid metal in place while preserving contact between the liquid metal and liquid electrolyte.

The cell in Figure 1.3g allow ec-LLS growth where nucleation occurs solely at the interface between the liquid metal film and the single-crystalline semiconductor substrate. Provided the substrate is lattice-matched to the intended solute crystal, the result would be electrodeposition of *epitaxial* films (i.e. epifilms). Epitaxy is highly desirable in semiconductor film deposition and is generally unthinkable for covalent semiconductor electrodeposition, particularly at low temperatures. We dubbed ec-LLS experiments where macroscopic epitaxial films are produced electrochemical liquid phase epitaxy (ec-LPE).

The ec-LPE concept was first realized with the electrodeposition of Ge epifilms.[40] Figure 1.4a summarizes electrochemical data obtained when thin liquid *e*-GaIn films were used for Ge ec-LLS. The inset highlights the simplicity of the electrochemical waveform, i.e. a constant negative bias was applied for several hours. Depending on the quality of the membrane and the ability of the cell to maintain the pressure necessary to constrain the liquid metal, the electrochemical response was purely steady-state. Disassembly of the cell and removal of the liquid metal revealed a large-area film strongly adhered to the wafer substrate (Figure 1.4b). The width of the film was dictated by the dimensions of the ec-LPE cell. A separate 'large' area ec-LPE cell afforded the electrodeposition of Ge epifilms spanning a 6" wafer substrate. Figure 1.4c illustrates the uniformity of these Ge epifilms. Irrespective of the width, the cell thickness was dictated by the total time and charge passed as well as the electrodeposition temperature. The continuity between the substrate and epifilm crystallinity was apparent in both dark-field scanning TEM and in selected area diffraction patterns (Figure 1.4d-f). Closer inspection of the interface

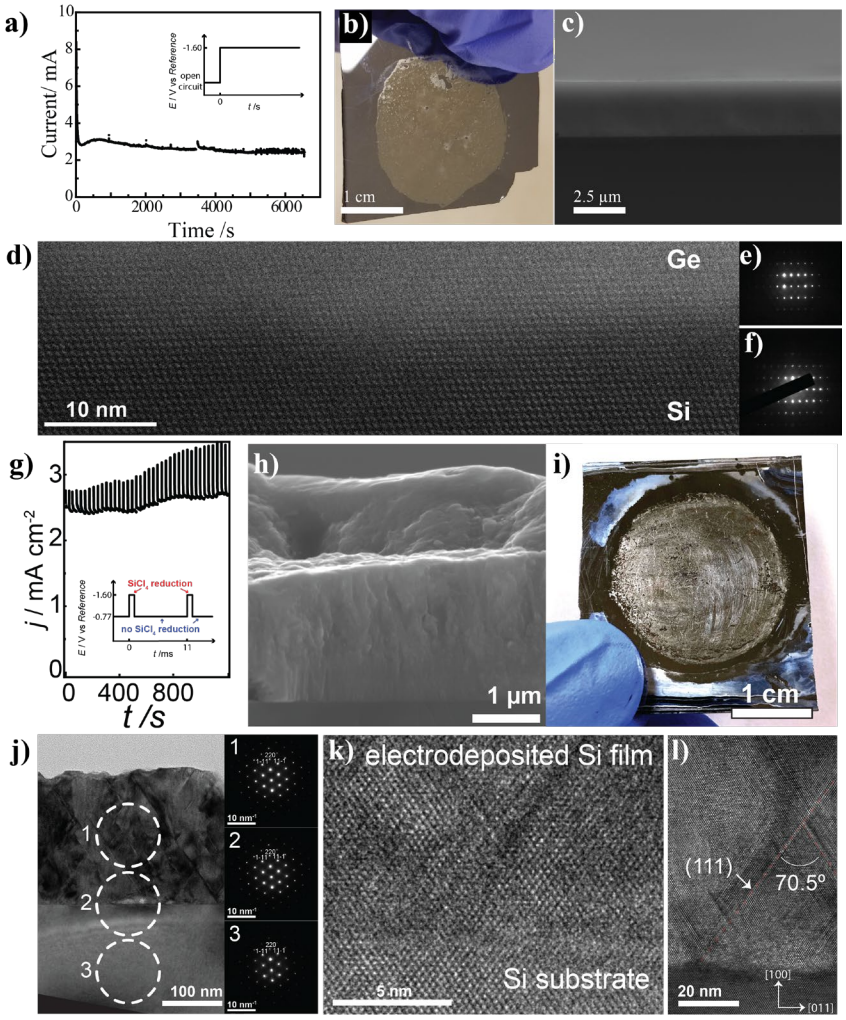

Figure 1.4 (a) Representative chronoamperometric trace of an ec-LPE deposition of a Ge film using the following conditions: $E = -1.6$ V vs E(Ag/AgCl), $T = 90$ °C, and an aqueous electrolyte containing 70 mM $Na_2B_4O_7$ and dissolved GeO_2 at a formal concentration of 225 mM. (b) Optical photograph of a Ge film prepared by ec-LPE with the same conditions as in (a) on top of a n^+-Si(100) seed substrate. (c) Scanning electron micrograph of a cross-section of a Ge film prepared by ec-LPE with the same conditions as in (a). The underlying seed substrate is n^+-Si(100). (d) Representative high resolution annular dark-field scanning transmission electron micrograph of the interface between the Ge film and Si substrate. Electron diffraction patterns for the Ge film and the Ge/Si interface are shown in (e) and (f), respectively. (g) Chronoamperometric data for Si ec-LPE performed on an n^+-Si(100) seed substrate using eutectic GaIn liquid metal thin-film electrodes within an ec-LPE cell filled with propylene carbonate containing 0.1 M $(C_4H_9)_4NCl$ with 0.5 M $SiCl_4$ at $T = 125$°C. (Inset) Excitation waveform (h) Cross-section scanning electron micrograph of Si film grown by ec-LPE (i) Plan view optical photograph of electrodeposited Si film prepared by ec-LPE at the conditions in Figure g. (j) Bright field transmission electron micrograph of a cross section of an epitaxial Si film prepared by ec-LPE on a n^+-Si(100). The dashed circles correspond to the position of the selected area aperture in 1-3. Insets: Partially indexed selected area electron diffraction patterns from just the epifilm, the epifilm-substrate interface, and the substrate respectively. (k) High magnification brightfield scanning transmission electron micrograph of Si epifilm grown by ec-LPE. (l) Representative high angle annular dark field high-resolution scanning transmission electron micrograph of the interface between the Si film and Si substrate.

between the substrate and the electrodeposited epifilm illustrated one of the most astounding aspects of ec-LPE. There was no evidence of an intervening oxide layer. The prevailing wisdom in semiconductor material synthesis and deposition is that the employed ec-LPE conditions are *anathema* to obtaining atomically clean interfaces. Yet, even though the electrodeposition was performed *with water* in a cell operated in *lab ambient* at nearly *room temperature*, epifilms were readily obtained.

An obvious target for low temperature ec-LPE is the preparation of Si epifilms. Low temperature growth of high quality crystalline Si is a major step towards non-toxic, inexpensive, environmentally responsible, and efficient photovoltaics.[41] Despite the early identification of Si ec-LLS processes for crystalline particles[42] and for crystalline nanowires,[24] Si ec-LPE proved significantly more challenging than Ge. In addition to requiring non-aqueous solvents and slightly elevated temperatures, the $SiCl_4$ precursor is prone to extensive side reactions at negative applied bias.[43] This aspect prevented growth of Si epifilms with thicknesses much beyond 10 nm.

Recently, Downes et al identified a strategy around this problem, using a pulsed electrodeposition waveform (Figure 1.4g) that prevented accumulation of deleterious side products at the liquid metal/electrolyte interface.[44] With this approach, macroscopic Si epifilms with micron thicknesses were readily obtained (Figure 1.4h,i). Again, the collected microscopic and diffraction data indicated the crystal structure of the electrodeposited films was a direct extension of the underlying substrate without any obvious sign of intervening oxide layer (Figure 1.4j-l).

A consistent feature in both epifilms types has been extensive but selective incorporation of one component (Ga) of the liquid metal electrodes. Interpreting this observation requires a microscopic view of the liquid metal structure.

1.3.3 Influence of the Local Atomic Structure and Composition of Liquid Metal Electrodes

A limitation of in-situ TEM is that the electron scatter caused by the liquid electrolyte substantially decreases the attainable imaging resolution. Similarly, traditional scanning probe methods useful for mapping the atomic structure of solid/liquid interfaces are ill-suited for liquid metal/liquid electrolyte contacts. As a result, other methods are necessary to interrogate the microscopic details of liquid metal interfaces. In this regard, X-ray reflectivity (XRR) stands alone in elucidating interface structure along the surface normal.[26]

XRR is a non-destructive technique which even in the absence of long-range order can access the molecular-scale interfacial structure.[45, 46] In these experiments, the specular reflection intensity at angle β is measured as a function of the incident angle (α), where $\alpha = \beta$. To maximize the resolution at the interface, shallow incident angles of approximately 0.1 to 5° are used. Although laboratory diffractometers with maximum photon fluxes of 10^9 photons per second are sufficient for XRR measurements of solid samples, liquid interfaces require higher fluxes to achieve the same spatial resolution.[46] This is because liquid metals are more prone to scattering and absorption losses, reducing the effective range in reflected signal and thus spatial resolution. For probing liquid metals most studies utilize synchrotron radiation sources with significantly higher photon fluxes (10^{10} to 10^{12} photons per second).

Another challenge when probing liquid interfaces via XRR is that liquids are not natively flat and will always align with its interface perpendicular to the forces of gravity. This means that to probe a liquid metal interface it is necessary to use a surface diffractometer which can change the incident X-ray relative to the sample and limit mechanical vibrations. The former is something laboratory diffractometers with lower photon fluxes can achieve by simply moving the anode source,[47] but at a beamline more advanced optical geometries are needed to deflect the beam. Fortunately, as interest in these measurements has grown, specialty diffractometers such as the Liquid Interfaces Scattering Apparatus (LISA) at the beamline P08 of PETRA III have been designed with these considerations in mind making data acquisition more accessible.[48]

XRR is the first technique to unambiguously identify one of the most unusual aspects of liquid metal interfaces – atomic layering both at the vapor[49-53] and liquid interfaces[21, 48, 54, 55] for a variety of unary and binary liquid metals. Specifically, a characteristic maximum is observed in the normalized XRR signal that corresponds to a quasi-Bragg peak arising from atomic layering in the near-surface region of the liquid metal. This peculiar atomic structure occurs because the stark when electronic differences between the liquid metal and the interfacial media are so great that the entropic penalty of organization is overcome by the free energy gain of minimizing interaction between the liquid metal atoms and the outside media.

When performing measurements on a liquid metal/liquid electrolyte interface a custom enclosed cell is required, similar to what has been described in Murphy B. et al.[56] Incident and reflected X-rays are able to penetrate through thin PEEK windows, a material that is transparent too X-rays as shown in Figure 1.5. The cell diameter is made ‘sufficiently’ large on a several

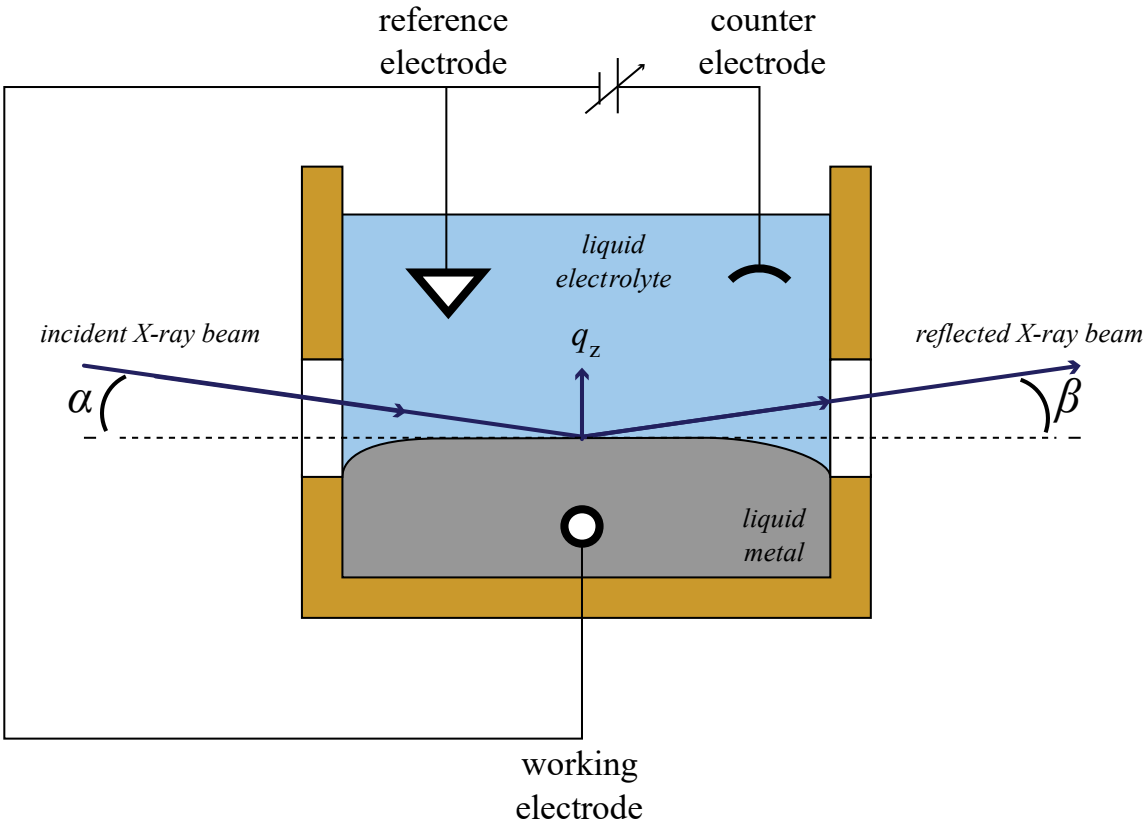

Figure 1.5 Schematic illustration of the electrochemical cell and the X-ray beam path used for in situ X-ray reflectivity measurements.

centimeter scale to minimize the local curvature observed by the X-ray beam. These local curvature effects are explored in more detail in Chapter 3 of this thesis. High photon energies above 18 keV and thus a synchrotron X-ray source is essential to penetrate the liquid electrolyte which can otherwise scatter or absorb a majority of the X-ray signal. The benefit of having a cell which is enclosed is that it can be maintained under an inert atmosphere to avoid any unintended effects of oxidation at the liquid metal interface. Additionally, electrode ports can be added to perform in-situ measurements under an electrochemical bias. Some of the first potential dependent XRR measurements for a pure Hg/NaF (*aq*) interface was conducted by Runge et al[57] with a similar cell set-up.

While data collection of the X-ray reflectivity curves can already be quite challenging, understanding the data also requires some form of mathematical modeling or fitting to interpret. For most liquid interfaces already explored, the so called 'Master Formula' for fitting the reflected signal (R) has been well described by Pershan & Nielson.[58] The most distilled form of this equation is presented as *Equation* 1.1.[59, 60]

$$\frac{R(q_z)}{R_F(q_z)} \approx \left| K_{bulk} \cdot K_{Surface} \right|^2$$

Equation 1.1

The scattering vector perpendicular to the surface, q_z is the common convention for denoting the incident angle (α), where $q_z = (4\pi/\lambda)\cdot\sin\alpha$ and λ is the wavelength of the X-rays. This equation states that when the reflected signal $R(q_z)$ is normalized by the Fresnel reflectivity of a perfectly flat interface, $R_F(q_z)$, the normalized signal depends on q_z in a manner that depends on two terms given in *Equation* 1.1. One term is related to the bulk electron density of the liquid metal under study, K_{bulk}. The other term describes the change in electron density in the direction normal to the surface plane, $K_{Surface}$.

In simplest terms, *Equation* 1.1 when $K_{Surface} \neq 1$, implies that the atoms at the liquid metal interface are not randomly distributed but exhibit a degree of ordering that deviates from the expectations of simple optical Fresnel reflectivity. Other functional forms of this equation for describing the behavior of liquid metals, often referred to as the distorted crystal model [DCM],[46, 49] is discussed in more detail in Chapter 2 and Chapter 3 of this thesis. Additionally, the dissertation of Runge B.[61] provides a detailed overview of the data collection and analysis for in-situ investigation of liquid interfaces, which also includes custom written python script that can be

adapted to mathematically describe the reflectivity data. Additional work published by Sartori et al[62] also includes useful Python code which can be accessed and adapted to describe XRR profiles of a liquid-liquid interface. Fitting the normalized experimental reflectivity data (R / R_F) effectively deconvolutes the individual electron density contributions normal to the liquid metal interface. Specifically, the functional form of the derivative of the interfacial electron density $f\left(d\rho_{e^-,\,interface}\right)$ accurately describe deviations from the known ideal behavior $f\left(\rho_{e^-}\right)$ of the interface. This includes explicit values of interfacial roughness, ion adsorption behavior, and ion coverage.

Preliminary in-situ XRR data was collected by the Maldonado group for Hg-In alloys under the most common conditions of Ge ec-LLS (in aqueous electrolyte containing 0.1 M $Na_2B_4O_7$) with a Hg-In alloy ($Hg_{0.3}In_{0.7}$).[21] Hg-In alloys are interesting because the amount of In in the alloy could be the same as in *e*-GaIn or even higher. In fact, Hg-In alloys with In contents ranging from 0 to ~70 at.% are all liquids at room temperature. Accordingly, Hg-In alloys represent a useful solvent system that ranges from being devoid of In to being primarily composed of In. The XRR data for the most In-rich Hg-In alloy are shown in Figure 1.6b compared to that of pure Hg in Figure 1.6a. A characteristic layering peak could be observed, although it was much more intense than for pure Hg. More interestingly, the data could only be fit with a model that corresponded to the outermost layer being composed almost entirely of Hg. This observation was consistent with this liquid metal behaving as an ideal mixture, where the component with the higher surface energy is predicted to have a more dilute fractional composition on the surface relative to its fractional composition in the bulk mixture if neither has an appreciable affinity for the outside medium.[63] Thus, these XRR data were the first direct insights on the atomic structure of a liquid metal/liquid electrolyte interface.

This surface segregation of Hg confirmed that the liquid metal structure and composition were malleable and depended strongly on the material being contacted. Since molten In at elevated temperatures completely wets crystalline Ge,[64] we posited that an opposite effect may occur once Ge nucleated and within Hg-In. That is, the low surface tension of 0.58 N m^{-1} at T = 25 °C for In/Ge relative to that for Hg/Ge (>1.1 N m^{-1}) should lead to an *accumulation* of In at a liquid metal/Ge crystal interface.[21] Accordingly, even though the solubility of Ge is essentially the same in pure Hg and in Hg-In alloys, the local environment of each Ge nucleus for crystal growth during ec-LLS should differ strongly within these two liquid metals (Figure 1.6c,d). Since In is well

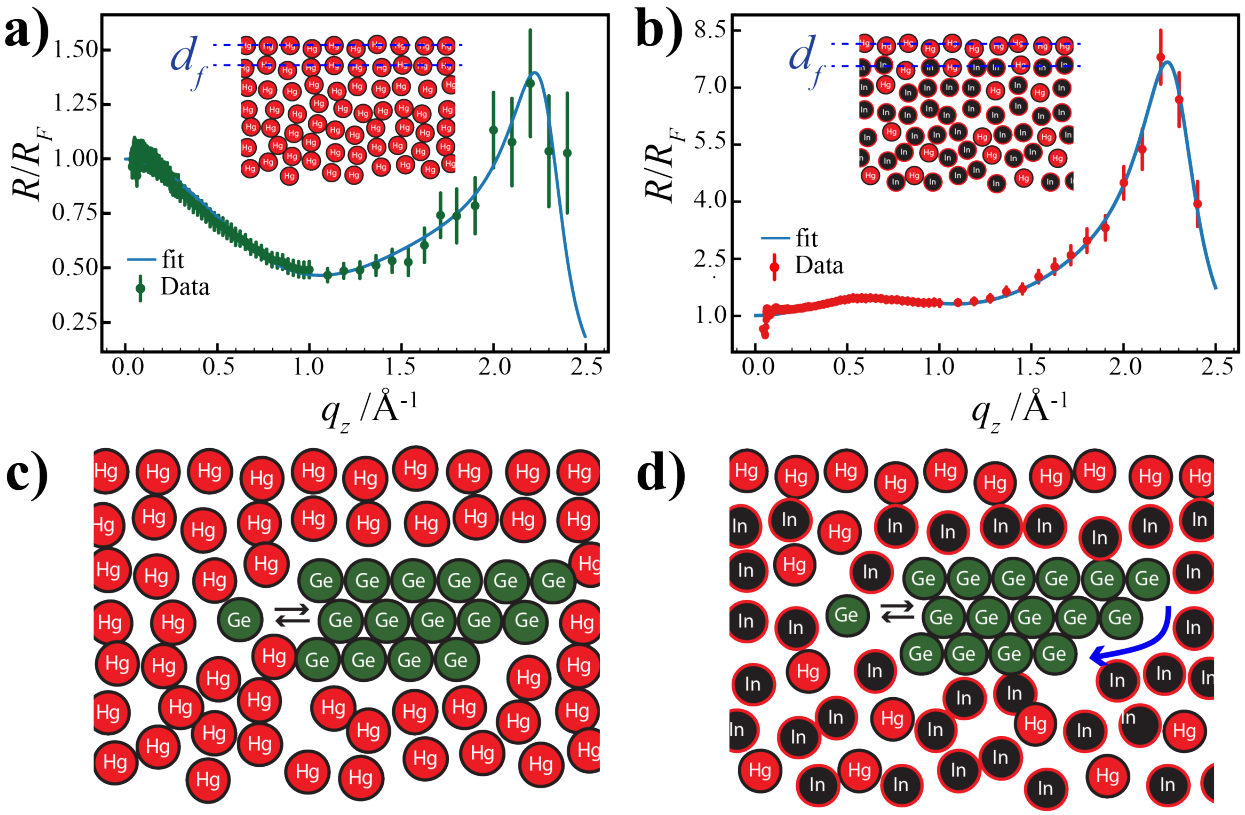

Figure 1.6 R_F-normalized X-ray reflectivity of (a) liquid Hg and (b) liquid $Hg_{0.3}In_{0.7}$ in 0.1 M $Na_2B_4O_7$ at a potential of $E = -1.4$ V. The solid lines in (a, b) indicate the best fit. Insets: Schematic representations of the interface structure for each liquid metal. Schematic depiction of Ge crystal nuclei growth in (c) pure Hg (d) and Hg_xIn_{1-x} where indium has a higher affinity for Ge facilitating better transport within the liquid metal and therefore causing larger Ge crystallites to be observed as In content increases.

documented as a 'surfactant' in vapor deposition of semiconductor films.[65, 66] we posited this effect may substantially change Ge ec-LLS crystal growth.

Figure 1.7 illustrates the resultant Ge crystal morphologies that we observed at a modest potential of -1.4 V vs *E*(Ag/AgCl) as a function of the In content in the Hg-In mixture. In pure Hg, the Ge crystals had the characteristic branched 'seaweed' structure indicative of fast crystal growth where the impinging zero-valent Ge atoms accumulated and remained where the flux was the highest. As the In content increased in the liquid metal, the leaf structure evolved into large grains, consistent with the premise that In at the crystal growth plane facilitated transported of the newly added zero-valent Ge, presumably to locales that minimized the overall free energy of the growing crystal surface. As a result, large faceted grains were exclusively obtained in the Hg-In alloys with the highest In content even though every other aspect of the ec-LLS process was identical. In total, these data indicated strongly that the liquid metal composition and structure could strongly influence the morphology of the product crystal.

With this same liquid metal solvent system, we separately explored the possibility that the liquid metal could also influence the *composition* of the ec-LLS product. We previously established that pure liquid metal solvent/electrodes in ec-LLS could also act as reactants.[18, 19] In this way, the product composition was necessarily dependent on the liquid metal identity. However, we posited that liquid metal alloys could further widen the synthetic fidelity if only one (or a subset) of components reacted with the electroreduced solute in ec-LLS.

For this purpose, we targeted the ec-LLS synthesis of In- and Pd- containing intermetallics. Such compounds are interesting as selective heterogeneous hydrogenation catalysts.[67] Simply melting solid In and solid Pd together will produce a variety of different compositions and phases, depending on the temperature and relative proportions. At room temperature, the most stable intermetallic compound is In_7Pd_3. We were curious whether this same composition would be formed if Pd was electrodeposited into various liquid Hg-In alloys at a constant potential of -1.85 V vs. *E*(Ag/AgCl). Using $Pd(CN)_2$ as the oxidized precursor in an alkaline aqueous electrolyte, we recently performed ec-LLS using open, bulk liquid Hg-In pools (Figure 1.8a,b). In this system, more solid material accumulated at the liquid metal/liquid electrolyte interface with higher In content in the liquid metal. X-ray diffraction data were collected for these materials and those collected for analogous experiments with solid In electrodes replacing the liquid metal electrodes.

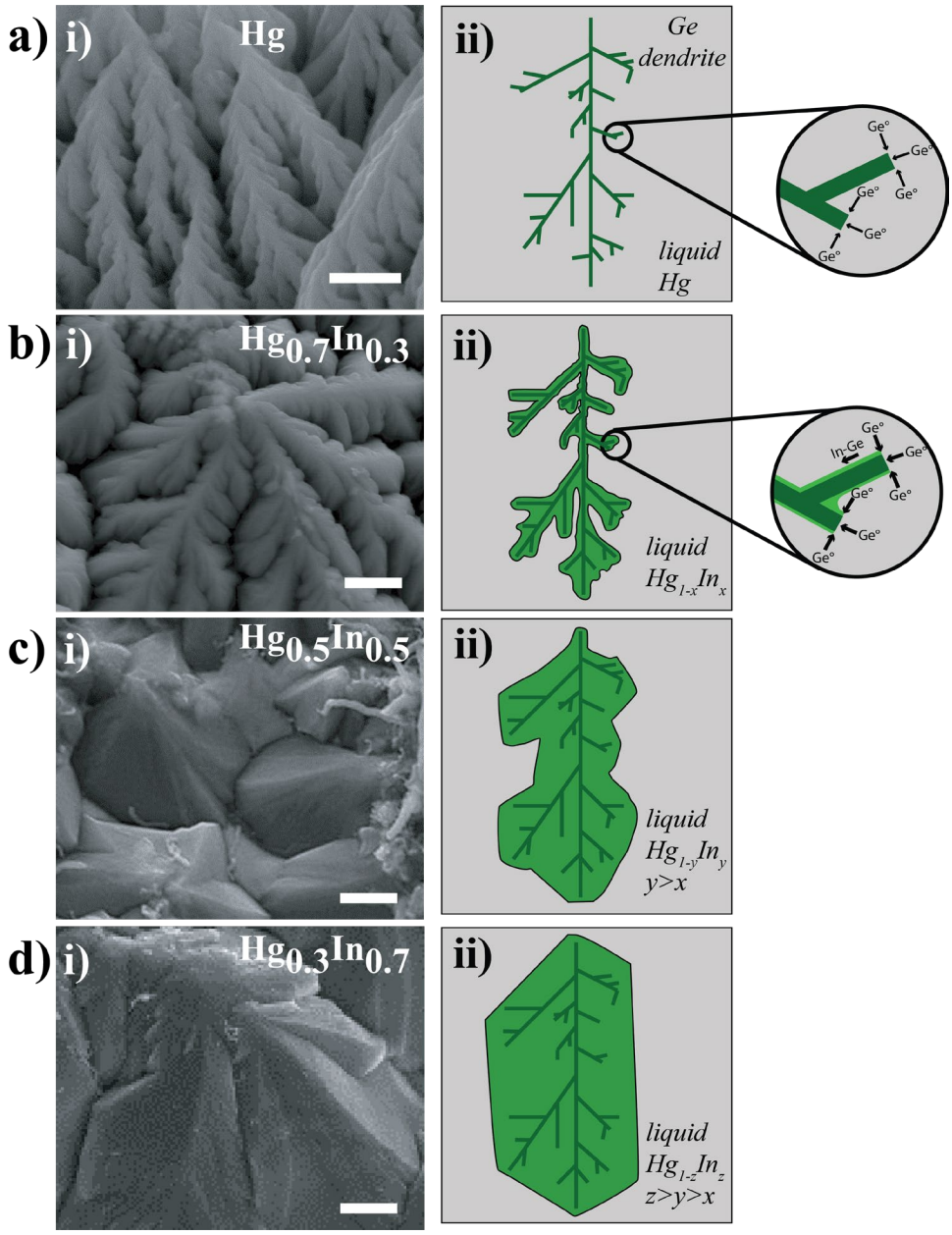

Figure 1.7 Scanning electron micrographs of as-prepared crystalline Ge electrodeposited with Hg, $Hg_{1-x}In_x$, and In electrodes from solutions containing 0.05 M GeO_2 and 0.01 M $Na_2B_4O_7$. Corresponding schematic depiction of the influence of In on the surface diffusion of Ge on the resultant morphology of the Ge crystallites as a function of In concentration. Scale bars: (a) 0.5 µm; (b, c, d) 1 µm.

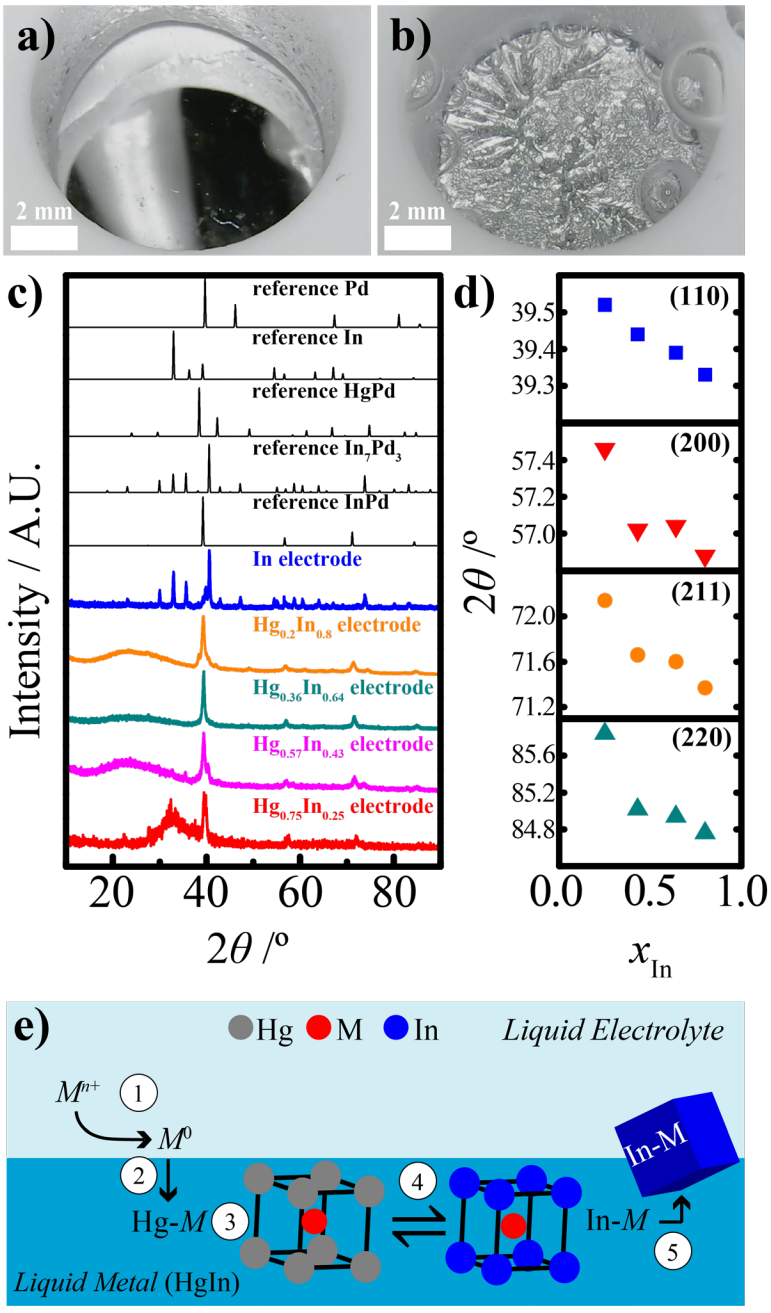

Figure 1.8 Photographs of Pd electrodeposited onto $Hg_{1-x}In_x$ alloy electrode at (a) $t = 0$ s and (b) $t = 7900$ s. (c) Powder X-ray diffractograms of Pd electrodeposited on $Hg_{1-x}In_x$ and solid In electrodes under the same reaction conditions. Reference peaks are shown for polycrystalline Pd, In, HgPd, In_7Pd_3, and InPd. (d) Shift in the peak position for the [100], [200], [211], and [220] InPd peaks as a function of the fraction of In in the Hg-In alloy used for material synthesis. (e) Schematic depiction of the formation of In-*M* intermetallics by ec-LLS. (1) M^{n+} is reduced at the Hg-In/electrolyte interface. (2) The resultant M^0 is dissolved into the Hg-In electrode and is solvated. (3) Nucleation occurs to form a Hg-*M* solid phase. (4) Lattice site exchange of In for Hg to for In-*M*. (5) Crystal growth and buoyancy of In-*M*.

The diffraction signatures of all of these materials were compared to the most probable crystalline phases spanning pure Pd, Hg-Pd compounds, or In-Pd compounds (Figure 1.8c).

Several points were notable in these X-ray diffraction data. First, the collected solids were not pure Pd, indicating chemical reaction between electrodeposited Pd and the electrode. Second, the material collected from solid In electrodes was exclusively In_7Pd_3, in accord with predictions based solely on thermodynamics. Third, the materials collected from the liquid Hg-In electrodes were *not* exclusively or predominantly In_7Pd_3. Rather, these products were consistent with the composition and crystal structure of InPd. The positions of the four principal InPd diffraction signals for the 110, 200, 211, and 220 crystallographic directions shifted to smaller 2θ values as the In content in the liquid metals increased (Figure 1.8d). These shifts were consistent with distortion in the lattice parameter for InPd because of Hg incorporation.

These facts were interpreted to indicate an ec-LLS process featuring metal exchange between the nascent nuclei/crystals and the liquid metal solvent (Figure 1.8e). We posit that Hg first reacts with the electrodeposited solute (Pd), rapidly forming an intermediate Hg-Pd phase. Electrodeposition of Pd using pure liquid Hg electrodes confirmed the existence of cubic HgPd but with low total mass yields, presumably because HgPd had limited stability in contact with Hg. In Hg-In electrodes, site exchange occurs between Hg and In to stabilize the solid and to form a In-Pd lattice matched phase with a similar (cubic) structure to Hg-Pd. The extent of the exchange between Hg and In at the lattice sites is a function of reaction rate, transport, and the activities of In and Hg in the liquid metal. In effect, InPd forms because HgPd is a reaction intermediate in this medium. Similar experiments performed with liquid Ga-In electrodes did not produce any InPd, further suggesting that HgPd was essential to the overall formation of InPd by ec-LLS under the employed conditions. Subsequent experiments with liquid Hg-In electrodes and other metal solutes indicate the basic premise described in Figure 1.8e is not unique to Pd.

1.4 Using Liquid Metal Electrodes a Reactant for Material Synthesis

Our group have previously established a variety of liquid metal systems which can directly influence the *composition* and *crystallinity* of an ec-LLS or ec-LPE product. Preliminary work using in situ X-ray reflectivity seem to suggest that there is local surface ordering at a liquid metal electrode interface which may contribute to the mechanisms of ec-LLS and thus the final product.[21] Despite this observation, single crystalline (*ordered*) film growth has been limited to the products of ec-LPE, which requires an external seeding substrate and complex custom cell design.[40, 68]

However, it was posited that this behavior can be achieved electrochemically under appropriate synthetic conditions that allow access to the local surface ordering of the liquid metal. This thesis explores this topic directly.

1.5 Overview of Thesis

In this thesis, the atomic understanding of liquid metals acquired via in-situ XRR is presented and subsequently leveraged to achieve novel variations of single crystalline inorganic crystal growth. The goals are to first characterize the liquid metal interfacial structure during previously established ec-LLS processes, to then identify potential synthetic pathways which can facilitate single crystalline products in accordance with the perceived interfacial structure and finally to recognize all possible aspects of reactions in liquid metal mediums that are operative when single crystalline growth is observed.

In Chapter 2, the local structure of the liquid metal/electrolyte interface for Hg electrodes immersed in aqueous solutions suitable for crystalline Ge electrodeposition was probed by *in situ* X-ray reflectivity. Series of X-ray reflectivity measurements were collected in both pure 0.1 M $Na_2B_4O_7$ solution and 0.1 M $Na_2B_4O_7$ with 0.05 M GeO_2 at potentials where there are no faradaic redox reactions. Quantitative analysis of these data indicates that the interface structure in pure $Na_2B_4O_7$ solution is indistinguishable from that of Hg immersed in NaF solution, suggesting non-specific adsorption of the borate ions. In GeO_2-containing electrolyte, the presence of Ge species could be detected over a wide potential regime. Between -0.86 and -0.46 V vs *E(*Ag/AgCl), the reflectivity data revealed the adsorption of dissolved H_2GeO_3 and/or $HGeO_3^-$ at a coverage that appears to be independent of potential. At potentials more positive than -0.5 V, an incomplete ultrathin film of a condensed phase forms via slow nucleation and growth at the Hg surface. This solid phase is consistent with a form of GeO_2 and tentatively assigned to polygermanates. This film likely forms through a condensation reaction driven by the concentration of $HGeO_3^-$ at the liquid Hg/electrolyte interface at positive potentials.

Chapter 3 aims to further the understanding of the interface between Hg_xIn_{1-x} and an aqueous $Na_2B_4O_7$ electrolyte during an applied potential bias. Aqueous $Na_2B_4O_7$ as a supporting electrolyte has been used previously during ec-LLS growth of Ge[21, 69, 70], but more importantly it has been shown to not form any strong chemical bonds with Hg and thus should not strongly influence the atomic structuring at the interface.[54] Using in-situ XRR, three liquid metal compositions ($Hg_{35}In_{65}$, $Hg_{50}In_{50}$, and $Hg_{95}In_{05}$) between -1.00 and -1.40 V vs *E*(Ag/AgCl) are

explored. Evidence of Hg surface enrichment limited to just the first layer at all bulk liquid metal compositions was clearly observed. Both the small angle scattering and large angle reflectivity data indicated the underlying layers had the bulk composition, irrespective of the value of the applied potential. This experimental behavior agrees with the single-layer segregation predicted by the Gibbs adsorption theorem and the general behavior observed in many liquid metal/vacuum interfaces, but the Hg enrichment was observed for both Hg-rich and In-rich bulk compositions. The pronounced Hg enrichment was consistent with regular solution behavior in the Hg-In system, especially a large negative enthalpy of mixing. A persistent and confirmed Yoneda signal in the diffuse scattering was also confirmed for the same range of compositions. The Yoneda peak showed a noticeable dependence on the radius of curvature but the data also suggested some dependence with the bulk composition. This work motivates further study of the Yoneda feature to determine whether information on the in-plane heterogeneity across the liquid metal/water interface can be ascertained.

In Chapter 4, the electrosynthesis of single-crystalline metallic and intermetallic particles with preferred orientation onto liquid metal electrodes is presented. Liquid gallium electrodes immersed in aqueous alkaline electrolytes without any molecular additive or external solid seeding substrates were used to electroreduce separately Pb^{2+}, Bi^{3+}, Pd^{2+}, and Mn^{2+}. The crystallinity, composition, and orientation of the electrodeposition products were characterized using scanning electron microscopy, transmission electron microscopy, selected area electron diffraction, grazing incidence X-ray diffraction, and energy dispersive X-ray spectroscopy. Electrodeposition of Pb and Bi results in the incipient formation of 2D nuclei that subsequently direct the growth of Pb and Bi single-crystals along the most closed packed [111] and [0001] directions, respectively. The absence of any intervening surface oxides and low electroreduction flux are necessary to avoid polycrystalline dendrite formation. Under comparable conditions, electrodeposition of Pd and Mn results in single crystalline intermetallic particles at the interface. Each crystal exhibits a preferred orientation consistent with the unique atomic packing of the near-surface region of liquid Ga. The presented study suggests a new concept in electrodeposition processes where the liquid metal structure imparts quasi-epitaxial growth in a system where the electrode material specifically has no crystallinity or long-range order. This study is thus the first demonstration of highly oriented electrodeposition at a liquid/liquid interface at ambient conditions, highlighting the unique solvation environment of liquid metal interfaces for forming thin metallic and intermetallic films.

Chapter 5 describes a method for obtaining previously unreported intermetallic phases, $Fe_{0.14\pm0.01}Ga_{0.86\pm0.01}$ and $Fe_{0.08\pm0.01}Co_{0.06\pm0.01}Ga_{0.86\pm0.01}$. Liquid gallium immersed in aqueous alkaline solution was used in a reaction between of Fe^{2+} and Co^{2+} species dissolved in solution. The atomic ordering at the liquid gallium interface results in a unique environment conducive to layered intermetallic growth. The crystallinity, composition, and orientation of the products were characterized using scanning electron microscopy, transmission electron microscopy, energy dispersive X-ray spectroscopy, selected area electron diffraction and MicroED. The predominate resultant crystals are thin hexagonal particles with a thickness no more than 200 nm and side lengths ≤ 5 μm requiring focused ion beam manipulation in sample preparation and isolation onto a conductivity probe for measurements of the resistivity. $Fe_{0.14\pm0.01}Ga_{0.86\pm0.01}$ and $Fe_{0.08\pm0.01}Co_{0.06\pm0.01}Ga_{0.86\pm0.01}$ are best characterized as having a layered structure, high degree (6-fold) of symmetry, and a hexagonal unit cell with $a = b = 8.22$ Å and $c = 11.8$ Å. Although a complete assignment of the lattice structure proved to be difficult due to ambiguity introduced by crystallographic defects, the estimated structure has a large atomic packing density and sub-units consistent with gallenene. Further studies on these new Ga based intermetallics are needed to further refine their respective structures and to explore their potential electronic properties.

In Chapter 6, room temperature and ambient pressure electrochemical liquid phase epitaxy (ec-LPE) of macroscopic Ge(100) films using uncompressed liquid metal electrodes has been achieved. Experiments were performed in aqueous electrolytes containing dissolved GeO_2 and $Na_2B_4O_7$ using either Hg, $Hg_{0.35}In_{0.65}$, Ga, or $Ga_{0.83}In_{0.17}$ (*e*-GaIn) working electrodes. The resultant crystalline Ge films were characterized via scanning electron microscopy, transmission electron microscopy, energy-dispersive X-ray spectroscopy, and selected area electron diffraction. *e*-GaIn was identified as the liquid metal composition that produced the most uniform and largest area Ge epi-films. Thickness profiles of the electrodeposited Ge films showed thicknesses that decreased at distances further from the three-phase boundary between the liquid metal, aqueous electrolyte, and solid seed substrate, consistent with the premise that In specifically facilitates nucleation and crystal growth via surface diffusion. This study thus establishes 'open' ec-LPE as a method to synthesize single crystalline semiconductors and makes recommendations for improving the prospects of 'open' ec-LPE based on the cumulative observations presented herein.

Chapter 7 provides an overview of all the previous chapters in this thesis in addition to highlighting key observations or insights on unresolved work. Observations are made using liquid

Ga as an electrode in contact with alkaline aqueous electrolyte. Unusual features in the cyclic voltammetry including an inverted oxidation current when scanning reductively were observed. The effects of scan rate or the applied potential range are explored and a potential mechanism to understand the unusual cyclic voltammetry profiles is presented, which is suggestive of Ga^{1+} species being adsorbed at the interface of the liquid metal. Efforts in obtaining a flat liquid Ga electrode is also discussed. Specifically, mechanically spreading liquid Ga on a piece of $CuGa_2$ improves the wettability of the liquid Ga even during applied electrochemical bias. Observations are made which show that the curvature of the liquid metal is unchanged over a large electrochemical window due to this improved interfacial wetting behavior. Methods are outlined for effectively separating synthesized particles from the liquid metal surface for characterization. Preliminary results on the electronic properties of $Fe_{0.08\pm0.01}Co_{0.06\pm0.01}Ga_{0.86\pm0.01}$ are obtained through single particle conductivity measurements. Recommendations are made for purifying the products of ec-LLS using this same approach on a Ge nanowire to promote electromigration of the impurities.

1.6 References

1. Czochralski, J., A new method for the measurement of the crystallization rate of metals. *Zeitschrift für physikalische Chemie* **1918,** *92*, 219-221.
2. Mauk, M. G., 6 - Liquid-Phase Epitaxy. In *Handbook of Crystal Growth (Second Edition)*, Kuech, T. F., Ed. North-Holland: Boston, 2015; pp 225-316.
3. Benbow, E. M.; Dalal, N. S.; Latturner, S. E., Crystal growth and magnetic behavior of R6T13−xAlxMy phases (R=La, Nd; T=Mn, Fe; M=main group) grown from lanthanide-rich eutectic fluxes. *Journal of Solid State Chemistry* **2009,** *182* (11), 3055-3062.
4. He, H.; Tyson, C.; Saito, M.; Bobev, S., Synthesis and structural characterization of the ternary Zintl phases AE3Al2Pn4 and AE3Ga2Pn4 (AE=Ca, Sr, Ba, Eu; Pn=P, As). *Journal of Solid State Chemistry* **2012,** *188*, 59-65.
5. Stojanovic, M.; Latturner, S. E., Growth of new ternary intermetallic phases from Ca/Zn eutectic flux. *Journal of Solid State Chemistry* **2007,** *180* (3), 907-914.
6. Kanatzidis, M. G.; Pöttgen, R.; Jeitschko, W., The Metal Flux: A Preparative Tool for the Exploration of Intermetallic Compounds. *Angewandte Chemie International Edition* **2005,** *44* (43), 6996-7023.
7. Sebastian, C. P.; Malliakas, C. D.; Chondroudi, M.; Schellenberg, I.; Rayaprol, S.; Hoffmann, R.-D.; Pöttgen, R.; Kanatzidis, M. G., Indium Flux-Growth of Eu2AuGe3: A New Germanide with an AlB2 Superstructure. *Inorganic Chemistry* **2010,** *49* (20), 9574-9580.
8. Kalantar-Zadeh, K.; Rahim, M. A.; Tang, J., Low Melting Temperature Liquid Metals and Their Impacts on Physical Chemistry. *Accounts of Materials Research* **2021,** *2* (8), 577-580.
9. Martin, A.; Du, C.; Chang, B.; Thuo, M., Complexity and Opportunities in Liquid Metal Surface Oxides. *Chemistry of Materials* **2020,** *32* (21), 9045-9055.
10. Zavabeti, A.; Ou, J. Z.; Carey, B. J.; Syed, N.; Orrell-Trigg, R.; Mayes, E. L. H.; Xu, C.; Kavehei, O.; O'Mullane, A. P.; Kaner, R. B.; Kalantar-zadeh, K.; Daeneke, T., A liquid metal reaction environment for the room-temperature synthesis of atomically thin metal oxides. *Science* **2017,** *358* (6361), 332.
11. Dong, R.; Zhang, T.; Feng, X., Interface-Assisted Synthesis of 2D Materials: Trend and Challenges. *Chemical Reviews* **2018,** *118* (13), 6189-6235.
12. Ghasemian, M. B.; Mayyas, M.; Idrus-Saidi, S. A.; Jamal, M. A.; Yang, J.; Mofarah, S. S.; Adabifiroozjaei, E.; Tang, J.; Syed, N.; O'Mullane, A. P.; Daeneke, T.; Kalantar-Zadeh, K., Self-Limiting Galvanic Growth of MnO2 Monolayers on a Liquid Metal—Applied to Photocatalysis. *Advanced Functional Materials* **2019,** *29* (36), 1901649.
13. Elsen, A.; Festersen, S.; Runge, B.; Koops, C. T.; Ocko, B. M.; Deutsch, M.; Seeck, O. H.; Murphy, B. M.; Magnussen, O. M., In situ X-ray studies of adlayer-induced crystal nucleation at the liquid–liquid interface. *Proceedings of the National Academy of Sciences* **2013,** *110* (17), 6663.
14. David, R.; Miki, N., Tunable Noble Metal Thin Films on Ga Alloys via Galvanic Replacement. *Langmuir* **2018,** *34* (36), 10550-10559.
15. Wang, S.; Mao, Q.; Ren, H.; Wang, W.; Wang, Z.; Xu, Y.; Li, X.; Wang, L.; Wang, H., Liquid Metal Interfacial Growth and Exfoliation to Form Mesoporous Metallic Nanosheets for Alkaline Methanol Electroreforming. *ACS Nano* **2022,** *16* (2), 2978-2987.
16. Kochat, V.; Samanta, A.; Zhang, Y.; Bhowmick, S.; Manimunda, P.; Asif Syed Asif, S.; Stender Anthony, S.; Vajtai, R.; Singh Abhishek, K.; Tiwary Chandra, S.; Ajayan Pulickel, M., Atomically thin gallium layers from solid-melt exfoliation. *Science Advances* **2018,** *4* (3), e1701373.

17. Fahrenkrug, E.; Maldonado, S., Electrochemical Liquid–Liquid–Solid (ec-LLS) Crystal Growth: A Low-Temperature Strategy for Covalent Semiconductor Crystal Growth. *Accounts of Chemical Research* **2015,** *48* (7), 1881-1890.
18. Fahrenkrug, E.; Gu, J.; Maldonado, S., Electrodeposition of Crystalline GaAs on Liquid Gallium Electrodes in Aqueous Electrolytes. *Journal of the American Chemical Society* **2013,** *135* (1), 330-339.
19. DeMuth, J.; Ma, L.; Fahrenkrug, E.; Maldonado, S., Electrochemical Liquid-Liquid-Solid Deposition of Crystalline Gallium Antimonide. *Electrochimica Acta* **2016,** *197*, 353-361.
20. DeMuth, J.; Ma, L.; Lancaster, M.; Acharya, S.; Cheek, Q.; Maldonado, S., Eutectic-Bismuth Indium as a Growth Solvent for the Electrochemical Liquid-Liquid-Solid Deposition of Germanium Microwires and Coiled Nanowires. *Crystal Growth & Design* **2018,** *18* (2), 677-685.
21. Pattadar, D.; Cheek, Q.; Sartori, A.; Zhao, Y.; Giri, R. P.; Murphy, B.; Magnussen, O.; Maldonado, S., Evidence for Facilitated Surface Transport during Ge Crystal Growth by Indium in Liquid Hg–In Alloys at Room Temperature. *Crystal Growth & Design* **2021,** *21* (3), 1645-1656.
22. Fahrenkrug, E.; Biehl, J.; Maldonado, S., Electrochemical Liquid–Liquid–Solid Crystal Growth of Germanium Microwires on Hard and Soft Conductive Substrates at Low Temperature in Aqueous Solution. *Chemistry of Materials* **2015,** *27* (9), 3389-3396.
23. Zhao, Z.; Yang, C.; Wu, L.; Zhang, C.; Wang, R.; Ma, E., Preparation and Characterization of Crystalline Silicon by Electrochemical Liquid–Liquid–Solid Crystal Growth in Ionic Liquid. *ACS Omega* **2021,** *6* (18), 11935-11942.
24. Ma, L.; Lee, S.; DeMuth, J.; Maldonado, S., Direct electrochemical deposition of crystalline silicon nanowires at T≥ 60° C. *RSC Advances* **2016,** *6* (82), 78818-78825.
25. Acharya, S.; Ma, L.; Maldonado, S., Critical Factors in the Growth of Hyperdoped Germanium Microwires by Electrochemical Liquid–Liquid–Solid Method. *ACS Applied Nano Materials* **2018,** *1* (10), 5553-5561.
26. Pershan, P. S.; Schlossman, M., *Liquid Surfaces and Interfacs: Synchrotron X-ray Methods.* Cambridge University Press: Cambridge, 2012.
27. Regan, M. J.; Pershan, P. S.; Magnussen, O. M.; Ocko, B. M.; Deutsch, M.; Berman, L. E., X-ray reflectivity studies of liquid metal and alloy surfaces. *Physical Review B* **1997,** *55* (23), 15874-15884.
28. Carim, A. I.; Collins, S. M.; Foley, J. M.; Maldonado, S., Benchtop Electrochemical Liquid–Liquid–Solid Growth of Nanostructured Crystalline Germanium. *Journal of the American Chemical Society* **2011,** *133* (34), 13292-13295.
29. Ma, L.; Gu, J.; Fahrenkrug, E.; Maldonado, S., Electrochemical Liquid-Liquid-Solid Deposition of Crystalline Ge Nanowires as a Function of Ga Nanodroplet Size. *Journal of the American Chemical Society* **2014,** *161* (7), D3044-D3050.
30. Fahrenkrug, E.; Gu, J.; Jeon, S.; Veneman, P. A.; Goldman, R. S.; Maldonado, S., Room-Temperature Epitaxial Electrodeposition of Single-Crystalline Germanium Nanowires at the Wafer Scale from an Aqueous Solution. *Nano Letters* **2014,** *14* (2), 847-852.
31. DeMuth, J.; Fahrenkrug, E.; Maldonado, S., Controlling Nucleation and Crystal Growth of Ge in a Liquid Metal Solvent. *Crystal Growth & Design* **2016,** *16* (12), 7130-7138.
32. Biswas, S.; O'Regan, C.; Petkov, N.; Morris, M. A.; Holmes, J. D., Manipulating the Growth Kinetics of Vapor–Liquid–Solid Propagated Ge Nanowires. *Nano Letters* **2013,** *13* (9), 4044-4052.

33. Kim, B. J.; Wen, C. Y.; Tersoff, J.; Reuter, M. C.; Stach, E. A.; Ross, F. M., Growth Pathways in Ultralow Temperature Ge Nucleation from Au. *Nano Letters* **2012,** *12* (11), 5867-5872.
34. Schwalbach, E. J.; Voorhees, P. W., Phase Equilibrium and Nucleation in VLS-Grown Nanowires. *Nano Letters* **2008,** *8* (11), 3739-3745.
35. Cheek, Q.; Fahrenkrug, E.; Hlynchuk, S.; Alsem, D. H.; Salmon, N. J.; Maldonado, S., In Situ Transmission Electron Microscopy Measurements of Ge Nanowire Synthesis with Liquid Metal Nanodroplets in Water. *ACS Nano* **2020,** *14*, 2869-2879.
36. Ross, F. M., Opportunities and challenges in liquid cell electron microscopy. *Science* **2015,** *350* (6267), aaa9886.
37. Han, C.; Islam, M. T.; Ni, C., In Situ TEM of Electrochemical Incidents: Effects of Biasing and Electron Beam on Electrochemistry. *ACS Omega* **2021,** *6* (10), 6537-6546.
38. Liu, N.; Zhou, G.; Yang, A.; Yu, X.; Shi, F.; Sun, J.; Zhang, J.; Liu, B.; Wu, C.-L.; Tao, X.; Sun, Y.; Cui, Y.; Chu, S., Direct electrochemical generation of supercooled sulfur microdroplets well below their melting temperature. *Proceedings of the National Academy of Sciences* **2019,** *116* (3), 765-770.
39. Grahame, D. C., The Electrical Double Layer and the Theory of Electrocapillarity. *Chemical Reviews* **1947,** *41* (3), 441-501.
40. Demuth, J.; Fahrenkrug, E.; Ma, L.; Shodiya, T.; Deitz, J. I.; Grassman, T. J.; Maldonado, S., Electrochemical Liquid Phase Epitaxy (ec-LPE): A New Methodology for the Synthesis of Crystalline Group IV Semiconductor Epifilms. *Journal of the American Chemical Society* **2017,** *139* (20), 6960-6968.
41. Maldonado, S., The Importance of New "Sand-to-Silicon" Processes for the Rapid Future Increase of Photovoltaics. *ACS Energy Letters* **2020,** *5* (11), 3628-3632.
42. Gu, J.; Fahrenkrug, E.; Maldonado, S., Direct Electrodeposition of Crystalline Silicon at Low Temperatures. *Journal of the American Chemical Society* **2013,** *135* (5), 1684-1687.
43. Downes, N.; Cheek, Q.; Maldonado, S., Electroreduction of Perchlorinated Silanes for Si Electrodeposition. *Journal of The Electrochemical Society* **2021,** *168* (2), 022503.
44. Downes, N.; DeMuth, J.; Waelder, J.; Cheek, Q. B.; Bartels, H.; Maldonado, S., Si Electrochemical Liquid Phase Epitaxy: Low-Temperature Growth of Hyperdoped Epitaxial Si Films. *Chemistry of Materials* **2022**.
45. Pershan, P. S., Review of the highlights of X-ray studies of liquid metal surfaces. *Journal of Applied Physics* **2014,** *116* (22), 222201.
46. Pershan, P. S.; Schlossman, M., *Liquid Surfaces and Interfaces: Synchrotron X-ray Methods*. Cambridge University Press: Cambridge, 2012.
47. Weiss, A. H.; Deutsch, M.; Braslau, A.; Ocko, B. M.; Pershan, P. S., Novel x-ray diffractometer for liquid surface studies. *Review of Scientific Instruments* **1986,** *57* (10), 2554-2559.
48. Murphy, B. M.; Greve, M.; Runge, B.; Koops, C. T.; Elsen, A.; Stettner, J.; Seeck, O. H.; Magnussen, O. M., A novel X-ray diffractometer for studies of liquid-liquid interfaces. *Journal of Synchrotron Radiation* **2014,** *21* (Pt 1), 45-56.
49. Regan, M. J.; Kawamoto, E. H.; Lee, S.; Pershan, P. S.; Maskil, N.; Deutsch, M.; Magnussen, O. M.; Ocko, B. M.; Berman, L. E., Surface Layering in Liquid Gallium: An X-Ray Reflectivity Study. *Physical Review Letters* **1995,** *75* (13), 2498-2501.

50. Magnussen, O. M.; Ocko, B. M.; Regan, M. J.; Penanen, K.; Pershan, P. S.; Deutsch, M., X-ray reflectivity measurements of surface layering in liquid mercury. *Physical Review Letters* **1995,** *74* (22), 4444-4447.
51. Tostmann, H.; DiMasi, E.; Pershan, P. S.; Ocko, B. M.; Shpyrko, O. G.; Deutsch, M., Surface structure of liquid metals and the effect of capillary waves: X-ray studies on liquid indium. *Physical Review B* **1999,** *59* (2), 783-791.
52. Shpyrko, O. G.; Streitel, R.; Balagurusamy, V. S. K.; Grigoriev, A. Y.; Deutsch, M.; Ocko, B. M.; Meron, M.; Lin, B.; Pershan, P. S., Surface Crystallization in a Liquid AuSi Alloy. *Science* **2006,** *313* (5783), 77-80.
53. Huber, P.; Shpyrko, O. G.; Pershan, P. S.; Tostmann, H.; DiMasi, E.; Ocko, B. M.; Deutsch, M., Wetting behavior at the free surface of a liquid gallium–bismuth alloy: an X-ray reflectivity study close to the bulk monotectic point. *Colloids and Surfaces A: Physicochemical and Engineering Aspects* **2002,** *206* (1), 515-520.
54. Hazelnis, J. P.; Sartori, A.; Cheek, Q. B.; Giri, R. P.; MacInnes, M. M.; Murphy, B. M.; Magnussen, O. M.; Maldonado, S., Detection of Ge-Containing Adlayers at the Liquid Hg/Water Interface by In Situ X-ray Reflectivity in Aqueous Borate Electrolytes Containing Dissolved GeO2. *The Journal of Physical Chemistry C* **2022,** *126* (18), 8177-8189.
55. Elsen, A.; Festersen, S.; Runge, B.; Koops, C. T.; Ocko, B. M.; Deutsch, M.; Seeck, O. H.; Murphy, B. M.; Magnussen, O. M., In situ X-ray studies of adlayer-induced crystal nucleation at the liquid-liquid interface. *Proceedings of the National Academy of Sciences* **2013,** *110* (17), 6663-8.
56. Murphy, B. M.; Festersen, S.; Magnussen, O. M., The Atomic scale structure of liquid metal–electrolyte interfaces. *Nanoscale* **2016,** *8* (29), 13859-13866.
57. Runge, B.; Festersen, S.; Koops, C. T.; Elsen, A.; Deutsch, M.; Ocko, B. M.; Seeck, O. H.; Murphy, B. M.; Magnussen, O. M., Temperature- and potential-dependent structure of the mercury-electrolyte interface. *Physical Review B* **2016,** *93* (16), 165408.
58. Pershan, P. S.; Als-Nielsen, J., X-Ray Reflectivity from the Surface of a Liquid Crystal: Surface Structure and Absolute Value of Critical Fluctuations. *Physical Review Letters* **1984,** *52* (9), 759-762.
59. Als-Nielsen, J.; McMorrow, D., Refraction and Reflection from Interfaces. In *Elements of Modern X-ray Physics*, Wiley: 2011; pp 69-112.
60. Als-Nielsen, J., X-ray studies of phase transitions on surfaces. *Physica B+C* **1984,** *126* (1), 145-148.
61. Runge, B. X-Ray Scattering Investigations of the Temperature and Potential Dependent Structure of the Mercury-Electrolyte Interface. Christian-Albrechts-Universit¨at zu Kiel, 2015.
62. Sartori, A.; Giri, R. P.; Fujii, H.; Hövelmann, S. C.; Warias, J. E.; Jordt, P.; Shen, C.; Murphy, B. M.; Magnussen, O. M., Role of chemisorbing species in growth at liquid metal-electrolyte interfaces revealed by in situ X-ray scattering. *Nature Communications* **2022,** *13* (1), 5421.
63. Dumke, M. F.; Tombrello, T. A.; Weller, R. A.; Housley, R. M.; Cirlin, E. H., Sputtering of the gallium-indium eutectic alloy in the liquid phase. *Surface Science* **1983,** *124* (2), 407-422.
64. Maruyama, T.; Matsuda, K.; Naritsuka, S., Multinuclear layer-by-layer growth on Ge(111) by LPE. *Journal of Crystal Growth* **2005,** *275* (1), e2155-e2160.
65. Won, D.; Weng, X.; Redwing, J. M., Effect of indium surfactant on stress relaxation by V-defect formation in GaN epilayers grown by metalorganic chemical vapor deposition. *Journal of Applied Physics* **2010,** *108*, 093511.

66. Won, D.; Weng, X.; Redwing, J. M., Metalorganic chemical vapor deposition of N-polar GaN films on vicinal SiC substrates using indium surfactants. *Applied Physics Letters* **2012,** *100*, 021913.
67. Yang, Y.; Wei, M., Intermetallic compound catalysts: synthetic scheme, structure characterization and catalytic application. *Journal of Materials Chemistry A* **2020,** *8* (5), 2207-2221.
68. Downes, N.; DeMuth, J.; Waelder, J.; Cheek, Q. B.; Bartels, H.; Maldonado, S., Si Electrochemical Liquid Phase Epitaxy: Low-Temperature Growth of Hyperdoped Epitaxial Si Films. *Chemistry of Materials* **2022,** *34* (24), 10861-10872.
69. Zhao, Z.; Sun, M.; Yang, C.; Zhang, C., Electrodeposition of crystalline germanium thin films by the electrochemical liquid-liquid-solid method. *Journal of Electroanalytical Chemistry* **2023,** *948*, 117829.
70. Zhang, T.; Fahrenkrug, E.; Maldonado, S., Electrochemical Liquid-Liquid-Solid Deposition of Ge at Hg Microdroplet Ultramicroelectrodes. *Journal of The Electrochemical Society* **2016,** *163* (9), D500-D505.

Chapter 2 Detection of Ge-Containing Adlayers at the Liquid Hg/Water Interface by In Situ X-Ray Reflectivity in Aqueous Borate Electrolytes Containing Dissolved GeO_2[2]

2.1 Preface

The following work details in-situ X-ray reflectivity (XRR) measurements of the liquid Hg interface using Ge ec-LLS conditions. The XRR data was collected by Andrea Sartori, Quintin Cheek, Rajendra P. Giri, and Molly MacInnes under the equal guidance of Stephen Maldonado, Bridget M. Murphy and Olaf M. Magnussen. Andrea Sartori and Joshua P. Hazelnis contributed equally to the XRR data analysis and interpretation. Joshua P. Hazelnis collected the potential of zero charge measurements. The writing, figures, and discussions of the work were equal in contribution between Joshua P. Hazelnis, Andrea Sartori, Stephen Maldonado, Bridget M. Murphy, and Olaf M. Magnussen.

2.2 Introduction

Room temperature liquid metal interfaces are potent reaction sites for the syntheses of inorganic, crystalline materials.[1-8] In general, the ductility of a liquid metal facilitates mechanical removal of material from its surface.[2, 9, 10] For the preparation of ultra-thin oxides, the surface tension of the liquid metal alloys helps dictate the surface oxide composition.[2] For electrodeposition of crystalline metals, metal salts, and covalent semiconductors, liquid metals are advantageous because they can serve as reaction solvents for species electroreduced at the solution/electrode interface.[11-16] Further development of liquid-metal-based material growth and processing requires detailed insight into the underlying interface structure and interface processes, similar to that obtained for growth at the solid-vapor and solid-liquid interface.[17, 18] However, atomic-scale data on liquid metal interfaces is currently scarce, mostly because these interfaces are difficult to access by structure-sensitive experimental techniques.

[2] Reprinted (adapted) with permission from Hazelnis, J. P.; Sartori, A.; Cheek, Q. B.; Giri, R. P.; MacInnes, M. M.; Murphy, B. M.; Magnussen, O. M.; Maldonado, S., Detection of Ge-Containing Adlayers at the Liquid Hg/Water Interface by In Situ X-ray Reflectivity in Aqueous Borate Electrolytes Containing Dissolved GeO2. *The Journal of Physical Chemistry C* 2022**,** *126* (18), 8177-8189. Copyright 2022 American Chemical Society.

Operando X-ray techniques have previously been used to probe electrode/electrolyte interfaces,[19] but one of the few methods that is capable of interrogating liquid metal interfaces is X-ray reflectivity (XRR). From XRR data, the interface structure along the surface normal can be directly determined with up to atomic resolution.[20] Historically, XRR measurements were essential in confirming atomic layering within the near surface region of liquid metals in contact with their vapor.[21-24] More recently, *in situ* XRR methods that probe liquid solution-liquid metal interfaces have been realized.[25-27] These methods employ high photon energies, which allow to access these deeply buried liquid-liquid interfaces due to their penetration depth. XRR measurements of pristine Hg electrodes in aqueous electrolytes were used to corroborate the electrocapillarity law, i.e. the maximum in surface tension and, consequently, the minimum in roughnesses of liquid metals at the potential of zero charge (E_{pzc}), as well as the polarization of the surface electron density profile according to the Schmickler-Henderson theory.[28] Similarly, the temperature-dependences of factors that govern the interfacial structure at water/liquid Hg contacts have been identified by XRR.[28] Two more recent sets of studies have illustrated the value of XRR in studying electrodeposition processes at water/liquid metal interfaces. XRR measurements combined with grazing incidence X-ray diffraction elucidated the initial steps in the nucleation and growth of lead halide crystals at liquid Hg electrolyte interfaces.[8, 29] Other XRR data have separately identified the surface composition and structure of liquid Hg-In alloy electrodes used to grow Ge crystals.[30]

This study utilizes XRR to determine *in situ* the interface between liquid Hg and aqueous $Na_2B_4O_7$ containing dissolved GeO_2. This electrolyte is of interest since electrodeposition of Ge nanowires,[14] microwires,[31] and epitaxial films[32] is possible with a variety of liquid metals. Still, little is known about the nature of the interface in this electrolyte, particularly when under potential control. Given the wealth of information on Hg interfaces, XRR analysis of liquid Hg electrodes in $Na_2B_4O_7$ (*aq*) represents an ideal starting point. Accordingly, the results from a series of potential-dependent XRR experiments and accompanying electrochemical measurements are presented that provide atomic-scale details on the Hg electrode surface in $Na_2B_4O_7$(*aq*), both with and without dissolved GeO_2. Notably, persistent adsorption of a Ge species is identified for the first time on Hg in solutions containing dissolved GeO_2. As demonstrated below, at sufficiently positive potentials, this adsorbate unexpectedly undergoes a transformation to a condensed phase at the water/Hg interface at positive potentials.

2.3 Experimental

2.3.1 Materials and Chemicals

Germanium (IV) oxide (99.999%, ChemPur), sodium tetraborate (99.998%, ChemPur), and mercury (99.999+%, ChemPur) were used as received. Water with a resistivity >18.2 MΩ·cm was used throughout.

2.3.2 Potential of Zero Charge Measurement

Measurements of E_{pzc} were performed using a custom-built, pendant-drop optical measurement system consisting of a digital camera (640 x 480p resolution) positioned perpendicular to a pendant Hg droplet (r = 695.2 um) immersed in an electrochemical cell with a flat optical window. A white-light, LED microscope ring light with a diffuser was placed opposite to the camera for illumination. Images were collected and processed with a custom ImageJ script using an algorithm[33, 34] for the surface tension as a function of the drop shape. Estimates of E_{pzc} were then obtained from the maximum of parabolic fits of the potential-dependent surface tension data. Cell temperature was monitored throughout the course of the experiment (25 ±1°C). All reported values were performed in triplicate and the error bars represent the sample standard deviation.

2.3.3 X-Ray Reflectivity Measurements

XRR measurements of the liquid metal-liquid electrolyte interfaces were performed using the Liquid Interface Scattering Apparatus (LISA) diffractometer[26] at beamline P08 of the PETRA III synchrotron source at DESY in Hamburg, Germany. A photon energy of 25 keV with a beam size of 0.4 mm (horizontal) and 0.1 mm (vertical) was chosen. Data were collected with a GaAs Lambda detector (1536 x 512 array of pixels with a pixel height of 55 μm). Beam attenuators were used to ensure that the count intensity was $\leq 10^5$ counts per pixel. Reflectivities were measured as a function of the incidence and exit angle $\alpha = \beta$ of the X-rays impinging on the interface, as shown schematically in Figure 1.5. The measured XRR intensity was obtained from integration of a detector area corresponding to a vertical and horizontal acceptance of 0.4° and 0.08°, respectively. The background intensity from X-ray scattering from bulk Hg and the electrolyte was determined at a 0.08° horizontal offset and subtracted from the main signal. The XRR curves were obtained

by normalizing the background-subtracted detector signal by the direct beam intensity and are presented as a function of q_z, where $q_z = (4\pi/\lambda)\cdot\sin\alpha$ and λ is the wavelength of the X-rays.

The sample was kept in a custom-designed electrochemical X-ray scattering cell similar to that described previously.[27] The closed cell featured a headspace separation gap of 26.5 mm between the top Hg interface and the top window and a radius of 2.75 cm for the Hg pool. The general beam path of the X-ray beam through thin PEEK windows is shown in Figure 1.5. Electrolyte solutions were purged with $N_2(g)$ for at least 30 minutes prior to injection into the cell and the headspace was kept under a slight positive pressure with $N_2(g)$ throughout all measurements. Upon assembly, the Hg electrode was held at a constant potential with respect to a saturated calomel electrode (SCE) for at least 15 minutes before the reflectivity measurements to ensure a stable interface. A digital, computer-controlled potentiostat (Ametek Modulab) was used throughout. Electrochemical data are presented in the polarographic ('Texas') convention, i.e. cathodic currents are plotted as positive and more negative potentials plotted to the right. All potentials are reported here with respect to SCE.

For XRR measurements collected at a constant applied potential, at least two XRR scans were taken. In these experiments, a random sequence of the applied potential values was used to eliminate the possibility of cumulative, systematic bias. A full set of angle-dependent XRR data from small (0.04 $Å^{-1}$) to large (2.5 $Å^{-1}$) values of the surface-normal scattering vector, q_z, took between 0.6 to 1.5 hours to collect, depending on the angle resolution at large q_z and signal integration time.

Fitting of XRR data was performed in a sequential process through custom-written python scripts. The first round of fitting focused on global optimization, using pre-defined upper and lower bounds for each fitting parameter. Subsequent fitting rounds were performed to refine the value of each parameter individually. The uncertainties in the reported fit parameters were calculated from a least squares analysis and denote the precision of that parameter towards the total fit rather than a sample standard deviation.

2.3.4 Modelling of XRR Data.

The experimental X-ray reflectivity curves, $R(q_z)$, were normalized by the Fresnel reflectivity, $R_F(q_z)$, of a perfectly sharp interface in the absence of any interfacial roughness, between Hg and the aqueous electrolyte. The deviations of $R(q_z)$ from $R_F(q_z)$ contain information

on the interface structure, in particular the distance-dependent electron density normal to the surface plane, $\rho_e(z)$. The relation between electron density profile and reflectivity is given by the so-called master formula,[35]

$$\frac{R(q_z)}{R_F(q_z)} = \left| \frac{1}{\rho_\infty} \int \frac{d\rho_e(z)}{dz} e^{izq_z} dz \right|^2$$

Equation 2.1

where ρ_∞ is equal to the difference in the electron densities of the bulk solvent and the bulk Hg.

The simplest model assuming coherent reflectivity employed here to describe $\rho_e(z)$ throughout the electrolyte, interface, and Hg electrode is described by *Equation* 2.2,

$$\rho_e(z) = \rho_{electrolyte}(z) + \rho_{DCM,Hg}(z)$$

Equation 2.2

where $\rho_{electrolyte}(z)$ and $\rho_{DCM,\,Hg}(z)$ represent the distance-dependent contributions of the electrolyte solution and the 'distorted crystal model' (DCM)[20, 24] for the Hg electrode, respectively. The electrolyte term is given by a complementary error function. The 'adlayer'[36] form of the distorted crystal model describes the outermost atomic Hg layer with a discrete Gaussian term and the subsequent Hg layers by a decay function resulting from an infinite series of Gaussians with increasing width.[8, 24, 25, 28, 37]

$$\rho_{electrolyte}(z) = \frac{1}{2}\rho_{e,H_2O}\left(\operatorname{erfc}\left(\frac{z - z_{H_2O}}{\sigma_{H_2O}\sqrt{2}}\right)\right)$$

Equation 2.3

$$\rho_{DCM,Hg}(z) = F_{Hg}(z) \otimes \left[\frac{\rho_{e,ad-Hg}}{\rho_{e,Hg}} \frac{1}{\sigma_{ad}\sqrt{2\pi}} e^{\frac{-(z-z_{ad})^2}{2\sigma_{ad}^2}} + \sum_{n=0}^{\infty} \frac{d}{\sqrt{\sigma_i^2 + n\sigma_b^2}\sqrt{2\pi}} e^{\frac{-(z-nd)^2}{2(\sigma_i^2 + n\sigma_b^2)}} \right]$$

Equation 2.4

In these expressions, z_{H_2O} , σ_{H_2O} , ρ_{H_2O} describe the position, width, and electron density of the electrolyte front. $\rho_{e,ad-Hg}$, σ_{ad} , z_{ad} are respectively the amplitude, root mean square displacement and position of the low density Hg adlayer, d is the spacing between the atomic layers of Hg, F_{Hg} (z) is the Fourier transform of the Hg atomic form factor, σ_i is the surface roughness (i.e. the combination of the intrinsic roughness and the effect of capillary waves),[28] and σ_b describes how

the roughness of each atomic layer increases with increasing layer number n.[20, 24] In this presentation, the ratio of adlayer and bulk electron densities corresponds to a fractional monolayer coverage, i.e. number of adlayer units per Hg atom on the surface.

Inserting *Equation* 2.2, *Equation* 2.3, and *Equation* 2.4 into *Equation* 2.1, we obtain an explicit dependence of $\frac{R(q_z)}{R_F(q_z)}$ with q_z.

$$\frac{R(q_z)}{R_F(q_z)} = \left| \left(\frac{1}{\rho_{e,Hg} - \rho_{e,H_2O}} \right) \left(\begin{array}{l} \left(\frac{f_{Hg}^0(q_z) + f_{Hg}^{'}}{Z_{Hg} + f_{Hg}^{'}} \right) \left(iq_z d \frac{e^{\frac{-q_z^2\sigma_i^2}{2}}}{\left(1 - e^{iq_z d - \frac{q_z^2\sigma_b^2}{2}}\right)} + iq_z \frac{\rho_{e,ad-Hg}}{\rho_{e,Hg}} e^{-\left(iq_z z_{ad} - \frac{q_z^2\sigma_{ad}^2}{2}\right)} \right) \\ -\rho_{e,H_2O} e^{-\left(iq_z z_{H_2O} - \frac{q_z^2\sigma_{H_2O}^2}{2}\right)} \end{array} \right) \right|^2$$

Equation 2.5

where $f_{Hg}^0(q_z)$ and $f_{Hg}^{'}$ are the angle-dependent Hg atomic form factor and the dispersion correction, respectively, and Z_{Hg} is the atomic number of Hg.

As discussed in the next section, fitting XRR data collected in solutions with dissolved GeO_2 and potentials more negative than -0.2 V with *Equation* 2.2 yielded notably larger values of $\rho_{e,ad-Hg}$. Accordingly, *Equation* 2.2 was refined to include a set of additional Gaussian terms, $\rho_{HGeO_3^-}(z)$, that constituted an 'adlayer' of H_2GeO_3/$HGeO_3^-$ (*Appendix Equation*.A.3, Appendix A). H_2GeO_3 and $HGeO_3^-$ are the predominant forms of dissolved GeO_2 at the solution pH of 9.13.[38, 39] In these fits, the terms that pertained to the Hg 'adlayer' were fixed at the values determined from the fits of the XRR data in the blank 0.1 M $Na_2B_4O_7$ electrolyte and corresponding potential. The position, width, and electron density of $\rho_{HGeO_3^-}(z)$ were free fit parameters.

The XRR data collected in the electrolyte with dissolved GeO_2 at -0.2 V could not be adequately fit in the same way even allowing for simple refinements to *Equation* 2.2. Instead, a two-step approach was adopted for fitting. First, a preliminary model was generated by adding multiple Gaussian terms without specific atomic form factors to *Equation* 2.2.

$$\rho_e(z) = \rho_{electrolyte}(z) + \sum_{m=1}^{3} \frac{\rho_{ad,m}}{\sigma_{ad}\sqrt{2\pi}} e^{\frac{-(z-z_{ad,m})^2}{2\sigma_{ad,m}^2}} + \rho_{DCM,Hg}(z)$$

Equation 2.6

The intent of these general Gaussian terms was to assess where excess electron density was needed to yield a good match to the data to inform a subsequent, structure-specific model. *Equation* 2.6 represents the fewest Gaussian terms necessary. Second, a more structure-specific model was explored based on the formation of GeO_2 at the water/Hg interface (*vide infra*). For brevity, the full expression of the electron density profile normal to the surface plane and of the resulting $\frac{R(q_z)}{R_F(q_z)}$ for this second model is given by *Appendix Equation*.A.11 in the Appendix A. *Equation* 2.7 is presented here to summarize the essence of this second model,

$$\rho_e(z) = \rho_{electrolyte}(z) + \rho_{DCM,Hg}(z) + \theta_{GeO_2} \cdot \left(\rho_{ad,Ge/GeO_2}(z) + \rho_{e,GeO_2}(z)\right) + (1-\theta_{GeO_2}) \cdot \rho_{ad,Ge/Hg}(z)$$

Equation 2.7

Equation 2.7 describes the Hg surface composition as the sum of two separate surface types, which coexist on length scales smaller than the X-ray coherence length. One fraction of the surface, θ_{GeO2}, was considered as having a solid bilayer of GeO_2 deposited on the Hg surface. In this part of the surface, the electron density was modeled by 2 additional Gaussian terms with Ge form factors and 6 additional Gaussian terms with O form factors. Based on the results of the preliminary model, the distances between these Gaussians were chosen to correspond to rutile GeO_2 oriented with the [110] direction along the surface normal. Furthermore, a third set of Gaussian terms with Ge and O atomic form factors that described specifically the accumulation of (solvated) $H_2GeO_3/HGeO_3^-$ at the water/GeO_2 interface was included. In the remaining surface fraction (i.e. '1- θ_{GeO2}'), an identical structure as Hg at the more negative potentials was assumed. This part of the surface was modeled by a set of Gaussians with Ge and O atomic form factors that described the adsorption of $H_2GeO_3/HGeO_3^-$ on the bare Hg surface.

2.4 Results

Figure 2.1 presents the voltammetric behavior of Hg immersed in either aqueous 0.1 M $Na_2B_4O_7$ or aqueous 0.1 M $Na_2B_4O_7$ with 0.05 M dissolved GeO_2. In the potential range from -0.1

to -0.9 V, Hg is neither electrochemically oxidized nor does it readily support H^+ reduction, as shown by the dashed line in Figure 2.1. Repeated scanning of Hg in the blank electrolyte over this potential range effected no change in voltammetric response. Although the potential range in Figure 2.1 was not sufficiently negative to support the $4e^-$ reduction of dissolved GeO_2, addition of dissolved GeO_2 to the $Na_2B_4O_7$ electrolyte results in a clear change in the voltammogram (solid line). A sizeable increase in oxidative current at potentials more positive than -0.2 V was noted in the presence of dissolved GeO_2. Similarly, there was a notable increase in reductive current in the potential range between -0.1 and -0.6 V of the potential sweep to more negative values. The corresponding anodic and cathodic charge densities (corrected for the contribution of double layer charging) were of comparable magnitude, i.e. 6.9 μC cm^{-2} and 10.5 μC cm^{-2}, respectively. The pronounced hysteresis between anodic and cathodic charge transfer rules out a simple reversible pseudo-capacitive process, such as electrochemical adsorption, and suggest a more complex behavior that involves nucleation and growth.

To determine the potential-dependent structure of the electrolyte/Hg interface, *in situ* XRR measurements were performed. First, XRR data were obtained in the blank aqueous $Na_2B_4O_7$ electrolyte and compared with data collected within the same synchrotron experiment in aqueous NaF. The NaF (*aq*)/Hg system is arguably the best studied liquid metal electrochemical system and considered as the prototypical case of a non-specifically adsorbing electrochemical double layer.[40-43] The extant XRR literature on this system supports this view and suggests that the interface is atomically abrupt [25, 28] and exhibits a similar surface layering as the vacuum/Hg interface.[24, 44]

The characteristic electron density profile along the surface normal, $\rho_e(z)$, for NaF (*aq*)/Hg (and similar interfaces between liquid metals and non-specifically adsorbing electrolyte)[20] is shown in Figure 2.2a. $\rho_e(z)$ contains contributions from the atomic surface layering in the Hg bulk (gray), a lower density Hg adlayer (green), and the electrolyte solution (blue). For low-Z ions, such as Na^+ and F^-, the X-ray scattering cross sections are similar to water and the electrolyte can thus be described by a single complementary error-function profile. Furthermore, Figure 2.2a depicts

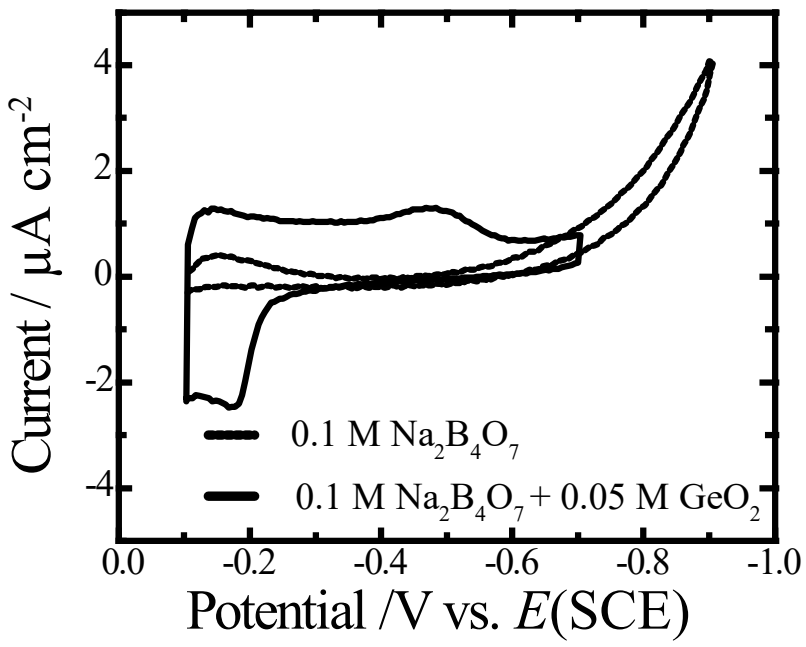

Figure 2.1 Voltammetric responses for a mercury electrode immersed in 0.1 M $Na_2B_4O_7$ (aq) (dashed line) and 0.1 M $Na_2B_4O_7$ + 0.05 M GeO_2 (aq) (solid line). Scan rate: 0.02 V s^{-1}

characteristic positions and widths that are employed as structural parameters in the models used to fit the data.

In the following, the XRR data are presented in the form of normalized reflectivity curves, R/R_F, plotted versus the surface normal scattering vector q_z (the corresponding experimentally measured X-ray reflectivities, $R(q_z)$, are presented in Figure 2.3. Figure 2.2b illustrates the characteristic shape of these XRR curves for Hg immersed in either 0.01 M NaF (*aq*) or 0.1 M $Na_2B_4O_7$ (*aq*) at the identical potential of -0.2 V. As clearly visible, the two curves are equivalent within the measurement errors over the entire q_z range. This observation is in accordance with the weak X-ray scattering of $Na_2B_4O_7$ and indicates a negligible influence of these electrolyte species on the Hg surface structure, suggesting the absence of strong chemisorption. R/R_F first decays up to $q_z \approx 1$ Å^{-1}, reflecting the finite roughness of the interface, and then increases up to a peak at $q_z \approx 2.2$ Å^{-1}. The latter is the 'pseudo-Bragg' peak, caused by the atomic Hg surface layering.[8, 21, 25, 28]

Quantitative structural data were obtained by fitting the R/R_F curves by the model function given by *Equation* 2.5, which resulted in the structure parameters given in Table 2.1. We first performed fits of the XRR data for Hg immersed in 0.01 M NaF (*aq*). Here, the electrolyte parameters (z_{H_2O} , ρ_{H_2O}) and the atomic layering distance in Hg (d) were set to established values for this system[28] while the parameters for the Hg adlayer (ρ_{ad}, z_{ad}) and the atomic roughnesses (σ_b and σ_i) were fitted. The subsequent fit of the XRR data for Hg immersed in 0.1 M $Na_2B_4O_7$ (*aq*) was performed in a similar fashion but with the position of the Hg adlayer fixed at the value obtained in NaF. Unsurprisingly, the fit parameters (Table 2.1) and the corresponding electron density profiles (Figure 2.2c) for the NaF and $Na_2B_4O_7$ datasets are statistically indistinguishable. More importantly, the fit parameters here are in good agreement with a previous detailed XRR study of the NaF (*aq*)/Hg system.[28] Together with the voltammetric data, this point verifies that the measurements reported here are sound and free of chemical contaminations which may otherwise disrupt the interfacial ordering. The data in Figure 2.2b,c imply the $Na_2B_4O_7$ (*aq*)/Hg interface is structurally similar to the NaF (*aq*)/Hg system despite differences in anion identity, ionic strength, and pH. As a result, these data support the contention that XRR data for Hg immersed in $Na_2B_4O_7$ (*aq*) afford a suitable reference point when changes are made to the electrolyte composition.

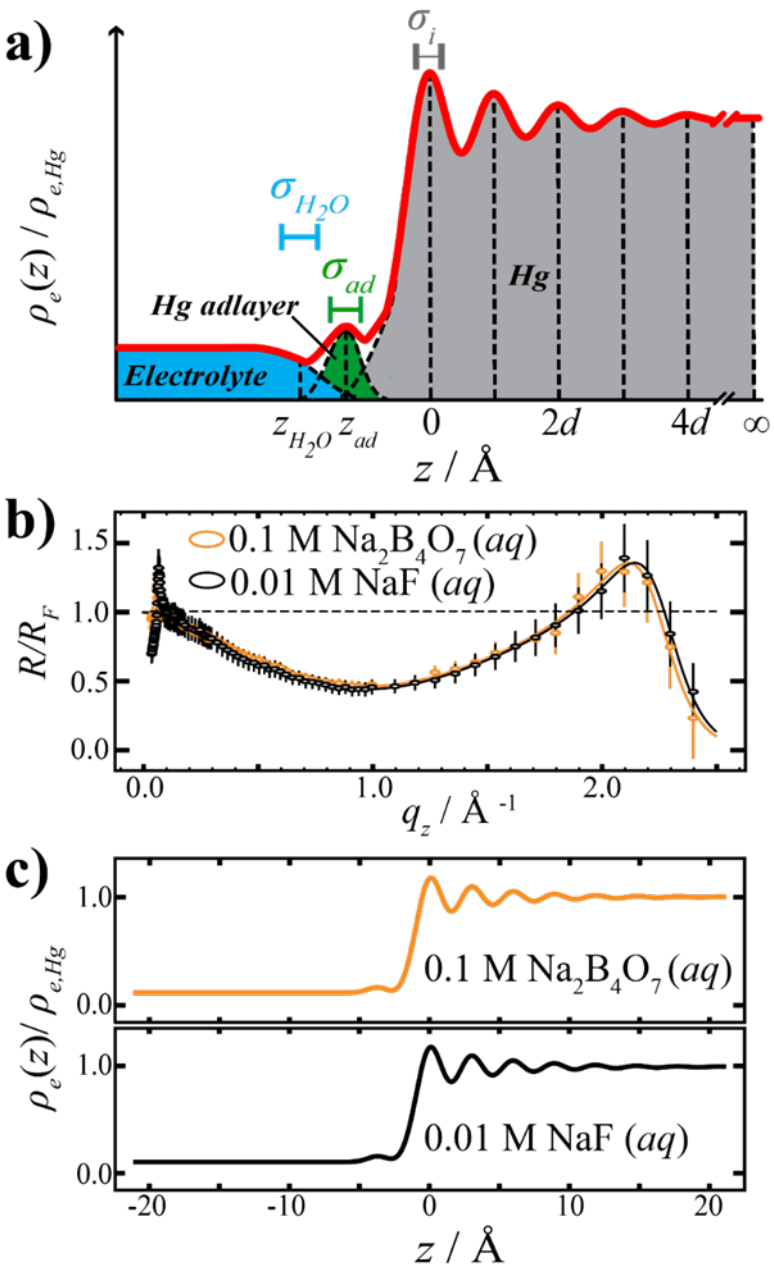

Figure 2.2 a) Schematic depiction of the model function for the electron density profile along the surface normal that was employed in the fitting of the XRR data. Contributions from the electrolyte, the Hg 'adlayer', and bulk Hg as well as the central fit parameters are indicated. b) Plot of the X-ray reflectivity normalized to the Fresnel reflectivity, R/R_F, vs. surface-normal momentum transfer, q_z, for a Hg electrode immersed in deaerated 0.1 M $Na_2B_4O_7$ (*aq*) (orange) or 0.01 M NaF(*aq*) (black) at -0.2 V. Solid lines denote best fits of the data with the model given by *Equation* 2.5. The resulting values of the model parameters are listed in Table 2.1. The corresponding electron density profiles are shown in c).

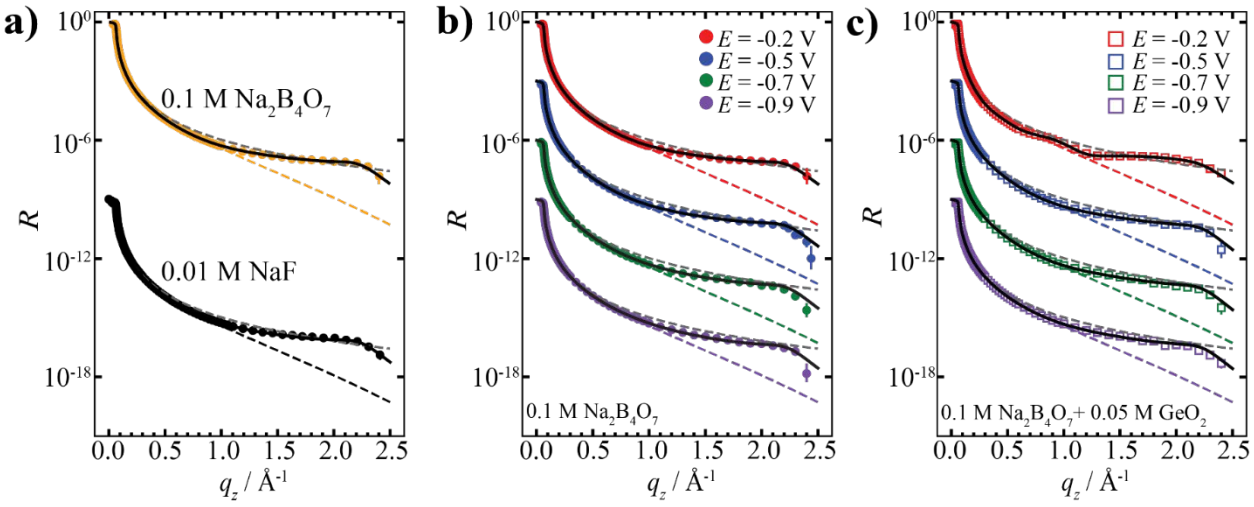

Figure 2.3 a) Plots of the absolute X-ray reflectivity vs. momentum transfer perpendicular to the surface for a Hg electrode immersed in deaerated electrolyte containing either 0.1 M $Na_2B_4O_7$(*aq*) or 0.01 M NaF(*aq*). These data were normalized in Figure 2.2 of the main text. b) Plots of the absolute X-ray reflectivity vs. momentum transfer perpendicular to the surface in 0.1 M $Na_2B_4O_7$(*aq*) at four different potentials: E = -0.2 V (red circles), -0.5 V (blue circles), -0.7 V (green circles), and -0.9 V (purple circles). These data were normalized in Figure 2.4 of the main text. c) Plots of the absolute X-ray reflectivity vs. momentum transfer perpendicular to the surface in 0.1 M $Na_2B_4O_7$ (*aq*) and 0.05 M GeO_2. For the data at E < -0.2 V, the solid black lines denote the corresponding best fit of the data using *Equation* 2.2, For the data at E = -0.2 V, the solid black lines indicate the best fit following the model of *Equation* 2.5. These data were normalized in Figure 2.5 of the main text. In all panels, curves are offset for visual clarity.

Table 2.1 Parameters of the best fits of the XRR data by *Equation* 2.5 [a,b,c]

Electrolyte	*Potential*	σ_{H2O} /Å	σ_i /Å	σ_b /Å	$\rho_{e,ad\text{-}Hg}/\rho_{e,Hg}$ /Å	σ_{ad} /Å	z_{ad} /Å
0.01 M NaF							
	-0.2 V	-0.95 ± 0.01	0.95 ± 0.01	0.48 ± 0.01	0.21 ± 0.01	0.95 ± 0.01	-3.64 ± 0.23
0.1 M $Na_2B_4O_7$							
	-0.2 V	-0.94 ± 0.01	-0.94 ± 0.01	0.49 ± 0.01	0.24 ± 0.01	0.94 ± 0.01	-3.64[b]
	-0.5 V	-0.97 ± 0.01	-0.97 ± 0.01	0.49[c]	0.21 ± 0.01	0.97 ± 0.01	-3.64[b]
	-0.7 V	-1.00 ± 0.01	-1.00 ± 0.01	0.49[c]	0.16 ± 0.01	1.00 ± 0.01	-3.64[b]
	-0.9 V	-1.01 ± 0.01	-1.01 ± 0.01	0.49[c]	0.10 ± 0.01	1.01 ± 0.01	-3.64[b]
0.1 M $Na_2B_4O_7$ + 0.05 M GeO_2							
	-0.5 V	-1.00 ± 0.01	-1.00 ± 0.01	0.49[c]	0.31 ± 0.01	1.00 ± 0.01	-3.64[b]
	-0.7 V	-1.01 ± 0.01	-1.01 ± 0.01	0.49[c]	0.27 ± 0.01	1.01 ± 0.01	-3.64[b]
	-0.9 V	-1.01 ± 0.01	-1.01 ± 0.01	0.49[c]	0.21 ± 0.01	1.01 ± 0.01	-3.64[b]

a. The data collected in 0.01 M NaF (*aq*) and in 0.1 M $Na_2B_4O_7$ (*aq*) based electrolyte were modelled using *Equation* 2.2 and $\rho_{e,ad-Hg} = 0.1\ \rho_{e,Hg}$, z_{H2O} = -1.00 Å, and d = 2.75 Å based on Reference 27. The data in 0.1 M $Na_2B_4O_7$ + 0.05 M GeO_2 (*aq*) at -0.2 V could not be described by this model and is thus not included here.

b. For data collected in 0.1 M $Na_2B_4O_7$ (*aq*) base electrolyte, z_{ad} was not a free fit parameter, but kept constant at its value obtained in fits of the data in 0.01 M NaF(*aq*) at-0.2 V.

c. For data collected in 0.1 M $Na_2B_4O_7$ (*aq*) base electrolyte, σ_b was obtained from the data in 0.1 M $Na_2B_4O_7$ (*aq*) at -0.2 V and then used as a constant value for the fits of the data at potentials < -0.2 V.

Subsequently, we assessed the potential dependence of the XRR curves in 0.1 M $Na_2B_4O_7$ (*aq*). Figure 2.4a shows the R/R_F data collected at several applied potentials. The best fits by *Equation* 2.5 are presented as solid black lines. They were performed using the same procedure described above but with the same Hg layering decay (i.e., fixed σ_b) as at -0.2 V. The latter was motivated by previous studies that showed that this decay is a Hg bulk property and not affected by the potential.[8] In the corresponding electron density profiles (Figure 2.4b) a characteristic behavior is apparent. The position of the 'pseudo-Bragg' peak at ≈ 2.2 Å^{-1} is potential-independent but its intensity decreases towards more negative potentials. A similar behavior was observed previously in the NaF (*aq*)/Hg system.[28] All of the data are well fit by *Equation* 2.5 using parameters for bulk Hg, bulk electrolyte, and the water/Hg interface that are in good agreement with the parameters reported in the literature for NaF (*aq*)/Hg.[25, 28] On the basis of these fits, the change in the intensity of the layering peak at different potentials can be attributed to changes in the interface roughness, σ_i, and $\rho_{e,ad-Hg}$ (Figure 2.4b, inset),[25, 28] in accord with previous XRR measurements of Hg immersed in NaF (*aq*).[37]

Figure 2.5 shows normalized X-ray reflectivity data collected at the same potentials as in Figure 2.4 but with dissolved GeO_2 added to the $Na_2B_4O_7$ (*aq*) electrolyte. At potentials equal to or more negative than -0.5 V, the R/R_F curves had the same general features as those shown in Figure 2.4. That is, they exhibited a smooth decay and subsequent rise to the 'pseudo-Bragg' peak with increasing q_z and are well described by the model function given by *Equation* 2.5. However, the measured data differed quantitatively from the measurements performed in the absence of dissolved GeO_2 suggesting a difference in structure or electron density at the liquid metal/electrolyte interface.

Figure 2.6 illustrates this point more directly. At applied potentials of -0.5, -0.7, and -0.9 V (Figure 2.6a), the differences in the XRR data measured in the absence and in the presence of dissolved GeO_2 are larger than the measurement standard deviations at $q_z \leq 1$ Å^{-1}. The fits to *Equation* 2.5 indicate that the differences in the data can largely be ascribed to an increase in the electron density of the 'adlayer' component (Figure 2.6b, Table 2.1). Figure 2.6b shows the fitted $\rho_{e,ad-Hg}$ values from the data in the presence and absence of dissolved GeO_2 as a function of potential. The two datasets have the same profile but the values in the presence of dissolved GeO_2 are uniformly higher. Assuming that the increased electron density from the enrichment of some

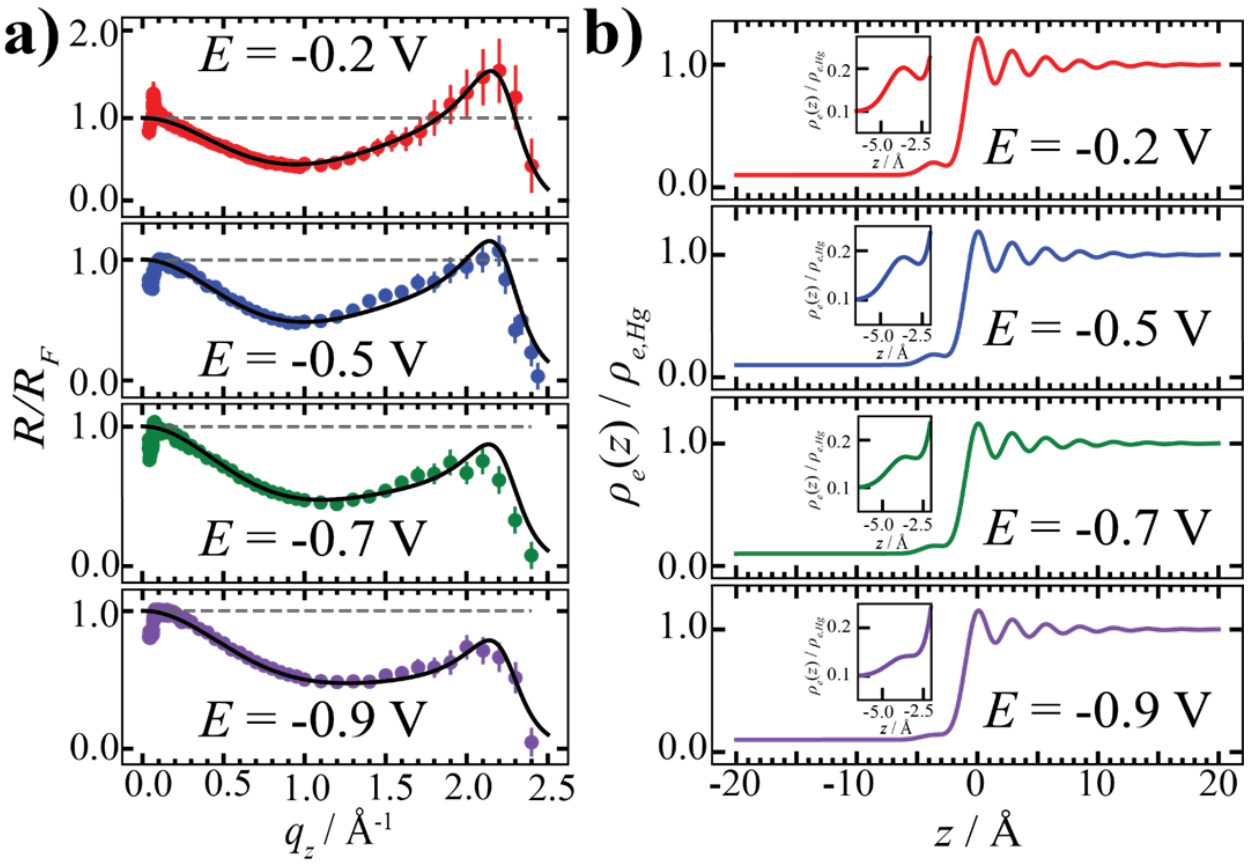

Figure 2.4 a) Plots of the normalized X-ray reflectivity curves for a Hg electrode immersed in 0.1 M $Na_2B_4O_7$ (*aq*) at -0.2 V (red), -0.5 V (blue), -0.7 V (green), -0.9 V (purple). Solid black lines denote the corresponding best fits of the data. Data were normalized to the Fresnel reflectivity. b) Electron density profiles corresponding to the best fits of the data in (a). Insets show an enlarged view of the electron density profile in the adlayer region (-5 Å^{-1} ≤ z ≤ -2 Å^{-1}).

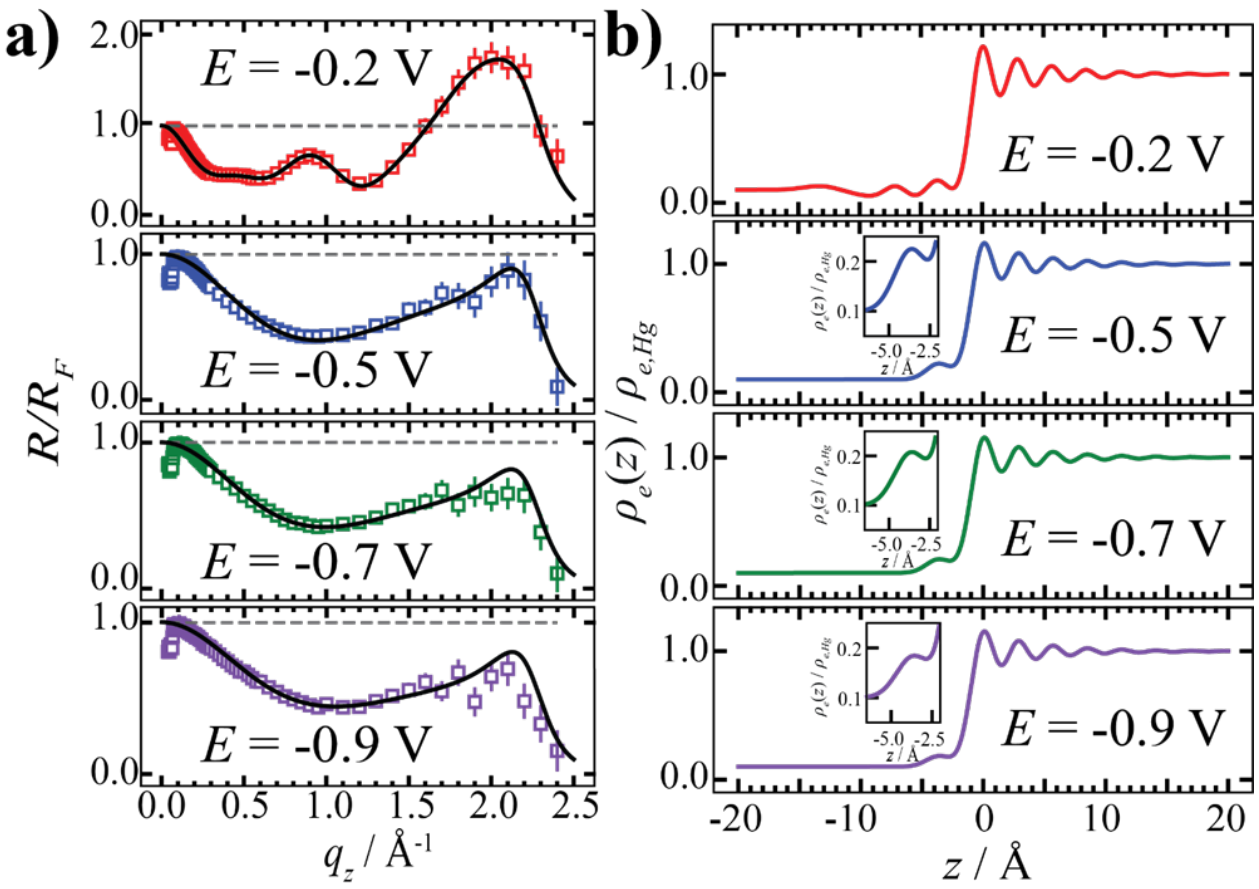

Figure 2.5 a) Plots of the normalized X-ray reflectivity curves for a Hg electrode immersed in deaerated electrolyte containing 0.1 M $Na_2B_4O_7$ + 0.05 M GeO_2 (*aq*) at -0.2 V (red), -0.5 V (blue), -0.7 V (green), and -0.9 V (purple). The XRR data at -0.2 V were recorded after keeping the potential for 15 min. at this value. The solid black lines denote the corresponding best fit of the data. b) Electron density profiles corresponding to the fitted data shown in (a). Insets show an enlarged view of the electron density profile in the adlayer region (-5 $Å^{-1} \leq z \leq$ -2 $Å^{-1}$).

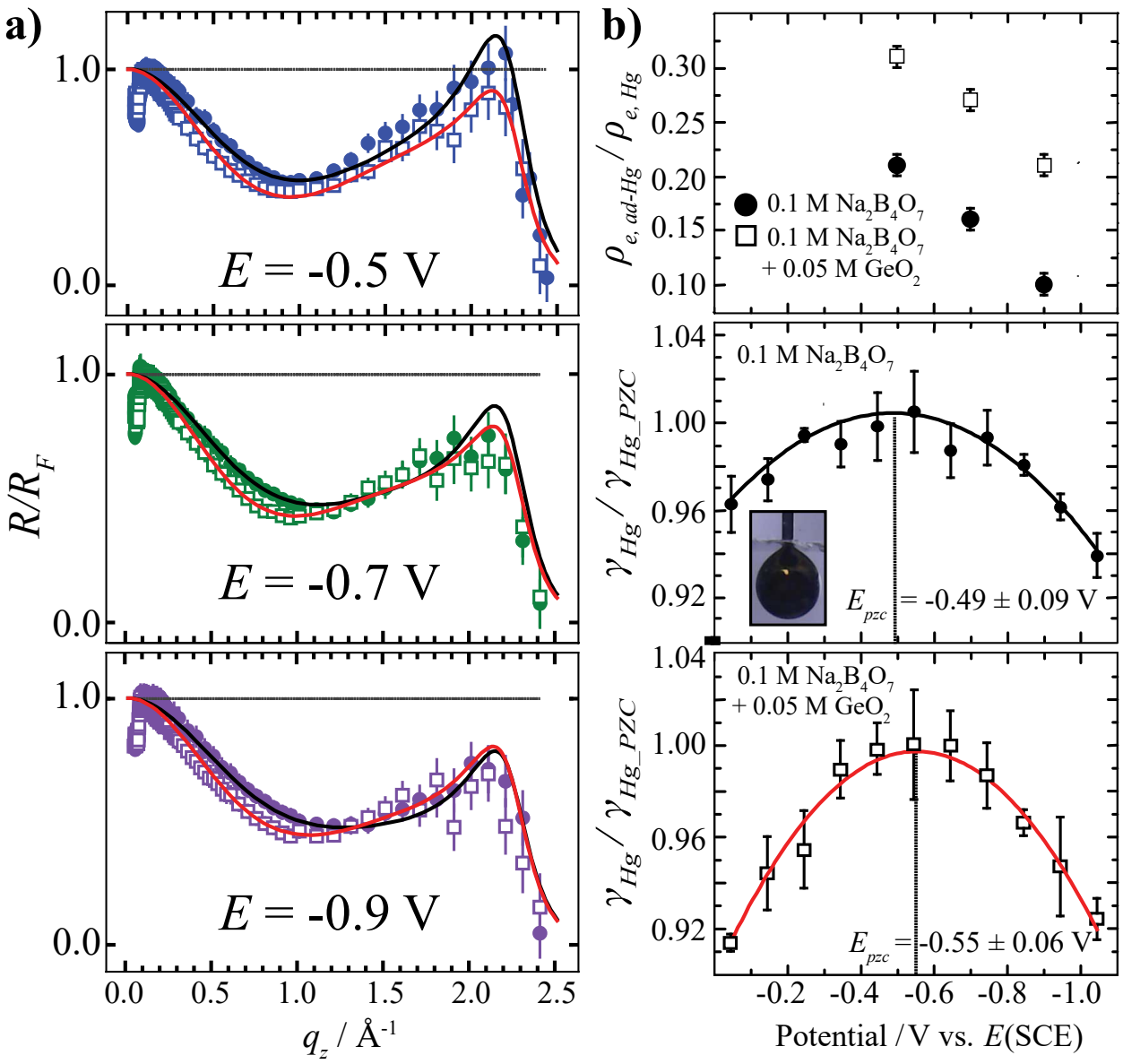

Figure 2.6 a) Comparison of the normalized X-ray reflectivity curves and corresponding fits for Hg electrodes immersed in either 0.1 M $Na_2B_4O_7$ (*aq*) (solid circles and black solid lines) or 0.1 M $Na_2B_4O_7$ + 0.05 M GeO_2 (*aq*) (hollow squares and red solid lines) at -0.50 V, -0.70 V, and -0.90 V. b) (top) Potential-dependent adlayer density determined from fits of the data in (a). (middle) Normalized surface tension, γ, measurements for Hg pendant drop electrodes (inset) in 0.1 M $Na_2B_4O_7$ (*aq*). (bottom) Normalized surface tension measurements for Hg pendant drop electrodes in 0.1 M $Na_2B_4O_7$ + 0.05 M GeO_2 (*aq*).

Ge-containing species at the Hg interface, the data collected in the presence of dissolved GeO_2 were fit again but with a modified version of *Equation* 2.5 (Appendix A). This modified model includes an additional 'adlayer' which specifically describes a molecule of H_2GeO_3 or $HGeO_3^-$ (i.e. the dominant species in bulk solution)[39] adsorbed at the interface through a hydrogen bond with the Hg surface. The purpose of this model was to quantify the contribution of H_2GeO_3 and/or $HGeO_3^-$ to the 'adlayer' peak in the electron density profile rather than obtain better fits of the data than shown in Figure 2.5 and Figure 2.6. For simplicity we refer to this 'adlayer' as describing adsorbed $HGeO_3^-$, but it is noted that XRR cannot distinguish between H_2GeO_3 and $HGeO_3^-$. In this refined model, $\rho_{e,ad-Hg}$ was set to the value obtained from the fit of the corresponding XRR data in neat 0.1 M $Na_2B_4O_7$ (*aq*) at the identical potential. Accordingly, the difference in electron density of the Hg 'adlayer' in Figure 2.6b can be re-interpreted as a coverage of $HGeO_3^-$ adsorbed at the Hg interface ($\theta_{HGeO3-/Hg}$). Over this range, $\theta_{HGeO3-/Hg}$ remains constant at a value of 0.20±0.01 monolayers.

The premise of adsorbed $HGeO_3^-$ at the Hg interface was further supported by separate estimates of E_{pzc} through surface tension measurements of Hg pendant drops (Figure 2.6b). The E_{pzc} value in 0.1 M $Na_2B_4O_7$ (*aq*) was -0.49±0.09 V, in close agreement with the reported value of E_{pzc}=-0.441 V in 0.01 M NaF (*aq*).[40] The apparent E_{pzc} value shifted negatively to -0.56±0.06 V when GeO_2 was dissolved in the $Na_2B_4O_7$ electrolyte, consistent with additional negative charge localized at the solution/Hg interface.

At -0.2 V, the XRR data are distinctly different. An additional peak is evident, centered at q_z = 0.85 Å^{-1}, that is less intense than the surface layering peak at q_z = 2.2 Å^{-1}. The prominence of the peak at q_z = 0.85 Å^{-1} depended somewhat on the duration the potential was held at ≥-0.2 V but was consistently observed when the applied potential was ≥ -0.2 V. However, independently of the duration, the R/R_F value at the center of this new peak was consistently below 1. The presence of the new peak implies the formation of a new structural feature at the interface on a length scale of $2\pi/0.85$ Å^{-1} ≈ 7 Å along the surface normal.

Dynamic XRR measurements were recorded during the course of a voltammetric experiment to determine if the differences in the data in Figure 2.4 and Figure 2.5 occurred instantly or evolved slowly over time. Figure 2.7 shows a single cyclic voltammetric sweep from -0.7 to -0.2 V and back to -0.7 V. In the steady-state experiments shown in Figure 2.4 and Figure 2.5, the XRR recorded at q_z = 0.3 Å^{-1} was significantly reduced in the presence of dissolved GeO_2

when the potential was changed from -0.5 to -0.2 V (by a factor of 1.5). Figure 2.7 indicates a similar behavior in the XRR signal intensity at q_z = 0.3 Å^{-1} during this voltammetric sweep. Specifically, the potential started to decrease in the negative going scan (red symbols) below -0.4 V, parallel to the increasing current in the CV. In the subsequent scan in positive direction (blue symbols), the XRR signal intensity increased again and reached the original intensity value at ≈-0.5 V. The noticeable hysteresis between negative and positive scan mirrors the hysteresis in the charge transfer observed in the CV indicates the surface transformation and restoration processes were kinetically distinct. XRR data were also recorded at q_z = 0.85 Å^{-1}, at the local maximum in Figure 2.5b. At this q_z value, the XRR intensity is expected to increase at more positive potentials according to the steady-state observations. Despite the poorer signal to noise at this q_z, which is caused by the lower XRR, this behavior is indeed observed in the potential sweep experiments. In total, these data indicated that the initial changes in the interface structure occur rapidly upon biasing the Hg electrode. However, the relative intensity changes are at both q_z positions much lower than those that would be expected from a comparison of the steady-state XRR curves at -0.5 and -0.2 V in Figure 2.5a. This point indicates that the formation of the interface structure that is responsible for the altered XRRs is a slow process and is in accordance with the observation that XRRs with a pronounced peak at q_z = 0.85 Å^{-1} are only found after longer waiting times at -0.2 V.

To obtain insight into the atomic-scale origin of the structural changes at the positive potential limit, several strategies were explored to fit the XRR data in GeO_2-containing electrolyte at -0.2 V. No satisfactory fits could be obtained with *Equation* 2.5 as written or by adding a $HGeO_3^-$ 'adlayer' as discussed above. This may be expected, as the presence of additional features in the R/R_F curve indicates that more complex interface structures are required to properly describe the data. For this purpose, a two-tiered fitting approach was adopted to identify the general and specific features of this solution/Hg interface structure. Based on the qualitative behavior of the XRR and the electrochemical data we attribute the structural changes to the formation of an ultrathin layer of a Ge compound at the Hg electrode surface.

The results of the fits with *Equation* 2.6 for the data collected at -0.2 V are shown in Figure 2.5 and Table 2.2. This generic fit provided no direct information on the specific identity of species accumulating at the solution/Hg interface but was useful in identifying where additional electron density, caused by Ge species at the surface, must be localized to produce the observed XRR curve (the contribution of oxygen species is much lower due to the lower Z and can be neglected in this

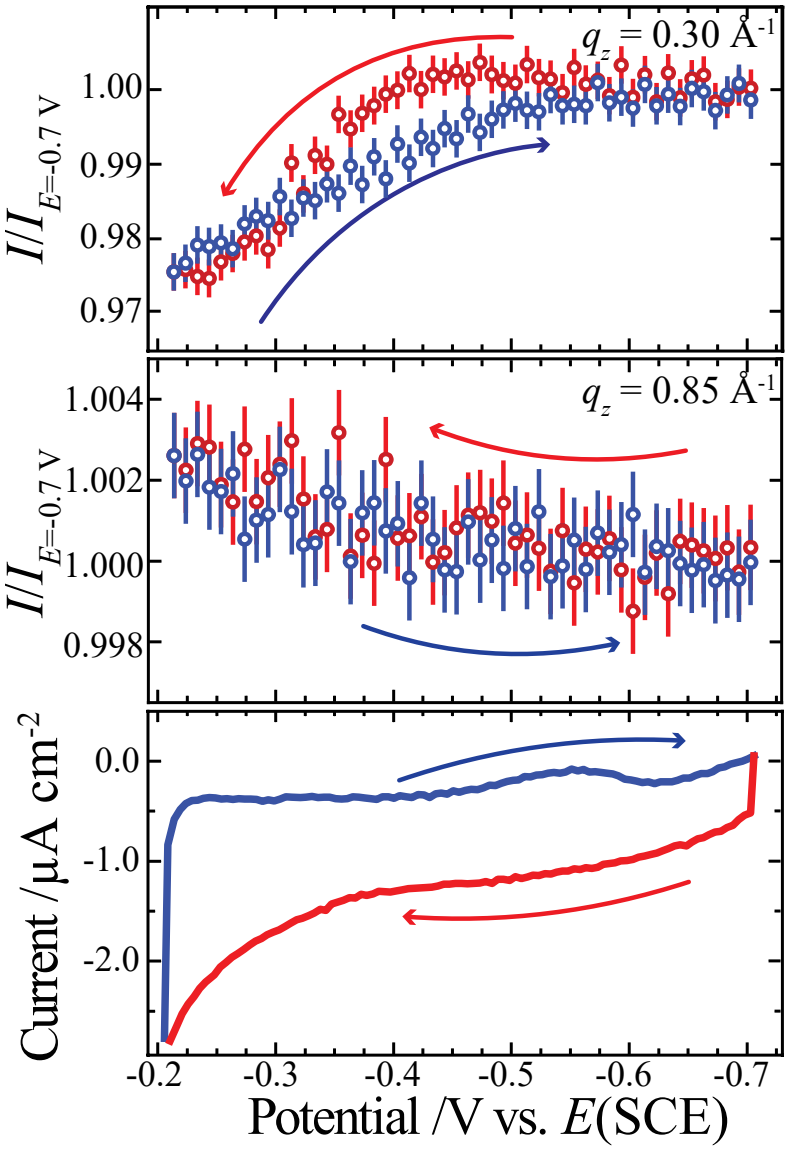

Figure 2.7 Plots depicting the reflected X-ray intensity at (top) $q_z = 0.30$ Å^{-1} and (middle) 0.85 Å^{-1}, recorded concurrently with (bottom) the electrochemical current during a voltammetric scan at 0.05 V s^{-1} for a Hg electrode immersed in 0.1 M $Na_2B_4O_7$ + 0.05 M GeO_2 (*aq*). The arrows denote the voltammetric sweep direction.

Table 2.2 Parameters of the best fits of the XRR data collected in 0.1 M $Na_2B_4O_7$ + 0.05 M GeO_2 at -0.2 V[a]

$\rho_e(z)$ described by *eq 6*				$\rho_e(z)$ described by *eq 7*			
Model Component	**Parameter**	**Value**	**Units**	**Model Component**	***Parameter***	***Value***	***Units***
Distorted Crystal Model	$\rho_{e,ad\text{-}Hg}/\rho_{e,Hg}$	0.22 ± 0.01	Å	Distorted Crystal Model	$\rho_{e,ad\text{-}Hg}/\rho_{e,Hg}$	0.22 ± 0.01	Å
	$\sigma_{ad,Hg}$	0.93 ± 0.01	Å		$\sigma_{ad,Hg}$	0.92 ± 0.01	Å
	$z_{ad,Hg}$	-3.64	Å		$z_{ad,Hg}$	-3.64	Å
	σ_b	0.49	Å		σ_b	0.49	Å
	σ_i	-0.93 ± 0.01	Å		σ_i	-0.92 ± 0.01	Å
	d	2.75	Å		d	2.75	Å
Electrolyte	$\rho_{e,H2O}/\rho_{e,Hg}$	0.10	-	Electrolyte	$\rho_{e,H2O}/\rho_{e,Hg}$	0.10	-
	z_{H2O}	-9.52 ± 0.37	Å		z_{H2O}	-6.55 ± 0.15	Å
	σ_{H2O}	-2.90 ± 0.10	Å		σ_{H2O}	-0.92 ± 0.01	Å
1st Gaussian	$\rho_{e,ad\text{-}1}/\rho_{e,Hg}$	0.18 ± 0.01	Å	$HGeO_3^-$ 'adlayer' on Hg	$z_{Ge,1}$	-3.75 ± 0.15	Å
	$z_{ad,1}$	-3.79 ± 0.13	Å		$z_{O,1}$	-2.09 ± 0.15	Å
	$\sigma_{ad,1}$	0.92 ± 0.08	Å		$z_{O,2}$	-4.60 ± 0.15	Å
2nd Gaussian	$\rho_{e,ad\text{-}2}/\rho_{e,Hg}$	0.25 ± 0.02	Å		$\sigma_{Ge} = \sigma_O$	0.92 ± 0.01	Å
	$z_{ad,2}$	-7.05 ± 0.03	Å		$\Theta_{HGeO3-/Hg}$	0.07 ± 0.02	Å
	$\sigma_{ad,2}$	0.92 ± 0.05	Å	GeO_2 Bilayer	$z_{Ge,1}$	-3.44 ± 0.25	Å
3rd Gaussian	$\rho_{e,ad\text{-}3}/\rho_{e,Hg}$	0.15 ± 0.02	Å		$z_{Ge,2}$	-6.61 ± 0.25	Å
	$z_{ad,3}$	-13.00 ± 0.13	Å		$z_{O,1\text{-}1}$	-2.19 ± 0.25	Å
	$\sigma_{ad,3}$	1.50 ± 0.14	Å		$z_{O,1\text{-}2}$	-3.44 ± 0.25	Å
					$z_{O,1\text{-}3}$	-4.69 ± 0.25	Å
					$z_{O,2\text{-}1}$	-5.36 ± 0.25	Å
					$z_{O,2\text{-}2}$	-6.61 ± 0.25	Å
					$z_{O,2\text{-}3}$	-7.86 ± 0.25	Å
					σ_{GeO2}	0.92 ± 0.01	Å
				$HGeO_3^-$ 'adlayer' on GeO_2	$z_{Ge,1}$	-12.60 ± 0.12	Å
					$z_{O,1}$	-10.94 ± 0.12	Å
					$z_{O,2}$	-13.45 ± 0.12	Å
					$\sigma_{Ge} = \sigma_O$	0.92 ± 0.01	Å
					$\Theta_{HGeO3-/GeO2}$	0.22 ± 0.02	Å
					θ_{GeO2}	0.27 ± 0.03	-

a. The full expressions for $\frac{R}{R_F}$ vs q_z using *Equation* 2.6 or Equation 2.7 are detailed in the Appendix A as *Appendix* Equation.A.2 and Appendix Equation.A.11, respectively.

first approach). Specifically, the fit implied a small Ge-Ge spacing along the surface normal of 3.26±0.13 Å (Table 2.2) near the Hg surface, consistent with rutile GeO_2 that is oriented with the [110] direction along the surface normal (3.17 Å).[45-47] A rutile crystal structure seems reasonable, since this phase is the thermodynamically stable polymorph at ambient temperature and pressure.[48] Attempts to verify the presence of a rutile phase at -0.2 V by in-plane X-ray diffraction studies were unsuccessful, however. This is not surprising, as the total amount of material is low (see below) and the crystals would be arranged in arbitrary in-plane orientation on the liquid Hg surface (i.e., form a two-dimensional powder), which would result in very weak diffraction peaks. Considering these aspects, the second phase of fitting for these data focused on a separate model with a presumed atomic structure based on GeO_2 in form of a (110)-oriented rutile polymorph (Figure 2.9a).

Fits with a GeO_2 bilayer that completely covered the Hg surface did provide qualitatively reasonable simulated XRR curves but the quantitative agreement was poor, particularly in the q_z ranges of 0.25 – 0.75 $Å^{-1}$ and 1.0 – 1.5 $Å^{-1}$ (Figure 2.8). However, a suitable fit was obtained when the surface was modelled with a partial coverage of rutile GeO_2 (Figure 2.9a). In this model, only a fraction θ_{GeO2} of the surface was considered to be covered by a film of solid, crystalline rutile GeO_2. This film was modelled as a rutile bilayer with a layer of adsorbed $HGeO_3^-$ on top. The remaining surface (i.e. '1 - θ_{GeO2}') was assumed to consist of an Hg electrode with adsorbed $HGeO_3^-$, as employed for modelling the XRR data at potentials negative of -0.2 V. This model satisfactorily fits the XRR data in GeO_2-containing solution at -0.2 V, resulting in a rutile coverage $\theta_{GeO2} = 0.27 \pm 0.01$ for the R/R_F curve shown in Figure 2.9b (Table 2.2). Analogous models where the atomic Ge and O positions reflected *a*-quartz or other rutile crystalline directions could not be absolutely ruled out but generally yielded slightly poorer fits.

2.5 Discussion

The data collectively support the premise that adsorbed Ge species are present on Hg electrodes immersed in solutions with dissolved GeO_2. However, the adsorbed species are not the same at all potentials. At comparatively negative potentials, the evidence points to the accumulation of solvated H_2GeO_3 and/or $HGeO_3^-$ at the Hg interface. At more positive potentials, the data implicate the growth of a condensed phase from the $HGeO_3^-$ adlayer. The condensation does not appear redox-based but instead the consequence of $HGeO_3^-$ accumulation on the Hg surface far from E_{pzc}. These points are elaborated below.

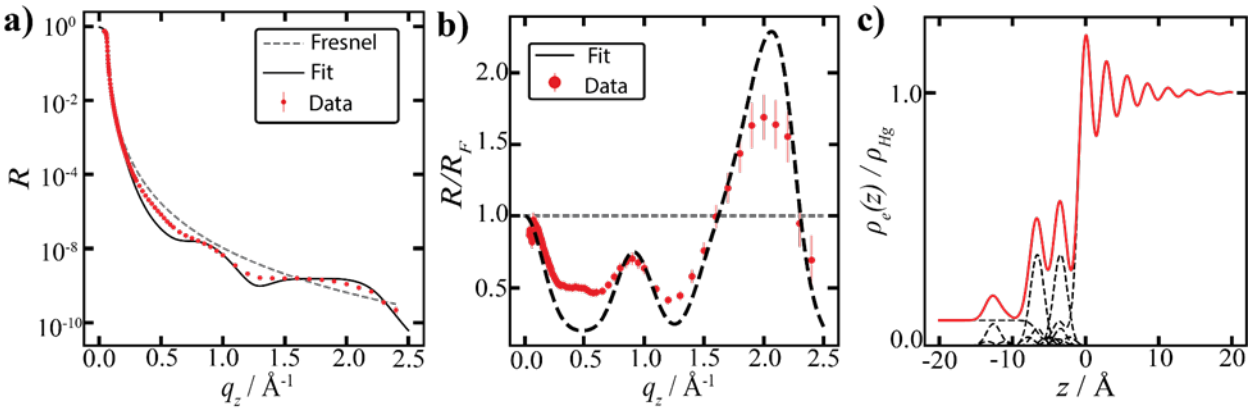

Figure 2.8 a) Plot of the absolute X-ray reflectivity vs. momentum transfer perpendicular to the surface for a Hg electrode immersed in deaerated electrolyte containing 0.1 M $Na_2B_4O_7$ (*aq*) and a formal concentration of 0.05 M GeO_2 at E = -0.2 V (closed red circles). The fit of the data using *Equation* 2.6 assuming Θ_{GeO2} = 1 and all other parameters listed in Table 2.2 is shown (black line). The Fresnel reflectivity of an interface with a monotonic electron density profile with no surface roughness is also presented (grey dashed line). b) The same XRR data as in (a) but normalized to the Fresnel reflectivity. c) Electron density profiles corresponding to the fitted data shown in (b).

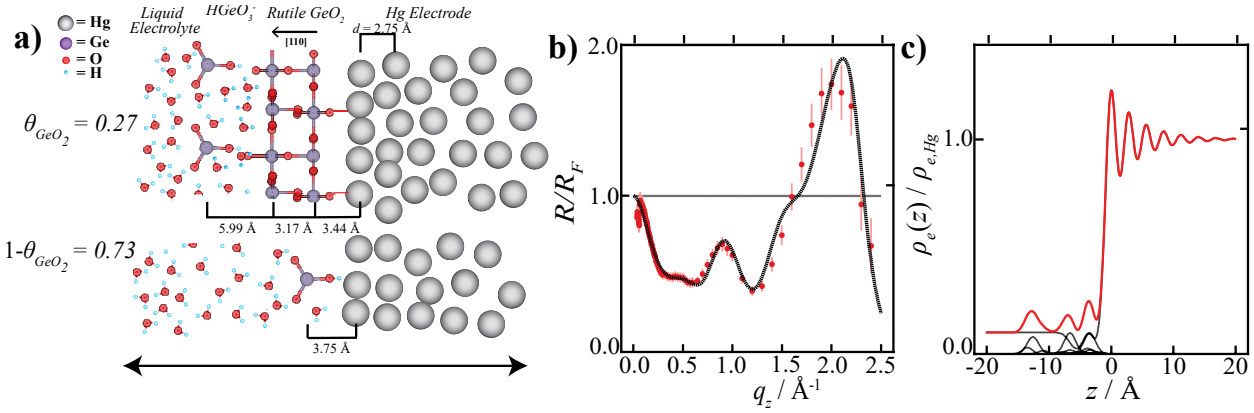

Figure 2.9 Interface structure of Hg electrodes in 0.1 M $Na_2B_4O_7$ + 0.05 M GeO_2 (*aq*) at -0.2 V. a) Schematic depiction of the three-component model (*Equation* 2.7) used to fit the XRR data at this potential, consisting of a surface fraction with a bilayer of solid GeO_2 (top) and a Hg surface with adsorbed $HGeO_3^-$ (bottom). The best fits were obtained with a rutile-like bilayer structure, oriented with the [110] direction along the surface normal, and a layer of adsorbed $HGeO_3^-$ on top. b) XRR curve shown in Figure 2.5a together with best fit by this model (dashed black line), corresponding to a bilayer coverage of $\theta_{GeO2} = 0.27 \pm 0.01$. c) Electron density profile corresponding to the fit shown in (b).

Hg/Electrolyte Interface at < -0.2 V Potentials Our studies show that Hg immersed in 0.1 M $Na_2B_4O_7(aq)$ has a similar E_{pzc} as in NaF(*aq*), exhibits only featureless double layer charging in voltammograms, and has an identical atomic layering within Hg. These observations are consistent with the premise that $Na_2B_4O_7(aq)$ is not forming strong chemical bonds with the Hg surface atoms. While fortuitous, this point could not be assumed *a priori* because extensive adsorption of $B_4O_7^{2-}$ on solid metal electrodes is known.[49] The reasons for the relative inertness of $B_4O_7^-$ anions towards Hg were not explored. Nevertheless, the XRR argue directly against any complicating chemistry between Hg and $B_4O_7^{2-}$ that alters the atomic structure of the Hg interface within the potential range explored here. Accordingly, $Na_2B_4O_7(aq)$ is a suitable base electrolyte for studies on the adsorption of Ge species.

The changes in the electrochemical behavior upon addition of GeO_2 to the electrolyte indicate adsorption of a $H_2GeO_3/HGeO_3^-$ species. The negative shift of E_{pzc} would be consistent with specific anion adsorption but chemisorption of a neutral species can also not be excluded. At the more negative potentials in the range explored here, the XRR data provide clear evidence that there is excess electron density at the water/Hg interface when GeO_2 is dissolved in the electrolyte. Although the XRR data are not definitive on the identity of the species, enrichment of the double layer with $HGeO_3^-$ and/or H_2GeO_3 is consistent with the cumulative observations. The chemisorption of $H_2GeO_3/HGeO_3^-$ at metal electrodes has been noted previously. At this same pH, molecular adlayers were previously observed on single crystalline Au electrodes by electrochemical scanning tunneling microscopy.[50] Ge-containing adsorbates in this electrolyte were separately identified on polycrystalline Au by surface-enhanced Raman measurements.[51] In the work here, the specific binding mode of $H_2GeO_3/HGeO_3^-$ to the Hg surface could not be unambiguously determined. However, the best fits were obtained with a separation distance of 2.09 Å between the O and Hg electron densities at the interface, suggestive of a bridging Ge-O-Hg bond. The $HGeO_3^-$ coverage of 0.20 ML (corresponding to a surface area per molecule of 45 $Å^2$) was less than the 0.33 ML (surface area per molecule of 20 $Å^2$) found previously on Au(111).[50] Considering that the coverage is constant over a wide potential range from -0.35 V below to 0.05 V more positive of E_{pzc}, adsorption of a neutral species (H_2GeO_3) appears more likely than adsorption of $HGeO_3^-$. Unambiguous clarification of the adsorbed species is difficult, however, because of the assumptions involved in determination of the coverage from the adlayer peak in the electron density profile (see above). Overall, the XRR data here indicate that the role

of chemisorbed $H_2GeO_3/HGeO_3^-$ should be considered when determining the mechanism(s) of Ge electrodeposition with Hg electrodes in this electrolyte.

Hg/Electrolyte Interface at ≥ -0.2 V In the presence of dissolved GeO_2, the XRR and CV data provide clear evidence for a structural transition at the Hg surface as the potential approaches -0.2 V. This transition has to be related to a surface phase containing Ge. However, neither Hg nor $HGeO_3^-$ are redox active at this potential, so a direct, redox-based oxide growth is difficult to rationalize. One possible interpretation of the voltammetric features in Figure 2.1 is a potential-dependent change in the protonation state of the adsorbate. That is, the Bronsted acid/base character of $H_2GeO_3/HGeO_3^-$ can be expressed as follows,[39]

$$OH^- + H_2GeO_3 \leftrightarrows HGeO_3^- + H_2O$$

Equation 2.8

In homogeneous solution, this reaction favors the products (i.e. deprotonation of $HGeO_3^-$, pK_A = 8.52) only at more alkaline pH values.[39] However, if localized at an electrode surface, the equilibrium of this acid/base reaction will couple to the electrostatic potential drop across the diffuse layer.[52] If the rates of protonation/deprotonation are sufficiently fast and the potential drop between the electrode surface and the adsorbate is negligible, the surface concentrations of H_2GeO_3 and $HGeO_3^-$ ($\left[H_2GeO_3\right]_s$ and $\left[HGeO_3^-\right]_s$, respectively) become dependent on the applied potential in the following manner, [52]

$$\ln\left(\frac{\left[HGeO_3^-\right]_s}{\left[H_2GeO_3\right]_s}\right) \approx \ln 10\left(pH - pK_A\right) + \frac{F}{RT}\left(E - E_{pzc}\right)$$

Equation 2.9

where F is the Faraday constant and R is the ideal gas constant.

If both H_2GeO_3 and $HGeO_3^-$ do not desorb from the electrode surface as a result of deprotonation/protonation, differentiating *Equation* 2.9 with respect to potential describes the rate at which the deprotonation/protonation of the adsorbate occurs as the potential is changed. This rate has the same underlying mathematical form[53, 54] as the reduction/oxidation of a redox

adsorbate and will elicit an electrochemical current that describes when the net charge of the adsorbate transitions through protonation/deprotonation states. That is, when the potential relative to E_{pzc} is positive enough, the adsorbed species will deprotonate, producing a current that is not associated with a redox reaction but has the same principle features.[55-57] This point is well known for self-assembled monolayers featuring terminal acid groups.[52, 55, 58] Accordingly, *Equation* 2.9 predicts that $HGeO_3^-$ will be the dominant species at sufficiently positive potentials, irrespective of solution pH. For example, a potential of 300 mV more positive than E_{pzc} will increase the surface concentration of $HGeO_3^-$ by a factor of ~10^5 at pH = 9.13 and T = 25 °C.

Although *Equation* 2.9 provides a possible rationale for the electrochemical data, changes in just the protonation state of the adsorbate would not elicit the observed XRR data. However, the following chemical equilibrium is known for $HGeO_3^-$,[39]

$$HGeO_3^-(aq) \leftrightarrows GeO_2(s) + OH^-(aq)$$

Equation 2.10

Equation 2.10 describes the conversion (precipitation) of solvated $HGeO_3^-$ into solid GeO_2. Mechanistically, such a process involves the formation of a Ge-O-Ge linkage between neighboring monomers of $HGeO_3^-$ (or a cogener).[59] We posit that a surface with predominantly adsorbed $HGeO_3^-$ would be subject to such a condensation reaction and would be consistent with the presented XRR data. That is, when adsorbed H_2GeO_3 is de-protonated because of a positive applied potential, the neighboring and newly formed $HGeO_3^-$ adsorbates undergo *Equation* 2.10 and form a new condensed phase at the Hg surface.

An electrochemically-coupled acid/base reaction that produces a film by precipitation would likely be limited to small thicknesses. The potential drop across the double layer would necessarily decrease when a dielectric (GeO_2) accumulates at the surface, thereby stopping the products of *Equation* 2.10 from being favored. Two facts support this premise. First, the relative dielectric constant of GeO_2 (5.2) is much smaller than that of water (80.4).[60, 61] Second, extremely long experiments (biasing at -0.2 V for days) were attempted to grow thicker films of GeO_2. In every trial, no macroscopic quantity of material was produced. This is in accordance with the XRR studies that find much less than a monolayer coverage even after keeping the potential for 15 min. at -0.20 V.

The XRR data argue against a description of extended rutile GeO_2 sheets for the phase identified by the XRR data, as they show clearly that the condensed phase formed at -0.2 V is readily removed by moving the electrode potential more negative than -0.5 V. Bulk rutile GeO_2 is relatively insoluble in water,[39] so simply shifting the electrode potential more negative would not necessarily be expected to remove or dissolve rutile GeO_2 from the Hg interface. In addition, it is not clear why hypothetical rutile GeO_2 sheets would be limited to a low incomplete surface coverage, as indicated by the data. These points suggest that an alternate form of GeO_2 is more likely under the investigated conditions.

Polygermanates are a class of macromolecular germanium oxyanions composed of edge-sharing GeO_6 octahedra and GeO_4 tetrahedra.[62-65] These oxyanions can exhibit a variety of sizes and structures, i.e. from linear chains to porous networks.[64, 65] In the solid-state, polygermanates are charge-stabilized by small cations. If the positive surface charge at an electrode surface, kept at potentials positive of E_{pzc}, similarly stabilizes polygermanate anions, polygermanates may be the relevant species indicated by the XRR data. Several points support this general premise. First, multiple polygermanates feature the same six-coordinate Ge arrangement as in rutile GeO_2, e.g. $Ge_7O_{15}^{2-}$,[64, 66, 67] consistent with the fitting results reported here. Second, the dissolution/removal of a charge-stabilized polygermanate anion at the Hg interface would be expected at more negative potentials, as observed here. Third, the XRR fits were consistent with both an incomplete surface coverage and defined bilayer structures, i.e. defined stoichiometry between the first and second Ge-O layers. Porous and cyclic polygermanates are known[64] that, if adsorbed, could conceivably still leave a significant fraction of an electrode surface exposed while still maintaining defined positions of the constituent Ge atoms. Porous polygermanates should also be much smaller than the X-ray coherence length, which justifies the use of a coherent reflectivity model.

Although the formation mechanism of polygermanates was not interrogated directly in this work, the possibility of their synthesis at liquid metal electrode surfaces is intriguing. Typically, polygermanates (and oxocondensates more generally) are prepared by heating saturated solutions of dissolved precursors in a closed vessel.[63] Elevated temperatures are necessary to increase solubility and lower activation barriers of formation. The data here could indicate that an alternative reaction route that doesn't require high temperatures is possible if the precursor species are adsorbed onto an electrode. If so, XRR features such as the hysteresis in Figure 2.7 should also contain information on the energetic barriers of formation, in analogous fashion to hysteresis

analysis in the voltammetry of conventional electrodeposition.[68] The known activation barrier for Ge-O-Ge linkage formation (36 kJ mol^{-1})[59] in homogeneous solution is sufficient to suggest that polygermanate formation/deconstruction at an electrode surface would not necessarily occur instantly following deprotonation of H_2GeO_3. The difference in the rates of deposition vs removal indicated by the hysteresis in the time-dependent XRR data are consistent with a strongly kinetically hindered nucleation and growth.[69, 70] Even more pronounced hysteresis was apparent in the electrochemical data obtained at faster scan rates than shown in Figure 2.7 but concomitant XRR measurements were not performed. Accordingly, additional work is needed to develop these points further. Nevertheless, the innate value of XRR for such studies is clear.

2.6 Conclusion

The work presented here provide insights how Ge species in aqueous solution interact with liquid Hg electrodes as a function of potential. Clear evidence for the adsorption of Ge species at the electrolyte-liquid metal interface over a wide potential range is found in electrolyte containing dissolved GeO_2. The collected XRR profiles atomic-scale data on the interface structure significantly go beyond that obtainable by electrochemical studies alone. Specifically, the work here illustrates that at least two different types of adlayers form on Hg in solutions containing dissolved GeO_2. At more negative potentials, adsorbed $H_2GeO_3/HGeO_3^-$ persists at Hg electrodes. At the most positive potentials, a condensed phase forms with atomic spacing consistent with polygermanates with a rutile GeO_2 sub-structure. The presented data suggest accumulation of oxyanions at a liquid metal electrode could present an alternative synthetic route for oxocondensates that are otherwise only obtained by hydrothermal reactions.[63] Thus, these observations incentivize further *in-situ* studies of Hg and other liquid metal electrodes in this electrolyte to elucidate the operative surface species during material syntheses. In total, the results presented here provide specific new insights on the surface chemistry of Hg in this electrolyte and illustrate the advantages of XRR as a tool for *in situ* studies of liquid metal electrode interfaces.

2.7 References

1. Martin, A.; Du, C.; Chang, B.; Thuo, M., Complexity and Opportunities in Liquid Metal Surface Oxides. *Chemistry of Materials* **2020,** *32* (21), 9045-9055.
2. Zavabeti, A.; Ou, J. Z.; Carey, B. J.; Syed, N.; Orrell-Trigg, R.; Mayes, E. L. H.; Xu, C.; Kavehei, O.; O'Mullane, A. P.; Kaner, R. B.; Kalantar-zadeh, K.; Daeneke, T., A liquid metal reaction environment for the room-temperature synthesis of atomically thin metal oxides. *Science* **2017,** *358* (6361), 332.
3. Daeneke, T.; Khoshmanesh, K.; Mahmood, N.; de Castro, I. A.; Esrafilzadeh, D.; Barrow, S. J.; Dickey, M. D.; Kalantar-zadeh, K., Liquid metals: fundamentals and applications in chemistry. *Chemical Society Reviews* **2018,** *47* (11), 4073-4111.
4. Dong, R.; Zhang, T.; Feng, X., Interface-Assisted Synthesis of 2D Materials: Trend and Challenges. *Chemical Reviews* **2018,** *118* (13), 6189-6235.
5. Zavabeti, A.; Zhang, B. Y.; de Castro, I. A.; Ou, J. Z.; Carey, B. J.; Mohiuddin, M.; Datta, R.; Xu, C.; Mouritz, A. P.; McConville, C. F.; O'Mullane, A. P.; Daeneke, T.; Kalantar-Zadeh, K., Green Synthesis of Low-Dimensional Aluminum Oxide Hydroxide and Oxide Using Liquid Metal Reaction Media: Ultrahigh Flux Membranes. *Advanced Functional Materials* **2018,** *28* (44), 1804057.
6. Ghasemian, M. B.; Mayyas, M.; Idrus-Saidi, S. A.; Jamal, M. A.; Yang, J.; Mofarah, S. S.; Adabifiroozjaei, E.; Tang, J.; Syed, N.; O'Mullane, A. P.; Daeneke, T.; Kalantar-Zadeh, K., Self-Limiting Galvanic Growth of MnO2 Monolayers on a Liquid Metal—Applied to Photocatalysis. *Advanced Functional Materials* **2019,** *29* (36), 1901649.
7. Alkathiri, T.; Dhar, N.; Jannat, A.; Syed, N.; Mohiuddin, M.; Alsaif, M. M. Y. A.; Datta, R. S.; Messalea, K. A.; Zhang, B. Y.; Khan, M. W.; Elbourne, A.; Pillai, N.; Ou, J. Z.; Zavabeti, A.; Daeneke, T., Atomically thin TiO2 nanosheets synthesized using liquid metal chemistry. *Chemical Communications* **2020,** *56* (36), 4914-4917.
8. Elsen, A.; Festersen, S.; Runge, B.; Koops, C. T.; Ocko, B. M.; Deutsch, M.; Seeck, O. H.; Murphy, B. M.; Magnussen, O. M., In situ X-ray studies of adlayer-induced crystal nucleation at the liquid–liquid interface. *Proceedings of the National Academy of Sciences* **2013,** *110* (17), 6663.
9. Kochat, V.; Samanta, A.; Zhang, Y.; Bhowmick, S.; Manimunda, P.; Asif Syed Asif, S.; Stender Anthony, S.; Vajtai, R.; Singh Abhishek, K.; Tiwary Chandra, S.; Ajayan Pulickel, M., Atomically thin gallium layers from solid-melt exfoliation. *Science Advances* **2018,** *4* (3), e1701373.
10. Tao, P.; Yao, S.; Liu, F.; Wang, B.; Huang, F.; Wang, M., Recent advances in exfoliation techniques of layered and non-layered materials for energy conversion and storage. *Journal of Materials Chemistry A* **2019,** *7* (41), 23512-23536.
11. Benbow, E. M.; Dalal, N. S.; Latturner, S. E., Crystal growth and magnetic behavior of R6T13−xAlxMy phases (R=La, Nd; T=Mn, Fe; M=main group) grown from lanthanide-rich eutectic fluxes. *Journal of Solid State Chemistry* **2009,** *182* (11), 3055-3062.
12. He, H.; Tyson, C.; Saito, M.; Bobev, S., Synthesis and structural characterization of the ternary Zintl phases AE3Al2Pn4 and AE3Ga2Pn4 (AE=Ca, Sr, Ba, Eu; Pn=P, As). *Journal of Solid State Chemistry* **2012,** *188*, 59-65.
13. Stojanovic, M.; Latturner, S. E., Growth of new ternary intermetallic phases from Ca/Zn eutectic flux. *Journal of Solid State Chemistry* **2007,** *180* (3), 907-914.

14. Carim, A. I.; Collins, S. M.; Foley, J. M.; Maldonado, S., Benchtop Electrochemical Liquid–Liquid–Solid Growth of Nanostructured Crystalline Germanium. *Journal of the American Chemical Society* **2011,** *133* (34), 13292-13295.
15. Kanatzidis, M. G.; Pöttgen, R.; Jeitschko, W., The Metal Flux: A Preparative Tool for the Exploration of Intermetallic Compounds. *Angewandte Chemie International Edition* **2005,** *44* (43), 6996-7023.
16. Sebastian, C. P.; Malliakas, C. D.; Chondroudi, M.; Schellenberg, I.; Rayaprol, S.; Hoffmann, R.-D.; Pöttgen, R.; Kanatzidis, M. G., Indium Flux-Growth of Eu2AuGe3: A New Germanide with an AlB2 Superstructure. *Inorganic Chemistry* **2010,** *49* (20), 9574-9580.
17. Budevski, E.; Staikov, G.; Lorenz, W. J., *Electrochemical Phase Formation and Growth: An Introduction to the Initial Stages of Metal Deposition*. VCH Verlagsgesellschaft mbH: Weinheim, 1996.
18. King, D. A.; Woodruff, D. P., *Growth and Properties of Ultrathin Epitaxial Layers*. El Sevier Ltd.: 1997; Vol. 8.
19. Abruña, H. D., X Rays as Probes of Electrochemical Interfaces. In *Modern Aspects of Electrochemistry No. 20*, Springer: 1989; pp 265-326.
20. Pershan, P. S.; Schlossman, M., *Liquid Surfaces and Interfacs: Synchrotron X-ray Methods.* Cambridge University Press: Cambridge, 2012.
21. Magnussen, O. M.; Ocko, B. M.; Regan, M. J.; Penanen, K.; Pershan, P. S.; Deutsch, M., X-ray reflectivity measurements of surface layering in liquid mercury. *Physical Review Letters* **1995,** *74* (22), 4444-4447.
22. DiMasi, E.; Tostmann, H.; Ocko, B. M.; Pershan, P. S.; Deutsch, M., X-ray reflectivity study of temperature-dependent surface layering in liquid Hg. *Physical Review B* **1998,** *58* (20), R13419-R13422.
23. Regan, M. J.; Pershan, P. S.; Magnussen, O. M.; Ocko, B. M.; Deutsch, M.; Berman, L. E., X-ray reflectivity studies of liquid metal and alloy surfaces. *Physical Review B* **1997,** *55* (23), 15874-15884.
24. Regan, M. J.; Kawamoto, E. H.; Lee, S.; Pershan, P. S.; Maskil, N.; Deutsch, M.; Magnussen, O. M.; Ocko, B. M.; Berman, L. E., Surface Layering in Liquid Gallium: An X-Ray Reflectivity Study. *Physical Review Letters* **1995,** *75* (13), 2498-2501.
25. Elsen, A.; Murphy, B. M.; Ocko, B. M.; Tamam, L.; Deutsch, M.; Kuzmenko, I.; Magnussen, O. M., Surface Layering at the Mercury-Electrolyte Interface. *Physical Review Letters* **2010,** *104* (10), 105501.
26. Murphy, B. M.; Greve, M.; Runge, B.; Koops, C. T.; Elsen, A.; Stettner, J.; Seeck, O. H.; Magnussen, O. M., A novel X-ray diffractometer for studies of liquid-liquid interfaces. *Journal of Synchrotron Radiation* **2014,** *21* (1), 45-56.
27. Murphy, B. M.; Festersen, S.; Magnussen, O. M., The Atomic scale structure of liquid metal–electrolyte interfaces. *Nanoscale* **2016,** *8* (29), 13859-13866.
28. Runge, B.; Festersen, S.; Koops, C. T.; Elsen, A.; Deutsch, M.; Ocko, B. M.; Seeck, O. H.; Murphy, B. M.; Magnussen, O. M., Temperature- and potential-dependent structure of the mercury-electrolyte interface. *Physical Review B* **2016,** *93* (16), 165408.
29. Festersen, S.; Runge, B.; Koops, C.; Bertram, F.; Ocko, B.; Deutsch, M.; Murphy, B. M.; Magnussen, O. M., Nucleation and Growth of PbBrF Crystals at the Liquid Mercury–Electrolyte Interface Studied by Operando X-ray Scattering. *Langmuir* **2020,** *36* (37), 10905-10915.

30. Pattadar, D.; Cheek, Q.; Sartori, A.; Zhao, Y.; Giri, R. P.; Murphy, B.; Magnussen, O.; Maldonado, S., Evidence for Facilitated Surface Transport during Ge Crystal Growth by Indium in Liquid Hg–In Alloys at Room Temperature. *Crystal Growth & Design* **2021,** *21* (3), 1645-1656.
31. Zhang, T.; Fahrenkrug, E.; Maldonado, S., Electrochemical Liquid-Liquid-Solid Deposition of Ge at Hg Microdroplet Ultramicroelectrodes. *Journal of The Electrochemical Society* **2016,** *163* (9), D500-D505.
32. Demuth, J.; Fahrenkrug, E.; Ma, L.; Shodiya, T.; Deitz, J. I.; Grassman, T. J.; Maldonado, S., Electrochemical Liquid Phase Epitaxy (ec-LPE): A New Methodology for the Synthesis of Crystalline Group IV Semiconductor Epifilms. *Journal of the American Chemical Society* **2017,** *139* (20), 6960-6968.
33. Hansen, F. K.; Rødsrud, G., Surface tension by pendant drop: I. A fast standard instrument using computer image analysis. *Journal of Colloid and Interface Science* **1991,** *141* (1), 1-9.
34. Daerr, A.; Mogne, A., Pendent_drop: an imagej plugin to measure the surface tension from an image of a pendent drop. *Journal of Open Research Software* **2016,** *4* (1), e3-e3.
35. Als-Nielsen, J.; McMorrow, D., Refraction and Reflection from Interfaces. In *Elements of Modern X-ray Physics*, Wiley: 2011; pp 69-112.
36. D'Evelyn, M. P.; Rice, S. A., A study of the liquid–vapor interface of mercury: Computer simulation results. *The Journal of Chemical Physics* **1983,** *78* (8), 5081-5095.
37. Duval, J. F. L.; Bera, S.; Michot, L. J.; Daillant, J.; Belloni, L.; Konovalov, O.; Pontoni, D., X-Ray Reflectivity at Polarized Liquid-Hg--Aqueous-Electrolyte Interface: Challenging Macroscopic Approaches for Ion-Specificity Issues. *Physical Review Letters* **2012,** *108* (20), 206102.
38. Isac-García, J.; Dobado, J. A.; Calvo-Flores, F. G.; Martínez-García, H., Chapter 13 - Green Chemistry Experiments. In *Experimental Organic Chemistry*, Isac-García, J.; Dobado, J. A.; Calvo-Flores, F. G.; Martínez-García, H., Eds. Academic Press: 2016; pp 417-484.
39. Pourbaix, M., *Atlas of electrochemical equilibria in aqueous solutions*. 2d English ed.; National Association of Corrosion Engineers: Houston, Tex., 1974; p 644 p.
40. Grahame, D. C., The Electrical Double Layer and the Theory of Electrocapillarity. *Chemical Reviews* **1947,** *41* (3), 441-501.
41. Grahame, D. C.; Larsen, R. P.; Poth, M. A., The Potential of the Electrocapillary Maximum of Mercury. *Journal of the American Chemical Society* **1949,** *71* (9), 2978-2983.
42. Grahame, D. C., Differential Capacity of Mercury in Aqueous Sodium Fluoride Solutions. I. Effect of Concentration at 25°. *Journal of the American Chemical Society* **1954,** *76* (19), 4819-4823.
43. Grahame, D. C., Capacity of the Electrical Double Layer between Mercury and Aqueous Sodium Fluoride. II. Effect of Temperature and Concentration. *Journal of the American Chemical Society* **1957,** *79* (9), 2093-2098.
44. Tostmann, H.; DiMasi, E.; Pershan, P. S.; Ocko, B. M.; Shpyrko, O. G.; Deutsch, M., Surface structure of liquid metals and the effect of capillary waves: X-ray studies on liquid indium. *Physical Review B* **1999,** *59* (2), 783-791.
45. Bradlyn, B.; Elcoro, L.; Cano, J.; Vergniory, M. G.; Wang, Z.; Felser, C.; Aroyo, M. I.; Bernevig, B. A., Topological quantum chemistry. *Nature* **2017,** *547* (7663), 298-305.
46. Vergniory, M. G.; Elcoro, L.; Felser, C.; Regnault, N.; Bernevig, B. A.; Wang, Z., A complete catalogue of high-quality topological materials. *Nature* **2019,** *566* (7745), 480-485.

47. Vergniory, M. G.; Wieder, B. J.; Elcoro, L.; Parkin, S. S. P.; Felser, C.; Bernevig, B. A.; Regnault, N., All Topological Bands of All Stoichiometric Materials. *Science (American Association for the Advancement of Science)* ***2022****, 376 (6595), eabg9094-eabg9094.*
48. Hill, V. G.; Chang, L. L. Y., Hydrothermal investigation of GeO2. *American Mineralogist* **1968,** *53* (9-10), 1744-1748.
49. Stevenson, K. J.; Gao, X.; W. Hatchett, D.; White, H. S., Voltammetric measurement of anion adsorption on Ag(111). *Journal of Electroanalytical Chemistry* **1998,** *447* (1), 43-51.
50. Liang, X.; Kim, Y.-G.; Gebergziabiher, D. K.; Stickney, J. L., Aqueous Electrodeposition of Ge Monolayers. *Langmuir* **2010,** *26* (4), 2877-2884.
51. Carim, A. I.; Gu, J.; Maldonado, S., Overlayer Surface-Enhanced Raman Spectroscopy for Studying the Electrodeposition and Interfacial Chemistry of Ultrathin Ge on a Nanostructured Support. *ACS Nano* **2011,** *5* (3), 1818-1830.
52. Smith, C. P.; White, H. S., Voltammetry of molecular films containing acid/base groups. *Langmuir* **1993,** *9* (1), 1-3.
53. Waelder, J.; Maldonado, S., Beyond the Laviron Method: A New Mathematical Treatment for Analyzing the Faradaic Current in Reversible, Quasi-Reversible, and Irreversible Cyclic Voltammetry of Adsorbed Redox Species. *Analytical Chemistry.* **2021,** *93* (37), 12672-12681.
54. Myland, J. C.; Oldham, K. B., Quasireversible cyclic voltammetry of a surface confined redox system: a mathematical treatment. *Electrochemistry Communications* **2005,** *7* (3), 282-287.
55. White, H. S.; Peterson, J. D.; Cui, Q.; Stevenson, K. J., Voltammetric Measurement of Interfacial Acid/Base Reactions. *The Journal of Physical Chemistry B* **1998,** *102* (16), 2930-2934.
56. Burgess, I.; Seivewright, B.; Lennox, R. B., Electric Field Driven Protonation/Deprotonation of Self-Assembled Monolayers of Acid-Terminated Thiols. *Langmuir* **2006,** *22* (9), 4420-4428.
57. Luque, A. M.; Mulder, W. H.; Calvente, J. J.; Cuesta, A.; Andreu, R., Proton Transfer Voltammetry at Electrodes Modified with Acid Thiol Monolayers. *Analytical Chemistry (Washington, DC, United States)* **2012,** *84*, 5778-5786.
58. Calvente, J. J.; Luque, A. M.; Andreu, R.; Mulder, W. H.; Olloqui-Sariego, J. L., Analytical Expressions for Proton Transfer Voltammetry: Analogy to Surface Redox Voltammetry with Frumkin Interactions. *Analytical Chemistry* **2013,** *85* (9), 4475-4482.
59. Trinh, T. T.; Rozanska, X.; Delbecq, F.; Tuel, A.; Sautet, P., The mechanism of the initial step of germanosilicate formation in solution: a first-principles molecular dynamics study. *Physical Chemistry Chemical Physics* **2016,** *18* (21), 14419-14425.
60. Murad, S. N. A.; Baine, P. T.; McNeill, D. W.; Mitchell, S. J. N.; Armstrong, B. M.; Modreanu, M.; Hughes, G.; Chellappan, R. K., Optimisation and scaling of interfacial GeO2 layers for high-κ gate stacks on germanium and extraction of dielectric constant of GeO2. *Solid-State Electronics* **2012,** *78*, 136-140.
61. Lee, C. H.; Tabata, T.; Nishimura, T.; Nagashio, K.; Kita, K.; Toriumi, A., Ge/GeO2 Interface Control with High Pressure Oxidation for Improving Electrical Characteristics. *ECS Transactions* **2019,** *19* (1), 165-173.
62. Smart, M. M.; McMillen, C. D.; Ivey, K.; Kolis, J. W., Chemistry of Metal Silicates and Germanates: The Largest Metal Polygermanate, K11Mn21Ge32O86(OH)9(H2O), with a 76 Å Periodic Lattice. *Inorganic Chemistry* **2020,** *59* (23), 16804-16808.
63. Everest, D. A.; Salmon, J. E., Studies in the chemistry of quadrivalent germanium. Part II. The depolymerisation of the pentagermanate ion with change of pH, and ion-exchange studies of

germanate solutions containing sulphate and orthophosphate. *Journal of the Chemical Society (Resumed)* **1955,** (0), 1444-1449.
64. Qin, C.; Gao, L.; Wang, E., Germanium: Inorganic Chemistry Based in part on the article Germanium: Inorganic Chemistry by Frank Glockling which appeared in the Encyclopedia of Inorganic Chemistry, First Edition. *Encyclopedia of Inorganic Chemistry* **2005**.
65. Ingri, N., Equilibrium Studies of Polyanions. 12. Polygermanates in Na(Cl) Medium. *Acta Chemica Scandinavica* **1963,** *17*, 597-617.
66. Vegas, A.; Jenkins, H. D. B., A revised interpretation of the structure of (NH4)2Ge7O15 in the light of the Extended Zintl-Klemm Concept. *Acta Crystallographica Section B* **2017,** *73* (1), 94-100.
67. Ingri, N.; Lundgren, G., The Crystal Structure of $Na_4Ge_9O_{20}$. *Acta Chemica Scandinavica* **1963,** *17*, 617-633.
68. Emery, S. B.; Hubbley, J. L.; Roy, D., Voltammetric and amperometric analyses of electrochemical nucleation: electrodeposition of copper on nickel and tantalum. *Journal of Electroanalytical Chemistry* **2004,** *568*, 121-133.
69. Guo, L.; Searson, P. C., On the influence of the nucleation overpotential on island growth in electrodeposition. *Electrochimica Acta* **2010,** *55* (13), 4086-4091.
70. Guo, L.; Oskam, G.; Radisic, A.; Hoffmann, P. M.; Searson, P. C., Island growth in electrodeposition. *Journal of Physics D: Applied Physics* **2011,** *44* (44), 443001.

Chapter 3 X-Ray Reflectivity and Scattering of Hg-In Alloy Electrodes

3.1 Preface

The following work details in-situ X-ray reflectivity (XRR) measurements of the liquid Hg-In electrode interfaces. The XRR data was collected by Andrea Sartori, Rajendra P. Giri, Henry Wu and Joshua P. Hazelnis under the equal guidance of Stephen Maldonado, Bridget M. Murphy and Olaf M. Magnussen. Andrea Sartori assisted in developing the code used for XRR data analysis and interpretation. Joshua P. Hazelnis performed all the fitting and data analysis. The writing, figures, and discussions of the work were equal in contribution between Joshua P. Hazelnis, Andrea Sartori, Stephen Maldonado, Bridget M. Murphy, and Olaf M. Magnussen.

3.2 Introduction

Liquid metals are potent media for the chemical and electrochemical syntheses of inorganic semiconductors, intermetallics, and metal alloys.[1-11] In many of these synthetic approaches, the liquid metals are inherently mixtures (e.g. solvent and solute),[7, 12, 13] sometimes consisting of several components.[14-16] Since the surface tension of liquid metals can be high, growth and/or segregation of materials with lower surface tension typically occurs at the surface.[17, 18] Accordingly, methodologies that provide insight on the composition and structure of liquid metal mixture interfaces are highly valuable.

Arguably the most direct method for studying the surface of a liquid metal is X-ray reflectivity (XRR). When performed at shallow angles, XRR can provide insight on the atomic structure along the surface normal of a liquid metal in contact with vacuum, ambient air, or water.[19-28] Extensive experimental XRR measurements and complementary theoretical work have been collected for pure elemental liquid metals including Hg,[27-32] Ga,[23, 25, 32-34], Bi,[35] Sn,[35, 36] K,[37] and In.[21] The interfaces of several binary liquid metal mixtures (Hg-Au,[38] Hg-Ga,[34] Ga-Bi,[39] Ga-Pb,[17] Ga-In,[23] Bi-In,[40] Ga-Sn,[41] Au-Si,[42] Au-Ge,[43] Pd-Ge,[19] and Na-K[44]) have also been studied by XRR. Among these systems, the majority were examined either at a single binary composition or within a narrow compositional range and all were studied in contact with just vacuum.

Liquid metal mixtures in contact with liquid phases underpin electrochemical synthetic routes.[1, 6, 11, 14, 45] Among these junction types, liquid Hg-In amalgams in contact with water are particularly interesting for several reasons. First, in general, very few liquid metals have been studied in electrochemical settings. The existing data on pure Hg electrodes suggest some features are functions of the applied potential.[27, 31] It is presently unclear if this aspect is unique to pure Hg or more general to other liquid metals. Second, Hg-In amalgam electrodes were previously utilized for the separate electrochemical growths of crystalline Ge and several transition metal intermetallics.[14-16] In all cases, the form of the as-obtained crystallites depended strongly on the bulk Hg-In composition. Third, the Hg-In binary system accommodates a wide range of bulk liquid compositions at room temperature since nearly 70 at.% In can be dissolved in Hg at T = 25 °C at standard pressure.[46] This binary system thus affords the possibility of evaluating surface structure across Hg-rich to In-rich bulk compositions. This feature is particularly interesting since amongst other investigated pure liquid metals, Hg is well known to have a complex surface structure that differs from that of the underlying bulk.[22, 26, 31, 35, 47] More recently, a pronounced enhancement in the diffuse scattering measured at low incidence angles has been observed at liquid Hg interfaces.[31] Such signatures are predicted to arise at the critical angle of the interface, i.e. a Yoneda signature,[48] and are often ascribed as indicators of surface heterogeneity across the surface plane.[49] Yoneda features have not been reported for most liquid metal surfaces and it is unclear if Hg is unique in this regard. More generally, it is not presently clear what factors are relevant to the detection of a Yoneda signal at a liquid metal interface. Analysis of this feature across Hg-In compositions would shed light on these basic questions.

Herein, this work reports XRR data on the interface between a set of Hg-In alloys ($Hg_{0.35}In_{0.65}$, $Hg_{0.50}In_{0.50}$, and $Hg_{0.95}In_{0.05}$) electrodes and an aqueous electrolyte at a series of applied biases. Analysis of experiments performed as a function of normalized incident angle ($q_z = (4\pi/\lambda)\cdot\sin\alpha_i$; where α_i is the incident angle of the X-ray beam with wavelength λ) and applied potential (E). At q_z values below the critical angle, diffuse scattering data across all bulk compositions are presented that show clear Yoneda features. (Figure 3.1) The factors that affect the observation of this signal are discussed. At q_z values much greater than the critical angle, the specular reflectivity data highlight the evolving surface characteristics (composition, roughness) as a function of bulk composition and applied potential.

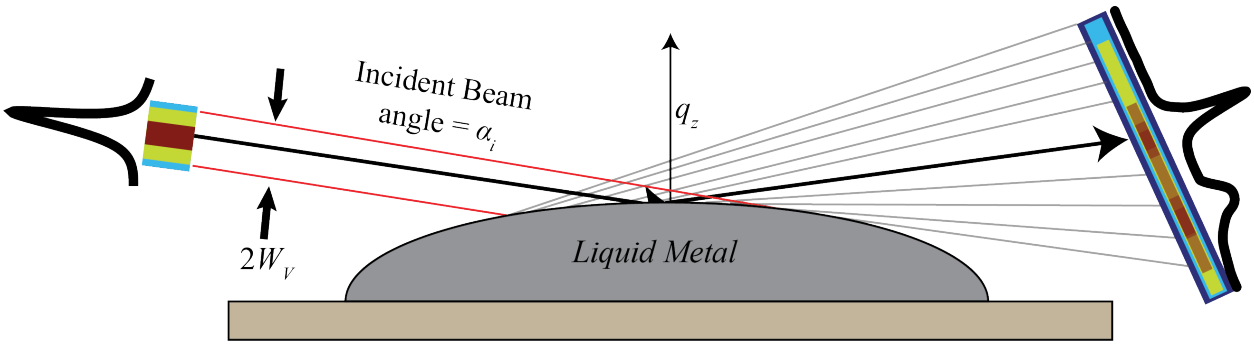

Figure 3.1 Schematic illustration of an X-ray reflectivity measurement where an X-ray beam of vertical height $2W_V$ at an incident angle, α_i interacts with the surface of a liquid metal.

3.3 Experimental

3.3.1 Materials

Aqueous 0.10 M $Na_2B_4O_7$ electrolyte solutions were prepared by measuring out the appropriate amount of $Na_2B_4O_7$ (99.998%, ChemPur) on a mass balance and subsequently mixing with nanopure water (resistivity >18.2 MΩ·cm) in a glass volumetric flask. Hg_xIn_{1-x} (x = 0.35, 0.50, 0.95) alloys were prepared by separately measuring the liquid Hg (99.999+%, ChemPur) and Indium shot (99.9999%, ChemPur) in the appropriate masses to generate a liquid metal of the desired composition with a volume of 25 mL. After measuring each component separately, they were stirred together in a clean 100 mL glass beaker to form a completely homogeneous mixture before transferring 20 of the 25 mL into a Hamilton 1025 TLL 25 mL syringe, leaving behind any surface oxide which may have formed. The syringe filled with 20 mL of Hg_xIn_{1-x} (x = 0.35, 0.50, 0.95 at%) was connected to the XRR cell and ≈ 15 mL of liquid metal was inserted into the cell following sufficient sparging of the electrolyte solution with N_2.

3.3.2 X-Ray Reflectivity Measurements and Analysis

XRR measurements were conducted using the same experimental cell and general procedure as previously described.[14, 27] (Figure 3.1) XRR measurements were conducted at beamline P08 using the Liquid Interface Scattering Apparatus (LISA) diffractometer of the Petra III synchrotron source at DESY in Hamburg, Germany.[50] A beam size of 0.4 mm horizontal ($2W_H$) by 0.1 mm vertical ($2W_V$) and photon energy of 25 keV and a wavelength (λ) of 0.04959 nm was used. Reflected intensities were collected with a GaAs Lambda detector (1536 x 512 array of pixels with a pixel height of 55 μm). Throughout data collection, beam attenuators ensured that the count intensity was ≤ 10^5 counts per pixel. The measured XRR intensity was obtained from integration of a detector area corresponding to a vertical and horizontal acceptance of 0.4° and 0.08°, respectively. The background intensity from X-ray scattering from bulk liquid metal and the electrolyte was determined at a 0.08° horizontal offset and subtracted from the main signal. The XRR curves were obtained by normalizing the background-subtracted detector signal by the direct beam intensity and are presented as a function of q_z.

Prior to first measurement, the cell was filled with 0.1 M $Na_2B_4O_7$(aq) electrolyte solutions and then purged with N_2(g) for at least 30 minutes. Throughout all measurements, the headspace of the cell was maintained under a slight positive N_2(g) pressure. After purging, 25 mL of Hg,

$Hg_{0.35}In_{0.65}$, $Hg_{0.50}In_{0.50}$, or $Hg_{0.95}In_{0.05}$ were injected into the cell. The liquid metal pool was then held at a constant potential with respect to an Ag/AgCl (sat. KCl) reference electrode via a digital, computer-controlled potentiostat (Ametek Modulab) for at least 15 minutes prior to reflectivity measurements to ensure a stable interface. All measurements were performed at lab temperature (T = 20 ± 5 °C).

Angle-dependent XRR data was collected for each Hg_xIn_{1-x} liquid metal composition, from small (0.04 $Å^{-1}$) to large (2.5 $Å^{-1}$) values of q_z. Depending on the integration time used, these scans required between 0.6 to 1.5 hours for collection. Each scan which was collected at a constant applied bias between -1.00 V and -1.40 V vs. Ag/AgCl (sat. KCl). At any given potential, scans were collected in duplicate or triplicate in a random sequence of applied potentials to avoid any systematic or cumulative bias in the data. The cell was held under potential control for the duration of reflectivity experiments and was not allowed to go to open-circuit in-between measurements. At every potential, the beam was aligned with the liquid surface in plane (x and y) and out of plane (z) using a set of independent motor positions to maximize the reflected intensity.

Custom-written python scripts included in Appendix B.2 were used to fit the normalized XRR data at q_z values much larger than the critical angle according to the 'master formula',[51]

$$\frac{R(q_z)}{R_F(q_z)} = \left| \left(\frac{1}{\rho_{e^-,HgIn,bulk} - \rho_{e^-,H_2O}} \right) \mathcal{F}\left(\frac{d\rho_{e^-}(z)}{dz} \right) \right|^2$$

Equation 3.1

where ρ_{e^-,H_2O} is the electron density of the bulk aqueous solution, $\rho_{e^-,HgIn,bulk}$ is the electron density of the bulk liquid metal, and $\mathcal{F}\left(\frac{d\rho_{e^-}(z)}{dz} \right)$ is the Fourier transform of the first derivative of the electron density along the axis (z) normal to the interface. The specific variants of the 'distorted crystal model'[20, 25] used in *Equation* 3.1 are described below. For every reported fit, multiple fitting rounds were performed to refine fit values and to minimize the cumulative χ^2 value.

For analysis of specular and diffuse scattering at small q_z values, *Equation* 3.1 was not used. Instead, data were first collected at fixed q_z values (0.08, 0.1 $Å^{-1}$, and 0.3 $Å^{-1}$) with a signal integration times of 10 s, 15 s, and 20 s respectively. Both the specular beam centered at α_i on the detector and the diffuse scattering were integrated along q_z with a single pixel resolution = 0.0006

± 0.0001 Å^{-1} and across q_x with a 12 pixel width = 0.0072 ± 0.0001 Å^{-1}. These integrated linescans were empirically fit with skewed Lorentzian profiles (*Equation* 3.2) using a custom python code included in Appendix B.3, to assign peak intensities (I), position ($q_{z,peak}$), width ($FWHM_{peak}$), and asymmetry (sk_{peak}),

$$I(q_z) = \left(1 + erf\left(\frac{sk_{peak}(q_z - q_{z,peak})}{FWHM}\right)\right) \times \left(\frac{I_{peak}}{1 + \left(\frac{q_z - q_{z,peak}}{FWHM}\right)^2}\right)$$

Equation 3.2

The uncertainties in the values I, $q_{z,peak}$, $FWHM_{peak}$, and sk_{peak} are reported as standard deviations across all the fits for a given measurement set.

3.4 Results

Figure 3.2a displays a representative detector image from a static scattering measurement at fixed incident angle (q_z = 0.10 Å^{-1}) of the specular and diffuse scattering. A prominent spot from the specular beam and a less intense secondary concentration of the diffuse scattering were observable. Integration of the region of interest highlighted by the orange box along q_z after normalization with respect to the specular peak intensity (I_0) yielded profiles as shown in Figure 3.2b. Figure 3.2b shows representative data for $Hg_{0.35}In_{0.65}$ (black), $Hg_{0.50}In_{0.50}$ (red), and $Hg_{0.95}In_{0.05}$ (blue). For all liquid metal compositions, the specular beam was centered at q_z = 0.100 ± 0.001 Å^{-1}. However, the width and overall noise of the specular peaks differed across compositions, with broader widths and lower I_0 values for larger bulk In concentrations. A secondary peak of maximum diffuse scattering was evident for all three compositions between q_z = 0.04 and 0.07 Å^{-1}. The asymmetric shape of the Yoneda peak across the three liquid metal compositions was similar, with a broad tailing toward q_z = 0 Å^{-1}. The intensity of the Yoneda peak (I_Y) also differed across the three Hg-In liquids, with the highest signal-to-noise observed for the largest In concentration, opposite the trend of the specular peak. Qualitatively, the integrated signal for scans collected with q_z = 0.08 Å^{-1} exhibited the same behavior, with a shift to $q_{z,peak}$ = 0.080 ± 0.001 Å^{-1} (Figure 3.3). For reference, static specular and diffuse scattering acquired at the larger q_z = 0.3 Å^{-1} showed a much more pronounced specular peak centered at q_z = 0.300 ± 0.001 Å^{-1}. At

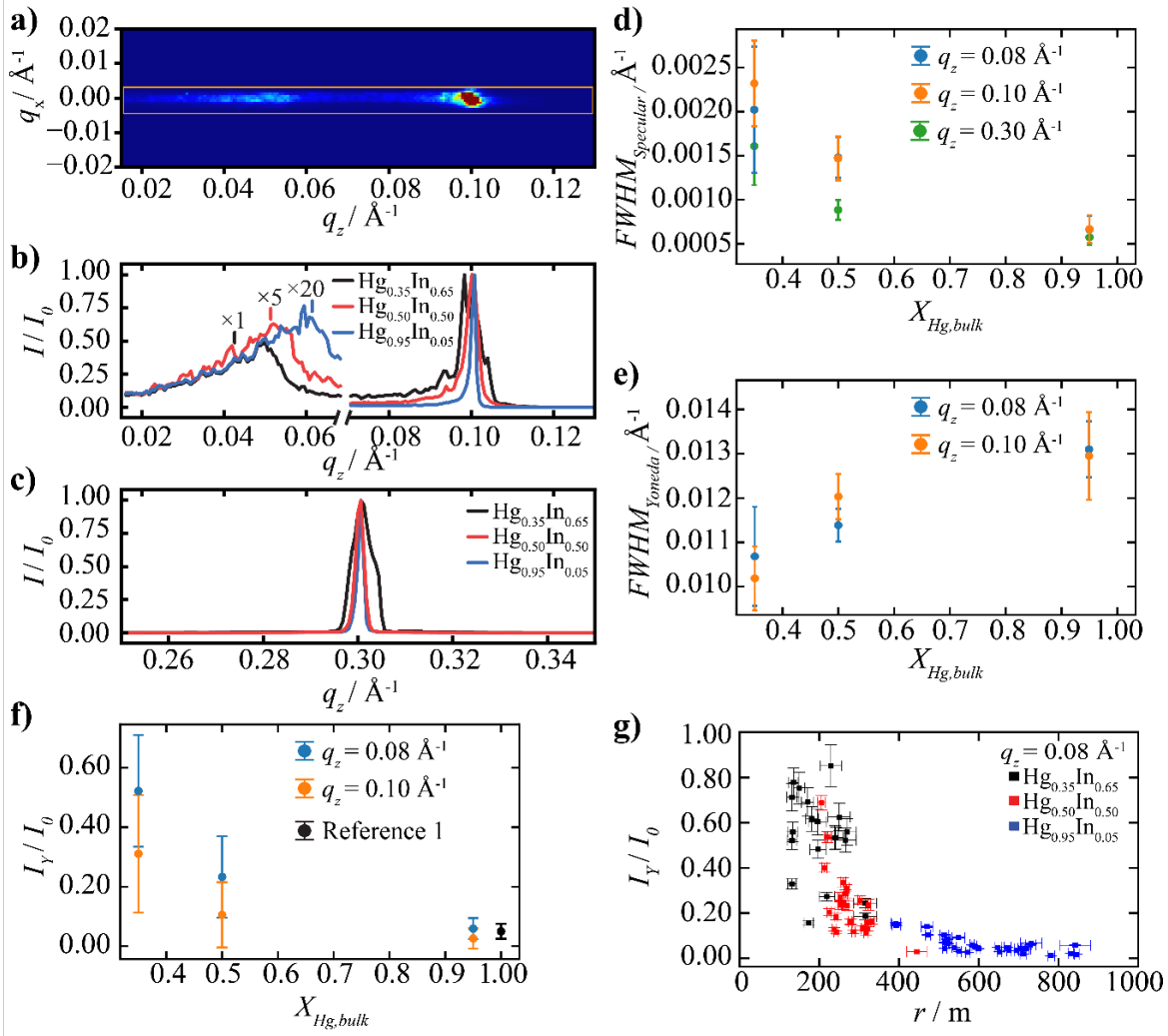

Figure 3.2 a) Example of the reflected beam signal from a liquid $Hg_{0.50}In_{0.50}$ immersed in 0.1 M $Na_2B_4O_7(aq)$ for a fixed incident angle q_z = 0.10 Å^{-1}. b) Line scans of the measured specular and diffuse scattering intensity integrated along q_z across the orange box in (a) for $Hg_{0.35}In_{0.65}$ (black), $Hg_{0.50}In_{0.50}$ (red), and $Hg_{0.95}In_{0.05}$ (blue). Intensities for q_z < 0.7 Å^{-1} scaled by 1, 5, 20 times, respectively. c) Example integrated profiles of the specular beam for the same liquid metals measured at q_z = 0.30 Å^{-1}. d) $FWHM_{Specular}$ as a function of Hg-In bulk composition. e) $FWHM_{Yoneda}$ as a function of Hg-In bulk composition. f) Normalized Yoneda intensity (I_Y/I_0) as a function of Hg-In bulk composition. g) Normalized Yoneda intensity as a function of radius of curvature (r) of the liquid metal for measurements with q_z = 0.08 Å^{-1}

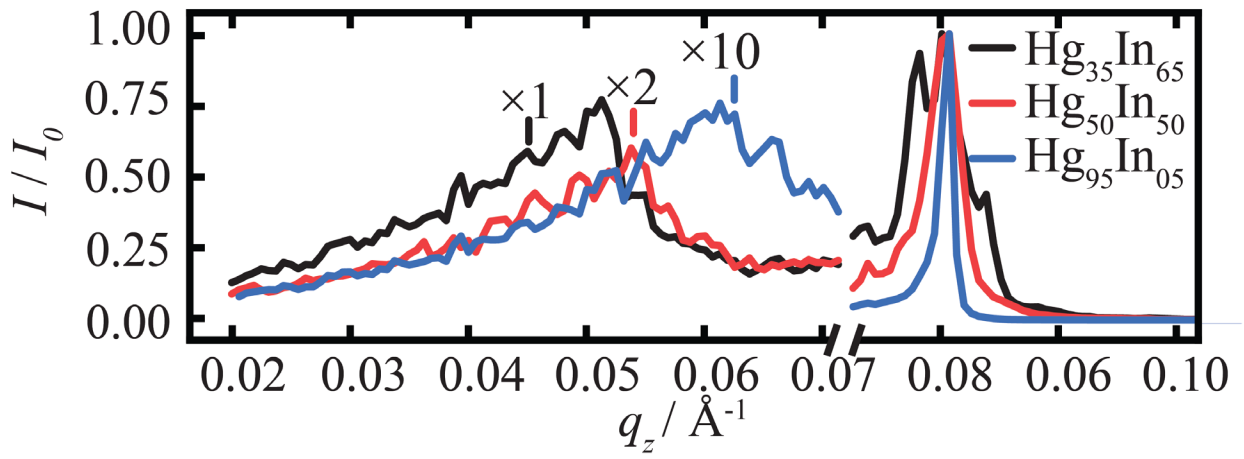

Figure 3.3 Example integration of the reflected beam intensity profile for $Hg_{35}In_{65}$ (black), $Hg_{50}In_{50}$ (red), and $Hg_{95}In_{05}$ (Blue) for incident angle $q_z = 0.08$ Å^{-1}. Intensity at angles smaller than $q_z \approx 0.7$ Å^{-1} scaled by 1, 2, 10 times, respectively.

this incident angle, the diffuse scattering was minimal (Figure 3.2c). Nevertheless, the broader character of the specular peak for $Hg_{0.35}In_{0.65}$ was still observed. The average intensity, peak positions, widths, and asymmetries for all the static scattering data as defined by *Equation* 3.2 are reported in Table 3.1.

The widths of the specular and Yoneda peaks in the static scattering measurements differed across the three bulk Hg-In compositions. Figure 3.2d shows the average $FWHM_{specular}$ values plotted against the Hg content in the liquid Hg-In mixture. Larger $FWHM_{specular}$ values were seen with lower bulk Hg concentrations. Figure 3.2e showed the opposite trend for $FWHM_{Yoneda}$, where smaller values were observed with lower bulk Hg concentrations, although the absolute change in average width was much less pronounced than for the specular peak. The normalized intensities of the Yoneda peak intensities (I_Y/I_0) also tracked with bulk Hg concentrations (Figure 3.2f). Normalization of the Yoneda signatures in this way accounted for fluctuations in the incident X-ray intensities, variation in counting times used during data collection, and comparison with previously reported I_Y values for pure Hg.[31] The smaller I_Y/I_0 values reported for pure Hg were in agreement with the trend seen here with increasing bulk Hg content.

The data were also assessed in terms of the apparent radius of curvature, r, of each liquid metal interface. In general, $r = mg/(2\pi\gamma)$, where m is the liquid metal mass, g is the gravitational constant, and γ is liquid metal surface tension. Since γ is a known function of the applied potential through electrocapillarity,[52, 53] the radius of curvature for a given measurement in this study will depend on the applied potential. Estimates of r for each measurement are possible through $FWHM_{specular}$ as described in *Equation* 3.3,[54]

$$r = \frac{W_v}{\left|\cos\left(FWHM_{specular} + \alpha_i\right) - \cos\left(\alpha_i\right)\right|}$$

Equation 3.3

where W_v is half the vertical incident beam height. With *Equation* 3.3, the I_Y/I_0 values for every measurement made in this work (i.e. across different incident angles, applied potential, and compositions) were plotted as a function of r (Figure 3.2g). The data showed an inverse correlation with r. The magnitude of this correlation depended on the value of q_z used for the static scattering measurements, as data collected at $q_z = 0.10$ Å^{-1} showed a less pronounced dependence on r (Figure 3.4). Overall, the data were clearly segmented along the r axis according to bulk composition, resulting in few measurements where the bulk compositions were different but the apparent r value

Table 3.1 Specular and Diffuse Scattering Features

liquid metal	q_z (Å^{-1})	$q_{z,specular}$ (Å^{-}	$FWHM_{specular}$ (Å^{-}	$sk_{specular}$	$q_{z,Yoneda}$ (Å^{-}	$FWHM_{Yoneda}$ (Å^{-}	sk_{Yoneda}	I_Y / I_0	r (m)
$Hg_{0.35}In_{0.65}$		0.079 ± 0.001	0.0020 ± 0.0007	-0.1 ± 0.2	0.051 ± 0.001	0.011 ± 0.001	-0.6 ± 0.2	0.52 ± 0.19	220 ±40
$Hg_{0.50}In_{0.50}$	0.08	0.081 ± 0.001	0.0015 ± 0.0002	-0.3 ± 0.1	0.054 ± 0.001	0.011 ± 0.001	-0.6 ± 0.1	0.23 ± 0.14	280 ± 50
$Hg_{0.95}In_{0.05}$		0.081 ± 0.001	0.0007 ± 0.0002	-0.3 ± 0.1	0.063 ± 0.001	0.013 ± 0.001	-0.2 ± 0.1	0.06 ± 0.04	640 ± 200
$Hg_{0.35}In_{0.65}$		0.100 ± 0.001	0.0023 ± 0.0005	-0.1 ± 0.2	0.050 ± 0.001	0.010 ± 0.001	-0.6 ± 0.1	0.31 ± 0.20	210 ± 20
$Hg_{0.50}In_{0.50}$	0.10	0.101 ± 0.001	0.0015 ± 0.0002	-0.3 ± 0.1	0.053 ± 0.001	0.012 ± 0.001	-0.7 ± 0.1	0.11 ± 0.11	280 ± 50
$Hg_{0.95}In_{0.05}$		0.101 ± 0.001	0.0007 ± 0.0002	-0.3 ± 0.1	0.060 ± 0.001	0.013 ± 0.001	-0.3 ± 0.1	0.03 ± 0.03	630 ± 100
$Hg_{0.35}In_{0.65}$		0.300 ± 0.001	0.0016 ± 0.0004	-	-	-	-	- - - -	270 ± 100
$Hg_{0.50}In_{0.50}$	0.30	0.301 ± 0.001	0.0009 ± 0.0001	-	-	-	-	- - - -	460 ± 60
$Hg_{0.95}In_{0.05}$		0.301 ± 0.001	0.0006 ± 0.0001	-	-	-	-	- - - -	710 ± 90

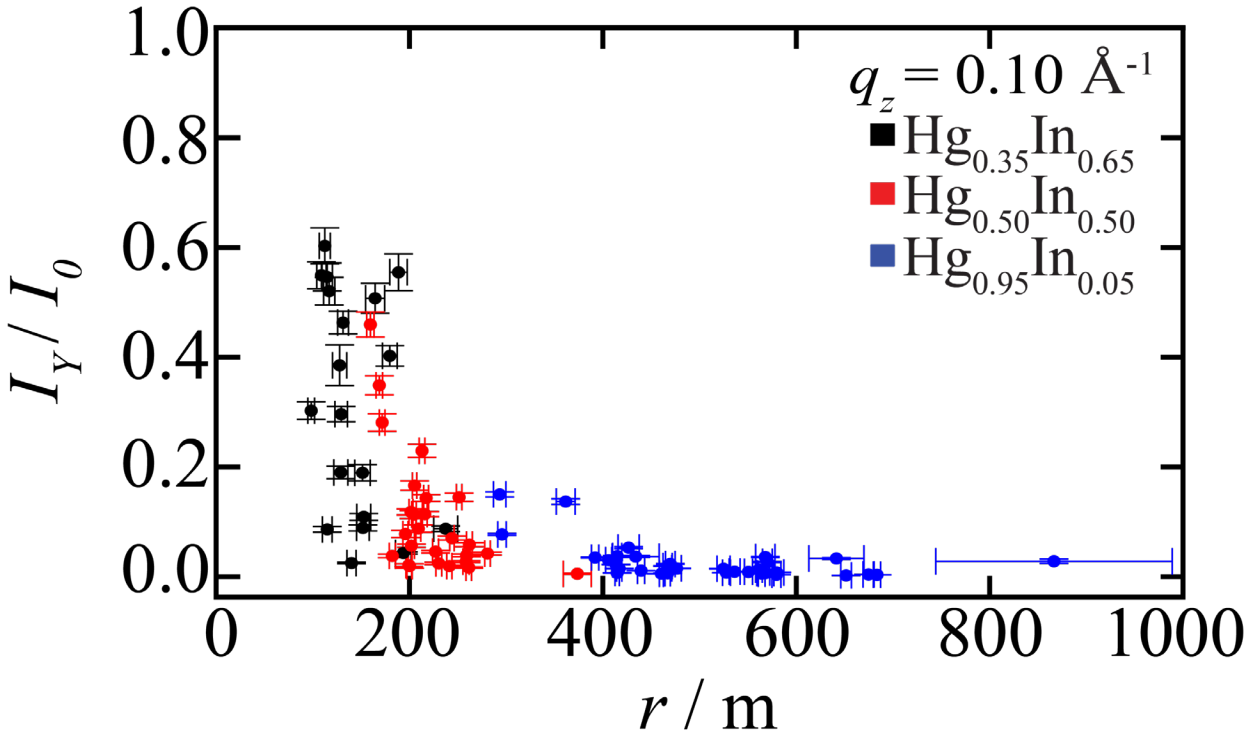

Figure 3.4 Yoneda intensity (I_Y / I_0) as a function of radius of curvature (r) of the liquid metal determined from *Equation* 3.3 and the fitted specular width from *Equation* 3.2 for the q_z = 0.10 Å^{-1} showing an increasing trend in intensity as the surface becomes more curved.

was the same. The best example of overlap is seen in Figure 3.2g at r = 260 ± 60 m. Over this range of r, there were 10 measurements for $Hg_{0.35}In_{0.65}$ and 24 measurements for $Hg_{0.50}In_{0.50}$. The respective average I_Y/I_0 values were 0.48 ± 0.20 and 0.24 ± 0.14, statistically distinct at the 99.9% confidence level.

All of the data in Figure 3.2 were acquired in static scattering measurements at a fixed incident angle and a constant applied potential, where the beam alignment was performed immediately prior to measurement but while the liquid metal was biased at the applied potential of interest. That is, at each applied potential, the beam position was optimized with respect to the specular beam intensity. All of the individual I_Y/I_0 values measured in this way (and summarized in Figure 2) at q_z = 0.10 Å^{-1} are shown in Figure 3.5a-c as a function of the applied potential. Globally, the measured I_Y/I_0 values did not exhibit an obvious dependence with potential for any liquid metal composition. Similar to I_Y/I_0, the position, width, and asymmetry of the Yoneda signal was invariant to potential. (Figure 3.6, Figure 3.7) However, analogous scattering measurements were performed where the applied potential was continuously varied (Figure 3.5d-f). In these experiments, the alignment was performed at the starting potential of the scan (denoted with a vertical dashed line in Figure 3.5d-f) and then the applied potential was swept without further realignment. These data exhibited a systematic influence of I_Y/I_0 with the applied potential, reflecting the effect of electrocapillarity. Although the profiles in Figure 3.5d-f resemble electrocapillarity curves and suggested perhaps a direct measurement of the potential dependence of γ for the liquid metal, the quantitative I_Y/I_0 profiles varied greatly as a function of beam position on the sample. For all liquid metal compositions, the height of the liquid metal interface increased at more negative potentials (Figure 3.8), indicating the beam alignment became less optimal as the potential was biased further away from the start potential. Accordingly, the utility of these measurements where the applied potential was actively changed without continuous realignment was limited. Accordingly, further analysis focused exclusively on static scattering measurements obtained at a fixed incident angle and a constant applied potential.

Figure 3.9 shows the average position of the Yoneda peak ($q_{z,peak,Yoneda}$) as a function of bulk liquid metal composition for data collected with both q_z = 0.08 and 0.10 Å^{-1}. The red line in Figure 3.9 denotes the expected critical angle ($q_c = 4\pi\sqrt{2\delta}\ /\ \lambda$) for the interface of each bulk Hg-In liquid and pure water, where δ is the real part of the refractive index and λ is the X-ray wavelength.[55] The measured $q_{z,peak,Yoneda}$ values were consistently ≤ 5 % of the expected critical

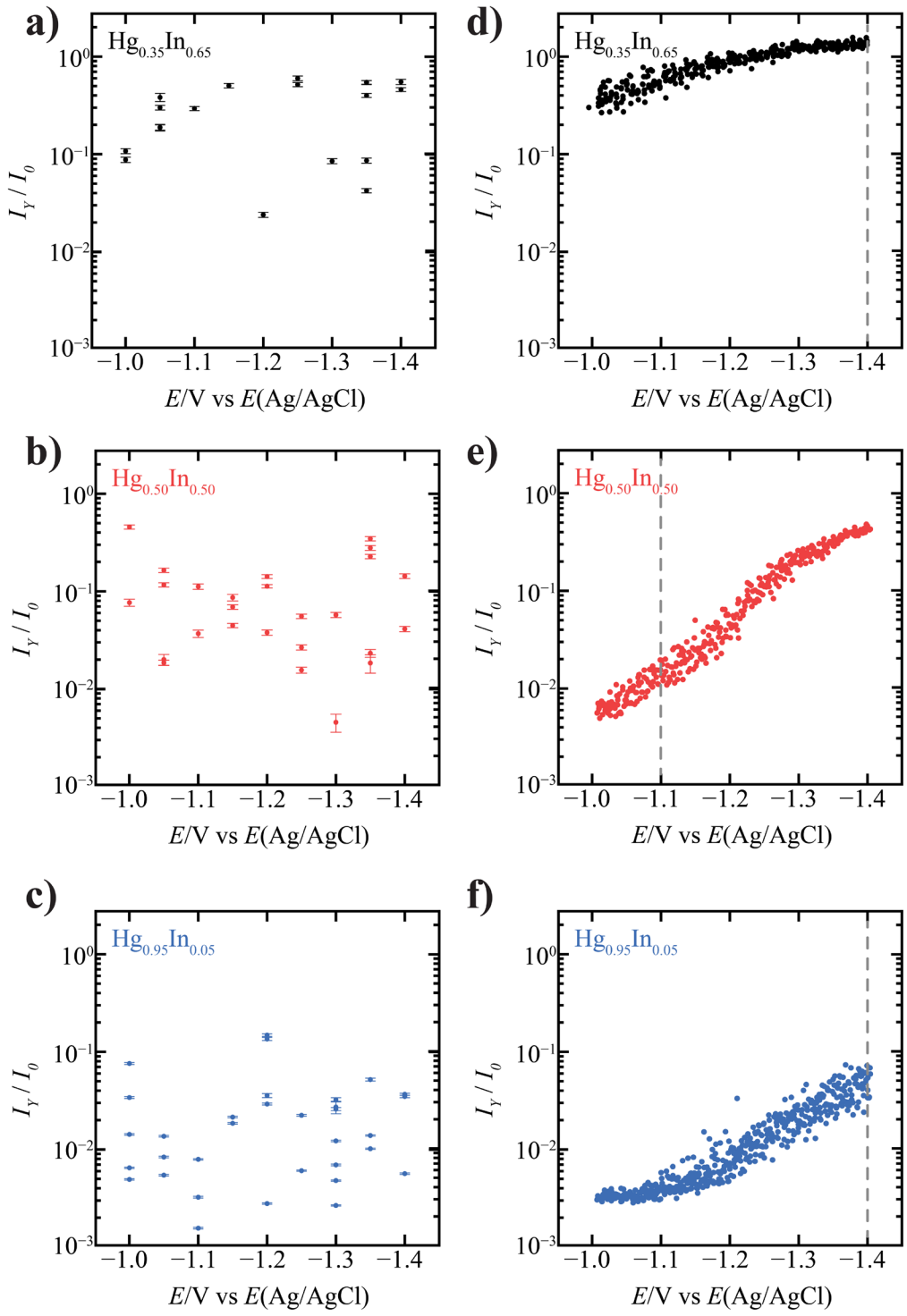

Figure 3.5 Potential dependence of I_Y/I_0 for a) $Hg_{0.35}In_{0.65}$, b) $Hg_{0.50}In_{0.50}$, and c) $Hg_{0.95}In_{0.05}$ electrodes when the measurement was performed at a constant applied potential and the incident beam was aligned at this potential. Analogous measurements were performed for d) $Hg_{0.35}In_{0.65}$, e) $Hg_{0.50}In_{0.50}$, and f) $Hg_{0.95}In_{0.05}$ electrodes where the potential was continuously scanned at 10 mV s^{-1} between -1.00 V to -1.40 V while scattering data was recorded. The dashed vertical lines denote the initial potential where the incident beam was aligned. All measurements were performed using an incident angle of $q_z = 0.10$ $Å^{-1}$

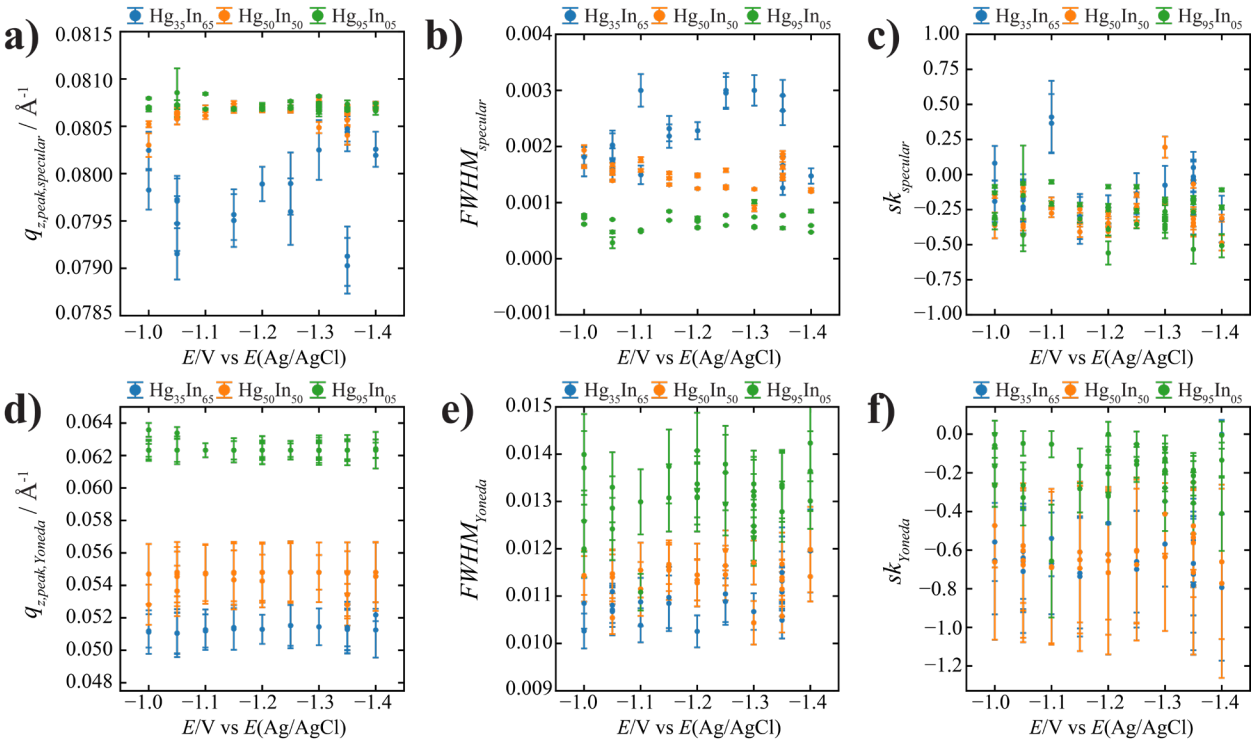

Figure 3.6 Plots of a) $q_{z,peak,specular}$ b) $FWHM_{specular}$ c) $sk_{specular}$ d) $q_{z,peak,Yoneda}$ e) $FWHM_{Yoneda}$ and f) sk_{Yoneda} versus applied potential (E) for fitting the diffuse scans of $Hg_{35}In_{65}$ (blue circle), $Hg_{50}In_{50}$ (orange circle), $Hg_{95}In_{05}$ (green circle) at a fixed incident angle of $q_z = 0.08$ Å^{-1} using *Equation* 3.2.

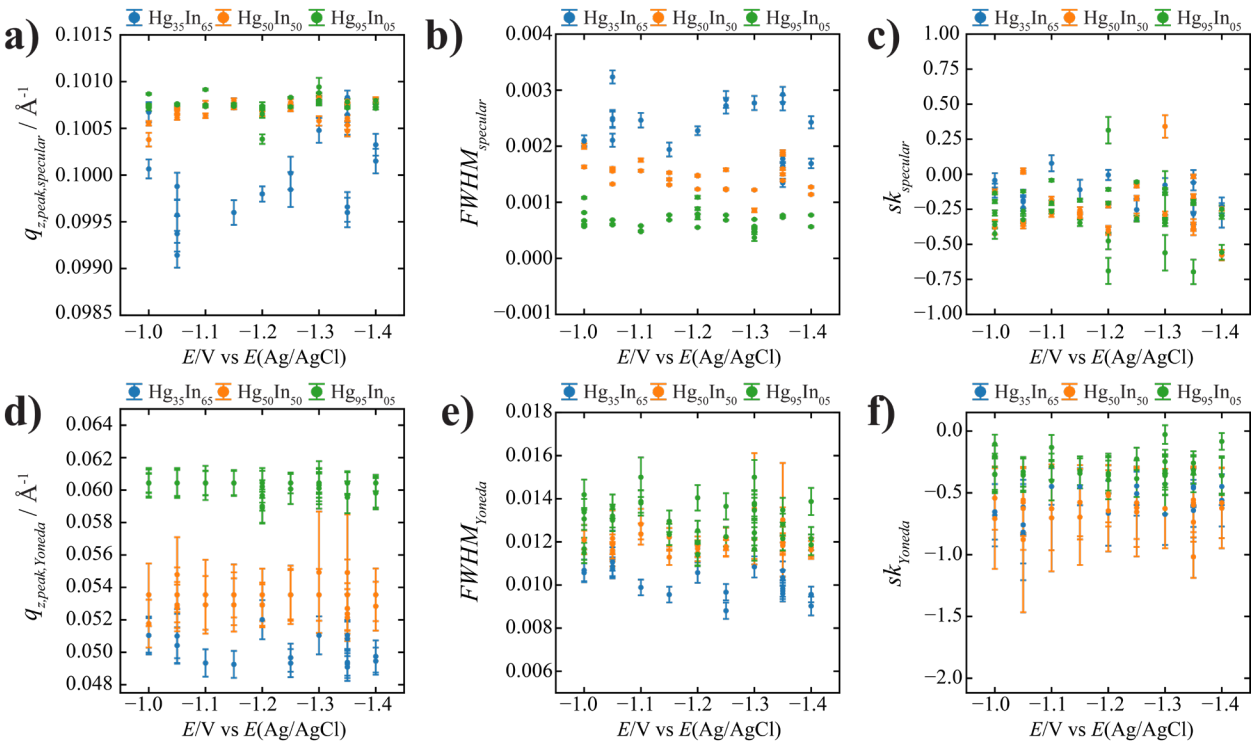

Figure 3.7 Plots of a) $q_{z,peak,specular}$ b) $FWHM_{specular}$ c) $sk_{specular}$ d) $q_{z,peak,Yoneda}$ e) $FWHM_{Yoneda}$ and f) sk_{Yoneda} versus applied potential (E) for fitting the diffuse scans of $Hg_{35}In_{65}$ (blue circle), $Hg_{50}In_{50}$ (orange circle), $Hg_{95}In_{05}$ (green circle) at a fixed incident angle of $q_z = 0.10$ Å^{-1} using *Equation* 3.2.

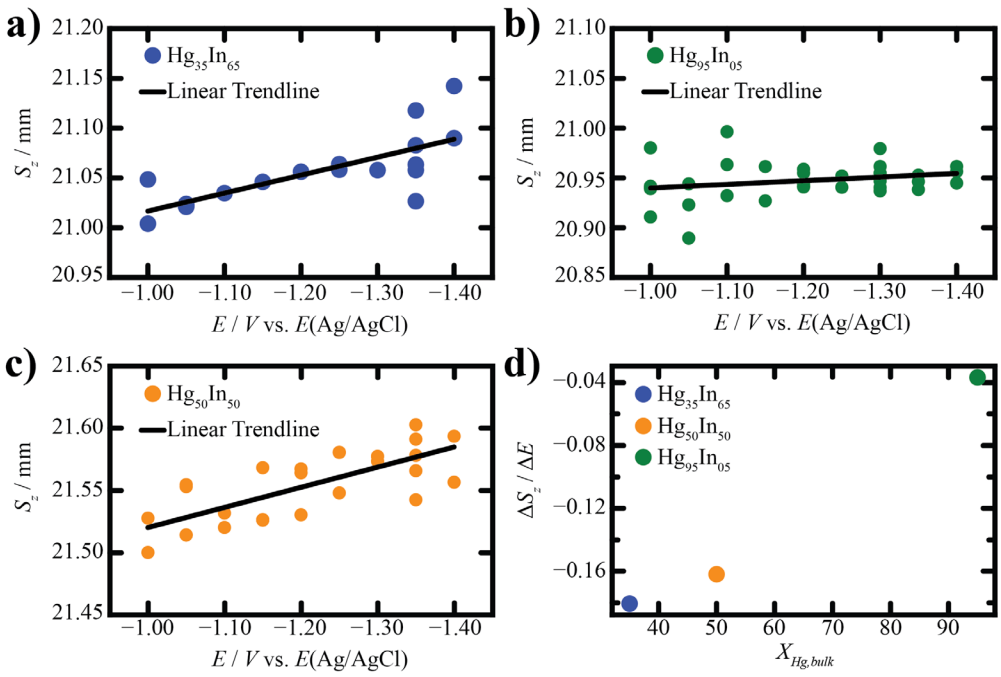

Figure 3.8 Plot of the a) $Hg_{35}In_{65}$ b) $Hg_{50}In_{50}$ c) $Hg_{95}In_{05}$ sample alignment (S_z) versus applied potential (E). d) Slope of the linear trendlines ($\Delta S_z / \Delta E$) used to fit the data in a-c versus liquid metal composition.

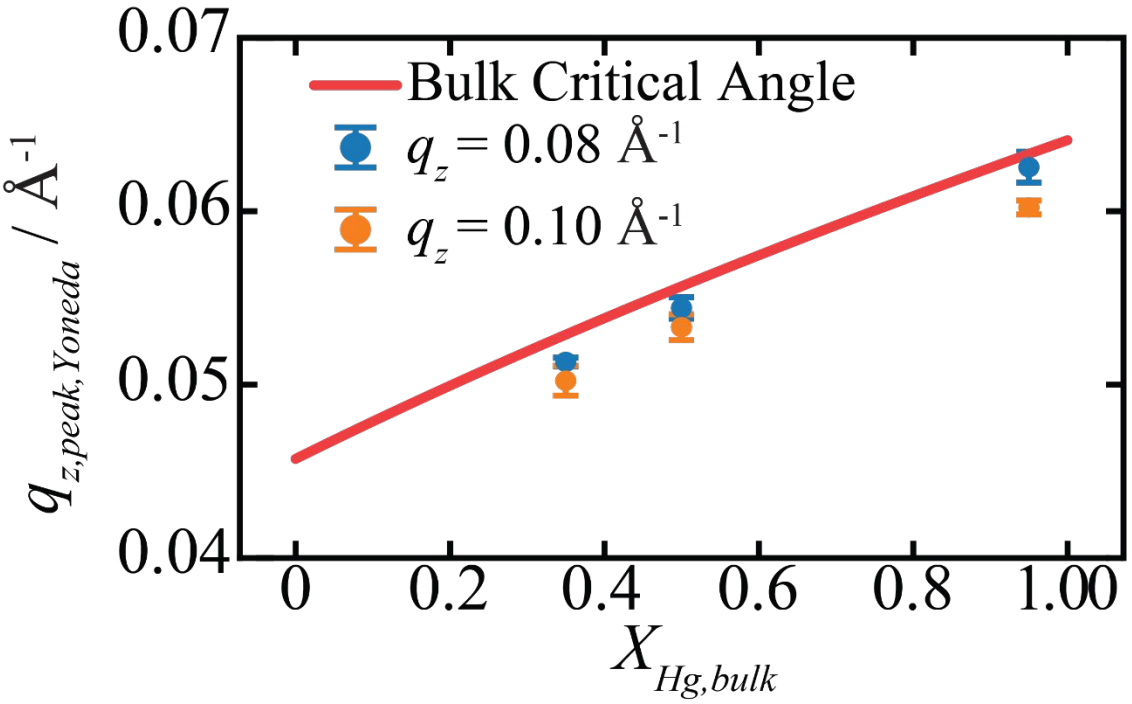

Figure 3.9 Plot of the normalized $q_{z,peak,Yoneda}$ position as function of Hg-In for fixed q_z = 0.08 Å^{-1} (blue circles) and q_z = 0.10 Å^{-1} (orange circles). The red line is the calculated value of the critical angle for the Hg-In/water interface assuming the refractive index of the bulk Hg-In composition.

angle for all liquid metal compositions, indicating that position of this peak in the diffuse scattering was sensitive to the *bulk* composition. This point is consistent with an X-ray penetration depth of the evanescent wave at the critical angle $(1 / q_c) \geq 15$ Å for all three Hg-In alloys at these incident angles. That is, the data in Figure 3.9 indicate that any possible change in composition at the surface in these Hg-In liquids did not extend significantly into the bulk.

Analysis of XRR data for $q_z > q_c$ was performed to separately assess the surface composition and structure. Figure 3.10 shows the normalized XRR data obtained at several different potentials for the three Hg-In compositions. The corresponding raw XRR data are displayed in Figure 3.11. The data in Figure 3.10 are the discrete symbols, with the error bars representing the inherent Poisson noise of the detector, calculated as the square root of the background corrected signal. Generally, the change in applied potential did not effect a substantial change in the XRR profile for a given liquid metal composition. For $Hg_{0.35}In_{0.65}$ and $Hg_{0.50}In_{0.50}$, the intensities of the normalized XRR profiles were equal to or slightly above the Fresnel behavior of the interface (i.e. $R(q_z)/R_F(q_z) \geq 1$) until $q_z > 1.0$ Å^{-1}. For $Hg_{0.95}In_{0.05}$, the data more closely matched prior reports for pure Hg/water interfaces,[26-28, 30, 31] where the XRR profiles deviated more broadly from the Fresnel reflectivity prior to the quasi-Bragg peak. The quasi-Bragg peak was most intense for $Hg_{0.35}In_{0.65}$. For all three Hg-In bulk compositions, the quasi-Bragg peak was centered at $q_z = 2.22 \pm 0.03$ Å^{-1}.

To fully evaluate the data, a modified form of the 'distorted crystal model' (DCM) denoted as the 'first layer'[20] model was used to describe the normalized XRR signal. In this model, the normalized reflectivity has contributions from the layer of liquid metal atoms at the interface (FirstLayer) and the aqueous electrolyte (Electrolyte) is described in *Equation* 3.4,

$$\frac{R(q_z)}{R_F(q_z)} = \left| \left(\frac{1}{\rho_{e^-,HgIn,bulk} - \rho_{e^-,H_2O}} \right) \left[\mathcal{F}\left(\frac{d\rho_{e^-,DCM}(z)}{dz} \right) + \mathcal{F}\left(\frac{d\rho_{e^-,FirstLayer}(z)}{dz} \right) + \mathcal{F}\left(\frac{d\rho_{e^-,Electrolyte}(z)}{dz} \right) \right] \right|^2$$

Equation 3.4a

$$\mathcal{F}\left(\frac{d\rho_{e^-,DCM}(z)}{dz} \right) = \left(\frac{f^0_{HgIn,bulk}(q_z) + f'_{HgIn,bulk}}{Z_{HgIn,bulk} + f'_{HgIn,bulk}} \right) \left(iq_z d\rho_{e^-,HgIn,bulk} \frac{e^{-q_z\left(iz_{bulk}+d\right) - \frac{q_z^2\left(\sigma_i^2+\sigma_b^2\right)}{2}}}{\left(1 - e^{q_z d - \frac{q_z^2\sigma_b^2}{2}}\right)} \right)$$

Equation 3.4b

$$\mathcal{F}\left(\frac{d\rho_{e^-,FirstLayer}(z)}{dz}\right)=\left(\frac{f^{0}_{HgIn,surface}(q_z)+f'_{HgIn,surface}}{Z_{HgIn,surface}+f'_{HgIn,surface}}\right)\left(iq_z d_{first}\left(\rho_{e^-,first}-\rho_{e^-,HgIn,bulk}\right)e^{-\left(iq_z z_{bulk}-\frac{q_z^2\sigma_{first}^2}{2}\right)}\right)$$

Equation 3.4c

$$\mathcal{F}\left(\frac{d\rho_{e^-,Electrolyte}(z)}{dz}\right)=\left(\frac{f^{0}_{H_2O}(q_z)+f'_{H_2O}}{Z_{H_2O}+f'_{H_2O}}\right)\left(-\rho_{e^-,H_2O}e^{-\left(iq_z z_{H_2O}-\frac{q_z^2\sigma_{H_2O}^2}{2}\right)}\right)$$

Equation 3.4d

where the $f_n^0(q_z)$ terms are the angle-dependent atomic form factors for material *n*, the f_n' terms are the dispersion corrections for material *n*, and the Z_n terms are the average atomic numbers for material *n*. The $f_n^0(q_z)$, f_n', and Z_n terms for the bulk and surface of the Hg-In liquid metals were calculated separately. *Equation* 3.5 describes these terms for the Hg-In surface (first) layer,

$$f_{HgIn,first}(q_z)=X_{Hg,first}f_{Hg}(q_z)+\left(1-X_{Hg,first}\right)f_{In}(q_z)$$

Equation 3.5a

$$f'_{HgIn,first}(E)=X_{Hg,first}f'_{Hg}(E)+\left(1-X_{Hg,first}\right)f'_{In}(E)$$

Equation 3.5b

$$Z_{HgIn,first}=X_{Hg,first}Z_{Hg}+\left(1-X_{Hg,first}\right)Z_{In}$$

Equation 3.5c

where $X_{Hg,first}$ and $X_{In,first}$ are the atomic fractions of Hg and In, respectively, in the first layer. Analogous expressions were used to describe the terms for the bulk of the Hg-In liquid metal.

The atomic fractions were fit through the corresponding electron density, $\rho_{e^-,first}$. The connection between $\rho_{e^-,first}$ and the fraction of Hg atoms in the first layer ($X_{Hg,first}$) is given in *Equation* 3.6,

$$\rho_{e^-,first} = X_{Hg,first} SLD_{Hg} + X_{In,first} SLD_{In}$$

Equation 3.6

where the scattering length densities, SLD,[55] denote how strongly X-rays will scatter through a given element. Given that $X_{Hg,first} + X_{In,first} = 1$, ***Equation* 3.7** follows.

$$X_{Hg,first} = \frac{\rho_{e^-,first} - SLD_{In}}{SLD_{Hg} - SLD_{In}}$$

Equation 3.7

Operationally, a value of $\rho_{e^-,first}$ less than $\rho_{e^-,bulk}$ denotes the first layer of the liquid metal was less electron dense than the underlying bulk liquid metal composition (i.e. In-rich). Correspondingly, a value of $\rho_{e^-,first}$ greater than $\rho_{e^-,bulk}$ corresponded to a Hg-rich surface.

Using *Equation* 3.4 - *Equation* 3.7, three variations of *Equation* 3.4 were applied to fit the data. The first approach used values of $\rho_{e^-,first}$ that set $X_{Hg,first}$ equal to the value predicted by the Gibbs adsorption theorem assuming no excess interaction energy (Table 3.2 and Table 3.3).[14, 56] At standard temperature and pressure, this approach predicted $X_{Hg,first}$ = 0.79, 0.88, 0.99, for $Hg_{0.35}In_{0.65}$, $Hg_{0.50}In_{0.50}$, and $Hg_{0.95}In_{0.05}$, respectively. The second approach assumed that the surface was pure Hg (i.e. $\rho_{e^-,first} = SLD_{Hg}$ so that $X_{Hg,first}$ = 1.0 for all cases). The third approach allowed $\rho_{e^-,first}$ to vary so that the value of $X_{Hg,first}$ was effectively a fit parameter bound between 0 and 1. The general qualities of these three approaches are summarized below, but the solid lines in Figure 3.10 correspond to fits with the third approach. Those fit parameters are summarized in Table 3.4. The corresponding electron density plots are shown in Figure 3.12. A fourth approach where $\rho_{e^-,first} = \rho_{e^-,bulk}$ so that $X_{Hg,first} = X_{Hg,bulk}$ was also initially explored but not considered further since the fits were uniformly poor for all conditions.

Across the three primary fitting approaches, several aspects in the fitting parameters were consistent. First, adequate fits could not be obtained if the roughness of the first layer (σ_{first}) was set equal to the roughness of the bulk layer immediately below the first layer (σ_i). This point was in stark contrast to prior XRR fits of liquid Hg/water interfaces.[31] The values of σ_{first} and σ_i were most dissimilar for $Hg_{0.35}In_{0.65}$ and most similar for $Hg_{0.95}In_{0.05}$. Second, σ_{first} was consistently

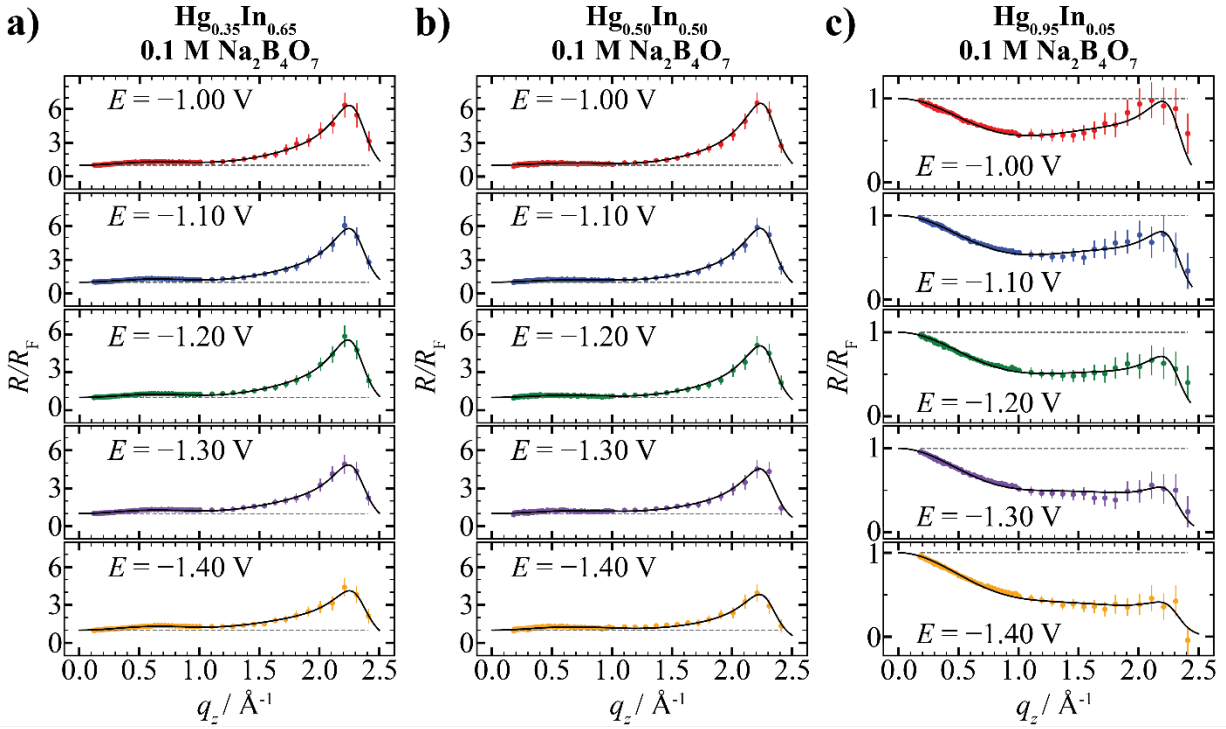

Figure 3.10 Plots of the normalized X-ray reflectivity curves (R/R_F) for a) $Hg_{0.35}In_{0.65}$, b) $Hg_{0.50}In_{0.50}$, and c) $Hg_{0.95}In_{0.05}$, electrodes immersed in 0.1 M $Na_2B_4O_7$ (*aq*) at applied potentials of −1.00 V (red), −1.10 V (blue), −1.20 V (green), −1.30 V (purple), −1.40 V (yellow) vs *E*(Ag/AgCl). Solid black lines denote the corresponding best fits of the data using the third approach outlined in the text. Data were normalized to the Fresnel reflectivity, R_F (denoted by grey dashed line).

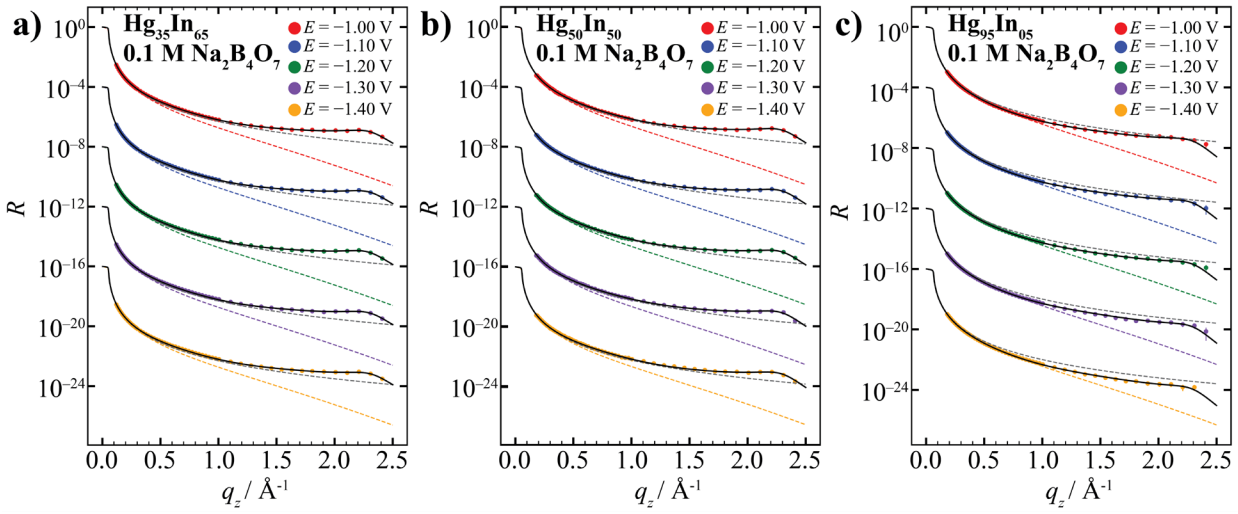

Figure 3.11 Plots of the absolute X-ray reflectivity vs. momentum transfer perpendicular to the surface for a a) $Hg_{35}In_{65}$ b) $Hg_{50}In_{50}$ or $Hg_{95}In_{05}$ deaerated electrolyte containing 0.1 M $Na_2B_4O_7(aq)$ at potentials of: E = -1.00 V (red circles), -1.10 V (blue circles), -1.20 V (green circles), -1.30 V (purple circles), and -1.40 V (yellow circles).These data were normalized in Figure 3.10 of the main text. In all panels, curves are offset for visual clarity

Table 3.2 Values of Best Fit for $X_{Hg,First}$ = Gibbs Adsorption Theorem for Ideal Solution Behavior[a]

liquid metal	E / V[b]	$X_{Hg,first}$[c]	$\rho_{e^-,first}$ / $\rho_{e^-,Hg\text{-}In,bulk}$	$\rho_{e^-,H2O}$ / $\rho_{e^-,Hg\text{-}In,bulk}$	z_{H2O} (Å)	σ_{H2O} (Å)	σ_b (Å)	σ_i (Å)	σ_{first} (Å)	d_{first} (Å)	d (Å)
$Hg_{0.35}In_{0.65}$	-1.00	0.79	1.27	0.17	-0.12	-0.66	0.43	0.83 ± 0.01	0.96 ± 0.01	2.99 ± 0.01	2.70 ± 0.04
	-1.10	0.79	1.27	0.17	-0.12	-0.66	0.43	0.84 ± 0.01	0.96 ± 0.01	2.96 ± 0.01	2.70 ± 0.01
	-1.20	0.79	1.27	0.17	-0.12	-0.66	0.43	0.85 ± 0.01	0.97 ± 0.01	2.99 ± 0.01	2.71 ± 0.01
	-1.30	0.79	1.27	0.17	-0.12	-0.66	0.43	0.87 ± 0.01	0.97 ± 0.01	2.98 ± 0.01	2.70 ± 0.01
	-1.40	0.79	1.27	0.17	-0.12	-0.66	0.43	0.88 ± 0.01	0.98 ± 0.01	2.97 ± 0.01	2.70 ± 0.01
$Hg_{0.50}In_{0.50}$	-1.00	0.88	1.21	0.15	-0.12	-0.66	0.43	0.83 ± 0.01	0.94 ± 0.01	2.95 ± 0.01	2.70 ± 0.01
	-1.10	0.88	1.21	0.15	-0.12	-0.66	0.43	0.85 ± 0.01	0.95 ± 0.01	2.95 ± 0.01	2.72 ± 0.01
	-1.20	0.88	1.21	0.15	-0.12	-0.66	0.43	0.88 ± 0.01	0.95 ± 0.01	2.92 ± 0.01	2.73 ± 0.01
	-1.30	0.88	1.21	0.15	-0.12	-0.66	0.43	0.90 ± 0.01	0.95 ± 0.01	2.94 ± 0.01	2.75 ± 0.01
	-1.40	0.88	1.21	0.15	-0.12	-0.66	0.43	0.91 ± 0.01	0.97 ± 0.01	2.96 ± 0.01	2.70 ± 0.01
$Hg_{0.95}In_{0.05}$	-1.00	0.99	1.02	0.12	-0.12	-0.66	0.43	1.06 ± 0.01	1.09 ± 0.01	2.98 ± 0.01	2.70 ± 0.01
	-1.10	0.99	1.02	0.12	-0.12	-0.66	0.43	1.08 ± 0.01	1.11 ± 0.01	2.99 ± 0.01	2.70 ± 0.01
	-1.20	0.99	1.02	0.12	-0.12	-0.66	0.43	1.09 ± 0.01	1.12 ± 0.01	2.96 ± 0.01	2.70 ± 0.01
	-1.30	0.99	1.02	0.12	-0.12	-0.66	0.43	1.12 ± 0.01	1.14 ± 0.01	2.98 ± 0.01	2.70 ± 0.01
	-1.40	0.99	1.02	0.12	-0.12	-0.66	0.43	1.14 ± 0.01	1.17 ± 0.01	2.98 ± 0.01	2.70 ± 0.01

a. in 0.1 M $Na_2B_4O_7$ (*aq*)
b. vs. *E*(Ag/AgCl)
c. atomic fraction on 0 – 1 scale

Table 3.3 Values of Best Fit for $X_{Hg,First} = 1.00$ (Full Hg Coverage)[a]

liquid metal	E / V[b]	$X_{Hg,first}$[c]	$\rho_{e\text{-},first}$ / $\rho_{e\text{-},Hg\text{-}In,bulk}$	$\rho_{e\text{-},H2O}$ / $\rho_{e\text{-},Hg\text{-}In,bulk}$	z_{H2O} (Å)	σ_{H2O} (Å)	σ_b (Å)	σ_i (Å)	σ_{first} (Å)	d_{first} (Å)	d (Å)
$Hg_{0.35}In_{0.65}$	-1.00	1.00	1.40	0.17	-0.12	-0.66	0.43	0.78 ± 0.01	1.21 ± 0.01	3.35 ± 0.02	2.70 ± 0.01
	-1.10	1.00	1.40	0.17	-0.12	-0.66	0.43	0.79 ± 0.01	1.21 ± 0.01	3.32 ± 0.01	2.70 ± 0.01
	-1.20	1.00	1.40	0.17	-0.12	-0.66	0.43	0.80 ± 0.01	1.22 ± 0.01	3.34 ± 0.01	2.70 ± 0.02
	-1.30	1.00	1.40	0.17	-0.12	-0.66	0.43	0.81 ± 0.01	1.22 ± 0.01	3.34 ± 0.01	2.69 ± 0.02
	-1.40	1.00	1.40	0.17	-0.12	-0.66	0.43	0.82 ± 0.01	1.22 ± 0.01	3.33 ± 0.01	2.68 ± 0.01
$Hg_{0.50}In_{0.50}$	-1.00	1.00	1.28	0.15	-0.12	-0.66	0.43	0.81 ± 0.01	1.02 ± 0.01	3.04 ± 0.02	2.69 ± 0.01
	-1.10	1.00	1.28	0.15	-0.12	-0.66	0.43	0.83 ± 0.01	1.03 ± 0.01	3.05 ± 0.01	2.70 ± 0.01
	-1.20	1.00	1.28	0.15	-0.12	-0.66	0.43	0.84 ± 0.01	1.04± 0.01	3.02 ± 0.01	2.69 ± 0.01
	-1.30	1.00	1.28	0.15	-0.12	-0.66	0.43	0.86 ± 0.01	1.05± 0.01	3.05 ± 0.01	2.71 ± 0.01
	-1.40	1.00	1.28	0.15	-0.12	-0.66	0.43	0.88 ± 0.01	1.05± 0.01	3.05 ± 0.01	2.73 ± 0.01
$Hg_{0.95}In_{0.05}$	-1.00	1.00	1.02	0.12	-0.12	-0.66	0.43	1.06 ± 0.01	1.09 ± 0.01	2.98 ± 0.01	2.70 ± 0.01
	-1.10	1.00	1.02	0.12	-0.12	-0.66	0.43	1.08 ± 0.01	1.11 ± 0.01	2.99 ± 0.01	2.70 ± 0.01
	-1.20	1.00	1.02	0.12	-0.12	-0.66	0.43	1.09 ± 0.01	1.12 ± 0.01	2.96 ± 0.01	2.70 ± 0.01
	-1.30	1.00	1.02	0.12	-0.12	-0.66	0.43	1.12 ± 0.01	1.14 ± 0.01	2.98 ± 0.01	2.70 ± 0.01
	-1.40	1.00	1.02	0.12	-0.12	-0.66	0.43	1.14 ± 0.01	1.17 ± 0.01	2.98 ± 0.01	2.70 ± 0.01

a. in 0.1 M $Na_2B_4O_7$ (*aq*)
b. vs. *E*(Ag/AgCl)
c. atomic fraction on 0 – 1 scale

Table 3.4 Fit Parameters for XRR Data in Figure 4[a]

liquid metal	E / V[b]	$X_{Hg,\,first}$[c]	$\rho_{e\text{-},\,first}$ / $\rho_{e\text{-},Hg\text{-}In,bulk}$	$\rho_{e\text{-},\,H2O}$ / $\rho_{e\text{-},Hg\text{-}In,bulk}$	z_{H2O} (Å)	σ_{H2O} (Å)	σ_b (Å)	σ_i (Å)	σ_{first} (Å)	d_{first} (Å)	d (Å)
$Hg_{0.35}In_{0.65}$	-1.00	0.93 ± 0.02	1.36 ± 0.01	0.17	-0.12	-0.66	0.43	0.79 ± 0.01	1.12 ± 0.02	3.21 ± 0.01	2.69 ± 0.03
	-1.10	0.93 ± 0.02	1.36 ± 0.01	0.17	-0.12	-0.66	0.43	0.80 ± 0.01	1.13 ± 0.01	3.21 ± 0.01	2.69 ± 0.01
	-1.20	0.92 ± 0.02	1.35 ± 0.01	0.17	-0.12	-0.66	0.43	0.81 ± 0.01	1.13 ± 0.01	3.21 ± 0.01	2.70 ± 0.01
	-1.30	0.93 ± 0.02	1.36 ± 0.01	0.17	-0.12	-0.66	0.43	0.82 ± 0.01	1.14 ± 0.01	3.22 ± 0.01	2.69 ± 0.01
	-1.40	0.95 ± 0.02	1.37 ± 0.01	0.17	-0.12	-0.66	0.43	0.83 ± 0.01	1.15 ± 0.01	3.22 ± 0.01	2.70 ± 0.01
$Hg_{0.50}In_{0.50}$	-1.00	0.98 ± 0.02	1.27 ± 0.01	0.15	-0.12	-0.66	0.43	0.81 ± 0.01	1.04 ± 0.01	3.09 ± 0.01	2.70 ± 0.01
	-1.10	1.00 ± 0.02	1.28 ± 0.01	0.15	-0.12	-0.66	0.43	0.83 ± 0.01	1.04 ± 0.01	3.09 ± 0.01	2.70 ± 0.01
	-1.20	0.98 ± 0.02	1.27 ± 0.01	0.15	-0.12	-0.66	0.43	0.84 ± 0.01	1.06 ± 0.01	3.09 ± 0.01	2.70 ± 0.01
	-1.30	1.00 ± 0.02	1.28 ± 0.01	0.15	-0.12	-0.66	0.43	0.86 ± 0.01	1.06 ± 0.01	3.09 ± 0.01	2.70 ± 0.01
	-1.40	1.03 ± 0.02	1.30 ± 0.01	0.15	-0.12	-0.66	0.43	0.88 ± 0.01	1.07 ± 0.01	3.06 ± 0.01	2.70 ± 0.01
$Hg_{0.95}In_{0.05}$	-1.00	0.99 ± 0.02	1.02 ± 0.01	0.12	-0.12	-0.66	0.43	1.06 ± 0.01	1.08 ± 0.01	2.97 ± 0.01	2.70 ± 0.01
	-1.10	1.00 ± 0.02	1.02 ± 0.01	0.12	-0.12	-0.66	0.43	1.08 ± 0.01	1.11 ± 0.01	2.97 ± 0.01	2.70 ± 0.01
	-1.20	1.00 ± 0.02	1.02 ± 0.01	0.12	-0.12	-0.66	0.43	1.09 ± 0.01	1.12 ± 0.01	2.97 ± 0.01	2.70 ± 0.01
	-1.30	0.99 ± 0.02	1.01 ± 0.01	0.12	-0.12	-0.66	0.43	1.11 ± 0.01	1.13 ± 0.01	2.98 ± 0.01	2.70 ± 0.01
	-1.40	1.00 ± 0.02	1.02 ± 0.01	0.12	-0.12	-0.66	0.43	1.14 ± 0.01	1.17 ± 0.01	2.98 ± 0.01	2.70 ± 0.01

a. in 0.1 M $Na_2B_4O_7$ (*aq*)
b. vs. *E*(Ag/AgCl)
c. atomic fraction on 0 – 1 scale

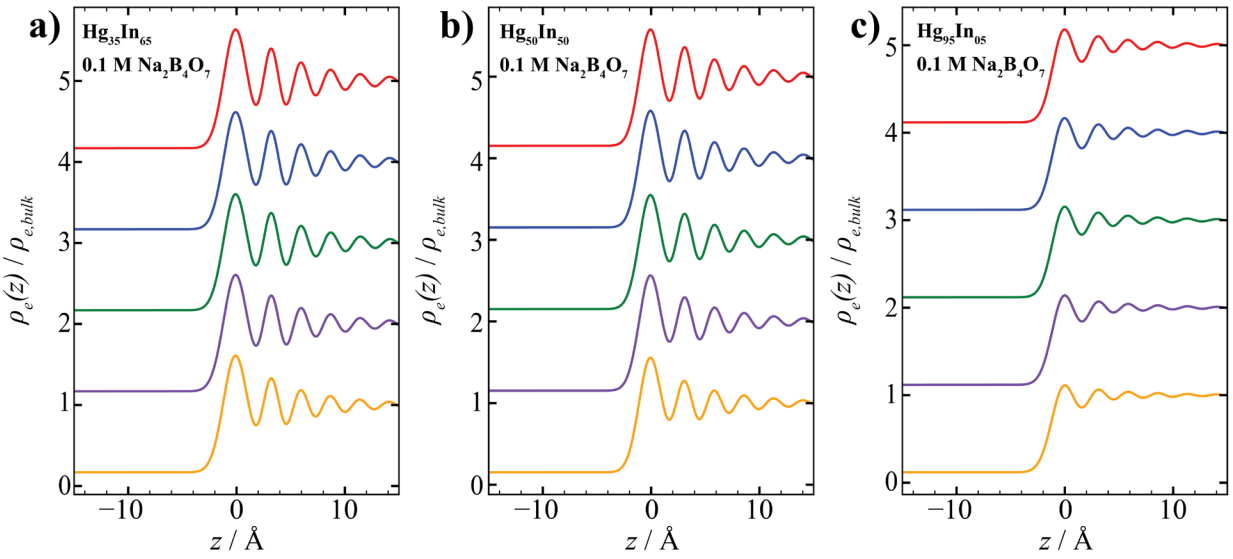

Figure 3.12 Electron density profiles corresponding to the best fits of the data shown in Figure 3.10 of the main text at potentials of: E = -1.00 V (red), -1.10 V (blue), -1.20 V (green), -1.30 V (purple), and -1.40 V (yellow). Profiles are offset for visual clarity.

larger than σ_i, a notable feature because the reported intrinsic roughness for pure In[21] is smaller than the value for pure Hg.[26, 31] Third, σ_i values increased at more negative potentials for all three bulk compositions (Figure 3.13, Table 3.4). This feature was consistent with the potential dependent behavior previously described for pure Hg in multiple aqueous electrolytes.[27, 31] The slopes of the lines in Figure 3.13 were-0.10 Å V^{-1}, -0.17 Å V^{-1}, and -0.19 Å V^{-1} for $Hg_{0.35}In_{0.65}$, $Hg_{0.50}In_{0.50}$, and $Hg_{0.95}In_{0.05}$, respectively. For reference, the reported potential dependence of σ_{first} for pure Hg in contact with NaF (*aq*) was -0.24 Å V^{-1}.[31] Additionally, σ_{first} also increased with more negative potentials (Table 3.4). However, none of the other fitting parameters showed a strong correlation with changes in potential. (Figure 3.14). Fourth, the layer spacing in the bulk liquid metal, *d*, for all compositions and potentials was 2.70 ± 0.01 Å, consistent with previous reports for both pure Hg and In.[14, 19, 21, 22, 26]

For $Hg_{0.35}In_{0.65}$, neither the approach based on the simple Gibbs adsorption theorem nor the approach assuming $X_{Hg,first} = 1$ fit all of the data adequately. Fits with significantly lower χ^2 values were obtained when $\rho_{e^-,first}$ corresponded to an intermediate value where $X_{Hg,first} = 0.93 \pm 0.02$. For $Hg_{0.50}In_{0.50}$, the approach based on the simple Gibbs adsorption theorem again did not describe the data accurately in the range of $q_z \leq 1.0$ Å^{-1}. Allowing $\rho_{e^-,first}$ (i.e. $X_{Hg,first}$) to vary yielded the best fits with values of 1.00 ± 0.02, consistent with the approach assuming a pure Hg surface layer. For $Hg_{0.95}In_{0.05}$, there was minimal difference in the fits with the three approaches since the Gibbs adsorption theorem predicted a nearly pure Hg surface composition. Allowing $\rho_{e^-,first}$ to vary yielded fits where $X_{Hg,first}$ remained between 0.99 ± 0.02 and 1.00 ± 0.02. Figure 3.15a summarizes the $X_{Hg,first}$ values fitted from the XRR data as a function of bulk composition. Figure 3.15b shows the corresponding d_{first} values for the fits that allowed $\rho_{e^-,first}$ (i.e. $X_{Hg,first}$) to vary. These values were generally in line with the d_{first} values previously reported in fits of XRR data for pure In and Hg.[21, 31]

3.5 Discussion

The presented data support the following points. First, the Yoneda signature is not unique to pure liquid Hg. Yoneda peaks were confirmed for all three liquid Hg-In bulk compositions, with the shape invariant to bulk composition, applied potential, radius of curvature, and surface roughness. Second, the intensity of the Yoneda features was strongly sensitive to the radius of curvature, less sensitive to the bulk composition, and no exhibited no intrinsic dependences on the

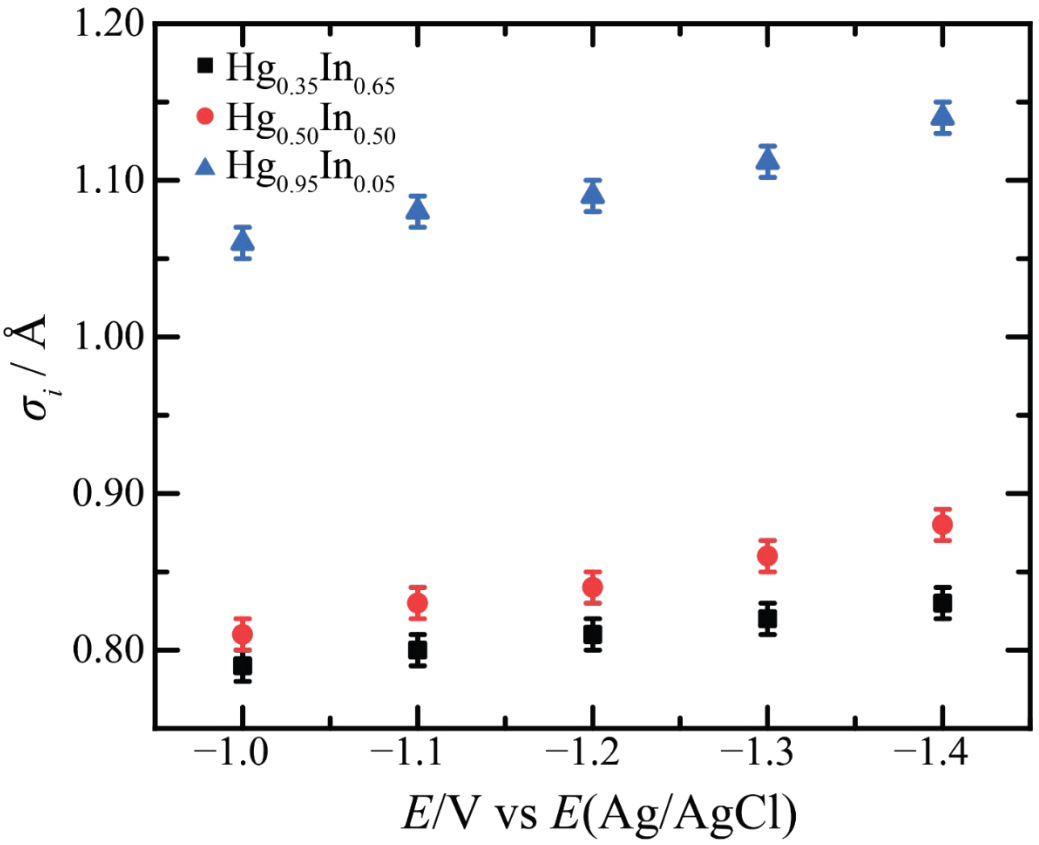

Figure 3.13 Plot of σ_i vs. applied potential for $Hg_{0.35}In_{0.65}$ (black squares), $Hg_{0.50}In_{0.50}$ (red circles), and $Hg_{0.95}In_{0.05}$ (blue triangles) electrodes immersed in 0.1 M $Na_2B_4O_7$ (*aq*).

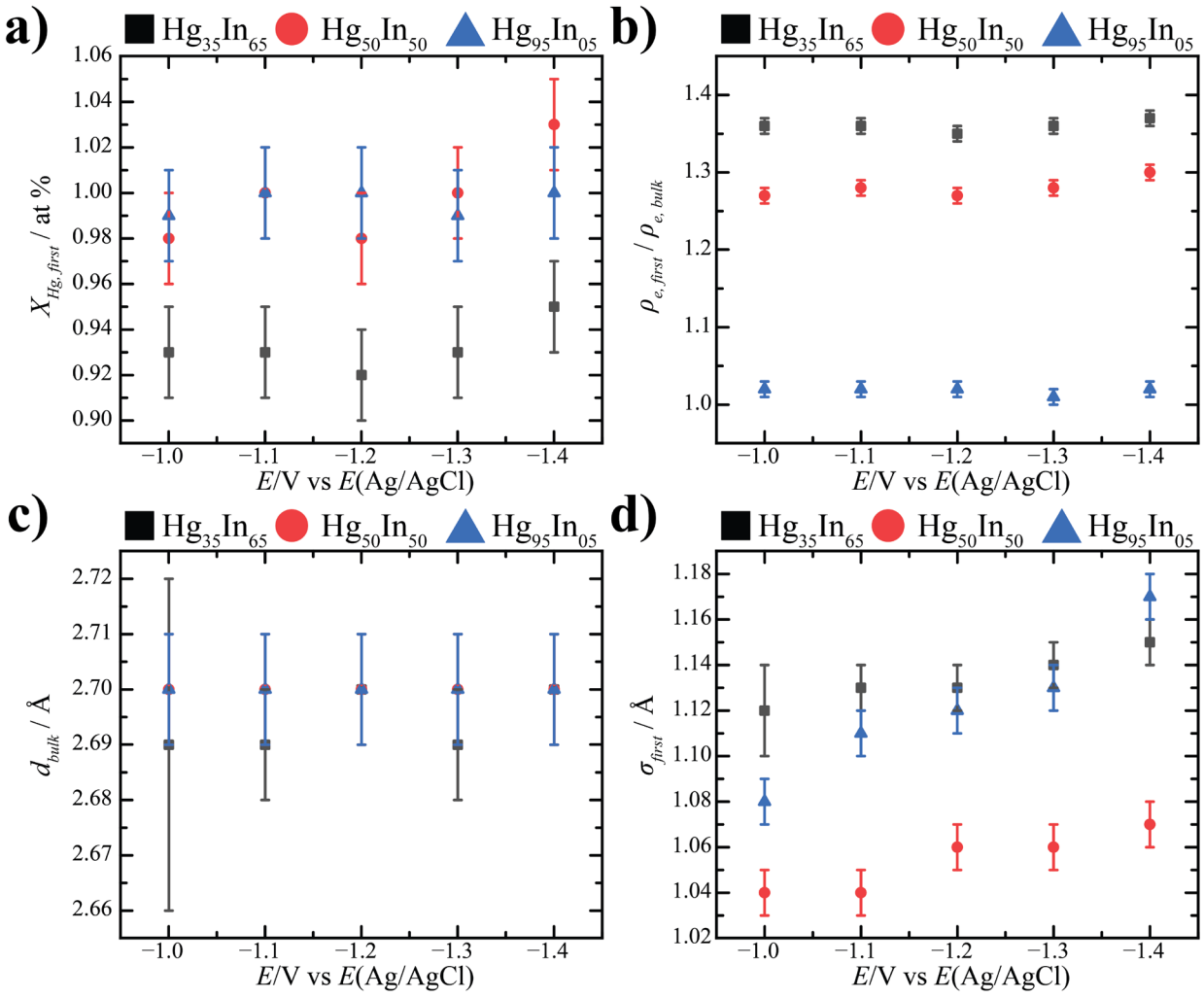

Figure 3.14 Trends in a) $X_{Hg,first}$ b) $\rho_{e,first}$ / $\rho_{e,bulk}$ c) d_{bulk} and d) σ_{first} versus the applied potential (E) as determined by the fit of the data in Figure 3.10 using *Equation* 3.4. Results for $Hg_{35}In_{65}$, $Hg_{50}In_{50}$, and $Hg_{95}In_{05}$ are the black squares, red circles, and blue triangles, respectively.

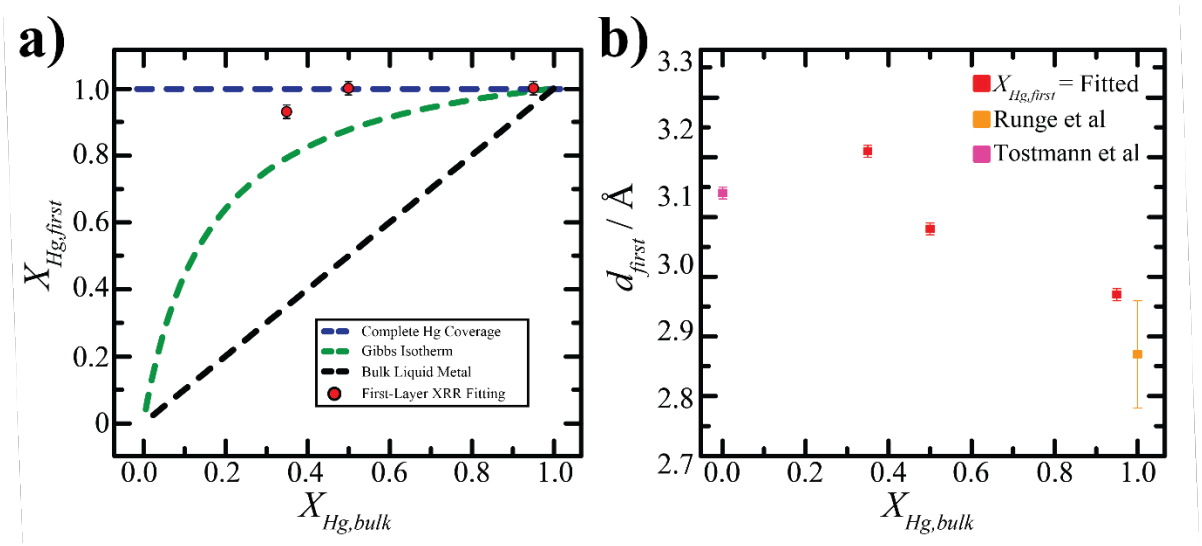

Figure 3.15 a) Plot of the fitted $X_{Hg,first}$ values for the data in Figure 4 compared to the bulk composition (dashed black line), the predicted first layer composition from the Gibbs adsorption theorem (dashed green line), and the assumption of a pure Hg surface (dashed blue line). b) Plot of d_{first} values from the fitting approach where $X_{Hg,first}$ was allowed to vary. Values of d_{first} for pure Hg (2.87 ± 0.09 Å) and pure In (3.14 ± 0.01 Å) are taken from the literature.

applied potential and the surface roughness. Third, the composition of all three Hg-In liquid metals could be described by a single Hg-rich surface layer on top of layers with the bulk liquid metal composition. The surface layer compositions were inconsistent with simple Gibbs adsorption, instead suggesting a negative (repulsive) interaction energy between Hg and In. These points are discussed below.

3.5.1 Observance of Yoneda Signatures at Liquid Metal Interfaces

Despite roughly 3 decades of XRR measurements, a pronounced Yoneda signal from liquid metal interfaces has not been observed outside of the aforementioned report of a very weak, potential-dependent Yoneda signal from a liquid Hg electrode immersed in aqueous electrolyte.[31] There are no other detailed reports on small-angle diffuse scattering, raising the possibility that the liquid Hg/water may somehow be unique. In this regard, liquid Hg is well known to exhibit unusual XRR responses, where the data suggest the outermost surface layer is less dense than the bulk.[26, 27, 31, 35, 57] A less dense surface structure is not known in any other liquid metal. Nevertheless, the data reported here confirm that Yoneda signals are not isolated to Hg/water junctions, with a Yoneda maximum in the diffuse scattering data for all three Hg-In mixtures under all investigated conditions. With regards to the connection between Yoneda signals and surface layer density, the XRR data for all three Hg-In compositions were clearly consistent with a surface layer that was *more dense* than the underlying bulk liquid metal. Hence, the appearance of the Yoneda feature does not directly implicate anything specific to pure liquid Hg/water interfaces.

The specific information contained within the Yoneda signature is less clear. Generally, a Yoneda feature arises due to total internal reflection at the critical angle, with the intensity accentuated by surface roughness.[48, 58-60] However, this basic premise does not seem consistent with the presented data. The results here indicate that the height fluctuations of the liquid metal/water interface, as indicated by σ_i and/or σ_{first}, that affect specular X-ray reflectivity at large q_z do not correlate with the Yoneda peak intensity. Specifically, the XRR data for $Hg_{0.35}In_{0.65}$ exhibited the smallest values of σ_i and σ_{first} but the corresponding scattering data showed the largest Yoneda intensities. Conversely, the XRR data for $Hg_{0.95}In_{0.05}$ showed the largest values of σ_i and σ_{first} but this surface exhibited the smallest Yoneda intensities. Thus, the results in this work suggest that 'roughness' of a liquid metal along the surface normal direction (i.e. z-axis) is not the primary source of the Yoneda feature.

Empirically, the data are clear that the Yoneda intensity tracked strongly with sample curvature. In principle, such an effect may be expected. Diffuse scattering at an interface with greater curvature occurs because an incident beam with a finite footprint will experience a range of incident angles. Referring to Figure 1.1, photons impinging to the left of the apex are at slightly larger incident angles and will only contribute to broadening the specular reflectance. Photons to the right of the apex are incident at smaller angles, too shallow for specular reflection. Instead, these photons will be scattered off the surface. For those photons incident at a position corresponding to an incident angle equal to the critical angle, the scattering is enhanced because of total internal reflection and corresponding field enhancement. Photons further to the right of this point will be scattered but without this enhancement. This latter aspect is generally reflected in the higher Yoneda intensities at the shallower angle q_z = 0.08 Å^{-1} (Figure 3.3) than at q_z = 0.10 Å^{-1}. However, the argument for curvature being the sole determinant in the observation of the intense Yoneda signals is not consistent with the decay of the diffuse scattering towards q_z = 0. With regards to curvature, the expectation might be that the scatter profile would change with different *r* values. In this work, *r* changed considerably (Figure 3.5) but the scattering signal decay towards q_z = 0 did not appear different (Figure 3.2a).

The fact that *r* was not conserved in these measurements is a consequence of the different surface tensions of the Hg-In liquids. Since the surface tension of pristine liquid In is significantly higher than pristine liquid Hg (0.556 mN m-1 vs 0.485 N m^{-1}),[26, 61] Hg-In liquids with higher In content naturally have larger surface tensions.[52, 53, 62] In the present work, all measurements were performed in the same *in-situ* XRR electrochemical cell that had both a fixed volume of 15 cm^3 and cell radius (r_{cell}) of 2.75 cm. For Hg-rich liquids, this cell is sufficiently large to afford low curvature (i.e. flat) liquid metal/water interfaces (electrocapillarity effects notwithstanding) since $r_{cell} > r = mg/(2\pi\gamma)$. For In-rich liquids, the same r_{cell} was actually smaller than optimal, i.e. $r_{cell} < r$, indicating these liquid metals couldn't achieve the same level of 'flatness'. Accordingly, it is tempting to ascribe the unusually large Yoneda signal for $Hg_{0.35}In_{0.65}$ as due solely to curvature. Still, while that may be a contributing factor, measurements with $Hg_{0.35}In_{0.65}$ and $Hg_{0.50}In_{0.50}$ with the same operative radius of curvature (= 260 ± 60 m) were statistically distinct. Moreover, if increased curvature were the sole factor in determining the intensity of a Yoneda feature, it is unclear why low-angle diffuse X-ray scattering from liquid metal droplets does not exhibit an

equally (or more) pronounced Yoneda feature.[54, 63] Hence, the data in this work suggests that thes Yoneda features are influenced by more than just curvature.

The prior report of Yoneda signals at Hg/water interfaces[31] raised the possibility that the feature was intrinsically potential dependent as a result of electrocapillarity. The results here provide some clarity and context on this premise. The Yoneda signal for a liquid metal electrode, if visible, will assuredly be sensitive to the applied potential if it is altered during diffuse scattering measurements. However, the sensitivity is a result of misalignment caused by the potential-dependent change in surface tension (i.e. change in *r*). When the beam alignment is optimized for a given applied potential, there is no significant potential dependence outside of random error. Hence, the Yoneda signal is not a direct reporter of the electrocapillarity curve of a liquid metal electrode or the potential of zero charge (i.e. the applied potential where the surface tension is maximized).

An intriguing possibility that remains is the intensity of the Yoneda feature is a function of heterogeneity in composition across the liquid metal/water interface. This point is consistent with the data for $Hg_{0.35}In_{0,65}$ since its surface had the highest In content. Still, there is no insight from the present data how the Hg and In are distributed across any Hg-In interface. A descriptive model of the Yoneda response is necessary to understand whether the diffuse scatter near the critical angle has such information embedded within. Unfortunately, the Born approximation[64] underlying *Equation* 3.4 is not applicable[20] and an alternative, first-principles approach is needed.

3.5.2 Chemistry of Hg-rich Surface Layer in Hg-In Liquids

The large-angle XRR data for all three Hg-In compositions are best explained with Hg enrichment confined to the outermost atomic layer, i.e. the underlying atomic layers have the bulk composition. Even for $Hg_{0.35}In_{0.65}$ where In is by far the majority component in the bulk, Hg accumulated at the interface and surface segregation reversal[65] was not observed. Since single-layer segregation is a key assumption of the Gibbs adsorption theorem,[66-68] the Gibbs framework is useful for further analysis of the fitted $X_{Hg,first}$ values.

For a liquid mixture, a common inference of the Gibbs adsorption theorem is that the component with a lower surface tension will have a higher atomic fraction in the surface layer relative to in the bulk. However, the most general way to express the atomic fraction of the surface

(first) layer in liquid Hg-In relative to the bulk composition, the surface tensions of Hg and In, and the temperature is through *Equation* 3.8,[69]

$$X_{Hg,first} = \frac{1}{\left(\frac{X_{Hg,bulk}}{1-X_{Hg,bulk}}\right) e^{\frac{-A}{k_B T}\left(\gamma_{Hg}-\gamma_{In}\right)} e^{\frac{w}{4k_B T}\left(X_{Hg,bulk}^2-\left(1-X_{Hg,bulk}\right)^2\right)} + 1}$$

Equation 3.8

where A is the average area per atom in the binary liquid alloy, k_B is the Boltzmann constant, T is the temperature, and w is the excess interaction energy between Hg and In relative to the interaction energies (**E**) between Hg-Hg and In-In in the liquid (i.e. $w = \mathbf{E}_{Hg\text{-}In} - \mathbf{E}_{Hg\text{-}Hg}/2 - \mathbf{E}_{In\text{-}In}/2$).[40, 65] For clarity, w is akin to the enthalpy of mixing which also defines whether the liquid mixture is an ideal or regular solution. A negative value of w would indicate an association (pairing) between Hg and In in the liquid, resulting in *more* surface enrichment (i.e. larger $X_{Hg,first}$) than if the solution were ideal. Conversely, a positive value of w would suggest repulsion between Hg and In in the liquid, causing *less* surface enrichment (i.e. smaller $X_{Hg,first}$) than if the solution were ideal. Figure 3.15a plots the ideal solution case, with $w = 0$.

The larger fitted $X_{Hg,first}$ values than predicted for an ideal solution (Figure 3.15a and Table 3.4) indicate the Hg-In liquids are regular solutions with negative w. At room temperature and assuming an average atomic area of ~ 7 Å^2, the fitted $X_{Hg,first}$ value for $Hg_{0.35}In_{0.65}$ was consistent with -4.0 x10^{-20} J per atom. The reported enthalpy of mixing for liquid $Hg_{0.35}In_{0.65}$ is ~ -2.1 kJ mol^{-1} (-3.5 x10^{-21} J per atom).[70] The factor of 10 difference may reflect the limitation in the absolute accuracy of *Equation* 3.8 when $|w|$ is large[69] or the propagation of uncertainty in the fitting or both. Nevertheless, the XRR analysis is clear that the Hg-In system has a strong pairing in the liquid. The general agreement between the *in-situ* XRR measurements and the prior calorimetric data further underscores the point that the applied potential does not appear to disrupt or alter the metallurgical characteristics of the liquid metal.

Finally, with regards to the chemical behavior of Hg-In electrodes, the present data also are useful in interpreting curious reports on the electrodeposition of intermetallic compounds with these liquids. Specifically, the electrosynthesis of several binary intermetallics composed of In and various transition metals were achieved through electrodeposition of the respective transition metal onto liquid Hg-In.[15, 16] Two unusual aspects were noted. First, the materials were mostly devoid of any Hg (save for occlusions) and instead were In-based.[15, 16] Second, the data indicated the binary

intermetallic crystals had phases inconsistent with those that would be produced if the corresponding transition metal had just been dissolved in pure liquid In and precipitated. Instead, the obtained compositions and crystalline polymorphs were closely matched to the crystal structures of the most stable binary Hg-transition metal intermetallic. These aspects suggested that the Hg and In components in the Hg-In liquids reacted sequentially, in spite of the aforementioned pairing of Hg-In in the bulk liquid. The displacement of Hg-metal bonds with In-metal bonds could be rationalized in terms of the greater lability as Hg is a d^{10} metal.[71, 72] However, the initial formation of Hg intermetallics was unclear. The XRR data here offer a straightforward rationale for those observations. Electrodeposition will place the transition metal adatom initially within a 'sea' of predominantly Hg atoms. If the metallurgical reaction outpaces dissolution into the bulk liquid metal, the initial cluster/nuclei that form should have the chemical character of a Hg-transition metal binary compound. If these nuclei then seed further crystal growth, the crystallographic growth will be dictated by Hg- (instead of In-) intermetallic lattice structures.

3.6 Conclusion

The work presented here provides insight on the composition and structure of liquid Hg-In electrode interfaces in aqueous solutions. Evidence of Hg surface enrichment limited to just the first layer at all bulk liquid metal compositions was clearly observed. Both the small angle scattering and large angle reflectivity data indicated the underlying layers had the bulk composition, irrespective of the value of the applied potential. This experimental behavior agrees with the single-layer segregation predicted by the Gibbs adsorption theorem and the general behavior observed in many liquid metal/vacuum interfaces, but the Hg enrichment was observed for both Hg-rich and In-rich bulk compositions. The pronounced Hg enrichment was consistent with regular solution behavior in the Hg-In system, especially a large negative enthalpy of mixing. A persistent and confirmed Yoneda signal in the diffuse scattering was also confirmed for the same range of compositions. The Yoneda peak showed a noticeable dependence on the radius of curvature but the data also suggested some dependence with the bulk composition. This work motivates further study of the Yoneda feature to determine whether information on the in-plane heterogeneity across the liquid metal/water interface can be ascertained.

3.7 References

1. Wu, H.; Hazelnis, J. P.; Maldonado, S., Understanding and Expanding the Prospects for Electrosynthesis with Liquid Metal Electrodes. *Accounts of Chemical Research* **2023,** *56* (7), 846-855.
2. Zeng, M.; Li, L.; Zhu, X.; Fu, L., A Liquid Metal Reaction System for Advanced Material Manufacturing. *Accounts of Materials Research* **2021,** *2* (8), 669-680.
3. Daeneke, T.; Khoshmanesh, K.; Mahmood, N.; de Castro, I. A.; Esrafilzadeh, D.; Barrow, S. J.; Dickey, M. D.; Kalantar-zadeh, K., Liquid metals: fundamentals and applications in chemistry. *Chemical Society Reviews* **2018,** *47* (11), 4073-4111.
4. Aukarasereenont, P.; Goff, A.; Nguyen, C. K.; McConville, C. F.; Elbourne, A.; Zavabeti, A.; Daeneke, T., Liquid metals: an ideal platform for the synthesis of two-dimensional materials. *Chemical Society Reviews* **2022,** *51* (4), 1253-1276.
5. Givargizov, E. I., Fundamental aspects of VLS growth. *Journal of Crystal Growth* **1975,** *31*, 20-30.
6. Redwing, J. M.; Miao, X.; Li, X., 9 - Vapor-Liquid-Solid Growth of Semiconductor Nanowires. In *Handbook of Crystal Growth (Second Edition)*, Kuech, T. F., Ed. North-Holland: Boston, 2015; pp 399-439.
7. Luzhnaya, N. P., Growth from metal solutions. *Journal of Crystal Growth* **1968,** *3-4*, 97-107.
8. Hazelnis, J. P.; Nguyen, T. T.; Wu, H.; Maldonado, S., Open Electrochemical Liquid Phase Epitaxial Growth of Crystalline Ge Films. *ACS Applied Materials & Interfaces* **2025**.
9. Derby, J. J.; Atherton, L. J.; Gresho, P. M., An integrated process model for the growth of oxide crystals by the Czochralski method. *Journal of Crystal Growth* **1989,** *97* (3), 792-826.
10. Scheel, H. J., Introduction to liquid phase epitaxy. *Liquid Phase Epitaxy of Electronic, Optical and Optoelectronic Materials* **2007,** *19* (8).
11. Trentler, T. J.; Hickman, K. M.; Goel, S. C.; Viano, A. M.; Gibbons, P. C.; Buhro, W. E., Solution-Liquid-Solid Growth of Crystalline III-V Semiconductors: An Analogy to Vapor-Liquid-Solid Growth. *Science* **1995,** *270* (5243), 1791-1794.
12. Ma, L.; Lee, S.; DeMuth, J.; Maldonado, S., Direct electrochemical deposition of crystalline silicon nanowires at T ≥ 60 °C. *RSC Advances* **2016,** *6* (82), 78818-78825.
13. Fahrenkrug, E.; Maldonado, S., Electrochemical Liquid–Liquid–Solid (ec-LLS) Crystal Growth: A Low-Temperature Strategy for Covalent Semiconductor Crystal Growth. *Accounts of Chemical Research* **2015,** *48* (7), 1881-1890.
14. Pattadar, D.; Cheek, Q.; Sartori, A.; Zhao, Y.; Giri, R. P.; Murphy, B.; Magnussen, O.; Maldonado, S., Evidence for Facilitated Surface Transport during Ge Crystal Growth by Indium in Liquid Hg–In Alloys at Room Temperature. *Crystal Growth & Design* **2021,** *21* (3), 1645-1656.
15. Wu, H.; Hazelnis, J. P.; Maldonado, S., Electrochemical Liquid-Liquid-Solid Growth of Ag-In Crystals with Liquid Indium Alloy Electrodes. *ChemElectroChem* **2024**.
16. Wu, H.; Maldonado, S., Electrodeposition of Pd Intermetallics using Hg-In by the Electrochemical Liquid-Liquid-Solid Method. *Journal of The Electrochemical Society* **2022,** *169* (11), 112514.
17. Yang, B.; Li, D.; Huang, Z.; Rice, S. A., Structure of the liquid-vapor interface of a dilute alloy of Pb in Ga. *Physical Review B* **2000,** *62* (19), 13111-13120.
18. Huber, P.; Shpyrko, O. G.; Pershan, P. S.; Tostmann, H.; DiMasi, E.; Ocko, B. M.; Deutsch, M., Wetting behavior at the free surface of a liquid gallium–bismuth alloy: an X-ray

reflectivity study close to the bulk monotectic point. *Colloids and Surfaces A: Physicochemical and Engineering Aspects* **2002,** *206* (1), 515-520.
19. Pershan, P. S., Review of the highlights of X-ray studies of liquid metal surfaces. *Journal of Applied Physics* **2014,** *116* (22), 222201.
20. Pershan, P. S.; Schlossman, M., *Liquid Surfaces and Interfaces: Synchrotron X-ray Methods*. Cambridge University Press: Cambridge, 2012.
21. Tostmann, H.; DiMasi, E.; Pershan, P. S.; Ocko, B. M.; Shpyrko, O. G.; Deutsch, M., Surface structure of liquid metals and the effect of capillary waves: X-ray studies on liquid indium. *Physical Review B* **1999,** *59* (2), 783-791.
22. DiMasi, E.; Tostmann, H.; Ocko, B. M.; Pershan, P. S.; Deutsch, M., X-ray reflectivity study of temperature-dependent surface layering in liquid Hg. *Physical Review B* **1998,** *58* (20), R13419-R13422.
23. Regan, M. J.; Pershan, P. S.; Magnussen, O. M.; Ocko, B. M.; Deutsch, M.; Berman, L. E., X-ray reflectivity studies of liquid metal and alloy surfaces. *Physical Review B* **1997,** *55* (23), 15874-15884.
24. Magnussen, O. M.; Ocko, B. M.; Deutsch, M.; Regan, M. J.; Pershan, P. S.; Abernathy, D.; Grübel, G.; Legrand, J.-F., Self-assembly of organic films on a liquid metal. *Nature* **1996,** *384* (6606), 250-252.
25. Regan, M. J.; Kawamoto, E. H.; Lee, S.; Pershan, P. S.; Maskil, N.; Deutsch, M.; Magnussen, O. M.; Ocko, B. M.; Berman, L. E., Surface Layering in Liquid Gallium: An X-Ray Reflectivity Study. *Physical Review Letters* **1995,** *75* (13), 2498-2501.
26. Magnussen, O. M.; Ocko, B. M.; Regan, M. J.; Penanen, K.; Pershan, P. S.; Deutsch, M., X-ray reflectivity measurements of surface layering in liquid mercury. *Physical Review Letters* **1995,** *74* (22), 4444-4447.
27. Hazelnis, J. P.; Sartori, A.; Cheek, Q. B.; Giri, R. P.; MacInnes, M. M.; Murphy, B. M.; Magnussen, O. M.; Maldonado, S., Detection of Ge-Containing Adlayers at the Liquid Hg/Water Interface by In Situ X-ray Reflectivity in Aqueous Borate Electrolytes Containing Dissolved GeO2. *The Journal of Physical Chemistry C* **2022,** *126* (18), 8177-8189.
28. Elsen, A.; Festersen, S.; Runge, B.; Koops, C. T.; Ocko, B. M.; Deutsch, M.; Seeck, O. H.; Murphy, B. M.; Magnussen, O. M., In situ X-ray studies of adlayer-induced crystal nucleation at the liquid-liquid interface. *Proceedings of the National Academy of Sciences* **2013,** *110* (17), 6663-8.
29. Festersen, S.; Runge, B.; Koops, C.; Bertram, F.; Ocko, B.; Deutsch, M.; Murphy, B. M.; Magnussen, O. M., Nucleation and Growth of PbBrF Crystals at the Liquid Mercury–Electrolyte Interface Studied by Operando X-ray Scattering. *Langmuir* **2020,** *36* (37), 10905-10915.
30. Sartori, A.; Giri, R. P.; Fujii, H.; Hövelmann, S. C.; Warias, J. E.; Jordt, P.; Shen, C.; Murphy, B. M.; Magnussen, O. M., Role of chemisorbing species in growth at liquid metal-electrolyte interfaces revealed by in situ X-ray scattering. *Nature Communications* **2022,** *13* (1), 5421.
31. Runge, B.; Festersen, S.; Koops, C. T.; Elsen, A.; Deutsch, M.; Ocko, B. M.; Seeck, O. H.; Murphy, B. M.; Magnussen, O. M., Temperature- and potential-dependent structure of the mercury-electrolyte interface. *Physical Review B* **2016,** *93* (16), 165408.
32. Magnussen, O. M.; Regan, M. J.; Kawamoto, E. H.; Ocko, B. M.; Pershan, P. S.; Maskil, N.; Deutsch, M.; Lee, S.; Penanen, K.; Berman, L. E., X-ray reflectivity studies of the surface structure of liquid metals. *Physica B: Condensed Matter* **1996,** *221* (1), 257-260.

33. Kawamoto, E. H.; Lee, S.; Pershan, P. S.; Deutsch, M.; Maskil, N.; Ocko, B. M., X-ray reflectivity study of the surface of liquid gallium. *Physical Review B* **1993,** *47* (11), 6847-6850.
34. Anton, P.; Uwe, K.; Hartmut, M.; Johann, P., In situ x-ray reflectivity study of the oxidation kinetics of liquid gallium and the liquid alloy. *Journal of Physics: Condensed Matter* **1998,** *10* (5), 971.
35. Pershan, P. S.; Stoltz, S. E.; Shpyrko, O. G.; Deutsch, M.; Balagurusamy, V. S. K.; Meron, M.; Lin, B.; Streitel, R., Surface structure of liquid Bi and Sn: An x-ray reflectivity study. *Physical Review B* **2009,** *79* (11), 115417.
36. Shpyrko, O. G.; Grigoriev, A. Y.; Steimer, C.; Pershan, P. S.; Lin, B.; Meron, M.; Graber, T.; Gerbhardt, J.; Ocko, B.; Deutsch, M., Anomalous layering at the liquid Sn surface. *Physical Review B* **2004,** *70* (22), 224206.
37. Shpyrko, O.; Huber, P.; Grigoriev, A.; Pershan, P.; Ocko, B.; Tostmann, H.; Deutsch, M., X-ray study of the liquid potassium surface: Structure and capillary wave excitations. *Physical Review B* **2003,** *67* (11), 115405.
38. DiMasi, E.; Tostmann, H.; Ocko, B. M.; Huber, P.; Shpyrko, O. G.; Pershan, P. S.; Deutsch, M.; Berman, L. E., Resonant X-ray Scattering from the Surface of a Dilute Liquid Hg-Au Alloy. *Materials Research Society Proceedings* **1999,** *590* (1), 183-188.
39. Huber, P.; Shpyrko, O.; Pershan, P. S.; Ocko, B.; DiMasi, E.; Deutsch, M., Short-range wetting at liquid gallium-bismuth alloy surfaces: X-ray measurements and square-gradient theory. *Physical Review B* **2003,** *68* (8), 085409.
40. DiMasi, E.; Tostmann, H.; Shpyrko, O. G.; Huber, P.; Ocko, B. M.; Pershan, P. S.; Deutsch, M.; Berman, L. E., Pairing Interactions and Gibbs Adsorption at the Liquid Bi-In Surface: A Resonant X-Ray Reflectivity Study. *Physical Review Letters* **2001,** *86* (8), 1538-1541.
41. Lei, N.; Huang, Z.; Rice, S. A., Structure of the liquid–vapor interface of a Sn:Ga alloy. *The Journal of Chemical Physics* **1997,** *107* (10), 4051-4060.
42. Shpyrko, O. G.; Streitel, R.; Balagurusamy, V. S. K.; Grigoriev, A. Y.; Deutsch, M.; Ocko, B. M.; Meron, M.; Lin, B.; Pershan, P. S., Crystalline surface phases of the liquid Au-Si eutectic alloy. *Physical Review B* **2007,** *76* (24), 245436.
43. Pershan, P. S.; Stoltz, S. E.; Mechler, S.; Shpyrko, O. G.; Grigoriev, A. Y.; Balagurusamy, V. S. K.; Lin, B. H.; Meron, M., Surface structure of the liquid Au72Ge28 eutectic phase: X-ray reflectivity. *Physical Review B* **2009,** *80* (12), 125414.
44. Tostmann, H.; DiMasi, E.; Pershan, P. S.; Ocko, B. M.; Shpyrko, O. G.; Deutsch, M., Microscopic surface structure of liquid alkali metals. *Physical Review B* **2000,** *61* (11), 7284-7287.
45. Zeng, M.; Fu, L., Controllable Fabrication of Graphene and Related Two-Dimensional Materials on Liquid Metals via Chemical Vapor Deposition. *Accounts of Chemical Research* **2018,** *51* (11), 2839-2847.
46. Okamoto, H., Hg-In (Mercury-Indium). *Journal of Phase Equilibria and Diffusion* **2012,** *33* (2), 159-160.
47. Calderín, L.; González, L. E.; González, D. J., Ab initio molecular dynamics study of the free surface of liquid Hg. *Physical Review B* **2013,** *87* (1), 014201.
48. Yoneda, Y., Anomalous Surface Reflection of X Rays. *Physical Review* **1963,** *131* (5), 2010-2013.
49. Fukuto, M.; Heilmann, R. K.; Pershan, P. S.; Badia, A.; Lennox, R. B., Monolayer/bilayer transition in Langmuir films of derivatized gold nanoparticles at the gas/water interface: An x-ray scattering study. *The Journal of Chemical Physics* **2004,** *120* (7), 3446-3459.

50. Murphy, B. M.; Greve, M.; Runge, B.; Koops, C. T.; Elsen, A.; Stettner, J.; Seeck, O. H.; Magnussen, O. M., A novel X-ray diffractometer for studies of liquid-liquid interfaces. *Journal of Synchrotron Radiation* **2014,** *21* (Pt 1), 45-56.
51. Als-Nielsen, J.; McMorrow, D., Refraction and Reflection from Interfaces. In *Elements of Modern X-ray Physics*, Wiley: 2011; pp 69-112.
52. Butler, J. N., The Zero-Charge Potential of Indium Amalgams in Perchloric Acid. *The Journal of Physical Chemistry* **1966,** *70* (7), 2312-2318.
53. Butler, J. N., Interfacial Tension of Indium Amalgams in 0.1 M Perchloric Acid at 25°. *The Journal of Physical Chemistry* **1965,** *69* (11), 3817-3825.
54. Konovalov, O. V.; Belova, V.; La Porta, F.; Saedi, M.; Groot, I. M. N.; Renaud, G.; Snigireva, I.; Snigirev, A.; Voevodina, M.; Shen, C.; Sartori, A.; Murphy, B. M.; Jankowski, M., X-ray reflectivity from curved surfaces as illustrated by a graphene layer on molten copper. *Journal of Synchrotron Radiation* **2022,** *29* (Pt 3), 711-720.
55. Henke, B. L.; Gullikson, E. M.; Davis, J. C., X-Ray Interactions: Photoabsorption, Scattering, Transmission, and Reflection at E = 50-30,000 eV, Z = 1-92. *Atomic Data and Nuclear Data Tables* **1993,** *54* (2), 181-342.
56. Dumke, M. F.; Tombrello, T. A.; Weller, R. A.; Housley, R. M.; Cirlin, E. H., Sputtering of the gallium-indium eutectic alloy in the liquid phase. *Surface Science* **1983,** *124* (2), 407-422.
57. Murphy, B. M.; Festersen, S.; Magnussen, O. M., The Atomic scale structure of liquid metal–electrolyte interfaces. *Nanoscale* **2016,** *8* (29), 13859-13866.
58. Inoue, K.; Kitahara, A.; Matsushita, K.; Kikkawa, H.; Nakabayashi, F.; Ageishi, N.; Terauchi, H.; Sakata, O.; Takahashi, I., Study of solid/solid interface by transmitted x-ray reflectivity. *Surface and Interface Analysis* **2005,** *37* (2), 185-189.
59. Kozhakhmetov, S. K.; Kozhakhmetova, T. A.; Kim, L. M.; Yessimov, S. T., Anomalous scattering of ultrasoft X-rays: a new technique to study the structure of surface solid layers. *Nuclear instruments & methods in physics research. Section A, Accelerators, spectrometers, detectors and associated equipment* **2001,** *470* (1).
60. Guentert, O. J., Study of the Anomalous Surface Reflection of X Rays. *Journal of Applied Physics* **1965,** *36* (4), 1361-1366.
61. Iida, T.; Guthrie, R. I. L., *The physical properties of liquid metals*. Clarendon Press ; Oxford University Press: Oxford: Oxford ; New York, 1988; Vol. Oxford: Oxford ; New York.
62. Olsen, D. A.; Johnson, D. C., THE SURFACE TENSION OF MERCURY-THALLIUM AND MERCURY-INDIUM AMALGAMS. *The Journal of Physical Chemistry* **1963,** *67* (12), 2529-2531.
63. Festersen, S.; Hrkac, S. B.; Koops, C. T.; Runge, B.; Dane, T.; Murphy, B. M.; Magnussen, O. M., X-ray reflectivity from curved liquid interfaces. *Journal of Synchrotron Radiation* **2018,** *25* (2), 432-438.
64. Stoev, K.; Sakurai, K., Recent theoretical models in grazing incidence X-ray reflectometry. *The Rigaku Journal* **1997,** *14* (2), 22-37.
65. Osborne, M. J.; Lacks, D. J., Surface segregation in liquid mixtures with strong interspecies attraction. *Physical Review E* **2004,** *70* (1), 010501.
66. Cahn, J. W.; Hilliard, J. E., Free Energy of a Nonuniform System. I. Interfacial Free Energy. *The Journal of Chemical Physics* **1958,** *28* (2), 258-267.
67. White, D., The surface tension of liquid metals and alloys. *Metallurgical Reviews* **1968,** *13* (1), 73-96.

68. Alberty, R. A., On the derivation of the Gibbs adsorption equation. *Langmuir* **1995,** *11* (9), 3598-3600.
69. Guggenheim, E. A., *Mixtures : the theory of the equilibrium properties of some simple classes of mixtures solutions and alloys*. Clarendon Press: 1952.
70. Gierlotka, W.; Jarosz, P.; Chen, S.-w., Liquid phase vapor pressure measurement and thermodynamics assessment of the Hg–In binary system. *Thermochimica Acta* **2009,** *491* (1), 29-34.
71. Cadenbach, T.; Bollermann, T.; Gemel, C.; Tombul, M.; Fernandez, I.; Hopffgarten, M. v.; Frenking, G.; Fischer, R. A., Molecular Alloys, Linking Organometallics with Intermetallic Hume−Rothery Phases: The Highly Coordinated Transition Metal Compounds [M(ZnR)n] (n ≥ 8) Containing Organo−Zinc Ligands. *Journal of the American Chemical Society* **2009,** *131* (44), 16063-16077.
72. Cable, R. E.; Schaak, R. E., Solution Synthesis of Nanocrystalline M−Zn (M = Pd, Au, Cu) Intermetallic Compounds via Chemical Conversion of Metal Nanoparticle Precursors. *Chemistry of Materials* **2007,** *19* (16), 4098-4104.

Chapter 4 Electrosynthesis of Quasi-Epitaxial Crystals on Liquid Metals[3]

4.1 Preface

The following work highlights a new concept in ec-LLS in which single crystalline inorganic materials can be achieved at a liquid-liquid interface. All experimental work was performed by Joshua P. Hazelnis. The writing and discussions of the work were equal in contribution between Joshua P. Hazelnis and Stephen Maldonado. Zhongrui Li is acknowledged for assistance with X-ray diffraction sample alignments. The Michigan Center for Materials Characterization is acknowledged for the use of microscopy instrumentation and staff assistance.

4.2 Introduction

Synthetic strategies that produce inorganic crystals with control and precision are necessary for (opto)electronic, sensing, and energy conversion technologies. Among the many current methods, strategies that leverage liquid metals as reaction media were historically among the first to be developed.[1] Resurgent interest in liquid metals has pushed their use to the forefront again, particularly for crystalline nanomaterials.[2] The general appeals of liquid metals are their physical malleability, their solvent characteristics towards inorganic solutes of interest, and the thermodynamic tendency for surface enrichment in oxides on liquid metal mixtures.

In addition to these aspects, liquid metals have one other potentially significant but otherwise under-exploited attribute. Unlike molecular liquids, liquid metals exhibit short-range atomic layering in the near surface region along the surface normal extending towards the bulk (Figure 4.1).[3-6] This atomic ordering is not crystalline per se since there is no evidence of persistent, long range, lateral ordering. Still, it is sufficient to yield a quasi-Bragg reflection at x-ray wavelengths.[6, 7] The surface layering likely arises from the abrupt change in electronic structure at liquid metal interfaces with air and water.[8] For crystallization, this near-surface atomic layering is thought to explain the observation of highly anisotropic metal crystal growth observed during

[3] Reprinted (adapted) with permission from Hazelnis, J. P.; Maldonado, S., Electrosynthesis of Quasi-Epitaxial Crystals on Liquid Metals. *Journal of the American Chemical Society* 2023, *145* (50), 27616-27625. Copyright 2023 American Chemical Society.

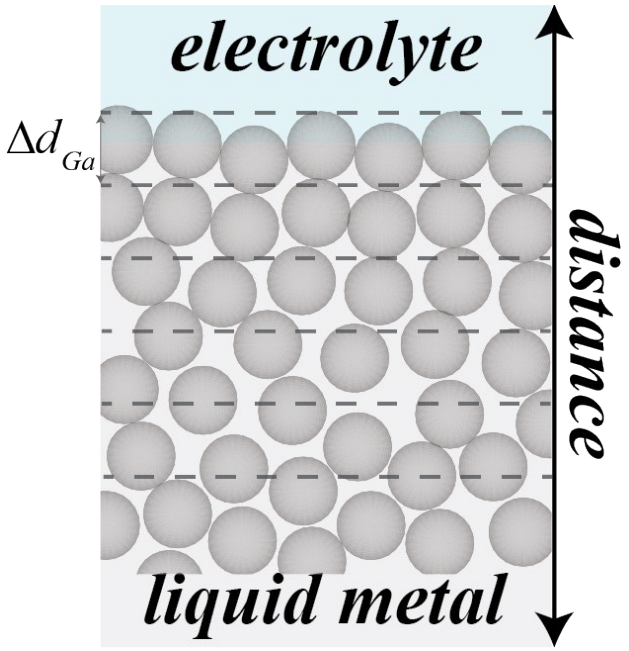

Figure 4.1 Schematic depiction of the short-range in-plane atomic layering in the near surface region of a liquid metal/electrolyte interface which decreases monotonically into the bulk liquid metal. Atomic layers (dashed grey lines) are defined by the diameter of a Ga atom (Δd_{Ga}) to highlight deviations of the atomic layering as the short-range order behavior trends toward that of a liquid traversing deeper into the bulk away from the electrolyte.

surface freezing of dilute liquid metal alloys under vacuum.[9-12] Presently, there is no indication that near-surface atomic layering is specifically influential in any other syntheses based on liquid metals.

Our group is generally interested in electrodepositions performed with liquid metals, where nucleation and growth of inorganic crystals is possible with electrochemical rather than thermal stimuli and can be performed in lab ambient rather than evacuated chambers.[13, 14] The appeal is that electrochemical synthetic reactions can be initiated/terminated precisely with extremely simple control hardware. Several types of inorganic crystals can be prepared this way.[13, 14] However, controlling their crystal type and orientation requires the presence of a separate, external solid (seed) surface.[15, 16] That is, epitaxy in electrodepositions with liquid metals has thus far only been possible with an additional, non-native solid/liquid interface.

Herein, this work demonstrates a new concept in the electrosynthesis of crystalline inorganic materials. This report tests the hypothesis that it is possible to electrodeposit crystalline metals with a preferred orientation at a liquid metal electrode interface that itself has no solid crystallinity, no external additives/binding agents in solution, and does not include an external solid seed substrate. The experiments described herein report on the separate electrodepositions of Pb, Bi, Pd, and Mn onto liquid Ga at constant, ambient temperature. The results show that when the liquid Ga/electrolyte interface is devoid of oxides, self-segregation and directed crystal growth of the metallic materials at the interface is possible. For metals that are immiscible with liquid Ga, electrodeposition under low flux conditions results in single-crystals of the metal solutes with a preferred orientation. For metals that are miscible with liquid Ga, electrodeposition at low flux conditions produces intermetallic single-crystals with a preferred orientation. In both cases, the observed crystal orientations are consistent with nucleation planes defined by the atomic packing density of atomic layers within Ga, suggesting that the intrinsic atomic structure of the near surface region of the liquid metal is key.

4.3 Experimental

4.3.1 Electrochemical Cell

A potentiostat (Autolab PGSTAT302N, Metrohm) and custom Teflon electrochemical cell were used for all electrochemical measurements (Figure 4.2a). All measurements were performed in triplicate and open to air in ambient. The working electrode was a 2.035 ± 0.007 g liquid Ga

droplet (99.99999% Pure, Fisher Scientific) in contact with a Pt wire ohmic contact housed in a quartz glass capillary with a 1.30 mm diameter. A teflon bowl with a diameter of 0.90 cm and depth of 0.60 cm contained the liquid Ga (Figure 4.2a). The surface area of the Ga electrode in contact with the liquid electrolyte was approximately 1.89 cm^2 after subtraction of the area of the ohmic contact capillary (diameter = 0.13 cm).

The cell was placed on a hotplate set to $T = 65°C$ to ensure Ga remained liquid throughout the duration of the electrodeposition experiments. A platinum (Pt) wire was used as the counter electrode. A BASi alkaline Hg/HgO half cell was used as the reference electrode (1.25 M NaOH filling solution). All potentials are reported with respect to this reference. The electrolyte was 1.25 M trace metal grade NaOH (99.99%, Sigma Aldrich) which was further purified before use by presoaking a separate (sacrificial) pool of Ga at $T = 65°C$ for at least 1 week to getter metal cations. Subsequent iron levels (one of the dominant metal contaminant in alkaline salts)[17] in the electrolyte were measured from aliquots via inductively coupled plasma mass spectrometry (ICP-MS) and determined to stabilize after removing no greater than 0.08 ppm. A leach rate of 0.034 mg Ga hr^{-1} was also determined experimentally via ICP-MS. This is in good agreement with previous reports of the anodic corrosion of Ga in alkaline solutions.[18] Therefore, as a consequence of the presoaking process to getter metal cations, the electrolytes will be sufficiently saturated with Ga ions. All electrochemical data are plotted with a positive current density denoting a reduction process and with more negative potentials to towards the right side (i.e. 'Texas' convention).

4.3.2 Pb Electrodeposition

A stock solution of 15.1 ± 0.3 mM $Pb(ClO_4)_2$ (99.995+%, Sigma Aldrich, $MW = 424.1$ g mol^{-1}) was prepared using the pre-treated stock 1.25 M NaOH. Electrodepositions were performed under potentiostatic control. Prior to each experiment, 25 mL of blank 1.25 M NaOH electrolyte was introduced to the cell and a bias was applied for 15 minutes prior to spiking in 5 mL of the as-prepared 15.1 ± 0.3 mM $Pb(ClO_4)_2 \cdot H_2O$ stock dilution, giving a final dilution of 2.5 ± 0.1 mM $Pb(ClO_4)_2$. The applied potential was maintained for another 180 minutes after the Pb^{2+} precursor was spiked in.

4.3.3 Bi Electrodeposition

Bi_2O_3 was prepared utilizing an adapted synthetic method to what was reported by Vivier et al.[19] Synthesis of Bi_2O_3 was done by preparing a solution of 9.5 mM $Bi(NO_3)_3$ to 1.25 M NaOH

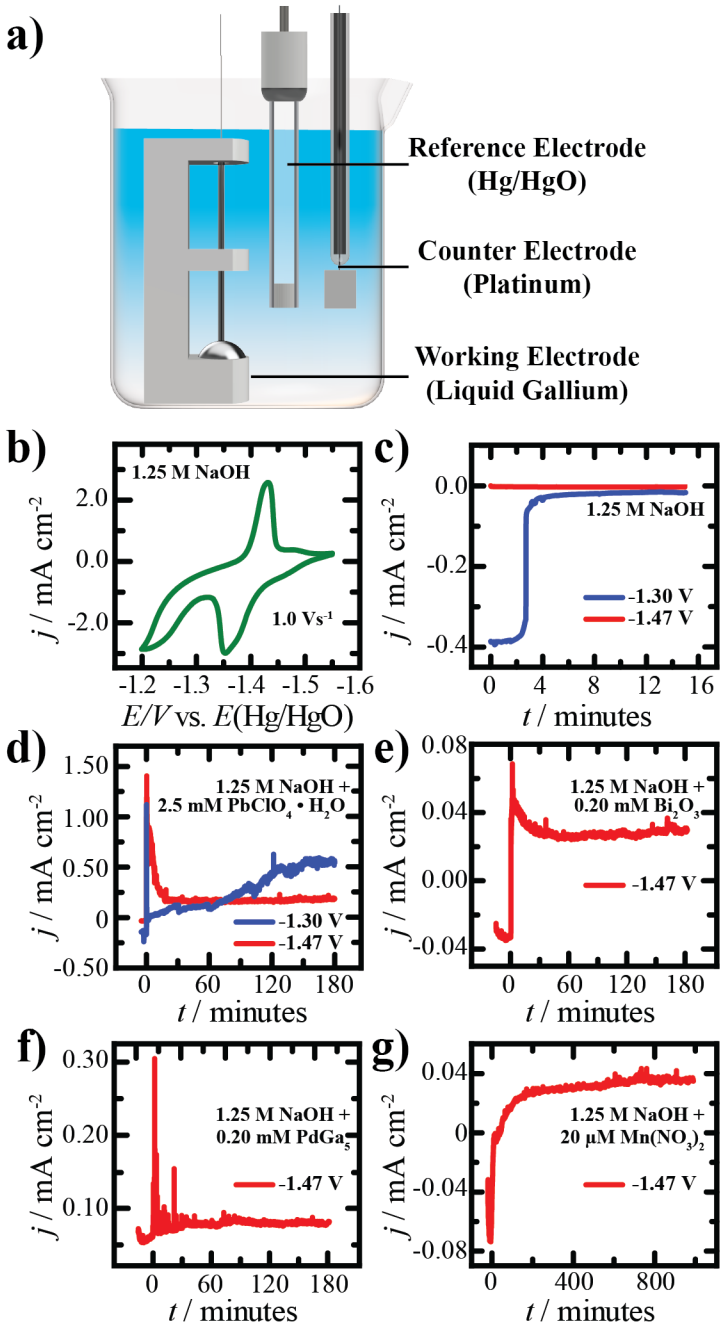

Figure 4.2 a) Schematic depicting the electrochemical cell with a liquid Ga working electrode for electrodeposition and cyclic voltammetry measurements. b) Cyclic Voltammetry of a blank 1.25 M NaOH electrolyte in contact with a liquid Ga working electrode at 1.0 V s^{-1}. c) Current-time transient responses from potential step experiments to (blue) -1.30 V and (red) -1.47 V (red) vs. Hg/HgO (1.25M NaOH) in blank 1.25 M NaOH solution for an initial 15 minutes prior to electrodeposition. d-g) Current-time transients for electrodeposition potentials of -1.30 V (blue) and -1.47 V (red) where t = 0 minutes is defined as the time when an aliquot of d) 15 mM $PbClO_4$, **e)** 1. 0 ± 0.01 mM Bi_2O_3, f) 1.20 ± 0.01 mM $PdCl_2$, or g) 0.120 mM $Mn(NO_3)_2$ is spiked in.

solution at room temperature in a polypropylene centrifuge tube. The precipitated solution was centrifuged and rinsed with nanopure water (Barnsted Nanopure >18.2 MΩ cm) three times before transferring to a glass vial and drying overnight in an oven at 100°C. The final Bi_2O_3 salt was placed on benchtop open to air prior to use. For electrodeposition, 24 mL of blank pre-treated 1.25 M NaOH(*aq*) electrolyte was added to the cell, the target bias for electrodeposition was then applied for 15 minutes before spiking in 6 mL solution of 0.98 ± 0.04 mM Bi_2O_3 to electrodeposit at a concentration of 0.20 ± 0.01 mM Bi_2O_3.The applied potential was maintained for another 180 minutes following the spike.

4.3.4 Pd Electrodeposition

Stock solutions of either 12.1 ± 0.6 or 1.2 ± 0.1 mM $PdCl_2$ (VWR, ≥ 99.99%) in 1.25 M NaOH solution was prepared for electrodeposition. 25 mL of 1.25 M NaOH(*aq*) solution was added to the electrochemical cell, the target bias for electrodeposition was applied for 15 minutes, and then 5 mL of the stock $PdCl_2$ solution was spiked to yield a final concentration of either 2.0 ± 0.1 mM or 0.2 ± 0.02 mM $PdCl_2$ while continuing the applied bias.

4.3.5 Mn Electrodeposition

A stock solution of alkaline 120μM $Mn(NO_3)_2$ was prepared by adding 5 μL of 1 mg mL^{-1} of Mn^{2+} in 5% (v/v) HNO_3 (Acros Organics, ThermoFisher Scientific) to 1.25 M NaOH(*aq*). Electrodeposition was performed by first applying -1.47 V for 15 minutes in the blank electrolyte and then spiking 5 mL of the stock Mn^{2+} solution to a final concentration of 20 μM. Electrodeposition was performed for 16.5 hours to produce enough material at the Ga electrode interface for ex-situ characterization (*vide supra*). Experiments with concentrations at the 10^{-3} M level were not possible due to substantial precipitation of $Mn(OH)_2$.

4.3.6 Materials Characterization

Scanning electron microscopy (SEM) was performed with a JEOL JSM-7800FLV field-emission scanning electron microscope with Schottky-type field-emission electron source to confirm the crystals were successfully isolated and transferred onto the Si substrate while maintaining the original orientation relative to the liquid Ga interface. The same SEM microscope used for imaging was also used for EDS and electron backscattering diffraction (EBSD) analyses. All SEM imaging was collected in back-scattered electron mode. The accelerating voltage for

SEM/EDS was 20 keV and 25 keV for EBSD. Manual measurements of the average particle size and particle counting was performed using the Fiji distribution of the open source software ImageJ.[20] EBSD data were collected while on the frozen Ga interface, at a 70-degree tilt via an Oxford NordlysMax^2 electron backscatter diffraction system. Indexing of the Kikuchi bands and orientation mapping was performed using the Oxford AztecHKL acquisition software.

Several methods were attempted for TEM analysis, including simple 'touch printing.[21] 'Touch printing' with target solid substrates resulted in the transfer of some particles off the surface of liquid Ga but always with a high coating of liquid Ga, complicating further crystallographic and composition analysis. Instead, TEM samples were prepared by first placing a clean Si wafer section onto a hotplate and slowly heating between 40-60°C while "streaking" the frozen Ga droplet across, allowing the crystals at the immediate interface and a minimal amount of residual Ga to be spread along the substrate for collection or further characterization. The act of freezing did not cause or alter any 'innate' particle morphology, as compared to observations from 'touch transfer'. Samples for cross-sectional TEM analysis were then prepared via FIB lift out and thinning using a Thermo Fisher Helios G4 PFIB UXe with a Schottky Field Emitter electron beam source, inductively coupled Xe Gas plasma ion beam source to avoid Ga contamination from the beam, and a Multichem gas injector. The procedure was performed by first placing a protective carbon layer with approximately 100 nm thickness via electron-beam-assisted chemical vapor deposition (CVD) with a 2 kV accelerating voltage and 13 nA beam current. Following, an ion-beam-assisted CVD (IBA-CVD) of a thick (3-4 μm) Pt:C (80:20 mixture) capping layer at 8.00 kV and 0.10 nA ion beam accelerating voltage and current, respectively, was performed. Trenches of the dimensions 20 μm x 23.5 μm x 20 μm (length x width x depth) were then milled into the Si substrate above and below the capped portion of the electrodeposited metal crystal using a 30 kV accelerating voltage and 60 nA beam current. An Omniprobe AutoProbe 200 micromanipulator equipped with a standard tungsten probe tip (Ted Pella) was then affixed to the Pt:C cap of the sample via a carbon IBA-CVD weld and subsequently transferred and welded onto a Mo Fib lift-out grid. During ion beam thinning of the electrodeposited metal crystals on the grid, there was poor adhesion with the residual Si substrate and Pt:C cap layers. Pt was used with IBA-CVD to backfill the gaps between the sample and the cap and/or Si substrate in between thinning steps.

TEM characterization was performed immediately following sample preparation to minimize oxidation of the thinned samples. TEM imaging was performed using a Thermo Fisher

Talos F200X G2 S/TEM X-FEG with a high-brightness Schottky type field emission gun and Gatan One View bottom mount camera. TEM samples were aligned to a major zone axis by using a double tilt holder and analyzing the Kikuchi bands of the sample. All HR-TEM images were subsequently acquired using bright field conditions, meaning that regions of the structure with heavier atoms should appear darker than that of lighter atoms. Additionally, an approximately 100 nm diameter selected area aperture was used for collecting selected area electron diffraction patterns for each sample.

Grazing incidence X-Ray diffraction was performed using a Rigaku Ultima IV Diffractometer with a 2.2 kW Cu Kα radiation long-fine focus tube and a scintillation count detector. The X-ray tube runs at 40 kV and 44 mA, and the Cu Kα line (wavelength 1.5406 Angstrom) used for excitation was obtained using a Kβ filter. The specimen was placed on a thin stage and aligned with a Z-scan prior to each measurement. The divergence, scattering, and receiving slits were set at 1 mm. The distance from the goniometer rotation axis to the detector was set at 285 mm. A scintillation count detector was used to collect the X-ray signal. Diffraction patterns were collected from 2θ = 10° to 90° with a step size of 0.05° and a counting time of 5 seconds.

4.4 Results

4.4.1 Electrochemical Behavior of Ga in 1.25 M NaOH Electrolyte

The extant literature on Ga electrode/water interfaces suggest that an interfacial oxide is always present[22, 23] although the Pourbaix diagram[23] suggests a clean metal/water interface at extreme negative potentials. To ascertain this possibility, the electrochemical behavior of liquid Ga was assessed with a pool electrode housed in a Teflon bowl (Figure 4.2a). In 1.25 M NaOH(*aq*), the open-circuit potential (OCP) of liquid Ga was near -1.47 V vs. Hg/HgO (1.25 M NaOH). Cyclic voltammetric sweeps at a scan rate of 1 V s^{-1} about this potential denoted a quasi-reversible redox process (Figure 4.2b). A pair of reductive and anodic waves corresponding to $8x10^{-2}$ and $-1x10^{-1}$ C cm^{-2}, respectively, were noted, corresponding to an oxide coverage of 2 x 10^{-7} mol cm^{-2} (i.e. ~ 100 nm thick, assuming a stoichiometry consistent with Ga_2O_3). Biasing the Ga electrode just negative of OCP resulted in a slight residual cathode current of -3.1 ± 0. 3 μA cm^2 (Figure 4.2c). Conversely, stepping the potential to -1.3 V induced a large anodic current that persisted for 3 min before decaying towards zero. The decay towards zero current at -1.3 V suggested an eventual

saturation of a thick surface gallium oxide at long times. Overall, these data implied that the Ga interface was likely unavoidably coated with an interfacial oxide at potentials more positive than OCP but possibly free of oxides at potentials more negative than OCP.

Metal electrodepositions were subsequently performed at -1.47 V. All metal cations of interest had standard potentials at much more positive potentials. Table 4.1 compiles the standard reduction potentials (E^0) for the four redox couples electrodeposited in this work ($Mn^{2+/0}$, $Bi^{3+/0}$, $Pb^{2+/0}$, and $Pd^{2+/0}$).[24, 25] In all cases, E^0 values are listed with respect to *E*.(Hg/HgO, 1.25 M NaOH).[26] The general electrodeposition process for all metals was as follows. The liquid Ga electrode was first held at -1.47 V for 15 min in blank electrolyte 1.25 M NaOH(*aq*). At $t = 0$, an aliquot of metal salt solution was spiked in to reach a solution concentration of either 2.5 mM (Pb^{2+}), 0.2 mM (Pd^{2+} or Bi^{3+}) or 2 μM (Mn^{2+}), with the concentration of the latter metal cations limited by substantially lower solubility. In all cases at these concentrations, the current changed initially and then attained a non-zero steady-state (cathodic) value (Figure 4.2d-g). Despite varying concentrations of metal pre-cursors being used, the amount of charge passed was maintained within an order of magnitude. Specifically, the charges passed were 0.4 ± 0.1, 0.9 ± 0.4, 1.8 ± 0.4, and 2.0 ± 0.4 C cm^{-2} for the electrodeposition of Bi, Pd, Mn, and Pb, respectively. Separately, each current transient exhibited a noticeable level of noise, with the metals more active towards H_2 evolution eliciting more noise in the data.

Physically, the liquid Ga surface largely retained a shiny, mirror-like appearance. Notably, these current-time transients also lacked local maxima at long times (> 1 min) typical of either progressive or instantaneous nucleation at solid surfaces.[27] Local maxima were observed within the first 4 seconds after spiking in the metal salt precursor. (Figure 4.3) Instead of data points being collected at intervals of $t = 1.0$ second, data was instead collected every $t = 0.01$ second to better resolve the first 5 seconds following the spike in at $t = 0$ seconds of higher concentration electrodeposition solution. For comparison, control experiments were performed for Pb electrodeposition with liquid Ga electrodes biased at -1.3 V (Figure 4.2d, blue trace). These current-time transients differed, exhibiting a local maxima at long times consistent with electrodeposition at a solid surface. In these control experiments, copious dark dendrites formed on the surface, accumulating and then spilling over the side of the Teflon bowl. Corresponding elemental analysis indicated a large oxygen signal at the underlying Ga interface, consistent with the presence of an oxide present during Pb electrodeposition under this condition (Figure 4.4).

Table 4.1 Standard redox potentials (E^0) of the metal cations of interest in this work Mn^{2+}, Bi^{3+}, Pb^{2+}, and Pd^{2+}

Redox Couple	**Standard Reduction Potential *(E^0)* vs. Hg/HgO (1.25 M NaOH)**
Mn^{2+} / Mn^0	-1.282 V
Bi^{3+} / Bi^0	-0.515 V
Pb^{2+} / Pb^0	-0.228 V
Pd^{2+} / Pd^0	0.813 V

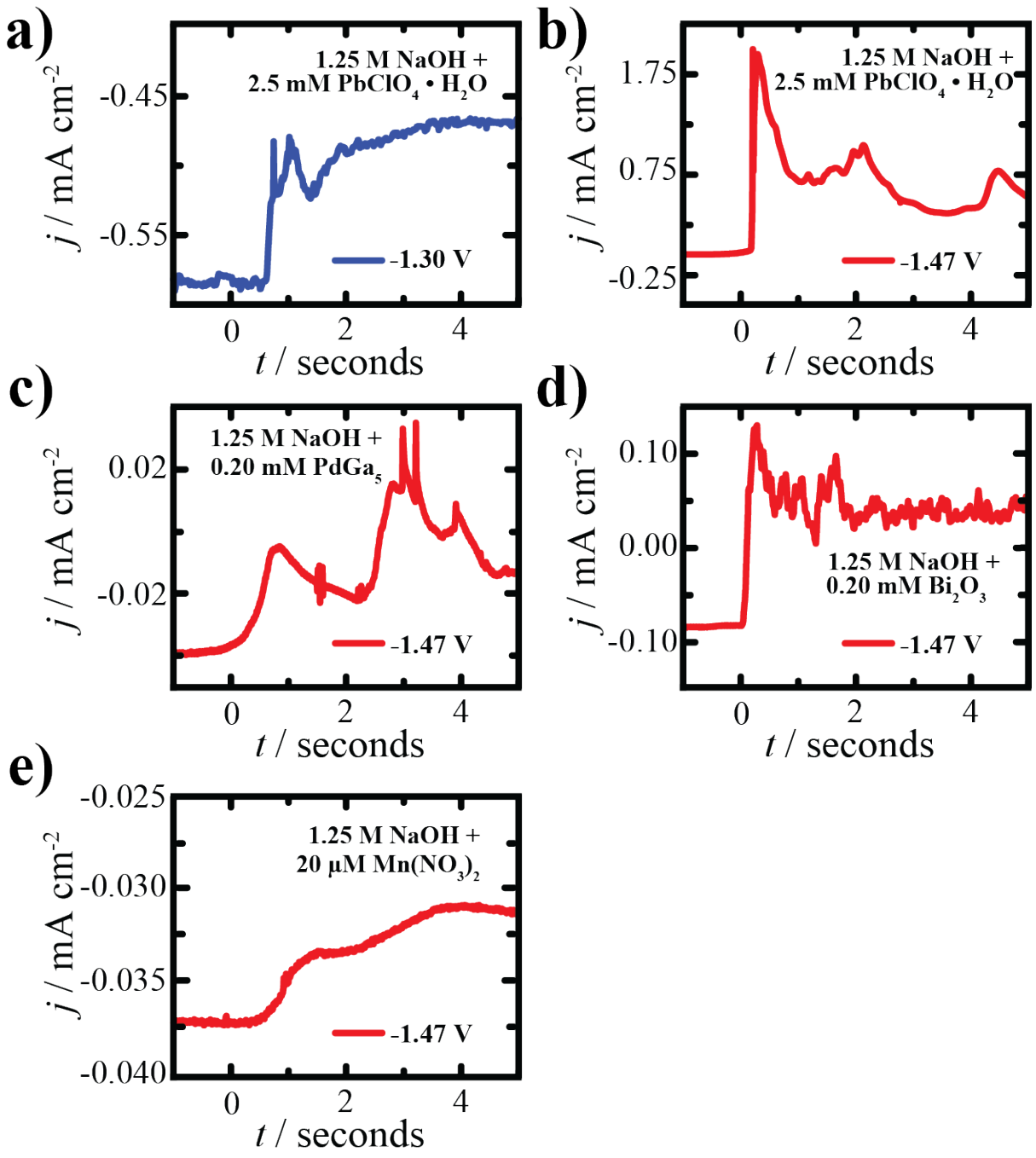

Figure 4.3 a) Current-time transients with data points collected every $t = 0.01$ second for electrodeposition potentials of -1.30 V (blue) and -1.47 V (red) where $t = 0$ seconds is defined as the time when an aliquot of a) 15 mM $PbClO_4$ b) 15 mM $PbClO_4$ c) 1.20 ± 0.01 mM $PdCl_2$, d) 1. 0 ± 0.01 mM Bi_2O_3 or e) 0.120 mM $Mn(NO_3)_2$ is spiked in.

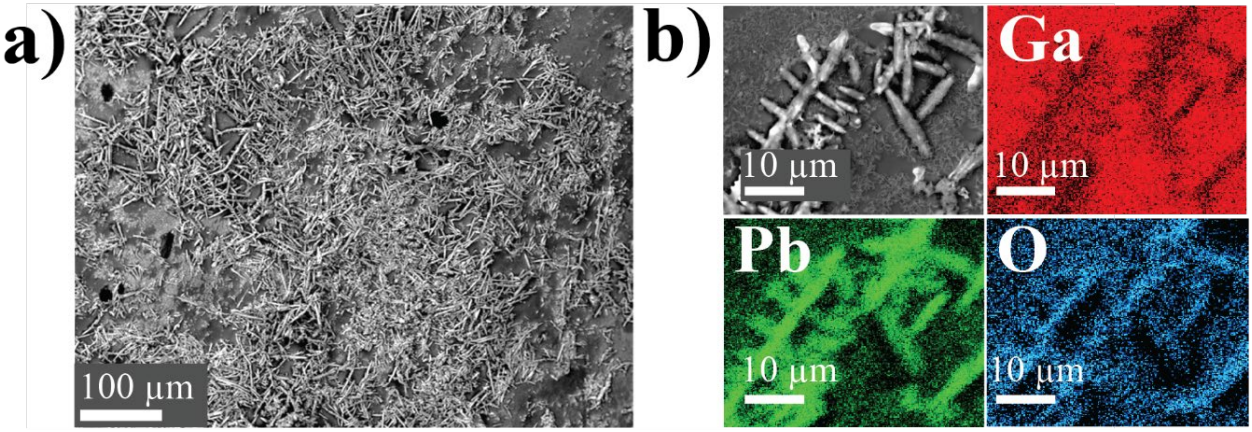

Figure 4.4 a) SEM analysis of a liquid Ga electrode following electrodeposition of 2.5 mM $PbClO_4$ ● H_2O at -1.30 V vs. Hg/HgO (1.25 M NaOH) b) EDS mapping of Ga, Pb and O at the liquid Ga electrode interface which maps the dendrites as Pb highlights an appreciable O signal otherwise not observed at -1.47 V.

For electrodeposition experiments performed at -1.47 V, the surfaces of the liquid Ga electrodes were examined by scanning electron microscopy (SEM). Upon termination of each experiment, the electrolyte was quickly removed, and the Ga liquid metal droplet was rinsed with copious water (Barnsted Nanopure >18.2 MΩ cm) to remove any excess salts. Flash freezing with liquid nitrogen was then performed to solidify the electrode surface without disturbing the particle orientation. The surfaces of the frozen Ga electrodes were then evaluated by SEM.

In all instances, these samples were devoid of dendrites. Instead in each case, the liquid metal surface was decorated with flat, thin (< 500 nm), metallic, and micron-wide particles (Figure 4.5a-d). The specific profile of these particles varied from discrete triangles and irregular coalesced shapes (Pb electrodeposition), triangles and straight parallel/coalescing lines (Bi electrodeposition), squares (Pd electrodeposition), and hexagons (Mn electrodeposition). Elemental analyses for each particle type confirmed that these structures were neither oxides nor composed of extraneous metals (Figure 4.5a-d insets).

Pb, Pd, and Bi electrodeposition experiments yielded similar particle coverages of ~ 0.3 ± 0.2 cm^{-2} , as estimated by SEM. The average side lengths for Pb triangular particles were 8 ± 8 μm (N = 203) and for Bi triangular particles were 2 ± 2 μm (N = 218). The square particles produced through Pd electrodeposition had average side lengths of 14 ± 13 μm (N = 187). The overall high coverage resulted in many areas of overlapping particles. Mn electrodeposition experiments consistently yielded much lower non-uniform particle coverage of (0.10 ± 0.05 cm^{-2}). The electrodeposition of Mn formed hexagonal particles with an average side length of 9 ± 3 μm (N = 12).

Additional electrodepositions of 0.2 mM Bi^{3+} and 2.5 mM Pb^{2+} were performed at long times (t > 15 hours). (Figure 4.6) The charged passed at these longer times was 2.2 and 30 C cm^{-2} for Bi^{3+} and Pb^{2+}, respectively. Consequently, the resultant particles of each electrodeposition appeared more coalesced and either thicker (> 1 μm) in the case of Bismuth or larger side lengths (> 100 μm) for the Pb triangles. Likely due to the higher concentrations (2.5 mM) of Pb^{2+}, evidence of heterogeneous nucleation was also observed at longer times (> 5 hours) with an increasing current density. SEM of the sample also showed evidence of Pb dendrite patches which were not observed at t = 3 hours under the same conditions. (Figure 4.6c, inset)

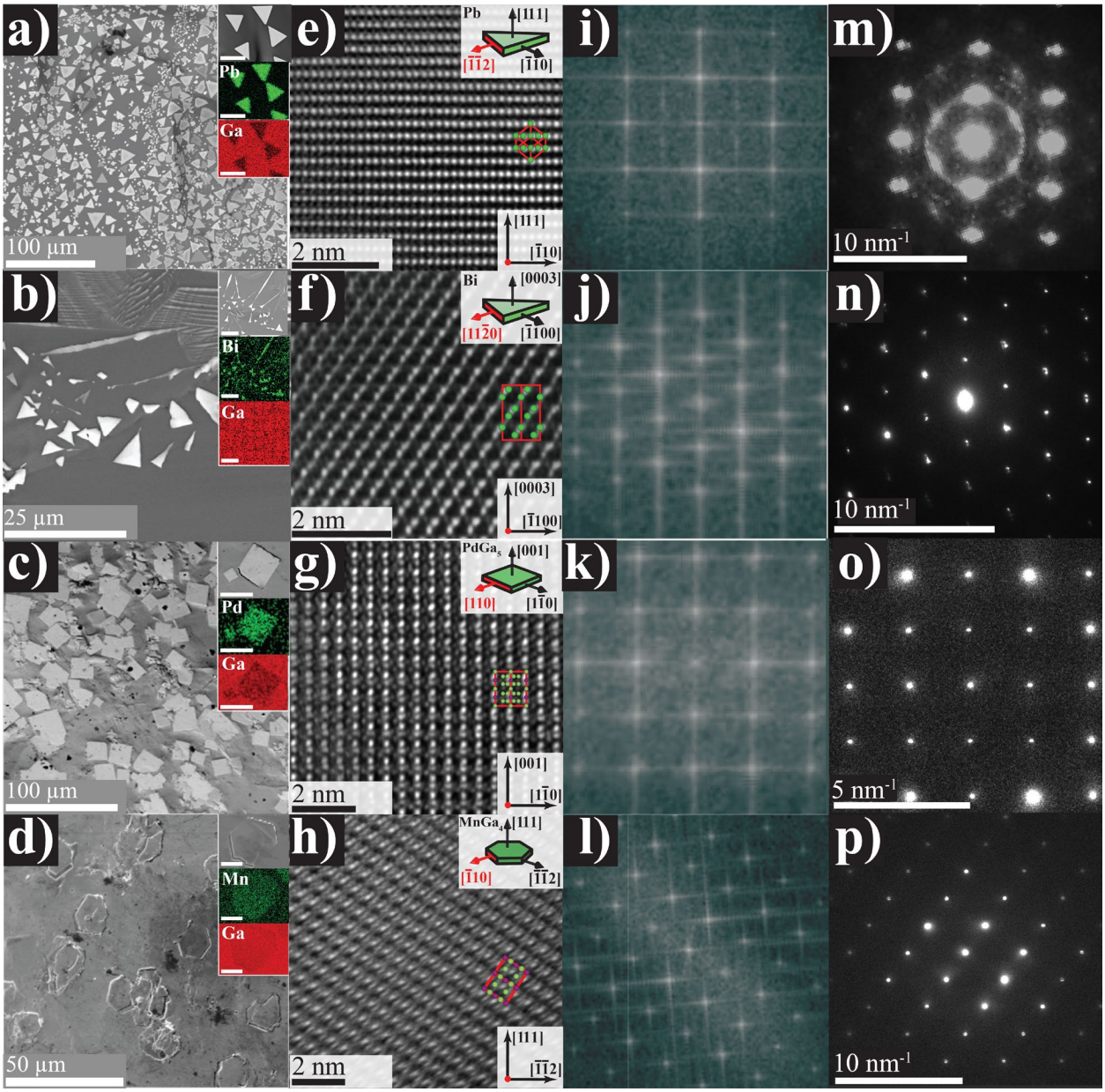

Figure 4.5 SEM and corresponding elemental mapping of the particles produced after metal electrodeposition at -1.47 V including a) Pb triangular particles (inset scale bar = 10 µm) b) Bi nanoribbons and triangular particles (inset scale bar = 25 µm) c) $PdGa_5$ square particles (inset scale bar = 25 µm) d) $MnGa_4$ nanoribbons and triangular particles (inset scale bar = 5 µm). Corresponding cross-sectional HR-TEM bright field image of the e) $[\bar{1}\bar{1}2]$ direction of a Pb triangular particle, f) $[11\bar{2}0]$ direction of a Bi triangular particle, g) [110] direction of a $PdGa_5$ square particle, h) $[\bar{1}10]$ direction $MnGa_4$ hexagonal particle with the face of the particle probed highlighted in red (inset) and a guiding overlay of the atomic arrangement corresponding to the unit cell viewed in that crystallographic direction for Ga (green) and Pd or Mn (purple). (i-l) Corresponding FFT of (e-h) respectively and experimental selected area electron direction for m) Pb, n) Bi, o) $PdGa_5$, and p) $MnGa_4$ in the orientation shown in (e-h) respectively.

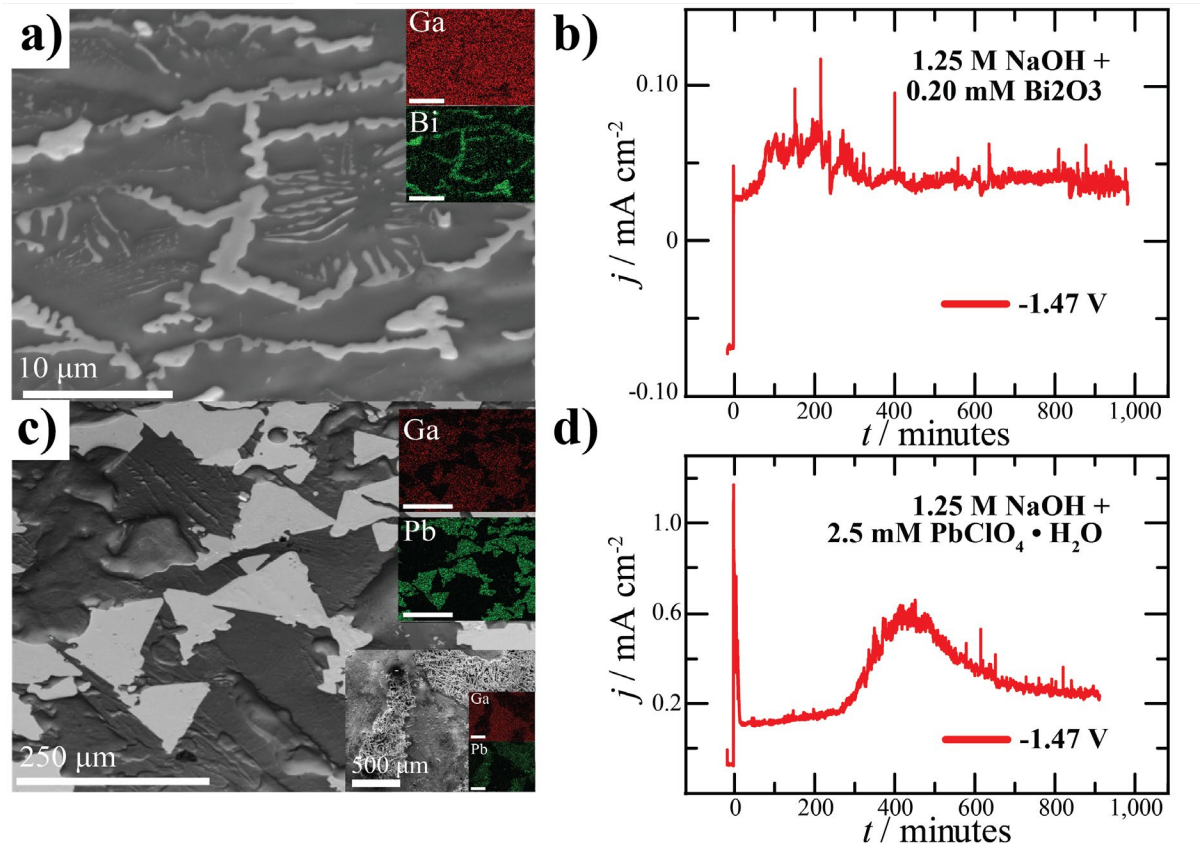

Figure 4.6 a) SEM/EDS analysis of a liquid Ga electrode following electrodeposition (t > 15 hours) of 0.20 mM Bi_2O_3 at -1.47 V vs. Hg/HgO (1.25 M NaOH) showing evidence of more coalesced and thicker triangles and nanoribbon Bi particles compared to electrodeposition at t = 3 hrs and b) corresponding current-time transient c) SEM/EDS analysis of a liquid Ga electrode following electrodeposition (t > 15 hours) of 2.5 mM $PbClO_4$ ● H_2O at -1.47 V vs. Hg/HgO (1.25 M NaOH) showing evidence of more coalesced and larger side length Pb triangles

Transmission electron microscopy (TEM) was separately performed on the materials produced from each of these electrodepositions for t = 3 hrs. Initial TEM sample preparation was attempted via 'touch printing'[21] a carbon-coated copper TEM grid to the liquid metal interface following electrodeposition. However, subsequent scanning electron microscopic imaging of the copper grids showed no instances of transfer of clean particles without a coating of liquid metal. Rather, the TEM grids featured an intolerably large amount of liquid Ga and Ga oxides. Accordingly, samples for transmission electron microscopic analysis were instead prepared after first freezing the bulk liquid metal, then slightly warming each frozen Ga droplet to melt the outer surface, and then streaking the surface across a clean Si wafer substrate. This approach transferred the crystals and limited liquid Ga to the solid substrate without perturbing the original orientation with respect to the liquid metal surface plane. Focused ion beam (FIB) milling was used to cut, to thin, and to lift out a cross section from each particle type (Figure 4.7). These thinned sections were then welded to a grid and analyzed by scanning transmission electron microscopy (TEM, Figure 4.5e-h). For these analyses, arbitrary triangular particles after Pb electrodeposition, square particles after Pd electrodeposition, and hexagonal particles after Mn electrodeposition were chosen since these morphologies constituted of 100% of the discrete particles observed in each case. For analysis of products from Bi electrodeposition, lines were the predominant (~75%) morphology but with evidence that the lines initiated and/or terminated at the vertex of triangle particles. Accordingly, we selected these minority morphologies for analysis.

In each case, bright field high resolution imaging (HR-TEM) was performed, with the plane of the image corresponding to the red plane indicated in the inset, i.e. orthogonal to the plane of the liquid metal electrode. For Pb, the real space image (Figure 4.5e) and the corresponding reciprocal space image (Figure 4.5i) of the particles were consistent with a cubic lattice structure where the [111] direction was perpendicular to the liquid metal surface (and parallel to the image plane). Wider field of view selected-area-electron-diffraction (SAED) data corroborated this assignment of the crystal orientation (Figure 4.5m). In the case of Pb, a polycrystalline ring was also visible in the SAED data, arising from PbO produced by the rapid oxidation of the sample in area following FIB thinning. The corresponding data for Bi particles (Figure 4.5f, j, n) indicated the rhombohedral lattice structure but otherwise similar conclusions, i.e. single crystals with an identifiable orientation where the [0001] direction was orthogonal to the liquid metal surface plane. The Bi structure can be described and indexed as rhombohedral, pseudocubic or hexagonal,[28] but

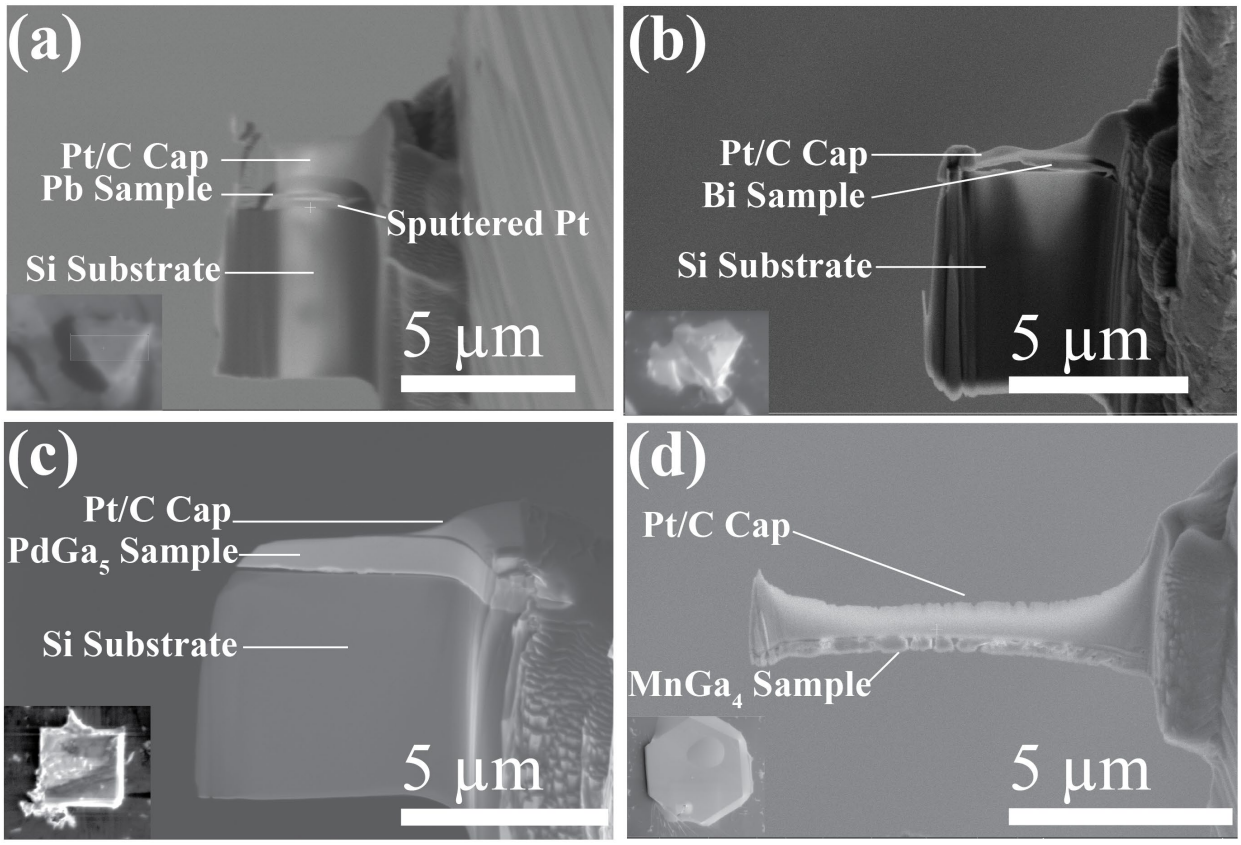

Figure 4.7 SEM of the final TEM sample prepared for analysis by plasma focused ion beam milling with corresponding liftout site (inset) for a) a Pb triangular particle, b) a Bi triangular particle, c) a $PdGa_5$ square particle, and d) a $MnGa_4$ hexagonal particle.

we note that this work adopts the hexagonal (hkil) Miller-Bravais notation of rhombohedral (R-3MH) Bi to avoid any ambiguity. Further, the SAED data for all Pb and Bi particles yielded lattice constants consistent with pure metal particles ($a = b = c = 0.495$ nm for Pb[29] and $a = b = 0.455$ nm and $c = 1.19$ nm for Bi[30]), suggesting negligible incorporation of Ga.

For Pd and Mn electrodepositions, the products were similarly single-crystalline. The real space (Figure 4.5g) and reciprocal space (Figure 4.5k) HR-TEM particles produced from Pd electrodeposition were consistent the tetragonal lattice structure of $PdGa_5$. This composition was confirmed by SAED data (Figure 4.5o), where lattice constants consistent with stoichiometric $PdGa_5$ were obtained (i.e. $a = b = 0.645$ nm, and $c = 1.00$ nm). Separate scanning TEM energy dispersive X-ray (STEM-EDX) analyses further supported this assignment (Figure 4.8). The orientation of the $PdGa_5$ particles were consistent with the [001] direction normal to the surface plane of liquid Ga. Separately, the real space (Figure 4.5h) and reciprocal space (Figure 4.5l) HR-TEM images of particles produced during Mn electrodeposition suggested cubic $MnGa_4$ as the sole products. This composition was confirmed by corresponding SAED data (Figure 4.5p) which yielded lattice constants (i.e. $a = b = c = 0.559$ nm) consistent with pure $MnGa_4$ and STEM-EDX data (Figure 4.9). These particles were consistently oriented with the [111] vector perpendicular to the surface plane of the liquid Ga electrode.

To separately confirm the orientation and to assess the effects of applied potential and concentration on the crystal orientation, grazing incidence X-ray diffraction was performed on undisturbed, frozen Ga surfaces (Figure 4.10). The products from Pb and Pd electrodepositions were more amenable for these studies since the lower concentrations required for Bi and Mn electrodepositions resulted in less total material collected, severely limiting the attainable signal-to-noise in the diffraction data. In these cases, electron back scatter diffraction (EBSD) were attempted to corroborate the orientation assignments.

Specifically, EBSD measurements were attempted on the as-prepared electrodeposited Bi lines (Figure 4.11). The material presented in the forward-scattered electron detector image appeared disorder because of the curvature of the sample. Nevertheless, the corresponding crystalline orientation map as determined from Kikuchi patterns collected at each pixel. These data indicated all Bi crystals were oriented so that the {0001} direction was perpendicular to the plane of the liquid metal electrode. For Mn^{2+} electrodeposition, bulk diffraction data collection was challenging due to the limited quantity and density of product material arising from the low

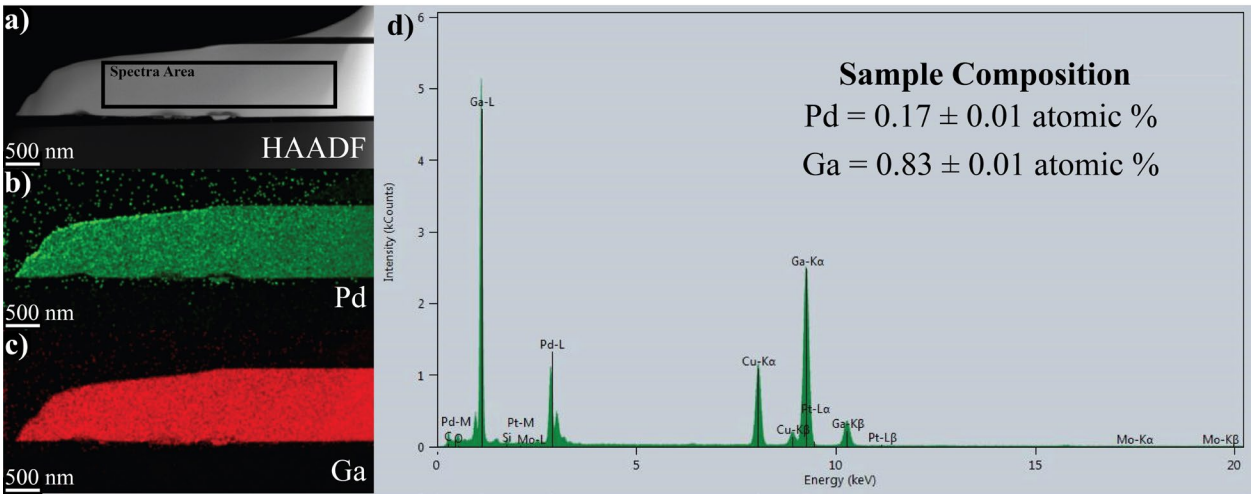

Figure 4.8 STEM-EDX analysis of the 0.2 mM Pd^{2+} electrodeposition at -1.47 V onto a liquid Ga electrode. a) HAADF image of the Pd particle area with the spectra area for EDX acquisition indicated. b) EDX mapping for Pd and c) Ga d) EDX Spectra for the spectra area indicated in (a) with the calculated sample composition for Pd and Ga noted in atomic % without considering contributions of the TEM grid or sample spacers.

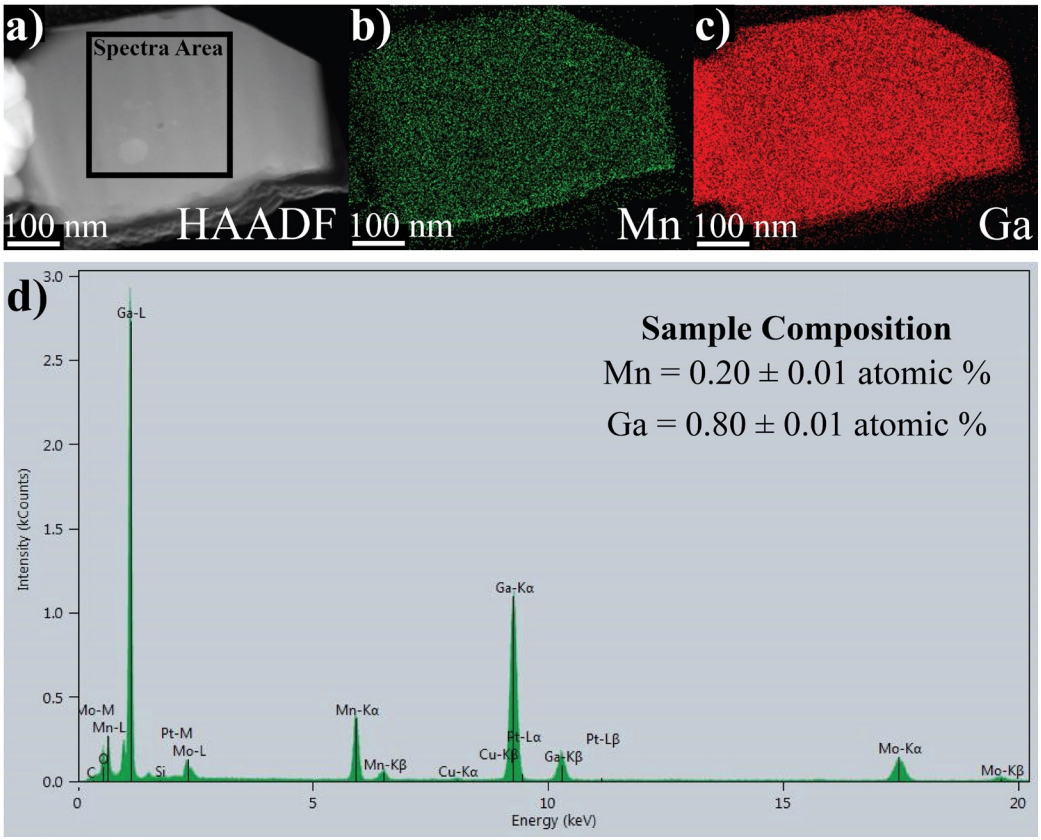

Figure 4.9 STEM-EDX analysis of the 20 µM Mn^{2+} electrodeposition at -1.47 V onto a liquid Ga electrode. a) HAADF image of the Mn particle area with the spectra area for EDX acquisition indicated. b) EDX mapping for Mn and c) Ga. d) EDX Spectra for the spectra area indicated in (a) with the calculated sample composition for Mn and Ga noted in atomic % without considering contributions of the TEM grid or sample spacers.

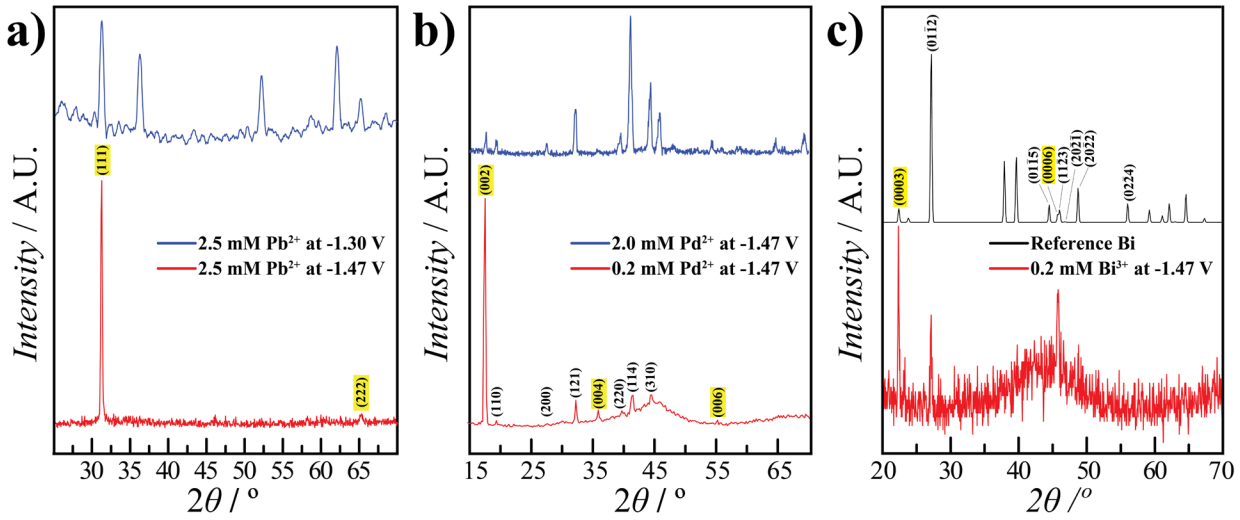

Figure 4.10 Grazing incidence x-ray diffraction data of the Ga electrode interface following electrodeposition in 1.25 M NaOH electrolyte containing either a) 2.5 mM $PbClO_4 \bullet H_2O$ at -1.30 V (blue) and -1.47 V (red) with peaks corresponding to the {111} preferred orientation of the deposition product Pb highlighted in yellow, b) 2.0 mM $PdClO_4$ (blue) and 0.2 mM $PdClO_4$ (red) with peaks corresponding to the {001} preferred orientation of the deposition product $PdGa_5$ highlighted in yellow c) 0.2 mM Bi_2O_3 at -1.47 V (red) and corresponding reference XRD spectra for a polycrystalline Bi sample with peaks corresponding to the preferred {0001}orientation of the electrodeposition product Bi highlighted in yellow.

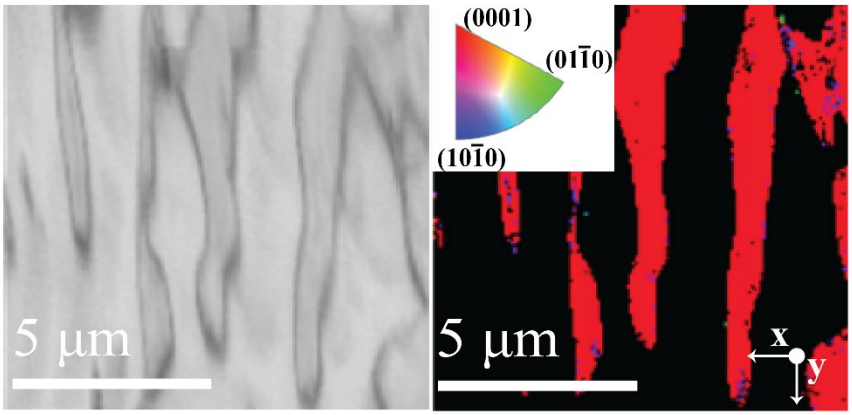

Figure 4.11 (left) Forward-scattered Electron Detector Image of thin, elongated electrodeposited Bi crystals on a frozen Ga interface. (right) The corresponding electron backscatter diffraction map indicating orientation mapping.

solubility of Mn^{2+} in the 1.25 M NaOH electrolyte and the significantly more negative E^0 value (Table 4.1), even after long (16.5 h) reaction times. These particles were also significantly thinner, with a maximum thickness between 200-300 nm (Figure 4.12). These hexagons were sufficiently fragile that they often fragmented upon collection and transfer to a solid surface. Electron backscatter diffraction could not be consistently obtained for these materials with Kikuchi patterns with sufficient signal-to-noise for analysis.

Electrodeposition of Pb performed at -1.47 V exhibited only a single peak for the (111) plane (Figure 4.10a), in accord with the premise of preferred orientation inferred from the HR-TEM images and electron diffraction. In contrast, experiments performed at -1.30 V exhibited X-ray diffraction peaks at 2θ = 31.3°, 36.3°, 52.3°, 62.2°, and 65.3°, indexed to the (111), (020), (220), (311), and (222) planes, respectively. The relative intensities of these signals was in accord with randomly oriented, polycrystalline Pb.[31]

$PdGa_5$ with a predominant orientation was evident in the X-ray diffraction data collected from experiments performed at -1.47 V at low concentrations but not at high concentrations (Figure 4.10b). Specifically, at low concentrations the family of {001} diffraction peaks (i.e. (002), (004), and (006)) were evident, with the signal for the (002) direction at 2θ = 17.7° as overwhelmingly the most intense. Additional peaks appeared at 2θ = 19.4°, 27.6°, 32.2°, 35.9°, 39.5°, 41.1°, 44.3°, and 55.0° indexed to the (110), (200), (121), (004), (220), (114), (310), and (006) planes, respectively. Although the (001) diffraction signal was not visible in the tetragonal lattice because of the 2_1 screw axis in this lattice type,[32] the observation of the dominant (002) signal was consistent with the [001] direction as normal to the liquid metal surface plane since they belong to the same family of directions. The appearance of other directions in Figure 4.10b as minor peaks was attributed to the difficulty of obtaining frozen liquid metal surfaces with absolutely no curvature. Increasing the precursor concentration by a factor of 10 resulted in the appearance of several additional peaks with dramatically different relative intensities. The overall pattern of peaks in this case was consistent with a collection of crystallites with randomized orientations with respect to the surface plane of Ga. For Bi electrodeposition (Figure 4.10c), the signal-to-noise was poor but the dominant signal was the diffraction peak along the [0003] direction, consistent with the assigned orientation of the [0001] vector as normal to the liquid metal surface plane.

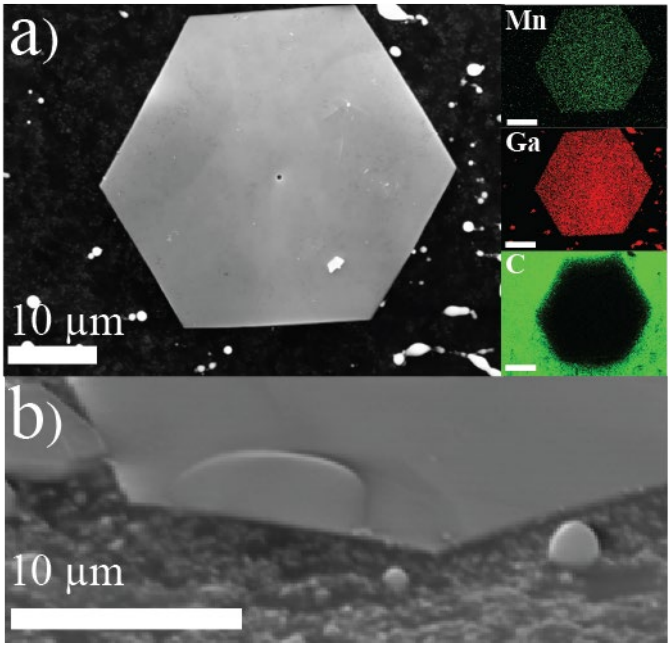

Figure 4.12 a) SEM of a $MnGa_4$ hexagon which was isolated onto carbon tape from the interface of liquid Ga for further attempted EBSD analysis with corresponding EDS mapping b) Different $MnGa_4$ hexagon also isolated onto carbon tape and imaged at a 52° tilt angle.

4.5 Discussion

The presented data supports three key points. First, electrodeposition with a preferred orientation can occur at a liquid metal-electrolyte interface without binding agents, additives, or external solid seeding substrates. Second, the orientation of the as-synthesized crystals suggests the crystallographic plane with the highest packing density of atoms is oriented along the surface plane. Third, factors that affect the quasi-epitaxial crystal growth are evident, with the rate of electroreduction and absence of oxides at the liquid metal interface as important. These points are further discussed below.

4.5.1 Probable Source of Preferred Orientation

All previously reported electrodeposition strategies that produce single-crystalline products utilized at least one of the following four concepts. (*1*) Electrodeposition of a metal layer onto a single-crystalline solid electrode that is epitaxially matched to the desired product film can produce single-crystalline metal films.[33] (*2*) Electrodeposition on a solid electrode with a high lattice mismatch can also yield single-crystalline films if periodic sites between the two materials overlap to form a stable boundary (coincidence site lattice epitaxy).[34, 35] (*3*) Initial electrodeposition of a less noble metal crystal on a solid surface followed by controlled galvanic or electrolytic metal replacement with a more noble element can produce single-crystalline materials with a preferred orientation.[36] (*4*) A chelating/binding reagent in the supporting electrolyte can direct electrodeposition with a preferred orientation through selective adsorption to specific crystallographic planes.[37]

The presented experiments argue against *any* of these four concepts as possible explanations for the directed crystal growth observed here. The possible inclusion of an unintended solid surface within Ga and/or at the Ga/water interface is unlikely. Prior to each electrodeposition, thorough cleaning of both the Teflon components and Ga was performed to mitigate the possibility of macroscopic solid impurities within the cell or electrolyte in every single experiment. The method used to prepare the alkaline electrolyte was sufficient to getter metal impurities as measured by inductively coupled plasma emission (ICP). There was no indication of separate intermetallic crystals from metal impurities separately reacting with Ga in these experiments.

The possible presence and influence of gallenene[38] from surface freezing of Ga is also remote. All electrodepositions were performed intentionally under active heating to ensure the

bulk and surface of Ga were molten. Additionally, previous studies demonstrated gallenene could only be prepared and retrieved from a liquid Ga interface with an external solid seed.[38] To date, there are no reports of spontaneous gallenene formation through surface freezing at elevated temperatures. Additionally, although solid gallenene could conceivably promote directed growth for some materials through coincidence site lattice epitaxy, it is improbable that this mechanism is equally operative for all four crystal types shown here.

The data also rule out the possibility of an appreciable gallium oxide serving as a solid nucleating surface in metal electrodeposition at more negative potentials in this electrolyte. The presented data show no accumulation of gallium oxides at the liquid Ga/electrolyte interface at -1.47 V, in agreement with the reported Pourbaix diagram for Ga/water contacts at standard temperature and pressure.[23] Although the limited sensitivities of scanning electron microscopy and energy dispersive spectroscopic measurements allow for the possibility of an ultra-thin gallium oxide film, its hypothetical importance is also likely negligible. Interfacial gallium oxide layers are uniformly amorphous or poorly crystalline.[39-41] Accordingly, consistent and complete lattice matching with Pb, Bi, $PdGa_5$, and $MnGa_4$ so as to seed the systematic growth of each material along specific directions is without precedent. Rather, a gallium oxide would most likely just increase the probability of nucleation but without any preferred orientation or direction (Figure 4.13a). The data collected at -1.30 V where an interfacial gallium oxide is clearly present and polycrystalline dendritic growth is observed (Figure 4.4) is in line with this premise. Although acidic electrolytes may also be useful in removing surface oxides, alkaline conditions are preferrable to minimize the competition with H_2 evolution at the employed negative potentials.

Since the electrolyte had no additional additives, the only species of relevance were the supporting counter ions. There is precedent for chemisorbed ions directing electrochemical inorganic crystal growth at a liquid metal/electrolyte contact.[42, 43] Chemisorption of halides to the Hg/water interface was previously used to sequester Pb^{2+} released anodically from Hg-Pb amalgams at positive potentials. The halides coordinated with the Pb^{2+} emitted from the Hg interface. The initial adlayer seeded the oriented growth of larger crystals extending into bulk water.[43] However, the halides in that work were strongly bound to the liquid metal amalgam surface. Additionally, the halides acted as reactants with leached metal cations and eventually were constituent species in the eventual crystal. Neither aspect is relevant to the work shown here. The perchlorate and hydroxide anions have significantly weaker binding affinity for Ga than Ga, with

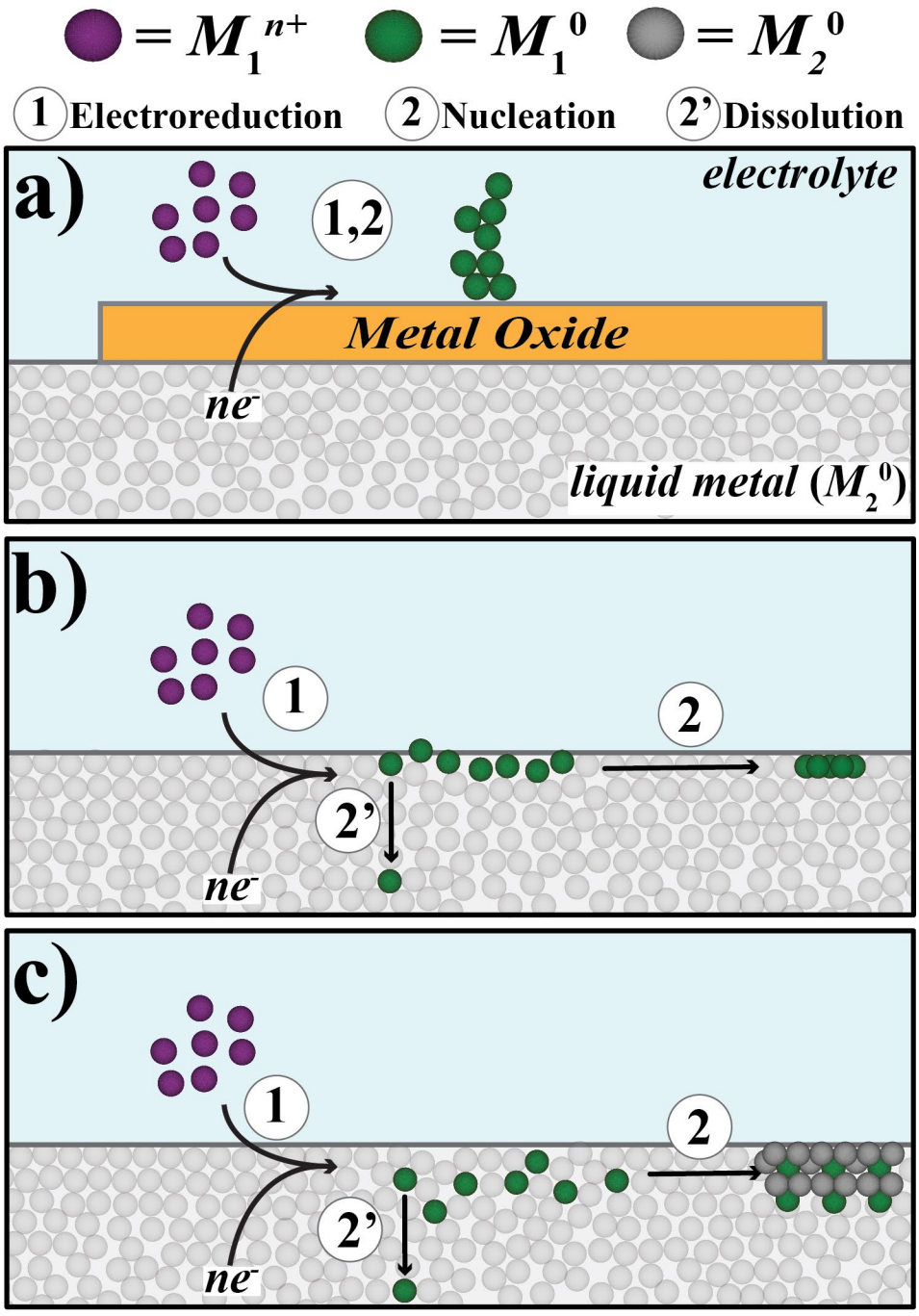

Figure 4.13 Graphical summary of the key electrodeposition steps in nucleus formation by quasi-epitaxy starting with the (1) electrochemical reduction of a dissolved metal precursor (M_1^{n+}) to achieve one of three observed products: a) polycrystalline metal (M_1^0) dendrites by heterogeneous nucleation on the solid surface oxide, b) single crystalline M_1^0 by nucleation of M_1^0 via self-segregation at the interface in a close-packed form, or c) single crystalline intermetallic via nucleation governed by the in-plane packing of M_2^0. In both (b) and (c), a fraction of electrodeposited metal atoms do not participate in nucleation at the interface and will instead dissolve into the liquid metal bulk (M_2^0).

perchlorates generally regarded as the least Lewis basic of all common electrolyte anions.[44, 45] Neither perchlorate nor hydroxide appeared in any detectable quantity in the collected metallic crystals.

4.5.2 Origin of Preferred Orientation

The primary observations of this work are consistent with the premise that liquid Ga itself is imparting directionality to the resultant crystals. In the dilute liquid metal Ga-Pb and Ga-Bi alloys formed by electrodeposition, segregation of the Pb and Bi components occurs since neither solute is miscible with liquid Ga.[46] That is, as soon as appreciable levels of Pb and Bi are introduced, the liquid metal mixtures self-segregate into a solute-rich surface surrounding a Ga-rich bulk. This point is well-established in the behavior of these same liquid alloys when heated and then cooled under vacuum.[9, 10, 46-48]

As long as the solute-rich surface remains molten (i.e. either at high temperatures when the composition is held constant or at short times during isothermal electrodeposition), the solute-rich surface attains a nearly close-packed, hexatic structure.[9, 10] Based on prior X-ray reflectivity studies,[4-6, 8, 49] the atomic layering extends from the solute-rich surface to the near-surface region of the bulk since both are in contact with dissimilar materials. When the solute-rich surface attains a sufficiently high solute concentration for nucleation (i.e. either at cold temperatures when the composition is held constant or at long times during isothermal electrodeposition), thin (~25 Å) nuclei form across the solute-rich surface layer. If nucleation occurs without substantial nuclear rearrangement, the most probable structure of these nuclei must be two-dimensional sheets with a high atomic density (Figure 4.13b). Within the two pure metal lattices, the Pb(111) and Bi(0001) planes have the highest in-plane atomic packing density, respectively.[50] The crystal faces parallel to the liquid metal surface were conclusively identified as these specific planes.

Electrodepositions of Pd and Mn shared this same principal observation. In both resultant intermetallic compounds, the product crystals were again oriented in a manner consistent with the planes featuring the highest atomic densities being coincident with the surface plane of the liquid metal. In both of these metal electrodepositions, the presence of a surface-segregated, solute-rich phase separated from the Ga-rich bulk was unlikely. Both Pd and Mn are miscible with liquid Ga. Accordingly, the Pd and Mn solutes were likely instantly and fully solvated by Ga upon dissolution into the liquid metal. Nuclei with a consistent structure (and subsequent crystal growth with a

preferred orientation) would still be possible if the following two points were true (Figure 4.13c). First, introduction of the electrodeposited metal solute does not destroy the atomic layering within liquid Ga. This point implies that the solvation shell around each metal solute near the liquid metal/water interface would resemble the atomic layering of liquid Ga. Second, if nucleation again occurs without substantial nuclear rearrangement, the most probable structure for nuclei would be two-dimensional sheets of solutes with a similar arrangement of solvated Ga atoms. This latter point is analogous to the condition for the observation of Pb and Bi crystals with preferred orientation but also requires that the structure of the nuclei specifically mirror the atomic arrangement of the lattice plane with the highest atomic densities of Ga in the resultant intermetallic.

Both intermetallic crystal structures are more complex than the close-packed face centered cubic and rhombohedral motifs of Pb and Bi, respectively. In the $PdGa_5$ lattice, the {001} family of planes has the highest atomic packing density. When viewed along a perpendicular axis, the {001} planes consist of pure Ga and Pd sheets. Interestingly, the atomic densities of the two distinct Ga sheets combine to a packing density of 0.072 atom $Å^2$. (Figure 4.14, Table 4.2)

This value is consistent with the packing density of a hypothetical Ga atomic layer where each atom has 5 in-plane nearest neighbors. (Figure 4.15, Table 4.3) The prevalence of five-fold coordination in the atomic layering within liquid metal interfaces has been predicted and observed previously.[51] An analogous analysis for $MnGa_4$ (Figure 4.16, Table 4.4) similarly suggests that the orientation of the crystal is consistent with the crystallographic direction where the sub-planes of Ga atoms sum up to an atomic packing density comparable to that of a putative Ga layer with 5 in-plane nearest neighbors (0.076 atoms $Å^2$). Accordingly, the preferred orientation of both the Pd and Mn intermetallic crystals are consistent with the premise that the structure of the initial nuclei specifically mirror the stratified atomic arrangement of the near-surface region of liquid Ga.

4.5.3 Factors that Prevent 'Quasi-Epitaxial' Crystal Growth in Electrodepositions with Liquid Metal Electrodes

The experiments performed here highlight an aspect that prevents 'quasi-epitaxial' crystal growth in electrodepositions with liquid metal electrodes. Quasi-epitaxial electrodeposition was only observed when the introduction of solute to the liquid metal by electroreduction was sufficiently slow. We found that controlling the precursor concentration in solution was the most

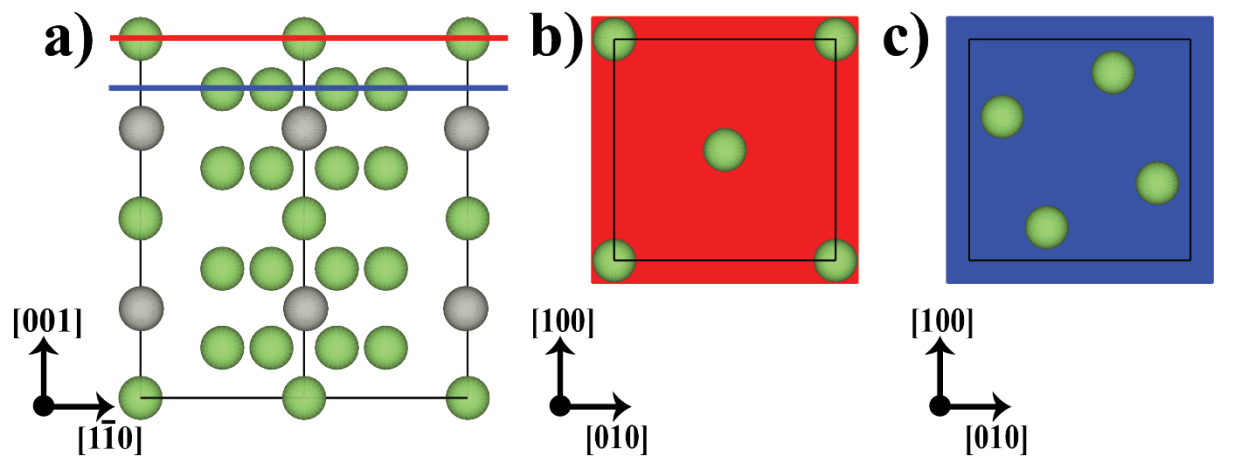

Figure 4.14 a) Tetragonal $PdGa_5$ projected along the [110] crystallographic cross-section with the perpendicular [001] direction pointed upwards. Two planes belonging to the {001} are highlighted in b) red and c) blue which are considered for the packing arrangement prior to Pd atom insertion within the liquid Ga layers at the interface.

Table 4.2 Packing density calculation for the $PdGa_5$ planes highlighted in Figure 4.14 along the perpendicular [001] direction to the liquid Ga interface

Plane	Number of Atoms	Area ($Å^2$)	Packing Density (atoms $Å^{-2}$)
(001) - Red	**1.00**	**41.58**	**0.024**
(001) - Blue	**2.00**	**41.58**	**0.048**

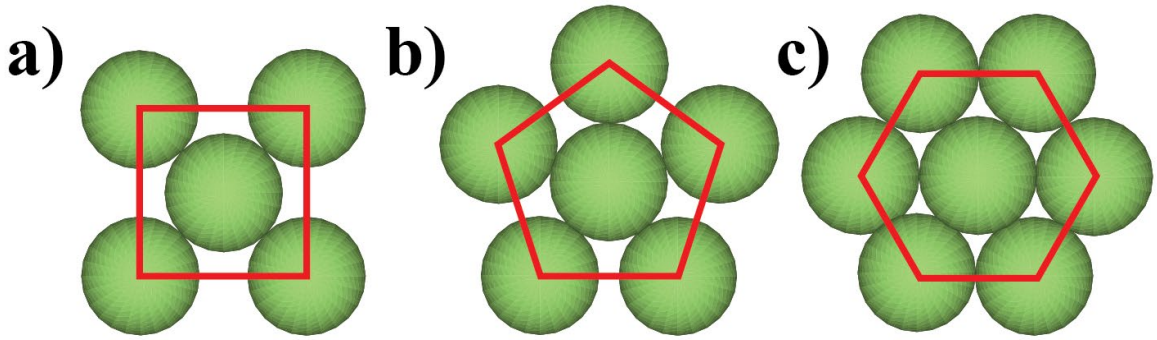

Figure 4.15 Potential a) cubic b) pentagonal or c) hexagonal in-plane packing arrangements the liquid Ga surface layers with the defined planar area highlighted in red.

Table 4.3 Packing density calculation for the possible in-plane ordering arrangement of liquid Ga layers nearest the liquid Ga/electrolyte interface shown in Figure 4.15.

		Atomic Radius = 1.36 Å	
Type of Packing	**Number of Atoms**	**Area ($Å^2$)**	**Packing Density (atoms $Å^{-2}$)**
Square	**1.00**	**14.80**	**0.068**
Pentagonal	**1.33**	**17.59**	**0.076**
Hexagonal	**1.50**	**19.22**	**0.078**

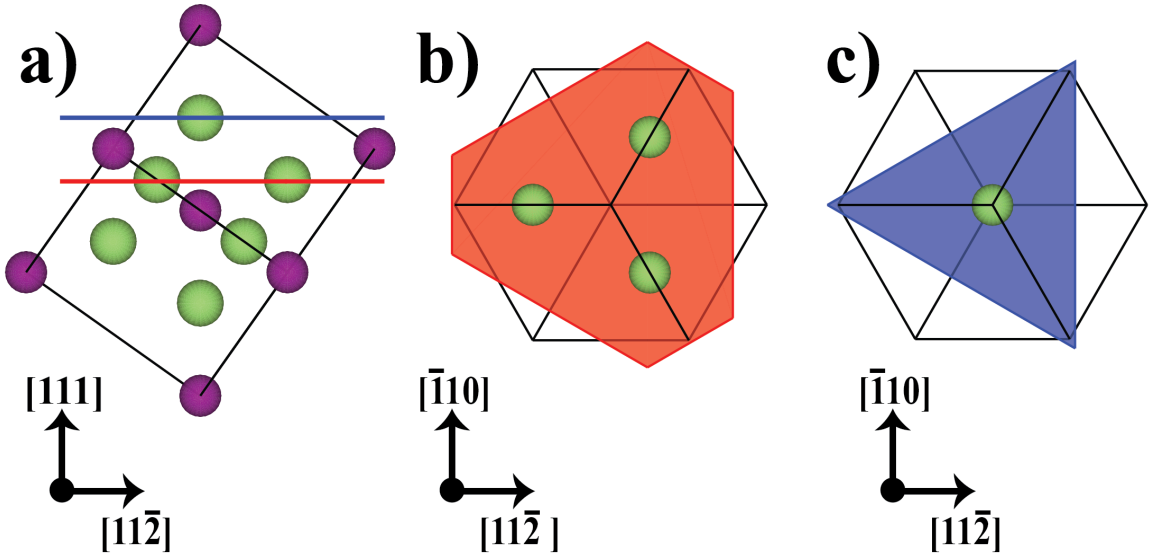

Figure 4.16 a) Cubic $MnGa_4$ projected along the [$\bar{1}$10] crystallographic cross-section with the perpendicular [111] direction pointed upwards. Two planes belonging to the {111} are highlighted in b) red and c) blue which are considered for the packing arrangement prior to Mn atom insertion within the liquid Ga layers at the interface.

Table 4.4 Packing density calculation for the $MnGa_4$ planes highlighted in Figure 4.16 along the perpendicular [111] direction to the liquid Ga interface.

Plane	Number of Atoms	Area ($Å^2$)	Packing Density (atoms $Å^{-2}$)
(111) - Red	**1.50**	**27.10**	**0.055**
(111) - Blue	**0.50**	**27.10**	**0.018**

effective system property in limiting the reaction flux. As long as the precursor concentrations were kept below a minimum concentration, the resultant crystals exhibited quasi-epitaxy. For Pb and Pd, these concentrations were determined to be 0.2 mM and 2.5 mM, respectively. The monodispersity of the particle morphology depended much more critically on time, where short times (< 180 min) produced singular particle shapes, at the expense of lower total particle densities. It is not clear from these data if the atomic ordering within the near-surface region of the liquid metal was compromised during the timescale of nucleation, the prevalence of secondary nucleation on the nascent crystals started to outpace nucleation in the liquid metal, or both. Nevertheless, additional experiments that reveal both the atomic structure and dynamics at these liquid metal interfaces would be informative on this front and to identify *apriori* the optimal time and concentration points for any liquid metal-metal cation electrodeposition combination.

Additionally, the experiments here, in conjunction with the aforementioned reports on surface freezing of liquid metal alloys, highlight factors that are not determinative in the synthesis of single-crystals with a preferred orientation in liquid metals. The electrodeposition experiments performed here were at ambient pressure and constant temperature. The majority of reports on crystal growth by surface freezing of liquid metals are in vacuum and with deliberate temperature changes. Accordingly, we interpret these aspects as not critical to the orientation of the resultant crystals.

Separately, the electrodeposition experiments here resolve a subtle disagreement in the surface freezing literature. In surface freezing experiments, the continued growth of large crystals is generally not possible with dilute alloys since the mole fraction of the solute is finite and kept constant. Nevertheless, large single-crystals have been predicted[47] if a sufficient supply of solute and fast diffusional transport were maintained. A competing hypothesis[47] alternatively suggested that instantaneous spinodal phase separation should always occur at liquid metal surfaces, which would result in macroscopic crystals with no preferred orientation. The observations reported here are consistent with the former prediction.

Finally, the possible implications of the term ‘quasi-epitaxy’ merit mention. Although the orientation of the single crystals shown here strongly support the contention that the liquid metal structure influences nucleation, the data are agnostic to whether the atomic structure of the liquid metal affects crystal growth. The observed crystal morphologies were all consistent with crystal growth occurring faster along planes with higher surface energies, i.e. to maximize the area of the

facet with the lowest surface energy.[52, 53] Similarly, there was no obvious in-plane ordering of any crystallites along the surface of undisturbed liquid metal electrodes. This point is in strong contrast to observations of crystallites nucleated and grown by conventional epitaxy on a single-crystalline solid substrate,[35] but is fully in line with the structural features of a liquid metal. Since there is no evidence of a long-lived, long-range, in-plane ordering across the surface of a liquid metal/water interface, there should be no expectation of correlated in-plane crystallite orientations. This point was manifested in the experiments with Pb, Pd, and Mn electrodeposition. The peculiar straight parallel lines along the $[11\bar{2}0]$ growth direction observed in the Bi electrodeposition experiments were consistent with prior reports of conventional epitaxial growth of Bi on solid surfaces.[54-56] Further examination of this system is warranted to determine what factor(s) produced these features.

4.6 Conclusions

This work introduces the concept of 'quasi-epitaxial' electrodeposition on liquid metal surfaces, i.e. the atomic layering within liquid metal electrodes effects non-random nuclei structures which lead to preferred orientation in electrodeposited crystals. Quasi-epitaxy occurs without any external solid seed and occurs in ambient, aqueous media. The presented data suggest that the initial nuclei have a structure influenced by the atomic packing in the near-surface layers within Ga, most likely featuring five-fold in-plane nearest neighbors. Although the presented data highlight the quasi-epitaxial principle on the formation of known phases and polymorphs, this work opens the possibility that quasi-epitaxy of new phases and crystalline structures may be obtained by electrodeposition at liquid metal electrode interfaces. Specifically, the unique solvation environment of liquid metal interfaces could facilitate structures not known in bulk phase diagrams, as has already been noted in some liquid metal systems.[57, 58] Further interrogation of liquid metal/liquid electrolyte interfaces with atomic specificity and fast temporal resolution would be helpful to better clarify the details concerning crystal growth.

4.7 References

1. Mauk, M.; Capper, P., Liquid Phase Epitaxy of Electronic, Optical, and Optoelectronic Materials. Wiley: 2007.
2. Liquid Metal as a New Reaction Medium. In *Liquid Metals*, 2022; pp 153-215.
3. Murphy, B. M.; Festersen, S.; Magnussen, O. M., The Atomic scale structure of liquid metal–electrolyte interfaces. *Nanoscale* **2016,** *8* (29), 13859-13866.
4. Elsen, A.; Murphy, B. M.; Ocko, B. M.; Tamam, L.; Deutsch, M.; Kuzmenko, I.; Magnussen, O. M., Surface layering at the mercury-electrolyte interface. *Physical Review Letters* **2010,** *104* (10), 105501.
5. Regan, M. J.; Kawamoto, E. H.; Lee, S.; Pershan, P. S.; Maskil, N.; Deutsch, M.; Magnussen, O. M.; Ocko, B. M.; Berman, L. E., Surface Layering in Liquid Gallium: An X-Ray Reflectivity Study. *Physical Review Letters* **1995,** *75* (13), 2498-2501.
6. Magnussen, O. M.; Ocko, B. M.; Regan, M. J.; Penanen, K.; Pershan, P. S.; Deutsch, M., X-ray reflectivity measurements of surface layering in liquid mercury. *Physical Review Letters* **1995,** *74* (22), 4444-4447.
7. Regan, M. J.; Pershan, P. S.; Magnussen, O. M.; Ocko, B. M.; Deutsch, M.; Berman, L. E., X-ray reflectivity studies of liquid metal and alloy surfaces. *Physical Review B* **1997,** *55* (23), 15874-15884.
8. Shpyrko, O.; Fukuto, M.; Pershan, P.; Ocko, B.; Kuzmenko, I.; Gog, T.; Deutsch, M., Surface layering of liquids: The role of surface tension. *Physical Review B* **2004,** *69* (24), 245423.
9. Yang, B.; Gidalevitz, D.; Li, D.; Huang, Z.; Rice Stuart, A., Two-dimensional freezing in the liquid–vapor interface of a dilute Pb:Ga alloy. *Proceedings of the National Academy of Sciences* **1999,** *96* (23), 13009-13011.
10. Li, D.; Jiang, X.; Yang, B.; Rice, S. A., Phase transitions in the liquid-vapor interface of dilute alloys of Bi in Ga: New experimental studies. *The Journal of Chemical Physics* **2005,** *122* (22), 224702.
11. Cahn, J. W., Critical point wetting. *The Journal of Chemical Physics* **2008,** *66* (8), 3667-3672.
12. Ebner, C.; Saam, W. F., New reentrant wetting phenomena and critical behavior near bulk critical points. *Physical Review Letters* **1987,** *58* (6), 587-590.
13. Fahrenkrug, E.; Maldonado, S., Electrochemical Liquid–Liquid–Solid (ec-LLS) Crystal Growth: A Low-Temperature Strategy for Covalent Semiconductor Crystal Growth. *Accounts of Chemical Research* **2015,** *48* (7), 1881-1890.
14. Wu, H.; Hazelnis, J. P.; Maldonado, S., Understanding and Expanding the Prospects for Electrosynthesis with Liquid Metal Electrodes. *Accounts of Chemical Research* **2023,** *56* (7), 846-855.
15. Demuth, J.; Fahrenkrug, E.; Ma, L.; Shodiya, T.; Deitz, J. I.; Grassman, T. J.; Maldonado, S., Electrochemical Liquid Phase Epitaxy (ec-LPE): A New Methodology for the Synthesis of Crystalline Group IV Semiconductor Epifilms. *Journal of the American Chemical Society* **2017,** *139* (20), 6960-6968.
16. Downes, N.; DeMuth, J.; Waelder, J.; Cheek, Q. B.; Bartels, H.; Maldonado, S., Si Electrochemical Liquid Phase Epitaxy: Low-Temperature Growth of Hyperdoped Epitaxial Si Films. *Chemistry of Materials* **2022,** *34* (24), 10861-10872.
17. Márquez, R. A.; Kawashima, K.; Son, Y. J.; Castelino, G.; Miller, N.; Smith, L. A.; Chukwuneke, C. E.; Mullins, C. B., Getting the Basics Right: Preparing Alkaline Electrolytes for Electrochemical Applications. *ACS Energy Letters* **2023,** *8* (2), 1141-1146.

18. Hurlen, T.; V»land, T.; Lunde, G., Anodic dissolution of liquid gallium. *Electrochimica Acta* **1964,** *9* (11), 1433-1437.
19. Vivier, V.; Régis, A.; Sagon, G.; Nedelec, J. Y.; Yu, L. T.; Cachet-Vivier, C., Cyclic voltammetry study of bismuth oxide Bi2O3 powder by means of a cavity microelectrode coupled with Raman microspectrometry. *Electrochimica Acta* **2001,** *46* (6), 907-914.
20. Schindelin, J.; Arganda-Carreras, I.; Frise, E.; Kaynig, V.; Longair, M.; Pietzsch, T.; Preibisch, S.; Rueden, C.; Saalfeld, S.; Schmid, B.; Tinevez, J.-Y.; White, D. J.; Hartenstein, V.; Eliceiri, K.; Tomancak, P.; Cardona, A., Fiji: an open-source platform for biological-image analysis. *Nature Methods* **2012,** *9* (7), 676-682.
21. Zavabeti, A.; Ou, J. Z.; Carey, B. J.; Syed, N.; Orrell-Trigg, R.; Mayes, E. L. H.; Xu, C.; Kavehei, O.; O'Mullane, A. P.; Kaner, R. B.; Kalantar-zadeh, K.; Daeneke, T., A liquid metal reaction environment for the room-temperature synthesis of atomically thin metal oxides. *Science* **2017,** *358* (6361), 332-335.
22. Hong, B.; Wang, Y.; Wei, X.; Huang, Q.; Wang, X.; Fujita, T.; Wei, Y., EQCM study on the electrochemical redox behavior of gallium in alkaline solution. *Hydrometallurgy* **2020,** *194*, 105344.
23. Chung, Y.; Lee, C.-W., Electrochemistry of Gallium. *Journal of Electrochemical Science and Technology* **2013,** *4* (1), 1-18.
24. Bard, A. a.; International Union of, P.; Applied, C., *Standard Potentials in Aqueous Solution*. First edition. ed.; Taylor and Francis: 2017.
25. Baur, E.; Latttnann, W., Über die Potentiale der Wismutoxyde und Über den Alkalischen Wismutsammler. *Zeitschrift für Elektrochemie und angewandte physikalische Chemie* **1934,** *40* (8), 582-585.
26. Kawashima, K.; Márquez, R. A.; Son, Y. J.; Guo, C.; Vaidyula, R. R.; Smith, L. A.; Chukwuneke, C. E.; Mullins, C. B., Accurate Potentials of Hg/HgO Electrodes: Practical Parameters for Reporting Alkaline Water Electrolysis Overpotentials. *ACS Catalysis* **2023,** *13* (3), 1893-1898.
27. Milchev, A.; Krastev, I., Two-dimensional progressive and instantaneous nucleation with overlap: The case of multi-step electrochemical reactions. *Electrochimica Acta* **2011,** *56* (5), 2399-2403.
28. Hofmann, P., The surfaces of bismuth: Structural and electronic properties. *Progress in Surface Science* **2006,** *81* (5), 191-245.
29. Swanson, H. E.; Tatge, E.; United States. National Bureau of, S., *Standard X-ray diffraction powder patterns. Vol. I, Data for 54 inorganic substances*. National Bureau of Standards: [Washington, D.C.], 1953; Vol. [Washington, D.C.].
30. Pilloni, M.; Ennas, G.; Cabras, V.; Denotti, V.; Kumar, V. B.; Musinu, A.; Porat, Z.; Scano, A.; Gedanken, A., Thermal and structural characterization of ultrasonicated BiSn alloy in the eutectic composition. *Journal of Thermal Analysis and Calorimetry* **2015,** *120* (3), 1543-1551.
31. Gontad, F.; Lorusso, A.; Klini, A.; Loufardaki, A.; Panareo, M.; Fotakis, C.; Perrone, A., Picosecond and subpicosecond pulsed laser deposition of Pb thin films. *Physical Review Special Topics - Accelerators and Beams* **2013,** *16* (9), 093401.
32. Nespolo, M., International Tables for Crystallography, Volume A, Space-group symmetry. Edited by Mois I. Aroyo. Wiley, 2016. ISBN 978-0-470-97423-0. *Acta Crystallographica Section A: Foundations and Advances* **2017,** *73* (3), 274-276.

33. Möller, F. A.; Magnussen, O. M.; Behm, R. J., Electrodeposition and Anodic Dissolution of Ni on Au(100): an in situ STM Study*. *Zeitschrift für Physikalische Chemie* **1999,** *208* (1-2), 57-75.
34. Hull, C. M.; Switzer, J. A., Electrodeposited Epitaxial Cu(100) on Si(100) and Lift-Off of Single Crystal-like Cu(100) Foils. *ACS Applied Materials & Interfaces* **2018,** *10* (44), 38596-38602.
35. Switzer, J. A.; Liu, R.; Bohannan, E. W.; Ernst, F., Epitaxial Electrodeposition of a Crystalline Metal Oxide onto Single-Crystalline Silicon. *The Journal of Physical Chemistry B* **2002,** *106* (48), 12369-12372.
36. Liang, X.; Zhang, Q.; Lay, M. D.; Stickney, J. L., Growth of Ge Nanofilms Using Electrochemical Atomic Layer Deposition, with a "Bait and Switch" Surface-Limited Reaction. *Journal of the American Chemical Society* **2011,** *133* (21), 8199-8204.
37. Wang, H.; Liang, Z.; Tang, M.; Chen, G.; Li, Y.; Chen, W.; Lin, D.; Zhang, Z.; Zhou, G.; Li, J.; Lu, Z.; Chan, K.; Tan, T.; Cui, Y., Self-Selective Catalyst Synthesis for CO2 Reduction. *Joule* **2019,** *3* (8), 1927-1936.
38. Kochat, V.; Samanta, A.; Zhang, Y.; Bhowmick, S.; Manimunda, P.; Asif, S. A. S.; Stender, A. S.; Vajtai, R.; Singh, A. K.; Tiwary, C. S.; Ajayan, P. M., Atomically thin gallium layers from solid-melt exfoliation. *Science Advances* **2018,** *4* (3), e1701373.
39. Regan, M.; Tostmann, H.; Pershan, P. S.; Magnussen, O.; DiMasi, E.; Ocko, B.; Deutsch, M., X-ray study of the oxidation of liquid-gallium surfaces. *Physical Review B* **1997,** *55* (16), 10786.
40. Plech, A.; Klemradt, U.; Metzger, H.; Peisl, J., In situ x-ray reflectivity study of the oxidation kinetics of liquid gallium and the liquid alloy. *Journal of Physics: Condensed Matter* **1998,** *10* (5), 971.
41. Chabala, J. M., Oxide-growth kinetics and fractal-like patterning across liquid gallium surfaces. *Physical Review B* **1992,** *46* (18), 11346.
42. Festersen, S.; Runge, B.; Koops, C.; Bertram, F.; Ocko, B.; Deutsch, M.; Murphy, B. M.; Magnussen, O. M., Nucleation and Growth of PbBrF Crystals at the Liquid Mercury–Electrolyte Interface Studied by Operando X-ray Scattering. *Langmuir* **2020,** *36* (37), 10905-10915.
43. Sartori, A.; Giri, R. P.; Fujii, H.; Hövelmann, S. C.; Warias, J. E.; Jordt, P.; Shen, C.; Murphy, B. M.; Magnussen, O. M., Role of chemisorbing species in growth at liquid metal-electrolyte interfaces revealed by in situ X-ray scattering. *Nature Communications* **2022,** *13* (1), 5421.
44. Linert, W.; Camard, A.; Armand, M.; Michot, C., Anions of low Lewis basicity for ionic solid state electrolytes. *Coordination Chemistry Reviews* **2002,** *226* (1), 137-141.
45. Davies, J.; Hartley, F., Complexes of the platinum metals containing weak donor ligands. *Chemical Reviews* **1981,** *81* (1), 79-90.
46. Issanin, A.; Turchanin, A.; Freyland, W., Electron spectroscopy and scanning tunneling microscopy study of quasi-two-dimensional freezing at the liquid/vapor interface of Ga-Bi alloys. *The Journal of Chemical Physics* **2004,** *121* (23), 12005-12009.
47. Huber, P.; Shpyrko, O.; Pershan, P. S.; Ocko, B.; DiMasi, E.; Deutsch, M., Short-range wetting at liquid gallium-bismuth alloy surfaces: X-ray measurements and square-gradient theory. *Physical Review B* **2003,** *68* (8), 085409.

48. Dogel, S.; Nattland, D.; Freyland, W., Complete wetting transitions at the liquid-vapor interface of gallium-bismuth alloys: Single-wavelength and spectroscopic ellipsometry studies. *Physical Review B* **2005,** *72* (8), 085403.
49. Pershan, P. S., X-ray scattering: Liquid metal/vapor interfaces. *The European Physical Journal Special Topics* **2011,** *196* (1), 109-120.
50. Halka, V.; Freyland, W., Thermal stability of surface freezing films in Ga-based alloys: An x-ray photoelectron spectroscopy and scanning tunneling microscopy study. *The Journal of Chemical Physics* **2007,** *127* (3), 034702.
51. Reichert, H.; Klein, O.; Dosch, H.; Denk, M.; Honkimäki, V.; Lippmann, T.; Reiter, G., Observation of five-fold local symmetry in liquid lead. *Nature* **2000,** *408* (6814), 839-841.
52. Li, L.; Goodrich, C.; Yang, H.; Phillips, K. R.; Jia, Z.; Chen, H.; Wang, L.; Zhong, J.; Liu, A.; Lu, J., Microscopic origins of the crystallographically preferred growth in evaporation-induced colloidal crystals. *Proceedings of the National Academy of Sciences* **2021,** *118* (32), e2107588118.
53. Lin, H.; Liu, J.-X.; Fan, H.; Li, W.-X., Compensation between Surface Energy and hcp/fcc Phase Energy of Late Transition Metals from First-Principles Calculations. *The Journal of Physical Chemistry C* **2020,** *124* (20), 11005-11014.
54. Kowalczyk, P. J.; Mahapatra, O.; McCarthy, D. N.; Kozlowski, W.; Klusek, Z.; Brown, S. A., STM and XPS investigations of bismuth islands on HOPG. *Surface Science* **2011,** *605* (7), 659-667.
55. Miki, K.; Owen, J. H. G.; Bowler, D. R.; Briggs, G. A. D.; Sakamoto, K., Bismuth-induced structures on Si(001) surfaces. *Surface Science* **1999,** *421* (3), 397-418.
56. Miki, K.; Bowler, D. R.; Owen, J. H. G.; Briggs, G. A. D.; Sakamoto, K., Atomically perfect bismuth lines on Si(001). *Physical Review B* **1999,** *59* (23), 14868-14871.
57. Shpyrko, O. G.; Streitel, R.; Balagurusamy, V. S.; Grigoriev, A. Y.; Deutsch, M.; Ocko, B. M.; Meron, M.; Lin, B.; Pershan, P. S., Surface crystallization in a liquid AuSi alloy. *Science* **2006,** *313* (5783), 77-80.
58. Mechler, S.; Yahel, E.; Pershan, P. S.; Meron, M.; Lin, B., Crystalline monolayer surface of liquid Au–Cu–Si–Ag–Pd: metallic glass former. *Applied Physics Letters* **2011,** *98* (25), 251915.

Chapter 5 Discovery of Metal-Ga Intermetallics via 'Quasi'-Epitaxy at Liquid Ga/Water Interfaces

5.1 Preface

The following work expands upon the new concept in ec-LLS introduced in Chapter 4, 'quasi'-epitaxy for obtaining previously unreported intermetallic phases. All synthetic procedures were performed by Joshua P. Hazelnis. Former undergraduate student, Navpreet Singh and Joshua P. Hazelnis performed the ICP-MS data collection. Focus ion beam sample preparation was performed by Allen Hunter and Joshua P. Hazelnis. (S)TEM characterization was performed by Tao Ma and Joshua P. Hazelnis. All microED data was collected by Tao Ma. Matthew R. Crawley from the University at Buffalo is acknowledged for assistance with microED data interpretation. The writing and discussions of the work were equal in contribution between Joshua P. Hazelnis and Stephen Maldonado. The Michigan Center for Materials Characterization is acknowledged for the use of microscopy instrumentation and staff assistance.

5.2 Introduction

Liquid metals are useful platforms for developing and expanding materials chemistry.[1, 2] Gallium (Ga) is a popular choice for a wide-range of low temperature processes and reactions because of its low melting point and mild toxicity. For example, liquid Ga has been a shape-changing and stimuli-responsive material[3, 4] as well as a potent reaction solvent for synthesizing 1D semiconductor nanowires,[5, 6] 2D metal oxide sheets,[7, 8] and 3D bulk inorganic crystals and films.[9, 10] In these contexts, the rapidly growing number of Ga-based discoveries/advances in materials chemistry has been reviewed recently.[1, 2, 11]

Notwithstanding innovations in high temperature metal flux chemistry,[12-14] studies that identify new/expanded reactivity of liquid Ga at low (room) temperature are scant. A primary factor for the dearth of reaction studies is the rapidity of oxide growth on clean liquid Ga when exposed to lab ambient.[15] Even when immersed in most liquid environments, Ga is often shrouded by a complex and non-uniform oxide layer(s).[16] The net result is an impression that liquid Ga is

relatively inert. However, the rapid amalgamation with metals like aluminum is a reminder that Ga can be a quite potent reactant. The challenge is to access that reactivity.

This study builds upon prior synthetic work that use liquid Ga as an electrode immersed in a liquid (aqueous) electrolyte to unlock latent and unique metallurgical reactivity. Specifically, single-crystalline growth at liquid Ga interfaces with preferential orientation dictated by the near surface, in-plane atomic ordering is a new and underexplored idea.[9] Although the concept of 'quasi'-epitaxy has been introduced, it is not clear if it is only applicable for a specific set of materials (e.g. Pb, Bi)[9] or if it can be leveraged more generally for synthesis.

Generally, the reactions between Ga and iron (Fe) are well known and studied.[17] Fe-Ga compounds have garnered intense interest over the past two decades because of magnetostrictive behavior of some alloys (e.g. Galfenol).[18-20] The metallurgy of Fe and Ga has been scrutinized heavily, with several refinements proposed in the phase diagram.[21] Although much recent work has illustrated the possibility of suppressing the growth of thermodynamically favored crystalline phases,[22] no new phases or compounds have been discovered.

In this work, we demonstrate that Ga shows unusual and unexpected reactivity towards Fe in alkaline solutions under reaction conditions sufficient to maintain an oxide-free surface and a low flux that facilitate 'quasi'-epitaxial material growth. This report describes the unexpected discovery of new Fe-Ga materials formed specifically at this liquid gallium/liquid water interface. Additionally, the consequence of adding another similar first row transition metal, cobalt (Co), is also explored.[23] The atomic structure of the as-prepared materials represent forms of matter not previously identified or predicted within the relevant binary[17] or ternary phase diagrams.[24] The details of the rapid synthesis of Fe-Ga and Fe-Co-Ga structures and their implications on the recently introduced 'quasi'-epitaxial growth mechanism discussed below.

5.3 Experimental

5.3.1 Chemical and Materials

Gallium (99.99%, Thermo Fisher Scientific), Cobalt(II) perchlorate hexahydrate (99.999%, Thermo Fisher Scientific), Iron (II) perchlorate hydrate (98%, Sigma Aldrich), and Sodium Hydroxide (99.99%, Sigma Aldrich) were used as received. Water purified through a Barnstead Nanopure filtration system to a resistivity of 18 MΩ•cm was used throughout.

5.3.2 Electrolyte Characterization

Inductively coupled plasma mass spectrometry (ICP-MS) analysis of the electrolyte purity was performed using a Perkin-Elmer Nexion 2000 ICP-MS in kinetic energy discrimination mode using Helium to avoid overlapping signal from ArO^+ with the most abundant iron isotope (Fe^{56}). (Figure 5.1) A droplet of liquid Ga was immersed in a Teflon container containing 60 mL of 1.25 M NaOH heated to T =70°C for $t \approx 100$ h. Aliquots (1 mL) were collected in regular time intervals and stored in polypropylene centrifuge tubes prior to analysis. Calibration solutions of 1, 5, 10, 25, 50, and 70 μg L^{-1} were prepared via serial dilutions.

5.3.3 Electron Microscopy Sample Preparation

Samples for cross-sectional and plan-view analysis were prepared via focused ion beam (FIB) milling lift out and thinning (Figure 5.2). A Thermo Fisher Helios G4 PFIB UXe station with an inductively coupled Xe Gas plasma-ion beam source was used to avoid Ga contamination during FIB cutting. A Multichem gas injector and Schottky Field Emitter electron beam source were also used. Lift-out was performed on sacrificial Si wafer substrates. Hexagonal particles were first transferred onto these Si supports by gently rubbing a liquid Ga droplet coated with hexagonal particles across the wafer surface. A protective carbon layer of 50-100 nm thickness was then deposited onto the hexagonal particles via electron-beam-assisted chemical vapor deposition with a 2 kV accelerating voltage and 13 nA beam current. For plan-view sample preparation, samples were subsequently lifted out using a standard tungsten probe tip (Ted Pella) at a 45° angle after trenches of the dimensions 20 μm x 20 μm x 20 μm (length x width x depth) were FIB milled into the Si substrate with a 30 kV accelerating voltage and 60 nA beam current. After lift-out, the samples were affixed to a Mo FIB lift-out grid on a 45° pre-tilted stub holder (TED Pella) and further thinned with the ion beam. For cross-sectional cuts, a thick (3-4 μm) Pt:C (80:20 mixture) capping layer was deposited by ion-beam-assisted chemical vapor deposition prior to lift-out. This cap was necessary to protect the sample during subsequent ion beam thinning. Lift-out was performed at 0° for these samples.

5.3.4 Electron Microscopy

A JEOL JSM-7800FLV field-emission scanning electron microscope (SEM) with Schottky-type electron source was used for imaging, electron dispersive spectroscopy (EDS), and electron backscattering diffraction (EBSD) analysis of sets of hexagonal particles. All SEM imaging was performed in secondary electron mode with a 20 keV accelerating voltage.

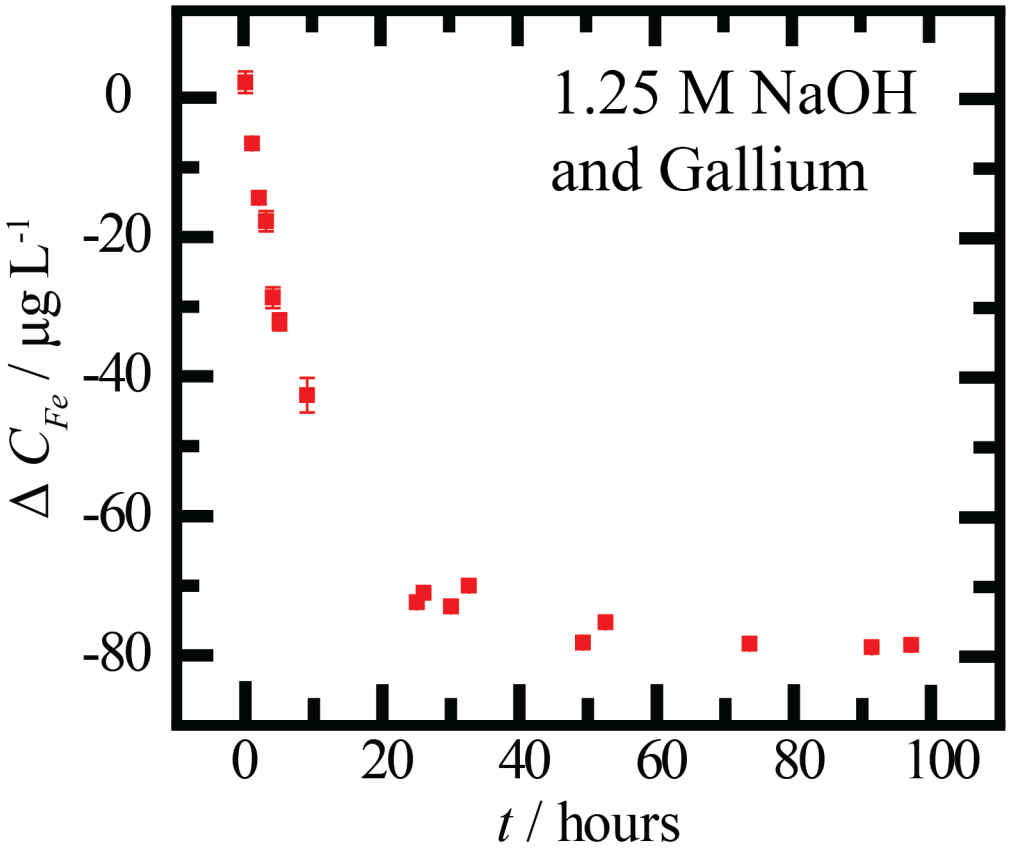

Figure 5.1 ICP-MS concentration profile showing the measured change in Fe concentration (ΔC_{Fe}) with time (t) over ≈100 hours for a 1.25 M NaOH (aq) solution in contact with liquid Ga.

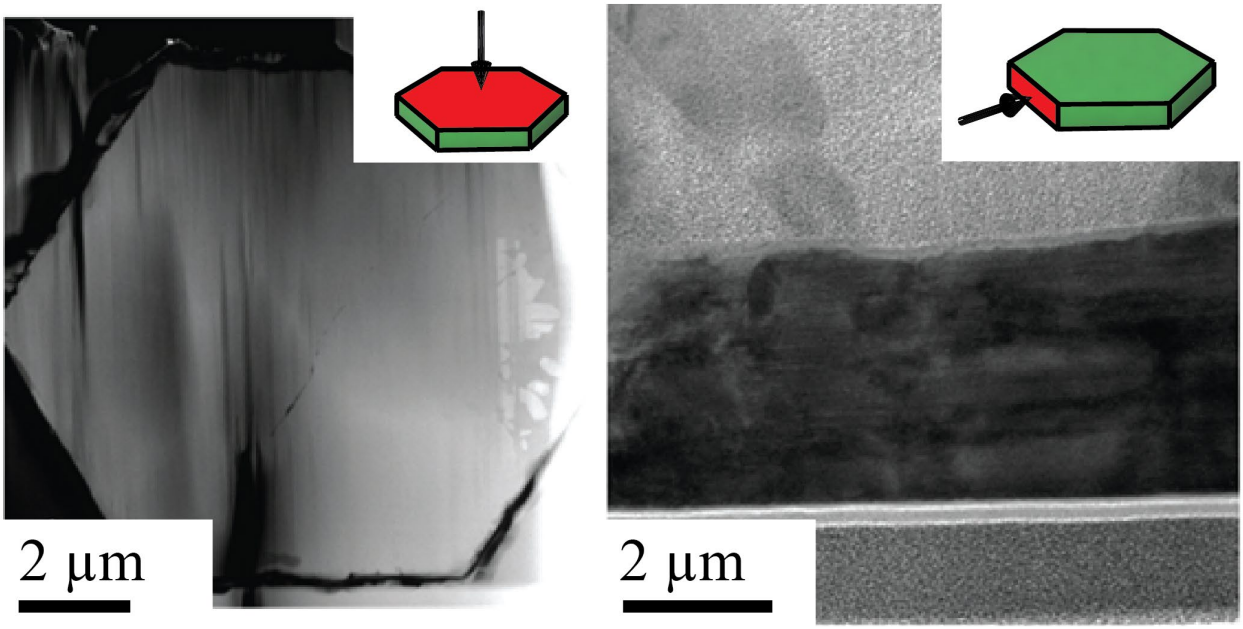

Figure 5.2 Example FIB samples prepared for (S)TEM characterization. The inset graphic denotes the viewing angle for each corresponding crystal image.

For individual particle analysis, transmission electron microscopy (TEM) was employed. A Thermo Fisher Talos F200X G2 S/TEM X-FEG instrument with a high-brightness Schottky type field emission gun and Gatan One View bottom mount camera or high-speed 4k × 4k in-situ imaging was used. A 100 nm diameter selected area aperture was inserted during the collection of all electron diffraction patterns. Scanning transmission electron microscopy (STEM) was performed exclusively in the Spectra 300 Probe-Corrected S/TEM instrument. Prior to taking HAADF images, samples were aligned to a major zone axis by using a double tilt holder and analyzing the Kikuchi bands of the sample. All high-resolution HAADF images and corresponding EDS were collected using a 300 keV beam. EDS imaging was performed and analyzed using VELOX software. Simulations of HAADF images from the predicted crystal structures were performed using the open source abTEM code.[25]

Microcrystal electron diffraction (microED) measurements were performed with Fischione Tomography Model 2020 holder. MicroED measurements were obtained for ± 70° tilt angles with a 2.51 pm electron wavelength (200 keV) and a camera length of 835.62 mm, as determined via pixel calibration (0.00715701 nm^{-1} per pixel) and magnification. A total of 343 frames were collected with an exposure time of 6.25 frames s^{-1} during active tilting. MicroED measurements were also performed in a Thermo Fisher Spectra 300 Probe-Corrected S/TEM at 300 keV with a Ceta-S bottom mount CMOS camera capable of 4k x 4k resolution at 40 frames s^{-1}. With this setup, a total of 1839 frames from -70° to +70° were collected at approximately 0.05° per frame without beam precession.

5.3.5 MicroED Data Workup

For micro-ED analysis, the raw output frame data of each dataset was obtained in a .dm4 format and was loaded into a custom written python script using the py4DSTEM python package. Each frame was treated as a 2x2 pixel array and was normalized to a pixel intensity scale of -100 to 220. A region of interest was integrated around the center electron beam diffraction spot and fitted with a Gaussian distribution in the x and y dimensions to identify and align the center pixel of each frame. A subsequent radial integration was than performed for each frame around that center pixel to give a profile of d-spacing for the electron diffraction spots in inverse space. To simulate the corresponding powder x-ray diffraction patterns for the hexagonal particles, the *d*-spacing values were converted to 2θ values using Bragg's law and the wavelength of a Cu K_α x-ray source (1.54 Å). Example code used is provided in the Appendix D, Section C.2. Individual

microED frames were processed and treated as a single crystal dataset using the PETS2 electron diffraction software.[26]

5.4 Results

5.4.1 Synthesis of Transition Metal-Ga Hexagonal Particles

Reactions between liquid Ga electrodes (3.61 ± 0.01 g; 0.59 ± 0.01 cm^3) and dissolved transition metal cations were performed in 1.25 M NaOH(*aq*) solution at open circuit (E = -1.47 V vs. E(Hg/HgO)). Slightly elevated temperatures (T = 40 to 80°C) were required to ensure Ga remained molten throughout. At the end of the timed reaction, the surface of the Ga electrode was covered with hexagonal particles.

Since commercially available alkali hydroxides have residual Fe at the sub-ppm or higher levels,[27] initial experiments were focused on the reactivity of latent Fe^{3+} with liquid Ga. ICP-MS analysis was performed to determine the rate dissolved Fe^{2+} cations reacted with Ga. The change in Fe^{2+} concentration (ΔFe^{2+}) was monitored as a function of time for a 1.25 M NaOH solution in contact with a Ga droplet over the course of approximately 100 hours (Figure 5.1). In the first 9 hours, a linear decrease in Fe^{2+} was observed (R^2 = 0.93). After 50 h, the total loss of Fe^{2+} achieved a plateau value of -78 ± 2 μg L^{-1}. This amount was not the total Fe^{2+} content since adding more Ga to solution would further increase the total Fe^{3+} loss, indicating that the interfacial reaction with Ga was not limited by the total Fe^{2+} content.

After 50 h, the surface of the liquid Ga electrodes still looked optically clean, i.e. a dull coating suggestive of an oxide was not observed. To better assess the microscopic structure of the interface, the Ga electrodes were flash frozen using liquid N_2, then rinsed with Nanopure water, dried with a dry N_2(g) stream, and finally analyzed SEM. Figure 5.3 illustrates a representative example of a Ga interface after such a reaction, where the surface was decorated with flat, hexagonal platelet particles. The average side lengths and thicknesses of these particles were 5.0 ± 0.5 μm and 0.2-0.4 μm, respectively. Preliminary EDS measurements indicated these particles contained Fe but were not pure metallic Fe.

Additional reactions were subsequently performed in solutions with added dissolved Fe $(ClO_4)_2$ at concentrations of 1 mg L^{-1}, 10 mg L^{-1}, and 28 mg L^{-1}. With 1 or 10 mg L^{-1} of Fe(II) was dissolved in solution, the same hexagonal plates were obtained (Figure 5.6) with the same lengths and thicknesses. The key difference was a noticeably higher total surface density coverage than

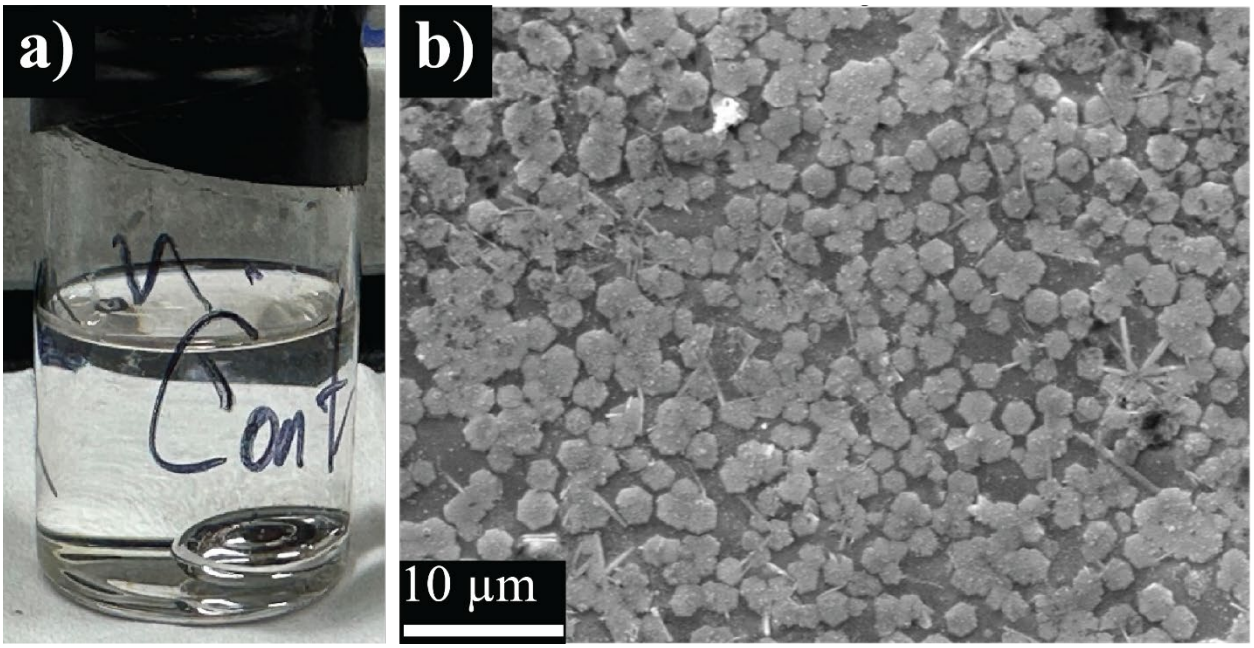

Figure 5.3 a) Picture of the glass vial where liquid Ga is reacted in alkaline aqueous solution of 1.25 M NaOH with Fe(II) and Co(II) of varying observations. b) SEM of the principle observation of the reaction which is the formation of hexagonal particles at the liquid metal interface. The reaction shown is the liquid metal surface after reacting with 10 mg L^{-1} Fe(II) salt dissolved in solution for t = 48 hours.

previously. With an added concentration of 28 mg L^{-1}, the predominant structure of the particles accumulated at the Ga surface were not hexagonal but cuboid instead. These cubes were suggestive of crystalline Fe^0 particles,[28] as estimated by SEM-EDS. (Figure 5.4)

Reactions were also performed in the presence of other added metal salts. For example, Figure 5.6 also shows representative images of Ga surfaces after reaction with 1.25 M NaOH aqueous solutions containing dissolved $Co(ClO_4)_2$ at concentrations of 1 and 10 mg L^{-1}. With 1 mg L^{-1} of Co^{2+} in solution hexagonal platelets were observed but with smaller side lengths = 2.5 μm. When imaged by SEM, most of these particles appears partially submerged into the Ga although still visible at the surface, i.e. they appeared less buoyant. This observation changed when the solution also contained 10 mg L^{-1} of added Fe^{2+}. The particles appeared to be large hexagons that nucleated a smaller hexagon on its basal plane. When the concentration of added Co^{2+} was 10 mg L^{-1}, there were mostly dendritic particles composed of mostly/entirely of Co^0, as estimated by SEM-EDS (Figure 5.5). Even when platelets were observed, they were covered with Co nuclei and filament protrusions.

The precise composition of any particle imaged while still on a Ga surface was difficult to ascertain by EDS analysis. For the particles synthesized in solutions containing only dissolve Fe^{2+}, initial EDS analysis of the particles isolated on carbon tape, confirmed the presence of only Fe and Ga. (Figure 5.7) Notably, there was no detectable levels of oxygen or any other heteroatom consistent with constituents of the reaction solutions. However, for more precise measurement of elemental composition, assorted hexagonal platelets were removed from the Ga surfaces and studied by STEM-EDS. Following the lift-off and FIB milling procedure outlined above and shown in Figure 5.2, high-angle annular dark field (HAADF) STEM/EDS imaging was performed on cross-sectional cut hexagonal particles. Figure 5.8 shows cross-sections of hexagonal platelets from syntheses with just aqueous Fe^{2+} solutions and aqueous solutions containing Fe^{2+} and Co^{2+}. Elemental mapping showed uniformity in the maps for Fe and Ga for particles made with just aqueous Fe^{2+} solutions. Integration of the signal across the sample area yielded a composition of $Fe_{0.14\pm0.01}Ga_{0.86\pm0.01}$. Importantly, the highest Ga composition in a known Fe-Ga compound is 75 at. % (i.e. $FeGa_3$).[17] The stoichiometry of Fe:Ga in these platelets was definitively not 1:3. Similar homogeneity in the Fe, Co, and Ga signals were observed for the particles synthesized with aqueous solutions containing Fe^{2+} and Co^{2+}. Integration from the mapping yielded a nominal composition of $Fe_{0.08\pm0.01}Co_{0.06\pm0.01}Ga_{0.86\pm0.01}$.

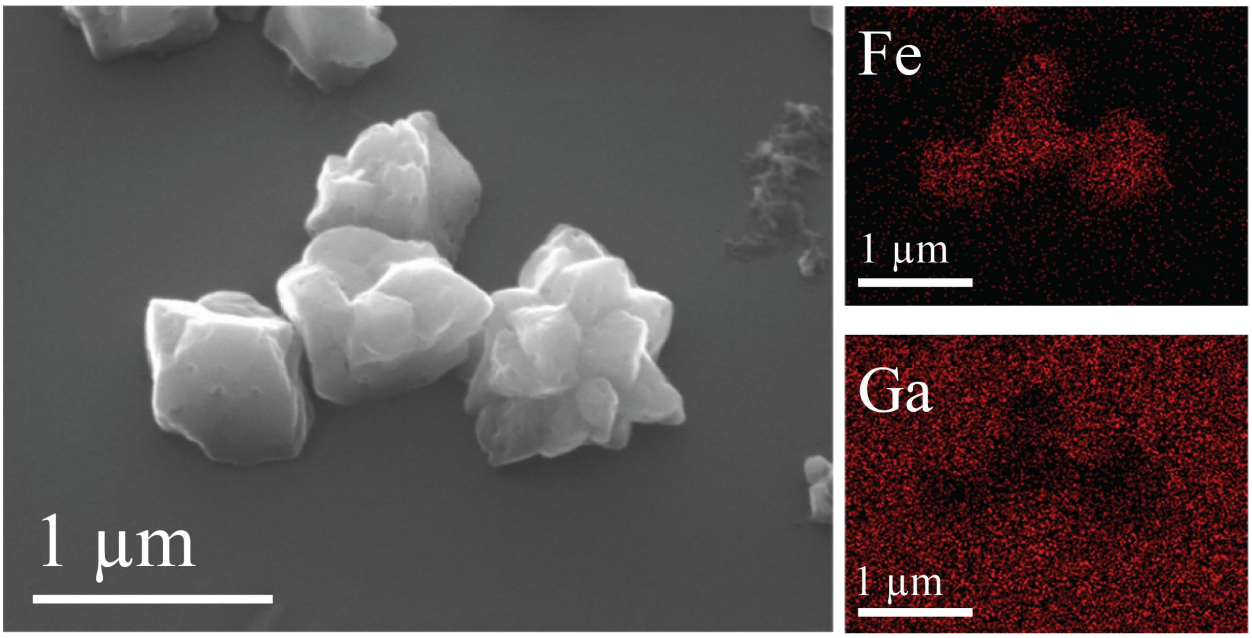

Figure 5.4 SEM of the Ga interface following a reaction with a 0.5 mM Fe(II) $(ClO_4)_2$ ● xH_2O solution showing cubic particles that formed

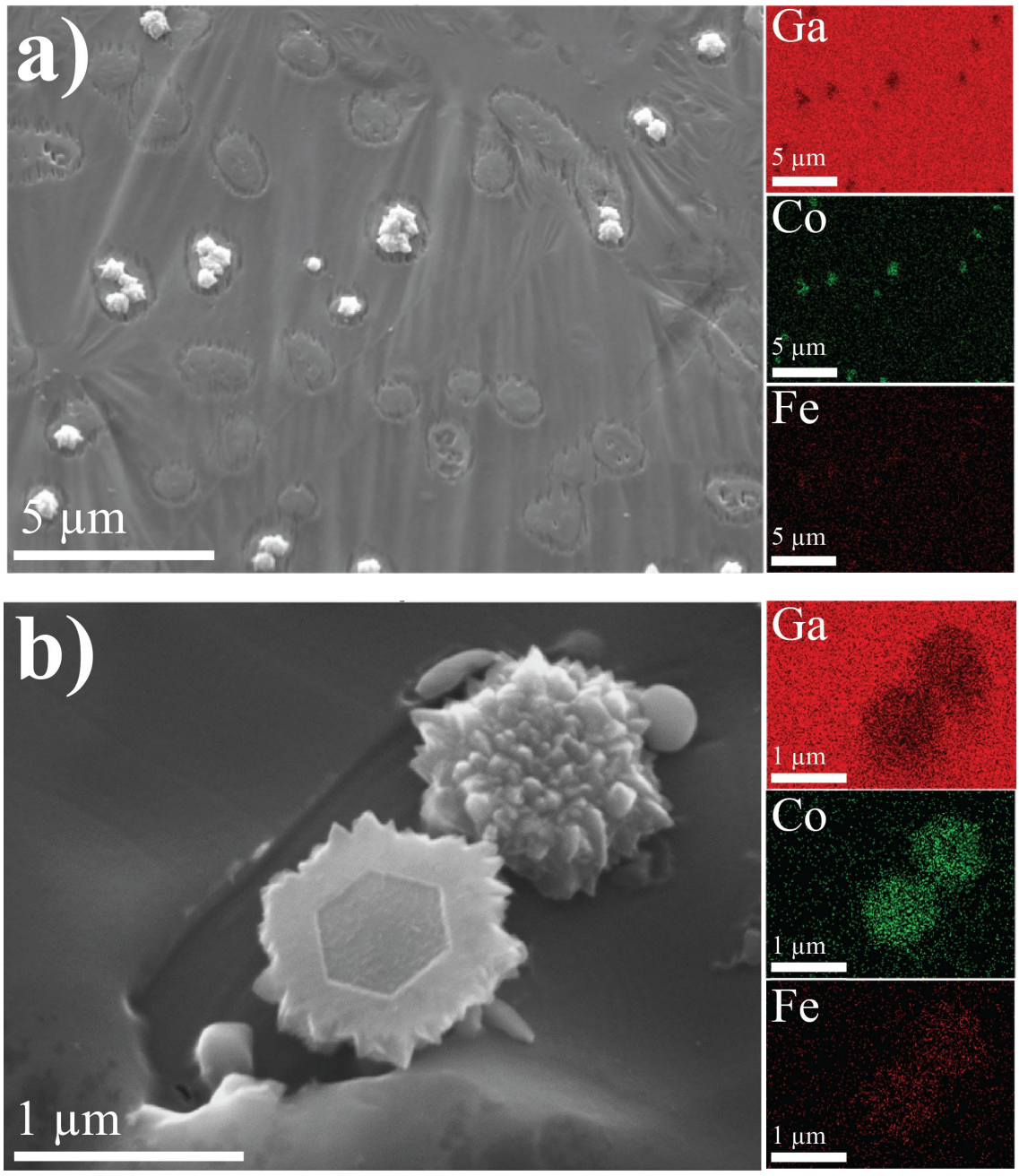

Figure 5.5 Representative SEM and EDS of the Ga interface following the reaction with 10,000 µg L^{-1} Co(II) and a) 1,078 µg L^{-1} Fe(II) or b) 10,078 µg L^{-1} Fe(II) dissolved in 1.25 M NaOH (*aq*) solution

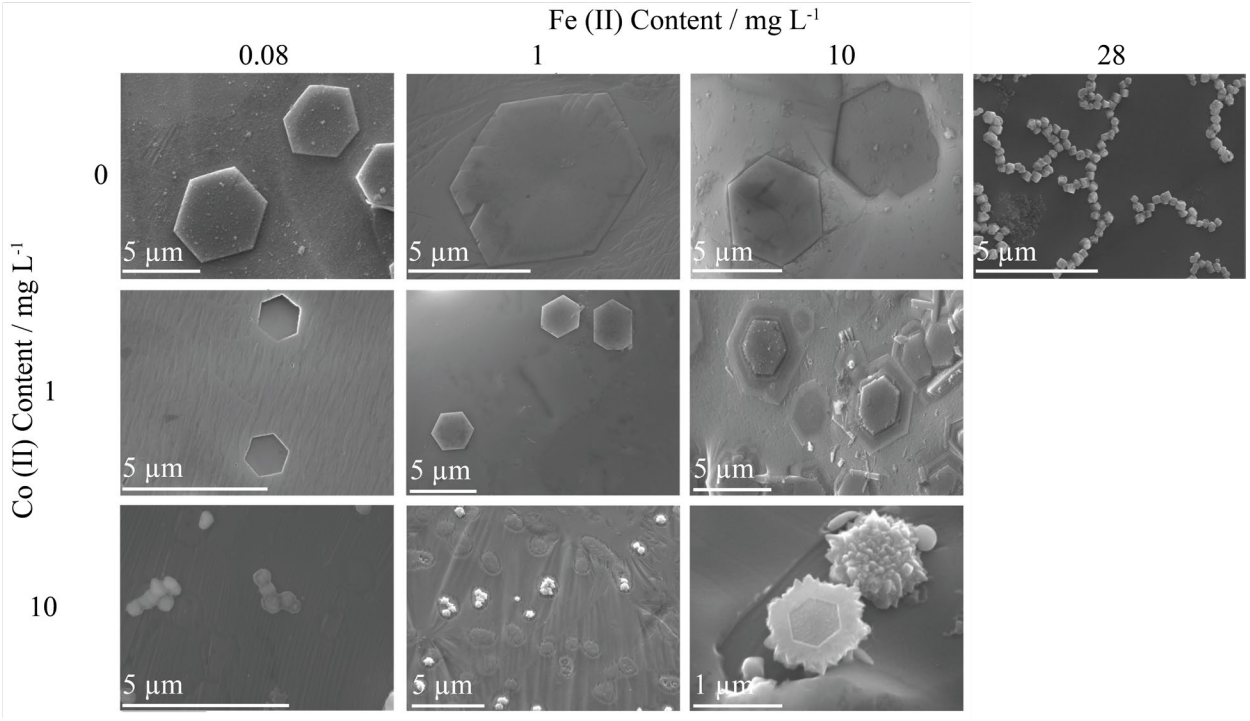

Figure 5.6 SEM analysis of synthesized $Fe_{0.85}Ga_{0.15}$ and $Fe_{0.08\pm0.01}Co_{0.06\pm0.01}Ga_{0.86\pm0.01}$ Particles using varied amounts of Fe(II) and Co(II) concentration in 1.25 M NaOH solution.

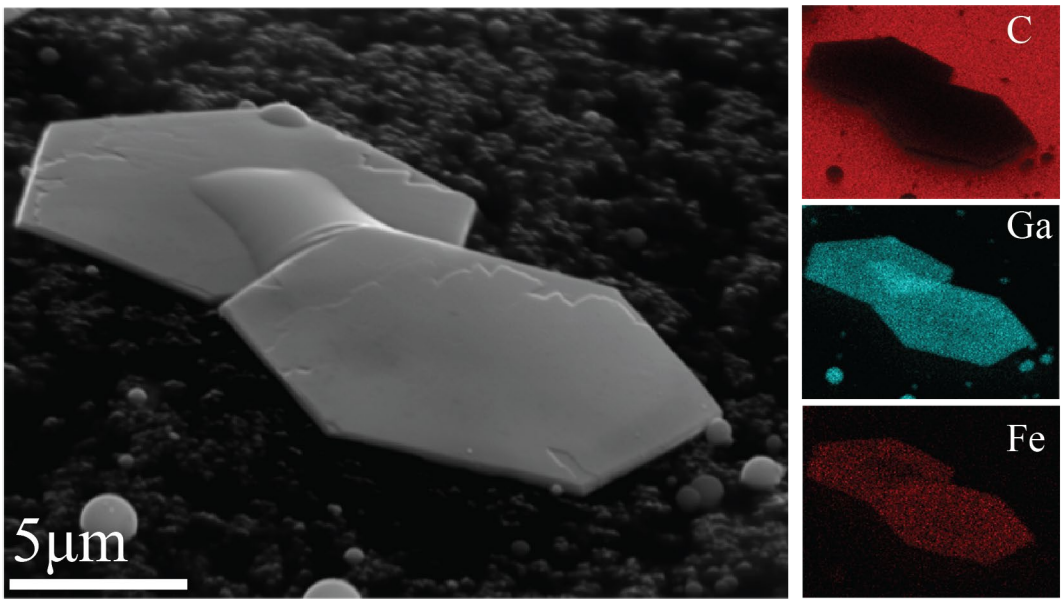

Figure 5.7 Representative SEM and EDS of the $Fe_{0.14\pm0.01}Ga_{0.86\pm0.01}$ hexagons lifted off the liquid Ga interface

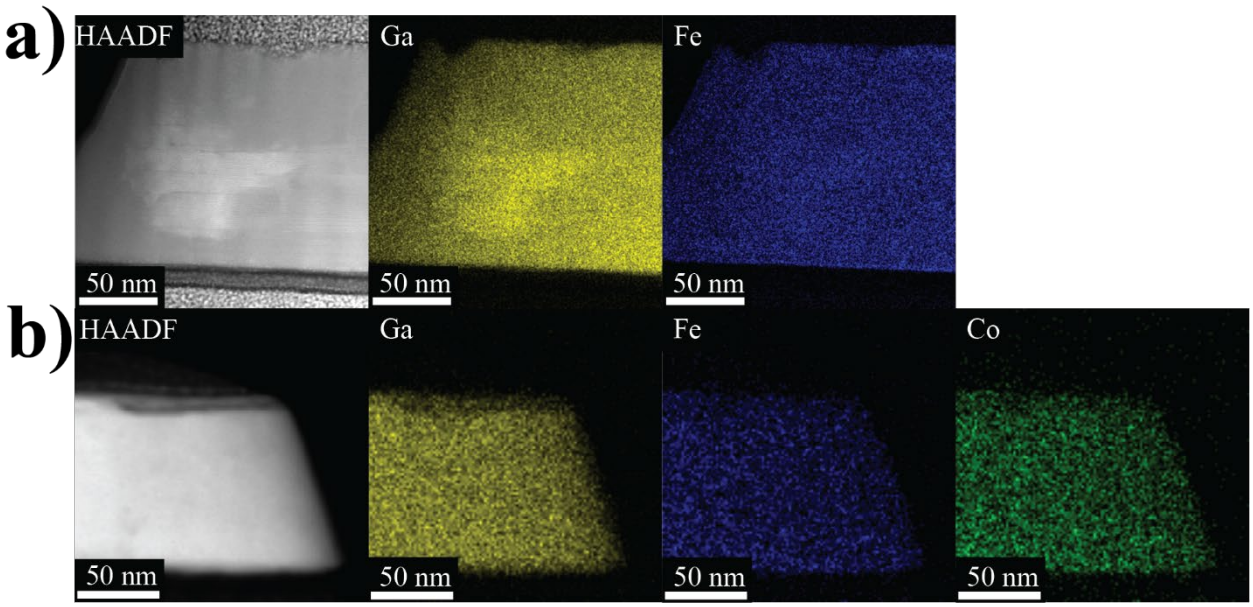

Figure 5.8 Collected EDX data for the a) $Fe_{15}Ga_{85}$ and b) $Fe_{0.08\pm0.01}Co_{0.06\pm0.01}Ga_{0.86\pm0.01}$ hexagonal particles

Figure 5.9 shows multiple high magnification HAADF STEM cross-sections of $Fe_{0.14\pm0.01}Ga_{0.86\pm0.01}$ and $Fe_{0.08}Co_{0.06}Ga_{0.86}$ hexagonal particles. In these images, the lighter contrast corresponds to heavier elements while darker contrast corresponds to lighter elements. The inset of each panel in Figure 5.9 describes the viewing direction and the plane at which the sample was cross-sectioned. In the plan-view direction, looking down the face of a thinned $Fe_{0.14\pm0.01}Ga_{0.86\pm0.01}$ hexagon, the atomic resolution was poor but a clear 6-fold symmetry was observed. Notably, the limited resolution was not an artifact of imaging conditions but instead was a property of these types of particles. Separately, the middle and right panels of Figure 5.9 show cross-sectional views different by 30°. In either of these views, a much more complex, layered arrangement of atoms was evident.

Comparing the data for $Fe_{0.14\pm0.01}Ga_{0.86\pm0.01}$ and $Fe_{0.08\pm0.01}Co_{0.06\pm0.01}Ga_{0.86\pm0.01}$ hexagonal particles in Figure 5.9, the plan-view images yielded much sharper images, indicating a more defined structure. Nevertheless, many similarities between $Fe_{0.14\pm0.01}Ga_{0.86\pm0.01}$ and $Fe_{0.08\pm0.01}Co_{0.06\pm0.01}Ga_{0.86\pm0.01}$ were clear. First, both hexagonal $Fe_{0.14\pm0.01}Ga_{0.86\pm0.01}$ and $Fe_{0.08\pm0.01}Co_{0.06\pm0.01}Ga_{0.86\pm0.01}$ particles had 6-fold symmetry. Second, the measured hexagonal side lengths in the top-left and bottom-left panels of Figure 5.9 was 4.8 Å, marked by the orange hexagon overlay. Third, the honeycomb array (denoted by the green hexagon overlay) of atomic columns were rotated 30° with respect to the outer hexagons and had smaller side lengths of 2.7 Å. Integrated differential phase contract (iDPC) images[29] were also collected specifically for the $Fe_{0.08\pm0.01}Co_{0.06\pm0.01}Ga_{0.86\pm0.01}$ particles along the plan-view direction (Figure 5.10) to specifically rule out the possible inclusion of lighter elements (i.e C and H) which are not detected by STEM-EDS analysis. No 'light' elements were detected.

The cross-sectional HAADF images of $Fe_{0.08\pm0.01}Co_{0.06\pm0.01}Ga_{0.86\pm0.01}$ were nearly identical to the analogous images of $Fe_{0.14\pm0.01}Ga_{0.86\pm0.01}$. The perpendicular cross-sectional directions were definitively layered with the same symmetry. Additionally, the layering appeared to be ordered along both directions, with the smallest repeating unit (7-layer stack) possessing a length of 11.8 Å and an average atomic layer spacing of 1.97 Å. Over a large imaging area, in either cross-sectional direction, numerous stacking faults were apparent in the images of $Fe_{0.14\pm0.01}Ga_{0.86\pm0.01}$ (**Figure 5.11**). Similar stacking faults were not observed in $Fe_{0.08\pm0.01}Co_{0.06\pm0.01}Ga_{0.86\pm0.01}$.

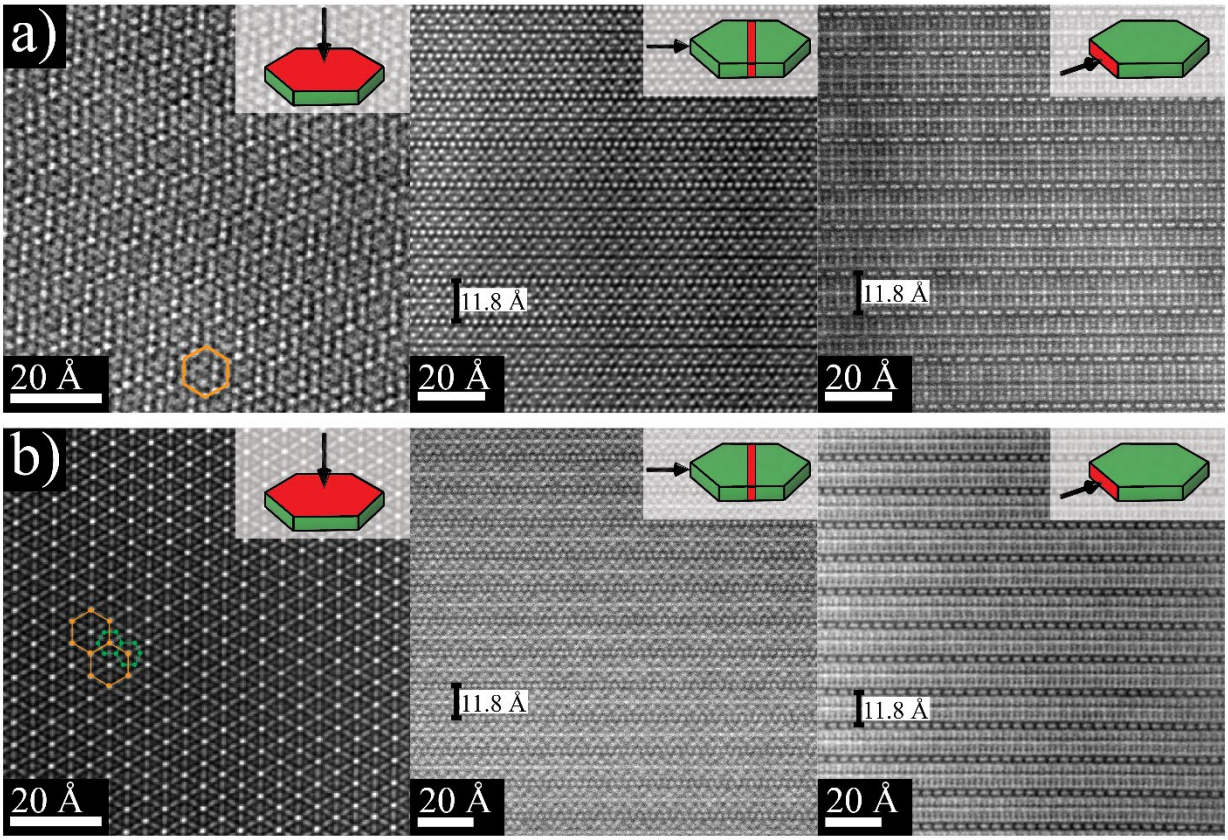

Figure 5.9 HAADF images of the plan-view [left], cross-section along the hexagon corner [middle] and side [right] for the a) $Fe_{0.85}Ga_{0.15}$ and b) $Fe_{0.08\pm0.01}Co_{0.06\pm0.01}Ga_{0.86\pm0.01}$ particles. Orange and green hexagons are used to denote the repeating honeycomb features observed imaging the plan-view direction, particularly for the $Fe_{0.08\pm0.01}Co_{0.06\pm0.01}Ga_{0.86\pm0.01}$ structure. A repeating 7-layer stack was observed for both $Fe_{0.08\pm0.01}Co_{0.06\pm0.01}Ga_{0.86\pm0.01}$ and $Fe_{0.14\pm0.01}Ga_{0.86\pm0.01}$ both cross-sectional directions with a measured height of 11.8 Å.

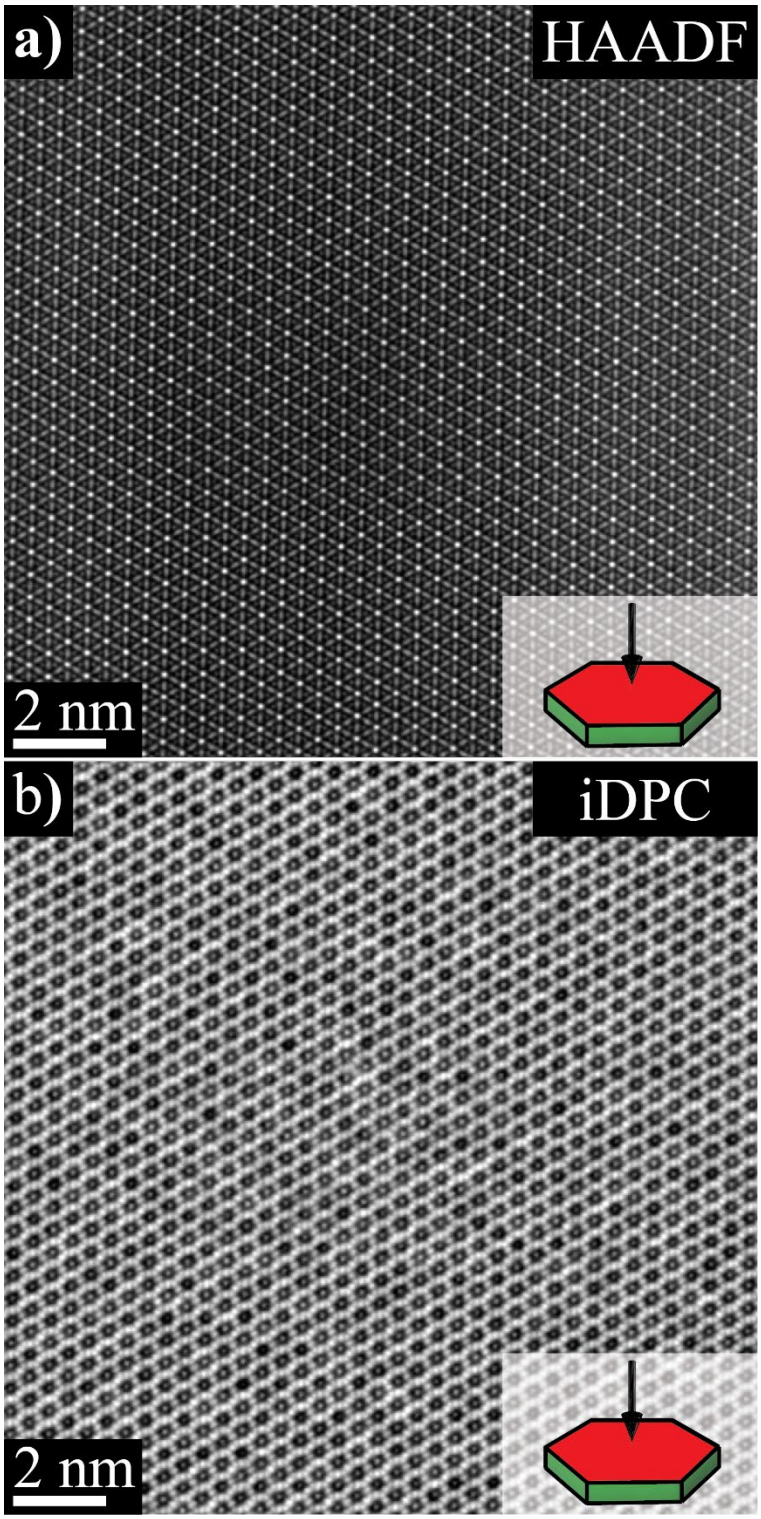

Figure 5.10 a) High angular dark-field (HAADF) and corresponding b) integrated differential phase contrast (iDPC) image of the $Fe_{0.08\pm0.01}Co_{0.06\pm0.01}Ga_{0.86\pm0.01}$ plan-view

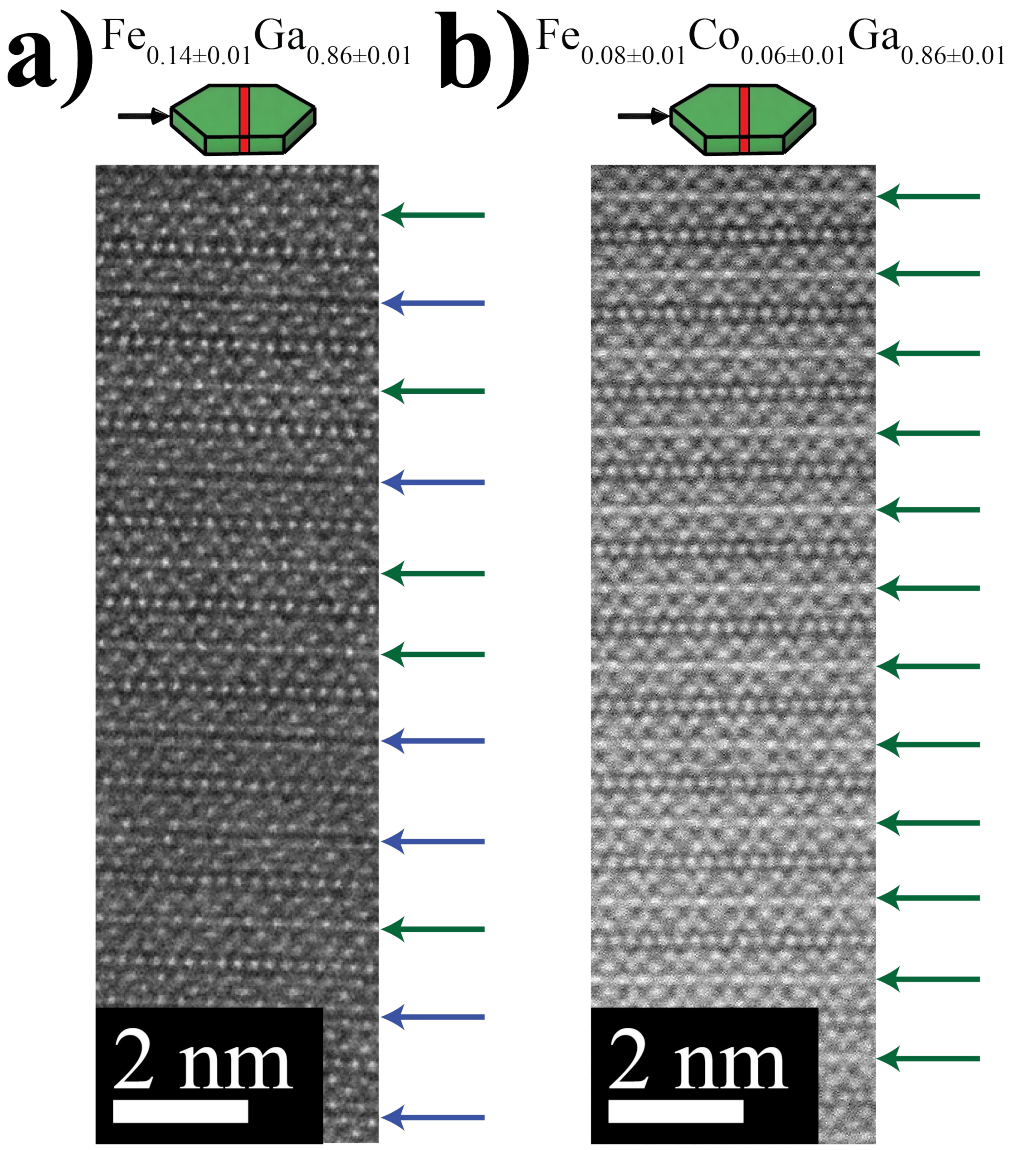

Figure 5.11 Comparison of the cross-sectional HAADF imaging looking down an axis intersecting the corner of the hexagonal a) $Fe_{0.14\pm0.01}Ga_{0.86\pm0.01}$ and $Fe_{0.08\pm0.01}Co_{0.06\pm0.01}Ga_{0.86\pm0.01}$ particles. Green arrows represent the repeating 7-layer stack, and blue arrows represent the non-periodic stacking faults observed in the $Fe_{0.14\pm0.01}Ga_{0.86\pm0.01}$ structure.

A set of selected area electron diffraction (SAED) patterns were collected for $Fe_{0.14\pm0.01}Ga_{0.86\pm0.01}$ and $Fe_{0.08\pm0.01}Co_{0.06\pm0.01}Ga_{0.86\pm0.01}$ hexagonal platelets (Figure 5.12, insets show orientation of crystal relative to incident beam). Both plan-view electron diffraction patterns for $Fe_{0.14\pm0.01}Ga_{0.86\pm0.01}$ and $Fe_{0.08\pm0.01}Co_{0.06\pm0.01}Ga_{0.86\pm0.01}$ showed discrete diffraction spots rather than only concentric rings, highlighting the single-crystalline nature of each hexagon platelet and indicating the HAADF observations of the local structure extend throughout. Additionally, the symmetries of the patterns were consistent with a high degree of 6-fold symmetry. The more and less intense spots within the pattern are denoted with yellow and red circles in Figure 5.12a,b for clarity, respectively. Each can be separately indexed with the innermost set of diffraction spots having a d-spacing of about 4.11 Å and the next more intense reflections having a *d*-spacing of 7.11 Å. The halo or ring in the electron diffraction pattern of $Fe_{0.08\pm0.01}Co_{0.06\pm0.01}Ga_{0.86\pm0.01}$ is due to some of the amorphous Pt and C capping material within the electron diffraction area and not representative of the sample.

The innermost spot of the electron diffraction pattern can be used as a reference point to estimate the lattice parameters along a perpendicular direction. Denoting the plan-view direction as the 'c-axis' then the *d*-spacing reflects lattice parameters *a* and *b*. With the prevalence of 6-fold symmetry, the pattern could be indicative of the cubic [111], hexagonal [0001], or trigonal [0001] crystallographic directions. Due to the distinct lack of 4-fold symmetry in the HAADF images, the cubic [111] assignment is unlikely. Therefore, the net conclusion of the plan-view diffraction data is that this structure is either trigonal or hexagonal with lattice parameters $a = b = 4.11$ Å or $a = b = 8.22$ Å, respectively.

The appearance of 'extra' less intense, satellite peaks (Figure 5.12, red circles) within the diffraction pattern can arise because of several different crystallographic properties.[30-33] One interpretation is that the 'satellite' spots arise from stacking or twinning defects within the structure.[33] While stacking defects are clearly identified in the HAADF images of $Fe_{0.14\pm0.01}Ga_{0.86\pm0.01}$ viewed along the c- axis, such defects were *not* observed in the HAADF images of $Fe_{0.08\pm0.01}Co_{0.06\pm0.01}Ga_{0.86\pm0.01}$. Because the primary electron diffraction patterns are otherwise identical, stacking faults are unlikely to be the source of these extra spots because they are similarly apparent in the diffraction of $Fe_{0.08\pm0.01}Co_{0.06\pm0.01}Ga_{0.86\pm0.01}$. A second possibility is the presence of a higher-symmetry superstructure.[34] Specifically, a higher symmetry which can arise when atomic occupancies or charge occupancies exhibit periodic ordering, leading to additional features in the

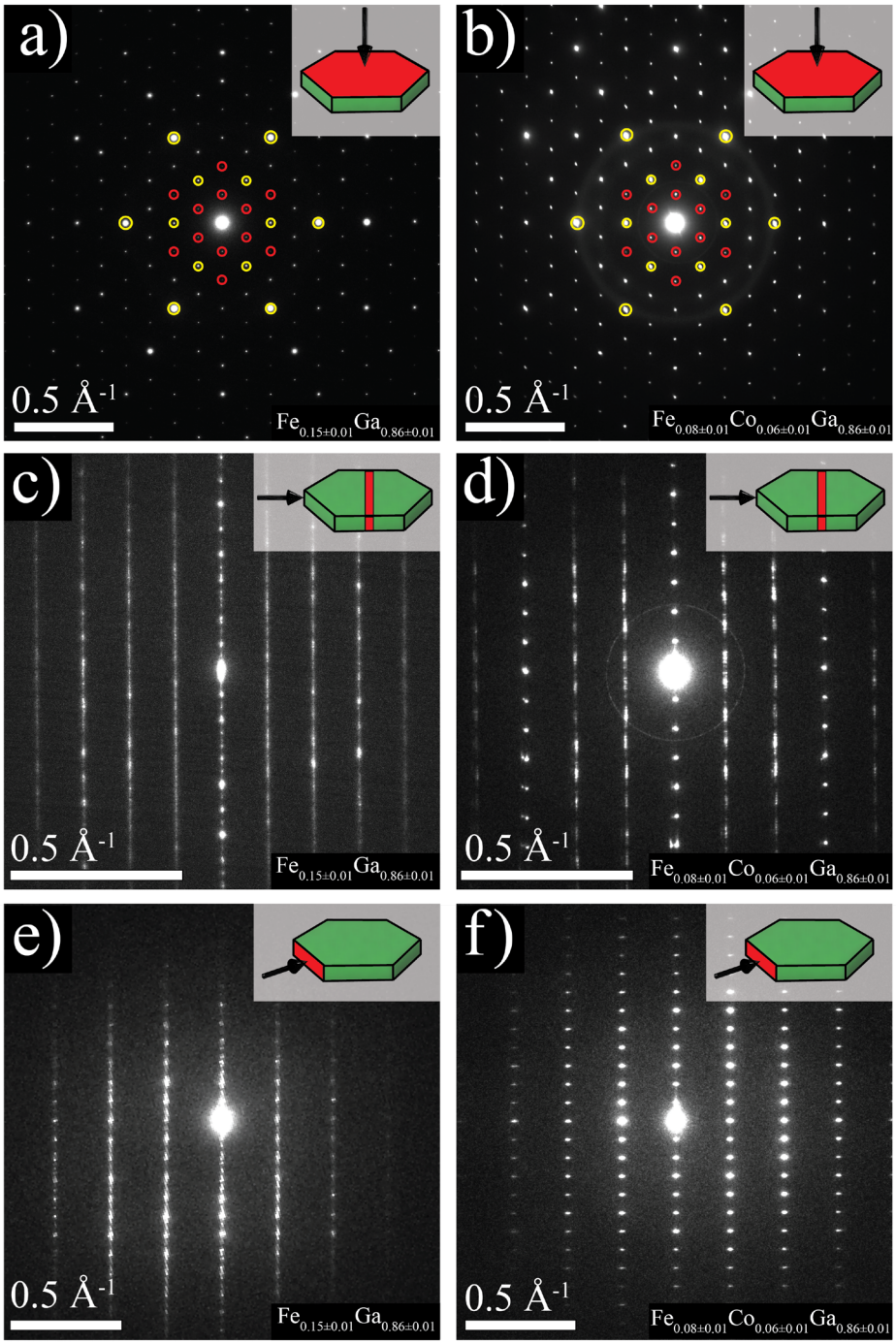

Figure 5.12 Selected area electron diffraction (SAED) of the a) $Fe_{0.85}Ga_{0.15}$ and b) $Fe_{0.08\pm0.01}Co_{0.06\pm0.01}Ga_{0.86\pm0.01}$ particle plan-view with the less intense (red) and more intense (yellow) spots circled for clarity, c) $Fe_{0.85}Ga_{0.15}$ and d) $Fe_{0.08\pm0.01}Co_{0.06\pm0.01}Ga_{0.86\pm0.01}$ cross-section along the hexagon corner, and e) $Fe_{0.85}Ga_{0.15}$ and f) $Fe_{0.08}Co_{0.06}Ga_{0.86}$ cross-section along the hexagon side

diffraction pattern. The occupancy of the sites for Fe and/or Co sites cannot be ascertained from diffraction data along this axis alone. A final possibility is that the lattice structure has some parrllels to hexagonal $BaTiO_3$, which has a hexagonal close-packed structure rather than some higher-symmetry defect.[35]

Electron diffraction patterns were also collected along the cross-sectional directions perpendicular to the face of the hexagon. Figure 5.12c,d show the resultant electron diffraction patterns looking down an intersecting axis of the hexagon corner for $Fe_{0.14\pm0.01}Ga_{0.86\pm0.01}$ and $Fe_{0.08\pm0.01}Co_{0.06\pm0.01}Ga_{0.86\pm0.01}$, respectively. The pattern collected for $Fe_{0.14\pm0.01}Ga_{0.86\pm0.01}$ in Figure 5.12c shows significantly more vertical streaking than the corresponding pattern for $Fe_{0.08\pm0.01}Co_{0.06\pm0.01}Ga_{0.86\pm0.01}$. This point is consistent with a higher presence of atomic stacking faults in $Fe_{0.14\pm0.01}Ga_{0.86\pm0.01}$ along the *c*-axis. The lattice parameter *c* can thus be estimated based on the measured *d*-spacing of the clear (i.e. non-streaked) spots. The data indicate a value of 11.8 Å, in good agreement with the measured thickness of the 7-layer repeating stack observed in the cross-sectional HAADF images. The remaining 'streaking' in other areas of the pattern along with splitting of the individual diffraction spots suggest structural defects along an off-axis direction, including potentially 'twisting'[36] of the individual atomic layers. The other cross-sectional directional perpendicular to the hexagonal particle edge showed similar aspects. (Figure 5.12e,f) The streaking was consistent in the $Fe_{0.14\pm0.01}Ga_{0.86\pm0.01}$ pattern along the *c*-axis, affected by the same stacking fault. Correspondingly, the pattern from $Fe_{0.08\pm0.01}Co_{0.06\pm0.01}Ga_{0.86\pm0.01}$ had no 'streaking.' The absence of streaking in one of the two cross-sectional directions suggests that any structural defect present only disrupts symmetry in one direction. Nonetheless, the cross-sectional SAED data was consistent with structure having the lattice parameter c = 11.8 Å.

The complexity of the selected area electron diffraction data was sufficient that a clear assignment of the crystal structure was not possible. To probe structural information further, microED was performed. Individual hexagonal platelets were analyzed by tilting the sample along the plan-view direction from a -70 to 70° angle while subsequently recording the electron diffraction as discrete frames (Figure 5.13a).[37] The advantage of having multiple incident angles is that solutions of the single crystal lattice structure are possible. Representative sets of electron diffraction frames for $Fe_{0.14\pm0.01}Ga_{0.86\pm0.01}$ and $Fe_{0.08\pm0.01}Co_{0.06\pm0.01}Ga_{0.86\pm0.01}$ are shown in Figure 5.13b and Figure 5.13c. Each frame was individually analyzed using the open-source PETS2 software package.[26] Although the alignment with the face of the particle was the same in both

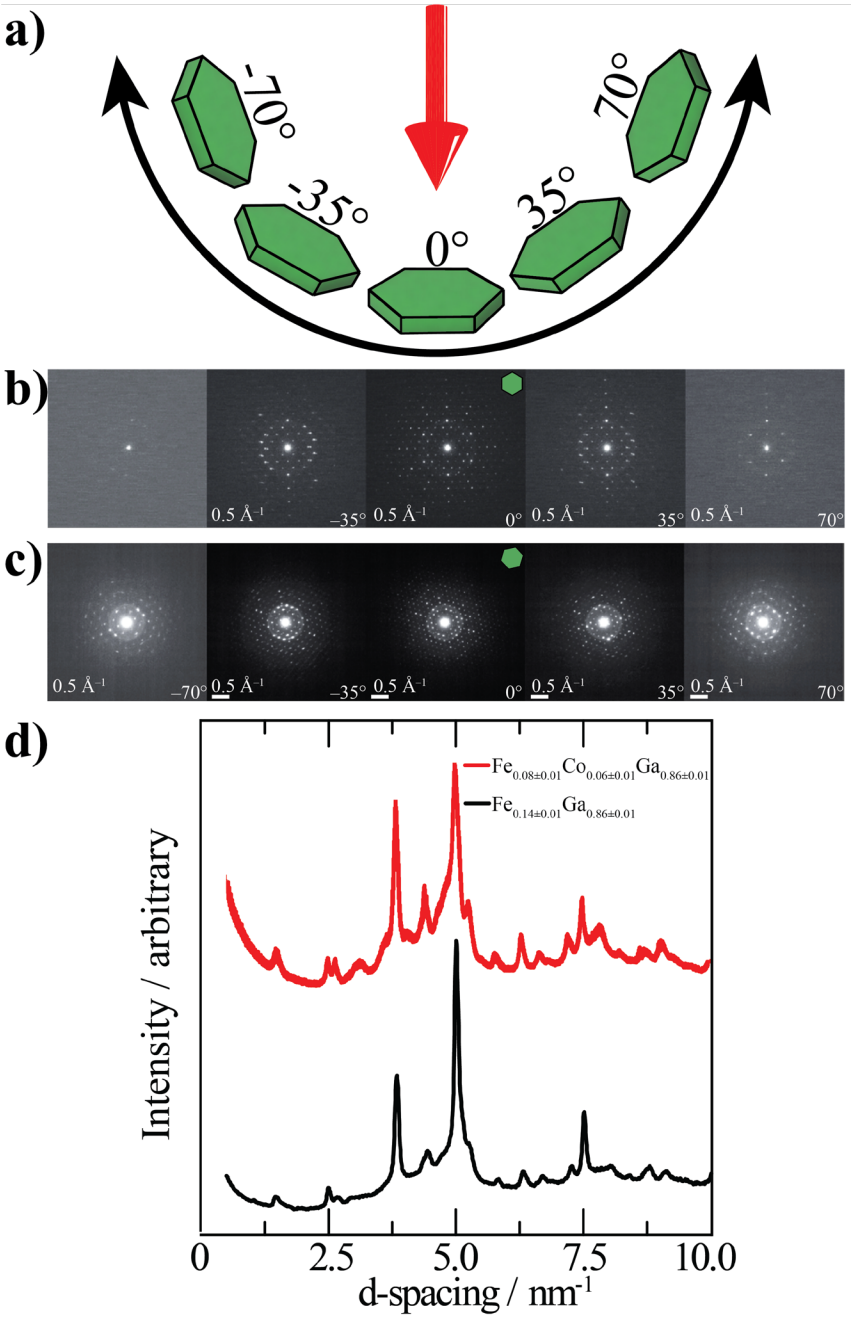

Figure 5.13 a) Schematic depiction of the microED experimental analysis of the hexagonal particles. Example microED frame data from -70° to 70° tilt angles for the b) $Fe_{0.14\pm0.01}Ga_{0.86\pm0.01}$ and c) $Fe_{0.08\pm0.01}Co_{0.06\pm0.01}Ga_{0.86\pm0.01}$ particles with frame nearest 0° having rotation orientation indicated with a green hexagon. Contrast and brightness have been adjusted to improve clarity. d) Plotted radial integrations of the -70° to 70° tilt angles for the $Fe_{0.14\pm0.01}Ga_{0.86\pm0.01}$ and $Fe_{0.08\pm0.01}Co_{0.06\pm0.01}Ga_{0.86\pm0.01}$ particles.

cases, the rotation of the particle differed as indicated by the green hexagon in the top right of each 0° frame. The rotation effected a difference in the incident axis at large angles. In both cases, streaking and splitting of the individual diffraction spots was consistently observed particularly at higher tilt angles. Contrast and brightness of the individual frames have been adjusted to improve clarity. For both $Fe_{0.08\pm0.01}Co_{0.06\pm0.01}Ga_{0.86\pm0.01}$ and $Fe_{0.14\pm0.01}Ga_{0.86\pm0.01}$, *a* and *b* parameters were readily extracted and were ~8 Å in both cases when a hexagonal (not trigonal) unit cell indexing is assumed. The crystallographic c-axis was estimated to be ~ 36 Å from the best refinement of the peaks along this direction. Although larger than what was estimated from the selected area diffraction data of $Fe_{0.08\pm0.01}Co_{0.06\pm0.01}Ga_{0.86\pm0.01}$, it is almost exactly 3 times larger than the measured distance of 11.8 Å. Accordingly, the larger value alludes to the possibility of higher order symmetry along the *c*-axis. The streaking observed in the extracted reflections hampered experimental space group determination due to overlap in the refined peak signal.

The cumulative microED data stacks still proved useful for determining an analogous *powder* diffraction pattern. Conventional powder X-ray diffraction of the hexagonal platelets was difficult as the amount of material collected would also be mixed with a large excess of bulk Ga which was difficult to separate. However, radial integration of all frames resulted in effective powder diffraction patterns for the two types of hexagonal platelets (Figure 5.13d). Each pattern showed the same sets of peaks with only slight variation in intensity. This similarity further corroborated the premise that the underlying lattice structure of the two types of hexagonal platelets was the same. When comparing these integrated patterns with the database of known powder diffraction patterns of pure Ga polymorphs and Ga-containing intermetallics, from the Inorganic Crystal Structure Database (ICSD)[38], no match was found (Figure 5.14). The net assessment from the microED analysis was that the data were consistent with this being a novel hexagonal structure with $a = b \approx 8$ Å and $c = 11.8$ Å or some multiple of 11.8 Å, depending on whether higher order symmetry was present along the c-axis. This point could not be explicitly resolved due to the excess 'streaking' in the individual electron diffraction data.

To ascertain the atomic positions of Fe, Co, and Ga within the new structure, atomic resolution HAADF STEM was performed on $Fe_{0.08\pm0.01}Co_{0.06\pm0.01}Ga_{0.86\pm0.01}$ in conjunction with correlated EDS mapping. Figure 5.15 shows imaging results along the same three viewing directions. These data show that the Fe and Co atoms share the same lattice sites. The cross-sectional EDS showed that there are only 2 layers which contain Fe and Ga sites, with the other 5

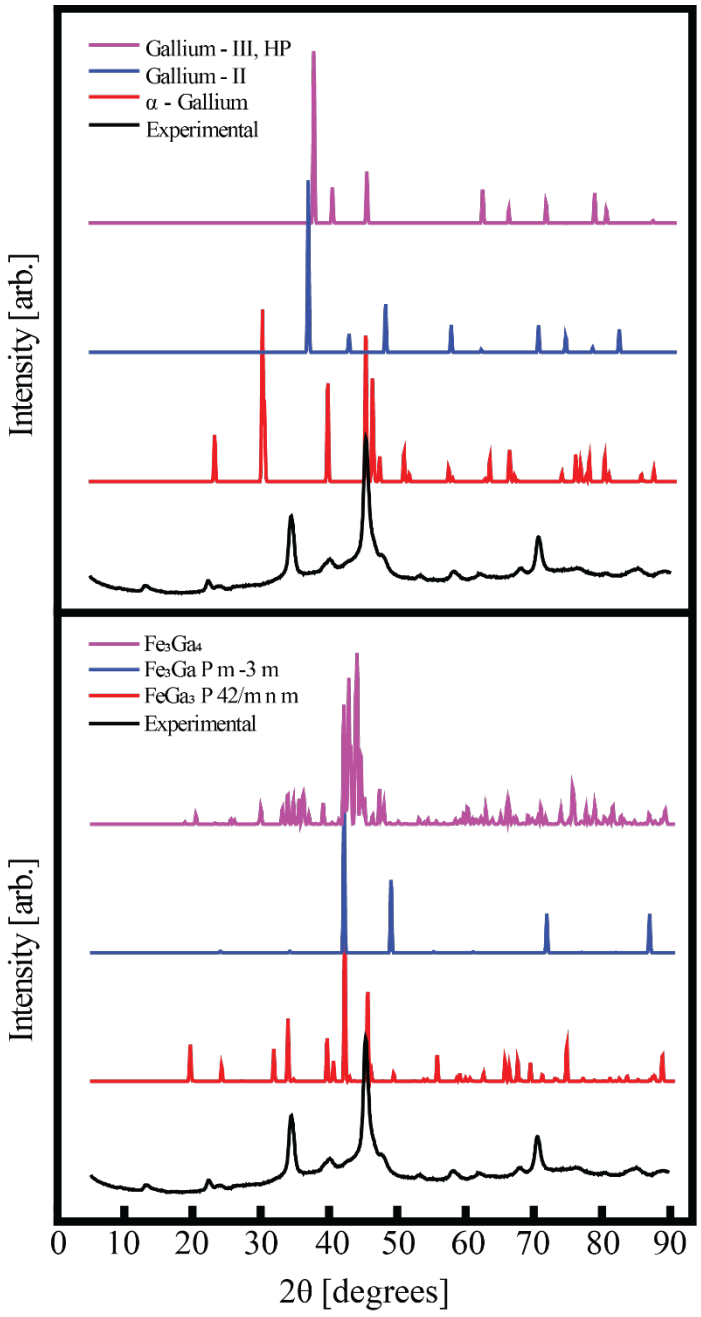

Figure 5.14 Radially integrated $Fe_{0.14\pm0.01}Ga_{0.86\pm0.01}$ experimental microED data plotted as a function of with 2θ using $Cu_{K\alpha}$ (1.54 Å) and the custom Python code presented in Section S4 compared to the powder X-ray diffraction profiles of common pure Ga and Fe-Ga phases.

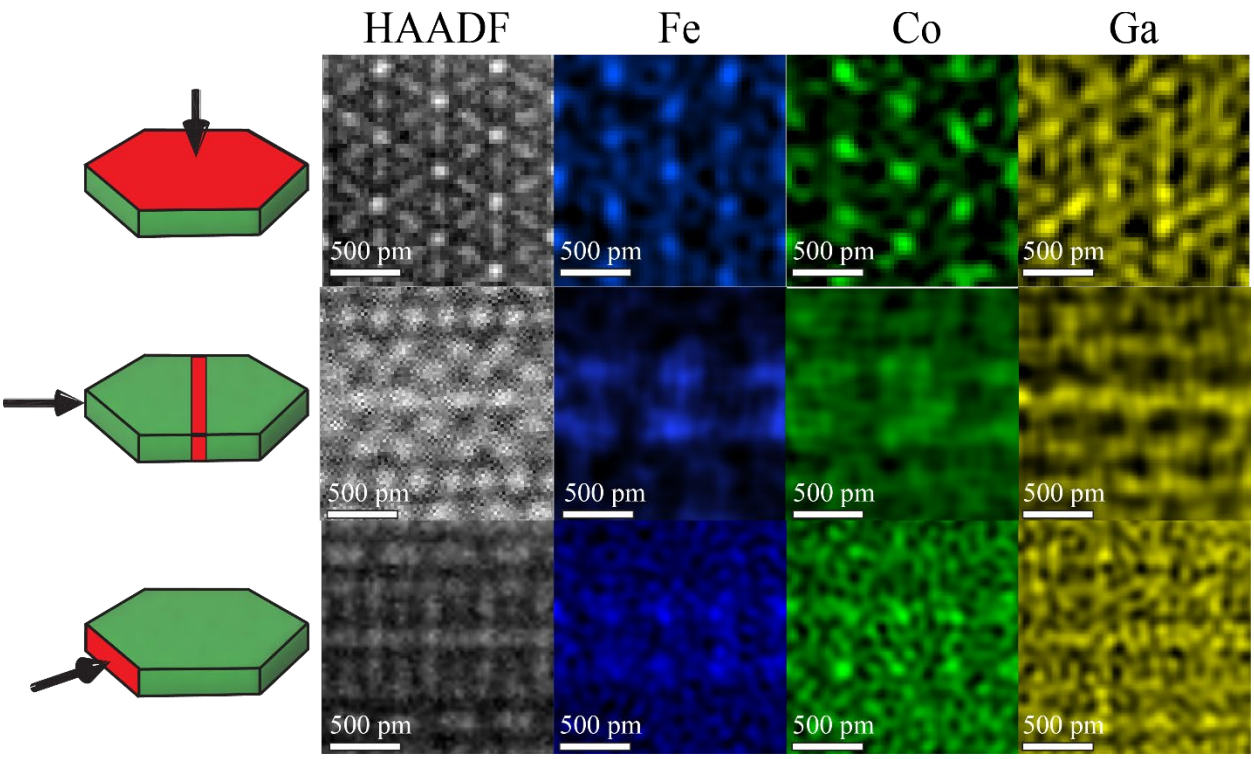

Figure 5.15 Spatially correlated, atomic resolution HAADF STEM images and EDS maps of a hexagonal $Fe_{0.08\pm0.01}Co_{0.06\pm0.01}Ga_{0.86\pm0.01}$ platelet.

layers of the repeating unit made up of entirely Ga. Additionally Fe and Co atoms overlap with the brightest spots in the HAADF plan-view, which define the corners of the largest hexagonal feature shown in Figure 5.9. EDS data was also collected on the $Fe_{0.14\pm0.01}Ga_{0.86\pm0.01}$ in the cross-sectional directions, showing that the position of the Fe sites was similar to the position identified for the $Fe_{0.08\pm0.01}Co_{0.06\pm0.01}Ga_{0.86\pm0.01}$ structure. (Figure 5.16)

5.5 Discussion

The presented data supports three key points. First, a new type of transition metal-Ga intermetallic compound has been synthesized. This new class of intermetallic compounds features a noticeably large atomic packing density and sub-units consistent with gallenene.[39] Second, this structure is unlike any previously reported but is in line with the concept of 'quasi'-epitaxy at liquid metal interfaces. Third, interfacial liquid metal structure that favors 'quasi'-epitaxy can produce new materials wholly unpredicted from the bulk metallurgy of the constituent elements. These points are further discussed below.

5.5.1 Lattice Structure

The bulk phase diagram of Fe-Ga suggests that the binary intermetallic with the highest Ga content is tetragonal $FeGa_3$.[17] That is, in mixtures of Fe and Ga, there are no other known *crystalline* materials that have a higher content of Ga. However, $FeGa_3$ was definitively not the assignment for the hexagonal platelets observed in the reactions reported here. The high Ga content and distinct the atomic arrangement wholly incompatible with a tetragonal unit cell[40, 41] were clear on this point.

The cumulative materials characterization reported here were consistent with the points that these new Ga intermetallics are layered, that they have a high degree (6-fold) of symmetry, and they have a hexagonal unit cell with $a = b = 8.22$ Å and $c = 11.8$ Å. However, the complete assignment of the lattice structure of these new Ga intermetallics has proven difficult because of the ambiguity introduced by crystallographic defects. Nevertheless, these unit cell parameters suggest some clear points about the atomic columnar distances in each of the 3 directions and atomic positions of the Fe/Co sites.

In $Fe_{0.14\pm0.01}Ga_{0.86\pm0.01}$, Fe sites were displaced from one repeating unit to the next due to the presence of a stacking fault along the c-axis. (Figure 5.11) Undoubtedly, this contributed to the vertical streaking in the corresponding selected area electron diffraction patterns and the poor

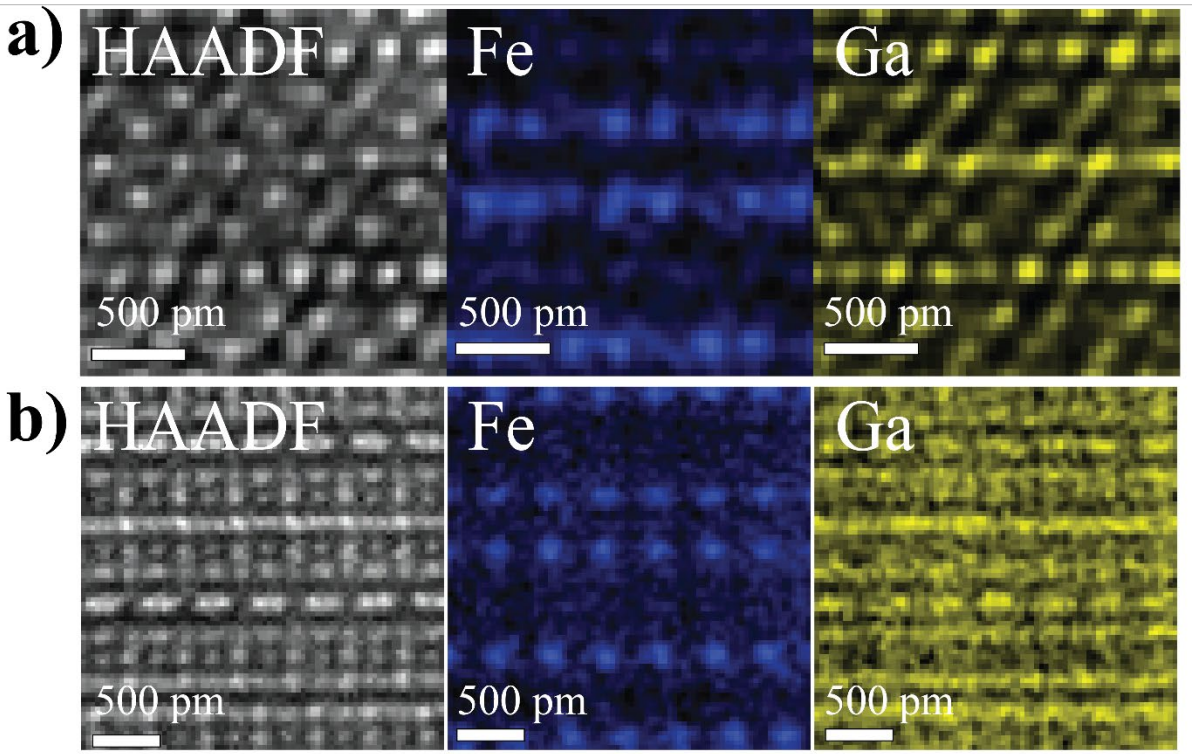

Figure 5.16 Atomic resolution (S)TEM-EDX of $Fe_{0.14\pm0.01}Ga_{0.86\pm0.01}$ along the hexagonal particle a) corner and b) side

resolution of plan-view STEM data. However, those values of *a*, *b*, and *c* in a hexagonal framework correspond to a 66 atom unit cell. A unit cell based on the atomic positions apparent in the HAADF/STEM data was constructed with a P6/mmm space group (Figure 5.17a). While other hexagonal space groups were potentially plausible, P6/mmm was best matched to the observed symmetry and structural features. Using the lattice site locations of Fe/Co and Ga from the HAADF/STEM data, the corresponding lattice structure would have a ratio of 12:44 for the Fe/Co and Ga sites, yielding a composition of $(FeCo)_{0.18}Ga_{0.82}$. This stoichiometry is within 3 atomic % of the measured composition.

The structure shown in Figure 5.17a was used to generate simulated HAADF images using abTEM in Figure 5.17b.[25] The simulated structures yielded a significant amount of agreement to the data in Figure 5.15. First, the hexagonal arrangement of atoms was accurately accounted for in the plan-view direction. Second, the relative intensities of each atomic column were preserved. Third, most atomic layers within the cross-sectional directions were accurately matched with the experimental data. This was particularly evident when looking down the axis intersecting the corner of the hexagon. However, some discrepancies prevent total confirmation of the unit cell assignment. Uncertainty was introduced by the possible twisting between layers. Such structural features could be defects or could be a part of the true unit cell. The most densely packed (0.077 atoms $Å^{-1}$), central layer is one example of the simulated intensities not being a direct match to the experimental HAADF image. Part of the discrepancy may be due to the poor resolution of this layer compared to all other layers in HAADF imaging, due to a seemingly higher packing of atoms. It could also be the case that if a twist in the structure was present, changing the columnar alignment of atom within this layer, resolution would be hindered. Accordingly, the validity of the exact structure drawn in Figure 5.17a may not be absolute, but it captures the essential features of the 'true' lattice structure.

5.5.2 Quasi-Epitaxy

The proposed unit cell for $Fe_{0.14\pm0.01}Ga_{0.86\pm0.01}$ and $Fe_{0.08\pm0.01}Co_{0.06\pm0.01}Ga_{0.86\pm0.01}$ contains layers of noticeably high in-plane atomic packing. Specifically, in the layers indicated in Figure 5.18, the atomic packing densities are 0.051, 0.051, 0.051, and 0.077 atoms $Å^{-2}$. (Figure 5.18, Table 5.1) These in-plane packing densities are higher than in any known Fe-Ga intermetallic. For example, the family of crystallographic planes in $FeGa_3$ with the highest total packing density is the (111) with 0.214 atoms $Å^{-2}$. The packing densities decrease in order across the following (001),

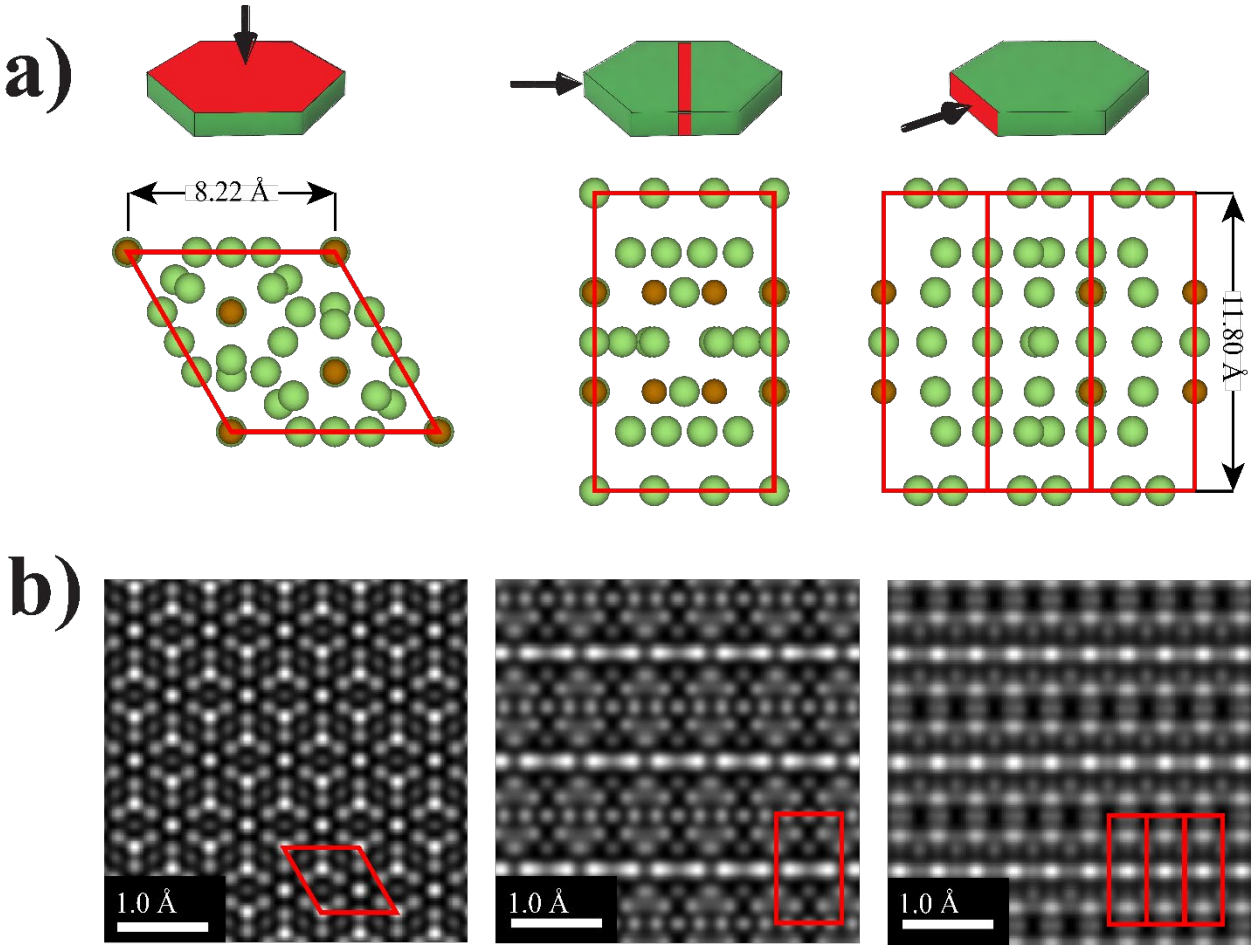

Figure 5.17 a) Estimated hexagonal unit cell structure with $a = b = 8.22$ Å and $c = 11.8$ Å of $Fe_{0.14\pm0.01}Ga_{0.86\pm0.01}$ and $Fe_{0.08\pm0.01}Co_{0.06\pm0.01}Ga_{0.86\pm0}$. Green spheres denote Ga atoms and brown spheres denote Fe or Co atomic sites. b) Simulated HAADF images for the structure shown in part a with the respective unit cell outlined in red.

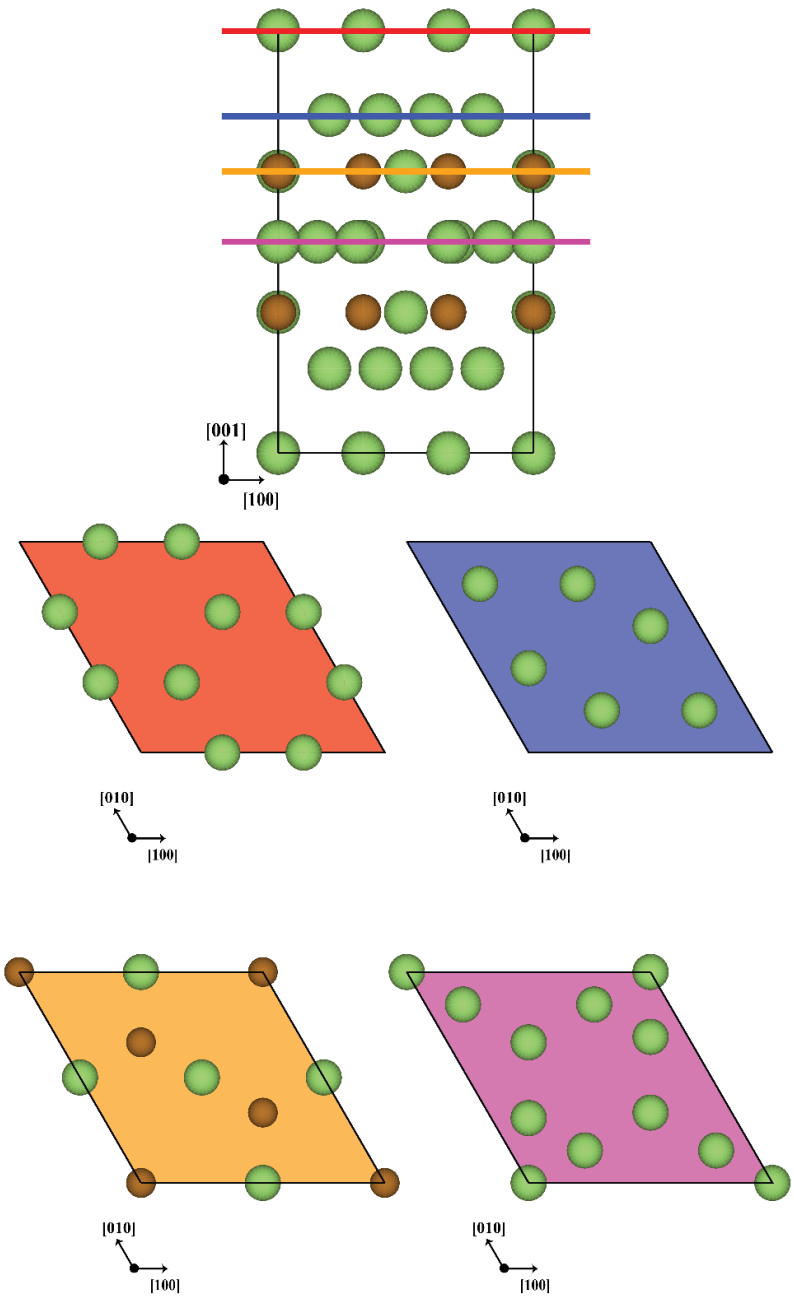

Figure 5.18 The estimated structure of hexagonal $Fe_{0.14\pm0.01}Ga_{0.86\pm0.01}$ and $Fe_{0.08\pm0.01}Co_{0.06\pm0.01}Ga_{0.86\pm0.01}$ projected along the [010] crystallographic cross section with sliced projections within the {001} family of planes shown. These slices are colored red (layer 1), blue (layer 2), yellow (layer 3), and pink (layer 4) are considered when calculating the total (Table 5.1) and Ga packing densities (Table 5.4). Green atoms are Ga and brown are Fe or Fe/Co in $Fe_{0.08\pm0.01}Co_{0.06\pm0.01}Ga_{0.86\pm0.01}$.

Table 5.1 Calculated total packing densities in the estimated $Fe_{0.14\pm0.01}Ga_{0.86\pm0.01}$ and $Fe_{0.08\pm0.01}Co_{0.06\pm0.01}Ga_{0.86\pm0.01}$ structures

$Fe_{0.14\pm0.01}Ga_{0.86\pm0.01}$ & $Fe_{0.08\pm0.01}Co_{0.06\pm0.01}Ga_{0.86\pm0.01}$ (a = b = 8.22 Å and c = 11.8 Å)					
Lattice Plane	**Atomic Layer**	**Total Number of Atoms**	**Area ($Å^2$)**	**Packing Density (atoms $Å^{-2}$)**	**Total Packing Density (atoms $Å^{-2}$)**
001	1 (red)	3	58.52	0.051	0.231
	2 (blue)	3		0.051	
	3 (orange)	3		0.051	
	4 (purple)	4.5		0.077	

(110), and (100) planes (Figure 5.19, Table 5.2). This point is relevant in the context of understanding crystal growth in the context of 'quasi'-epitaxy.

As developed previously,[9] preferential crystal growth can occur at the surface of a liquid metal even without formal crystallinity. The atomic layering that occurs naturally at a liquid metal in contact with air/water/vacuum extends from the outer surface towards the bulk interior.[42-44] Although this structure only persists along the surface normal vector (rather than in three dimensions), the result is that solvation environment of solutes dissolved in a liquid metal can be dramatically different near the interface as compared to deeper in the bulk.

A driving premise in 'quasi'-epitaxy at liquid metal interfaces is the highest packing density plane of a crystal closely resembles the atomic packing density of a 5-fold Ga coordination environment (0.076 Ga atoms $Å^{-2}$, Figure 4.15). The idea is then that the barrier for nucleation is low because the solid crystal structure and liquid solvation shell are physically similar. Accordingly, the prediction is that the crystals that exhibit 'quasi' epitaxy will be grown in a direction with a packing density resembling the solvation environment in the layered liquid metal surface region. Conversely, crystals that do not have a plane with a similar structure will not form. This hypothesis was proposed for $PdGa_5$[001]and $MnGa_4$[111] single crystals when grown previously at liquid Ga/water interfaces, but the crystals that were observed also grew along the lowest energy surface direction. The possibility that those previous Ga intermetallic products were formed exclusively to minimize surface energy rather than following the layered Ga surface structure could not be distinguished. The data presented here address this hypothesis without ambiguity.

The lowest surface energy plane of $FeGa_3$ is (111). If minimizing the lowest surface energy was the only factor in 'quasi'-epitaxy, then a $FeGa_3$ crystal grown along the [111] direction should have been obtained. The data clearly argue against this point. The (111) surface plane of $FeGa_3$ also does *not* match the 5-fold in-plane packing of Ga atoms. Even summing the planar packing densities of any two adjacent atomic layers along the [111] direction in $FeGa_3$ gives a density of either 0.071 Ga atoms $Å^{-2}$ or 0.084 Ga atoms $Å^{-2}$. These densities are akin to a 4- or 6-fold in-plane nearest neighbor Ga structure, respectively. There are layers along the [001] direction in $FeGa_3$ that resemble a 5-fold planar Ga packing structure (**Table 5.3**) but with too low of an in-planar packing density. In other words, if a material has a highest packing-density surface plane that does not match the in-plane surface structure of 5-fold Ga, it will not form via 'quasi'-epitaxy.

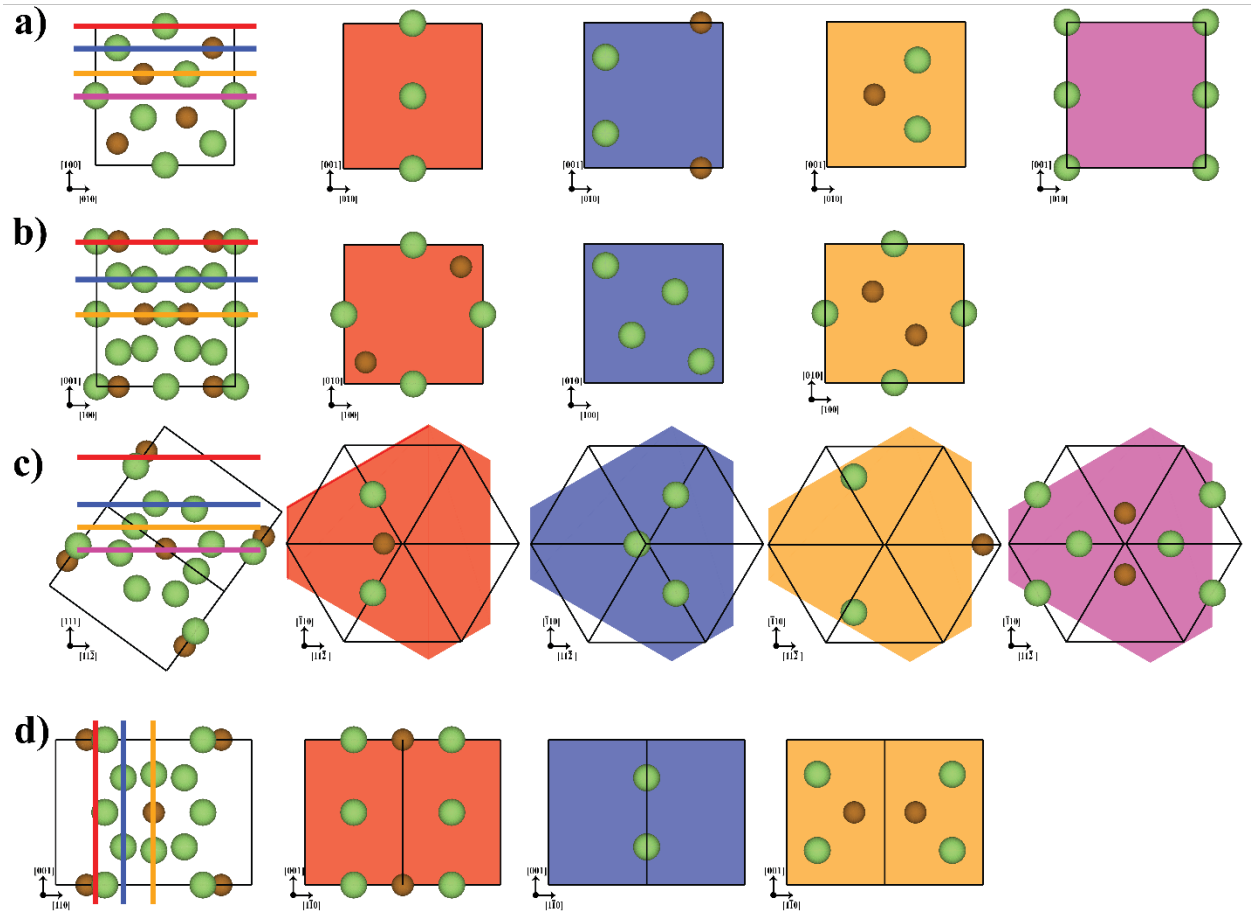

Figure 5.19 The thermodynamic expected phase, tetragonal $FeGa_3$ projected along the a) [001] b) [010] c) [110] and d) [110] crystallographic cross sections with sliced projections within the {100}, {001}, {111}, and {110} family of planes shown alongside each of these projections, respectively. These slices are colored red (layer 1), blue (layer 2), yellow (layer 3), and pink (layer 4) where applicable are considered when calculating the total (Table 5.2) and Ga packing densities (Table 5.3). Green atoms are Ga and brown are Fe.

Table 5.2 Calculated total packing densities of $FeGa_3$

$FeGa_3$ (a = b = 6.27 Å and c = 6.556 Å)					
Lattice Plane	**Atomic Layer**	**Total Number of Atoms**	**Area (Å^2)**	**Packing Density (atoms Å^{-2})**	**Total Packing Density (atoms Å^{-2})**
100	1 (red)	1.0	41.1	0.024	0.122
	2 (blue)	1.5		0.036	
	3 (orange)	1.5		0.036	
	4 (purple)	1.0		0.024	
001	1 (red)	2.0	39.3	0.051	0.153
	2 (blue)	2.0		0.051	
	3 (orange)	2.0		0.051	
111	1 (red)	1.5	35.1	0.043	0.214
	2 (blue)	1.5		0.043	
	3 (orange)	1.5		0.043	
	4 (purple)	3.0		0.085	
110	1 (red)	3.0	56.9	0.053	0.123
	2 (blue)	1.0		0.018	
	3 (orange)	3.0		0.053	

Table 5.3 Calculated packing densities of Ga atoms in $FeGa_3$

FeGa3 (a = b = 6.27 Å and c = 6.556 Å)				
Lattice Plane	**Atomic Layer**	**Number of Ga Atoms**	**Area ($Å^2$)**	**Ga Packing Density (atoms $Å^{-2}$)**
100	1 (red)	1	41.11	0.024
	2 (blue)	1		0.024
	3 (orange)	1		0.024
	4 (purple)	1		0.024
001	1 (red)	1	39.31	0.025
	2 (blue)	2		0.051
	3 (orange)	1		0.025
111	1 (red)	1	35.09	0.028
	2 (blue)	1.5		0.043
	3 (orange)	1		0.028
	4 (purple)	2		0.057
110	1 (red)	2	56.85757	0.035
	2 (blue)	1		0.018
	3 (orange)	2		0.035

Table 5.4 Calculated Ga atom packing densities in the estimated $Fe_{0.14\pm0.01}Ga_{0.86\pm0.01}$ and $Fe_{0.08\pm0.01}Co_{0.06\pm0.01}Ga_{0.86\pm0.01}$ structures

$Fe_{0.14\pm0.01}Ga_{0.86\pm0.01}$ & $Fe_{0.08\pm0.01}Co_{0.06\pm0.01}Ga_{0.86\pm0.01}$ (a = b = 8.22 Å and c = 11.8 Å)				
Lattice Plane	**Atomic Layer**	**Number of Ga Atoms**	**Area ($Å^2$)**	**Ga Packing Density (atoms $Å^{-2}$)**
001	1 (red)	3	58.52	0.051
	2 (blue)	3		0.051
	3 (orange)	1.5		0.026
	4 (purple)	4.5		0.077

In contrast, summing up the planar packing densities of individual layers in the unit cell of the hexagonal platelets possess a Ga packing density equal to 0.077 Ga atoms $Å^{-2}$. Specifically, the layer which contains the Fe or Co atoms and the nearest neighboring layer with Ga atom packing densities of 0.051 Ga atoms $Å^{-1}$ and 0.026 atoms $Å^{-1}$, respectively. (Figure 5.18, Table 5.4) We posit that this structure forms (and follows 'quasi'-epitaxial growth) because it is much more closely resembles the liquid Ga atomic structure. Dissolved Fe and Co atoms serve as atomic 'binders' to hold the Ga atoms in places and promote precipitation. The average Fe-Ga bond distance is estimated to be 2.37 Å in this layer, which is in close agreement to the reported bonding distance of 2.41 Å in $FeGa_3$.[45] Simply, the liquid Ga atomic structure *facilitated* the formation of this new type of Ga intermetallic.

The intervening layers of this new intermetallic structure have Ga packing densities of 0.077 Ga atoms $Å^{-2}$ (i.e. like in the liquid phase) and 0.051 Ga atoms $Å^{-2}$, akin to gallenene. Gallenene[46] is a two-dimensional sheet of gallium analogous to graphene, but with a buckled-plane structure.[39] However, in this context, its structure is similar to a close-packed layer of Ga atoms with the absence of one atom in the center of each hexagon of the honeycomb lattice. The occurrence of a gallenene sub-structure is interesting because it suggests this class of Ga intermetallics contains weak, out of plane van-der-waals cohesion as in more common layered materials (e.g. graphite, MoS_2, and WSe_2).[47, 48] These materials all share the propensity for exfoliation, or easy 'peeling' apart of the layers. Preliminary efforts were attempted to exfoliate these hexagonal platelets through the 'scotch-tape approach.'[48] Analysis of the surface planes post peeling were consistent with exfoliation, i.e. layered behavior (Figure 5.20).

This work additionally reinforces the following points about 'quasi'-epitaxial growth. (1) The liquid metal/electrolyte interface must be 'clean' or devoid of any interfacial oxides, which can hinder reactivity with the underlying bulk. (2) The rate of reaction must be sufficiently slow to maintain single crystalline growth. (3) The plane with the highest atomic packing density in the product material must show some agreement with the in-plane packing structure of the liquid metal. This work also adds new insight on optimal reaction conditions

The presented experiments support these three factors as being operative when directed crystal growth is observed at a liquid metal interface. The reaction products were only observed in alkaline aqueous electrolytes (1.25 M NaOH, pH > 14). These conditions apparently maintained a

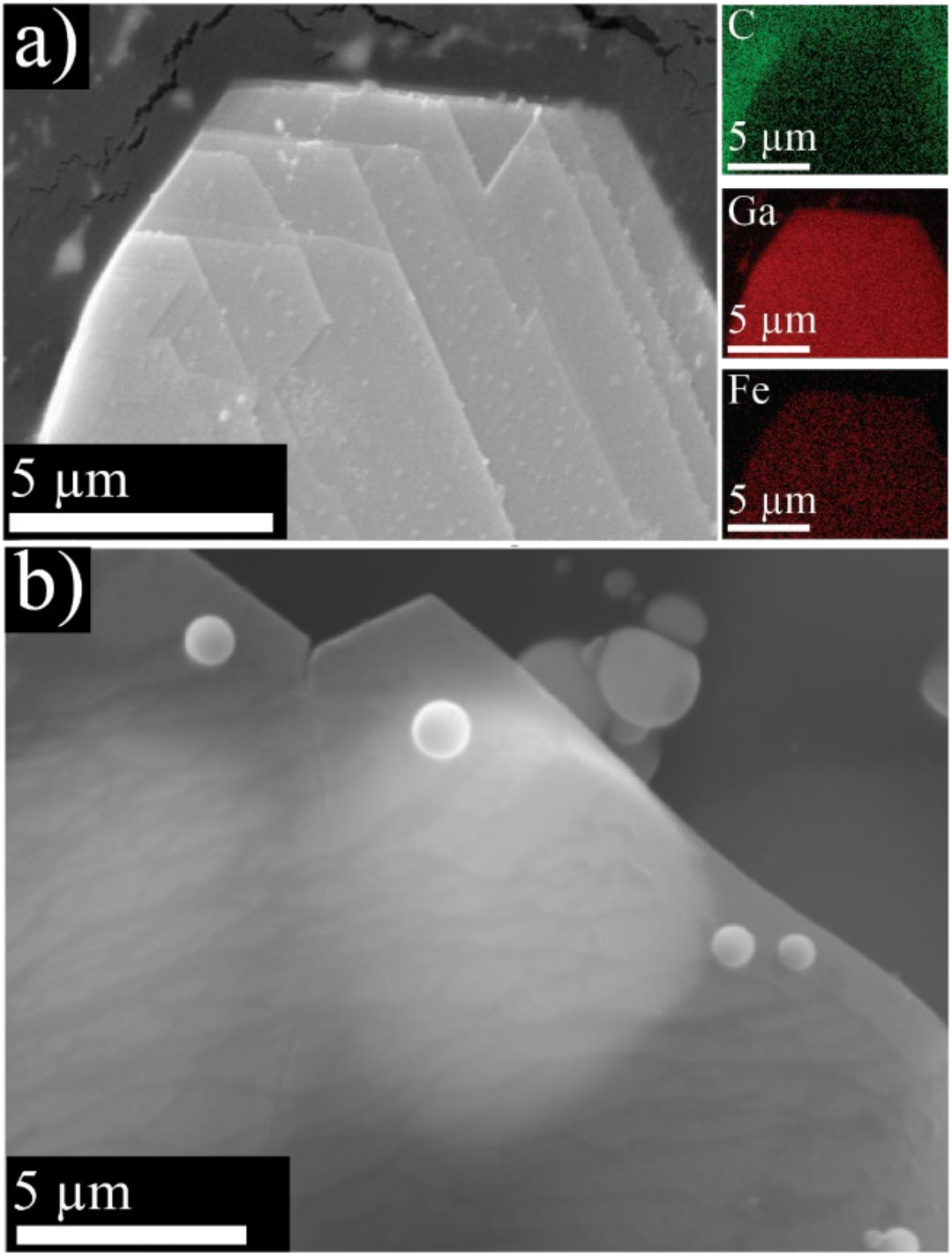

Figure 5.20 SEM and EDS of a) a gold coated $Fe_{0.14\pm0.01}Ga_{0.86\pm0.01}$ particle on scotch tape following exfoliation and b) section of the $Fe_{0.14\pm0.01}Ga_{0.86\pm0.01}$ exfoliated particle which appears transparent when imaged with a 12 kV electron beam.

clean Ga/water interface, as predicted by the Pourbaix diagram at standard temperature and pressures.[49, 50] Additionally, while no external electrochemical bias was necessary, the measured open-circuit potential of -1.47 V vs. *E*(Ag/AgCl) was sufficiently negative to inhibit native oxide growth and consistent with previous literature reports of the anodic dissolution of Ga in alkaline solution.[9, 51, 52] Moreover, the reactions also were promoted by comparatively *slow* metal ion fluxes, as determined by the dissolved concentrations in water. Increasing the concentration of dissolved Fe resulted in the accumulation of metallic Fe particles, not the new intermetallic.

Reactions involving multiple metal solutes and Ga were clearly established here. In these experiments, by introducing a secondary Co^{2+} reactant, afforded introduction of Co into the compound without compromising the basic structure. This is reasonable due to the nearly identical covalent bond radii of Fe (1.16 Å) and Co (1.11 Å),[53] allowing for direct substitution with little expected change to the respective bond lengths. The only notable difference between them is their respective electronic structure or valence electron count.[54] Previous studies have primarily focused on comparing the behaviors of lightly doped $(FeCo)_xGa_{1-x}$ due to these structural similarities but unique differences in electronic properties.[54] Thus the structural similarities between $Fe_{0.14\pm0.01}Ga_{0.86\pm0.01}$ and $Fe_{0.08\pm0.01}Co_{0.06\pm0.01}Ga_{0.86\pm0.01}$ is unsurprising but this study motivates future experiment exploring their respective electronic properties.

5.6 Conclusion

This work expands upon the applications and understanding of 'quasi'-epitaxial growth at a liquid metal surface by describing a method for obtaining previously unreported intermetallic phases, $Fe_{0.14\pm0.01}Ga_{0.86\pm0.01}$ and $Fe_{0.08\pm0.01}Co_{0.06\pm0.01}Ga_{0.86\pm0.01}$. Specifically, reactions involving multiple metals solutes at the surface of liquid Ga in alkaline aqueous solutions was sufficient to maintain an oxide-free surface and a low flux that facilitates 'quasi'-epitaxial material growth. $Fe_{0.14\pm0.01}Ga_{0.86\pm0.01}$ and $Fe_{0.08\pm0.01}Co_{0.06\pm0.01}Ga_{0.86\pm0.01}$ are best characterized as having a layered structure, high degree (6-fold) of symmetry, and a hexagonal unit cell with $a = b = 8.22$ Å and $c = 11.8$ Å. Although a complete assignment of the lattice structure proved to be difficult due to ambiguity introduced by crystallographic defects, the estimated structure has a large atomic packing density and sub-units consistent with gallenene. Additionally, the presented data supports the idea that the atomic packing in the near-surface layers of liquid Ga structurally influenced the formation of these phases. Further studies on these new Ga based intermetallics are needed to further refine their respective structures and to explore their potential electronic properties.

5.7 References

1. Hu, Q.; Hu, F.; Sun, D.; Zhang, K., Responsive Gallium-Based Liquid Metal Droplets: Attributes, Fabrication, Response Behaviors, and Applications. *Coatings* **2024,** *14* (8), 935.
2. Tang, S.-Y.; Tabor, C.; Kalantar-Zadeh, K.; Dickey, M. D., Gallium Liquid Metal: The Devil's Elixir. *Annual Review of Materials Research* **2021,** *51* (Volume 51, 2021), 381-408.
3. Chrimes, A. F.; Berean, K. J.; Mitchell, A.; Rosengarten, G.; Kalantar-zadeh, K., Controlled Electrochemical Deformation of Liquid-Phase Gallium. *ACS Applied Materials & Interfaces* **2016,** *8* (6), 3833-3839.
4. Agarwal, R.; Mohamad, A., Gallium-based liquid metals as smart responsive materials: Morphological forms and stimuli characterization. *Advances in Colloid and Interface Science* **2024,** *329*, 103183.
5. Seifner, M. S.; Sistani, M.; Zivadinovic, I.; Bartmann, M. G.; Lugstein, A.; Barth, S., Drastic Changes in Material Composition and Electrical Properties of Gallium-Seeded Germanium Nanowires. *Crystal Growth & Design* **2019,** *19* (5), 2531-2536.
6. Sunkara, M. K.; Sharma, S.; Miranda, R.; Lian, G.; Dickey, E. C., Bulk synthesis of silicon nanowires using a low-temperature vapor–liquid–solid method. *Applied Physics Letters* **2001,** *79* (10), 1546-1548.
7. Zhao, S.; Zhang, J.; Fu, L., Liquid Metals: A Novel Possibility of Fabricating 2D Metal Oxides. *Advanced Materials* **2021,** *33* (9), 2005544.
8. Goff, A.; Aukarasereenont, P.; Nguyen, C. K.; Grant, R.; Syed, N.; Zavabeti, A.; Elbourne, A.; Daeneke, T., An exploration into two-dimensional metal oxides, and other 2D materials, synthesised via liquid metal printing and transfer techniques. *Dalton Transactions* **2021,** *50* (22), 7513-7526.
9. Hazelnis, J. P.; Maldonado, S., Electrosynthesis of Quasi-Epitaxial Crystals on Liquid Metals. *Journal of the American Chemical Society* **2023,** *145* (50), 27616-27625.
10. Fahrenkrug, E.; Gu, J.; Maldonado, S., Electrodeposition of Crystalline GaAs on Liquid Gallium Electrodes in Aqueous Electrolytes. *Journal of the American Chemical Society* **2013,** *135* (1), 330-339.
11. Ding, Y.; Zeng, M.; Fu, L., Surface Chemistry of Gallium-Based Liquid Metals. *Matter* **2020,** *3* (5), 1477-1506.
12. Lan, H.; Wang, L.; He, R.; Huang, S.; Yu, J.; Guo, J.; Luo, J.; Li, Y.; Zhang, J.; Lin, J.; Zhang, S.; Zeng, M.; Fu, L., 2D quasi-layered material with domino structure. *Nature Communications* **2023,** *14* (1), 7225.
13. Mukanova, A.; Tussupbayev, R.; Sabitov, A.; Bondarenko, I.; Nemkaeva, R.; Aldamzharov, B.; Bakenov, Z., CVD graphene growth on a surface of liquid gallium. *Materials Today: Proceedings* **2017,** *4* (3), 4548-4554.
14. Lan, H.; Li, Y.; Liu, J.; Hu, W.; Zhu, X.; Ma, Y.; Niu, L.; Zhang, Z.; Jia, S.; Li, L.; Chen, Y.; Wang, J.; Zeng, M.; Fu, L., Self-Limiting Synthesis of Ultrathin Ge(110) Single Crystal via Liquid Metal. *Small* **2022,** *18* (9), 2106341.
15. Kim, J.-H.; Kim, S.; Dickey, M. D.; So, J.-H.; Koo, H.-J., Interface of gallium-based liquid metals: oxide skin, wetting, and applications. *Nanoscale Horizons* **2024,** *9* (7), 1099-1119.
16. Creighton, M. A.; Yuen, M. C.; Susner, M. A.; Farrell, Z.; Maruyama, B.; Tabor, C. E., Oxidation of Gallium-based Liquid Metal Alloys by Water. *Langmuir* **2020,** *36* (43), 12933-12941.

17. Mohamed, A. K.; Palacheva, V. V.; Cheverikin, V. V.; Zanaeva, E. N.; Cheng, W. C.; Kulitckii, V.; Divinski, S.; Wilde, G.; Golovin, I. S., The Fe–Ga phase diagram: Revisited. *Journal of Alloys and Compounds* **2020,** *846*, 156486.
18. Estrine, E. C.; Hein, M.; Robbins, W. P.; Stadler, B. J. H., Composition and crystallinity in electrochemically deposited magnetostrictive galfenol (FeGa). *Journal of Applied Physics* **2014,** *115* (17), 17A918.
19. Summers, E. M.; Lograsso, T. A.; Wun-Fogle, M., Magnetostriction of binary and ternary Fe–Ga alloys. *Journal of Materials Science* **2007,** *42* (23), 9582-9594.
20. Schnurr, S.; Wiedwald, U.; Ziemann, P.; Verchenko, V. Y.; Shevelkov, A. V., Structural and thermoelectric properties of TMGa3 (TM = Fe, Co) thin films. *Beilstein Journal of Nanotechnology* **2013,** *4*, 461-466.
21. Golovin, I. S.; Palacheva, V. V.; Mohamed, A. K.; Balagurov, A. M., Structure and Properties of Fe–Ga Alloys as Promising Materials for Electronics. *Physics of Metals and Metallography* **2020,** *121* (9), 851-893.
22. Meisenheimer, P. B.; Steinhardt, R. A.; Sung, S. H.; Williams, L. D.; Zhuang, S.; Nowakowski, M. E.; Novakov, S.; Torunbalci, M. M.; Prasad, B.; Zollner, C. J.; Wang, Z.; Dawley, N. M.; Schubert, J.; Hunter, A. H.; Manipatruni, S.; Nikonov, D. E.; Young, I. A.; Chen, L. Q.; Bokor, J.; Bhave, S. A.; Ramesh, R.; Hu, J. M.; Kioupakis, E.; Hovden, R.; Schlom, D. G.; Heron, J. T., Engineering new limits to magnetostriction through metastability in iron-gallium alloys. *Nature Communications* **2021,** *12* (1), 2757.
23. Priputen, P.; Drienovský, M.; Noga, P.; Kusý, M.; Černičková, I.; Janovec, J., Isothermal section of Ga-Co-Cu phase diagram at 830 °C and its peculiarities. *Journal of Alloys and Compounds* **2019,** *785*, 1173-1179.
24. Raghavan, V., Co-Fe-Ga (Cobalt-Iron-Gallium). *Journal of Phase Equilibria and Diffusion* **2008,** *29* (5), 438-439.
25. Madsen, J.; Susi, T., The abTEM code: transmission electron microscopy from first principles. *Open Research Europe* **2021,** *1* (24).
26. Palatinus, L.; Brázda, P.; Jelínek, M.; Hrdá, J.; Steciuk, G.; Klementová, M., Specifics of the data processing of precession electron diffraction tomography data and their implementation in the program PETS2. 0. *Structural Science* **2019,** *75* (4), 512-522.
27. Liu, L.; Twight, L. P.; Fehrs, J. L.; Ou, Y.; Sun, D.; Boettcher, S. W., Purification of Residual Ni and Co Hydroxides from Fe-Free Alkaline Electrolyte for Electrocatalysis Studies. *ChemElectroChem* **2022,** *9* (15), e202200279.
28. Chen, Y.-X.; Chen, S.-P.; Chen, Q.-S.; Zhou, Z.-Y.; Sun, S.-G., Electrochemical preparation of iron cuboid nanoparticles and their catalytic properties for nitrite reduction. *Electrochimica Acta* **2008,** *53* (23), 6938-6943.
29. Li, X.; Lazić, I.; Huang, X.; Wirix, M.; Wang, L.; Deng, Y.; Niu, T.; Wu, D.; Yu, L.; Sun, F., Imaging biological samples by integrated differential phase contrast (iDPC) STEM technique. *Journal of Structural Biology* **2022,** *214* (1), 107837.
30. Cayron, C., Diffraction artefacts from twins and stacking faults, and the mirage of hexagonal, polytypes or other superstructures. *Scripta Materialia* **2021,** *194*, 113629.
31. Meng, Y. S.; Ceder, G.; Grey, C. P.; Yoon, W. S.; Shao-Horn, Y., Understanding the Crystal Structure of Layered LiNi0.5Mn0.5 O 2 by Electron Diffraction and Powder Diffraction Simulation. *Electrochemical and Solid-State Letters* **2004,** *7* (6), A155.
32. Andrews, K. W.; Dyson, D. J.; Keown, S. R., *Interpretation of electron diffraction patterns*. Springer: 1967.

33. Boulineau, A.; Croguennec, L.; Delmas, C.; Weill, F., Reinvestigation of Li2MnO3 Structure: Electron Diffraction and High Resolution TEM. *Chemistry of Materials* **2009,** *21* (18), 4216-4222.
34. Zandbergen, H. W.; Foo, M.; Xu, Q.; Kumar, V.; Cava, R. J., Sodium ion ordering in NaxCoO2: Electron diffraction study. *Physical Review B* **2004,** *70* (2), 024101.
35. Maunders, C.; Etheridge, J.; Wright, N.; Whitfield, H. J., Structure and microstructure of hexagonal Ba3Ti2RuO9 by electron diffraction and microscopy. *Structural Science* **2005,** *61* (2), 154-159.
36. Sung, S. H.; Goh, Y. M.; Yoo, H.; Engelke, R.; Xie, H.; Zhang, K.; Li, Z.; Ye, A.; Deotare, P. B.; Tadmor, E. B.; Mannix, A. J.; Park, J.; Zhao, L.; Kim, P.; Hovden, R., Torsional periodic lattice distortions and diffraction of twisted 2D materials. *Nature Communications* **2022,** *13* (1), 7826.
37. Mu, X.; Gillman, C.; Nguyen, C.; Gonen, T., An Overview of Microcrystal Electron Diffraction (MicroED). *Annual Review of Biochemistry* **2021,** *90*, 431-450.
38. Zagorac, D.; Müller, H.; Ruehl, S.; Zagorac, J.; Rehme, S., Recent developments in the Inorganic Crystal Structure Database: theoretical crystal structure data and related features. *Applied Crystallography* **2019,** *52* (5), 918-925.
39. Gaston, N., 5 - Gallenene. In *Xenes*, Molle, A.; Grazianetti, C., Eds. Woodhead Publishing: 2022; pp 107-119.
40. Häussermann, U.; Boström, M.; Viklund, P.; Rapp, Ö.; Björnängen, T., FeGa3 and RuGa3: Semiconducting Intermetallic Compounds. *Journal of Solid State Chemistry* **2002,** *165* (1), 94-99.
41. Brokman, A.; Weger, M.; Schapink, F. W.; de Haan, C. D., Electron diffraction comparative study of the tetragonal phases in YBa2Cu3Ox compounds. *Solid State Communications* **1988,** *65* (6), 473-475.
42. Regan, M. J.; Kawamoto, E. H.; Lee, S.; Pershan, P. S.; Maskil, N.; Deutsch, M.; Magnussen, O. M.; Ocko, B. M.; Berman, L. E., Surface Layering in Liquid Gallium: An X-Ray Reflectivity Study. *Physical Review Letters* **1995,** *75* (13), 2498-2501.
43. Pershan, P. S., Review of the highlights of X-ray studies of liquid metal surfaces. *Journal of Applied Physics* **2014,** *116* (22), 222201.
44. Pershan, P. S.; Schlossman, M., *Liquid Surfaces and Interfaces: Synchrotron X-ray Methods*. Cambridge University Press: Cambridge, 2012.
45. Wagner, F. R.; Cardoso-Gil, R.; Boucher, B.; Wagner-Reetz, M.; Sichelschmidt, J.; Gille, P.; Baenitz, M.; Grin, Y., On Fe–Fe Dumbbells in the Ideal and Real Structures of FeGa3. *Inorganic Chemistry* **2018,** *57* (20), 12908-12919.
46. Kochat, V.; Samanta, A.; Zhang, Y.; Bhowmick, S.; Manimunda, P.; Asif, S. A. S.; Stender, A. S.; Vajtai, R.; Singh, A. K.; Tiwary, C. S.; Ajayan, P. M., Atomically thin gallium layers from solid-melt exfoliation. *Science Advances* **2018,** *4* (3), e1701373.
47. Li, H.; Wu, J.; Yin, Z.; Zhang, H., Preparation and Applications of Mechanically Exfoliated Single-Layer and Multilayer MoS2 and WSe2 Nanosheets. *Accounts of Chemical Research* **2014,** *47* (4), 1067-1075.
48. Zhou, Q.; Xia, G.; Du, M.; Lu, Y.; Xu, H., Scotch-tape-like exfoliation effect of graphene quantum dots for efficient preparation of graphene nanosheets in water. *Applied Surface Science* **2019,** *483*, 52-59.
49. Chung, Y.; Lee, C.-W., Electrochemistry of Gallium. *Journal of Electrochemical Science and Technology* **2013,** *4* (1), 1-18.

50. Pourbaix, M., Atlas of electrochemical equilibria in aqueous solutions. *National Association of Corrosion Engineers International* **1966**.
51. Corbett, J. D., Solutions of Gallium (I) Salts in Aqueous Base. *Inorganic Chemistry* **1963,** *2* (3), 634-636.
52. Hurlen, T., Anodic dissolution of liquid gallium in alkaline solutions. *Electrochimica Acta* **1964,** *9* (11), 1449-1452.
53. Pyykkö, P.; Atsumi, M., Molecular Single-Bond Covalent Radii for Elements 1–118. *Chemistry – A European Journal* **2009,** *15* (1), 186-197.
54. Likhanov, M. S.; Verchenko, V. Y.; Nasonova, D. I.; Gippius, A. A.; Zhurenko, S. V.; Demikhov, E. I.; Kuo, C. N.; Lue, C. S.; Young, B. L.; Shevelkov, A. V., Crystal structure and magnetic properties of intermetallic semiconductor FeGa3 lightly doped by Co and Ni. *Journal of Alloys and Compounds* **2018,** *745*, 341-346.

Chapter 6 Open Electrochemical Liquid Phase Epitaxial Growth of Crystalline Ge Films[4]

6.1 Preface

The following work highlights an alternative, more facile approach for performing ec-LPE in which single crystalline inorganic epi-films can be achieved by immersing a Ge seeding wafer into a liquid metal pool at benchtop conditions. Experimental work was shared between Joshua P. Hazelnis, Tung T. Nguyen, and Henry Wu. Contact angle and cross-sectional measurements with corresponding data interpretation were performed by Tung T. Nguyen. Epi-films were prepared equally by Joshua P. Hazelnis, Tung T. Nguyen, and Henry Wu. All linear sweep voltammetry and electrochemical analysis was performed by Joshua P. Hazelnis. Focused ion beam samples were all prepared by Joshua P. Hazelnis for (S)TEM characterization which was performed equally by Joshua P. Hazelnis and Henry Wu. Other than the contact angle and cross-sectional epi-film analysis, all data work-up, figure preparation and writing were equal in contribution between Joshua P. Hazelnis and Stephen Maldonado. Lauren Rich is acknowledged for helpful discussions. The financial support of the University of Michigan College of Engineering and technical support from the Michigan Center for Materials Characterization is also acknowledged.

6.2 Introduction

The development of innovative, more sustainable methods for semiconductor manufacture is growing in importance for three interconnected reasons.[1-3] First, the societal demand for semiconductor-based technologies is increasing substantially, with no signs of abatement.[4] Second, the current strategies for semiconductor synthesis and production have inordinately large environmental footprints.[5, 6] Third, in the case of covalent semiconductors like silicon (Si) and germanium (Ge), the infrastructure required to produce material with target properties for optoelectronic use is extreme. For example, new facilities for producing ultra-pure Si for solar and electronics cost upwards of $10B - $20B to construct, to operate, and to maintain.[7] Similarly,

[4] Reprinted (adapted) with permission from Hazelnis, J. P.; Nguyen, T. T.; Wu, H.; Maldonado, S., Open Electrochemical Liquid Phase Epitaxial Growth of Crystalline Ge Films. *ACS Applied Materials & Interfaces* 2025. Copyright 2025 American Chemical Society.

hyperdoped covalent semiconductors[8-10] that exhibit improved or novel optical and electrical properties[10-12] require chemical vapor deposition,[8] molecular beam epitaxy,[9] ion implantation,[13] or gas immersion laser doping[14] to synthesize. While versatile, none of these techniques can be described as simple, 'benchtop', or inexpensive. Accordingly, identification of simpler, more facile, and less costly semiconductor manufacturing methods has value from many perspectives.

Previously, our group developed an electrochemical strategy for producing group IV and III-V semiconductors at ambient conditions with relatively modest instrumentation.[15-18] This electrochemical approach does not require volatile precursors, elevated temperatures, or produce substantive (stoichiometric) waste products. Instead, it leverages the idea that liquid metals can be used to both reduce an oxidized precursor dissolved in a liquid electrolyte and to provide the resultant solute a separate medium to accumulate, nucleate, and grow as a crystal. This approach is generally described as electrochemical liquid-liquid-solid (ec-LLS) crystal growth.[19, 20]

In the context of crystalline semiconductor film deposition, an important advancement of the ec-LLS idea was previously introduced as electrochemical liquid phase epitaxy (ec-LPE).[21, 22] In ec-LPE, the liquid metal is sufficiently thin that the dissolved solute can diffuse, accumulate, and nucleate at a bottom solid seeding interface, thereby affording epitaxial film growth (Figure 6.1a). In its original conception, ec-LPE required a custom pressurized electrochemical cell with a highly engineered porous membrane to overcome the electrocapillarity[23, 24] of liquid metal films that disrupts their flatness, i.e. the application of a potential tends to deform liquid metal films into discrete droplets in the absence of strong wetting of the substrate. Although wafer-scale epitaxial films (epi-films) coverages were possible in the original 'compressed' ec-LPE strategy, the cell construction and assembly were sufficiently cumbersome to make high throughput growths difficult. The resultant epi-films produced also had high levels (i.e. above the equilibrium solubility) of liquid metal incorporation.[21, 22]

Herein, this work explores and details an alternative approach to the ec-LPE concept for room-temperature growth of semiconductor epi-films. The intent of this work is to determine whether epitaxy can be achieved without compression. Specifically, the simplest approach to achieve a thin liquid metal in contact with both a liquid electrolyte and solid seed substrate is simply to immerse the solid substrate into a liquid metal pool electrode during electroreduction and grow crystals at the three-phase boundary of the liquid metal, liquid electrolyte, and solid substrate (Figure 6.1b). This 'open' ec-LPE strategy has never been explored before. This work

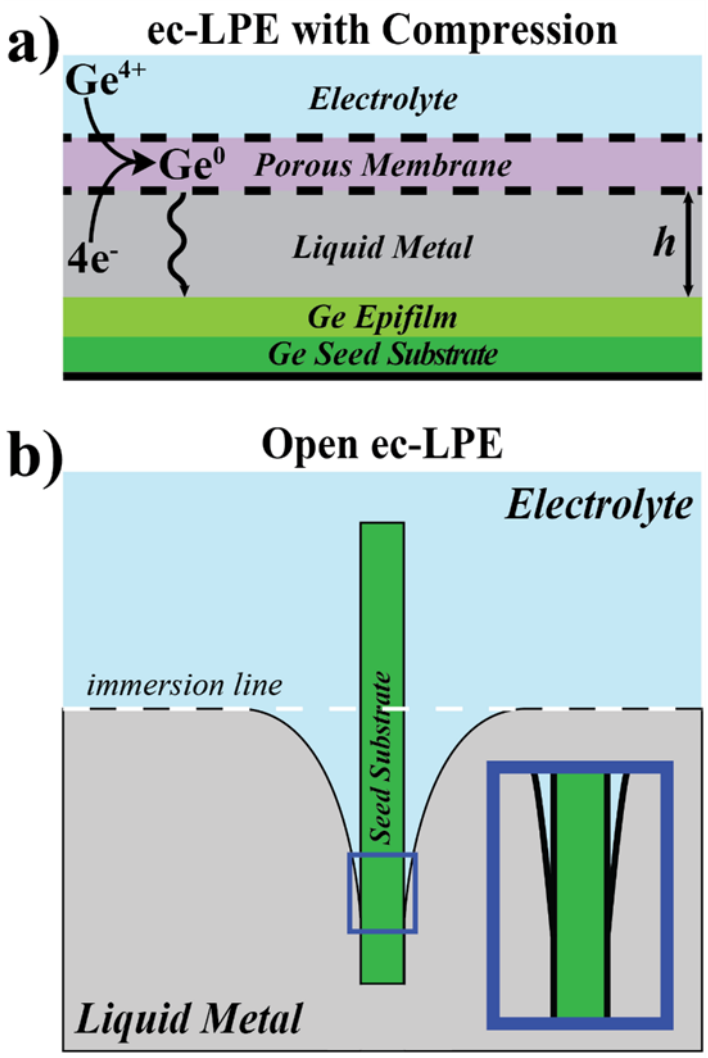

Figure 6.1 a) Schematic depiction of electrochemical liquid phase epitaxy (ec-LPE) with compression where electroreduced solute dissolves through a porous membrane in the liquid metal with a thickness *h* and diffuses to a boundary with a solid to nucleate at that interface. Preferential heterogeneous nucleation at the liquid metal/seed substrate interface is probable when *h* is sufficiently small with the compressive membrane ensuring the electrocapillarity does not change *h*. b) Schematic depiction of open ec-LPE where a seed substrate is immersed into a liquid metal electrode pool. The white line denotes the macroscopic view of how far the seed substrate is immersed in the liquid metal. The blue box denotes where the three-phase boundaries occur between the liquid metal, liquid electrolyte, and solid seed substrate.

assesses whether any epitaxial electrodeposition can be realized at or near the three-phase boundary (blue box, Figure 6.1b, inset) where the liquid metal may be sufficiently thin to promote nucleation at the liquid metal/solid substrate interface vs at the liquid metal/liquid electrolyte interface. Four different liquid metal compositions (Hg, $Hg_{0.35}In_{0.65}$, Ga, and $Ga_{0.83}In_{0.17}$) are described here to identify aspects that favor or disfavor this approach. Insights for realizing high 'open' ec-LPE film growths are discussed.

6.3 Experimental

6.3.1 Materials and Chemicals

Indium shot (In, 99.99%, Alfa Aesar), gallium (Ga, 99.99%, Thermo Fisher), mercury (Hg, triply distilled, D.F. Goldsmith), (99.9%, Sigma-Aldrich), germanium(IV) oxide (99.999%, ChemPur), sodium tetraborate (99.998%, ChemPur), methanol (ACS grade, BDH), hydrochloric acid (Certified ACS Plus, 36.5 to 38.0 %, ThermoFisher), and sodium hydroxide (pellets, 99.99%, Sigma-Aldrich) were used as received. Nanopure water (>18.2 MΩ•cm, Barnstead Nanopure) was used throughout. Electrode supports for contacting the liquid metal pool electrodes consisted either of tungsten foil (W, 99.95%, mm thick, Alfa Aesar). The growth substrates used were diced sections of Ge (100) wafers (double side polished, P-doped, 10-15 Ω•cm, University Wafer).

6.3.2 Liquid Metal Alloy Preparation

Eutectic gallium indium (*e*-GaIn) was prepared mixing liquid Ga and In shot in a 10 mL glass scintillation vial at 82.8 % at. and 17.2 % at., respectively. The mixture was heated in an oven at 100°C for ~ 30 minutes followed by thorough mixing with a glass transfer pipette. Similarly, a stock of $Hg_{0.35}In_{0.65}$ was prepared by adding liquid Hg and In shot to a 10 mL glass scintillation vial to atomic fractions of 35 and 65 at. %, respectively. Both components were carefully stirred using a clean glass transfer pipette.

6.3.3 Electrochemical cell

Electrodepositions were carried out in a custom quartz glass cell consisting of a bottom plate, a cell cap, and a mount for reverse hold tweezers (Figure 6.2). Tungsten foil (2 cm x 2 cm) was used as an ohmic contact between the steel base plate and liquid metal working electrode. The area between the liquid metal working electrode and tungsten foil was sealed using an O-ring (X-

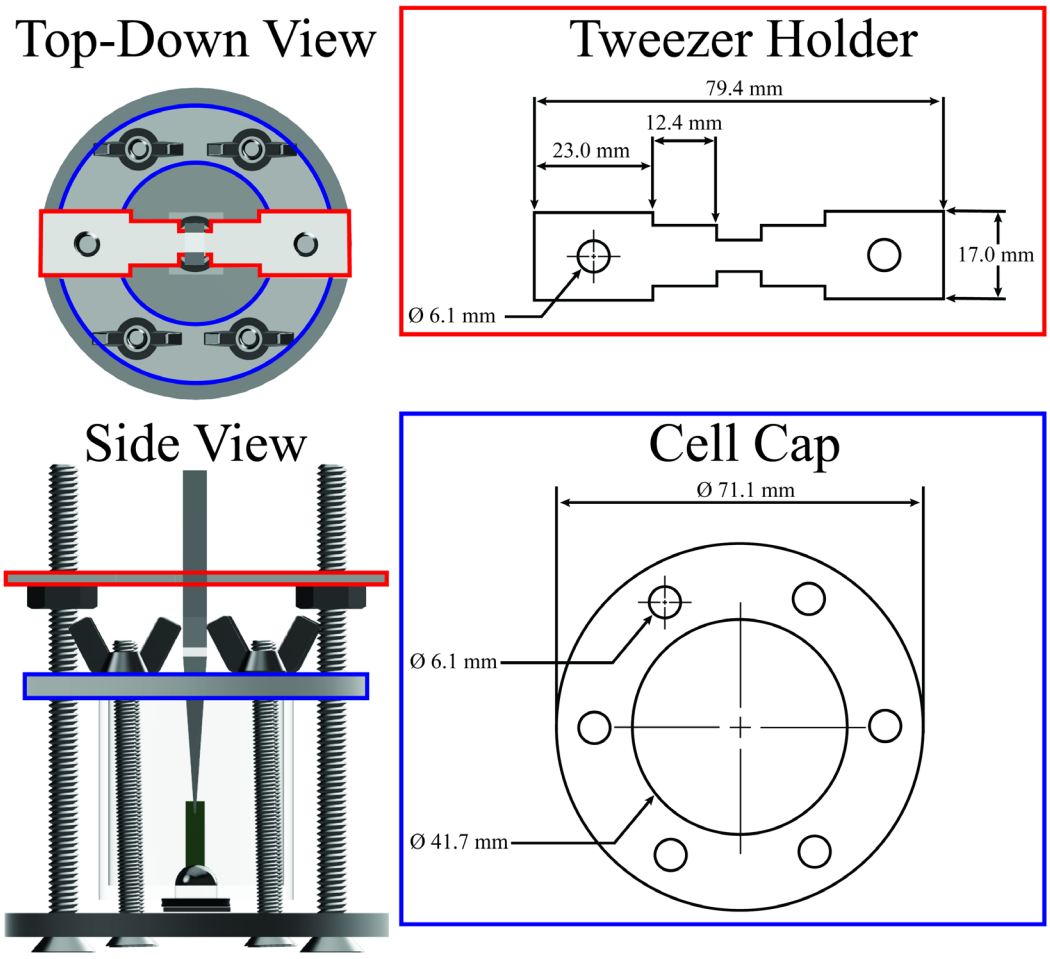

Figure 6.2 Sketch and specification of the PMMA tweezer holder [red] and cell cap [blue] for the custom O-ring cell used for electrodeposition with corresponding top-down and side view schematics of the electrochemical cell.

Profile Chemical-Resistant Viton® Fluoroelastomer O-Rings, McMaster-Carr). An acrylic cap was placed on top of the quartz glass cell for compression and attached to the steel base plate.

Custom cell parts were laser cut from 3/16" PMMA using an Omtech MF2028-80 80W CO_2 Laser Engraver. This includes a "tweezer holder" to lock a pair of ceramic reverse lock tweezers in place while inserting the Ge (001) seeding wafer during electrodeposition and a cell cap which can be modified by adding ports for the reference, counter and N_2 sparging line when performing air-free linear sweep voltammetry. A top-down and side view of the electrochemical cell schematic are included with each part highlighted (tweezer holder = red and cell cap = blue) for clarity.

The counter, reference, and working electrodes were a platinum wire (BASi, MW-2030), a Ag wire coated with AgCl and immersed in saturated KCl(*aq*) and separated from the test solutions with a double junction, and a liquid metal pool, respectively. For the working electrode, either 3.00 ± 0.05 g of liquid Ga, or *e*-GaIn or 4.5 ± 0.1 g of Hg or $Hg_{0.35}In_{0.65}$ were used. A larger amount of Hg containing liquid metals was used to compensate for the higher density and thus smaller volume as compared to the Ga containing liquid metals. To maintain molten Ga during electrodeposition, the cell was placed on a warm hot plate (Thermofisher Isotemp) set to 60°C to keep the cell at a measured steady-state temperature of 31°C. Electrodepositions with all other liquid metal compositions were performed without external heating at lab ambient temperatures (20-25°C). Electrical contact with the liquid metal working electrode was made by externally contacting the base plate of the cell. All currents densities were normalized by the estimated surface area of the liquid metal in contact with the electrolyte (~1.38 cm^2) and not by the area of the immersed Ge wafer.

6.3.4 Linear Sweep Voltammetry

Linear sweep voltammetry data for each of the four liquid metal working electrode compositions were collected using a 30 mL aqueous electrolyte solution consisting of 0.1 M $Na_2B_4O_7$, both with and without dissolved 0.05 M GeO_2. Controls were also performed using a 0.01 M $Na_2B_4O_7$ supporting electrolyte solution. Prior to data collection, the electrolyte was sparged with N_2(g) for at least 15 minutes. The system remained under an inert N_2(g) atmosphere for the entirety of the experiment. Crystal growth substrates were not inserted into the liquid metal

pool during these voltammetric sweeps. In each case, the applied bias was swept reductively using a Solartron 1176A potentiostat. All reported potentials are referenced to *E*(Ag/AgCl, sat. KCl).

6.3.5 Electrodeposition of Ge Films

In electrolyte consisting of 0.1 M $Na_2B_4O_7(aq)$ and 0.05 M $GeO_2(aq)$, an external bias of -1.5 V vs. *E*(Ag/AgCl, sat. KCl) was applied to each type of liquid metal working electrode for t = 3 h using either a Solartron 1176A or a Princeton Applied Research Model EG&G 363 potentiostat. A wafer section (previously rinsed with methanol and dried with N_2) was then mechanically inserted into the liquid metal electrode pool at an immersion depth of 3 mm from the liquid metal/electrolyte interface as determined by measuring the distance between the acrylic piece used to hold the reverse holder ceramic tweezers and the bottom of the cell with calipers prior to electrodeposition. After t = 3 h, the wafer section was removed from the liquid metal. Excess liquid metal was mechanically wiped away using a kimwipe (Kimtech) and residual liquid metal was removed by soaking the wafer section in concentrated HCl for 20 to 30 minutes, followed by copious rinsing with nanopure water.

6.3.6 Contact Angle Measurements

The wetting characteristics between the liquid metal working electrode and Ge(100) were analyzed via independent contact angle measurements. A 25 μL droplet of either pure Ga, *e*-GaIn, $Hg_{0.35}In_{0.65}$ or pure Hg was placed onto a Ge(100) wafer. Since these measurements were done in air, the initial liquid metal oxide skin was removed using a drop of 1.25 M concentrated aqueous NaOH stock solution prior to imaging with a digital camera (640× 480 pixels resolution) positioned perpendicular to the droplet wafer surface. All measurements were performed in triplicate and the contact angles were measured using the angle tool in FIJI ImageJ analysis software.[25]

6.3.7 Materials Characterization

Scanning electron microscopy (SEM) images and energy dispersive spectroscopy (EDS) maps were obtained using a JEOL JSM-7800FLV scanning electron microscope equipped with an Everhart-Thornley secondary electron detector and Oxford xMaxN 80mm^2 silicon-drift energy-dispersive x-ray spectrometer. All SEM and EDS data were acquired using an accelerating voltage of 18kV and processed in Oxford Aztec v.3.3 EDS software. Cross-sectional SEM images were

obtained along the direction normal to the liquid metal/electrolyte interface to measure the thickness of the electrodeposited Ge film. All SEM micrographs were acquired in secondary electron mode and thus the image contrast relates to the local topography of the imaging area. Electron backscatter diffraction (EBSD) was also performed using an Oxford NordlysMax^2 EBSD Camera but at an accelerating voltage of 25 kV. Kikuchi patterns from the electrodeposited Ge film were collected. These data were used to calculate and to index corresponding pole figures using the Oxford AztecHKL software.

Prior to transmission electron microscopic (TEM) characterization, samples were prepared by focused ion beam (FIB) milling using a Thermo Fisher HeliosG4 PFIB UXe equipped with a Schottky Field Emitter electron beam source and Multichem gas injector. (Figure 6.3) Xe plasma FIB was intentionally used to avoid introducing additional Ga from the ion beam. An area of electrodeposition near the liquid metal/electrolyte interface was first identified followed by electron-beam-assisted chemical vapor deposition of a ~100 nm protective carbon layer on a 20 x 5 µm area at a 3 kV accelerating voltage and 13 nA beam current. Once protected from ion beam damage, a Pt/C (80:20 mixture) capping layer was added using ion-beam-assisted CVD with an accelerating voltage of 8.00 kV and 1 nA beam currents. With a 30 kV accelerating voltage and 15 nA ion beam currents, two trenches of ~20 µm depth were made on either side of the deposited capping layer to fully expose the electrodeposited Ge and underlying seed wafer for liftout using an Omniprobe AutoProbe 200 micromanipulator equipped with a standard tungsten probe tip (Ted Pella). The final lamella was attached to a copper FIB lift-out grid and thinned down via the ion beam to a uniform thickness of <200 nm for STEM characterization.

Transmission electron microscopy (TEM) characterization was performed on the electrodeposited Ge cross-section sample using a Thermo Fisher Talos F200X G2 S/TEM with Gatan One View bottom mount camera. TEM, high angular annular dark field (HAADF) imaging, EDX, and selected area electron diffraction patterns were collected as described below.

Prior to analysis, a FEI double tilt holder was utilized to align each sample with a major crystallographic zone axis perpendicular to the incident electron beam. All HR-TEM images were acquired under bright field conditions at 200kV with the heavier atoms within the sample appearing darker than that of lighter atoms. If samples had a high amount of liquid metal incorporation, these contrast differences allowed for facile identification of the Ge substrate/electrodeposition interface. When collecting SAED patterns, a 100 nm diameter selected

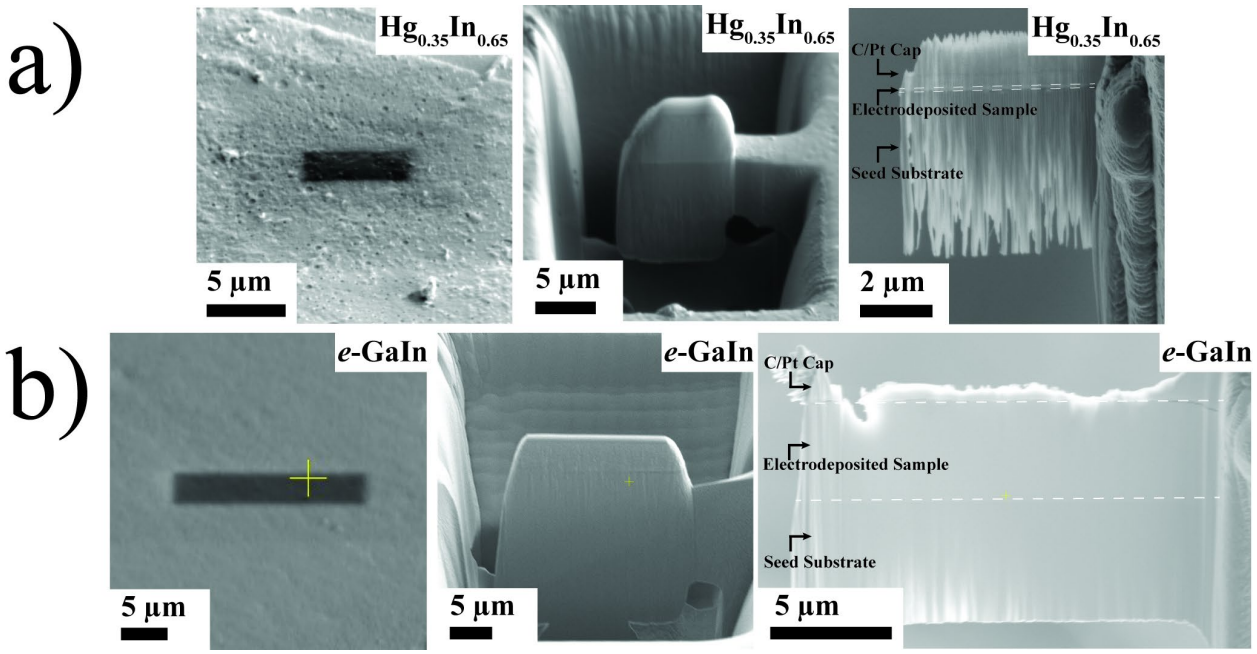

Figure 6.3 SEM of the final TEM sample prepared by plasma focused ion beam milling with corresponding liftout site for Ge electrodeposited film using a) $Hg_{0.35}In_{0.65}$ and b) *e*-GaIn

area aperture was used to focus the beam on either the electrodeposition area or Ge substrate. HAADF images along the sample interface were taken prior to collecting EDX spectra. All EDX spectra is an average of 50-100 scans over the sample area.

6.4 Results

6.4.1 Wetting Characteristics

The wetting of each liquid metal composition on crystalline Ge was performed prior to initiating any 'open' ec-LPE experiments via liquid metal contact angles measurements (Figure 6.4). In these measurements, a new solid crystalline Ge surface was used for each liquid metal composition to avoid residual liquid metal contamination between droplets. 25 μL aliquots of liquid metal were dispensed onto crystalline Ge wafer sections. To avoid the possibility of the wetting behavior being dictated by the native surface oxide[26] of each liquid metal droplet, all measurements were performed with both the liquid metal and solid Ge wafer section immersed in 1.25 M NaOH(*aq*). The data shown in Figure 6.4 are representative examples for each case, where 5 replicates for each liquid metal (*e*-GaIn, Ga, $Hg_{0.35}In_{0.65}$, Hg) were performed. In strong base, the liquid metal droplets spontaneously ball up. Hg and $Hg_{0.35}In_{0.65}$ exhibited similarly high contact angles (α), (133± 2)° and (129± 2)°, respectively. In contrast, the wetting angles (α) for Ga and *e*-GaIn were noticeably smaller, (117 ± 3)° and (116 ± 5)°, respectively.

6.4.2 Linear Sweep Voltammetry

Linear sweep voltammetry responses were recorded between -0.85 to -1.70 V at a scan rate of 0.01 V s^{-1} to identify differences in the activity for proton/water reduction in 0.1 M $Na_2B_4O_7$ amongst pure Ga, *e*-GaIn, Hg, and $Hg_{0.35}In_{0.65}$ (Figure 6.5). Every voltammogram was initiated at the rest potential and then swept cathodically. For Hg and $Hg_{0.35}In_{0.65}$, the activity for proton/water reduction did not differ significantly in blank 0.1 M $Na_2B_4O_7$ electrolyte. One notable difference was the reduction peak observed at E = -0.97 V with $Hg_{0.35}In_{0.65}$, consistent with the reduction of In-containing oxides which form spontaneously at open circuit in air and in water.[27] *e*-GaIn exhibited a similar reduction peak at E = -1.06 V. The currents for proton/water reduction were noticeably largest for liquid Ga, exhibiting the largest current density of 2.7 mA cm^{-2} at -1.7 V.

Upon the addition of 0.05 M GeO_2, a clear increase in the total current was observed for all liquid metal working electrodes at the most negative potentials. This increase was smallest for

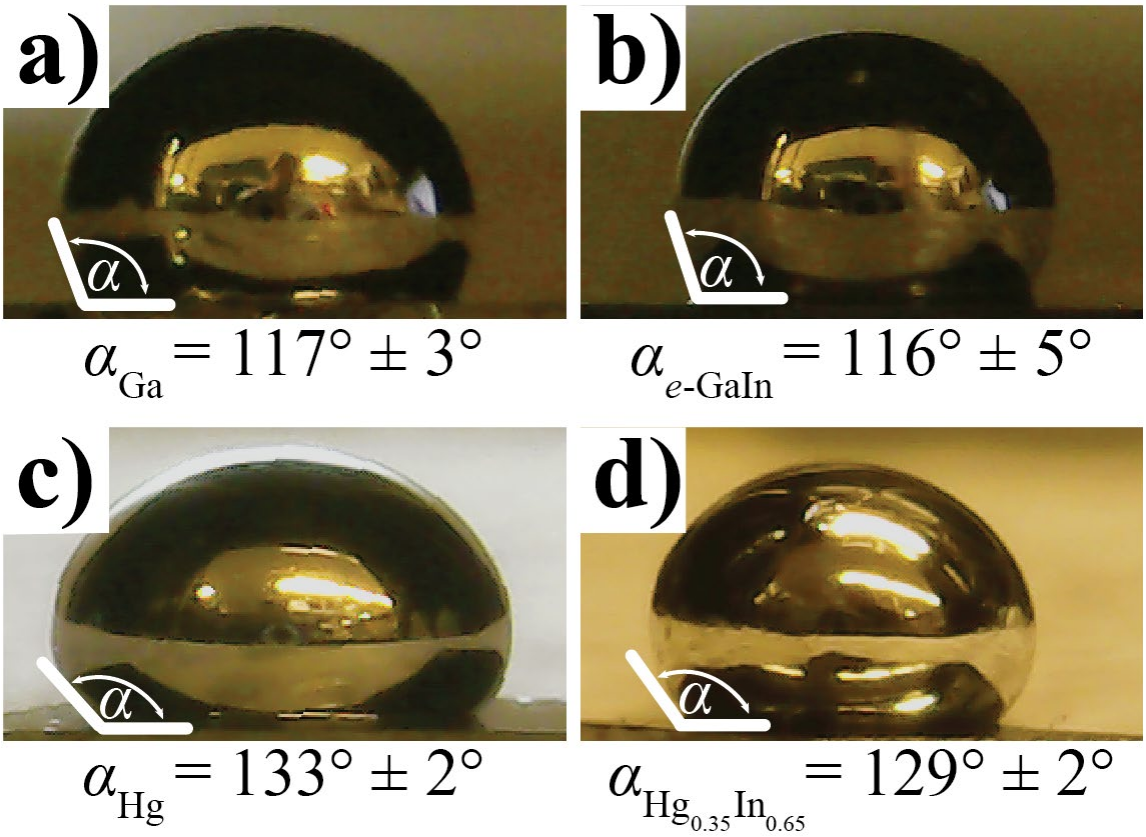

Figure 6.4 Wetting contact angle, α measurements between a Ge(100) wafer substrate and either liquid a) Ga, b) *e*-GaIn, c) Hg, or d) $Hg_{0.35}In_{0.65}$.

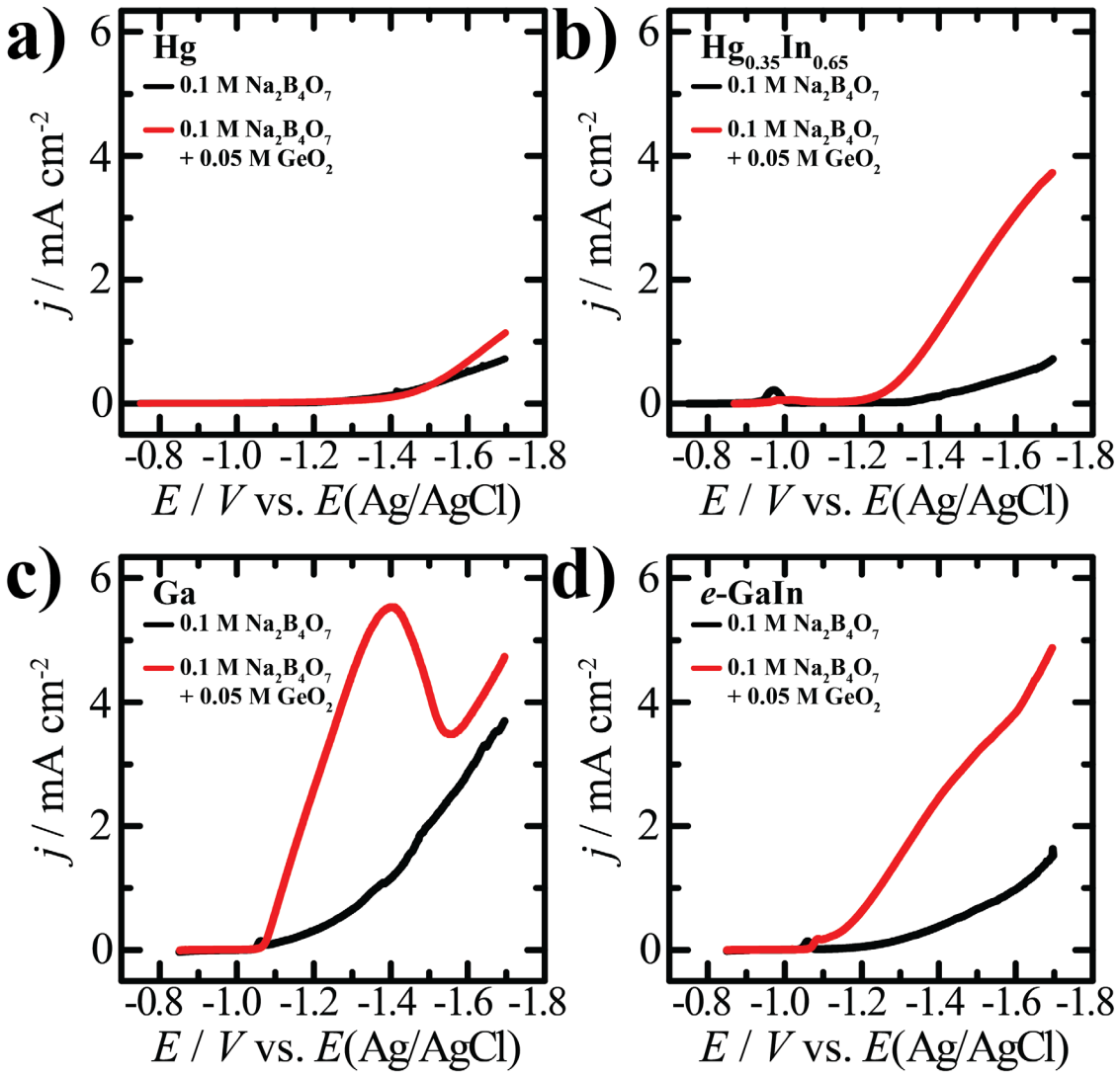

Figure 6.5 Linear sweep voltammetric responses for liquid a) Hg, b) $Hg_{0.35}In_{0.65}$, c) Ga, and d) *e*-GaIn in N_2 purged aqueous 0.1 M $Na_2B_4O_7$, both (black line) without and (red line) with 0.05 M GeO_2.

liquid Hg. For both $Hg_{0.35}In_{0.65}$ and *e*-GaIn, the reduction currents were noticeably higher at potentials more negative than -1.25 V, indicating the presence of In accelerated the rate of reduction of dissolved GeO_2. However, the largest reductive currents were observed with liquid Ga, where a clear peak was noted. This peak did not depend linearly with the square root of scan rate, implying it was not diffusive in nature. Upon repetitive scanning, the magnitude of the peak decreased but the current overall remained large. (Appendix E*,* Appendix Figure D.2) Curiously, for all liquid metals, the magnitude of the currents for the reduction of dissolved GeO_2 decreased significantly if the concentration of $Na_2B_4O_7$ was lowered to 0.01 M (Figure 6.6).[27]

6.4.3 'Open' ec-LPE

To facilitate electroreduction of dissolved GeO_2 with minimal parallel proton/water reduction, 'open' ec-LPE experiments were attempted with a constant bias of -1.5 V in aqueous electrolyte containing 0.1 M $Na_2B_4O_7$ and 0.05 M GeO_2. In each experiment, a clean Ge wafer section was inserted into the liquid metal pool immediately after the initial application of bias. These wafer sections were held in place with an insulated, ceramic-coated self-closing tweezer.

Current-density vs time transients were recorded for all liquid metals following the application of the bias. Figure 6.7a shows representative chronoamperometric responses for each liquid metal type. In general, the current density slowly decayed on the time scale of minutes to tens of minutes. The quasi-steady-state current densities were low for Hg-containing liquid metals but highest for liquid *e*-GaIn, in contrast to the voltammetry results. The initial 0.25 h typically showed some instability in the current at the beginning of each experiment. Hg electrodes exhibited the most instability, with pronounced oscillatory behavior initially (Figure 6.7a, inset). Although the duration of the oscillations varied somewhat between trials, they were consistently observed with liquid Hg in the open ec-LPE cell. For all four liquid metal types, the liquid metal surface concurrently darkened and roughened over time (Figure 6.7b). Additionally, a small number of macroscopic bubbles accumulated at the liquid metal/electrolyte interface (Figure 6.7b, bottom). After 3 h, the wafer section was emersed from the liquid metal, removed from the cell, cleaned of excess liquid metal, and the resultant electrodeposited film(s) was analyzed.

Despite similarities in the electrochemical responses, each of the four types of liquid metal working electrodes yielded distinctly different electrodeposited Ge films. With pure Hg, no contiguous electrodeposited Ge film was observed on the wafer section (Figure 6.9a). Higher

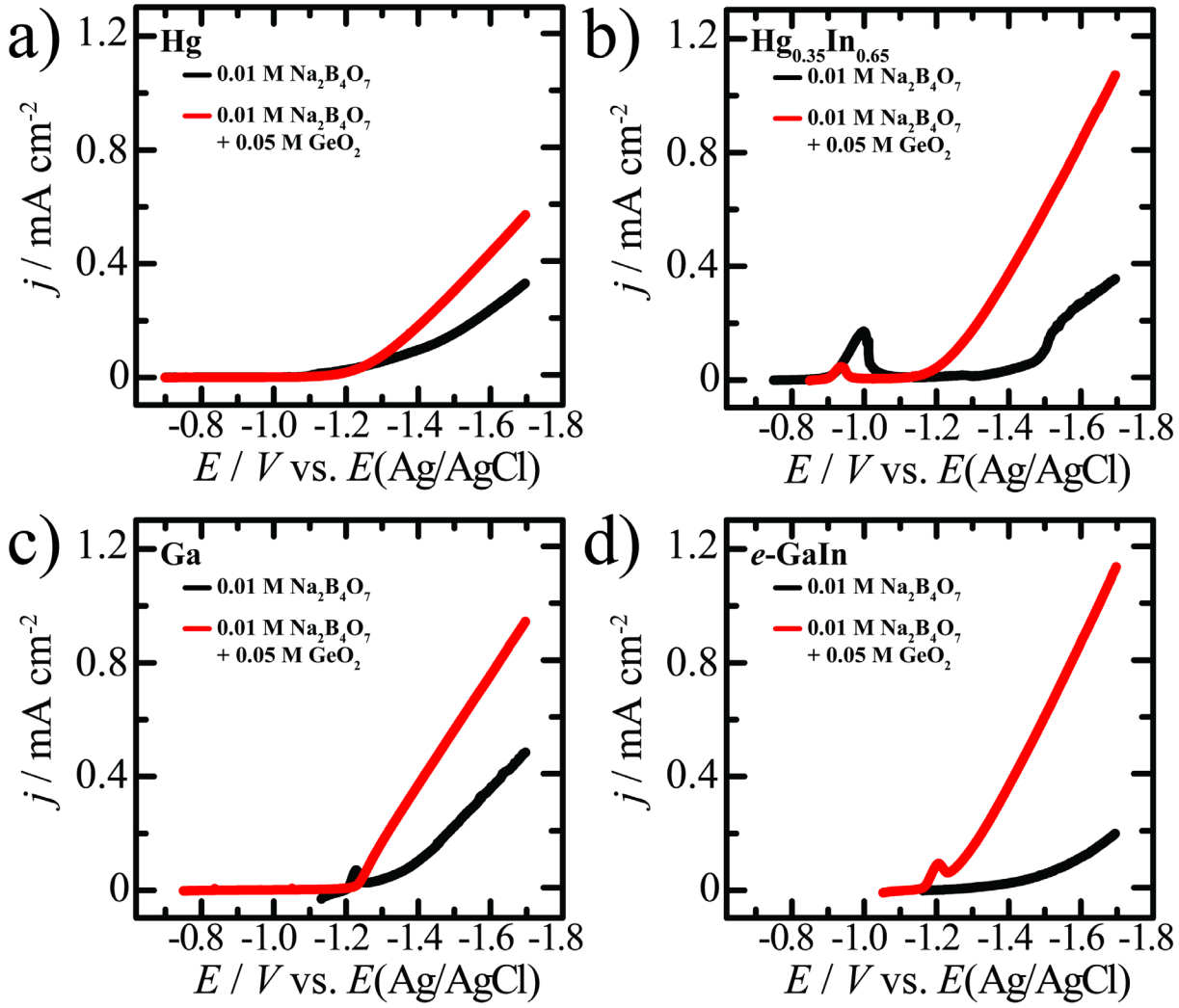

Figure 6.6 Linear sweep voltammetry of a) Hg b) $Hg_{0.35}In_{0.65}$ c) Ga and d) *e*-GaIn in 0.01 M $Na_2B_4O_7$ electrolyte with [red] and without [black] the addition of 0.05 M GeO_2.

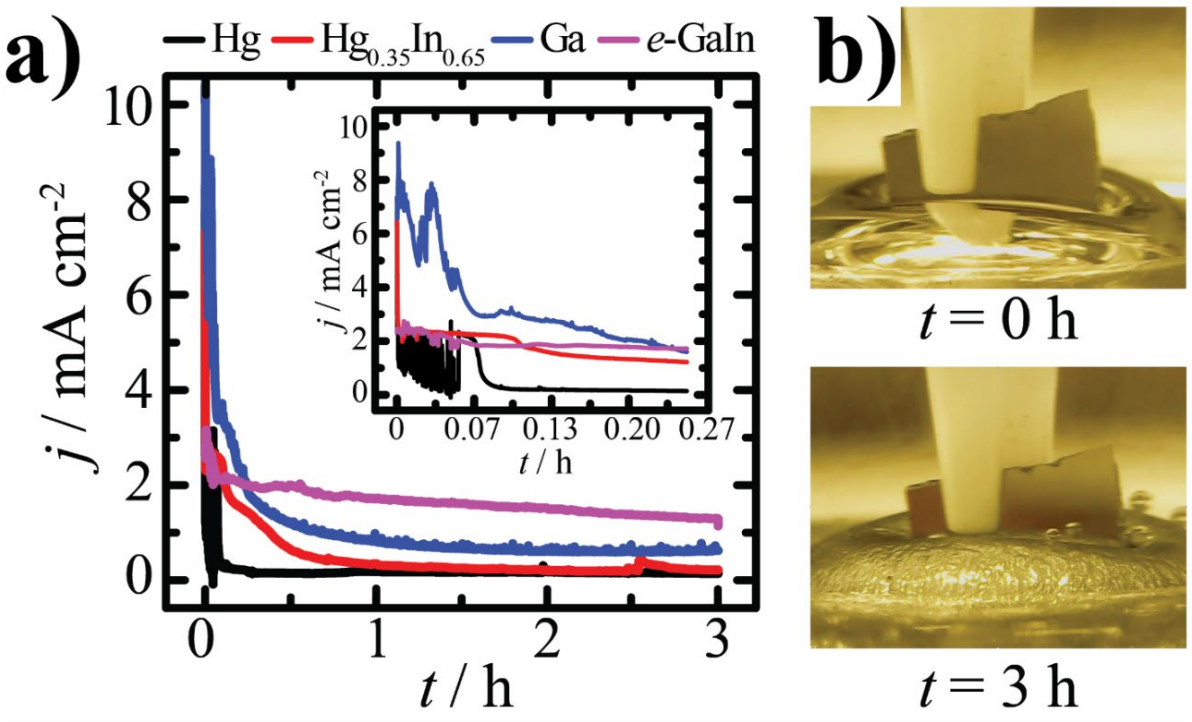

Figure 6.7 a) Representative current-time responses for the chronoamperometric electrodeposition of 0.05 M GeO_2 in aqueous 0.1 M $Na_2B_4O_7$ using either liquid Hg, $Hg_{0.35}In_{0.65}$, Ga, or *e*-GaIn. In all traces, the applied bias was -1.5 V vs. *E*(Ag/AgCl). Zoomed-in view of the first 0.25 h (inset). b) Optical photographs of a Ge(100) wafer section immersed into liquid *e*-GaIn at (top) $t = 0$ h and (bottom) $t = 3$ h of the experiment.

magnification imaging by SEM (Figure 6.9b) further confirmed the absence of appreciable Ge nuclei on the substrate surface, indicating that epitaxial growth did not occur. In contrast, for experiments performed with $Hg_{0.35}In_{0.65}$, an appreciable fraction of the substrate was coated with an electrodeposited Ge film (Figure 6.9c), with the top and bottom of the area covered by the film denoted by the dotted blue and dot-dashed orange lines. The top boundary of the film appeared approximately 2 ± 0.1 mm below the immersion level of the wafer (i.e. white lines in Figure 6.1b). The bottom of the film extended to the bottom edge of the Ge seed substrate. Higher magnification SEM images (Figure 6.9d, inset) showed these films had a high density of circular pits that exposed the underlying surface of the wafer section. Electron back-scatter diffraction (EBSD) measurements of the top of the electrodeposited films (Figure 6.9e) yielded Kikuchi patterns in agreement with Ge(100), i.e. the crystallographic orientation of the underlying wafer section. Identical Kikuchi patterns collected over multiple regions of the films confirmed uniform orientation along the (100) direction. The corresponding pole figures showed only sharp poles consistent with the film orientation being aligned with the [100] direction perpendicular to the film surface. (Figure 6.9f) Cross-sectional analyses showed the film thickness to be 370 ± 120 nm. (Figure 6.8)

'Open' ec-LPE experiments performed with pure liquid Ga also produced macroscopic electrodeposited Ge films, albeit with significantly narrower coverages (Figure 6.9g). These films were strongly adherent to the wafer section surface, spanning the region between the three-phase contact line of the Ge substrate, liquid metal, and liquid electrolyte to a depth ~ 500 μm towards the bottom edge. High magnification SEM images (Figure 6.9h) indicated that these electrodeposited Ge films contained a lower but still noticeable density of circular pits, as seen in the films grown with $Hg_{0.35}In_{0.65}$. Cross-section analyses showed these films were less thick than the $Hg_{0.35}In_{0.65}$ films with an average thickness of 140 ± 30 nm. (Figure 6.8) Nevertheless, EBSD measurements confirmed the (100) orientation of the film (Figure 6.9i-j), consistent with the crystallinity of the seed substrate. 'Open' ec-LPE experiments conducted with *e*-GaIn as the liquid metal yielded the largest area Ge films. These film areas spanned from the immersion line down to a depth ~ 2 mm towards the bottom edge (Figure 6.9k) and occurred on both sides of the seed wafer section (Figure 6.10). SEM imaging of these films (Figure 6.9l) indicated a contiguous coverage with a much lower density of circular pits. Despite the high surface roughness of the epi-films lowering the EBSD signal to noise, measured Kikuchi patterns and corresponding pole

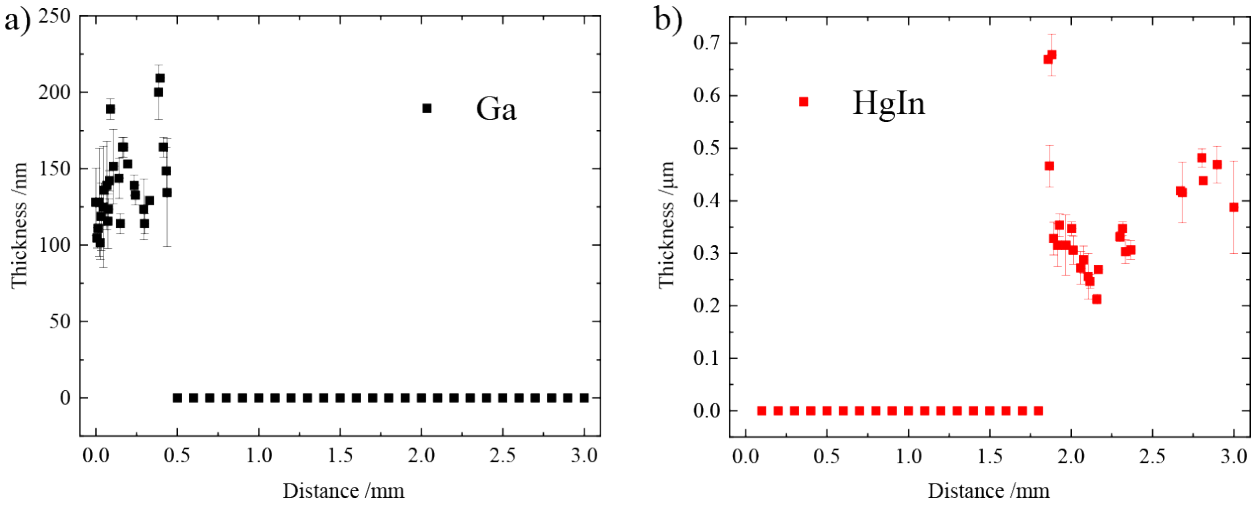

Figure 6.8 Plot of the thickness electrodeposited Ge film using a) Ga and b) $Hg_{0.35}In_{0.65}$ as a function of distance (x) from the interface between liquid metal, substrate, and electrolyte

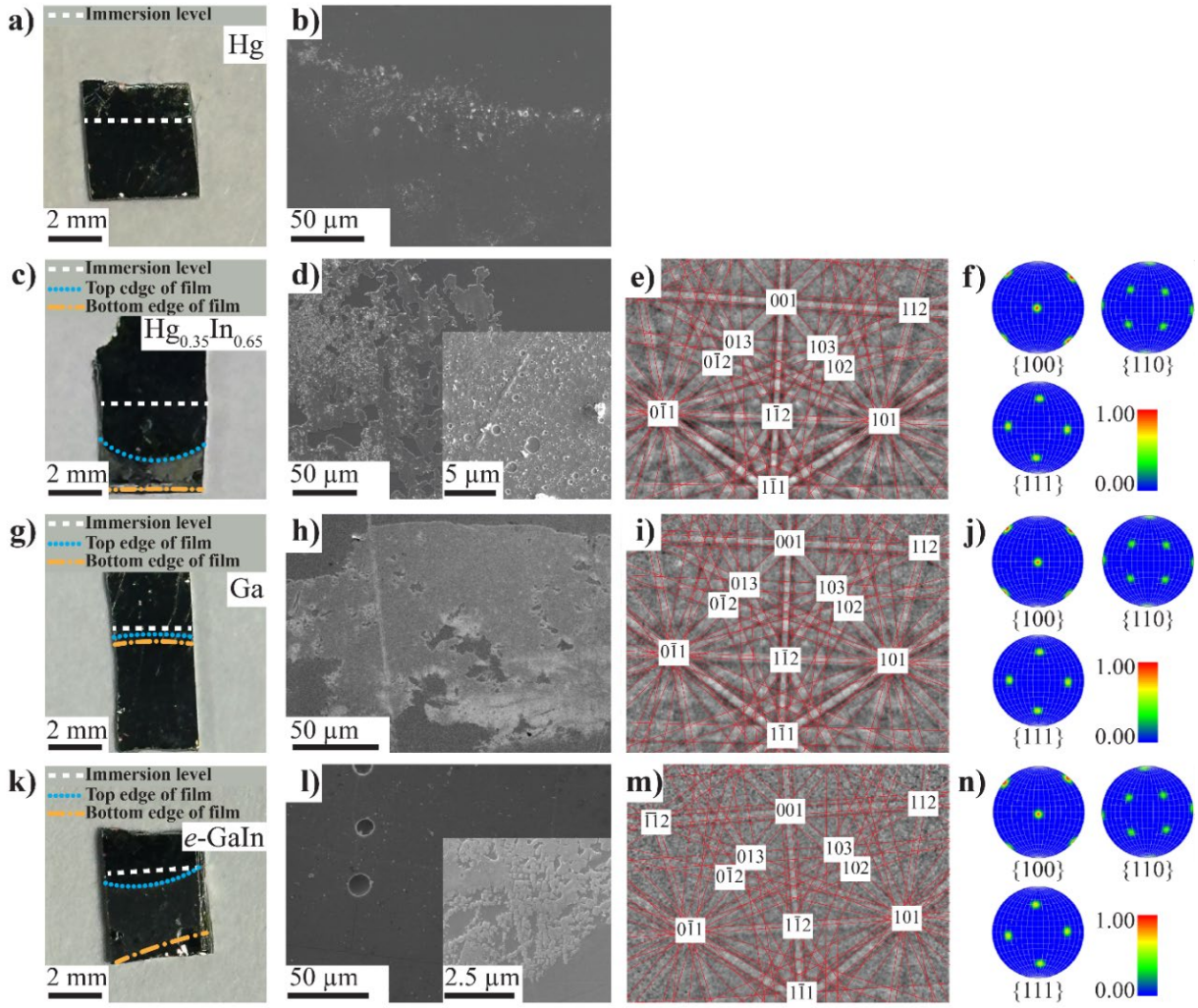

Figure 6.9 Representative images of various Ge(100) wafer sections following 3 h attempts at 'open' ec-LPE of Ge epi-films using either liquid a,b) Hg, c-f) $Hg_{0.35}In_{0.65}$, g-j) Ga, or k-n) *e*-GaIn. Panels a), c), g) and k) show the macroscopic view of the resultant films. The immersion level of each wafer section is indicated with a white dashed line. The top of the epi-film is denoted with a blue dotted line. The bottom edge of the epi-film is marked with an orange dot-dashed line. Panels b, d), h) and l) illustrate representative scanning electron micrographs of the top edge of the electrodeposited material. Inset in l shows the nuclei observed towards the bottom edge of the *e*-GaIn film. Panels e-f), i-j), and m-n) indicate the representative Kikuchi patterns and corresponding pole figures measured by electron back scatter diffraction for each film prepared with liquid $Hg_{0.35}In_{0.65}$, Ga, and *e*-GaIn, respectively.

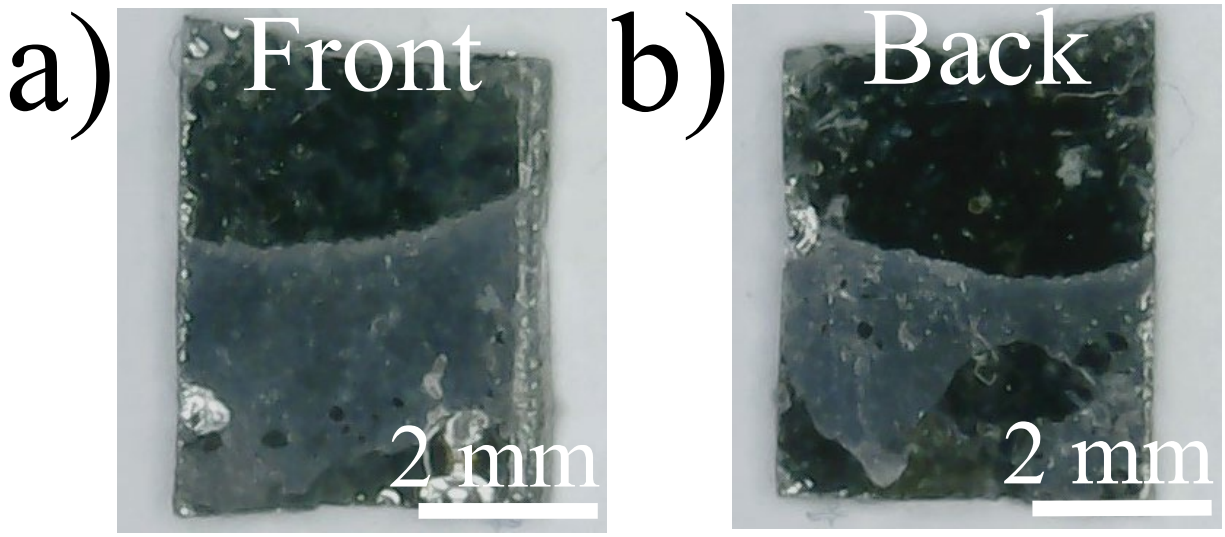

Figure 6.10 Optical micrographs of the a) front and b) back of the Ge electrodeposited film using *e*-GaIn at -1.5 V vs. Ag/AgCl in 0.1 M $Na_2B_4O_7$ and 0.05 M GeO_2 for 3 hours

figures separately denoted exclusive (100) growth (Figure 6.9m-n). At the lower film edge (i.e. closest to the bottom of the seed substrate) where the film was more discontinuous, discrete and obvious square Ge crystallites were seen (Figure 6.9l, inset). The shape and orientation of these nuclei were separately in accord with expectations of crystallites grown off the (100) surface plane.[28]

Since the epi-films grown with *e*-GaIn were noticeably thicker than the other films, the thickness dependence as a function of position was examined by cross-sectional SEM (Figure 6.11). For Ge films prepared with liquid *e*-GaIn at -1.5 V with t = 1 and 3 h, the thickest section was always the region nearest to the three-phase boundary (Figure 6.11a,b). For both times, the epi-film thicknesses decreased rapidly along the direction perpendicular to the immersion line until reaching a plateau (Figure 6.11a,b). Between these two experimental times, the maximum thickness of 8 ± 2 μm was obtained for t = 3 h. Additional experiments were repeated with *e*-GaIn and much longer run times (t = 18 h) in an attempt to increase film coverage and/or thickness. Curiously and contrary to expectations, these experiments consistently yielded epi-films that did not extend all the way to the bottom edge of the seed substrate. Instead, they had comparatively flat profiles and thicknesses that were actually much *less* than for epi-films grown for t = 3 h (Figure 6.11c). Moreover, these epi-films abruptly stopped much closer to the three-phase boundary edge. SEM analysis of the region just below this three-phase contact showed square Ge (100) nuclei suggestive of epitaxy but likely re-dissolution of the electrodeposited films (Figure 6.12). Controls were performed where a previously electrodeposited Ge film by open ec-LPE with *e*-GaIn for t = 3 h was re-immersed into a fresh volume of liquid *e*-GaIn in contact with 0.1 M $Na_2B_4O_7$ blank electrolyte solution. An applied bias was maintained at -1.5 V vs. E(Ag/AgCl, sat. KCl) while this film was immersed in the fresh liquid metal for t = 18 h. Under these conditions, there was no active Ge electrodeposition but otherwise every other aspect was identical to an 'open' ec-LPE experiment. In these control experiments, the Ge film thickness and areal coverage unambiguously decreased (Figure 6.13), suggesting that electrodeposited Ge can redissolve back into the liquid metal if it is not saturated with Ge.

The thickness-distance profiles were quantitatively analyzed (Figure 6.11d), with the following assumptions. First, the three phase boundary between the liquid metal, seed substrate, and electrolyte was site of initial nucleation. Second, the rates of Ge adatom dissolution into the liquid metal and transport of Ge adatoms along the liquid metal surface to the three-phase boundary

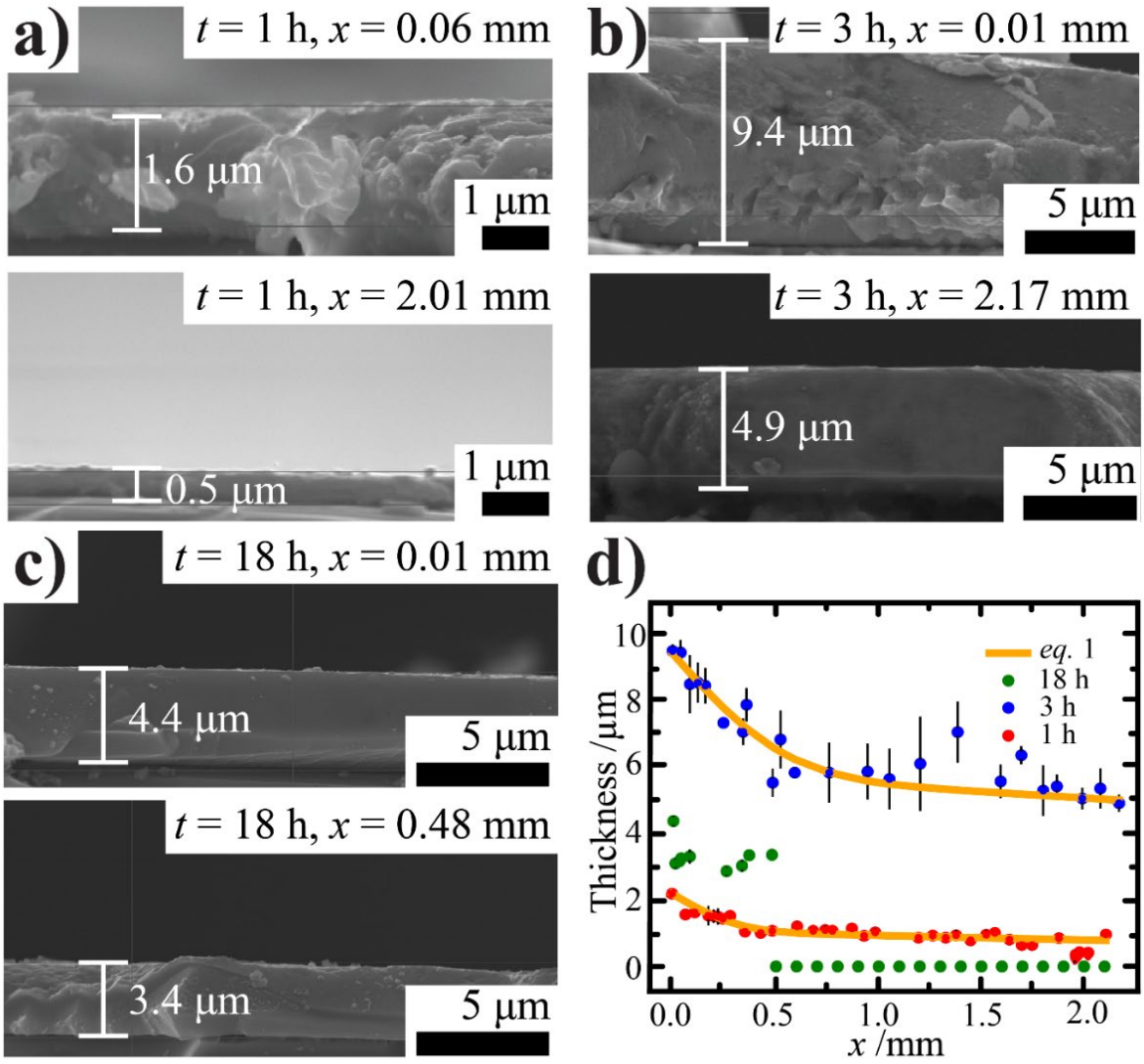

Figure 6.11 a-c) Cross-sectional scanning electron micrographs at two different positions along the vector perpendicular to the white lines in Figure 6.9 for Ge epi-films electrodeposited with liquid *e*-GaIn pool electrodes biased at -1.5 V vs. *E*(Ag/AgCl) for *t* = a) 1 h, b) 3h, and c) 18 h. d) Thickness vs distance along the vector perpendicular to the white lines in Figure 6.9 for Ge epi-films prepared with liquid *e*-GaIn biased at -1.5 V vs. *E*(Ag/AgCl) for *t* = 1, 3, and 18 h. The lines are the best fits according to *Equation* 6.1.

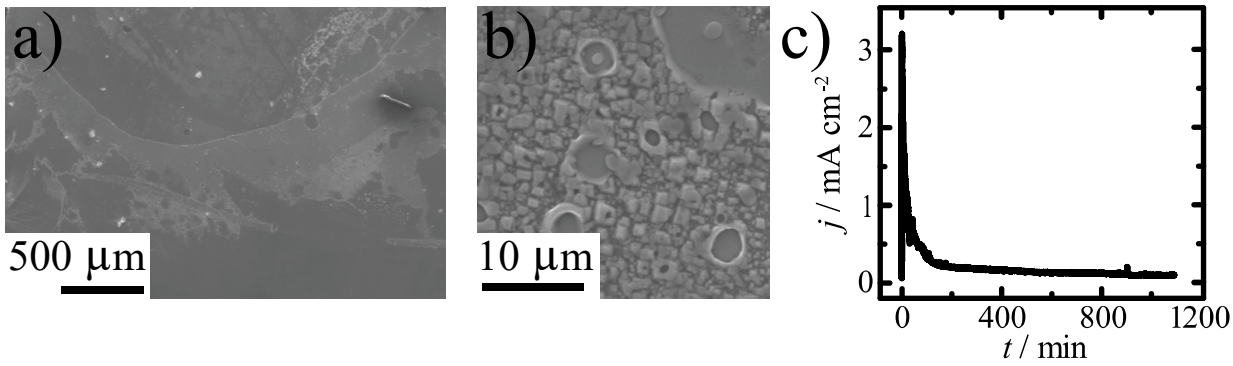

Figure 6.12 Scanning electron micrograph of the Ge electrodeposited film in plain a) and close-up b) views using Ga for 18 hours and the corresponding current-transient curve c)

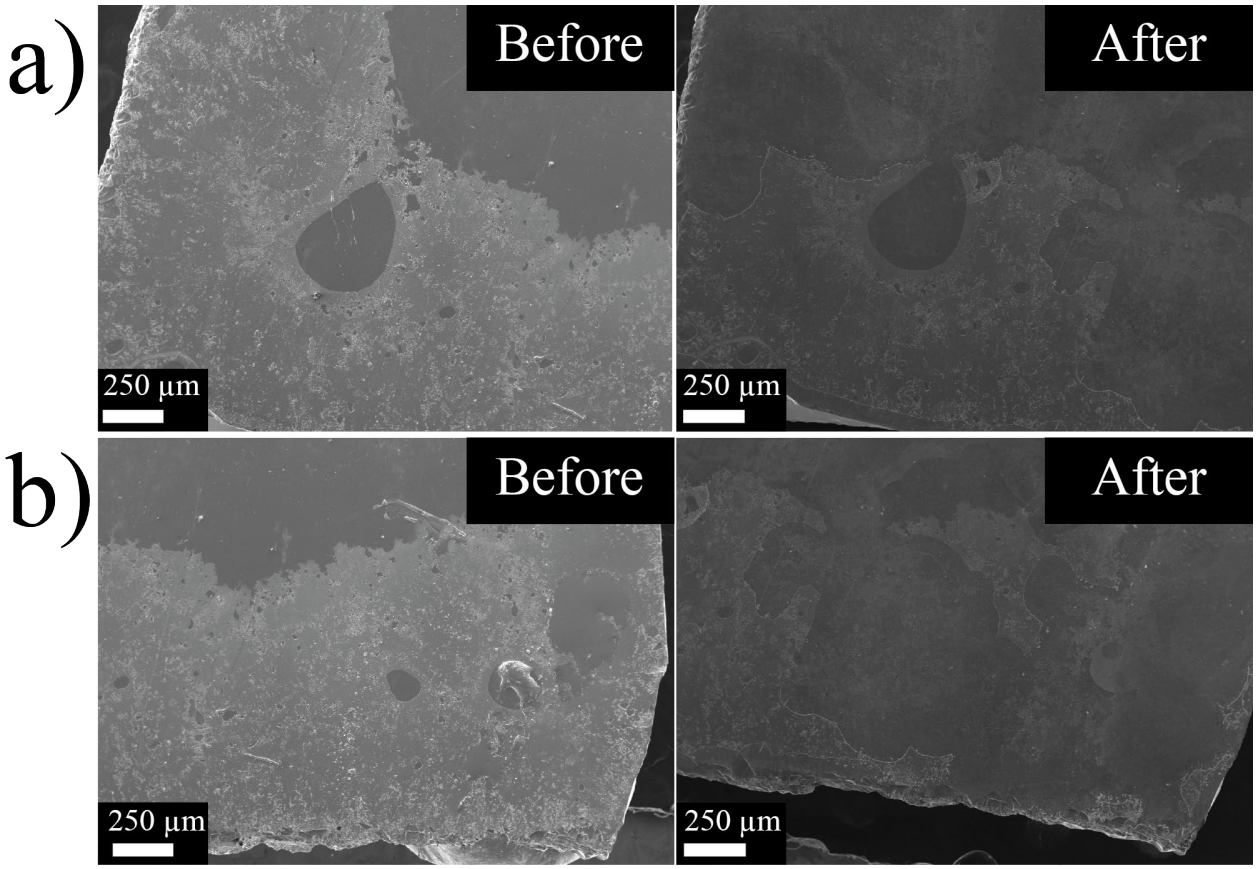

Figure 6.13 Scanning electron micrographs of a) bottom left and b) top right of an electrodeposited Ge film using *e*-GaIn before and after submerged in *e*-GaIn droplet under -1.5 V vs. Ag/AgCl in 0.1 M $Na_2B_4O_7$ for 18 hours

were not rate-limiting. Third, since no epi-films were seen above the immersion line, the flux of electroreduced Ge to the three-phase boundary caused nucleation and growth of the epi-film down into the liquid metal/seed substrate interface but not up across the seed substrate/electrolyte interface. Accordingly, the thickness profile was assumed analogous to the concentration profile expected for the product of a redox process at an electrode interface, i.e. one-dimensional diffusion produces a gradient described by a complementary error function (erfc) where the maximum amount of product is at the electrode interface and its concentration decays along the vector perpendicular to the surface of the electrode. The argument of 'erfc' includes the product of the experimental time, t, and a constant describing the magnitude of diffusion, D.[29, 30]

An initial model based on the aforementioned assumptions and just one diffusive process could not accurately describe the data in Figure 6.11. Since the thickness-distance profiles decayed to a non-zero thickness, the profiles were then modeled as the summation of two distinct diffusive processes using *Equation* 6.1,

$$T(x) = T_0\left(\operatorname{erfc}\left(\frac{x}{2\sqrt{D_1 t}}\right) + \operatorname{erfc}\left(\frac{x}{2\sqrt{D_2 t}}\right)\right)$$

Equation 6.1

where $T(x)$ is the film thickness at position x along the vector perpendicular to the immersion line, D_n is the diffusion coefficient of the nth process, and T_0 is the max thickness of the film based on the flux of Ge atoms into the liquid metal. In this treatment, T_0 was taken to be ½ of the max film thickness. The data for the experiments performed with t = 1 and 3 h were described by diffusion constants of 9 x10^{-8} and 6 x 10^{-5} cm^2 s^{-1}. The smaller diffusion constant was broadly consistent with diffusion of In adatoms along a solid surface (e.g. ~3 x 10^{-7} cm^2 s^{-1} for In on solid tungsten at 25 °C).[31] The larger diffusion constant was similar to solute diffusion at room temperature within bulk liquid Ga (~10^{-5} cm^2 s^{-1}).[32, 33]

The film/substrate intferfaces for the films grown with *e*-GaIn and $Hg_{0.35}In_{0.65}$ were examined in more detail with TEM and STEM imaging (see Figure 6.3 for information on sample preparation). HAADF STEM images of the substrate/film interface of the experiments performed with $Hg_{35}In_{65}$ showed a high density of defects, evidenced as darkened regions (Figure 6.14a,c). Dark areas in HAADF STEM images denote regions with less electron density, corresponding to void space within the epi-film at the interface. We interpret these voids to be the same circular pits observable in Figure 6.9. High resolution TEM imaging corroborated this point, with a clear

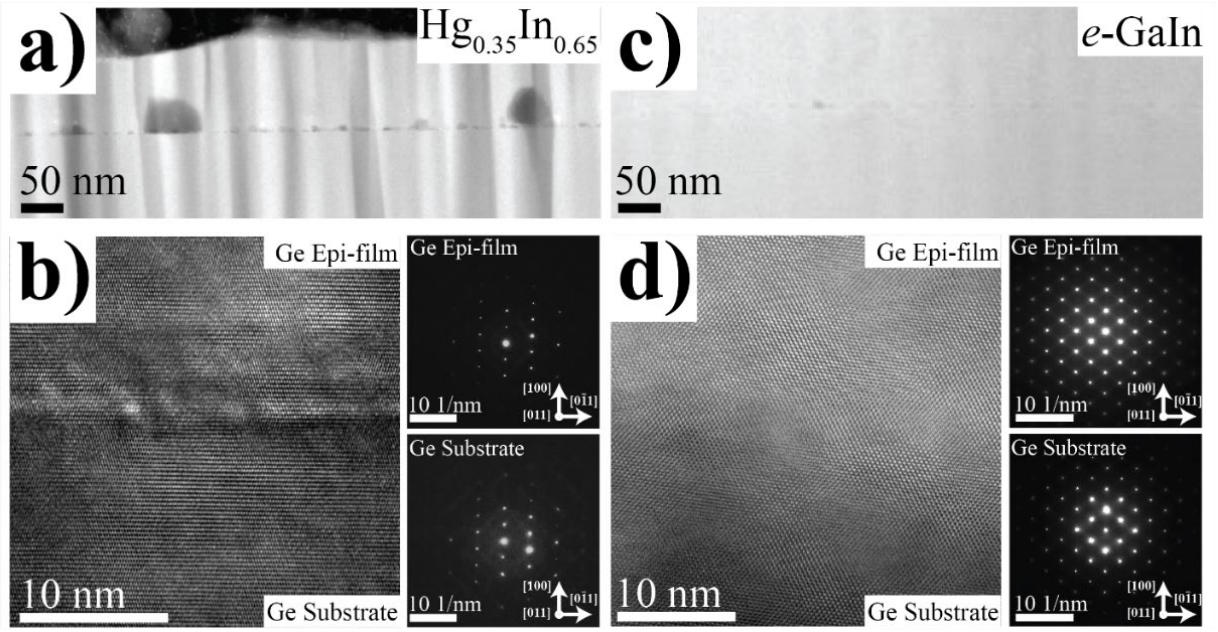

Figure 6.14 Cross-sectional electron micrographs of the interface between a Ge(100) seed substrate and electrodeposited Ge-epifilm using either liquid a,b) $Hg_{0.35}In_{0.65}$ or c,d) *e*-GaIn liquid metal electrodes. Panels a) and c) illustrate high-angle annular dark-field (HAADF) scanning transmission electron micrographs of the respective interfaces. Panels b) and d) show high resolution bright-field images of the respective interfaces, with selected area electron diffraction images obtained from the respective seed substrate and Ge epi-films.

change in contrast at the interface between the two regions. (Figure 6.14b) The interface for epi-films produced with *e*-GaIn showed no discontinuities or obvious defects across the junction (Figure 6.14d). Selected area diffraction of both the electrodeposited film area and the Ge(100) substrate was also performed for both films (Figure 6.14b,d). Both sets of patterns are indexed similarly to the Ge[011] cross-sectional direction, consistent with epitaxial growth. Streaking between spots was consistently observed in the patterns obtained for the epitaxial Ge films grown with *e*-GaIn, indicating twinning defects throughout the crystal structure along the [111] direction, in accord with prior ec-LPE reports.[22] These same twinning defects can be observed in the TEM images for the epitaxial Ge films grown with *e*-GaIn and were not apparent in the electrodeposited Ge films prepared with $Hg_{0.35}In_{0.65}$. Additionally, no appreciable Hg incorporation was detected, while In was measured by EDX at 2.0 ± 0.3 at %. (Figure 6.15) For comparison, Ga and In were incorporated at 15 ± 2 at % and 1 ± 0.1 at %, respectively, for the films grown with *e*-GaIn. (Figure 6.16)

6.5 Discussion

The presented data support three key points. First, epitaxial growth of electrodeposited Ge films by ec-LPE was achieved without any externally applied pressure to mitigate electrocapillarity of the liquid metal, confirming the possibility of 'open' ec-LPE. Second, there was a clear dependence on the efficacy of 'open' ec-LPE with different liquid metals. However, the utility of a liquid metal for 'open' ec-LPE did not correlate solely with either the electrochemical activity for H_2 evolution, with the wetting with crystalline Ge, or with Ge solubility. Rather, amongst the group of Hg- and Ga- containing liquid metals, the best films were observed with liquid metals containing In. Third, the presented results suggest what aspects more refined versions of 'open' ec-LPE should possess. These points are further discussed below.

6.5.1 Epitaxial Germanium Films

These experiments established that the three-phase boundary involving a liquid metal, liquid electrolyte, and solid substrate facilitates epitaxial crystal growth during electrodeposition. The exact position of the three-phase boundary relative to the macroscopic interpretation of the immersion line depends on the wettability of the liquid metal towards the solid substrate. Upon immersion of the wafer into the liquid metal, the metal surface bends downwards, forming a meniscus. The data are clear that the larger the wetting contact angle is, the deeper the actual three-

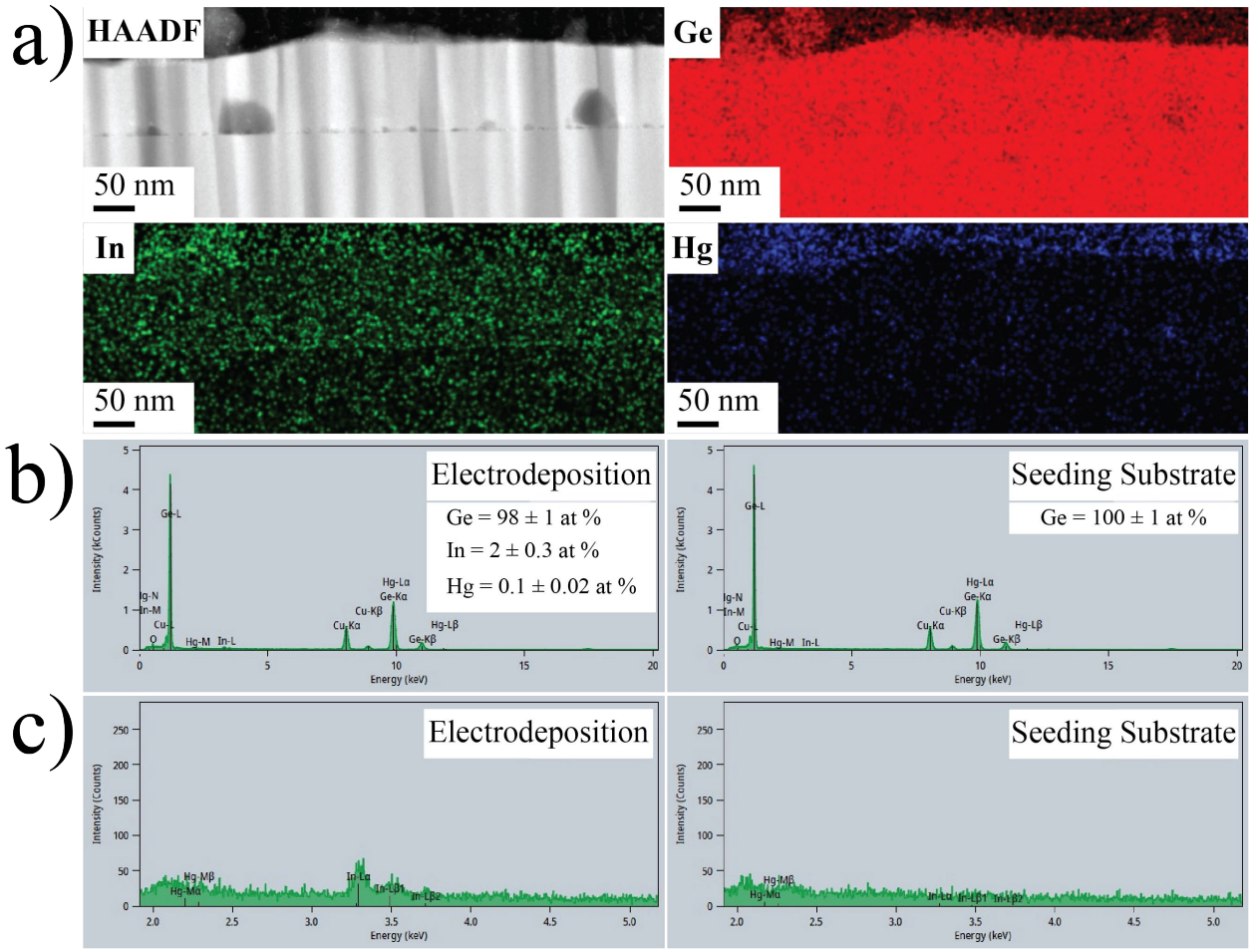

Figure 6.15 a) High-angle annular dark field scanning transmission electron micrograph (HAADF – STEM) of the interface between the Ge film grown using $Hg_{0.35}In_{0.65}$ and Ge substrate with corresponding energy dispersive spectroscopy signal for Ge, In and Hg with the corresponding b) EDS spectra showing the peak signals of each element. c) Zoomed EDS spectra in the region around the less intense Hg and In peak signal.

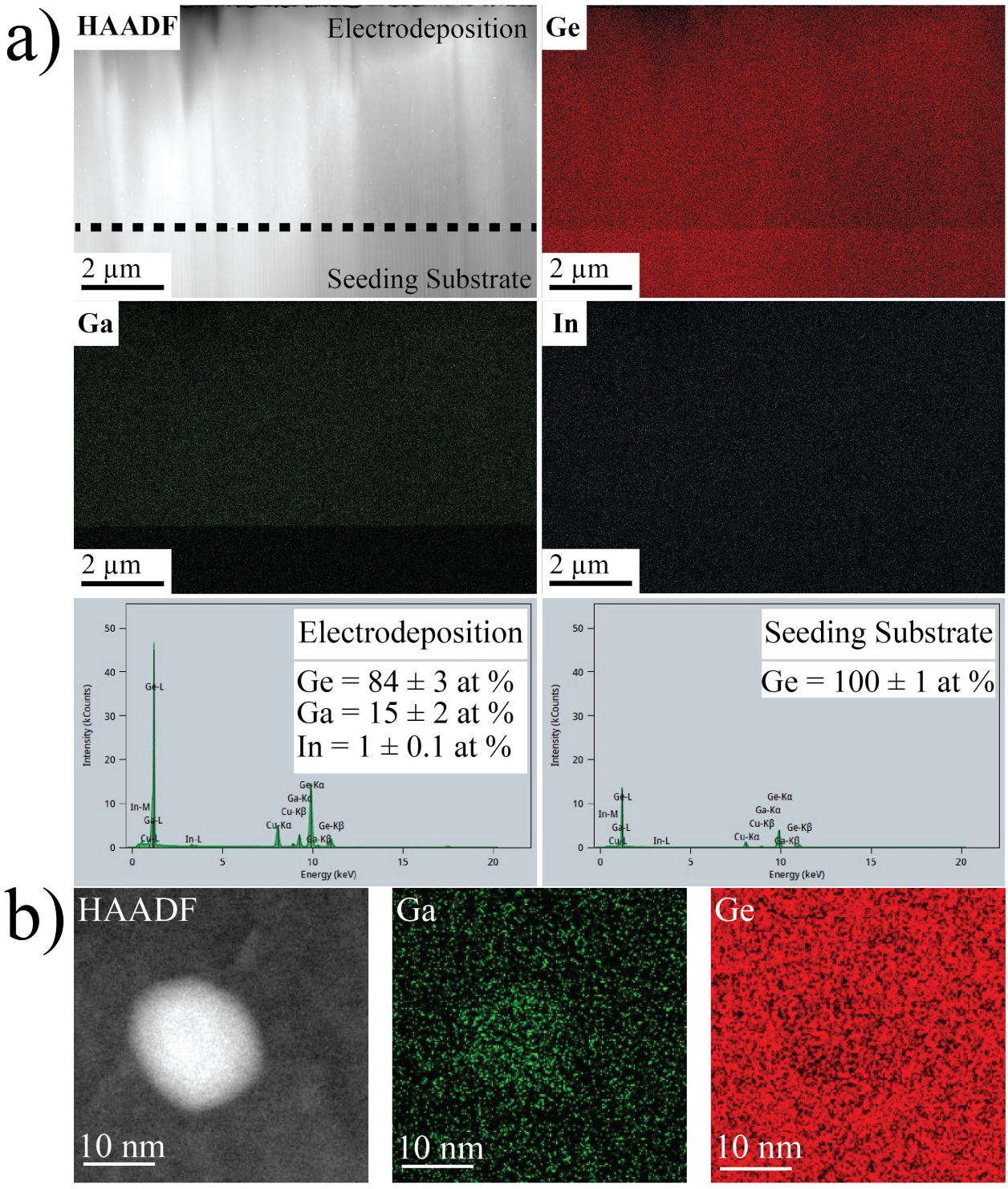

Figure 6.16 a) High-angle annular dark field scanning transmission electron micrograph (HAADF – STEM) of the interface between the Ge film grown using *e*-GaIn and Ge substrate with corresponding energy dispersive spectroscopy signal for Ge, Ga, and In. b) HAADF – STEM image of Ga droplet occluded in the Ge electrodeposited film with corresponding energy dispersive spectroscopy signal for Ge and Ga.

phase boundary is (relative to the macroscopic immersion line). The data also indicate that no matter where the three-phase boundary occurs, there is always the possibility of sufficiently thin liquid metal to allow electroreduced solute atoms to nucleate on the liquid metal/solid interface rather than the liquid metal/liquid electrolyte interface. Accordingly, the possibility of 'open' ec-LPE has been established.

Previous reports of ambient-condition semiconductor ec-LPE had four defining characteristics:[21, 22] (*1*) film crystallinity defined by the underlying seeding wafer; (*2*) liquid metal incorporation in the electrodeposited films; (*3*) prevalence of twinning defects that alleviated the strain of the liquid metal incorporation; and (*4*) junctions devoid of interfacial oxides. The presented data are consistent with the notion that 'open' ec-LPE produces electrodeposited semiconductor films that possess these same four characteristics. In this way, this report implicitly affirms that these four observables are not consequences of the original conception of ec-LPE, i.e the use of a pressurized cell with a compressive membrane or metal wetting layers that facilitate wetting between the liquid metal and the seed substrate. Instead, these observables seem to be direct possibilities in any electrodeposition where the crystal growth is seeded by a solid substrate in contact with a liquid metal electrode.

One apparent challenge with the 'open' ec-LPE approach regarding the quality of epi-films is the presence of bubbles. The formation of circular voids within the electrodeposited Ge films was consistent with the entrapment of a gas bubble (i.e. H_2) during the film growth. The 'open' ec-LPE approach appears prone to this possibility since proton/water reduction can occur at the three-phase boundary. In the prior 'closed ec-LPE' reports, the nucleation and crystal growth regions were physically separated from the aqueous electrolyte. No steps were taken here to suppress the possibility of bubble formation, but the presented data clearly support the idea that media that inhibit bubble formation will decrease their impact on film growth. Specifically, the current density for H_2 evolution with *e*-GaIn was five times smaller than the corresponding current density with $Hg_{0.35}In_{0.65}$ and pure Ga. Accordingly, these films featured noticeably lower densities of circular pits. This observation suggests that other steps that minimize bubble formation (e.g. changing the surface tension of the liquid electrolyte,[34-37] identifying other liquid metal compositions with even lower activity for proton/water reduction) ought to improve the film quality with respect to the density of circular voids.

6.5.2 Liquid Metal Characteristics

This work established clearly that the activity of the liquid metal for electroreduction of dissolved GeO_2, the wetting contact angle between the liquid metal and solid crystalline Ge, and the solubility of Ge in the liquid metals were not individually the defining factors that facilitated the 'open' ec-LPE process. Liquid Ga exhibited the highest currents for electroreduction of dissolved GeO_2. Liquid Ga also possesses the highest solubility for Ge at room temperature ($\leq$ 1 at. %),[38, 39] much higher than the solubility exhibited by Hg (3×10^{-8} at %)[40] and the inferred solubility for *e*-GaIn since the solubility of Ge in liquid In is much lower (10^{-2} to 10^{-3} at. %).[41] Yet liquid Ga consistently yielded very minimal evidence of Ge epi-films. Similarly, neither the highest or lowest wetting contact angles were correlated with successful growths, as evidenced by the meager film growths with both liquid Hg and liquid Ga. The absolute wetting contact angles also were not directly predictive, as liquid Ga and *e*-GaIn had statistically indistinguishable values while *e*-GaIn was demonstratively more conducive for the 'open' ec-LPE concept. Similarly, $Hg_{0.35}In_{0.65}$ exhibited a noticeably higher wetting contact angle than liquid Ga but still yielded much larger area epi-films.

The consistent attribute of the liquid metal that was correlated with successful film growth was the inclusion of In. As indicated above, the primary action of In is likely not to significantly increase the bulk solubility of the liquid metal towards the solute (i.e. Ge in this work). Instead, the presence of In seems to facilitate two other aspects of ec-LPE. First, In seems to increase the probability of heterogeneous nucleation. The miniscule nucleation of Ge in liquid Hg and liquid Ga are consistent with this premise. Second, as noted previously,[27, 42] In can be a surfactant in crystal growth processes.[43, 44] The smaller diffusion coefficients determined from fits of Figure 6.11 are consistent with surface diffusion of In along a solid (non-reactive) surface. In contrast, the surface diffusivities of Ge adatoms on analogous solid surfaces is known to be markedly slower (e.g. ~3×10^{-13} cm^2 s^{-1} for Ge on Si(100) at 250 °C),[45] too slow to be relevant in the data in Figure 6.11. Hence, we infer that In acts as a surfactant in this system and specifically facilitates transport of Ge along the solid surface of the growing crystal front, introducing new Ge at the three-phase boundary move along the solid nascent epi-film (Figure 6.17). This process causes the epi-film thickness to fall off rapidly at even short distances away from the three-phase boundary because surface diffusion along the solid surface is slow relative to the total experimental time. If surface diffusion were the only pathway to grow the epi-film, then the epi-films should never extend down to an appreciable depth. However, this was clearly not the case with *e*-GaIn. We surmise that the

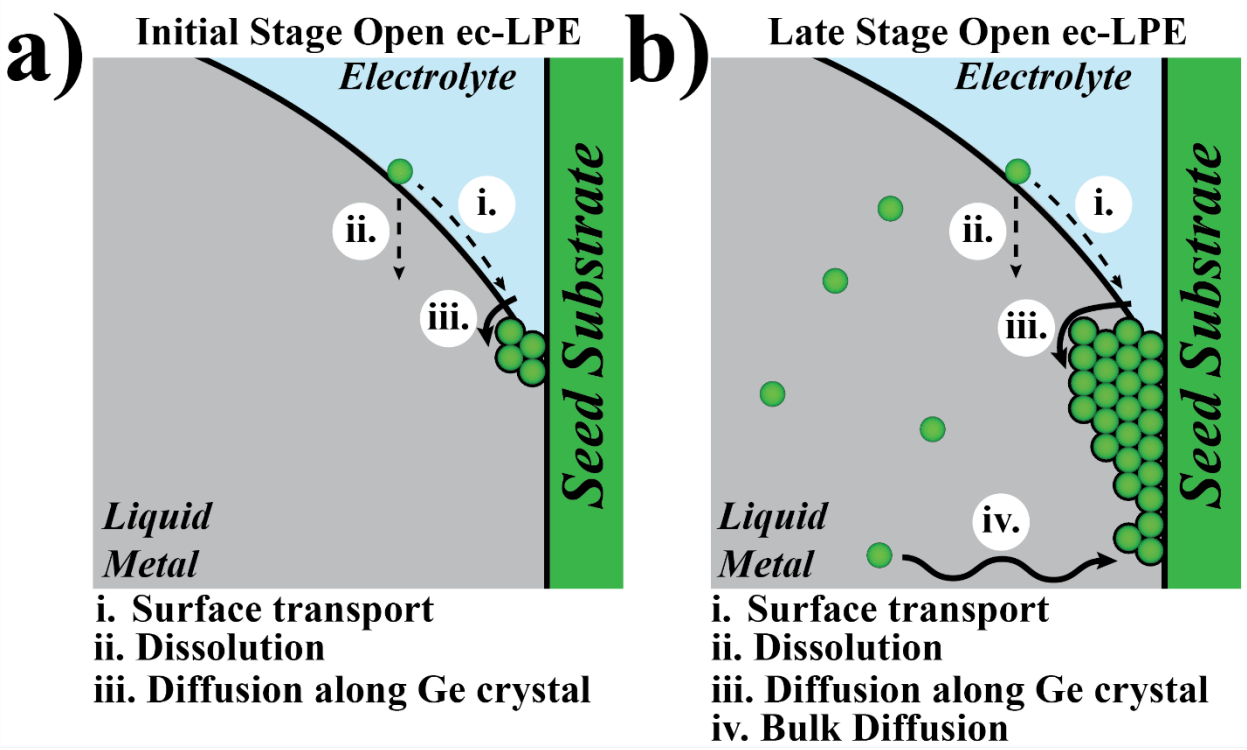

Figure 6.17 Schematic depiction of the a) initial and b) latter stages of the 'open' ec-LPE process at the three-phase boundary. The dashed arrow labeled 'i.' denotes transport of electroreduced Ge adatoms along the liquid metal surface. The dashed arrow labeled 'ii.' indicates the dissolution of electroreduced Ge adatoms into the bulk liquid metal. The solid arrow labeled 'iii.' illustrates diffusion of electroreduced Ge adatoms along the solid surface of a Ge crystal. The solid arrow labeled 'iv.' shows the diffusion of Ge dissolved in the bulk liquid metal. The assumption in this work is that the solid arrows are rate-limiting with respect to epi-film growth while the dashed arrows are not.

larger area epi-films obtained with liquid *e*-GaIn are only possible because of a second diffusive pathway. Specifically, solute diffusion through the liquid metal can also supply adatoms to the crystal growth front (Figure 6.17). Since diffusion through a non-viscous liquid is orders of magnitude faster, the thickness profile ought to be both flatter and extend further down the substrate. At present, it seems unlikely that the presence of In specifically changes the bulk diffusivity since the viscosity of *e*-GaIn is not appreciably different than Ga.[46, 47] Moreover, slight variations in the value of D_2 in modeling with *Equation* 6.1 did not appreciably affect differences in the thickness-distance fits. Only diminutions of D_2 by an order of magnitude worsened the fits, which are not physically plausible. Accordingly, once films are nucleated, it is likely that film growths can proceed similarly with or without In in the liquid metal. However, the practical challenge of changing liquid metal compositions during a growth limit the utility of this concept.

6.5.3 Suggestions for refined 'open' ec-LPE Strategies

Based on the presented evidence, it seems clear that 'open' ec-LPE will require the use of liquid metals with surfactant species. Besides In, elements such as Sn,[48] Bi,[49] or Sb[50] ought to be considered as potential constituents in a target liquid metal alloy composition. Naturally, their inclusion will affect the metal alloy melting point and thus may define what operating temperatures (and correspondingly electrolytes) are best for 'open' ec-LPE. Irrespective, the data also speak to a more practical point about growing large area epi-films by 'open' ec-LPE.

The static approach taken here, i.e. leave the seed substrate immersed at a constant, fixed depth in the liquid metal, clearly did not yield films with arbitrarily large areal coverages. Although this aspect might improve with a hypothetical 'better' liquid metal, it remains unlikely that epi-films uniformly coating a large wafer substrate could be produced in exactly this manner. However, we can envision a process where the seed substrate is translocated vertically during an 'open' ec-LPE process (Figure 6.18). In this way, the three-phase boundary constantly moves and therefore extends the depth (along the substrate surface in a vector normal to the three-phase boundary) that the epi-films would be deposited.

This concept is quite common in traditional melt crystal growths, where a 'puller' vertically displaces a seed crystal to draw out a crystalline boule.[51] Moreover, in conventional LPE, translocation of a liquid metal growth solvent along/across a deposition substrate is a well-established strategy.[52] The data presented here suggest three things about performing 'open' ec-

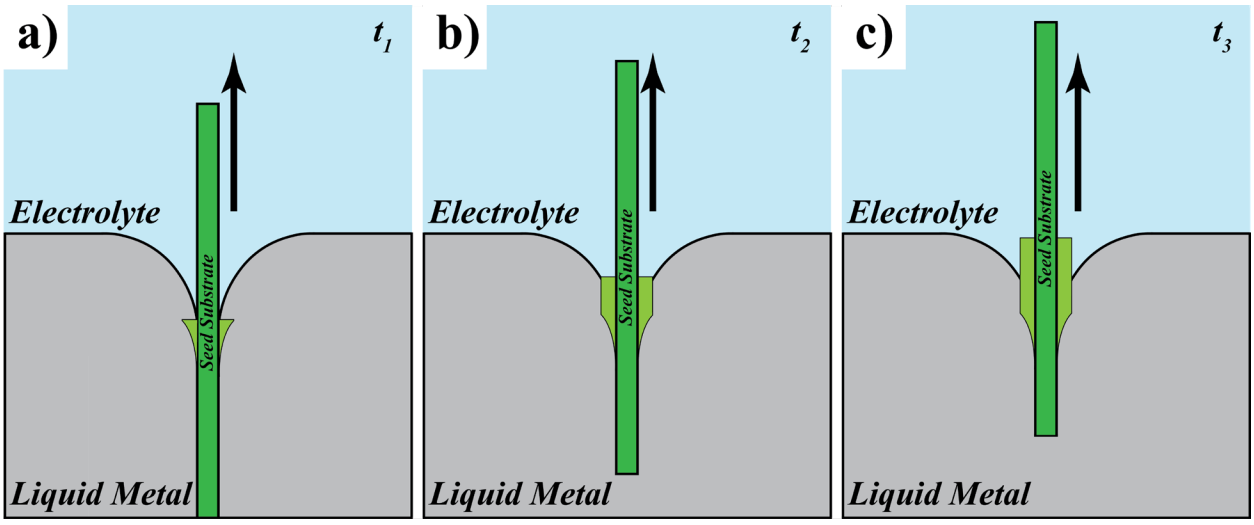

Figure 6.18 Schematic depiction of three different time points a) t_1 < b) t_2 < c) t_3 in a hypothetical 'open' ec-LPE process where the seed substrate is vertically translocated through the liquid metal pool electrode.

LPE with translocation. First, the liquid metal should be pre-saturated with the solute (i.e. Ge in this work) to limit re-dissolution of the epi-film into the liquid metal far away from the three-phase boundary. Pre-saturation would also minimize the initial induction time to just reach the critical supersaturation point to start epi-film growth. Second, to further avoid any epi-film re-dissolution back into the liquid metal, vertical translocation where the substrate is pulled up through the liquid metal would likely be more efficient (Figure 6.18). Doing so might also help dislodge/remove bubbles from parasitic solvent electrolysis processes. Third, the rate of vertical translocation should be chosen in consultation with the operative kinetic and mass transport velocities that define the epi-film deposition rate. A beneficial aspect of electrochemistry is that the kinetics for the electroreduction step can be precisely regulated through the chosen applied bias/current. Accordingly, it may be possible to optimize the speed by which an epi-film could be deposited by 'open' ec-LPE with careful selection of the electrochemical parameters.

6.6 Conclusions

This work introduces the concept of 'open' ec-LPE, a method enabling single-crystal semiconductor growth at room temperature and ambient pressures. The data presented suggests that Ge(100) epi-films can be synthesized electrochemically on an external Ge seeding substrate using a liquid metal electrode. Liquid metals such as Hg, $Hg_{35}In_{65}$, Ga, and *e*-GaIn were employed in this study. Despite differences in wetting interactions and solubility toward Ge, the most successful film growth occurred with In-containing liquid metals ($Hg_{35}In_{65}$ and *e*-GaIn). This can be attributed to the well-established role of In as a surface surfactant, which facilitates the transport of Ge to the crystal growth plane. Among these, Ge epi-films grown from *e*-GaIn exhibited the highest uniformity and coverage. Further investigation into minimizing bubble formation within the electrolyte, as well as the exploration of other liquid metal compositions, could broaden the potential of 'open' ec-LPE. Additional effort in performing 'open' ec-LPE with translocation can be a new method for creating contiguous large area semiconductor films. Such methods appear imminently suitable for the facile synthesis of hyperdoped group IV semiconductor epi-films. More extensive study with other liquid metal compositions is needed to determine if epi-films with higher purities are possible.

6.7 References

1. Gan, C. L.; Chung, M.-H.; Zou, Y.-S.; Huang, C.-Y.; Takiar, H., Technological sustainable materials and enabling in semiconductor memory industry: A review. *e-Prime - Advances in Electrical Engineering, Electronics and Energy* **2023,** *5*, 100245.
2. Chandrasekaran, N. In *Intelligent, Data-Driven Approach to Sustainable Semiconductor Manufacturing*, 2022 6th IEEE Electron Devices Technology & Manufacturing Conference (EDTM), 6-9 March 2022; 2022; pp 1-5.
3. Zhu, S.; Hu, H.; Yang, H.; Qu, Y.; Li, Y., Mini-Review of Best Practices for Greenhouse Gas Reduction in Singapore's Semiconductor Industry. *Processes* **2023,** *11* (7), 2120.
4. Mohammad, W.; Elomri, A.; Kerbache, L., The Global Semiconductor Chip Shortage: Causes, Implications, and Potential Remedies. *IFAC-PapersOnLine* **2022,** *55* (10), 476-483.
5. Ma, L.; Yu, Z.; Ma, W.; Qing, S.; Wu, J., Assessment and Study on the Impact on Environment by Multi-crystalline Silicon Preparation by Metallurgical Route. *Silicon* **2019,** *11* (3), 1383-1391.
6. Myronov, M., Chapter 3 - Molecular Beam Epitaxy of High Mobility Silicon, Silicon Germanium and Germanium Quantum Well Heterostructures. In *Molecular Beam Epitaxy (Second Edition)*, Henini, M., Ed. Elsevier: 2018; pp 37-54.
7. Kshetri, N.; Voas, J., Where's the Silicon? *Computer* **2021,** *54* (8), 11-12.
8. Xu, C.; Wallace, P. M.; Ringwala, D. A.; Menéndez, J.; Kouvetakis, J., Fabrication of Ge:Ga Hyperdoped Materials and Devices Using CMOS-Compatible Ga and Ge Hydride Chemistries. *ACS Applied Materials & Interfaces* **2018,** *10* (43), 37198-37206.
9. Strohbeen, P. J.; Brook, A. M.; Sarney, W. L.; Shabani, J., Superconductivity in hyperdoped Ge by molecular beam epitaxy. *AIP Advances* **2023,** *13* (8).
10. Tong, Z.; Bu, M.; Zhang, Y.; Yang, D.; Pi, X., Hyperdoped silicon: Processing, properties, and devices. *Journal of Semiconductors* **2022,** *43* (9), 093101.
11. Spitzer, W. G.; Trumbore, F.; Logan, R., Properties of heavily doped n-type germanium. *Journal of Applied Physics* **1961,** *32* (10), 1822-1830.
12. von den Driesch, N.; Stange, D.; Wirths, S.; Mussler, G.; Holländer, B.; Ikonic, Z.; Hartmann, J. M.; Stoica, T.; Mantl, S.; Grützmacher, D.; Buca, D., Direct Bandgap Group IV Epitaxy on Si for Laser Applications. *Chemistry of Materials* **2015,** *27* (13), 4693-4702.
13. Hellings, G.; Wuendisch, C.; Eneman, G.; Simoen, E.; Clarysse, T.; Meuris, M.; Vandervorst, W.; Posselt, M.; De Meyer, K., Implantation, Diffusion, Activation, and Recrystallization of Gallium Implanted in Preamorphized and Crystalline Germanium. *Electrochemical and Solid-State Letters* **2009,** *12* (12), H417.
14. Barkby, J. W.; Moro, F.; Perego, M.; Taglietti, F.; Lidorikis, E.; Kalfagiannis, N.; Koutsogeorgis, D. C.; Fanciulli, M., Fabrication of nitrogen-hyperdoped silicon by high-pressure gas immersion excimer laser doping. *Scientific Reports* **2024,** *14* (1), 19640.
15. Fahrenkrug, E.; Gu, J.; Maldonado, S., Electrodeposition of Crystalline GaAs on Liquid Gallium Electrodes in Aqueous Electrolytes. *Journal of the American Chemical Society* **2013,** *135* (1), 330-339.
16. DeMuth, J.; Ma, L.; Fahrenkrug, E.; Maldonado, S., Electrochemical Liquid-Liquid-Solid Deposition of Crystalline Gallium Antimonide. *Electrochimica Acta* **2016,** *197*, 353-361.
17. Gu, J.; Fahrenkrug, E.; Maldonado, S., Direct Electrodeposition of Crystalline Silicon at Low Temperatures. *Journal of the American Chemical Society* **2013,** *135* (5), 1684-1687.

18. Carim, A. I.; Collins, S. M.; Foley, J. M.; Maldonado, S., Benchtop Electrochemical Liquid–Liquid–Solid Growth of Nanostructured Crystalline Germanium. *Journal of the American Chemical Society* **2011,** *133* (34), 13292-13295.
19. Wu, H.; Hazelnis, J. P.; Maldonado, S., Understanding and Expanding the Prospects for Electrosynthesis with Liquid Metal Electrodes. *Accounts of Chemical Research* **2023,** *56* (7), 846-855.
20. Fahrenkrug, E.; Maldonado, S., Electrochemical Liquid–Liquid–Solid (ec-LLS) Crystal Growth: A Low-Temperature Strategy for Covalent Semiconductor Crystal Growth. *Accounts of Chemical Research* **2015,** *48* (7), 1881-1890.
21. Demuth, J.; Fahrenkrug, E.; Ma, L.; Shodiya, T.; Deitz, J. I.; Grassman, T. J.; Maldonado, S., Electrochemical Liquid Phase Epitaxy (ec-LPE): A New Methodology for the Synthesis of Crystalline Group IV Semiconductor Epifilms. *Journal of the American Chemical Society* **2017,** *139* (20), 6960-6968.
22. Downes, N.; DeMuth, J.; Waelder, J.; Cheek, Q. B.; Bartels, H.; Maldonado, S., Si Electrochemical Liquid Phase Epitaxy: Low-Temperature Growth of Hyperdoped Epitaxial Si Films. *Chemistry of Materials* **2022,** *34* (24), 10861-10872.
23. Yu, R.; Han, J.; Chi, Y.; Zheng, J.; Fuchs, R.; Ghasemian, M. B.; Rahim, M. A.; Tang, S. Y.; Mao, G.; Kalantar-Zadeh, K., Impact of minor alloy components on the electrocapillarity and electrochemistry of liquid metal fractals. *Advanced Functional Materials* **2024,** *34* (31), 2301348.
24. Eaker, C. B.; Dickey, M. D., Liquid metal actuation by electrical control of interfacial tension. *Applied Physics Reviews* **2016,** *3* (3), 031103.
25. Schindelin, J.; Arganda-Carreras, I.; Frise, E.; Kaynig, V.; Longair, M.; Pietzsch, T.; Preibisch, S.; Rueden, C.; Saalfeld, S.; Schmid, B.; Tinevez, J.-Y.; White, D. J.; Hartenstein, V.; Eliceiri, K.; Tomancak, P.; Cardona, A., Fiji: an open-source platform for biological-image analysis. *Nature Methods* **2012,** *9* (7), 676-682.
26. Eaker, C. B.; Khan, M. R.; Dickey, M. D., A Method to Manipulate Surface Tension of a Liquid Metal via Surface Oxidation and Reduction. *The Journal of Visualized Experiments* **2016,** (107), e53567.
27. Pattadar, D.; Cheek, Q.; Sartori, A.; Zhao, Y.; Giri, R. P.; Murphy, B.; Magnussen, O.; Maldonado, S., Evidence for Facilitated Surface Transport during Ge Crystal Growth by Indium in Liquid Hg–In Alloys at Room Temperature. *Crystal Growth & Design* **2021,** *21* (3), 1645-1656.
28. Mo, Y. W.; Savage, D. E.; Swartzentruber, B. S.; Lagally, M. G., Kinetic pathway in Stranski-Krastanov growth of Ge on Si(001). *Physical Review Letters* **1990,** *65* (8), 1020-1023.
29. Anderson, L. B.; Reilly, C. N., Teaching electroanalytical chemistry: Diffusion-controlled processes. *Journal of Chemical Education* **1967,** *44* (1), 9.
30. Allen J. Bard, L. R. F., Henry S. White, *Electrochemical Methods: Fundamentals and Applications*. 3rd ed.; John Wiley & Sons: 2022.
31. Morris, M. A.; Barnes, C. J.; King, D. A., Monolayer and multilayer surface diffusion, growth mode and thermal stability of indium on W {100}. *Surface Science* **1986,** *173* (2), 618-638.
32. Shahzad, A.; Yang, F.; Steffen, J.; Neiss, C.; Panchenko, A.; Goetz, K.; Vogel, C.; Weisser, M.; Embs, J. P.; Petry, W.; Lohstroh, W.; Görling, A.; Goychuk, I.; Unruh, T., Atomic diffusion in liquid gallium and gallium-nickel alloys probed by quasielastic neutron scattering and molecular dynamic simulations. *Journal of Physics: Condensed Matter* **2024,** *36* (17), 175403.

33. Blagoveshchenskii, N.; Novikov, A.; Puchkov, A.; Savostin, V.; Sobolev, O., Self-diffusion in liquid gallium and hard sphere model. *EPJ Web of Conferences* **2015,** *83*, 02018.
34. Weissenborn, P. K.; Pugh, R. J., Surface Tension and Bubble Coalescence Phenomena of Aqueous Solutions of Electrolytes. *Langmuir* **1995,** *11* (5), 1422-1426.
35. Qiu, H.; Obata, K.; Yuan, Z.; Nishimoto, T.; Lee, Y.; Nagato, K.; Kinefuchi, I.; Shiomi, J.; Takanabe, K., Quantitative Description of Bubble Formation in Response to Electrolyte Engineering. *Langmuir* **2023,** *39* (14), 4993-5001.
36. Xu, Q.; Nakajima, M.; Ichikawa, S.; Nakamura, N.; Roy, P.; Okadome, H.; Shiina, T., Effects of surfactant and electrolyte concentrations on bubble formation and stabilization. *Journal of Colloid and Interface Science* **2009,** *332* (1), 208-214.
37. Craig, V. S. J.; Ninham, B. W.; Pashley, R. M., Effect of electrolytes on bubble coalescence. *Nature* **1993,** *364* (6435), 317-319.
38. Olesinski, R. W.; Abbaschian, G. J., The Ga−Ge (Gallium-Germanium) system. *Bulletin of Alloy Phase Diagrams* **1985,** *6* (3), 258-262.
39. Trumbore, F. A.; Porbansky, E. M.; Tartaglia, A. A., Solid solubilities of aluminum and gallium in germanium. *Journal of Physics and Chemistry of Solids* **1959,** *11* (3), 239-245.
40. Guminski, C., The Ge-Hg (Germanium-Mercury) System. *Journal of Phase Equilibria* **1999,** *20* (3), 344-346.
41. Olesinki, R. W.; Kanani, N.; Abbaschian, G. J., The Ge-In (Germanium-Indium) system. *Bulletin of Alloy Phase Diagrams* **1985,** *6* (6), 536-539.
42. Cheek, Q.; Fahrenkrug, E.; Hlynchuk, S.; Alsem, D. H.; Salmon, N. J.; Maldonado, S., In Situ Transmission Electron Microscopy Measurements of Ge Nanowire Synthesis with Liquid Metal Nanodroplets in Water. *ACS Nano* **2020,** *14* (3), 2869-2879.
43. Qwah, K. S.; Farzana, E.; Wissel, A.; Monavarian, M.; Mates, T.; Speck, J. S., Indium as a surfactant: Effects on growth morphology and background impurity in GaN films grown by ammonia-assisted molecular beam epitaxy. *APL Materials* **2022,** *10* (8), 081107.
44. Voigtländer, B.; Zinner, A.; Weber, T.; Bonzel, H. P., Modification of growth kinetics in surfactant-mediated epitaxy. *Physical Review B* **1995,** *51* (12), 7583-7591.
45. Oguz Er, A.; Elsayed-Ali, H. E., Electronically enhanced surface diffusion during Ge growth on Si(100). *Journal of Applied Physics* **2011,** *109* (8), 084320.
46. Dickey, M. D.; Chiechi, R. C.; Larsen, R. J.; Weiss, E. A.; Weitz, D. A.; Whitesides, G. M., Eutectic Gallium-Indium (EGaIn): A Liquid Metal Alloy for the Formation of Stable Structures in Microchannels at Room Temperature. *Advanced Functional Materials* **2008,** *18* (7), 1097-1104.
47. Balyakin, I. A.; Yuryev, A. A.; Filippov, V. V.; Gelchinski, B. R., Viscosity of liquid gallium: Neural network potential molecular dynamics and experimental study. *Computational Materials Science* **2022,** *215*, 111802.
48. Anderson, T. J.; Ansara, I., The Ga-Sn (gallium-tin) system. *Journal of Phase Equilibria* **1992,** *13* (2), 181-189.
49. Gancarz, T., The thermophysical properties of Bi-Ga alloys. *Journal of Molecular Liquids* **2022,** *363*, 119912.
50. Zhang, L.; Tang, H. F.; Schieke, J.; Mavrikakis, M.; Kuech, T. F., The addition of Sb as a surfactant to GaN growth by metal organic vapor phase epitaxy. *Journal of Applied Physics* **2002,** *92* (5), 2304-2309.
51. Zharikov, E. V., Problems and recent advances in melt crystal growth technology. *Journal of Crystal Growth* **2012,** *360*, 146-154.

52. Mauk, M. G., 6 - Liquid-Phase Epitaxy. In *Handbook of Crystal Growth (Second Edition)*, Kuech, T. F., Ed. North-Holland: Boston, 2015; pp 225-316.

Chapter 7 Unresolved Work

7.1 Preface

This section provides an overview of the work presented in prior sections of this thesis and highlights work which is still ongoing or unresolved. The Au-patterned electrodes discussed in Section 7.6 were provided by the group of Robert Hovden from the University of Michigan's Materials Science & Engineering Department. Conductivity measurements outlined in Section 7.6 was performed by Tung Nguyen. All other data was collected and analyzed by Joshua P. Hazelnis.

7.2 Overview

This thesis expands upon the understanding of room temperature liquid metals for inorganic crystal growth via in-situ X-ray reflectivity. Specifically, the interfacial behavior of pure Hg and Hg_xIn_{1-x} amalgams has been described under ec-LLS growth conditions. Chapter 2 demonstrates the effectiveness of in-situ XRR for probing ec-LLS processes by collecting measurements of the pure Hg interface in both pure 0.1 M $Na_2B_4O_7$ solution and 0.1 M $Na_2B_4O_7$ with 0.05 M GeO_2 at potentials where there are no faradaic redox reactions. The first conclusion was that using $Na_2B_4O_7$ as a supporting electrolyte was indistinguishable from pure Hg immersed in NaF solutions, suggesting non-specific adsorption with the local ordering of Hg maintained. The second was that with the presence of dissolved H_2GeO_3 and/or $HGeO_3^-$, adsorption not only occurred but could be detected and quantified. At sufficiently positive potentials (> -0.5 V vs. SCE), the accumulation of adsorbed species best matched the formation of monolayer coverage polygermanates via a condensation reaction which was previously believed to only form during hydrothermal synthetic processes. Chapter 3 furthers this work by extending in-situ XRR to binary Hg_xIn_{1-x} systems to systematically investigate the effects of applied potential and liquid metal composition on the liquid metal/ liquid electrolyte interface. Hg_xIn_{1-x} show behavior of Hg surface enrichment which disagrees with the mathematically predicted first-layer atomic compositions from the Gibbs Adsorption Isotherm for an ideal mixture. A persistent and confirmed Yoneda signal in the diffuse scattering was also confirmed for the same range of Hg_xIn_{1-x} compositions.

The Yoneda peak showed a noticeable dependence on the radius of curvature, but the data also suggested some dependence with the bulk composition. This work motivates further study of the Yoneda feature to determine whether information on the in-plane heterogeneity across the liquid metal/water interface can be ascertained.

This thesis has also expanded on the utility of ec-LLS and ec-LPE by describing ways in which the interfacial order of liquid metals can be leveraged for preparing single crystalline inorganic materials. Specifically, interfacial order similar to what has been identified via in-situ X-ray reflectivity (XRR), allows for the synthesis of single crystalline metallic and semiconducting materials at room temperature and ambient environments. Chapter 4 presented the first known example of electrochemically driven, single crystalline metallic growth on a liquid-liquid interface. Liquid Ga at constant, ambient conditions was used to separately electrodeposit pure single crystalline forms of Pb, Bi, $PdGa_5$, and $MnGa_4$. Low flux electrodeposition onto a 'clean' Ga interface devoid of oxides, caused self-segregation and directed crystal growth of the metallic material to be observed. Short range order and the atomic packing density of atomic layers within Ga dictated the observed crystal orientations. Chapter 5 further supports this idea by the observation that the phases $FeGa_3$ or $CoGa_3$, based on the binary phase diagrams, were not observed when Fe or Co was reacted with liquid Ga, respectively. The nearly identical structures of $FeGa_3$ and $CoGa_3$ do not have nucleation planes which match closely with the atomic packing density of Ga. Instead under identical low flux electrodeposition conditions, a subset of new layered intermetallics were observed. The estimated structure based on extensive microscopy characterization matched much closely with a 5-fold Ga in-plane packing density. Chapter 6 redefined the interface by introducing a seeding substrate directly into liquid metal pools of Hg, $Hg_{0.35}In_{0.65}$, Ga, and *e*-GaIn during electrodeposition of Ge which promoted epitaxial growth. The presented technique 'open' ec-LPE, is a facile approach to traditional ec-LPE which does not necessitate mechanical compression to maintain a flat liquid metal. This work highlighted that despite differences in wetting and solubility towards Ge, the highest coverage epi-films were consistently observed using In-containing liquid metals (*e*-GaIn and $Hg_{0.35}In_{0.65}$) due to the role of In as a surface surfactant. This work motivates additional studies using an 'open' ec-LPE type approach with translocation for creating contiguous large area semiconductor films.

7.3 Context of Future Directions

For future ec-LLS experiments targeting single crystalline inorganic materials, it is important to further understand the mechanisms discussed for liquid Ga and the influence of the atomic packing density of interfacial atomic layers. If it is true that the packing density of a liquid metal directly influences the crystal orientation of the resultant phase, as Chapter 4 and Chapter 5 seem to suggest, then changing the material precursor or liquid metal should afford a new electrochemical pathway for obtaining known or potentially unreported single crystalline inorganics. Section 5.3 describes initial electrochemical experiments for understanding the interface of liquid Ga under identical conditions used for facilitating single crystalline growth. Unexpected features in the cyclic voltammetry include an inverted oxidation current when scanning reductively was observed, suggesting the presence of some parallel chemical process. The scan rate dependence, effects of applied potential range, and results when using a solid instead of liquid Ga electrode are presented but a complete mechanism is not fully understood. Preliminary data and previously reported literature seem to suggest the presence of an unstable Ga^{1+} species at the interface which may be driving the observed reactivities. Future work to progress this project and to further the electrochemical understanding of Ga is outlined.

Many of the systems, including liquid Ga, have not yet been investigated via in-situ characterization. Some of this arises from the inherent difficulties in probing large liquid metal pools in a similar way to what has been outlined in Chapter 2 and Chapter 3 for Hg and Hg_xIn_{1-x}, respectively. Section 5.4 outlines some initial efforts in creating optically 'flat' liquid metal electrodes to significantly enhance the throughput of in-situ XRR experimentation. The premise of this work relies on forming a conductive intermetallic alloy film which contains some form of the liquid metal component to promote interfacial wetting without introducing experimental impurities to the liquid metal pool. Specifically, a Cu-Ga alloy is targeted and electrochemically investigated as a proof of concept for improving interfacial wetting. Experiments to elucidate potential impurities which may be introduced into the liquid metal or identifying other potential substrates were not performed, but future experiment suggestions are made.

Lastly, one of the biggest challenges when trying to characterize small amounts of inorganic material on the surface of a liquid metal is finding unique ways to isolate them. This is especially true when the particles like those shown in Chapter 5 are compositionally similar to the composition of the bulk liquid metal. Section 5.5 details some of the efforts which have been made

to probe the properties of particles synthesized on liquid metal electrodes. Specifically, a method to isolate single particles and probe the electrical conductivity properties is presented. Additional recommendations are made on how this might be performed more effectively in the future and is particularly important as the prospects for liquid metal electrode expand to novel materials.

7.4 Electrochemistry of Gallium

Despite the use of gallium for nearly a century in electronic applications,[1, 2] there are many questions which remain unanswered on the chemistries observed at the interface of liquid Ga under electrochemical bias.[3-6] This is increasingly important for not just the work proposed in this thesis on unique inorganic crystal growth behavior using liquid Ga, but also the plethora of electrochemical devices which take advantage of the conductive and flexible properties.[7-9] This thesis focuses closely on the characteristics of liquid Ga in alkaline aqueous media, a topic which has been highly debated in literature.[3-5] The general consensus seems to suggest the following points[3-6, 10-12]: (1) Anodic oxidation of Ga in alkaline media forms some combination of oxide or hydroxide species which passivates the surface. (2) There are likely some unstable Ga^{1+} species localized at the interface which can undergo a spontaneous disproportionation reaction. (3) The interface is dynamic with corrosion and dissolution of Ga species being an operative part of any accurate mechanism.

The goal of this section is not to accurately describe the operative mechanisms but rather describe the process for careful electrochemical data collection and subsequent observations of Ga in alkaline aqueous media. It is this author's opinion that a likely contributing factor to the debated understanding of this system is due to inconsistencies in the reported electrochemical data.[3] While scan rate dependence, repeated cycling, and differences between liquid and solidified Ga have been explored across multiple studies, there is no comprehensive study which seems to accurately describe these behaviors in totality. The following discussion describes preliminary attempts to do just that and a best guess at some of the chemical reactions which may contribute to these observations. It is important to note that the author's interpretation of the data is at best an informed hypothesis and is meant to help guide any future work but should not be taken as fact.

Cyclic voltammetry of liquid Ga electrodes was collected using a similar electrochemical set-up as what was described in Section 4.3.1. The exact electrochemical set-up is depicted in Figure 7.1. For the working electrode, a Teflon bowl with a diameter of 0.90 cm and depth of 0.60 cm housed a liquid Ga droplet with an approximate surface area of 1.89 cm^2. Electrical contact

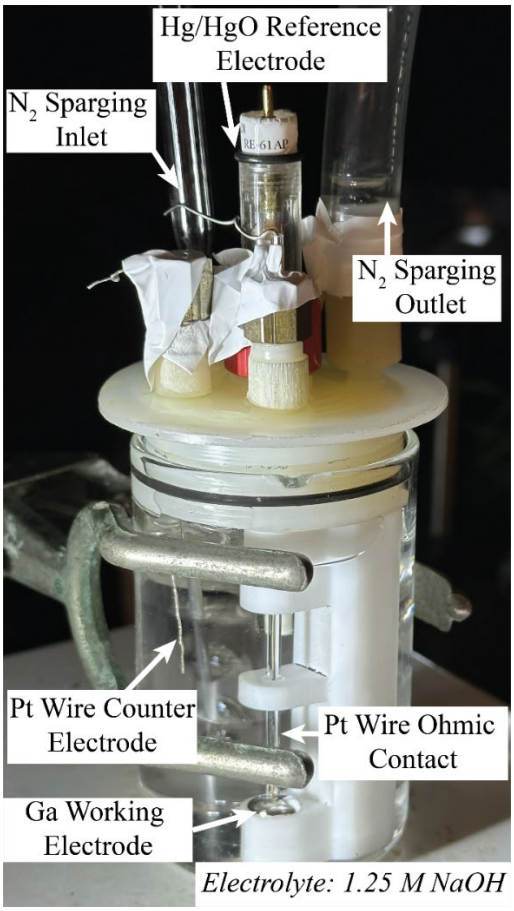

Figure 7.1 Picture of the electrochemical cell used for the electrochemical characterization of liquid Ga in aqueous 1.25 M NaOH electrolyte. The liquid Ga pool was housed in a custom Teflon bowl and contacted using a Pt wire. The counter electrode was a pure Pt wire, the reference a Hg/HgO (1.25 M NaOH) and the cell was maintained under inert N_2 atmosphere.

was made to the liquid Ga (2.00 ± 0.10 g, 99.99%) by inserting a Pt wire encased in a quartz glass capillary to avoid exposure of the wire to the surrounding electrolyte solution. The counter and reference electrodes were Pt wire and Hg/HgO (1.25 M NaOH), respectively. All measurements were made using a stock 1.25 M NaOH (aq) solution (99.99%, Trace metal grade) with an expected pH > 14. The cell was sealed with a plastic cap with an inlet tube connected to a glass pipette and outlet tube to sparge and subsequently maintain a positive N_2 (g) pressure for the duration of the electrochemical measurements. This was a method to simplify the electrochemical data and avoid any contributions of ambient oxygen. A potentiostat (Autolab PGSTAT302N,Metrohm) was used for all measurements. The cell was placed on a hot plate set too 65°C to avoid the Ga electrode freezing. All data are reported in 'Texas Convention' where positive and negative currents correspond to, reductive and oxidative processes respectively.

Initial measurements over two different potential ranges were performed on the liquid Ga electrode in 1.25 M NaOH and are shown in Figure 7.2. Each plot shows the recorded signal for 35 cycles at 10 mV s^{-1} collected in repetition, without allowing the system to go to OCP (-1.47 V vs. Hg/HgO. The last scan (cycle 35) is highlighted in red to emphasis the observed changes in the profile due to this repeated cycling. In each case, two distinct peaks are observed. The first of which appears on the oxidative scan (scanning from negative to positive potentials) and is centered at approximately -1.38 V vs. Hg/HgO in both cases. The shape of this peak is very distinct, with a sharp discontinuation in the oxidative current rather than a typical gaussian type peak shape. Although the exact cause of this feature within the cyclic voltammetry is unknown, it may be some due to an adsorption type process. This is because similar features have been observed for adsorption processes at the surface of a mercury hanging drop electrode (HMDE).[13] This would be consistent with the idea that there are adsorbed oxide or oxyhydroxide species present at these alkaline conditions. However, further work would be needed to confirm or reject this hypothesis.

The other curious feature in the cyclic voltammetry is the presence of the 'inverted peak', i.e oxidative currents when scanning reductively. This is not the first time that such a feature has been observed on liquid Ga in alkaline media[10] and it has also been observed for adsorption processes at the surface of liquid Hg[14] and Au[13]. The behavior of the peak was found to change during repeated electrochemical cycling dependent strongly on the electrochemical potential window. If the liquid Ga electrode was repeatedly cycled between -1.35 and -1.47 V vs. Hg/HgO the oxidative and 'inverted peak' on the reductive scan would monotonically decrease and

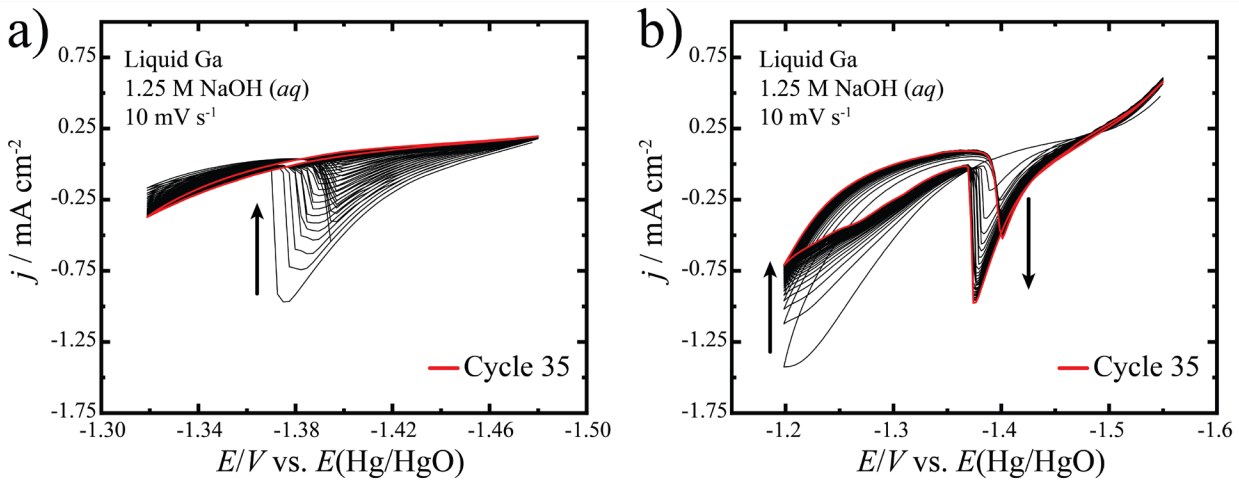

Figure 7.2 Cyclic Voltammetry of liquid Ga in 1.25 M NaOH (*aq*) solution at a scan rate of 10 mV s^{-1}. A total of 35 cycles were performed from a) -1.32 V to -1.47 V or b) -1.20 V to -1.55 V with the last cycle highlighted in red to clearly represent the change in the voltametric profile over time.

eventually disappear. (Figure 7.2a) However, when the electrochemical window used for cycling was expanded from -1.20 to -1.55 V vs. Hg/HgO both peaks would immediately increase in oxidative current intensity within the first couple of scans. (Figure 7.2b) Additionally, a pronounced oxidative feature was observed between -1.20 and -1.30 V vs. Hg/HgO. One possible explanation for these cumulative observations is, species which either accumulate or adsorb onto the liquid Ga surface at potentials more positive than -1.20 V vs. Hg/HgO are directly influencing the behavior of the oxidative and 'inverted' peaks. A more comprehensive study is needed to confirm whether this is actually the case.

The scan rate dependence and its influence on the resultant profile was also explored. Figure 7.3 shows the results of changing scan rate for the liquid Ga / 1.25 M NaOH (aq) system, between 100 and 1,000 mV s^{-1} at 100 mV increments. At 100 mV s^{-1}, the overall profile looks similar to the profile at 10 mV s^{-1} shown in Figure 7.2. Specifically, regions more positive of -1.20 V vs. Hg/HgO show a pronounced oxidative current, the oxidative peak centered around -1.38 V vs. Hg/HgO still has an overall 'sharp' appearance, and the distinct presence of an 'inverted peak' on the reductive scan slightly negative of -1.4 V vs. Hg/HgO. The main difference between 10 mV s^{-1} and 100 mV s^{-1} scan rates are the slightly pronounced reductive signal just before the 'inverted peak' when using the faster scan rates.

As the scan rate is incrementally increased, a few changes in each of these three features are observed. (Figure 7.3) The first is that the 'inverted peak' begins to disappear and a more gaussian shaped reductive peak appears in its place. A nearly complete disappearance of the 'inverted peak' is observed at a scan rate $\geq$ 500 mV s^{-1}. The second observation is that the oxidation peak originally centered around -1.38 V vs. Hg/HgO at slower scan rates becomes incrementally more broad and shifts to more positive potentials. Lastly, the oxidative feature more positive of -1.20 V vs. Hg/HgO has an increasing oxidative current with an increasing scan rate. Additionally, at the slowest scan rates $\leq$ 600 mV s^{-1}, the appearance of a more defined oxidative peak can be observed. It is this author's opinion that these trends with scan rate suggest that the underlying processes contributed to these peaks have some non-zero kinetic dependence and change when scanned sufficiently fast. This is particularly true of the 'inverted peak' which is observed to be completely lost at faster scan rates.

To confirm whether or not the observed behaviors were unique to liquid Ga, a solid electrode was characterized in the same way. (Figure 7.4) In this case, instead of using the set-up

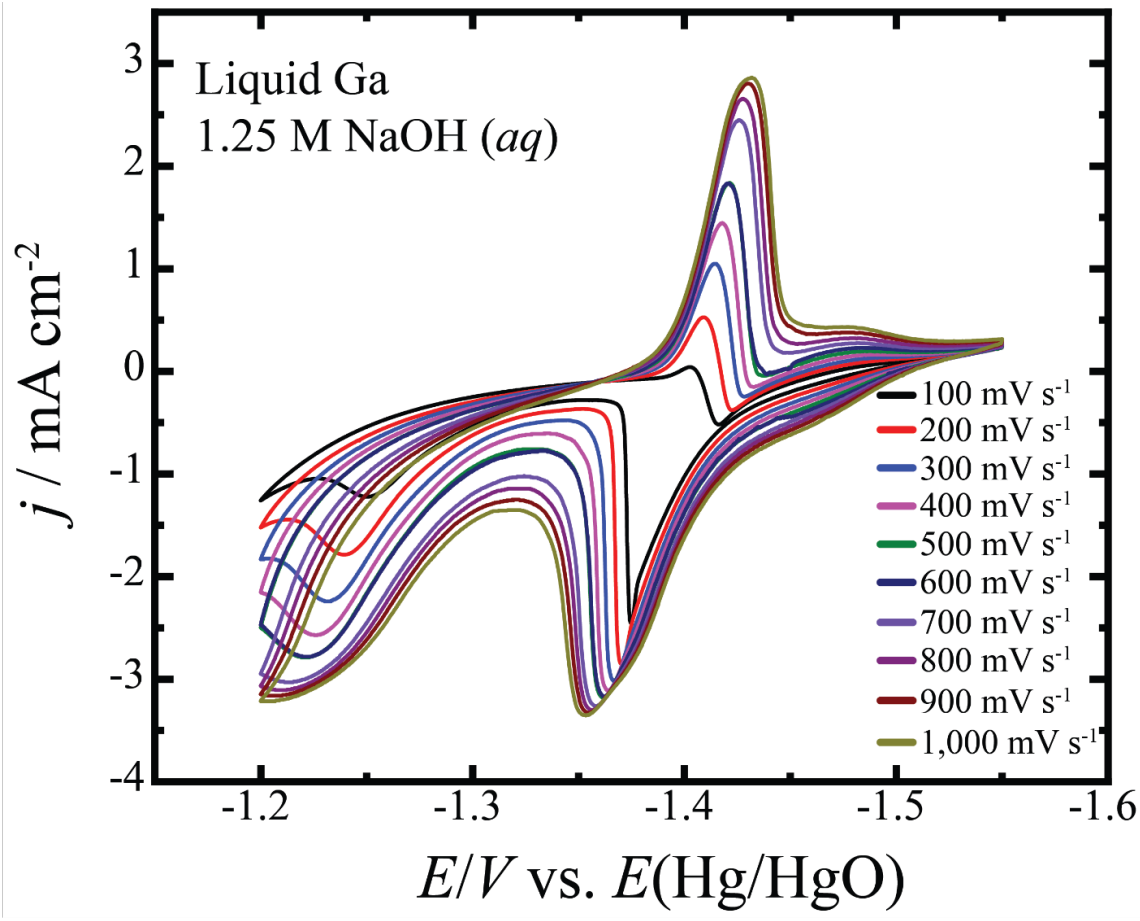

Figure 7.3 Cyclic Voltammetry of liquid Ga in 1.25 M NaOH (*aq*) solution at scan rates of 100 to 1,000 mV s^{-1} in 100 mV intervals.

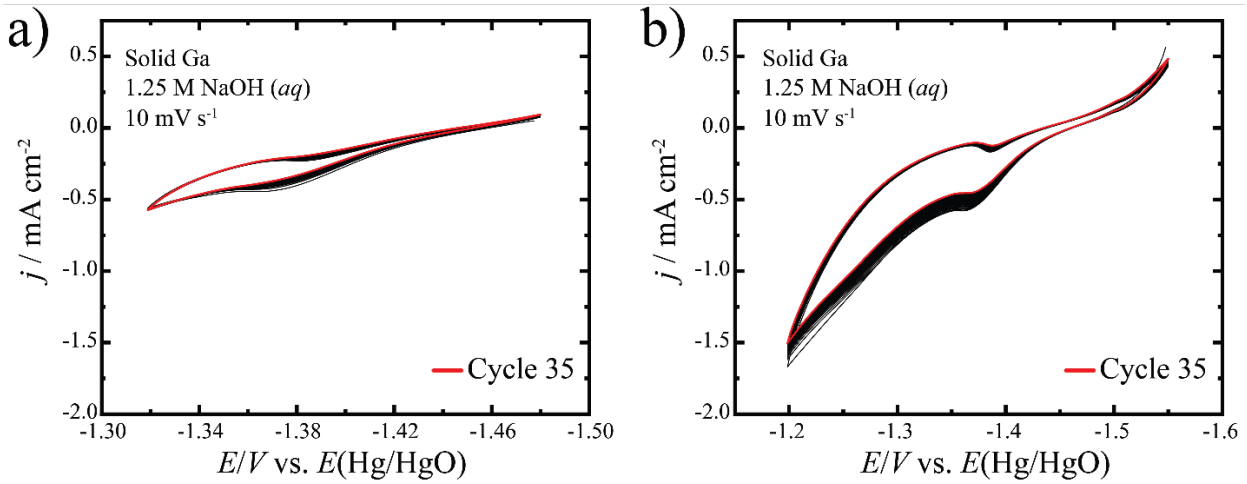

Figure 7.4 Cyclic Voltammetry of solid Ga on a FTO glass substrate in 1.25 M NaOH (*aq*) solution at a scan rate of 10 mV s^{-1}. A total of 35 cycles were performed from a) -1.32 V to -1.47 V or b) -1.20 V to -1.55 V with the last cycle highlighted in red to clearly represent the change in the voltametric profile over time.

exactly as shown in Figure 1a, liquid Ga was instead smeared onto the conductive side of an FTO electrode and flash frozen with liquid N_2. This electrode dipped into the 1.25 M NaOH (aq) electrolyte solution, taking care as to not submerge the alligator clip used to make electrical contact. Experiments were performed in a clean quartz glass beaker which was loosely sealed using parafilm. The counter and reference electrodes used were the same Pt wire and Hg/HgO (1.25 M NaOH), respectively. The electrolyte solution was sparged with N_2 (g) and N_2 (g) was allowed to flow over the top of the electrolyte solution during data collection.

The observations made using a solid Ga electrode were different than the ones made for liquid Ga. For one, although an oxidative feature was observed around -1.38 V vs. Hg/HgO, it was not nearly as 'sharp' in appearance nor were the oxidative currents as large. Second, although a slight 'inverted peak' was observed when scanning reductively, it was consistently at much lower current magnitudes. Lastly, the behaviour over multiple scans was inversely proportional to what was observed for liquid Ga and the extent of this change was significantly more subtle.

7.4.1 Proposed Operative Reactions

The following adsorption based mechanisms are proposed based on the collected experimental data in combination with the chemical reactions predicted by the Pourbaix diagram of Ga[3, 15] and previously literature reports. [3-6, 10-12] The summary of these reactions are the author's interpretation of the voltametric features observed, particularly for liquid Ga, including the 'inverted peak'. As mentioned previously, the following mechanism is only proposed based on the author's interpretation of the data, but additional work would be necessary to confirm its accuracy.

For one, in the potential regions more negative than the 'inverted peak' (-1.40 V vs. Hg/HgO) the surface of Ga is likely populated with Ga-H bonds in accordance with *Equation* 7.1.

$$GaH + OH^- \rightleftharpoons Ga^0 + H_2O + 1e^-$$

Equation 7.1

It is assumed that these bonds are relatively strong due to pure Ga showing poor efficacy for HER[16], as further supported by the relatively low reductive currents in the experimentally obtained data at the most negative potentials. Therefore, it is assumed that the rate of this reaction is likely quite slow.

If this is true, it would imply that the Ga atoms are oxidized as Ga^{1+}, which would be unstable and could undergo subsequent disproportionation to Ga^0 and H_2(g) via *Equation* 7.2.

$$2GaH \rightleftharpoons 2Ga^{0} + H_{2}$$

Equation 7.2

This HER reaction would again be expected to occur at a very slow rate. This would especially be the case when more H_2 is present in solution favoring reactivity towards GaH, which is the case at sufficiently negative potentials. Due to this anticipated stability of GaH, it is likely that one would need to scan to a sufficiently positive potential for them to be removed from the interface. This would also mean that there is likely no redox current observed for this $1e^-$ oxidation process when the GaH fully populates the surface due to the strength of the Ga-H bond.

At more positive potentials, the direct oxidation of Ga^0 would be expected to occur. This could either be as Ga^{3+} or in a less stable Ga^{1+} form. Possible chemical reactions for this oxidation is provided in *Equation* 7.3 and *Equation* 7.4.

$$Ga^{0} + 3OH^{-} \rightleftharpoons Ga(OH)_{3} + 3e^{-}$$

Equation 7.3

$$Ga^{0} + OH^{-} \rightleftharpoons GaOH + 1e^{-}$$

Equation 7.4

This could plausibly occur for any bare Ga^0 exposed at the liquid metal surface, where *Equation* 7.3 occurs at some less positive potential than *Equation* 7.4. Like the unstable Ga^{1+} form GaH, GaOH could also undergo a disproportionation reaction according to *Equation* 7.5.

$$3GaOH \rightleftharpoons 2Ga^{0} + Ga(OH)_{3}$$

Equation 7.5

This reaction almost certainly has a faster expected rate constant than the disproportionation of GaH due to the ionic rather than covalent characteristic of this bond making it weaker, thus easier to break. The direct combination of *Equation* 7.4 and *Equation* 7.5 is *Equation* 7.6:

$$2GaOH + OH^{-} \rightleftharpoons Ga^{0} + Ga(OH)_{3} + 1e^{-}$$

Equation 7.6

which implies that there must be some GaOH present on the liquid Ga interface for some oxidation current to be observed.

In this case, the shape of the oxidative peak which initially appears at -1.38 V vs. Hg/HgO is likely dictated by whether *eqn*. 6 occurs or not. In other words, oxidative current only passes if GaOH is present and subsequent disproportion can occur. The probability of this occurring is less likely at more positive potentials where Ga_2O_3 would otherwise dominate which could be why at slower scan rates the current suddenly 'drops' due to the loss of all adsorbed GaOH on the oxidative sweep.

Conversely, on the cathodic scan, this process is effectively reversed and some non-zero amount of GaOH is reformed and adsorbed. If the scan rate is slow, it will kinetically allow for the disproportionation in *eqn*. 6 and thus a net oxidative current. However, if the scan rates are sufficiently fast, outpacing disproportionation, a one electron reduction of GaOH can occur and a net reductive current is observed instead. When the Ga is solidified, kinetically everything is expected to be much slower which could be one reason why all of the observed features are less pronounced compared to that of liquid Ga.

These initial observations motivate more careful electrochemical studies, possibly coupled with in-situ characterization to either confirm or reject the proposed reactions. Similar studies have already been conducted where the change in mass[5] or surface tension[4] was probed during electrochemical cycling to make more informed conclusions on what may actually be occurring. Nonetheless, a definitive mechanism is not yet fully understood nor is the mechanism proposed confirmed to be accurate.

7.5 Flat Liquid Metal Electrodes

Design of a flat liquid Ga electrode has been explored by mechanically spreading it over a wettable conductive substrate ($CuGa_2$). Substrates were prepared via a direct chemical reaction at room-temperature facilitated by concentrated acid (HCl). The work in Chapter 4 and Chapter 5 suggested that the surface structure of liquid Ga itself imparted directionality to the resultant crystals. In surface freezing of heated liquid alloys under vacuum, segregation of metal solutes can yield preferential crystal growth.[17-21] The prevailing explanation is that a hexatic phase forms above the melting point that facilitates the formation of a close-packed solid nucleus upon freezing. The relevance of this pathway for electrodepositions performed at a constant temperature remains an open question.

One way the surface structure of liquid Ga can be more effectively probed to study this question, is through similar in-situ X-ray methods like what has been presented in Chapter 2 and

Chapter 3 for pure Hg and $Hg_{1-x}In_{1-x}$ under an applied electrochemical bias. For the X-ray reflectivity measurements in this thesis, an electrochemical cell with a flat, bulk pool of the liquid metal with a 5.5 cm diameter was used. (Figure 1.5) However, these measurements were primarily made with a supporting electrolyte, $Na_2B_4O_7$ (aq) which did not showing any strong adsorption or change in the liquid interface for pure Hg, similar to the well-studied NaF system.[22] This meant that repetitious experiments could be made varying the applied electrochemical bias without fear of any aging effects. To probe the interfacial structure of liquid Ga during crystal growth, multiple liquid metal pools would have to be used.

Ideally, the use of a flat, thin liquid metal film will be desirable to enable more detailed structural analyses, faster operando measurements, and better control in materials synthesis. As this geometry suppresses curvature, liquid metal samples of much lower lateral extension (≤ 1 cm) can be realized, which will lead to one order of magnitude lower X-ray absorption and background scattering by the electrolyte. The latter will result in much higher signal-to-background ratios, allowing significant reduced data acquisition times for XRR and GIXS as well as kinetic studies with sub-second time resolution.[23] It is this author's opinion that such films also (i) enable faster and better controlled supersaturation of the liquid metal by the deposited species, (ii) be better suited for studies of the electrocatalytic behavior, and (iii) may open up long-term prospects for studies by other in situ/operando methods, e.g. X-ray absorption spectroscopy.

Previous studies have shown that *e*-GaIn and pure Ga liquid metals in the presence of HCl removes the surface metal oxides and will readily wet a Cu substrate.[24, 25] This is due to the formation of $CuGa_2$ which shows strong metallic bonding characteristics at the liquid Ga/$CuGa_2$ interface. Thus, an electrode was prepared by mixing a liquid Ga droplet with concentrated HCl on the surface of a piece of Cu foil. (Figure 7.5) Visually, the film does show some roughness despite it being seemingly quite thin. One possible suggestion would be to employ some form of mechanical or chemical polishing of the Cu substrate to achieve the 'optical' smoothness needed for an X-ray measurement. Nonetheless, Ga wetted Cu foil electrodes were also made into platform electrodes (Figure 7.5b-c) to better visualize the interface with an applied electrochemical bias. Specifically, electrical contact was made to the backside of the wetted Cu foil using a Cu wire and silver print. This was then threaded through a glass capillary and sealed with a chemical resistant 2-part epoxy.



Figure 7.5 a) As prepared Cu/$CuGa_2$/Ga foil electrode by mechanically spreading Ga across the Cu foil in the presence of concentrated HCl. b) Top and c) side view of the Cu/$CuGa_2$/Ga foil electrode in a 'platform' configuration to better probe the characteristics of the liquid metal/electrolyte interface.

For electrochemical characterization, a custom-quartz glass cell fitted with a flat optical glass window to view the 'platform' electrode inserted into the bottom of the cell via an optical camera. (Figure 7.6) Additional liquid Ga was placed onto the surface of the electrode to avoid having any of the underlying $CuGa_2$ substrate exposed. (Figure 7.5c) In an aqueous electrolyte solution of $Na_2B_4O_7$, three repeated cyclic voltammograms were collected over a wide potential range, -1.0 to -1.7 V vs. *E*(Ag/AgCl) at a scan rate of 10 mV s^{-1} to gauge the stability of the liquid Ga interface. (Figure 7.6b-c) At the most negative applied potentials, a large increase in reductive current is observed likely due to HER,[16] supported by the appearance of bubbles at the interface. At more positive potentials an oxidative and reductive peak is observed which are consistent with the formation and reduction of Ga_2O_3. If the liquid Ga does not have a strong wetting reaction with the Cu/$CuGa_2$ foil, then it should have a more pronounced curvature once the liquid metal oxide is removed.[26]

Despite being at sufficiently negative reduction potentials to observe oxide reduction (< -1.47 V vs. *E*(Ag/AgCl),[3, 27] the liquid Ga/electrolyte interface did not optically appear to change. (Figure 7.6d) This observation would be consistent with the liquid Ga having a favorable bonding reaction with the $CuGa_2$.[25] This observation was also maintained even when electrodepositing Ge with 0.50 M GeO_2 in solution at the most negative potential, -1.7 V vs. *E*(Ag/AgCl), for $t > 18$ hours. (Figure 7.6e)

These preliminary observations suggest that mechanically spreading a liquid metal over a wettable conductive substrate is a plausible approach for maintaining a flat Ga electrode. Some considerations which were not accounted for here but are worth considering for future experimentation are: (1) Does the material from the Cu/$CuGa_2$ substrate introduce undesired impurities into the bulk liquid Ga? (i.e leeching of Cu atoms into the bulk) (2) Can the liquid metal be made 'optically' flat to support small angle X-ray measurements? (3) Are there other wettable substrates worth considering? (i.e substrates which are photolithographically patterned rather than an intermetallic with a favorable wetting interaction)[28]

7.6 Isolating and Characterizing Products of Liquid Metal Electrodeposition

After performing the work outlined in this thesis, it is the author's opinion that one of the biggest challenges of electrodepositing inorganic particles onto a liquid metal electrode is the difficulty in separating them from the bulk. This challenged seemed to be more evident when the target inorganic materials are formed in small quantities and on the nano or micron scale, like the

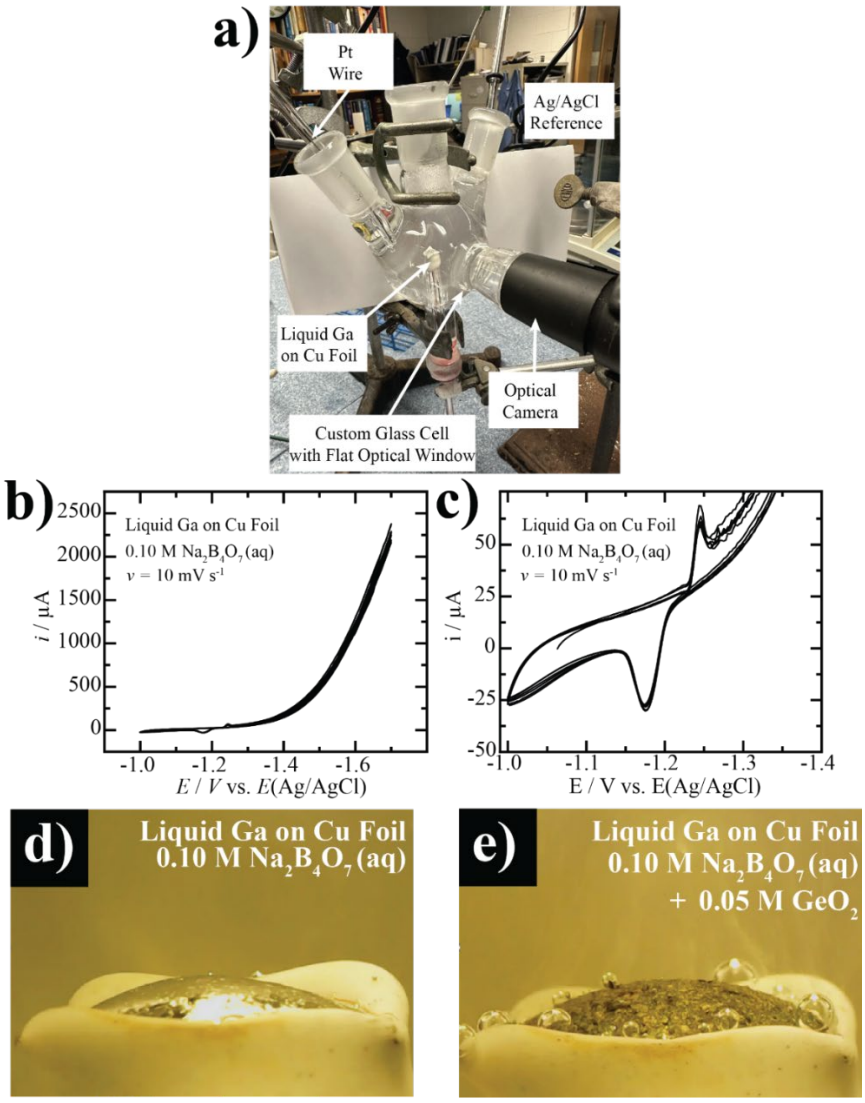

Figure 7.6 a) Custom electrochemical cell fitted with a flat quartz-glass window to view and video with an optical camera the behavior of the $Cu/CuGa_2/Ga$ 'platform' electrodes shown in Figure 7.5 when an electrochemical bias is applied. b) Cyclic voltammetry from -1.0 to -1.7 V vs. Ag/AgCl in an aqueous 0.1 M $Na_2B_4O_7$ electrolyte solution in contact with the $Cu/CuGa_2/Ga$ 'platform' electrode. c) Zoom-in on the cyclic voltammetry shown in b to highlight the peak features present at more positive potentials. d) Interface of the liquid Ga/electrolyte in a blank 0.1 M $Na_2B_4O_7$ electrolyte solution. e) Interface after holding at negative -1.7 V vs. Ag/AgCl for t > 18 hours in 0.1 M $Na_2B_4O_7$ and 0.05 M GeO_2. Accumulation of Ge crystallites and hydrogen bubbles are observed but the interfacial curvature is unchanged.

products of 'quasi'-epitaxial growth discussed in Chapter 4 and Chapter 5. Although some methods were briefly discussed in those chapters, the purpose of this section is to detail the methods which were explored for isolating these materials and showcasing preliminary electrical measurements of single particles ($Fe_{0.08\pm0.01}Co_{0.06\pm0.01}Ga_{0.86\pm0.01}$).

Taking inspiration from methods used for isolating and exfoliating layered materials,[29] tape was found to be a very effective method for isolating particles which were grown on a liquid Ga surface. Specifically, some form of tape (i.e scotch, carbon, Kapton) with a strong adhesive layer is pressed into the surface of a liquid metal following a reaction. In the author's experience, this was found to work best when the surface was completely dry and free from liquids such as an electrolyte solution. Following this, some amount of target material and bulk liquid metal would be observed to have been transferred onto the tape. For liquid Ga, one way to remove the bulk was by chemically reducing the oxide which may have formed in air with 1.25 M NaOH solutions[26, 30] and subsequently rinsing with copious amounts of nanopure water.

Figure 7.7 shows the observations of tape lift-off of hexagonal particles of $Fe_{0.14\pm0.01}Ga_{0.86\pm0.01}$ and $Fe_{0.08\pm0.01}Co_{0.06\pm0.01}Ga_{0.86\pm0.01}$, like those synthesized in Chapter 5, from a liquid Ga surface. As can be seen in the image taken at a 50x microscope magnification in Figure 7.7b, many hexagonal particles transferred with very little bulk Ga left behind. If a conductive tape like carbon is used, this was determined to be an effective method for preliminary SEM-EDS analysis like what is shown for these same hexagonal particles in Chapter 5. It also allows for precise optical measurements to be made, such as Raman spectroscopy where the presence of an adhesive did not hinder appear to hinder data collection in any way. The shortcoming of this method is that once the particles are affixed onto the adhesive of the tape, it was found to be difficult to separate them again. Attempts at dissolving the adhesive using solvents such as acetone did remove some of the adhesive from the tape backing but left too much dissolved adhesive in solution that even via centrifugation and drop casting, particles were not successfully isolated.

Other methods which have been reported for TEM sample preparation was also explored, but showed similar levels of success. These included polymethyl methacrylate (PMMA) assisted transfer,[31, 32] "Touch Printing" (i.e touching a non-adhesive material to a sample to facilitate a transfer),[33] or use of Crystalbond adhesives made by Ted Pella.[34] All of these approaches, like tape, rely on the successful transfer of material between the liquid metal and a substrate. The benefit of these approaches, however, is that either there is no adhesive, or it can be more easily removed if

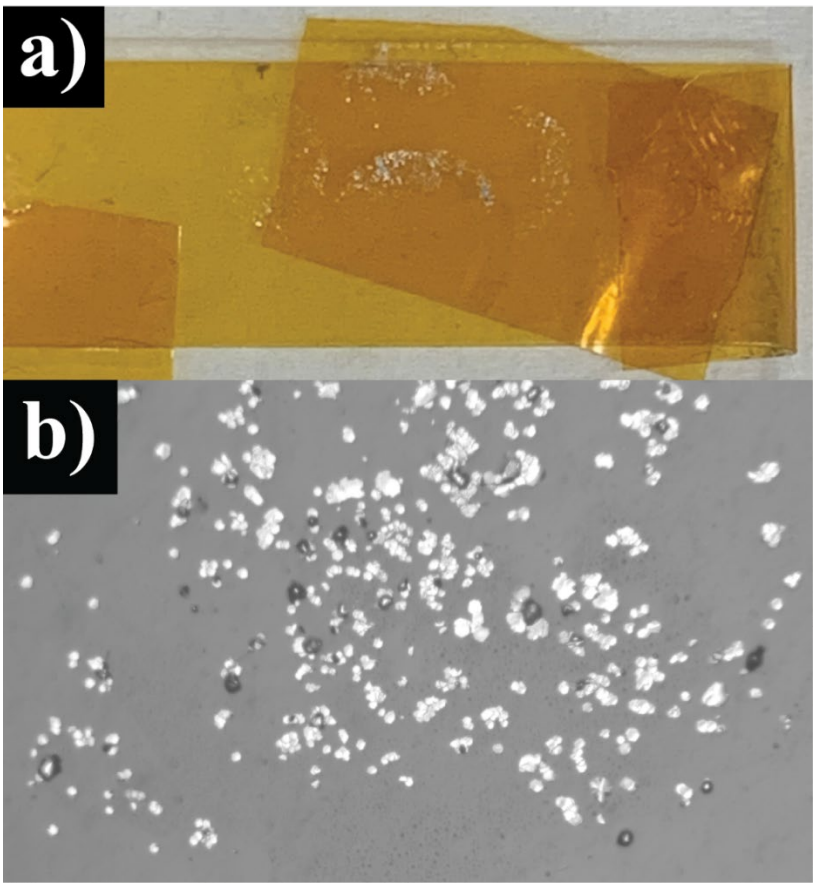

Figure 7.7 a) Picture of a piece of Kapton tape after touching the interface of liquid Ga which had been decorated with particles. Subsequent contact with 1.25M NaOH was performed to remove any bulk liquid metal that may have transferred. b) Image taken with a 50x microscope objective of the piece of tape shown in part a showing hexagonal particles which were transferred.

present. It is the author's opinion that these methods would have worked better if larger amounts of product material were produced during the liquid metal-based reactions at the interface, increasing the probability of successful transfer and thus isolation. However, this unfortunately was not the direct observations made during the work of this thesis.

Instead, a method was developed which not only successfully transferred particles from the liquid Ga surface to a substrate but was done so in the absence of any adhesive layers. Following a reaction with liquid Ga, liquid N_2 was used to flash freeze the surface producing an ingot of Ga coated in particles which may have formed. (Figure 7.8a) Since the melting point of Ga is slightly above room-temperature (29.8°C)[7], particles on the surface of the Ga ingot were transferred by gently streaking the ingot onto a substrate such as a Si wafer at a slightly elevated temperature. (Figure 7.8b) Although some amount of the bulk liquid metal would also be observed to transfer, the particles were now on top of a substrate in the absence of an additional adhesive layer making it possible to transfer them via some form of micromanipulation.

One effective method for isolating and preparing the transferred particles for characterization was focused ion beam manipulation.[35, 36] This technique couples scanning electron microscopy with a focused ion beam, micromanipulator, and gas injector to serve as an effective tool for cutting, polishing or positioning material on the nanoscale.[36] Procedures which utilized this technique for the preparation of (S)TEM samples, have already been outlined in Chapter 4 and Chapter 5. In this section, the use of this technique is described for isolating single particles on an Au-patterned electrode array to probe the electrical properties of the novel $Fe_{0.14\pm0.01}Ga_{0.86\pm0.01}$ and $Fe_{0.08\pm0.01}Co_{0.06\pm0.01}Ga_{0.86\pm0.01}$ introduced in this thesis.

Au-patterned SiO_2 electrodes were prepared by bottom contact lift-off photolithography patterning.[37] Specifically, 60 nm deep trenches were patterned into a 500 nm SiO_2 layer atop a Si wafer via ion beam etching with Ar (g). Subsequently, 10 nm of Ti followed by 50 nm of Au was deposited into the etches trenches via e-beam evaporation at a rate of 4 Å s^{-1}. The final electrodes were polished using a 100 nm micropolishing film prior to use. The final electrodes were made up of six independent Au electrode strips 5 μm wide and spaced 5 μm apart.

Hexagonal particles were transferred from the substrate in Figure 7.8 onto the Au-patterned electrode array using a Thermo Fisher Helios G4 PFIB UXe equipped with a Schottky Field Emitter electron beam source, inductively coupled Xe gas plasma, Omniprobe AutoProbe 200 micromanipulator equipped with a standard tungsten probe tip (Ted Pella), and a multichem gas

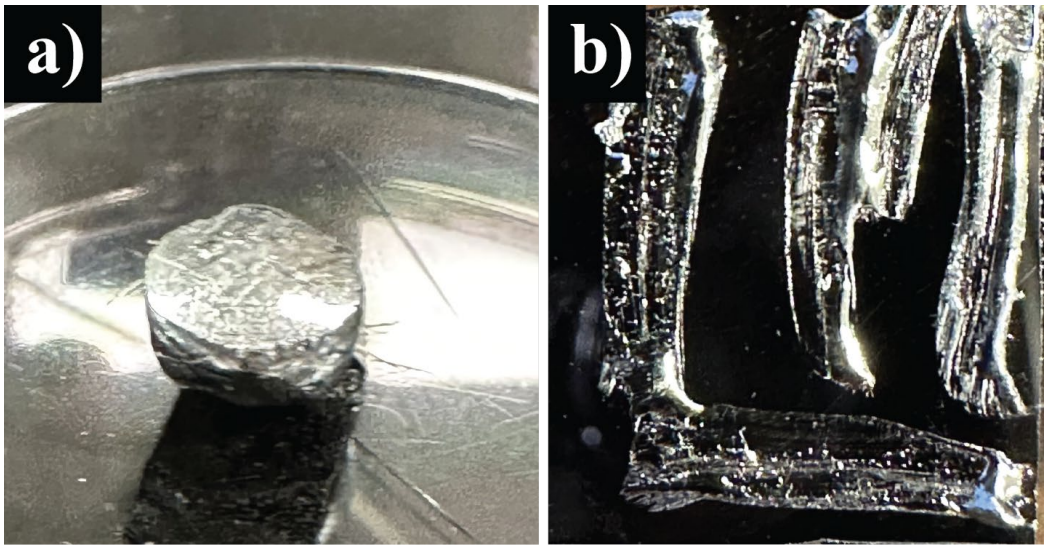

Figure 7.8 a) Picture of a typical Ga ingot which has been frozen with liquid N_2 following electrodeposition of particles on the surface. b) Image of a Si wafer after an ingot like what is shown in part a is gently 'streaked' onto the wafer to transfer particles of interest which may be contained on the surface.

delivery system. First the micromanipulator was inserted and aligned close to a $Fe_{0.08\pm0.01}Co_{0.06\pm0.01}Ga_{0.86\pm0.01}$ particle before being attached via a carbon ion-beam assisted chemical vapor deposition (IBA-CVD). (Figure 7.9a) This was specifically done using low 8.00 kV and 0.1-0.3 nA beam voltage and currents, respectively to avoid damaging the sample. Once attached, the $Fe_{0.08\pm0.01}Co_{0.06\pm0.01}Ga_{0.86\pm0.01}$ hexagon was lifted by moving the tip of the needle slowly away from the substrate surface (Figure 7.9b). Depending on how strongly the particle was adhered to the surface, the particle would sometimes fragment during this step. Once the $Fe_{0.08\pm0.01}Co_{0.06\pm0.01}Ga_{0.86\pm0.01}$ hexagon was free from the substrate on the tip of the needle, it was subsequently moved to a spot on the Au-electrode array between two Au electrode strips and cut free from the needle. (Figure 7.9c-d) Lastly, Pt electrical contacts were made via IBA-CVD at higher 15-60 nA beam currents between the Au electrode and each side of the particle. (Figure 7.9e)

Once electrically connected to two of the Au electrodes, current-potential (i-v) curves were measured using a Keithley 4200 semiconductor parameter analyzer. (Figure 7.10a) Specifically, an electrochemical bias of ±100 mV was applied across the $Fe_{0.08\pm0.01}Co_{0.06\pm0.01}Ga_{0.86\pm0.01}$ hexagonal particle eliciting a linear current response in accordance with Ohm's Law, $V = \underline{i}R$. The slope ($1 / R$) of the *i-V* curve shown in Figure 7.10b was determined by fitting the data with a line, and the resistance was thus determined to be approximately 104 Ω. Due to the challenges in preparing these individual particles for measurement, a standard deviation was not determined.

Based on the estimated thickness (50-200 nm) of the probed $Fe_{0.08\pm0.01}Co_{0.06\pm0.01}Ga_{0.86\pm0.01}$ particle, the conductivity $\sigma = R \cdot A$ is measured to be around 1.9×10^5 to 4.8×10^5 S m^{-1}, which is between the reported conductivity values of lightly Co doped $FeGa_3$ (1.0×10^4 S m^{-1})[38] and pure liquid metal Ga (6×10^4 S m^{-1})[39] at ambient conditions. Temperature dependent measurements were attempted to elucidate any superconducting properties $Fe_{0.08\pm0.01}Co_{0.06\pm0.01}Ga_{0.86\pm0.01}$ may or may not exhibit due to it being a novel layered material.[40] However, a 4-point probe would be more appropriate for these measurements to effectively eliminate any influences of contact or lead resistance and only measure the voltage drop across the sample.[41, 42]

This same approach can be used to isolate and probe other products of ec-LLS such as Ge nanowires.[43-45] Given the increased density at which nanowires can be growth, lifting off a Ge nanowire from the surface of a substrate is trivial compared to the $Fe_{0.08\pm0.01}Co_{0.06\pm0.01}Ga_{0.86\pm0.01}$ particles. (Figure 7.11). One common observation when growing Ge nanowires from a liquid metal

electrode is that the liquid metal tends to incorporate into the final wire[43, 44] like what was described for the epitaxial Ge films prepared via 'open' ec-LPE in Chapter 6. It is this author's opinion that a possible future application for removing these impurities post-process is via electromigration, the electrical induced movement of atoms in a conductor due to an applied electric field.[46-50] While this remains relatively unexplored for the products of ec-LLS electromigration of impurities in materials such as CdZnTe has been demonstrated.[47] A single wire microwire like what is shown in Figure 7.11, could be an effective platform for studying this phenomenon for purifying products of ec-LLS and motivates future experiments.

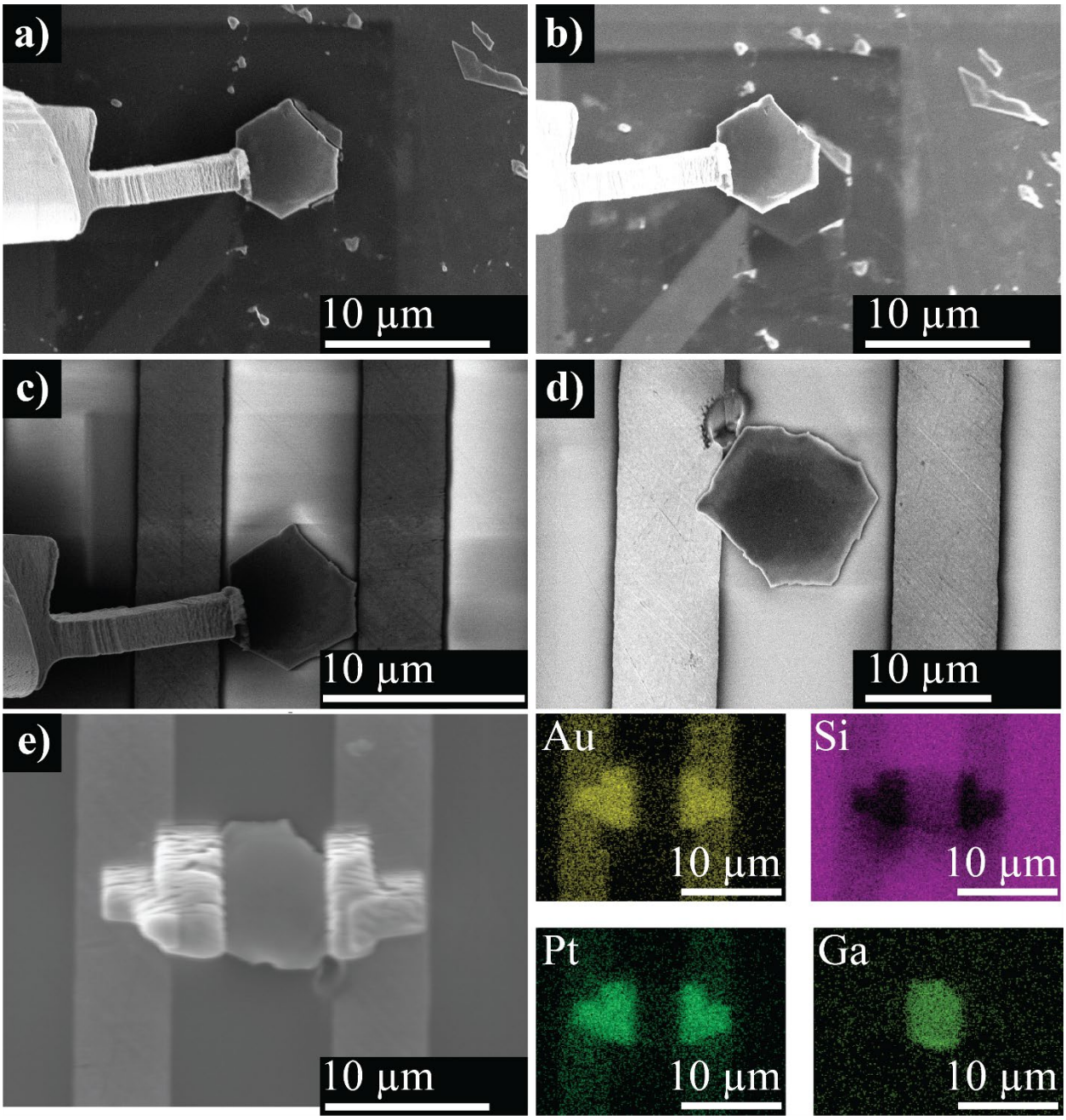

Figure 7.9 SEM images of a single particle FIB transfer onto an Au patterned electrode array. a) Attachment of the omniprobe needle to the particle. b) Initial lift-off from the substrate surface which fragments a piece of the particle. c) Movement of the particle the Au patterned electrode area. d) Particle cut free from the omniprobe needle. e) Platinum is patterned between the Ga-based hexagonal particle and the Au electrodes to make electrical contact. Corresponding EDS is shown.

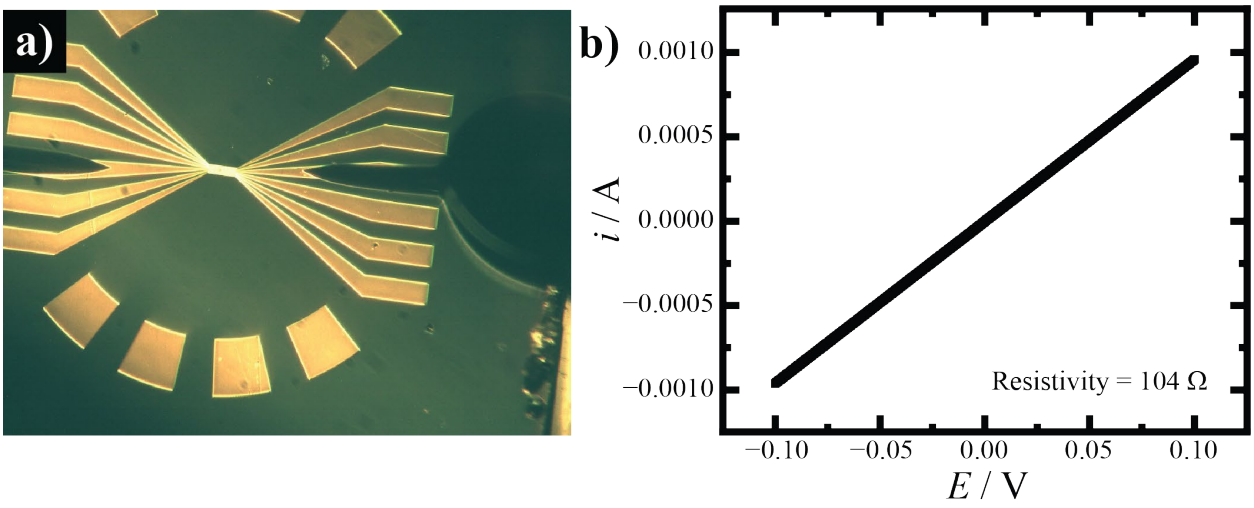

Figure 7.10 a) Optical image of the 2-probe measurement performed by making contact to the Au electrode strips. b) i-v curve response when the potential bias is swept from ± 0.10 V across the as prepared $Fe_{0.08\pm0.01}Co_{0.06\pm0.01}Ga_{0.86\pm0.01}$ particle shown in Figure 7.9.

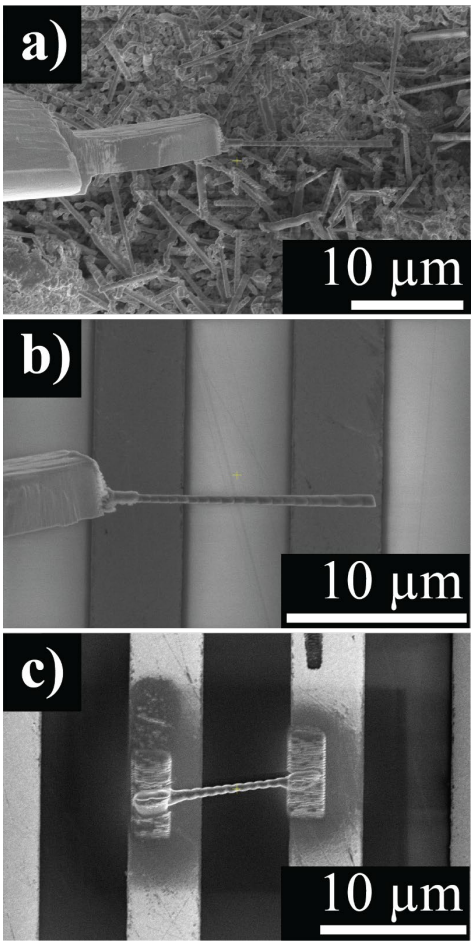

Figure 7.11 Using the FIB procedure in Figure 7.9 but for a Ge nanowire. a) Ge NW is affixed to the omniprobe needle. b) The Ge NW is brought near the Au patterned electrode array prior to being cut free from the needle. c) Platinum is patterned between the Ge NW and the Au electrodes to make electrical contact.

7.7 References

1. Fogg, H. C., A Review of the Electrochemistry of Gallium. *Transactions of The Electrochemical Society* **1934,** *66* (1), 107.
2. Bockris, J. O. M.; Enyo, M., Electrodeposition of Gallium on Liquid and Solid Gallium Electrodes in Alkaline Solutions. *Journal of The Electrochemical Society* **1962,** *109* (1), 48.
3. Chung, Y.; Lee, C.-W., Electrochemistry of Gallium. *Journal of Electrochemical Science and Technology* **2013,** *4* (1), 1-18.
4. Rashid-Nadimi, S.; Okatenko, V.; Song, M.; Shetty, Y.; Bachmann, A. L.; Mehrabian, N.; Hillaire, K.; Nithyanandam, P.; Daniels, K.; Kiani, A.; Dickey, M. D., The Role of Electrochemical Oxidation on the Interfacial Tension of Eutectic Gallium Indium. *ACS Electrochemistry* **2025,** *1* (1), 103-114.
5. Hong, B.; Wang, Y.; Wei, X.; Huang, Q.; Wang, X.; Fujita, T.; Wei, Y., EQCM study on the electrochemical redox behavior of gallium in alkaline solution. *Hydrometallurgy* **2020,** *194*, 105344.
6. Gladyshev, S.; Akcil, A.; Abdulvaliev, R.; Tastanov, Y.; Beisembekova, K.; Temirova, S., Kinetic study of gallium electrochemical reduction in alkaline solution. *Hydrometallurgy* **2013,** *140*, 95-101.
7. Tang, S.-Y.; Tabor, C.; Kalantar-Zadeh, K.; Dickey, M. D., Gallium Liquid Metal: The Devil's Elixir. *Annual Review of Materials Research* **2021,** *51* (Volume 51, 2021), 381-408.
8. Agarwal, R.; Mohamad, A., Gallium-based liquid metals as smart responsive materials: Morphological forms and stimuli characterization. *Advances in Colloid and Interface Science* **2024,** *329*, 103183.
9. Reis Carneiro, M.; Majidi, C.; Tavakoli, M., Gallium-Based Liquid–Solid Biphasic Conductors for Soft Electronics. *Advanced Functional Materials* **2023,** *33* (41), 2306453.
10. Varadharaj, A.; Rao, G. P., Cyclic voltammetric studies on gallium film electrodes in alkaline media. *Proceedings of the Indian Academy of Sciences - Chemical Sciences* **1990,** *102* (2), 177-187.
11. Hurlen, T., Anodic dissolution of liquid gallium in alkaline solutions. *Electrochimica Acta* **1964,** *9* (11), 1449-1452.
12. Perkins, R., Gallium oxidation in alkaline solution. *Journal of The Electrochemical Society* **1972,** *119* (6), 713-715.
13. Miah, M. R.; Ohsaka, T., Observation of 'inverted peak' during molecular oxygen reduction at Au electrode in alkaline media. *Electrochimica Acta* **2007,** *52* (22), 6378-6385.
14. Roman, A. J.; Sevilla, J. M.; Pineda, T.; Blázquez, M., A study on maxima and inverted peaks in cyclic voltammetry. Electrochemical reduction of pyridine-4-aldoxime at an HMDE. *Journal of Electroanalytical Chemistry* **2001,** *517* (1), 15-19.
15. Pourbaix, M., Atlas of electrochemical equilibria in aqueous solutions. *National Association of Corrosion Engineers International* **1966**.
16. Liu, C.; Ma, J.; Fu, Z.; Zhao, P.; Bai, M.; Gao, Y.; Zhao, M.; He, Y.; Xiao, H.; Jia, J., Gallium-based materials for electrocatalytic and photocatalytic hydrogen evolution reaction. *International Journal of Hydrogen Energy* **2024,** *73*, 490-509.
17. Issanin, A.; Turchanin, A.; Freyland, W., Electron spectroscopy and scanning tunneling microscopy study of quasi-two-dimensional freezing at the liquid/vapor interface of Ga-Bi alloys. *The Journal of Chemical Physics* **2004,** *121* (23), 12005-12009.

18. Li, D.; Jiang, X.; Yang, B.; Rice, S. A., Phase transitions in the liquid-vapor interface of dilute alloys of Bi in Ga: New experimental studies. *The Journal of Chemical Physics* **2005,** *122* (22).
19. Yang, B.; Gidalevitz, D.; Li, D.; Huang, Z.; Rice Stuart, A., Two-dimensional freezing in the liquid–vapor interface of a dilute Pb:Ga alloy. *Proceedings of the National Academy of Sciences* **1999,** *96* (23), 13009-13011.
20. Huber, P.; Shpyrko, O.; Pershan, P. S.; Ocko, B.; DiMasi, E.; Deutsch, M., Short-range wetting at liquid gallium-bismuth alloy surfaces: X-ray measurements and square-gradient theory. *Physical Review B* **2003,** *68* (8), 085409.
21. Dogel, S.; Nattland, D.; Freyland, W., Complete wetting transitions at the liquid-vapor interface of gallium-bismuth alloys: Single-wavelength and spectroscopic ellipsometry studies. *Physical Review B* **2005,** *72* (8), 085403.
22. Runge, B.; Festersen, S.; Koops, C. T.; Elsen, A.; Deutsch, M.; Ocko, B. M.; Seeck, O. H.; Murphy, B. M.; Magnussen, O. M., Temperature- and potential-dependent structure of the mercury-electrolyte interface. *Physical Review B* **2016,** *93* (16), 165408.
23. Fuchs, T.; Briega-Martos, V.; Fehrs, J. O.; Qiu, C.; Mirolo, M.; Yuan, C.; Cherevko, S.; Drnec, J.; Magnussen, O. M.; Harrington, D. A., Driving Force of the Initial Step in Electrochemical Pt(111) Oxidation. *The Journal of Physical Chemistry Letters* **2023,** *14* (14), 3589-3593.
24. Kim, J.-H.; Kim, S.; Kim, H.; Wooh, S.; Cho, J.; Dickey, M. D.; So, J.-H.; Koo, H.-J., Imbibition-induced selective wetting of liquid metal. *Nature Communications* **2022,** *13* (1), 4763.
25. Cui, Y.; Liang, F.; Yang, Z.; Xu, S.; Zhao, X.; Ding, Y.; Lin, Z.; Liu, J., Metallic Bond-Enabled Wetting Behavior at the Liquid Ga/CuGa2 Interfaces. *ACS Applied Materials & Interfaces* **2018,** *10* (11), 9203-9210.
26. Eaker, C. B.; Khan, M. R.; Dickey, M. D., A Method to Manipulate Surface Tension of a Liquid Metal via Surface Oxidation and Reduction. *The Journal of Visualized Experiments* **2016,** (107), e53567.
27. Hazelnis, J. P.; Maldonado, S., Electrosynthesis of Quasi-Epitaxial Crystals on Liquid Metals. *Journal of the American Chemical Society* **2023,** *145* (50), 27616-27625.
28. Hirsch, A.; Lacour, S. P., A Method to Form Smooth Films of Liquid Metal Supported by Elastomeric Substrate. *Advanced Science* **2018,** *5* (10), 1800256.
29. Cheng, C.-W.; Shiu, K.-T.; Li, N.; Han, S.-J.; Shi, L.; Sadana, D. K., Epitaxial lift-off process for gallium arsenide substrate reuse and flexible electronics. *Nature Communications* **2013,** *4* (1), 1577.
30. Kim, J.-H.; Kim, S.; Dickey, M. D.; So, J.-H.; Koo, H.-J., Interface of gallium-based liquid metals: oxide skin, wetting, and applications. *Nanoscale Horizons* **2024,** *9* (7), 1099-1119.
31. Liu, J.; Fu, L., Controllable growth of graphene on liquid surfaces. *Advanced Materials* **2019,** *31* (9), 1800690.
32. Van Ngoc, H.; Qian, Y.; Han, S. K.; Kang, D. J., PMMA-Etching-Free Transfer of Wafer-scale Chemical Vapor Deposition Two-dimensional Atomic Crystal by a Water Soluble Polyvinyl Alcohol Polymer Method. *Scientific Reports* **2016,** *6* (1), 33096.
33. Zavabeti, A.; Ou, J. Z.; Carey, B. J.; Syed, N.; Orrell-Trigg, R.; Mayes, E. L. H.; Xu, C.; Kavehei, O.; O'Mullane, A. P.; Kaner, R. B.; Kalantar-zadeh, K.; Daeneke, T., A liquid metal reaction environment for the room-temperature synthesis of atomically thin metal oxides. *Science* **2017,** *358* (6361), 332-335.

34. Wandless, M.-V.; Nord, G. L. *Sample preparation techniques for transmission electron microscopy of geologic materials*; 2331-1258; US Geological Survey: 1986.
35. Friedensen, S.; Mlack, J. T.; Drndić, M., Materials analysis and focused ion beam nanofabrication of topological insulator Bi2Se3. *Scientific Reports* **2017,** *7* (1), 13466.
36. Cox, D. C., Introduction to Focused Ion Beam Nanometrology. Morgan & Claypool Publishers: 2015.
37. Ito, H.; Hasegawa, K.; Matsuki, T.; Kusumoto, S. In *Development of lift-off photoresists with unique bottom profile*, 2015 International Conference on Electronics Packaging and iMAPS All Asia Conference (ICEP-IAAC), 14-17 April 2015; 2015; pp 633-637.
38. Likhanov, M. S.; Verchenko, V. Y.; Bykov, M. A.; Tsirlin, A. A.; Gippius, A. A.; Berthebaud, D.; Maignan, A.; Shevelkov, A. V., Crystal growth, electronic structure, and properties of Ni-substituted FeGa3. *Journal of Solid State Chemistry* **2016,** *236*, 166-172.
39. Wang, X.; Repaka, D. V. M.; Suwardi, A.; Zhu, Q.; Wu, J.; Xu, J., Thermal and Electrical Properties of Liquid Metal Gallium During Phase Transition. *Transactions of Tianjin University* **2023,** *29* (3), 209-215.
40. Tokumoto, Y.; Hamano, K.; Nakagawa, S.; Kamimura, Y.; Suzuki, S.; Tamura, R.; Edagawa, K., Superconductivity in a van der Waals layered quasicrystal. *Nature Communications* **2024,** *15* (1), 1529.
41. Sun, L.; Wang, J.; Bonaccurso, E., Conductivity of individual particles measured by a microscopic four-point-probe method. *Scientific Reports* **2013,** *3* (1), 1991.
42. HASEGAWA, S.; SHIRAKI, I.; TANABE, F.; HOBARA, R.; KANAGAWA, T.; TANIKAWA, T.; MATSUDA, I.; PETERSEN, C. L.; HANSEN, T. M.; BOGGILD, P.; GREY, F., Electrical Conduction Through Surface Superstructures Measured by Microscopic Four-Point Probes. *Surface Review and Letters* **2003,** *10* (06), 963-980.
43. DeMuth, J.; Ma, L.; Lancaster, M.; Acharya, S.; Cheek, Q.; Maldonado, S., Eutectic-Bismuth Indium as a Growth Solvent for the Electrochemical Liquid-Liquid-Solid Deposition of Germanium Microwires and Coiled Nanowires. *Crystal Growth & Design* **2018,** *18* (2), 677-685.
44. Seifner, M. S.; Sistani, M.; Porrati, F.; Di Prima, G.; Pertl, P.; Huth, M.; Lugstein, A.; Barth, S., Direct Synthesis of Hyperdoped Germanium Nanowires. *ACS Nano* **2018,** *12* (2), 1236-1241.
45. Mahenderkar, N. K.; Liu, Y.-C.; Koza, J. A.; Switzer, J. A., Electrodeposited Germanium Nanowires. *ACS Nano* **2014,** *8* (9), 9524-9530.
46. Kumar, S.; Kumar, P.; Pratap, R., A model for electromigration induced flow in liquid metals. *Journal of Physics D: Applied Physics* **2017,** *50* (39), 39LT02.
47. Kim, K.; Kim, S.; Hong, J.; Lee, J.; Hong, T.; Bolotnikov, A. E.; Camarda, G. S.; James, R. B., Purification of CdZnTe by electromigration. *Journal of Applied Physics* **2015,** *117* (14).
48. Ho, P. S.; Kwok, T., Electromigration in metals. *Reports on Progress in Physics* **1989,** *52* (3), 301.
49. D'Heurle, F. M.; Rosenberg, R., Electromigration in Thin Films. In *Physics of Thin Films*, Hass, G.; Francombe, M. H.; Hoffman, R. W., Eds. Elsevier: 1973; Vol. 7, pp 257-310.
50. Epstein, S. G., Electromigration of a series of solutes in liquid bismuth. *Advances in Physics* **1967,** *16* (62), 325-332.

Appendices

Appendix A: Supporting Information for Chapter 2

A.1 Contents

This section contains supporting information for Chapter 2 entitled "*Detection of Ge-Containing Adlayers at the Liquid Hg/Water Interface by In Situ X-Ray Reflectivity in Aqueous Borate Electrolytes Containing Dissolved GeO_2.*' Section A.2 summarizes the explicit form of the 'master formula' using *Equation* 2.6 of the main text for $\rho_e(z)$. Section A.3 presents the explicit form of the 'master formula' using *Equation* 2.7 of the main text for $\rho_e(z)$ to describe adsorbed $H_2GeO_3/HGeO_3^-$. Section A.4 presents the full expression for the distance-dependent electron density profile normal to the surface plane for a Hg surface featuring a partial coating of GeO_2.

A.2 Refinement to *Equation* 2.2 to Describe Enrichment Hg Interface with General Gaussian Terms

The following expressions constitute a refinement to the model described by *Equation* 2.5 in the main text. In the approach presented below, additional Gaussian terms were included to account for the possibility of additional electron density throughout the solution/Hg interface. These new Gaussian terms do not pertain to any specific element and so they cannot give precise information of composition or structure. Instead, the intent of these general Gaussian terms was to assess where excess electron density was needed to yield a good match to the data. This information was used to generate the structure-specific model described in the next section.

$$\rho_e(z) = \frac{1}{2}\rho_{e,H_2O}\left(\operatorname{erfc}\left(\frac{z - z_{H_2O}}{\sigma_{H_2O}\sqrt{2}}\right)\right) + F_{Hg}(z) \otimes \left[+ \frac{\rho_{e,ad-Hg}}{\rho_{e,Hg}} \frac{1}{\sigma_{ad,Hg}\sqrt{2\pi}} e^{\frac{-\left(z - z_{ad,Hg}\right)^2}{2\sigma_{ad,Hg}^2}} + \sum_{n=0}^{\infty} \frac{d}{\sqrt{\sigma_i^2 + n\sigma_b^2}\sqrt{2\pi}} e^{\frac{-(z-nd)^2}{2\left(\sigma_i^2 + n\sigma_b^2\right)}} \right]$$
$$+ \left[\sum_{m=1}^{3} \rho_{ad,m} \frac{1}{\sigma_m\sqrt{2\pi}} e^{\frac{-(z-z_m)^2}{2\sigma_m^2}} \right]$$

Appendix Equation A.1

Inserting *Appendix Equation* A.1 into *Equation* 2.1 of the main text yields the following result.

$$\frac{R(q_z)}{R_F(q_z)} = \left| \frac{1}{\rho_{e,Hg} - \rho_{e,H_2O}} \left(\frac{f_{Hg}^0(q_z) + f'_{Hg}}{Z_{Hg} + f'_{Hg}} \left[iq_z d \frac{e^{\frac{-q_z^2\sigma_i^2}{2}}}{\left(1 - e^{iq_z d - \frac{q_z^2\sigma_b^2}{2}}\right)} + \frac{iq_z\rho_{ad}}{\rho_{e,Hg}} e^{-iq_z z_{ad} - \frac{q_z^2\sigma_{ad}^2}{2}} \right] - \rho_{e,H_2O} e^{iq_z z_{H_2O} - \frac{q_z^2\sigma_{H_2O}}{2}} \right. \right.$$
$$\left. \left. + \sum_{m=1}^{3} iq_z\rho_{ad,m} e^{-iq_z z_m - \frac{q_z^2\sigma_m^2}{2}} \right) \right|^2$$

Appendix Equation.A.2

A.3 Refinement to *Equation* 2.2 to Describe Enrichment of $H_2GeO_3/HGeO_3^-$ at Hg Interface

The following expressions constitute a refinement to the model described by *Equation* 2.5 in the main text. In the approach presented below, additional Gaussian terms were added that collectively describe a separate 'adlayer' of $HGeO_3^-$ in addition to the Hg 'adlayer' term. Appendix Figure.A.1 describes the employed model.

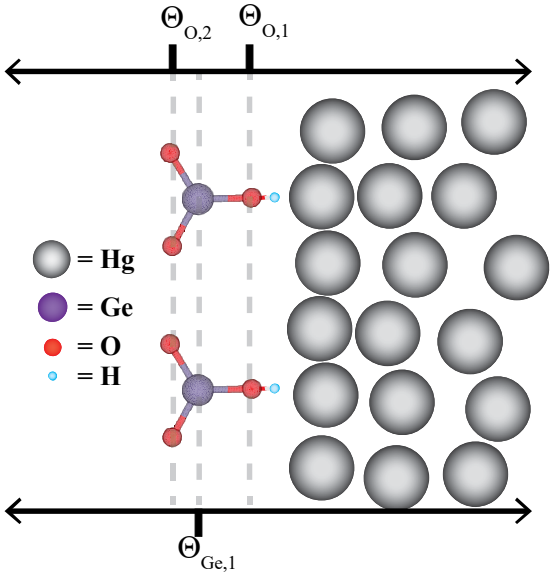

Appendix Figure.A.1 Pictorial representation of an 'adlayer'of $HGeO_3^-$ ions. The gray dashed lines indicate the layers of atoms that are described by a Gaussian term with the atomic form factors of either Ge or O, respectively.

In the following expressions, the term θ_{HGeO3-} corresponds to the fractional coverage of this 'adlayer'.

$$\rho_e(z)=\frac{1}{2}\rho_{e,H_2O}\left(\operatorname{erfc}\left(\frac{z-z_{H_2O}}{\sigma_{H_2O}\sqrt{2}}\right)\right)+F_{Hg}(z)\otimes\left[\frac{\rho_{e,ad-Hg}}{\rho_{e,Hg}}\frac{1}{\sigma_{ad,Hg}\sqrt{2\pi}}e^{\frac{-\left(z-z_{ad,Hg}\right)^2}{2\sigma_{ad,Hg}^2}}+\sum_{n=0}^{\infty}\frac{d}{\sqrt{\sigma_i^2+n\sigma_b^2}\sqrt{2\pi}}e^{\frac{-(z-nd)^2}{2\left(\sigma_i^2+n\sigma_b^2\right)}}\right]$$

$$+F_{Ge}(z)\otimes\left[\Theta_{HGeO_3^-/Hg}\frac{1}{\sigma_{ad}\sqrt{2\pi}}e^{\frac{-\left(z-z_{ad,Ge_j}\right)^2}{2\sigma_{ad,Ge}^2}}\right]+F_O(z)\otimes\left[\sum_{k=1}^{2}\Theta_{HGeO_3^-/Hg}\frac{1}{k\sigma_{ad,O}\sqrt{2\pi}}e^{\frac{-\left(z-z_{ad,O_k}\right)^2}{2\sigma_{ad,O}^2}}\right]$$

Appendix Equation.A.3

In this expression, $F_{Ge}(z)$ and $F_O(z)$ are the Fourier transforms of the Ge and O atomic form factors, respectively. The term $\Theta_{HGeO3-/Hg}$ has units of Å and describes the fractional coverage of the

$HGeO_3^-$ adlayer on bare Hg. Notably, the outer O atoms are twice as numerous as the inner O atoms.

The result of inserting *Appendix Equation*.A.2 in *Equation* 2.1 of the main text is given below,

$$\frac{R(q_z)}{R_F(q_z)}=\left|\frac{1}{\rho_{e,Hg}-\rho_{e,H_2O}}\left(\begin{array}{l}\dfrac{f^0_{Hg}(q_z)+f'_{Hg}}{Z_{Hg}+f'_{Hg}}\left[iq_z d\dfrac{e^{\frac{q_z^2\sigma_i^2}{2}}}{\left(1-e^{iq_z d-\frac{q_z^2\sigma_b^2}{2}}\right)}+\dfrac{iq_z\rho_{ad,e-Hg}}{\rho_{e,Hg}}e^{-iq_z z_{ad}-\frac{q_z^2\sigma_{ad}^2}{2}}\right]-\rho_{e,H_2O}e^{iq_z z_{H_2O}-\frac{q_z^2\sigma_{H_2O}}{2}} \\ +\dfrac{f^0_{Ge}(q_z)+f'_{Ge}}{Z_{Hg}+f'_{Ge}}iq_z\Theta_{HGeO_3^-/Hg}e^{-iq_z z_{ad,Gej}-\frac{q_z^2\sigma^2_{ad,Ge}}{2}}+\dfrac{f^0_O(q_z)+f'_O}{Z_{Hg}+f'_O}\sum_{k=1}^{2}\frac{1}{k}iq_z\Theta_{HGeO_3^-/Hg}e^{-iq_z z_{ad,O_k}-\frac{q_z^2\sigma^2_{ad,O}}{2}}\end{array}\right)\right|^2$$

Appendix Equation.A.4

where $f^0_{Ge}(q_z)$ and f'_{Ge} are the angle-dependent Ge atomic form factor and the dispersion correction, respectively, and $f^0_O(q_z)$ and f'_O are the angle-dependent O atomic form factor and the dispersion correction, respectively.

A.4 Description of the Distance-Dependent Electron Density Profile for a Hg interface Featuring a Partial Coverage of GeO_2

The explicit terms in each component of *Equation* 2.7 in the main text (reproduced here as *Appendix* Equation.A**.5**) are presented below in *Appendix* Equation.A**.6**-Appendix Equation**.A.10**. The general definitions for each term follow the description in the main text, except that subscripts *j* and *i* denote distinct Ge and O atoms, respectively.

$$\rho_e(z)=\rho_{e,electrolyte}+\rho_{DCM,Hg}+\left(1-\theta_{GeO_2}\right)\rho_{ad,Ge/Hg}+\theta_{GeO_2}\rho_{ad,Ge/GeO_2}+\theta_{GeO_2}\rho_{e,GeO_2}$$

Appendix Equation.A.5

$$\rho_{e,electrolyte} = \frac{1}{2}\rho_{e,H_2O}\left(\operatorname{erfc}\left(\frac{z - z_{H_2O}}{\sigma_{H_2O}\sqrt{2}}\right)\right)$$

Appendix Equation.A.6

$$\rho_{DCM,Hg} = F_{Hg}(z) \otimes \left[\frac{\rho_{e,ad-Hg}}{\rho_{e,Hg}} \frac{1}{\sigma_{ad,Hg}\sqrt{2\pi}} e^{\frac{-\left(z - z_{ad,Hg}\right)^2}{2\sigma_{ad,Hg}^2}} + \sum_{n=0}^{\infty} \frac{d}{\sqrt{\sigma_i^2 + n\sigma_b^2}\sqrt{2\pi}} e^{\frac{-(z-nd)^2}{2\left(\sigma_i^2 + n\sigma_b^2\right)}}\right]$$

Appendix Equation.A.7

$$\rho_{ad,HGeO_3^-/Hg} = F_{Ge}(z) \otimes \left[\Theta_{HGeO_3^-/Hg} \frac{1}{\sigma_{ad,Ge}\sqrt{2\pi}} e^{\frac{-\left(z - z_{ad,Ge_j}\right)^2}{2\sigma_{ad,Ge}^2}}\right] + F_O(z) \otimes \left[\sum_{k=1}^{2} k\Theta_{HGeO_3^-/GeO_2} \frac{1}{\sigma_{ad,O}\sqrt{2\pi}} e^{\frac{-\left(z - z_{ad,O_i}\right)^2}{2\sigma_{ad,O}^2}}\right]$$

Appendix Equation.A.8

$$\rho_{ad,HGeO_3^-/GeO_2} = F_{Ge}(z) \otimes \left[\Theta_{HGeO_3^-/GeO_2} \frac{1}{\sigma_{ad,Ge}\sqrt{2\pi}} e^{\frac{-\left(z - z_{ad,Ge_j}\right)^2}{2\sigma_{ad,Ge}^2}}\right] + F_O(z) \otimes \left[\sum_{k=1}^{2} k\Theta_{HGeO_3^-/GeO_2} \frac{1}{\sigma_{ad,O}\sqrt{2\pi}} e^{\frac{-\left(z - z_{ad,O_i}\right)^2}{2\sigma_{ad,O}^2}}\right]$$

Appendix Equation.A.9

$$\rho_{e,GeO_2} = \sum_{j=1}^{2}\left(F_{Ge}(z) \otimes \left[\Theta_{\text{Ge bi}\,j} \frac{1}{\sigma_{ad}\sqrt{2\pi}} e^{\frac{-\left(z - z_{ad,Ge_j}\right)^2}{2\sigma_{ad,Ge}^2}}\right] + F_O(z) \otimes \left[\sum_{k=1}^{3} \Theta_{\text{O bi}\,j,k} \frac{1}{\sigma_{ad,O}\sqrt{2\pi}} e^{\frac{-\left(z - z_{ad,O_i}\right)^2}{2\sigma_{ad,O}^2}}\right]\right)$$

Appendix Equation.A.10

In these expressions, $\Theta_{HGeO3-/Hg}$, $\Theta_{HGeO3-/GeO2}$, $\Theta_{Ge\ \text{bi},j}$, and $\Theta_{O\ \text{bi},j,k}$ have units of Å. The first terms describe the fractional coverages of the $HGeO_3^-$ adlayer on bare Hg and on GeO_2, respectively.

The last two terms describe the individual coverages of Ge and O atoms, respectively, that constitute a GeO_2 bilayer film with a rutile structure.

The result of the master formula in this case is given below,

$$\frac{R(q_z)}{R_F(q_z)}=\left|\frac{1}{\rho_{e,Hg}-\rho_{e,H_2O}}\left(\begin{array}{l}\dfrac{f^0_{Hg}(q_z)+f'_{Hg}}{Z_{Hg}+f'_{Hg}}\left[iq_z d\dfrac{e^{-\frac{q_z^2\sigma_f^2}{2}}}{\left(1-e^{iq_z d-\frac{q_z^2\sigma_b^2}{2}}\right)}+iq_z\dfrac{\rho_{e,ad-Hg}}{\rho_{e,Hg}}e^{-iq_z z_{ad}-\frac{q_z^2\sigma_{ad}^2}{2}}\right]-\rho_{H_2O}e^{iq_z z_{H_2O}-\frac{q_z^2\sigma_{H_2O}}{2}}\\ +\left(1-\theta_{GeO_2}\right)\left(\dfrac{f^0_{Ge}(q_z)+f'_{Ge}}{Z_{Hg}+f'_{Ge}}iq_z\Theta_{HGeO_3^-/Hg}e^{-iq_z z_{ad,Gej}-\frac{q_z^2\sigma_{ad,Ge}^2}{2}}+\dfrac{f^0_O(q_z)+f'_O}{Z_{Hg}+f'_O}\sum_{k=1}^{2}\dfrac{iq_z\Theta_{HGeO_3^-/Hg}}{k}e^{-iq_z z_{ad,Oj}-\frac{q_z^2\sigma_{ad,O}^2}{2}}\right)\\ +\theta_{GeO_2}\left(\dfrac{f^0_{Ge}(q_z)+f'_{Ge}}{Z_{Hg}+f'_{Ge}}iq_z\Theta_{HGeO_3/GeO_2}e^{-iq_z z_{ad,Gej}-\frac{q_z^2\sigma_{ad,Ge}^2}{2}}+\dfrac{f^0_O(q_z)+f'_O}{Z_{Hg}+f'_O}\sum_{k=1}^{2}iq_z\Theta_{HGeO_3/GeO_2}e^{-iq_z z_{ad,Ok}-\frac{q_z^2\sigma_{ad,O}^2}{2}}\right)\\ +\theta_{GeO_2}\sum_{j=1}^{2}\left(\dfrac{f^0_{Ge}(q_z)+f'_{Ge}}{Z_{Hg}+f'_{Ge}}iq_z\Theta_{Ge\ bi\ j}e^{-iq_z z_{ad,Gej}-\frac{q_z^2\sigma_{ad,Ge}^2}{2}}+\dfrac{f^0_O(q_z)+f'_O}{Z_{Hg}+f'_O}\sum_{k=1}^{3}iq_z\Theta_{O\ bi\ j,k}e^{-iq_z z_{ad,Ok}-\frac{q_z^2\sigma_{ad,O}^2}{2}}\right)\end{array}\right)^2\right|$$

Appendix Equation.A.11

Appendix Equation.A.**6**-Appendix Equation.**A.9** feature coverage parameters ($\Theta_{HGeO3-/Hg}$ and $\Theta_{HGeO3-/GeO2}$) that are necessarily linked by the rutile structure as shown in Appendix Figure A.**2**.

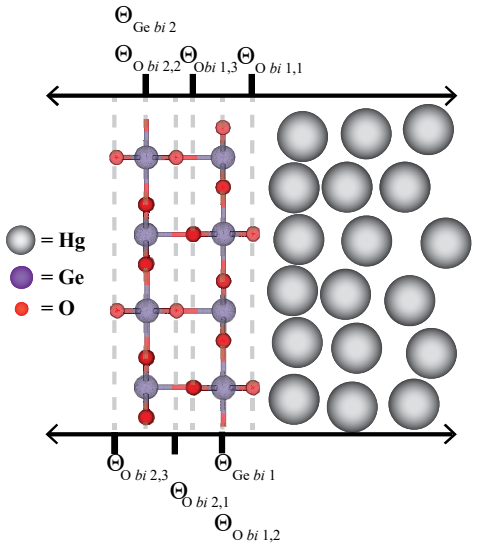

Appendix Figure A.2 Pictorial representation of a rutile bilayer of GeO_2 along the <110> direction used in fitting the data collected at E = -0.2 V. The gray dashed lines indicate the layers of atoms within each of the respective structures

which are described by Gaussian terms with the atomic form factors of Ge or O, respectively. Each layer is defined by a coverage (Θ), position (z), and roughness (σ). The relative positions of atoms within this structure are determined by the lattice bond distances and orientation.

Individual layers of atoms that together constitute GeO_2 are thus described with Gaussian terms for each atom in each layer that have fixed relative coverages (Θ) and positions (z). Roughness values for all Gaussian terms ($\sigma_{ad,Ge}$ and $\sigma_{ad,O}$) are set equal in magnitude to σ_i. The proportionalities for the Θ terms are determined by taking the ratio of Ge or O atoms in a given layer (as denoted by the gray dashed lines) to the Ge or O atoms in another. From Appendix Figure A**.2**, the proportionalities of each coverage term are described in the following expressions.

$$\Theta_{Ge\ bi1} = \Theta_{Ge\ bi2} = \Theta_{O\ bi1,2} = \Theta_{O\ bi2,2}$$

Appendix Equation.A.12

$$\frac{1}{2}\Theta_{Ge\ bi1} = \Theta_{O\ bi1,1} = \Theta_{O\ bi1,3} = \Theta_{O\ bi2,1} = \Theta_{O\ bi2,3}$$

Appendix Equation.A.13

Appendix B: Supporting Information for Chapter 3

B.1 Contents

This document contains supporting information for Chapter 3 entitled "*X-Ray Reflectivity and Scattering of Hg-In Alloy Electrodes*". Section B.2 contains python code used for fitting the reflectivity data of a Hg-In electrode interface. Section B.3 contains python code used to describe the Yoneda feature.

B.2 Full XRR Scan Fitting Python Code

The following section contains code adapted from Sartori et al[1] used to fit the 'full' XRR scans presented in Figure 3.10 for Hg_xIn_{1-x} electrodes. Specifically, the code implements *Equation* 3.4a to accurately describe the experimentally obtained normalized reflectivity curves (R / R_F). Below lists the primary considerations when using this code.

The main fitting file is provided in Section B.2.1 and is the primary file which must be updated and changed when fitting a given curve. The following parameters should be updated accordingly:

"out-filename" = savepath of .dat file

"saving" = naming convention of save file

"file_name" = text file of fitting parameter results

"path_graph" = Path on computer where fitting figures will be saved

"save" and "save_results" = True or False based on whether or not results should be saved

"comp" = bulk liquid metal composition as an atomic fraction (0 to 1)

"comp_first_layer" = composition of first layer as atomic fraction (0 to 1)

"layer_hgin" = this line of code is passed to DCMLayerPers file in Section B.2.2 and can be used to fix certain values or define initial values of any given fitting parameter

"layer_hgin.().fit" = True or False based on whether not a given parameter should be fit. At least one of these values should be set too True, otherwise the code will provide an error. Usually if one wants to run the code without any parameters fitting, set layer_hgin.density_w.fit = True and everything else false because this value is typically fixed and has a small min max range defined.

"layer_hgin.().fit_min" and "layer_hgin.().fit_max" = defines the minimum and maximum fitting range of any given parameter. For the code to properly report standard deviations of a given fit parameter, all parameters being fit must deviate from the starting value and not converge to a maximum or minimum value. Otherwise the standard deviation will be 'none'

"qz_min, qz_max" = range of q_z values to be fit. Useful if you only want to fit a section of a given reflectivity curve.

"df" = change to .csv file of the raw data to be fit

The other Sections B.2.2 through B.2.5 are called upon by the main fitting file and must be correctly named and referenced in the Fitting file header. Use of "XRR." is nomenclature that the file is in a subfolder named "XRR" saved locally on the computer.

B.2.1 Fitting File

```
import matplotlib
from matplotlib.ticker import MultipleLocator
import numpy
import pandas
import sympy
import matplotlib.pyplot as plt
import matplotlib.ticker as ticker
from matplotlib import rcParams

from xrr.model import ElectronDensityModel
from xrr.dcm_JH_edit_firstlayer_2025 import DCMLayer, DCMLayerPers
from xrr.layer import SlabLayer, GaussianLayer,SlabLayerWidth
from xrr.fit_lmFit import fit_model
import warnings


warnings.filterwarnings("ignore")
settings =dict(out_filename = r"E:\Beam Line Data\sept 2021 workup\processed round
13\Hg0.95In0.05_Borax/MinChi/Hg0.95In0.05_Borax_-1.40V_1.dat",
            # output file format default or motofit
            out_format = "default",
            save = False)
saving = "Hg95In05_Borax_-140V_1"
save_results = False
file_name=r"E:\Beam Line Data\sept 2021 workup\processed round 13\Hg0.95In0.05_Borax/MinChi/Hg0.95In0.05_Borax_-1.40V_1.txt"
path_graph=r"E:\Beam Line Data\sept 2021 workup\processed round 13\Hg0.95In0.05_Borax/MinChi/"

def fresnel(qc, qz, roughness=0, beta=0, wl=1):
   return (numpy.exp(-qz**2 * roughness**2) *
         abs((qz - numpy.sqrt((qz**2 - qc**2) + beta*32j*numpy.pi**2/wl**2)) /
         (qz + numpy.sqrt((qz**2 - qc**2) + beta*32j*numpy.pi**2/wl**2)))**2)


comp = 0.35 #Hg Composition and Atomic Percent
comp_first_layer = 0.35
################Critical Angles and SLD####################
delta1w=3.68895286E-07
delta2w=3.68836169E-07

deltaH2O= (delta1w+delta2w)*0.5

#######Mercury/Water##############

delta1m=3.56932765E-06
delta2m=3.56904411E-06

deltaHg= (delta1m+delta2m)*0.5
alphac_Hg_r =numpy.sqrt(2*(deltaHg))
qc_Hg = 4*numpy.pi* numpy.sin(alphac_Hg_r) / 0.4959
SLD_Hg = qc_Hg**2 / (16* numpy.pi)



alphac_Hg_r_H2O =numpy.sqrt(2*(deltaHg-deltaH2O))
qc_Hg_H2O = 4*numpy.pi* numpy.sin(alphac_Hg_r_H2O) / 0.4959
SLD_Hg_H2O = qc_Hg_H2O**2 / (16* numpy.pi)

#######Indium/Water##############
delta1i=1.99647548E-06
```

```
delta2i=1.99630472E-06

deltaIn=  (delta1i+delta2i)*0.5
alphac_In_r =numpy.sqrt(2*(deltaIn))
qc_In= 4*numpy.pi* numpy.sin(alphac_In_r) / 0.4959
SLD_In= qc_In**2 / (16* numpy.pi)


alphac_In_r_H2O =numpy.sqrt(2*(deltaIn-deltaH2O))
qc_In_H2O= 4*numpy.pi* numpy.sin(alphac_In_r_H2O) / 0.4959
SLD_In_H2O= qc_In_H2O**2 / (16* numpy.pi)

##############################

alphac = numpy.sqrt(2*((comp*deltaHg + (1-comp)*deltaIn)-deltaH2O))
qc = 4*numpy.pi* numpy.sin(alphac) / 0.4959
SLD = qc**2 / (16* numpy.pi)

############################################################


def formfactor_hgin(qz): #https://lampx.tugraz.at/~hadley/ss1/crystaldiffraction/atomicformfactors/formfactors.php
   S_hg = (12.689 +
      20.6809 * sympy.exp(-0.545*qz**2/(16*sympy.pi**2)) +
      19.0417 * sympy.exp(-8.4484*qz**2/(16*sympy.pi**2)) +
      21.6575 * sympy.exp(-1.5729*qz**2/(16*sympy.pi**2)) +
      5.9676 * sympy.exp(-38.3246*qz**2/(16*sympy.pi**2)))
   S_in = (4.9391 + 19.1624 * sympy.exp(-0.5476*qz**2/(16*sympy.pi**2)) +
        18.5596 * sympy.exp(-6.3776*qz**2/(16*sympy.pi**2)) +
       4.2948 * sympy.exp(-25.8499*qz**2/(16*sympy.pi**2)) +
       2.0396 * sympy.exp(-92.8029*qz**2/(16*sympy.pi**2)))
   S=S_hg*comp + S_in *(1-comp)
   return S



def formfactor_hgin_first_layer(qz): #https://lampx.tugraz.at/~hadley/ss1/crystaldiffraction/atomicformfactors/formfactors.php
   S_hg = (12.689 +
      20.6809 * sympy.exp(-0.545*qz**2/(16*sympy.pi**2)) +
      19.0417 * sympy.exp(-8.4484*qz**2/(16*sympy.pi**2)) +
      21.6575 * sympy.exp(-1.5729*qz**2/(16*sympy.pi**2)) +
      5.9676 * sympy.exp(-38.3246*qz**2/(16*sympy.pi**2)))
   S_in = (4.9391 + 19.1624 * sympy.exp(-0.5476*qz**2/(16*sympy.pi**2)) +
        18.5596 * sympy.exp(-6.3776*qz**2/(16*sympy.pi**2)) +
       4.2948 * sympy.exp(-25.8499*qz**2/(16*sympy.pi**2)) +
       2.0396 * sympy.exp(-92.8029*qz**2/(16*sympy.pi**2)))
   S=S_hg*comp_first_layer + S_in *(1-comp_first_layer)
   return S

hgin_Zeff_first_layer = (80 - (80/82.5)**2.37)*(comp_first_layer) + 48.0097 * (1-comp_first_layer)
hgin_Zeff = (80 - (80/82.5)**2.37)*(comp) + 48.0097 * (1-comp)
hgin_beta = (2.354E-07 *comp) + (2.8867E-08 *(1-comp)) #https://henke.lbl.gov/optical_constants/pert_form.html
hgin_qc = qc
wavelength = 0.4959 # in Angstrom

# ==== load data
df = pandas.read_csv("E:/Beam Line Data/sept 2021 workup/processed round
6/Hg0.35In0.65_Borax/Hg0.35In0.65_Borax_XRR_Hg0.35In0.65_Borax_-1.00V_appendlayering.dat", sep="\t")

qz = df["qz"]
alpha = numpy.arcsin(qz * wavelength / (4 * numpy.pi))

intensity = df["intensity_normalized"]
e_intensity = df["e_intensity_normalized"]
qz_smooth = numpy.linspace(0, 2.5, 1000)

# ==== prepare data normalized to Fresnel
fresnel_intens = fresnel(hgin_qc, qz, beta=hgin_beta, wl=wavelength)
fresnel_intens_smooth = fresnel(hgin_qc, qz_smooth, beta=hgin_beta, wl=wavelength)
intensity_norm = intensity/fresnel_intens
```

```
e_intensity_norm = e_intensity/fresnel_intens


# ==== create electron density model
m = ElectronDensityModel()

#                    df,    rhof,   sigmaf,  d,     sig i,   sig b,    Rho w = 1,   z water,   sig water)
layer_hgin = DCMLayerPers(3.21,  1.36,   1.12,   2.69,   0.79,    0.43,       1,       -0.12,      -0.66, hgin_Zeff, hgin_Zeff_first_layer,
position=0, formfactor=formfactor_hgin, formfactor_first_layer=formfactor_hgin_first_layer )
m.add(layer_hgin)


# ==== fit model to data
# == set qz limit for fit
qz_min, qz_max = 0.1, 2.5#0.15, 1.5#

mask = (qz >= qz_min) & (qz <= qz_max)

# == define which parameters to fit
fit=True
if fit:
   fit_para=True
else:
   fit_para=False

layer_hgin.density_w.fit = True
layer_hgin.density_w.fit_min = 0.999999999999#0.16999
layer_hgin.density_w.fit_max = 1.00#0.1701
layer_hgin.mu_w.fit = False
layer_hgin.mu_w.fit_min = -4
layer_hgin.mu_w.fit_max = -0.1
layer_hgin.sigma_w.fit = False
layer_hgin.sigma_w.fit_max =-0.65
layer_hgin.sigma_w.fit_min =-3

layer_hgin.d_mod.fit = False
layer_hgin.d_mod.fit_min= 2.80
layer_hgin.d_mod.fit_max= 3.40
layer_hgin.r_mod.fit = False
layer_hgin.r_mod.fit_min= 1.014
layer_hgin.r_mod.fit_max= 1.30
layer_hgin.s_mod.fit = False
layer_hgin.s_mod.fit_min= 1.06
layer_hgin.s_mod.fit_max= 1.50

layer_hgin.density.fit = False  # do not fit the mercury density

layer_hgin.d.fit = False
layer_hgin.d.fit_min=2.6
layer_hgin.d.fit_max=2.8
layer_hgin.sigma_i.fit = False # do fit the intrinsic roughness
layer_hgin.sigma_i.fit_min = 0.5
layer_hgin.sigma_i.fit_max= 1.2
layer_hgin.sigma_b.fit = False # do fit the roughness increase per layer
layer_hgin.sigma_b.fit_min = 0.4
layer_hgin.sigma_b.fit_max = 0.6

# == run the fit


z = numpy.linspace(-20, 20, 10000)
rho_guessed = m(z)
popt, perr, rrf_fitted = fit_model(m, qz[mask], intensity_norm[mask],
                           weights=qz[mask], plot=0)#, method='shgo')#,differential_evolution')#, ftol=          1e-3,xtol = 1e-3)#,glbtol=1e-7)

# == show fitted parameter values
params = m.get_params()
# ==== get initial parameters
_, fit_params = m.get_fit_func()
p_init = [p.value for p in fit_params]
```

```
for p in params:
    if p.fit:
        print("{0} = {1} +/- {2}".format(p.name, p.value, p.fit_error))



# ============================================================================
print("layer_hgin.density_w", layer_hgin.density_w.value, "+-", layer_hgin.density_w.fit_error)
print("layer_hgin.mu_w", layer_hgin.mu_w.value, "+-", layer_hgin.mu_w.fit_error)
print("layer_hgin.sigma_w", layer_hgin.sigma_w.value, "+-", layer_hgin.sigma_w.fit_error)


print("layer_hgin.sigma_i", layer_hgin.sigma_i.value, "+-", layer_hgin.sigma_i.fit_error)
print("layer_hgin.sigma_b", layer_hgin.sigma_b.value, "+-", layer_hgin.sigma_b.fit_error)
print("layer_hgin.d", layer_hgin.d.value, "+-", layer_hgin.d.fit_error)

print("layer_hgin.d_mod", layer_hgin.d_mod.value, "+-", layer_hgin.d_mod.fit_error)
print("layer_hgin.r_mod", layer_hgin.r_mod.value, "+-", layer_hgin.r_mod.fit_error)
print("layer_hgin.s_mod", layer_hgin.s_mod.value, "+-", layer_hgin.s_mod.fit_error)

metal_e_density = comp*SLD_Hg+(1-comp)*SLD_In
print(metal_e_density)

print("Hg content", ((layer_hgin.r_mod.value*metal_e_density)- SLD_In)/(SLD_Hg - SLD_In))

print('SLD Hg: ' + str(SLD_Hg))
print('SLD_In: ' + str(SLD_In))

print("Hg content with H2O", ((layer_hgin.r_mod.value*SLD)- SLD_In_H2O)/(SLD_Hg_H2O - SLD_In_H2O))

print('SLD Hg/H2O: ' + str(SLD_Hg_H2O))
print('SLD_In/H2O: ' + str(SLD_In_H2O))


# ============================================================================

if save_results:
    results = open(file_name,"w+")
    results.write("HgIn_fullXRR_-1400-632_640.dat")
    results.write("\n")
    results.write("sigma_i= "+ str(layer_hgin.sigma_i.value)+ " +- " +str(layer_hgin.sigma_i.fit_error))
    results.write("\n")
    results.write("sigma_b= "+ str(layer_hgin.sigma_b.value)+ " +- " +str(layer_hgin.sigma_b.fit_error))
    results.write("\n")
    results.write("d= "+str(layer_hgin.d.value)+ " +- " +str(layer_hgin.d.fit_error))
    results.write("\n")
    results.write("d_first= "+str(layer_hgin.d_mod.value)+ " + -" +str(layer_hgin.d_mod.fit_error))
    results.write("\n")
    results.write("r_first= "+str(layer_hgin.r_mod.value)+ " +- " +str(layer_hgin.r_mod.fit_error))
    results.write("\n")
    results.write("sigma_first= "+str(layer_hgin.s_mod.value)+ " +- " +str(layer_hgin.s_mod.fit_error))
    results.write("\n")
    results.write("mu_w= "+str(layer_hgin.mu_w.value)+ " +- " +str(layer_hgin.mu_w.fit_error))
    results.write("\n")
    results.write("sigma_w= "+str(layer_hgin.sigma_w.value)+ " +- " +str(layer_hgin.sigma_w.fit_error))
    results.write("\n")
    results.close()

# ============================================================================



# ========fix plot============================================================

RRF_fit=abs(rrf_fitted(qz_smooth, *popt))
```

```
# ============================================================================

# ==== plot data and fit (XRR-curve)
plt.rc('font', size=28)          # controls default text sizes
plt.rc('axes', titlesize=15)     # fontsize of the axes title
plt.rc('axes', labelsize=24)    # fontsize of the x and y labels
plt.rc('xtick', labelsize=15)    # fontsize of the tick labels
plt.rc('ytick', labelsize=15)    # fontsize of the tick labels
plt.rc('legend', fontsize=24)    # legend fontsize
plt.rc('figure', titlesize=15)  # fontsize of the figure title# ==== plot data and fit (XRR-curve)


matplotlib.rcParams['axes.linewidth'] = 2
matplotlib.rcParams['xtick.major.size'] = 10
matplotlib.rcParams['xtick.major.width'] = 3
matplotlib.rcParams['xtick.minor.size'] = 5
matplotlib.rcParams['xtick.minor.width'] = 1.5

matplotlib.rcParams['ytick.major.size'] = 10
matplotlib.rcParams['ytick.major.width'] = 3
matplotlib.rcParams['ytick.minor.size'] = 5
matplotlib.rcParams['ytick.minor.width'] = 1.5

fig = plt.figure("XRR Curve" , figsize=(12,8))
ax = fig.gca()
ax.set_yscale("log")

ax.plot(qz, fresnel(hgin_qc, qz, beta=hgin_beta, wl=wavelength), c="k", ls="--",label="Fresnel")
ax.errorbar(qz, intensity, yerr=e_intensity, ls="none", marker="o", mew=2.0,
         mec="#e31a1c", mfc="white", c="#fa9897", label="Data")

#Or to plot the XRR curve (not normalized to Rf):

#ax.plot(qz_smooth, rrf_fitted(qz_smooth, *p_init)*fresnel_intens_smooth,label="Initial para", c="green", alpha=0.2)
#
ax.plot(qz_smooth, RRF_fit*fresnel_intens_smooth,label="Fit", lw=3.0)

ax.xaxis.set_minor_locator(ticker.AutoMinorLocator())
#ax.yaxis.set_minor_locator(ticker.AutoMinorLocator())

ax.set_xlabel(r"$q_z$ /$\AA$$^{-1}$", fontsize=28)
ax.set_ylabel("$R$", fontsize=28)
ax.tick_params(which='both', direction='in')
plt.tick_params(labelsize=24)
plt.tight_layout()
# ax.set_title("E= -1700 mV vs $[Hg/HgSO_4]$")
ax.legend()
plt.tight_layout()
if save_results:
    plt.savefig(path_graph+ "XRR_Curve" + str(saving), dpi=300)

# ==== plot data and fit R/R0.7
fig = plt.figure("R/RF" , figsize=(12,8))
ax = fig.gca()


#Then, to plot R/Rf, add the following line where you plot the other R/Rf data:
#
# ============================================================================
#ax.plot(qz_smooth, rrf_fitted(qz_smooth, *p_init), label="Initial para", c="green", alpha=0.2)
# ============================================================================


ax.errorbar(qz, intensity_norm, yerr=e_intensity_norm, ls="none", marker="o", mew=2.0,
         mec="#e31a1c", mfc="white", c="#fa9897", label="Data")

ax.plot(qz_smooth, RRF_fit, label="Fit",lw=3.0 ) #str(layer_hgin.d_mod.value)+ " " +str(layer_hgin.r_mod.value)
```

```
ax.plot([0, 2.5], [1,1], ls="--", label="Fresnel", c="black")

ax.xaxis.set_minor_locator(ticker.AutoMinorLocator())
ax.yaxis.set_minor_locator(ticker.AutoMinorLocator())

ax.set_xlabel(r"$q_z$ /$\AA$$^{-1}$", fontsize=28)
ax.set_ylabel("$R/R_F$", fontsize=28)
ax.tick_params(which='both', direction='in')
plt.tick_params(labelsize=24)
plt.tight_layout()
# ax.set_title("")

ax.legend()
plt.tight_layout()
if save_results:
    plt.savefig(path_graph+ "RRf" + str(saving), dpi=300)

# ==== plot electron density model
fig = plt.figure("Electron Density" , figsize=(12,8))
ax = fig.gca()

z = numpy.linspace(-20, 20, 10000)
ax.plot(z, m(z), lw=3.0)
#ax.plot(z, rho_guessed, c="green", alpha=0.2)
for layer in m._layers:
   ax.plot(z, layer(z), c="k", ls="--", zorder=-1)

ax.xaxis.set_minor_locator(ticker.AutoMinorLocator())
ax.yaxis.set_minor_locator(ticker.AutoMinorLocator())

ax.set_xlabel("z /$\AA$", fontsize=28)
ax.set_ylabel(r"<$\rho$(z)>", fontsize=28)
ax.tick_params(which='both', direction='in')
plt.tick_params(labelsize=24)
plt.tight_layout()
# ax.set_title("E= -1700 mV vs $[Hg/HgSO_4]$")

if save_results:
    plt.savefig(path_graph+ "El_density" + str(saving), dpi=300)



   # plt.subplots_adjust( left= 0.075, right= 0.99, top=0.96)
plt.tight_layout()
plt.show()
# ================================================================================

if settings["save"]:
   save_header = (settings["out_format"] == "default")
   df = pandas.DataFrame()
   df["qz"] = qz
   df["intensity"] = intensity
   df["e_intensity"] = e_intensity
   df["intensity_normalized"] = intensity_norm
   df["e_intensity_normalized"] = e_intensity_norm
   df2 = pandas.DataFrame()
   df2["qz_smooth"]=qz_smooth
   df2["fit"]=abs(rrf_fitted(qz_smooth, *popt))
   df2["fresnel"]=fresnel(hgin_qc, qz_smooth, beta=hgin_beta, wl=wavelength)
   df3 = pandas.DataFrame()
   df3["z"]=z
   df3["elDen"]=m(z)

   df_f=pandas.concat([df,df2,df3],axis=1)
   df_f.to_csv(settings["out_filename"], sep="\t", index=False, header=save_header)
#
# plt.show()
# ================================================================================
```

B.2.2 DCMLayer and DCMPers File

Section B.2.2 is where *Equation* 3.4a is explicitly calculated. Specifically, defined as the variable "temp" in the subclass "DCMLayerPers". Although classes "DCMLayer" and "DCMModified" are included, they are not used in fitting for purposes of the work in this thesis. These would instead be used for other forms of the DCM model such as the adlayer case. The following changes need to be made to this file:

"d_w" should be set equal to the normalized electron density of the electrolyte, water. In this case, it is normalized by the bulk liquid metal composition. As such, change the value "self._s_density_w" is multiplied by.

"x_amount_of_Hg" = composition of the first_layer as an atomic fraction (0 to 1)

"ff_Hg_p_new.append(i*_)" and "ff_In_p_new.append(j*_)" = change the number multiplying *i* and *j* to the bulk atomic fractions of Hg and In, respectively.

```
import math
import sympy
import numpy as np
#import scipy
import xrr.gen as gen

from .layer import StackedLayer, LayerParameter, GaussianLayer,ErrorLayer



class DCMLayer(StackedLayer):

   display_layers = 25

   def __init__(self, d, si, sb,  r_beach, z_beach, sigma_beach, density_w, mu_w, sigma_w, Z, position=0, formfactor=lambda x: 1.0,
**kwargs):
      super(DCMLayer, self).__init__(**kwargs)
      self._s_d = sympy.Symbol(gen.name(), real=True, positive=True)
      self._s_position = sympy.Symbol(gen.name(), real=True, positive=True)
      self._s_si = sympy.Symbol(gen.name(), real=True, positive=True)
      self._s_sb = sympy.Symbol(gen.name(), real=True, positive=True)

      self.d = LayerParameter(d, self._s_d)
      self.position = LayerParameter(position, self._s_position)
      self.sigma_i = LayerParameter(si, self._s_si)
      self.sigma_b = LayerParameter(sb, self._s_sb)
      self.Z = Z
      self.form_factor = formfactor

      self.rho_ad=sympy.Symbol(gen.name(), real=True, positive=True)
      self.sigma_ad=sympy.Symbol(gen.name(), real=True, positive=True)
      self.z_ad=sympy.Symbol(gen.name(), real=True)

      self.r_beach = LayerParameter(r_beach, self.rho_ad)
      self.sigma_beach = LayerParameter(sigma_beach, self.sigma_ad)
      self.z_beach = LayerParameter(z_beach, self.z_ad)


      self._s_density_w= sympy.Symbol(gen.name(), real=True, positive=True)
```

```
    self._s_mu_w = sympy.Symbol(gen.name(), real=True)
    self._s_sigma_w = sympy.Symbol(gen.name(), real=True, positive=True)

    self.mu_w = LayerParameter(mu_w, self._s_mu_w)
    self.sigma_w = LayerParameter(sigma_w, self._s_sigma_w)
    self.density_w = LayerParameter(density_w, self._s_density_w)



    self._make_term()



def _make_term(self):

    mu_ad= self.z_ad
    sigma_ad= self._s_si #self.sigma_ad
    amp_ad=  self.rho_ad /(self.sigma_ad *  sympy.sqrt(2 * sympy.pi) )
    layer= GaussianLayer(amp_ad, mu_ad, sigma_ad)

    self.stack.append(layer)

    d_w=self._s_density_w * 0.169
    #Hg35In65 = 0.169
    # Hg50In50 = 0.152
    #Hg95In05 = 0.118


    mu_w=self._s_mu_w
    #s_w=(-1)*self._s_si
    s_w= self._s_sigma_w
    layer= ErrorLayer(d_w, mu_w, s_w)
    self.stack.append(layer)

    for n in range(self.display_layers):
        mu = self._s_d * n - self._s_position
        sigma = sympy.sqrt(n * self._s_sb**2 + self._s_si**2)
        amp = (self._s_d * self._s_density /
               (sigma * sympy.sqrt(2 * sympy.pi)))
        layer = GaussianLayer(amp, mu, sigma)
        self.stack.append(layer)



def structure_factor(self, qz, fit=False):
    f = (self.form_factor(qz) + 0.2) / (80 + 0.2)
    ff_Hg_p=[20.6809, 0.545, 19.0417, 8.4484, 21.6575, 1.5729, 5.9676, 38.3246, 12.6089]
    ff_H2O_p=[4.1916, 12.8573, 1.63969, 4.17236, 1.52673, 47.0179, -20.307,-0.01404, 21.9412]
    ff=(21.9412 +
    4.1916 * sympy.exp(-12.8573*qz**2/(16*sympy.pi**2)) +
    1.63969 * sympy.exp(-4.172363*qz**2/(16*sympy.pi**2)) +
    1.52673 * sympy.exp(-47.0179*qz**2/(16*sympy.pi**2))-
    20.307 * sympy.exp(0.01404*qz**2/(16*sympy.pi**2)))

    f_h2o = (ff + 0.012) / (80 + 0.012)
    s_w= self._s_sigma_w

    #s_w=(-1)*self._s_si
    sigma_ad= self._s_si
    dcm = 1j*  qz * self._s_d * (sympy.exp(- qz**2 * self._s_si**2 / 2.0) /
          (1 - sympy.exp(1j*qz * self._s_d - qz**2 * self._s_sb**2 / 2.0)))
    beach = 1j* qz * self.rho_ad * sympy.exp(1j * qz * self.z_ad - (qz**2 * sigma_ad**2) / 2.0 )
    # electrolyte=self._s_density_w* (1 - sympy.exp(-1j *qz * self._s_mu_w - qz**2 * self._s_sigma_w**2 /2 ))
    d_w=self._s_density_w #* 0.10318


    # electrolyte=-d_w* (sympy.cos(-qz * self._s_mu_w)-1j*sympy.sin(-qz*self._s_mu_w)) *sympy.exp(- qz**2 * s_w**2 /2)
```

```
        # electrolyte=-d_w* sympy.exp(-1j *qz * self._s_mu_w - qz**2 * s_w**2 /2 )
        electrolyte=-d_w* sympy.exp(1j *qz * self._s_mu_w - qz**2 * s_w**2 /2 )


        fac_sum_h2o=0
        fac_sum_hg=0
        for i in range(0,9,2):
            fac_sum_h2o+=ff_H2O_p[i]
            fac_sum_hg+=ff_Hg_p[i]


        factor_h2o=(fac_sum_h2o + 0.008) / (80 + 0.008)
        factor_hg=(fac_sum_hg + 0.2) / (80  + 0.2)

        #temp=  1/ (factor_hg*self._s_density + self._s_density_w ) * ( f *(dcm+ beach) + electrolyte)

        temp=1/ (factor_hg*self._s_density+factor_h2o* d_w )*( f *(dcm+ beach) +f_h2o* electrolyte)


        fac = self._substitute(temp, fit=fit)


        return fac




class DCMLayerPers(StackedLayer):
        # modification by Andrea 06/2019
    display_layers = 25

    def __init__(self,d_p, r_p,s_p, d, si, sb, density_w, mu_w, sigma_w, Z, Z_first, position=0, formfactor=lambda x:
1.0,formfactor_first_layer=lambda x: 1.0, **kwargs):


        super(DCMLayerPers, self).__init__(**kwargs)
        self._s_d = sympy.Symbol(gen.name(), real=True, positive=True)
        self._s_position = sympy.Symbol(gen.name(), real=True, positive=True)
        self._s_si = sympy.Symbol(gen.name(), real=True, positive=True)
        self._s_sb = sympy.Symbol(gen.name(), real=True, positive=True)

        self.d = LayerParameter(d, self._s_d)
        self.position = LayerParameter(position, self._s_position)
        self.sigma_i = LayerParameter(si, self._s_si)
        self.sigma_b = LayerParameter(sb, self._s_sb)
        self.Z = Z
        self.Z_first = Z_first
        self.form_factor = formfactor
        self.formfactor_first_layer = formfactor_first_layer

        self._s_r_mod = sympy.Symbol(gen.name(), real=True, positive=True)
        self._s_s_mod = sympy.Symbol(gen.name(), real=True, positive=True)
        self._s_d_mod = sympy.Symbol(gen.name(), real=True, positive=True)

        self.r_mod = LayerParameter(r_p, self._s_r_mod)
        self.s_mod = LayerParameter(s_p, self._s_s_mod)
        self.d_mod = LayerParameter(d_p, self._s_d_mod)


        self._s_density_w= sympy.Symbol(gen.name(), real=True, positive=True)
        self._s_mu_w = sympy.Symbol(gen.name(), real=True)
        self._s_sigma_w = sympy.Symbol(gen.name(), real=True, positive=True)

        self.mu_w = LayerParameter(mu_w, self._s_mu_w)
        self.sigma_w = LayerParameter(sigma_w, self._s_sigma_w)
        self.density_w = LayerParameter(density_w, self._s_density_w)
```

```
    self._make_term()


def _make_term(self):

    d_w=self._s_density_w*0.169
    #Hg35In65 = 0.169
    #Hg50In50 = 0.152
    #Hg95In05 = 0.118

    mu_w=self._s_mu_w
    s_w=self._s_sigma_w
    layer= ErrorLayer(d_w, mu_w, s_w)

    self.stack.append(layer)

    # first layer modification
    amp = self._s_d_mod *self._s_r_mod/ (self._s_s_mod * math.sqrt(2 * math.pi))
    mu = self._s_position
    sigma = self._s_s_mod
    layer = GaussianLayer(amp, mu, sigma)

    self.stack.append(layer)
    # normal DCM layers
    for n in range(0, self.display_layers):
        mu = self._s_d * n + self._s_d_mod
        sigma = sympy.sqrt(n * self._s_sb**2 + self._s_si**2)
        amp = (self._s_d * self._s_density /
               (sigma * math.sqrt(2 * math.pi)))
        layer = GaussianLayer(amp, mu, sigma)
        self.stack.append(layer)

def structure_factor(self, qz, fit=False):
    f = (self.form_factor(qz) + 0.2) / (self.Z + 0.2)

    x_amount_of_Hg = 0.35 #CHANGE % OF COMPOSITION

    Z_first_layer = (80 - (80/82.5)**2.37)*(x_amount_of_Hg) + 48.0097 * (1-x_amount_of_Hg)

    f_first_layer = (self.formfactor_first_layer(qz) + 0.2) / (Z_first_layer + 0.2)



    ff_Hg_p=[20.6809, 0.545, 19.0417, 8.4484, 21.6575, 1.5729, 5.9676, 38.3246, 12.6089]
    ff_Hg_p=np.array(ff_Hg_p)
    ff_In_p=[19.1624, 0.5476, 18.5596, 6.3776, 4.2948, 25.8499, 2.0396, 92.8029, 4.9391]
    ff_Hg_p_new=[]

    for i in ff_Hg_p:
        ff_Hg_p_new.append(i*0.35)

    ff_In_p_new=[]
    for j in ff_In_p:
        ff_In_p_new.append(j*0.65)

    ff_HgIn_p=np.array(ff_Hg_p_new)+np.array(ff_In_p_new)



    ff_Hg_p_first_layer=[]

    for i in ff_Hg_p:
        ff_Hg_p_first_layer.append(i*x_amount_of_Hg)

    ff_In_p_first_layer=[]
    for j in ff_In_p:
        ff_In_p_first_layer.append(j*(1-x_amount_of_Hg))

    ff_HgIn_first_layer=np.array(ff_Hg_p_first_layer)+np.array(ff_In_p_first_layer)
```

```
        ff_H2O_p=[4.1916, 12.8573, 1.63969, 4.17236, 1.52673, 47.0179, -20.307,-0.01404, 21.9412]
        ff=(21.9412 +
        4.1916 * sympy.exp(-12.8573*qz**2/(16*sympy.pi**2)) +
        1.63969 * sympy.exp(-4.172363*qz**2/(16*sympy.pi**2)) +
        1.52673 * sympy.exp(-47.0179*qz**2/(16*sympy.pi**2))-
        20.307 * sympy.exp(0.01404*qz**2/(16*sympy.pi**2)))

        f_h2o = (ff + 0.012) / (self.Z + 0.012)


        # modification by Andrea 06/2019

        dcm =   1j * qz * self._s_d *self._s_density* (sympy.exp(- qz**2 * self._s_si**2 / 2.0) /
              (1 - sympy.exp(1j*qz * self._s_d)* sympy.exp( - qz**2 * self._s_sb**2 / 2.0))) * sympy.exp(1j* qz*  (self._s_d_mod ))

        mod = 1j* qz  *(self._s_d_mod *self._s_r_mod) * sympy.exp(- (qz**2 * self._s_s_mod**2) / 2.0 )

        fac_sum_h2o=0
        fac_sum_hgin=0
        fac_sum_hgin_first_layer=0
        for i in range(0,9,2):
           fac_sum_h2o+=ff_H2O_p[i]
           fac_sum_hgin+=ff_HgIn_p[i]
           fac_sum_hgin_first_layer+=ff_HgIn_first_layer[i]

        factor_h2o=(fac_sum_h2o + 0.008) / (self.Z + 0.008)
        factor_hgin=(fac_sum_hgin + 0.2) / (self.Z  + 0.2)
        factor_hgin_first_layer=(fac_sum_hgin_first_layer + 0.2) / (self.Z_first  + 0.2)
        # electrolyte = -self._s_density_w * sympy.exp(-1j *qz * self._s_mu_w - qz**2 * self._s_sigma_w**2 /2 )
        s_w= self._s_sigma_w
        d_w= self._s_density_w
        electrolyte=-d_w* sympy.exp(1j *qz * self._s_mu_w - qz**2 * s_w**2 /2 )



        ##################TEMP EQUATION USED FOR FITTING################
        temp = 1/ (factor_hgin*self._s_density+factor_h2o* d_w *factor_hgin_first_layer )*( f_first_layer* mod +f* dcm + f_h2o*
electrolyte)
        ################################################################

        fac = self._substitute(temp, fit=fit)
        return fac


class DCMLayerModified(DCMLayer):

    display_layers = 25

    def __init__(self, rho_first, z_first, d, si, sb, density_w, mu_w, sigma_w, Z, position=0, formfactor=lambda x: 1.0, **kwargs):
        self._s_density_first = sympy.Symbol(gen.name(), real=True, positive=True)
        self._s_z_first = sympy.Symbol(gen.name(), real=True, positive=True)
        self.density_first = LayerParameter(rho_first, self._s_density_first)
        self.z_first = LayerParameter(z_first, self._s_z_first)
        super(DCMLayerModified, self).__init__(d, si, sb, density_w, mu_w, sigma_w, Z, position=0, formfactor=lambda x: 1.0, **kwargs)

    def _make_term(self):

        d_w=self._s_density_w
        mu_w=self._s_mu_w
        s_w=self._s_sigma_w
        layer= ErrorLayer(d_w, mu_w, s_w)
        self.stack.append(layer)

        # first layer modification
        amp = self._s_d * self._s_density_first / (self._s_si * math.sqrt(2 * math.pi))
        mu = self._s_z_first
        sigma = self._s_si
        layer = GaussianLayer(amp, mu, sigma)
        self.stack.append(layer)
```

```
        # normal DCM layers
        for n in range(1, self.display_layers):
            mu = self._s_d * n - self._s_position
            sigma = sympy.sqrt(n * self._s_sb**2 + self._s_si**2)
            amp = (self._s_d * self._s_density /
                   (sigma * math.sqrt(2 * math.pi)))
            layer = GaussianLayer(amp, mu, sigma)
            self.stack.append(layer)

    def structure_factor(self, qz, fit=False):
        f = (self.form_factor(qz) + 0.2) / (self.Z + 0.2) #(1 / ( 0.015)) *



        # modification by Andrea 03/2019

        dcm= (1j * qz* self._s_d * self._s_density * sympy.exp(- (qz**2 * self._s_si**2 )/2.0 ) * ( sympy.exp( 1j * qz * self._s_d - (qz**2 *
self._s_sb**2 )/2.0 ) / (1 - sympy.exp( 1j * qz * self._s_d - (qz**2 * self._s_sb**2 )/2.0 ))  ))
        mod= ( 1j * qz* self._s_d *  self._s_density_first  *  sympy.exp(( 1j * qz* self._s_z_first - (qz**2 * self._s_si**2 )/2.0 )  ))
        #mod= ( 1j * qz* self._s_d * ( self._s_density_first -self._s_density )  *  sympy.exp(( 1j * qz* self._s_z_first - (qz**2 * self._s_si**2
)/2.0 )  ))
        electrolyte = -self._s_density_w * sympy.exp(-1j *qz * self._s_mu_w - qz**2 * self._s_sigma_w**2 /2 )
        temp = 1/ (0.015 + self._s_density_w ) * ( f* (mod + dcm) + electrolyte) #65*

        fac = self._substitute(temp, fit=fit)
        return fac
```

B.2.3 XRR.Layer File

The file "XRR.Layer" file shown below is called by the fitting file in Section B.2.1 to define the variables and gaussian profiles across the interface. No changes need to be made to this file to use the fitting file.

```
import numpy
import scipy
import sympy

import xrr.gen as gen


class LayerParameter(object):

    def __init__(self, value, symbol, fit=False, fit_min=-numpy.inf,
                 fit_max=numpy.inf, fit_expr=None):
        super(LayerParameter, self).__init__()
        self.symbol = symbol
        self.value = value
        self._fit = fit
        self._min = fit_min
        self._max = fit_max
        self._fit_err = None
        self._symbol_name = symbol.name
        self._name = symbol.name
        self.symbol.name = gen.name()
        self._expr = fit_expr
        if fit_expr:
            self._fit = True

    @property
    def fit(self):
        return self._fit

    @fit.setter
    def fit(self, do_fit):
        self._fit = do_fit

    @property
    def fit_min(self):
        return self._min

    @fit_min.setter
    def fit_min(self, fit_min):
        self._min = fit_min

    @property
    def fit_max(self):
        return self._max

    @fit_max.setter
    def fit_max(self, fit_max):
        self._max = fit_max

    @property
    def fit_error(self):
        return self._fit_err

    @fit_error.setter
    def fit_error(self, err):
        self._fit_err = err
```

```
    @property
    def name(self):
        return self._name

    @name.setter
    def name(self, name):
        self._name = name

    @property
    def fit_expr(self):
        return self._expr

    @fit_expr.setter
    def fit_expr(self, fit_expr):
        self._expr = fit_expr
        self._fit = True


class Layer(object):

    def __init__(self, density=1, color="#A3A3A3"):
        super(Layer, self).__init__()
        self.z = sympy.Symbol("z", real=True)
        self._s_density = sympy.Symbol(gen.name(), real=True, positive=True)
        self.density = LayerParameter(density, self._s_density)
        self._master = None
        self._master_fit = None
        # self._term = sympy.numbers.Zero()
        self._term =sympy.core.numbers.Zero()
        self.color = color
        self.name = "layer"

    def __call__(self, z):
        z_sym = sympy.Symbol("z_model")
        expr = self.expr.subs(self.z, z_sym)
        f = sympy.lambdify(z_sym, expr, ("numpy", {"erf": scipy.special.erf}))
        return f(z)

    def get_expr(self, fit=False):
        return self._substitute(self._term, fit=fit)

    expr = property(get_expr)

    def set_name(self, name):
        self.name = name
        self.set_param_names()

    def set_param_names(self):
        for param in self.params:
            param.name = "{0}_{1}".format(self.name, param._symbol_name)

    @property
    def params(self):
        # find layer parameters
        attrs = list(self.__dict__.keys())
        def f(x):
            return (not x.startswith("_") and
                    isinstance(self.__dict__[x], LayerParameter))
        p_attrs = list(filter(f, attrs))
        params = list(map(lambda x: self.__dict__[x], p_attrs))
        return params

    def _substitute(self, expr, fit=False):
        # substitute parameters
        params = self.params
        if fit:
            # sort out fit parameters
            params = list(filter(lambda x: not x.fit, self.params))
        subs = list(map(lambda x: (x.symbol, x.value), params))
```

```
        return expr.subs(subs)

    def get_fit_parameters(self):
        params = self.params
        # get fit parameters
        params = list(filter(lambda x: x.fit, self.params))
        return params

    def structure_factor(self, qz, fit=False):
        if not fit and self._master is None:
            integrand = (-1)*sympy.diff(self._term, self.z) * sympy.exp(1j*qz*self.z)
            master = sympy.integrate(integrand, (self.z, -sympy.oo, sympy.oo))
            self._master = qz, self._substitute(master, False)
            return self._master[1]
        elif fit and self._master_fit is None:
            integrand =(-1)* sympy.diff(self._term, self.z) * sympy.exp(1j*qz*self.z)
            master = sympy.integrate(integrand, (self.z, -sympy.oo, sympy.oo))
            self._master_fit = qz, self._substitute(master, True)
            return self._master_fit[1]
        elif not fit and self._master is not None:
            old_qz, old_master = self._master
            master = old_master.subs(old_qz, qz)

            self._master = qz, master
            return self._master[1]
        elif fit and self._master_fit is not None:
            old_qz, old_master = self._master_fit
            master = old_master.subs(old_qz, qz)

            self._master_fit = qz, master
            return self._master_fit[1]


class StackedLayer(Layer):

    def __init__(self, **kwargs):
        super(StackedLayer, self).__init__(**kwargs)
        self.stack = []

    def get_expr(self, fit=False):
        # term = sympy.numbers.Zero()
        term =sympy.core.numbers.Zero()
        for layer in self.stack:
            term += layer.get_expr(fit=fit)
        return self._substitute(term, fit=fit)
    expr = property(get_expr)

    def set_name(self, name):
        super(StackedLayer, self).set_name(name)
        for d in enumerate(self.stack):
            n, layer = d
            layer_name = "{0}:{1}".format(name, n)
            layer.set_name(layer_name)


class GaussianLayer(Layer):

    c_master = None
    c_density = sympy.Symbol("c_density", real=True, positive=True)
    c_mu = sympy.Symbol("c_mu", real=True)
    c_sigma = sympy.Symbol("c_sigma", real=True, positive=True)
    c_z = sympy.Symbol("c_z", real=True)
    c_qz = sympy.Symbol("c_qz", real=True)

    def __init__(self, density, mu, sigma, **kwargs):
        super(GaussianLayer, self).__init__(density=density, **kwargs)
        self._s_mu = sympy.Symbol(gen.name(), real=True)
        self._s_sigma = sympy.Symbol(gen.name(), real=True, positive=True)
        self.mu = LayerParameter(mu, self._s_mu)
        self.sigma = LayerParameter(sigma, self._s_sigma)
```

```
        self._term = (self._s_density * sympy.exp(-(self.z - self._s_mu)**2 /
                    (2 * self._s_sigma**2)))

    def structure_factor(self, qz, fit=False):
        if self.c_master is None:
            expr = (self.c_density / (self.c_sigma *(sympy.sqrt(sympy.pi)))*sympy.exp(-(self.c_z - self.c_mu)**2 /
                  (2 * self.c_sigma**2)))
            integrand = (-1*sympy.diff(expr, self.c_z) *
                       sympy.exp(1j*self.c_qz*self.c_z))
            master = sympy.integrate(integrand,
                                (self.c_z, -sympy.oo, sympy.oo))
            self.__class__.c_master = master
        subs = [(self.c_qz, qz),
                (self.c_z, self.z),
                (self.c_density, self._s_density),
                (self.c_mu, self._s_mu),
                (self.c_sigma, self._s_sigma)]
        master_expr = self.c_master.subs(subs)
        master = self._substitute(master_expr, fit=fit)
        return master


class GaussianLayer2(StackedLayer):

    def __init__(self, density, mu, sigma, **kwargs):
        super(GaussianLayer2, self).__init__(**kwargs)


        self.rho_g=sympy.Symbol(gen.name(), real=True, positive=True)
        self.sigma_g=sympy.Symbol(gen.name(), real=True, positive=True)
        self.z_g=sympy.Symbol(gen.name(), real=True)

        self.density = LayerParameter(density, self.rho_g)
        self.sigma = LayerParameter(sigma, self.sigma_g)
        self.mu = LayerParameter(mu, self.z_g)

        self._make_term()


    def _make_term(self):

        z_g= self.z_g
        sigma_g= self.sigma_g
        amp=  self.rho_g #/(self.sigma_g *  sympy.sqrt(2 * sympy.pi) )
        layer= GaussianLayer(amp, z_g, sigma_g)

        self.stack.append(layer)

        #self.layer = (self.rho_g / (self.sigma_g *  (sympy.sqrt(sympy.pi)))* sympy.exp(-(self.z - self.z_g)**2 /
        #             (2 * self.sigma_g**2)))


    def structure_factor(self, qz, fit=False):
        g = 1j* qz * self.rho_g * sympy.exp(1j * qz * self.z_g - (qz**2 * self.sigma_g**2) / 2.0 )
        gau = self._substitute(g, fit=fit)
        return gau



class ErrorLayer(Layer):

    def __init__(self, density, mu, sigma, **kwargs):
        super(ErrorLayer, self).__init__(**kwargs)
        self.density.value = density
        self._s_mu = sympy.Symbol(gen.name(), real=True)
        self._s_sigma = sympy.Symbol(gen.name(), real=True, positive=True)
        self.mu = LayerParameter(mu, self._s_mu)
        self.sigma = LayerParameter(sigma, self._s_sigma)
        self._term =(0.5 * self._s_density * (sympy.erf((self.z - self._s_mu) /
                    (self._s_sigma*sympy.sqrt(2))) + 1))
```

```
class SlabLayer(Layer):

    def __init__(self, density, z0, z1, sigma, **kwargs):
        super(SlabLayer, self).__init__(**kwargs)
        self.density.value = density
        self._s_z0 = sympy.Symbol(gen.name(), real=True)
        self._s_z1 = sympy.Symbol(gen.name(), real=True)
        self._s_sigma = sympy.Symbol(gen.name(), real=True, positive=True)
        self.z0 = LayerParameter(z0, self._s_z0)
        self.z1 = LayerParameter(z1, self._s_z1)
        self.sigma = LayerParameter(sigma, self._s_sigma)
        rise = (0.5 * self._s_density * (sympy.erf((self.z - self._s_z0) /
              (self._s_sigma)) + 1))
        fall = (-0.5 * self._s_density * (sympy.erf((self.z - self._s_z1) /
              (self._s_sigma)) + 1))
        self._term = rise + fall


class SlabLayerWidth(Layer):

    def __init__(self, density, z0, width, sigma, **kwargs):
        super(SlabLayerWidth, self).__init__(**kwargs)
        self.density.value = density
        self._s_z0 = sympy.Symbol(gen.name(), real=True)
        self._s_width = sympy.Symbol(gen.name(), real=True, positive=True)
        self._s_sigma = sympy.Symbol(gen.name(), real=True, positive=True)
        self.z0 = LayerParameter(z0, self._s_z0)
        self.width = LayerParameter(width, self._s_width)
        self.sigma = LayerParameter(sigma, self._s_sigma)
        self._term = 0.5 * self._s_density * (sympy.erf((self.z - self._s_z0 + 0.5*self._s_width)/self._s_sigma) - sympy.erf((self.z - self._s_z0 -
0.5*self._s_width)/self._s_sigma))
        self._master_term = None

    def structure_factor(self, qz, fit=False):
        if self._master_term is None:
            rho = self._s_density
            z = self.z
            z0 = self._s_z0
            w = self._s_width
            s = self._s_sigma
            # derivative
            diff_a = (-1) *rho * sympy.exp(-((z-z0+0.5*w)/s)**2/(sympy.sqrt(sympy.pi)*s))
            diff_b = (-1) *rho * sympy.exp(-((z-z0-0.5*w)/s)**2/(sympy.sqrt(sympy.pi)*s))
            # master
            master_a = sympy.integrate(diff_a*sympy.exp(1j * qz * z), (z, -sympy.oo, sympy.oo))
            master_b = sympy.integrate(diff_b*sympy.exp(1j * qz * z), (z, -sympy.oo, sympy.oo))
            self._master_term = qz, master_a - master_b
        old_qz, master = self._master_term
        master = self._substitute(master.subs(old_qz, qz), fit=fit)
        return master
```

B.2.4 XRR Model Approach File

The file "XRR.Model" file shown below is called by the fitting file in Section B.2.1 to define the ElectronDensityModel class describing electron density contributions across the interface. No changes need to be made to this file to use the fitting file.

```
# -*- coding: utf-8 -*-
#import numpy
import sympy
import scipy.special

from .layer import Layer


class ElectronDensityModel(object):

    def __init__(self):
        super(ElectronDensityModel, self).__init__()
        self._layers = []

    def __call__(self, z):
        z_sym = sympy.Symbol("z_model")
        model = 0
        for layer in self._layers:
            model += layer.expr.subs(layer.z, z_sym)
        f = sympy.lambdify(z_sym, model, ("numpy", {"erf": scipy.special.erf}))
        return f(z)

    def get_master(self):
        qz = sympy.Symbol("qz", real=True)
        temp = 0
        for layer in self._layers:
            temp += layer.structure_factor(qz)
        master = abs(temp)**2

        return qz, master

    def get_fit_func(self):
        qz = sympy.Symbol("qz", real=True)
        fit_symbols, fit_params = [], []
        temp = 0
        for layer in self._layers:
            temp += layer.structure_factor(qz, fit=True)
            fit_params += filter(lambda x: x.fit, layer.params)
        master = abs(temp)**2

        fit_symbols = list(map(lambda x: x.symbol, fit_params))
        f = sympy.lambdify([qz] + fit_symbols, master,
                           ("numpy", {"erf": scipy.special.erf}))
        return f, fit_params

    def get_params(self):
        fit_params = []
        for layer in self._layers:
            fit_params += layer.params
        return fit_params

    def add(self, layer):
        if isinstance(layer, Layer):
            self._layers.append(layer)
            layer.set_name("layer_{0}".format(len(self._layers) - 1))
        else:
            raise TypeError()
```

B.2.5 XRR.lmfit File

The file "XRR.lmfit" file shown below is called by the fitting file in Section B.2.1 to define the nonlinear least-squares fitting approach using the lmfit library. No changes need to be made to this file to use the fitting file.

```
"""
Alternate fitting routine with lmfit
"""

import lmfit as lm
import numpy as np
#import pandas
import matplotlib.pyplot as plt
from time import time
from lmfit import fit_report

def fit_model(model, xdata, ydata, weights=1, verbose=True, plot=False, free_params=None, **kws):
    fitfunc, fit_params = model.get_fit_func()
    p_init = [p.value for p in fit_params]
    p_min = [p.fit_min for p in fit_params]
    p_max = [p.fit_max for p in fit_params]
    p_expr = [p.fit_expr for p in fit_params]
    p_name = [p.name for p in fit_params]

    # lmfit parameter class for holding params, supports expressions (constraints)
    # add free params first, remove later
    if not free_params:
        p = lm.Parameters()
        free_n = 0
    else:
        p = free_params
        free_n = len(p.valuesdict())
    for i in range(len(p_init)):
        if p_expr[i]:
            # name, value, vary, min, max
            p.add(p_name[i], vary=False, expr=p_expr[i])
        else:
            p.add(p_name[i], p_init[i], True, p_min[i], p_max[i])

    # plot initial values
    if plot:
        fig = plt.figure()
        ax = fig.add_subplot(111)
        plt.plot(xdata, ydata, 'ko', label='data')
        fit, = ax.plot(xdata, abs(fitfunc(xdata, *p_init)), 'r-', label='fit')
        plt.xlabel(r'$q_\mathrm{z}\>/\>\mathrm{\AA}^{-1}$')
        plt.ylabel(r'$R\>/\>R_\mathrm{F}$')
        plt.legend()
        plt.ion()
        plt.show()

    # residual function (difference model - data)
    def residual(pars, x, fx, data=None, eps=None, **kws):
        args = list(pars.valuesdict().values())[free_n:]
        model = abs(fx(x, *args))
        if data is None:
            return model
        if eps is None:
            return model - data
        return (model - data) / eps

    # iteration callback function
    def cb(pars, iter, resid, *fcn_args, **fcn_kws):
```

```
    # draw every plot iterations
    if plot and iter % plot == 0:
        fit.set_ydata(residual(pars, *fcn_args))
        plt.draw()
        plt.pause(.001)
    # print opt value every verbose iter
    if verbose and iter % verbose == 0:
        print(iter, np.sum(resid**2))

# lmfit minimizer object
minim = lm.Minimizer(residual, p,
    fcn_args=(xdata, fitfunc),
    fcn_kws={'data': ydata, 'eps': weights, 'verbose': verbose, 'plot': plot},
    iter_cb=cb)
# perform optimization
if verbose:
    print('iter | sum err²')
t0 = time()
opt = minim.minimize(**kws)
t1 = time() - t0
if verbose:
    print('optimization time = {:2.0f}h {:2.0f}m {:2.0f}s'.format(t1//3600, (t1%3600)//60, t1%60))
print(fit_report(opt))
# lm.report_fit(opt)
# set layer paramters to the obtained values, remove free params
p_opt = [v for v in opt.params.valuesdict().values()][free_n:]
p_err = [opt.params[k].stderr for k in opt.params.valuesdict().keys()][free_n:]
for n in range(len(fit_params)):
    fit_params[n].value = p_opt[n]
    fit_params[n].fit_error = p_err[n]
return p_opt, p_err, fitfunc
```

B.3 Code Used to Describe the Yoneda Feature

The code in this section implements *Equation* 3.2 to describe the behavior of the Yoneda feature like what is shown in Figure 3.2 and Figure 3.3. Specifically, the code fits the Yoneda and corresponding specular feature with a couple of skewed Lorentzian functions and linear background. The code fits each separately and then plots the final 'full' fit.

To use this code the following variables should be changed:

"scan_numbers" = should be updated as a list to represent the specific scans one wants to describe

'data_directory', 'experiment' and 'detector' = specific pathways or descriptors used to describe the location and name that the data is saved locally

'log_scale' = True or False to plot raw detector data and subsequent integration on log scale or not.

'save_max', 'max_out_filename', 'save_plot', 'save_plot_specular', 'save_plot_yoneda', 'plot_out_filename', 'save_profile','out_filename', 'save_results', 'fit_out_filename' = Series of parameters to define the desired functionality of the code with either True or False with subsequent defined save paths.

'Gauss' = define True or False depending on whether not a gaussian should be used instead of a Lorentzian

'init' and 'bounds' = the initial and boundary conditions for each fitting parameter and should be updated to accurately represent the peak conditions attempting to be fit by 'curve_fit'

```
import h5py
import numpy as np
import matplotlib.pyplot as plt
from matplotlib import rcParams
#from lisaspec.spec import SpecFile
#from matplotlib.ticker import MultipleLocator
#from matplotlib.patches import Rectangle
import hashlib
import os
import csv
import math
import pandas
from eigene.p08_detector_read import p08_detector_read
from PIL import Image
from sigfig import round
from scipy.special import erf
from matplotlib import rc
rc('text', usetex=True)

from scipy.optimize import curve_fit
import warnings

import time

import gc
```

```
start = time.time()

# scan_numbers = [786, 814, 826, 838, 850, 897, 928, 941, 962, 991, 1003, 1028,
#                 1054, 1067, 1124, 1142, 1177, 1223, 1279, 1331, 1372, 1386,
#                 1398, 1435, 1467, 1483, 1499, 1511] #Hg35In65 with qz = 0.08


# scan_numbers = [2104, 2144, 2189, 2217, 2239, 2265, 2278, 2307, 2341, 2353,
#                 2365, 2389, 2426, 2450, 2466, 2477, 2511, 2538, 2569, 2612,
#                 2637, 2653, 2710, 2727, 2751, 2789, 2817, 2855, 2895, 2906,
#                 2933, 2994, 3022] #Hg95In05 with qz = 0.08


# scan_numbers = [3340, 3368, 3387, 3412, 3442, 3458, 3484, 3522, 3535, 3561,
#                 3599, 3622, 3640, 3653, 3690, 3726, 3763, 3797, 3831, 3844,
#                 3870, 3885, 3912, 3942, 3970, 3996] #Hg50In50 with qz = 0.08



# scan_numbers = [787, 815, 827, 839, 851, 898, 929, 963, 992, 1004,
#                 1029, 1055, 1068, 1125, 1143, 1178, 1224, 1280, 1332, 1373, 1387,
#                 1399, 1436, 1468, 1484, 1500, 1512] #Hg35In65 with qz = 0.10

# scan_numbers = [2105, 2145, 2190, 2218, 2240, 2266, 2279, 2308, 2342, 2354,
#                 2366, 2390, 2427, 2451, 2467, 2478, 2512, 2539, 2570, 2613,
#                 2638, 2654, 2711, 2728, 2752, 2790, 2818, 2856, 2896, 2907,
#                 2934, 2995, 3023] #Hg95In05 with qz = 0.10

# scan_numbers = [3341, 3369, 3388, 3413, 3443, 3459, 3485, 3523, 3536, 3562,
#                 3600, 3623, 3641, 3654, 3691, 3727, 3764, 3798, 3832, 3845,
#                 3871, 3886, 3913, 3943, 3971, 3997] #Hg95In05 with qz = 0.10

scan_numbers = [3459]

# scan = [1257, 1350, 1351, 1352, 1413, 1591, 1613, 1653, 1689, 1725,
#         1765, 1802, 1813, 1856, 1894, 1929, 1967, 1968, 2014,
#         2133, 2179, 2206, 2207, 2228, 2229, 2253, 2292, 2325, 2377, 2406, 2407,
#         2409, 2411, 2439, 2493, 2524, 2553, 2581, 2609, 2625, 2699, 2741, 2768, 2771,
#         2772, 2776, 2801, 2835, 2872, 2918, 2955]


# scan = [3358, 3399, 3427, 3470, 3501, 3547, 3577,
#         3665, 3706, 3711, 3712, 3713, 3743, 3776, 3816, 3858, 3899, 3928, 3958,
#         3983, 3985, 4015, 4016, 4017, 4018, 4019, 4020, 4025, 4027, 4032, 4092,
#         4138]

# scan = [1591, 1613, 1653, 1689, 1725, 1765, 1802, 1813, 1856, 1894, 1929, 1967, 1968, 2014, 2018, 2019, 2021]

warnings.filterwarnings("ignore")
# == settings
settings = dict(
    data_directory=r"E:/Beam Line Data/sept 2021 workup/processed round 4/q_calc_spock_output/2021-09/hgin",
    experiment="maldonado_hgin",  # "align_lisa",
    detector="lambda",
    scan_number = scan_numbers,
    image_number= 0,
    use_flatfield=True,
    flatfield=r"E:/Beam Line Data/sept 2021 workup/Flatfield _ dark image\flatfield _darkimage/Module_2017-004_GaAs_25keV_flatfield.tif",
    use_mask=True,
    mask=r"E:/Beam Line Data/sept 2021 workup/Flatfield _ dark image/flatfield _darkimage/lambda_dark_00376_00000.nxs",
    multiple=True,
    log_scale= False,
    intensity_scale=(1, 15000),
    # plot colormap
    colormap="jet",
    # Specify which data to use for x and y dimensions. Supported
    # values are "pixels", "qx", "qy" and "qz". If reciprocal space
```

```
    # data is not found, "pixels" will be used.
    xdim="qz",
    ydim="qx",
    # regions of interest to display (x, y, w, h)
    # roisp = (140-10, 48, 20, 20),
    background=False,
    roi_offset=25,
    roi=(5, 52, 300, 12),
    # roi = (5, 86, 300, 12), #Hg35In65 and Hg95In05
    # save plot to this file:
    save_max = False,
    max_out_filename="E:/Beam Line Data/sept 2021 workup/processed round 6/Diffuse\0.10 qz/fit_max.txt",
    save_plot=False,
    save_plot_specular=False,
    save_plot_yoneda=False,
    plot_out_filename="F:/Beam Line Data/sept 2021 workup/processed round 11/diffuse_scans/qz 0.10 scans fit with lorentz/Hg35In65",
    save_profile=False,
    out_filename="F:/Beam Line Data/sept 2021 workup/processed round 11/diffuse_scans/Diffuse/0.0.08 qz/profile",
    save_results=False,
    fit_out_filename="F:/Beam Line Data/sept 2021 workup/processed round 11/diffuse_scans/qz 0.10 scans fit with lorentz/Hg35In65",
    gauss = False
    # plot title
    #plot_title="A Diffraction Measurement"
)

AXIS_LABELS = dict(pixels="pixels", qx=r"q$_x$ [$\AA^{-1}$]",
                   qy=r"q$_y$ [$\AA^{-1}$]", qz=r"q$_z$ [$\AA^{-1}$]")
if settings["use_flatfield"] == True:
    flatfield = np.array(Image.open(settings["flatfield"]))
if settings["use_mask"] == True:
    file_mask = h5py.File(settings["mask"], "r")
    img_mask = np.array(file_mask["/entry/instrument/detector/data"])[0]
    file_mask.close()
    mask = np.zeros_like(img_mask)
    mask[(img_mask > 1)] = 1
    mask = (mask == 1)
    mask_value = 0


def line(xdata, slope, intercept):
    return ([i*slope for i in xdata] + intercept)

def poly(xdata, slope1, slope2, intercept):
    list1 = [i**2 * slope1 for i in xdata]
    list2 = [i*slope2 for i in xdata]
    lists_of_lists = [list1,list2]
    polynomial = [sum(x) for x in zip(*lists_of_lists)]
    return polynomial

def gaussian(xdata, sk, amp, pos, sigma):
    skew = (1 + erf((sk * (xdata - pos)) / (sigma * np.sqrt(2))))
    return skew * amp * np.exp(-(xdata-pos)**2/(2*sigma**2))


def skew_gaussian(xdata, sk, amp, pos, sigma):
    skew = (1 + erf((sk * (xdata - pos)) / (sigma * np.sqrt(2))))
    return skew * amp * np.exp(-(xdata-pos)**2/(2*sigma**2))


def skew_lorentz(xdata, sk, amp, pos, sigma):
    skew = (1 + erf((sk * (xdata - pos)) / (sigma * np.sqrt(2))))
    return skew * amp * (1 / (1+((xdata - pos)/sigma)**2))

def skew_lorentz_poly(xdata, sk, amp, pos, sigma, slope1, slope2, intercept):
    skew = (1 + erf((sk * (xdata - pos)) / (sigma * np.sqrt(2))))

    list1 = [i**2 * slope1 for i in xdata]
    list2 = [i*slope2 for i in xdata]
    lists_of_lists = [list1,list2]
    polynomial = [sum(x) for x in zip(*lists_of_lists)]
```

```
    return (skew * amp * (1 / (1+((xdata - pos)/sigma)**2)) + polynomial)


def lorentz(xdata, amp, pos, sigma):
    return amp * (1 / (1+((xdata - pos)/sigma)**2))

def gaussian2(xdata, slope, intercept, amp_2, pos_2, sigma_2):
    # return amp * np.exp(-(xdata-pos)**2/(2*sigma**2)) +amp_2 * np.exp(-(xdata-pos_2)**2/(2*sigma_2**2))
    return ([i*slope for i in xdata] + intercept) + amp_2 * np.exp(-(xdata-pos_2)**2/(2*sigma_2**2))

def gaussian_yoneda(xdata, slope, intercept, amp, pos, sigma,amp_2, pos_2, sigma_2):

    return ( [i*slope for i in xdata] + intercept) + amp * np.exp(-(xdata-pos)**2/(2*sigma**2)) +amp_2 * np.exp(-(xdata-
pos_2)**2/(2*sigma_2**2))

def lorentz_yoneda_background(xdata, slope, intercept, sk, amp, pos, sigma,amp_2, pos_2, sigma_2):
    skew = (1 + erf((sk * (xdata - pos)) / (sigma * np.sqrt(2))))
    return ( [i*slope for i in xdata] + intercept) + (skew * amp * (1 / (1+((xdata - pos)/sigma)**2))) +amp_2 * (1 / (1+((xdata -
pos_2)/sigma_2)**2))

def skew_lorentz_yoneda(xdata, sk, amp, pos, sigma,amp_2, pos_2, sigma_2):
    skew = (1 + erf((sk * (xdata - pos)) / (sigma * np.sqrt(2))))
    return (skew * amp * (1 / (1+((xdata - pos)/sigma)**2))) +amp_2 * (1 / (1+((xdata - pos_2)/sigma_2)**2))

def lorentz_yoneda(xdata, amp, pos, sigma,amp_2, pos_2, sigma_2):
    return ( amp * (1 / (1+((xdata - pos)/sigma)**2))) +amp_2 * (1 / (1+((xdata - pos_2)/sigma_2)**2))

def gauss_yoneda(xdata, amp, pos, sigma,amp_2, pos_2, sigma_2):
    return amp * np.exp(-(xdata-pos)**2/(2*sigma**2)) + amp_2 * (1 / (1+((xdata - pos_2)/sigma_2)**2))

def skew_gauss_yoneda(xdata, sk, amp, pos, sigma,amp_2, pos_2, sigma_2):
    skew = (1 + erf((sk * (xdata - pos)) / (sigma * np.sqrt(2))))
    return skew * amp * np.exp(-(xdata-pos)**2/(2*sigma**2)) + amp_2 * (1 / (1+((xdata - pos_2)/sigma_2)**2))

def skew2_gauss_yoneda(xdata, sk, amp, pos, sigma, sk2, amp_2, pos_2, sigma_2):
    skew = (1 + erf((sk * (xdata - pos)) / (sigma * np.sqrt(2))))
    skew2 = (1 + erf((sk2 * (xdata - pos)) / (sigma * np.sqrt(2))))
    return skew * amp * np.exp(-(xdata-pos)**2/(2*sigma**2)) + skew2 * amp_2 * (1 / (1+((xdata - pos_2)/sigma_2)**2))

def skew2_lorentz_yoneda(xdata, sk, amp, pos, sigma, sk2, amp_2, pos_2, sigma_2):
    skew = (1 + erf((sk * (xdata - pos)) / (sigma * np.sqrt(2))))
    skew2 = (1 + erf((sk2 * (xdata - pos)) / (sigma * np.sqrt(2))))
    return (skew * amp * (1 / (1+((xdata - pos)/sigma)**2))) + skew2 * amp_2 * (1 / (1+((xdata - pos_2)/sigma_2)**2))


def skew2_lorentz_yoneda_poly(xdata, sk, amp, pos, sigma, sk2, amp_2, pos_2, sigma_2, slope1, slope2, intercept):
    skew = (1 + erf((sk * (xdata - pos)) / (sigma * np.sqrt(2))))
    skew2 = (1 + erf((sk2 * (xdata - pos)) / (sigma * np.sqrt(2))))
    list1 = [i**2 * slope1 for i in xdata]
    list2 = [i*slope2 for i in xdata]
    lists_of_lists = [list1,list2]
    polynomial = [sum(x) for x in zip(*lists_of_lists)]
    return (skew * amp * (1 / (1+((xdata - pos)/sigma)**2))) + (skew2 * amp_2 * (1 / (1+((xdata - pos_2)/sigma_2)**2)) + polynomial)

def skew2_lorentz_line(xdata, sk, amp, pos, sigma, slope, intercept):
    skew = (1 + erf((sk * (xdata - pos)) / (sigma * np.sqrt(2))))
    return (skew * amp * (1 / (1+((xdata - pos)/sigma)**2))) + ([i*slope for i in xdata] + intercept)



for scan in settings['scan_number']:
    Yoneda_pos = []
    Yoneda_int = []
    gc.collect()
    if settings["multiple"]:
        i = 0
        q_tot = []
        int_tot = []
        full_qz = []
        roi = settings["roi"]
```

```
for i in range(0, settings["image_number"]+1):
    # == load data
    det_filename = "{data_directory}/{experiment}_{0:05}/{detector}/{experiment}_{0:05}_00000.nxs".format(
        scan, **settings)  # "{data_directory}/.nx5".format(**settings)

    det_file = h5py.File(det_filename, "r")

    try:
        img = p08_detector_read(settings["data_directory"], settings["experiment"],
                        scan, settings["detector"])()[i]
    except IndexError:
        break

    img_res = img
    # print(img_res)
    # flatfield correction
    if settings["use_flatfield"] == True:
        img = img / flatfield
    if settings["use_mask"] == True:
        img[mask] = mask_value
    Q = None
    if "Q" in det_file["/entry/instrument/detector".format(settings["detector"])]:
        Q = np.array(
            det_file["/entry/instrument/detector/Q".format(settings["detector"])][i])

    rcParams["figure.figsize"] = 12, 8
    rcParams["font.size"] = 20
    rcParams["text.usetex"] = False
    rcParams["text.latex.preamble"] = r"\usepackage{sfmath}"
    #fig = plt.figure("Detector Image")
    # fig.patch.set_color("white")
    #ax = fig.gca()

    smin, smax = settings["intensity_scale"]

    # print(data)
    if settings["log_scale"]:
        data = np.log10(img_res)
        vmin = max(np.log10(smin), 0)
        vmax = np.log10(smax)

    else:
        data = img_res
        vmin, vmax = smin, smax

    # make xdata
    if settings["xdim"] == "pixels" or Q is None:
        xdata, _ = np.meshgrid(np.arange(img_res.shape[1]),
                               np.arange(img_res.shape[0]))

    elif settings["xdim"] == "qx":
        xdata = Q[:, :, 0] * 10
    elif settings["xdim"] == "qy":
        xdata = Q[:, :, 1] * 10
    elif settings["xdim"] == "qz":
        xdata = Q[:, :, 2] * 10
    # make ydata
    if settings["ydim"] == "pixels" or Q is None:
        _, ydata = np.meshgrid(np.arange(img_res.shape[1]),
                               np.arange(img_res.shape[0]))
    elif settings["ydim"] == "qx":
        ydata = Q[:, :, 0] * 10
    elif settings["ydim"] == "qy":
        ydata = Q[:, :, 1] * 10
    elif settings["ydim"] == "qz":
        ydata = Q[:, :, 2] * 10
    # plot data

    # ax.pcolormesh(xdata, ydata, data, cmap=settings["colormap"],
    #         vmin=vmin, vmax=vmax)
```

```
#making the profile in q
q_abs= []
q_x = []
qxy = []
q_xy_int = []
q_xy_i =[]
alpha = np.arcsin((0.4959*0.1)/(4*math.pi))
# print(np.sin(alpha))
int_working = 0
det_int=[]
y = 0
background_avg = 0
yon_int =[]
yon_pos =[]

spec_int = []
for a in range(roi[0],roi[0]+roi[2]):
    if y == 0:
        print('')
    else:
        beta = ((0.4959*xdata[0][a])/(2*math.pi))-np.sin(alpha)
        beta = np.arcsin(beta)
        # qxy_working = (2*math.pi/0.4959)*np.sqrt(np.cos(alpha)**2+np.cos(beta)**2-(2*np.cos(alpha)*np.cos(beta)*np.cos(0)))

        #FOR Hg95In05 Use 0.069 as upper bound
        #FOR Hg35In65 Use 0.060 as upper bound
        #FOR Hg50In50 Use 0.062 as upper bound


        if xdata[0][a] > 0.015 and xdata[0][a] < .062:
            det_int.append(int_working)
            q_abs.append(xdata[0][a])
        if xdata[0][a] > 0.09 and xdata[0][a] < 0.15:
            spec_int.append(int_working)
        if xdata[0][a] > 0.04 and xdata[0][a] < 0.07:
            yon_int.append(int_working)
            yon_pos.append(xdata[0][a])

        int_working = 0
    for b in range(roi[1],roi[1]+roi[3]):
        if np.isnan(data[b][a]) or data[b][a]<0:
            intensity_here=0
        else:
            if settings['background']:
                b1 = b - settings["roi_offset"]
                b2 = b + settings["roi_offset"]
                background_1 = np.sum(data[b1][a])
                background_2 = np.sum(data[b2][a])
                background_avg = np.average(
                    [background_1, background_2])

                if np.isnan(background_avg) or background_avg < 0:
                    if background_1 == background_2:
                        background_avg = 0
                    elif np.isnan(background_1) or background_1 < 0:
                        background_avg = background_2
                    else:
                        background_avg = background_1
            intensity_here = data[b][a]-background_avg

        int_working += (intensity_here)
    y += 1

# print('__________')
print('Yoneda pos: ' + str(yon_pos[yon_int.index(np.max(yon_int))]))
# print('__________')
# print('Yoneda int: ' + str(np.np.average(det_int[0:10])max(yon_int)) )
# print('__________')
# print('Spec_int: ' + str(np.max(spec_int)) )
```

```
        # print('__________')
        # print(spec_int)
        # print(min(spec_int))

        # fig = plt.figure()
        # ax4 = fig.add_subplot(111)
        q_abs_yoneda = q_abs
        det_int_yoneda = det_int

        # ax4.plot(q_abs, det_int,marker='o')
        # ax4.set_xlim(0.01,0.11)

        init = [ -1, max(yon_int), yon_pos[yon_int.index(np.max(yon_int))], 0.002]
        bounds=([-5, max(yon_int)-5000, yon_pos[yon_int.index(np.max(yon_int))] - 0.001,0.001], [0, max(yon_int) + 5000,
yon_pos[yon_int.index(np.max(yon_int))] + 0.001, 0.015])

        if settings['gauss'] == True:
            y_popt_g, y_pcov_g = curve_fit(skew_gaussian, q_abs, det_int, bounds=bounds, p0=init, maxfev=1000000)
        else:
            y_popt_g, y_pcov_g = curve_fit(skew_lorentz, q_abs, det_int, bounds=bounds, p0=init, maxfev=1000000)

        p_sigma = np.sqrt(np.diag(y_pcov_g))

        print('Scan :' + str(scan))
        # print('Image_Number: ' + str(i))
        # print('Slope        :'+str(y_popt_g[0]) + ' +/- ' + str(p_sigma[0]) )
        # # print('Slope2       :'+str(y_popt_g[1]) + ' +/- ' + str(p_sigma[1]) )
        # print('Intercept    :'+str(y_popt_g[1]) + ' +/- ' + str(p_sigma[1]) )
        print('Skew    :'+str(y_popt_g[0]) + ' +/- ' + str(p_sigma[0]) )
        print('Yoneda_Amp  :'+str(y_popt_g[1]) + ' +/- ' + str(p_sigma[1]))
        print('Yoneda_Pos  :'+str(y_popt_g[2]) + ' +/- ' + str(p_sigma[2]))
        print('Yoneda_Sigma:'+str(y_popt_g[3]) + ' +/- ' + str(p_sigma[3]))
        # print('Skew2    :'+str(y_popt_g[4]) + ' +/- ' + str(p_sigma[4]) )
        # print('Specular_Amp  :'+str(y_popt_g[5]) + ' +/- ' + str(p_sigma[5]))
        # print('Specular_Pos  :'+str(y_popt_g[6]) + ' +/- ' + str(p_sigma[6]))
        # print('Specular_Sigma:'+str(y_popt_g[7]) + ' +/- ' + str(p_sigma[7]))

        if settings['gauss'] == True:
            obs_yon = skew_gaussian(q_abs, y_popt_g[0], y_popt_g[1], y_popt_g[2], y_popt_g[3])
        else:
            obs_yon = skew_lorentz(q_abs, y_popt_g[0], y_popt_g[1], y_popt_g[2], y_popt_g[3])

        corr_matrix = np.corrcoef(det_int_yoneda, obs_yon)
        corr_yoneda = corr_matrix[0,1]
        R_sq_yon = corr_yoneda**2

        print('r_squared for Yoneda: ' + str(R_sq_yon))




        # chi_squared = 0
        # chi = []
        # for y in range(len(q_abs)):
        #     chi_calc = ((obs_yon[y] - det_int[y])**2) / det_int[y]
        #     if np.isnan(chi_calc) or chi_calc < 0 or chi_calc == math.inf:
        #         chi.append(0)
        #         chi_squared += 0
        #     else:
        #         chi.append(chi_calc)
        #         chi_squared += ((obs_yon[y] - det_int[y])**2) / det_int[y]


        if y_popt_g[1] > 0.00:
            Yoneda_pos.append(y_popt_g[1])
        if y_popt_g[0] > 0.00:
            Yoneda_int.append(y_popt_g[0])


        fig = plt.figure()
```

```
        fig.patch.set_color("white")
        ax = fig.add_subplot(211)

        ax.plot(q_abs, det_int, marker='o', ls="--")

        ax.vlines(y_popt_g[2], 0, np.max(
            skew_lorentz(q_abs, y_popt_g[0], y_popt_g[1], y_popt_g[2], y_popt_g[3])), ls="--", color='red')



        if settings["gauss"] == True:
            # ax.plot(q_abs, skew_gaussian(q_abs, y_popt_g[0], y_popt_g[1], y_popt_g[2], y_popt_g[3] ),label='Yoneda',color="black",
linewidth=2.0)
            # ax.plot(q_abs, skew_lorentz(q_abs,y_popt_g[4], y_popt_g[5],y_popt_g[6], y_popt_g[7]),label='Specular',color="blue",
linewidth=2.0)
            ax.plot(q_abs, skew_gaussian(q_abs, y_popt_g[0], y_popt_g[1], y_popt_g[2], y_popt_g[3]), label='Fit', color="red", linewidth=2.0)
        else:
            # ax.plot(q_abs, skew_lorentz(q_abs, y_popt_g[0], y_popt_g[1], y_popt_g[2], y_popt_g[3]),label='Yoneda',color="black",
linewidth=2.0)
            # ax.plot(q_abs, skew_lorentz(q_abs,y_popt_g[4], y_popt_g[5],y_popt_g[6], y_popt_g[7]),label='Specular',color="blue",
linewidth=2.0)
            ax.plot(q_abs, skew_lorentz(q_abs, y_popt_g[0], y_popt_g[1], y_popt_g[2], y_popt_g[3]), label='Fit', color="red", linewidth=2.0)



        if settings['log_scale'] == True:
            ax.set_ylabel('Log10(Pixel Intensity)')
        else:
            ax.set_ylabel('Pixel Intensity (arb.)')

        # ax.set_xlim(-0.01,0.157)
        ax.set_xlim(0.005, 0.13)
        ax.set_ylim(-50, max(yon_int) + 50000)
        ax2 = fig.add_subplot(212)
        ax2.pcolormesh(xdata, ydata, data, cmap=settings["colormap"],
                       vmin=vmin, vmax=vmax)
        # ax2.set_xlim(-0.01,0.157)
        ax2.set_ylim(-0.02, 0.02)

        ax2.set_xlim(0.005, 0.13)
        ax2.set_ylabel('qx (1/Å)')

        # top line
        x = xdata[roi[1], roi[0]:(roi[0]+roi[2]+5)]
        y = ydata[roi[1], roi[0]:(roi[0]+roi[2]+5)]
        ax2.plot(x, y, color="orange")
        # bottom line
        x = xdata[roi[1]+roi[3], roi[0]:(roi[0]+roi[2]+1)]
        y = ydata[roi[1]+roi[3], roi[0]:(roi[0]+roi[2]+1)]
        ax2.plot(x, y, color="orange")
        # left line
        x = xdata[roi[1]:(roi[1]+roi[3]+1), roi[0]]
        y = ydata[roi[1]:(roi[1]+roi[3]+1), roi[0]]
        ax2.plot(x, y, color="orange")
        # right line
        x = xdata[roi[1]:(roi[1]+roi[3]+1), roi[0]+roi[2]]
        y = ydata[roi[1]:(roi[1]+roi[3]+1), roi[0]+roi[2]]
        ax2.plot(x, y, color="orange")
        # roi name

        ax2.annotate(roi, (xdata[roi[1], roi[0]], ydata[roi[1], roi[0]]),
                     color='orange', ha="left", va="bottom", size=12)

        # ax3 = fig.add_subplot(313)
        # ax3.plot(q_abs, chi, label='Sum χ2: ' + str(round(chi_squared, sigfigs=4)
        #                                     ) + '\n' + 'avg χ2: ' + str(round(np.average(chi), sigfigs=4)))
        # ax3.set_xlim(-0.03, 0.15)
        # ax3.set_ylim(-0.01, 4)
```

```
        # ax3.set_ylabel('χ2')
        # ax3.set_xlabel('qz (1/Å)')
        # ax.set_title('Scan Number: ' + str(scan) + '    Avg Chi squared: ' + str(np.average(round(np.average(chi), sigfigs=3))))
        ax.set_title('Scan Number: ' + str(scan)  + '    $r^2$: ' + str(round(R_sq_yon,4)))
        # ax3.legend(fontsize=12)
        fig.align_ylabels()


        ######################Define Yoneda Fitted Variables ########################

        Yoneda_skew = y_popt_g[0]
        Yoneda_amp = y_popt_g[1]
        Yoneda_pos = y_popt_g[2]
        Yoneda_sig = y_popt_g[3]

        Yoneda_skew_sig = p_sigma[0]
        Yoneda_amp_sig = p_sigma[1]
        Yoneda_pos_sig = p_sigma[2]
        Yoneda_sig_sig = p_sigma[3]


        ###############################################################################
        if settings["save_plot_yoneda"]:
            if os.path.exists(settings["plot_out_filename"] + 'YONEDA_' + str(scan) + str(i) + '.png'):
                settings["save_plot"] = input(
                    "Plot output picture file already exists. Overwrite? [y/n] ") == "y"
            plt.savefig(settings["plot_out_filename"]+"_" + 'YONEDA_'  +
                        str(scan)+"_"+str(i)+".png", dpi=300)

################################################## SECOND ROUND OF FITS WITH FIXED PARAMS
#########################################################################


        #making the profile in q
        q_abs= []
        q_x = []
        qxy = []
        q_xy_int = []
        q_xy_i =[]
        alpha = np.arcsin((0.4959*0.1)/(4*math.pi))

        int_working = 0
        det_int=[]
        y = 0
        background_avg = 0
        yon_int =[]
        yon_pos =[]

        spec_int = []
        for a in range(roi[0],roi[0]+roi[2]):
            if y == 0:
                print('')
            else:
                beta = ((0.4959*xdata[0][a])/(2*math.pi))-np.sin(alpha)
                beta = np.arcsin(beta)
                # qxy_working = (2*math.pi/0.4959)*np.sqrt(np.cos(alpha)**2+np.cos(beta)**2-(2*np.cos(alpha)*np.cos(beta)*np.cos(0)))

                #FOR Hg95In05 Use 0.069 as lower bound
                #FOR Hg35In65 Use 0.060 as lower bound
                #FOR Hg50In50 Use 0.062 as upper bound

                if xdata[0][a] > 0.062 and xdata[0][a] < 0.15:
                    det_int.append(int_working)
                    q_abs.append(xdata[0][a])
                if xdata[0][a] > 0.08 and xdata[0][a] < 0.12:
                    spec_int.append(int_working)
                # if xdata[0][a] > 0.04 and xdata[0][a] < 0.07:
                #     yon_int.append(int_working)
                #     yon_pos.append(xdata[0][a])
```

```
                int_working = 0
            for b in range(roi[1],roi[1]+roi[3]):
                if np.isnan(data[b][a]) or data[b][a]<0:
                    intensity_here=0
                else:
                    if settings['background']:
                        b1 = b - settings["roi_offset"]
                        b2 = b + settings["roi_offset"]
                        background_1 = np.sum(data[b1][a])
                        background_2 = np.sum(data[b2][a])
                        background_avg = np.average(
                            [background_1, background_2])

                        if np.isnan(background_avg) or background_avg < 0:
                            if background_1 == background_2:
                                background_avg = 0
                            elif np.isnan(background_1) or background_1 < 0:
                                background_avg = background_2
                            else:
                                background_avg = background_1
                    intensity_here = data[b][a]-background_avg

                int_working += (intensity_here)
            y += 1

        q_abs_specular = q_abs
        det_int_specular = det_int

        # p1, p2, p3 = np.polyfit(q_abs, det_int, 2)


        slope_guess = (det_int[0]-det_int[-1]) / (q_abs[0] - q_abs[-1])

        init = [ 2, max(spec_int),0.10,0.0007, slope_guess, 0]
        bounds=([ -5, max(spec_int) - 100,0.095 ,0, slope_guess-50000000, -5000000], [5, max(spec_int) + 100, 0.105, 0.005,slope_guess +
50000000, 500000])

        if settings['gauss'] == True:
            y_popt_g, y_pcov_g = curve_fit(skew2_gauss_yoneda, q_abs, det_int, bounds=bounds, p0=init, maxfev=1000000)
        else:
            y_popt_g, y_pcov_g = curve_fit(skew2_lorentz_line, q_abs, det_int, bounds=bounds, p0=init, maxfev=1000000)

        p_sigma = np.sqrt(np.diag(y_pcov_g))

        print('Scan :' + str(scan))
        # print('Image_Number: ' + str(i))
        # print('Slope        :'+str(y_popt_g[0]) + ' +/- ' + str(p_sigma[0]) )
        # # print('Slope2        :'+str(y_popt_g[1]) + ' +/- ' + str(p_sigma[1]) )
        # print('Intercept     :'+str(y_popt_g[1]) + ' +/- ' + str(p_sigma[1]) )
        # print('Skew    :'+str(y_popt_g[0]) + ' +/- ' + str(p_sigma[0]) )
        # print('Yoneda_Amp  :'+str(y_popt_g[1]) + ' +/- ' + str(p_sigma[1]))
        # print('Yoneda_Pos  :'+str(y_popt_g[2]) + ' +/- ' + str(p_sigma[2]))
        # print('Yoneda_Sigma:'+str(y_popt_g[3]) + ' +/- ' + str(p_sigma[3]))
        print('Skew_specular    :'+str(y_popt_g[0]) + ' +/- ' + str(p_sigma[0]) )
        print('Specular_Amp  :'+str(y_popt_g[1]) + ' +/- ' + str(p_sigma[1]))
        print('Specular_Pos  :'+str(y_popt_g[2]) + ' +/- ' + str(p_sigma[2]))
        print('Specular_Sigma:'+str(y_popt_g[3]) + ' +/- ' + str(p_sigma[3]))
        print('slope :'+str(y_popt_g[4]) + ' +/- ' + str(p_sigma[4]))
        print('intercept :'+str(y_popt_g[5]) + ' +/- ' + str(p_sigma[5]))
        # print('background_pos:'+str(y_popt_g[6]) + ' +/- ' + str(p_sigma[6]))
        # print('background_sigma:'+str(y_popt_g[7]) + ' +/- ' + str(p_sigma[7]))

        if settings['gauss'] == True:
            obs_spec = skew2_gauss_yoneda(q_abs, y_popt_g[0], y_popt_g[1], y_popt_g[2], y_popt_g[3], y_popt_g[4], y_popt_g[5], y_popt_g[6],
y_popt_g[7])
        else:
            obs_spec = skew2_lorentz_line(q_abs, y_popt_g[0], y_popt_g[1], y_popt_g[2], y_popt_g[3], y_popt_g[4], y_popt_g[5])


        corr_matrix = np.corrcoef(det_int_specular, obs_spec)
```

```
corr_specular = corr_matrix[0,1]
R_sq_spec = corr_specular**2

print('r_squared for Specular: ' + str(R_sq_spec))


# chi_squared = 0
# chi = []
# for y in range(len(q_abs)):
#     chi_calc = ((obs_spec[y] - det_int[y])**2) / det_int[y]
#     if np.isnan(chi_calc) or chi_calc < 0 or chi_calc == math.inf:
#         chi.append(0)
#         chi_squared += 0
#     else:
#         chi.append(chi_calc)
#         chi_squared += ((obs_spec[y] - det_int[y])**2) / det_int[y]



fig = plt.figure()

fig.patch.set_color("white")
ax = fig.add_subplot(211)
# det_int[det_int<0] = 0
ax.plot(q_abs, det_int, marker='o', ls="--")

ax.vlines(y_popt_g[2], 0, np.max(
    skew2_lorentz_line(q_abs, y_popt_g[0], y_popt_g[1], y_popt_g[2], y_popt_g[3], y_popt_g[4], y_popt_g[5])), ls="--", color='red')
# ax.plot(q_abs, line(q_abs,y_popt_g[0], y_popt_g[1]),label='background',color="green", linewidth=2.0)



if settings["gauss"] == True:
    ax.plot(q_abs, skew_gaussian(q_abs, y_popt_g[0], y_popt_g[1], y_popt_g[2], y_popt_g[3] ),label='Yoneda',color="black",
linewidth=2.0)
    ax.plot(q_abs, skew_lorentz(q_abs,y_popt_g[4], y_popt_g[5],y_popt_g[6], y_popt_g[7]),label='Specular',color="blue", linewidth=2.0)
    ax.plot(q_abs, skew2_gauss_yoneda(q_abs, y_popt_g[0], y_popt_g[1], y_popt_g[2], y_popt_g[3], y_popt_g[4], y_popt_g[5],
y_popt_g[6], y_popt_g[7]), label='Fit', color="red", linewidth=2.0)
else:
    # ax.plot(q_abs, skew_lorentz(q_abs, skew, Yoneda_amp, Yoneda_pos, Yoneda_sigma),label='Yoneda',color="black", linewidth=2.0)
    ax.plot(q_abs, skew_lorentz(q_abs,y_popt_g[0], y_popt_g[1],y_popt_g[2], y_popt_g[3]),label='Specular',color="blue", linewidth=2.0)
    ax.plot(q_abs, line(q_abs, y_popt_g[4], y_popt_g[5]),label='line',color="orange", linewidth=2.0)
    ax.plot(q_abs, skew2_lorentz_line(q_abs, y_popt_g[0], y_popt_g[1], y_popt_g[2], y_popt_g[3], y_popt_g[4], y_popt_g[5]), label='Fit',
color="red", linewidth=2.0)



if settings['log_scale'] == True:
    ax.set_ylabel('Log10(Pixel Intensity)')
else:
    ax.set_ylabel('Pixel Intensity (arb.)')




ax.set_xlim(0.005, 0.13)
# ax.set_ylim(-50, Yoneda_amp + 50000)
ax2 = fig.add_subplot(212)
ax2.pcolormesh(xdata, ydata, data, cmap=settings["colormap"],
               vmin=vmin, vmax=vmax)
# ax2.set_xlim(-0.01,0.157)
ax2.set_ylim(-0.02, 0.02)

ax2.set_xlim(0.005, 0.13)
ax2.set_ylabel('qx (1/Å)')

# top line
x = xdata[roi[1], roi[0]:(roi[0]+roi[2]+5)]
y = ydata[roi[1], roi[0]:(roi[0]+roi[2]+5)]
ax2.plot(x, y, color="orange")
```

```
        # bottom line
        x = xdata[roi[1]+roi[3], roi[0]:(roi[0]+roi[2]+1)]
        y = ydata[roi[1]+roi[3], roi[0]:(roi[0]+roi[2]+1)]
        ax2.plot(x, y, color="orange")
        # left line
        x = xdata[roi[1]:(roi[1]+roi[3]+1), roi[0]]
        y = ydata[roi[1]:(roi[1]+roi[3]+1), roi[0]]
        ax2.plot(x, y, color="orange")
        # right line
        x = xdata[roi[1]:(roi[1]+roi[3]+1), roi[0]+roi[2]]
        y = ydata[roi[1]:(roi[1]+roi[3]+1), roi[0]+roi[2]]
        ax2.plot(x, y, color="orange")
        # roi name

        ax2.annotate(roi, (xdata[roi[1], roi[0]], ydata[roi[1], roi[0]]),
                    color='orange', ha="left", va="bottom", size=12)

        # ax3 = fig.add_subplot(313)
        # ax3.plot(q_abs, chi, label='Sum χ2: ' + str(round(chi_squared, sigfigs=4)
        #                                     ) + '\n' + 'avg χ2: ' + str(round(np.average(chi), sigfigs=4)))
        # ax3.set_xlim(-0.03, 0.15)
        # ax3.set_ylim(-0.01, 4)
        # ax3.set_ylabel('χ2')
        # ax3.set_xlabel('qz (1/Å)')
        # ax.set_title('Scan Number: ' + str(scan) + '   Avg Chi squared: ' + str(np.average(round(np.average(chi), sigfigs=3))))
        ax.set_title('Scan Number: ' + str(scan) + '    $r^2$ ' + str(round(R_sq_spec,4)))
        # ax3.legend(fontsize=12)
        fig.align_ylabels()

        Specular_skew = y_popt_g[0]
        Specular_amp = y_popt_g[1]
        Specular_pos = y_popt_g[2]
        Specular_sig = y_popt_g[3]
        Specular_slope = y_popt_g[4]
        Specular_intercept = y_popt_g[5]


        Specular_skew_sig = p_sigma[0]
        Specular_amp_sig = p_sigma[1]
        Specular_pos_sig =  p_sigma[2]
        Specular_sig_sig = p_sigma[3]
        Specular_slope_sig =  p_sigma[4]
        Specular_intercept_sig =  p_sigma[5]

        if settings["save_plot_specular"]:
            if os.path.exists(settings["plot_out_filename"] + 'SPECULAR_' + str(scan) + str(i) + '.png'):
                settings["save_plot"] = input(
                    "Plot output picture file already exists. Overwrite? [y/n] ") == "y"
            plt.savefig(settings["plot_out_filename"]+"_" + 'SPECULAR_'  +
                        str(scan)+"_"+str(i)+".png", dpi=300)
########################################################################################################################################
        #making the profile in q
        q_abs= []
        q_x = []
        qxy = []
        q_xy_int = []
        q_xy_i =[]
        alpha = np.arcsin((0.4959*0.1)/(4*math.pi))

        int_working = 0
        det_int=[]
        y = 0
        background_avg = 0
        yon_int =[]
        yon_pos =[]

        spec_int = []
        for a in range(roi[0],roi[0]+roi[2]):
            if y == 0:
```

```
            print('')
        else:
            beta = ((0.4959*xdata[0][a])/(2*math.pi))-np.sin(alpha)
            beta = np.arcsin(beta)
            # qxy_working = (2*math.pi/0.4959)*np.sqrt(np.cos(alpha)**2+np.cos(beta)**2-(2*np.cos(alpha)*np.cos(beta)*np.cos(0)))
            if xdata[0][a] > 0.015 and xdata[0][a] < 0.15:
                det_int.append(int_working)
                q_abs.append(xdata[0][a])
            if xdata[0][a] > 0.09 and xdata[0][a] < 0.105:
                spec_int.append(int_working)
            # if xdata[0][a] > 0.04 and xdata[0][a] < 0.07:
            #     yon_int.append(int_working)
            #     yon_pos.append(xdata[0][a])

            int_working = 0
        for b in range(roi[1],roi[1]+roi[3]):
            if np.isnan(data[b][a]) or data[b][a]<0:
                intensity_here=0
            else:
                if settings['background']:
                    b1 = b - settings["roi_offset"]
                    b2 = b + settings["roi_offset"]
                    background_1 = np.sum(data[b1][a])
                    background_2 = np.sum(data[b2][a])
                    background_avg = np.average(
                        [background_1, background_2])

                    if np.isnan(background_avg) or background_avg < 0:
                        if background_1 == background_2:
                            background_avg = 0
                        elif np.isnan(background_1) or background_1 < 0:
                            background_avg = background_2
                        else:
                            background_avg = background_1
                intensity_here = data[b][a]-background_avg

            int_working += (intensity_here)
        y += 1

    fig = plt.figure()

    fig.patch.set_color("white")
    ax = fig.add_subplot(211)

    # det_int[det_int<0] = 0
    ax.plot(q_abs, det_int, marker='o', ls="--", label = 'Raw Data')

    # q_abs_specular = []
    # q_abs_yoneda = []

    # for i in range(len(q_abs)):
    #     if q_abs[i] > 0.062:
    #         q_abs_specular.append(q_abs[i])
    #     else:
    #         q_abs_yoneda.append(q_abs[i])


    ax.plot(q_abs_specular, skew2_lorentz_line(q_abs_specular, Specular_skew, Specular_amp, Specular_pos, Specular_sig, Specular_slope,
Specular_intercept), label='Fit of Specular', color="black", linewidth=2.0)
    ax.plot(q_abs_yoneda,   skew_lorentz(q_abs_yoneda, Yoneda_skew, Yoneda_amp, Yoneda_pos, Yoneda_sig), label='Fit of Yoneda',
color="red", linewidth=2.0)
    ax.set_xlim(0.015, 0.13)
    ax.legend()

    if settings['log_scale'] == True:
        ax.set_ylabel('Log10(Pixel Intensity)')
    else:
        ax.set_ylabel('Pixel Intensity (arb.)')

    ax2 = fig.add_subplot(212)
```

```
    ax2.pcolormesh(xdata, ydata, data, cmap=settings["colormap"],
                   vmin=vmin, vmax=vmax)




    # ax2.set_xlim(-0.01,0.157)
    ax2.set_ylim(-0.02, 0.02)

    ax2.set_xlim(0.015, 0.13)
    ax2.set_ylabel('qx (1/Å)')

    # top line
    x = xdata[roi[1], roi[0]:(roi[0]+roi[2]+5)]
    y = ydata[roi[1], roi[0]:(roi[0]+roi[2]+5)]
    ax2.plot(x, y, color="orange")
    # bottom line
    x = xdata[roi[1]+roi[3], roi[0]:(roi[0]+roi[2]+1)]
    y = ydata[roi[1]+roi[3], roi[0]:(roi[0]+roi[2]+1)]
    ax2.plot(x, y, color="orange")
    # left line
    x = xdata[roi[1]:(roi[1]+roi[3]+1), roi[0]]
    y = ydata[roi[1]:(roi[1]+roi[3]+1), roi[0]]
    ax2.plot(x, y, color="orange")
    # right line
    x = xdata[roi[1]:(roi[1]+roi[3]+1), roi[0]+roi[2]]
    y = ydata[roi[1]:(roi[1]+roi[3]+1), roi[0]+roi[2]]
    ax2.plot(x, y, color="orange")
    # roi name

    # ax2.annotate(roi, (xdata[roi[1], roi[0]], ydata[roi[1], roi[0]]),
    #              color='orange', ha="left", va="bottom", size=12)

    # ax3 = fig.add_subplot(313)
    # ax3.plot(q_abs, chi, label='Sum χ2: ' + str(round(chi_squared, sigfigs=4)
    #                                     ) + '\n' + 'avg χ2: ' + str(round(np.average(chi), sigfigs=4)))
    # ax3.set_xlim(-0.03, 0.15)
    # ax3.set_ylim(-0.01, 4)
    # ax3.set_ylabel('χ2')
    # ax3.set_xlabel('qz (1/Å)')
    # ax.set_title('Scan Number: ' + str(scan) + '   Avg Chi squared: ' + str(np.average(round(np.average(chi), sigfigs=3))))
    ax.set_title('Scan Number: ' + str(scan) + '    $r^2$: ' + str(round(np.average([R_sq_yon, R_sq_spec]), 4)))

    plt.tight_layout()

    # ax3.legend(fontsize=12)
    fig.align_ylabels()



##################### Too Save the Files ##############################################################################



    plt.tight_layout()

    if settings["save_plot"]:
       if os.path.exists(settings["plot_out_filename"] + str(scan) + str(i) + '.png'):
          settings["save_plot"] = input(
             "Plot output picture file already exists. Overwrite? [y/n] ") == "y"
       plt.savefig(settings["plot_out_filename"]+"_" +
                   str(scan)+"_"+str(i)+".png", dpi=300)
    if settings["save_results"]:
```

```
    results = open(settings["fit_out_filename"] + ".txt", "a")
    # results.write(str(settings['scan_number'])+"_"+str(i)+"\n")
    # results.write(",")
    results.write(str(scan))
    results.write(",")
    results.write(str(Yoneda_skew))
    results.write(",")
    results.write(str(Yoneda_skew_sig))
    results.write(",")
    results.write(str(Yoneda_amp))
    results.write(",")
    results.write(str(Yoneda_amp_sig))
    results.write(",")
    results.write(str(Yoneda_pos))
    results.write(",")
    results.write(str( Yoneda_pos_sig))
    results.write(",")
    results.write(str( Yoneda_sig ))
    results.write(",")
    results.write(str(Yoneda_sig_sig))
    results.write(",")
    results.write(str(Specular_skew))
    results.write(",")
    results.write(str(Specular_skew_sig))
    results.write(",")
    results.write(str(Specular_amp))
    results.write(",")
    results.write(str(Specular_amp_sig))
    results.write(",")
    results.write(str(Specular_pos))
    results.write(",")
    results.write(str(Specular_pos_sig))
    results.write(",")
    results.write(str(Specular_sig))
    results.write(",")
    results.write(str(Specular_sig_sig))
    results.write(",")
    results.write(str(Specular_slope))
    results.write(",")
    results.write(str(Specular_slope_sig))
    results.write(",")
    results.write(str(Specular_intercept))
    results.write(",")
    results.write(str(Specular_intercept_sig))




    results.write(",")
    results.write(str(np.average([R_sq_yon, R_sq_spec])))
    results.write("\n")
    results.close()


if settings['save_max']:
    results = open(settings["max_out_filename"], "a")
    results.write(str(scan)+"_"+str(i)+"\n")
    results.write(str(max(det_int)))
    results.write("\n")
    results.close()

if settings["save_profile"]:

    df = pandas.DataFrame()
    df["Q"] = q_abs
    df["intensity"] = det_int

    df.to_csv(settings["out_filename"]+"_"+str(scan
                                    )+"_"+str(i)+".dat", sep="\t", index=False, header=True)
```

```
        end = time.time()
        print('Time Elapsed :' + str(end - start))
        # print(np.average(chi))


        # plt.savefig("C:/Users/jhaze/University of Michigan Dropbox/LSA-Maldonado
Group/Group_Business/Group_Documents/Manuscripts/Hazelnis_XRR of Hg-In/Figures/Yoneda_int_fit_Hg50In50_no detector
image.svg",format="svg")
        # plt.savefig("C:/Users/jhaze/University of Michigan Dropbox/LSA-Maldonado
Group/Group_Business/Group_Documents/Manuscripts/Hazelnis_XRR of Hg-In/Figures/Yoneda_int_fit_Hg50In50_no detector
image.png",format="png")



        plt.show()
        gc.collect()

#########################################################################################################################
#####
```

B.4 References

1. Sartori, A.; Giri, R. P.; Fujii, H.; Hövelmann, S. C.; Warias, J. E.; Jordt, P.; Shen, C.; Murphy, B. M.; Magnussen, O. M., Role of chemisorbing species in growth at liquid metal-electrolyte interfaces revealed by in situ X-ray scattering. *Nature Communications* **2022,** *13* (1), 5421.

Appendix C: Supporting Information for Chapter 5

C.1 Contents

This section contains supporting information for Chapter 5 entitled “Chapter 5 Discovery of Metal-Ga Intermetallics via ‘Quasi’-Epitaxy at Liquid Ga/Water Interfaces”. Section C.2 includes example Python code used to radially integrate the collected microED data. Section C.3 provides additional Python code used to convert microED frame data to .tif images.

C.2 Example Python Code Used to Radially Integrate MicroED Frame Data

The code included in this section takes raw .dm4 files from a microED dataset and radially integrates them around the aligned center pixel in order to estimate the present d-spacing values and thus a predicted PXRD pattern. The code works by first fitting the center pixel of each frame via 'curve_fit' with a gaussian distribution in both the x and y directions. In doing so, a corresponding (x,y) center pixel is determined for each frame. Ideally, this center pixel is the same for each frame but during microED data collection, some shift between frames is commonly observed. Once the center pixel of each frame is appropriately defined, radially integration can subsequently be performed using the function 'def radial_profile'. This returns the d-spacing values which have been converted too 2Θ values using the wavelength for a Cu Kα source (0.15418 nm). The final output of the code is a .csv file which sums up the radial integration contribution of all of the microED frames.

When running this code, the data directory where the raw data is saved locally on the computer should be updated accordingly as well as the save file paths. The code can also be modified to convert the d-spacing values using a different wavelength by changing the 0.15418 nm within the 'def radial_profile' function. Additionally, the initial boundary conditions used by 'curve_fit' to fit the center pixel may need to be updated to better match the raw input data file (i.e the center pixel is located somewhere different on the raw frame data than what is observed in this example dataset).

```
"""
Coded by: Joshua Hazelnis
Code Created: 09-01-2022

Used to Radially Integrate MicroED Frame Data
collected on a 4096x4096 pixel detector

Coding Language: Python
"""
import dm4reader
import py4DSTEM
import h5py
import matplotlib.pyplot as plt
from matplotlib import rcParams
import hashlib
import numpy as np
import os
import csv
import math
import pandas as pd
from scipy.optimize import curve_fit
import warnings
import ncempy
import math
warnings.filterwarnings("ignore")

# == settings
```

```
settings = dict(
            data_directory = r"E:\FeGa_Planview_SA40_CL840-2\Frames_Compiled",
            experiment='FeGa_Planview_SA40_CL840-2',
            hour ="Hour_00",
            minute = "Minute_00",
            second = range(0,54+1),
            frame = range(0,7+1),

            scale = 29.3151 / 4096, #1/nm per pixel
            # plot colormap
            colormap = "gray",
            intensity_scale = (-100, 220),

            # regions of interest to display (x, y, w, h)
            roi = (2000, 1950, 150, 150),

            #plotting
            plot_diffraction = False,
            plot_gaussian = False,
            radial_int = True,

            # save plot to this file:
            save_plot = False,
            radial_path = r"E:\FeGa_Planview_SA40_CL840-2\radial_int_2",
            save_diff = False,
            diff_path = r'Y:/Jphazeln\FeGa_Planview_SA40_CL840-2\diff_center'
            )

def gaussian(xdata, amp, pos, sigma):
    return amp * np.exp(-(xdata-pos)**2/(2*sigma**2))


def radial_profile(data, center, second, frame, save_path):
    y,x = np.indices((data.shape)) # first determine radii of all pixels

    r = np.sqrt((x-center[0])**2+(y-center[1])**2)
    bin_edges= np.linspace(0.5, 2925, 2926)
    # print(bin_edges)
    # radius of the image.
    r_max = np.max(r)
    ring_brightness, radius = np.histogram(r, weights=data, bins=bin_edges)
    # print(radius)
    dist_from_center = radius[1:]*settings['scale'] #1/nm

    theta_two = []
    for d in dist_from_center:
        d = d**-1
        theta = 0.15418 / (2*d)
        if theta > 1:
            theta_two.append(200)
        else:
            theta = math.asin(theta)
            theta_two.append(math.degrees(theta*2))


    if settings['save_plot']:
        path = save_path + '/Second_ '+ str(second) + ' Frame_ '+ str(frame) + '.png'
        fig.savefig(path)
        ############################
    return [dist_from_center, ring_brightness]

roi = settings['roi']

roi_pixels_x = range(roi[0],roi[0]+roi[2])
roi_pixels_y = range(roi[1],roi[1]+roi[3])
roi_pixels = [roi_pixels_x, roi_pixels_y]


brightness_tot = np.zeros(2925)
theta_addition = []
```

```
bright_addition = []
for second in settings['second']:
    for frame in settings['frame']:
        plt.show()
        try:
            pix_tot = []
            int_tot = []
            center_pix = []
            if second < 10:
                file = settings['data_directory'] + "/" +  settings['experiment'] + '_' + settings['hour'] + '_' + settings['minute'] + '_Second_0' + str(second)
+ '_Frame_000' + str(frame) + '.dm4'
            else:
                file = settings['data_directory'] + "/" + settings['experiment'] + '_' + settings['hour'] + '_' + settings['minute'] + '_Second_' + str(second) +
'_Frame_000' + str(frame) + '.dm4'

            dm = py4DSTEM.io.import_file(file)

            data = dm[:][:]

            vmin, vmax = settings['intensity_scale']

            pix_int_x = []
            pix_int_y = []
            pixel_pos_x = []
            pixel_pos_y = []

            for a in roi_pixels_x:
                for b in roi_pixels_y:
                    pixel_pos_x.append(a)
                    if np.isnan(data[b][a]) or data[b][a]<0:
                        intensity_here=0
                        pix_int_x.append(intensity_here)
                    else:
                        pix_int_x.append(data[b][a])


            bin_edges = np.arange(np.min([pixel_pos_x]), np.max(pixel_pos_x), 1)
            hist, edges = np.histogram(pixel_pos_x, bins=bin_edges, weights=pix_int_x)
            hist2, edges2 = np.histogram(pixel_pos_x, bins=bin_edges)
            result = np.divide(hist, hist2)
            edges=edges[1:len(edges)]
            pix_tot.extend(edges)
            int_tot.extend(result)

            init = [1000,roi[0]+int(roi[2]/2),15]
            # print(data[0][roi[0]+int(roi[2]/2)])
            bounds=([500, 2000,0], [3000, 2200, 100])
            y_popt_g, y_pcov_g = curve_fit(gaussian, edges, result, p0=init,bounds = bounds, maxfev = 100000)


            center_pix.append(y_popt_g[1])

            if settings['plot_gaussian']:
                fig = plt.figure()

                ax = fig.add_subplot(111)
                result[result<0] = 0
                plt.plot(edges, result,marker='o', ls="--")

                ax.vlines(y_popt_g[1], 0, np.max(gaussian(edges,y_popt_g[0], y_popt_g[1], y_popt_g[2])),ls="--", color='red' )
                ax.plot(edges, gaussian(edges,y_popt_g[0], y_popt_g[1], y_popt_g[2]),label='Fit',color="black")

                ax.set_xlim(roi[0],roi[0]+roi[2])

            for a in roi_pixels_y:
                for b in roi_pixels_x:
                    pixel_pos_y.append(a)
                    if np.isnan(data[a][b]) or data[a][b]<0:
                        intensity_here=0
                        pix_int_y.append(intensity_here)
```

```
        else:
            pix_int_y.append(data[a][b])

pix_tot = []
int_tot = []

bin_edges = np.arange(np.min([pixel_pos_y]), np.max(pixel_pos_y), 2)
hist, edges = np.histogram(pixel_pos_y, bins=bin_edges, weights=pix_int_y)
hist2, edges2 = np.histogram(pixel_pos_y, bins=bin_edges)
result = np.divide(hist, hist2)
edges=edges[1:len(edges)]
pix_tot.extend(edges)
int_tot.extend(result)

init = [1000,roi[1]+int(roi[3]/2),15]
# print(data[0][roi[0]+int(roi[2]/2)])
bounds=([500, 1950 ,0], [3000, 2100, 100])
y_popt_g, y_pcov_g = curve_fit(gaussian, edges, result, p0=init,bounds = bounds, maxfev = 100000)
# print( y_popt_g[0], y_popt_g[1], y_popt_g[2])

center_pix.append(y_popt_g[1])

if settings['plot_gaussian']:
    fig2 = plt.figure()

    ax2 = fig2.add_subplot(111)
    result[result<0] = 0
    plt.plot(edges, result,marker='o', ls="--")

    ax2.vlines(y_popt_g[1], 0, np.max(gaussian(edges,y_popt_g[0], y_popt_g[1], y_popt_g[2])),ls="--", color='red' )
    ax2.plot(edges, gaussian(edges,y_popt_g[0], y_popt_g[1], y_popt_g[2]),label='Fit',color="black")

    ax2.set_xlim(roi[1],roi[1]+roi[3])
    ax2.legend()

if settings['plot_diffraction']:
    fig3 = plt.figure()
    ax3 = fig3.add_subplot()
    plt.imshow(data, interpolation='nearest', cmap=settings['colormap'], vmin = vmin, vmax = vmax)
    # top line
    x = (roi[0],roi[0]+roi[2])
    y = (roi[1],roi[1])
    plt.plot(x, y, color="orange")
    # bottom line
    x = (roi[0],roi[0]+roi[2])
    y = (roi[1]+roi[3],roi[1]+roi[3])
    plt.plot(x, y, color="orange")
    # left line
    x = (roi[0],roi[0])
    y = (roi[1],roi[1]+roi[3])
    plt.plot(x, y, color="orange")
    # right line
    x = (roi[0]+roi[2],roi[0]+roi[2])
    y = (roi[1],roi[1]+roi[3])
    plt.plot(x, y, color="orange")
    ax3.set_title('Second: '+ str(second) + ' Frame: '+ str(frame))
    ax3.set_xlabel('pixels')
    ax3.set_ylabel('pixels')
    if settings['save_diff']:
        path = settings['diff_path'] + '/Second_ '+ str(second) + ' Frame_ '+ str(frame) + '.png'
        fig3.savefig(path)

if settings['radial_int']:
    [dist_from_center, ring_brightness] = radial_profile(data, center_pix, second, frame, settings['radial_path'])

    print('Second: ' + str(second))
    print('Frame: ' + str(frame))


    fig5 = plt.figure()
```

```
            ax5 = fig5.add_subplot()

            ax5.set_xlim([0.5, 20])
            ax5.set_ylim([0, 80000])
            ax5.set_title('Second: ' + str(second) + ' Frame: ' + str(frame))
            ax5.set_xlabel('d-spacing [1/nm]')
            ax5.set_ylabel('Pixel Intensity [arb.]')
            ax5.plot(dist_from_center, ring_brightness,linewidth = 0.75)
            plt.show()
            brightness_tot += ring_brightness

        except AssertionError:
            continue

np.savetxt("summation_all_frames_dspacing.csv", [dist_from_center, brightness_tot], delimiter=",")
```

C.3 Example Python Code Used to Convert MicroED (.mrc) Frame Data to .tif

The code in this section was written to convert raw microED frame data with the file extension '.mrc' to '.tif' format which is more commonly used in single crystal analysis software. To utilize this code the file path labelled 'mrc_file_path', where the raw .mrc file(s) are saved on the computer needs to be updated accordingly. Similarly, the output folder path (output_folder') where the converted '.tif' images will be saved needs to be updated accordingly.

```
"""
Created on Sun Jun  9 21:16:40 2024

@author: Josh
Coding Language: Python
Used to convert .mrc files to .tif
"""

import mrcfile
from PIL import Image
import numpy as np
import os

def convert_mrc_to_tiff(mrc_file_path, output_folder):
    # Ensure the output folder exists
    os.makedirs(output_folder, exist_ok=True)

    # Open the .mrc file with memory-mapped access
    with mrcfile.mmap(mrc_file_path, mode='r') as mrc:
        # Get the number of slices in the .mrc file
        num_slices = mrc.data.shape[0]

        for i in range(num_slices):
            # Extract each slice
            slice_data = mrc.data[i, :, :]

            # Convert the slice to uint16 if not already
            slice_data = slice_data.astype(np.uint16)

            # Convert the slice to a PIL Image
            image = Image.fromarray(slice_data)

            # Ensure the image is saved as 16-bit TIFF
            output_file_path = os.path.join(output_folder, f"slice_{i+1:03d}.tiff")
            image.save(output_file_path, format='TIFF', depth=16)
            print(f"Saved {output_file_path}")

##############################CHANGE FILE PATHS HERE#############################################################
mrc_file_path = 'E:/20240304/CoFeGa-PlanView/0019-Camera_Ceta_370_mm_1623-90203992fbb84264930b971c0c931fa1.mrc'
output_folder = 'E:/20240304/CoFeGa-PlanView/0019-Camera Raw Frames/tif'
#################################################################################################################
convert_mrc_to_tiff(mrc_file_path, output_folder)
```

Appendix D: Supporting Information for Chapter 6

D.1 Contents

This document contains supporting information for Chapter 6 entitled “Epitaxial Ge Film Electrodeposition Using Liquid Metal Electrodes: A Study on Ambient-Condition Semiconductor Electrosynthesis Without Compression”. Section D.2 presents additional voltammetric measurements on multiple liquid Ga pools.

D.2 Additional Voltammetric Measurements on Multiple Liquid Ga pools

We performed additional voltammetric measurements on multiple liquid Ga pools. The methodology for handling all electrodes was identical and summarized in the Experimental section of the main text. The set of three voltammograms below (each from a different aliquot of ultra-pure liquid Ga) highlights consistent and confounding observations. (Appendix Figure D.1)

First, in all cases where the electrolyte was composed of 0.1 M $Na_2B_4O_7$ and 0.05 M GeO_2, a redox wave overlapping with the initial stage of hydrogen evolution was observed. The magnitude was in the mA cm^{-2} range, significantly higher than what is expected for a simple $1e^-$ redox adsorbate (i.e. ~10^{-5} A cm^{-2}, Bard, A. J. and Faulkner, L. R. *Electrochemical Methods: Fundamentals and Applications*, 2nd edition) Second, repetitive cycling at a given scan rate (the plots here correspond to a scan rate of 10 mV s^{-1}) results in a decrease in the magnitude of the peak in question. This point is apparent for all three electrode responses shown below. (Appendix Figure D.1) Third, the initial (the first scan upon exposure to solution) peak position and magnitude was not absolutely consistent across otherwise identical electrodes & electrolytes, as observed across the voltammetric responses for electrode 3 (Appendix Figure D.1c) vs electrodes 1 & 2 (Appendix Figure D.1a-b). Fourth, the decrease in peak magnitude with scan rate was monotonic if repetitive cycling was performed, i.e. the same scan rate and the same starting and switching potentials are used. This aspect is apparent in electrodes 1 and 3 (Appendix Figure D.1a and Appendix Figure D.1c), where no experimental parameter changed between scans. This point remained true if there was a break between scans where the electrode went to open circuit (electrode 1) or if the cycles were continuous with no break in between (electrode 3). Fifth, the peak current magnitude and position change significantly if multiple scans are performed at different scan rates (but with the same starting and stopping points) in between the repetitive cycles. This fact is evident in the responses for electrode 2. (Appendix Figure D.1b)

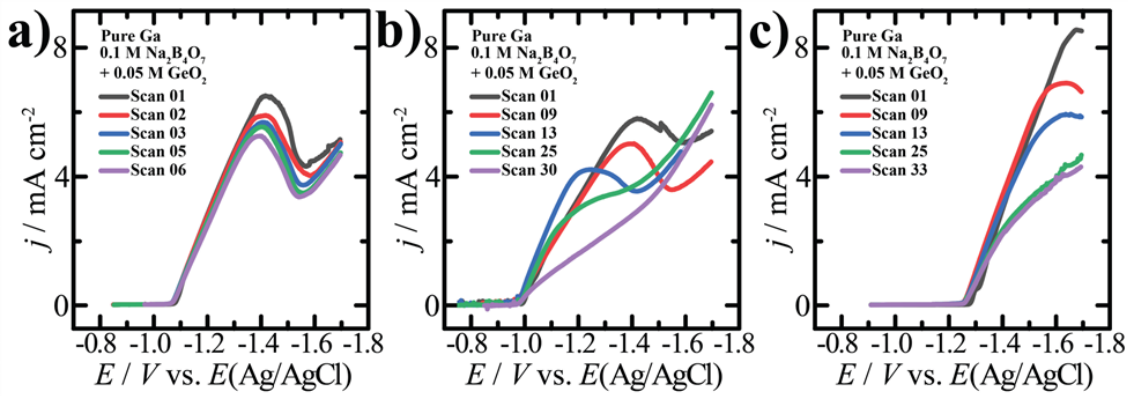

Appendix Figure D.1 Linear sweep voltammetry responses at 10 mV s^{-1} for three distinct liquid Ga electrodes in 0.1 M $Na_2B_4O_7$ and 0.05 M GeO_2 electrolyte solution where a) repetitive cycling with allowing the electrode to go to OCP in-between scans, b) repetitive 10 mV s^{-1} sweeps but with multiple sweeps not at 10 mV s^{-1} taken in-between and c) repetitive cycling without going to OCP was performed.

Sixth, background corrected scans showed a non-linear dependence between peak-current and scan rate. (Appendix Figure D.2)

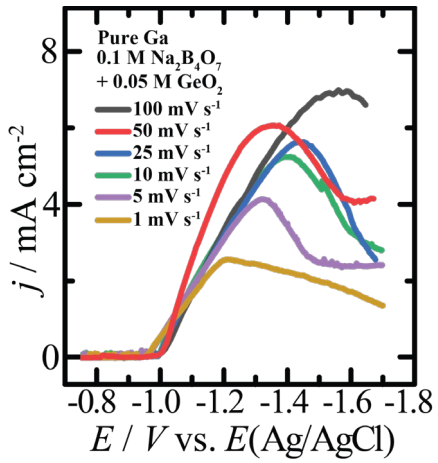

Appendix Figure D.2 Background corrected linear sweep voltammetry responses at 1, 5, 10, 50, and 100 mV s^{-1} for a liquid Ga electrode in 0.1 M $Na_2B_4O_7$ and 0.05 M GeO_2 electrolyte solution.

The specific features exhibited by liquid Ga electrodes are not described by any simple redox model. There is precedence for dissolved GeO_2 adsorbing onto a liquid Hg electrode surface and eliciting adsorptive type redox responses (Hazelnis, J. P.; Sartori, A.; Cheek, B. Q.; Giri, R. P.; MacInnes, Molly M.; Murphy, B. M.*; Magnussen, O. M.*; and Maldonado, S.* "Detection of Ge-Containing Adlayer at the Liquid Hg/Water Interface By In-Situ X-ray Reflectivity in Aqueous Borate Electrolytes Containing Dissolve GeO2" *J. Phys. Chem. C.*, **2022**, *126(18)*, 9177-8189).

However, the magnitude and dependence seen here would suggest either a very thick (100s of monolayers) coating and/or a strongly coupled chemical reaction that reacts with the reduced form. Additionally, the severe sensitivity towards both $Na_2B_4O_7$ and the particular surface history indicates that any adsorbate is participating in multiple preceding reactions. Similarly, the variation in otherwise identical electrodes implies that even subtle differences in the native surficial oxide may contribute greatly to the initial redox behavior.

A single mechanism that describes and contextualizes all experimental features remains unknown. Still, the reproducibility in the ec-LPE experiments performed with liquid Ga electrodes also implies that the chemistry of the pronounced redox wave observed in Figure 6.5 of the main text is also not the most germane factor. Moreover, the loss of this redox feature over prolonged electrochemical cycling (or current passage) coupled with the numerous prior reports of ec-LLS with liquid Ga cited in the main text further bolster the point that this feature is likely not critical to understanding crystal growth once nucleation has been achieved.